NASA CONTRACTOR REPORT

NASA CR 137970

INVESTIGATION OF NORMAL SHOCK INLETS FOR HIGHLY MANEUVERABLE AIRCRAFT

By Arnold W. Martin

Prepared under Contract No. NAS 2-8955 by

ROCKWELL INTERNATIONAL/LOS ANGELES AIRCRAFT DIVISION
Los Angeles, California

for

Ames Research Center
NATIONAL AERONAUTICS AND SPACE ADMINISTRATION

Rockwell International

NASA CONTRACTOR REPORT

NASA CR 137970

ERRATA

INVESTIGATION OF NORMAL SHOCK INLETS
FOR
HIGHLY MANEUVERABLE AIRCRAFT

By Arnold W. Martin

Prepared under Contract No. NAS 2-8955 by

ROCKWELL INTERNATIONAL/LOS ANGELES AIRCRAFT DIVISION
Los Angeles, California

for

Ames Research Center
NATIONAL AERONAUTICS AND SPACE ADMINISTRATION

Rockwell International

NASA Contractor Report NASA CR 137970

The following photographs in figures 1, 21 and 22 had poor contrast in the original issue of this report and are being rereleased.

TABLE OF CONTENTS

List of Illustrations

List of Illustrations

List Of Illustrations

List of Illustrations

INVESTIGATION OF NORMAL SHOCK INLETS FOR HIGHLY MANEUVERABLE AIRCRAFT

By Arnold W. Martin

ROCKWELL INTERNATIONAL/LOS ANGELES AIRCRAFT DIVISION
Los Angeles, California

SUMMARY

Performance characteristics of several fuselage-side-mounted normal shock inlets were obtained in wind tunnel tests at 0.9 Mach number at angles of attack from -8° to 40 degrees and angles of sideslip from -10° to 10°. Limited data were also obtained at 1.2 Mach number.

A sharp-lipped, kidney-shaped inlet was tested in two vertical positions both with a variable incidence canard located forward of the inlet and with the canard removed. Negligible inlet performance differences were observed between the canard-on and the canard-off configurations at low angles of attack and sideslip. At higher angles of attack and canard deflection angles not resulting in ingestion of the canard wake, inlet performance was improved by the flow-straightening action of the canard. At angles of attack resulting in canard wake ingestion, inlet performance penalties were severe.

Seven variations of a two-dimensional scarfed inlet were tested with the canard removed to investigate concepts for improving inlet performance at extreme angles of attack. In the first and basic configuration, the bottom lip was sharp, the leading edge radius being identical to those of the inlet side and top leading edges. In the second and third variations, the sharp bottom lip was replaced by, respectively, a lip of intermediate thickness and a lip of extreme thickness. In the fourth variation, a slat formed from the leading edge of the intermediate-thickness lip was translated forward. The same slat was translated upward for the fifth variation. A horizontal flow turning vane was located in the inlet and tested with the sharp bottom lip for variation 6, and with the thick bottom lip for variation 7. The best performance at high angles of attack was obtained with the slat lip translated upwards and with the thick lip. Total pressure recovery at a given mass flow ratio was approximately 10 percent higher for these configurations than for the basic configuration at an angle of attack of 30°.

The inlet configurations tested with the canard removed were insensitive to angles of sideslip from -10° to 10°. With the canard, total pressure recovery and mass flow ratio of the windward inlet were reduced in the order of 8 percent at a sideslip angle of 10°.

INTRODUCTION

A need has been established for a minimum weight, minimum complexity fighter aircraft which is highly maneuverable at transonic speed and is capable of sustained supersonic flight. Normal shock inlets best meet the requirements for minimum weight and complexity. Such inlets should have sharp lips to minimize drag at supersonic Mach numbers. However, sharp lips result in high distortion and total pressure losses at large angles of attack. The objective of this test program was to investigate concepts for obtaining both low cowl drag and good inlet performance at high angles of attack. Two types of aircraft were considered, one with a canard located forward of the inlet face, the other without a canard or with the canard located adjacent to or aft of the inlet face.

The first portion of the test program investigated the effect of a canard on inlet performance for a kidney-shaped inlet in each of two vertical locations. Specific objectives of these tests were to determine 1) whether the flow-aligning effect of a canard can be used to provide good high-angle-of-attack performance for a sharp-lip inlet, 2) whether canard wake ingestion can be avoided, and 3) whether inlet performance is acceptable when canard wake is ingested.

The second portion of the test program investigated a sharp-lip, two-dimensional inlet on a canardless forebody. A rectangular inlet of low width-to-height ratio was selected from two considerations. First, the sharp-lip separation effects are largely limited to the bottom cowl. Consequently most of the separation losses can be eliminated by modifying only the bottom cowl. Second, the design, installation and actuation of such devices as slat lips, turning vanes and inflatable lips are simplified with parallel inlet sides. The inlet face was scarfed to provide better performance at high angles of attack. It was also reasoned that the scarfing would have a beneficial effect on subsonic spillage drag inasmuch as excess flow will tend to spill over the thicker bottom lip.

Three concepts for improving high-angle-of-attack performance of the two-dimensional inlet were investigated. First, the cowl lip thickness was changed. Second, the concept of a wing leading edge slat was adapted to the bottom cowl. The third concept was the installation of a horizontal turning vane in the inlet.

The cowl lips of different thicknesses were a sharp-lip configuration selected from supersonic drag considerations, an intermediate configuration with thickness sufficient for adaption to a slat leading edge configuration, and a fat-lip configuration. The thickness of the fat lip was such that it would seem practical for a high performance aircraft only if the thickness could be varied with flight condition through some design concept such as an inflatable lip.

The slat lip configuration was tested with the slat translated upward and with the slat translated forward. During normal operation, the slat would be retracted, resulting in a contour identical to that of the intermediate thickness lip. The slat would not, therefore, introduce inlet performance or drag penalties at angles of attack where the slat was not required.

Conceptually, the horizontal turning vane would have actuators which would change vane leading edge and trailing edge deflection angles in accordance with the flight condition. In the test program, only a single fixed geometry configuration could be tested because of time and cost limitations.

SYMBOLS AND ABBREVIATIONS

A_c — capture area, sq. cm. (sq. in.)

CONF — model configuration

IDC — engine face station circumferential total pressure distortion parameter

$$IDC = \frac{IDC_1 + IDC_2}{2} \text{ or } \frac{IDC_4 + IDC_5}{2}, \text{ whichever is greater}$$

IDC_i — $\frac{RAVG-RMIN}{PT2}$ for ring i of engine face station total pressure rakes. i = 1, 2, 3, 4, 5

IDR — engine face station radial total pressure distortion parameter. IDR is the greater of IDR_1, IDR_2, IDR_3, IDR_4 and IDR_5

IDR_i — $\frac{PT2 - RAVG}{PT2}$ for the ring designated by the subscript

IDT — engine face station total pressure distortion parameter.

$$IDT = \frac{PT2MAX - PT2MIN}{PT2}$$

M — free stream mach number

MFR2 — measured mass flow at the engine face station divided by the mass flow which would pass through the area A_c at free stream conditions

M.S. — model station cm. (in.)

PSD( ) — power spectral density of the pressure designated by the bracket,

$$\left(\frac{\Delta PT}{PTO}\right)^2 \quad \frac{1}{HZ}$$

PTO — free stream total pressure

PT2	spatial average of engine face station total pressures
PT2MAX.	maximum individual probe total pressure at the engine face station
PT2MIN.	minimum individual probe total pressure at the engine face station
RAVG	average total pressure for the designated ring of engine face station total pressure probes (8 probes per ring)
RMIN	minimum single probe total pressure in the designated ring of engine face station total pressure probes
RMS ( )	root-mean-square amplitude of the designated pressure (divided by PTO) about its mean
SYM	plotting symbol used for associated curves
α	angle of attack, degrees
β	angle of sideslip, degrees
δ	canard deflection angle, degrees
Δ	increment in PT/PTO between contour lines in engine face station total pressure distribution plots

MODEL DESCRIPTION

The model consists of a fuselage forebody, fuselage side-mounted normal-shock inlets, and variable-incidence-angle canard surfaces located forward of the inlets. Construction of the model is such that the vertical location of the inlets can be varied, the right inlet can be replaced by a flow field rake, and the canards can be removed. Figure 1 shows (a) a sideview and the relative size of the model (b) a front view of the model with the kidney-shaped inlets installed in the upper shoulder position, and (c) the model with a two-dimensional inlet installed in the NASA Ames Research Center 14-foot Transonic Wind Tunnel. The model scale is approximately one-fourth that of a light-weight fighter aircraft.

Fuselage Forebody and Canard

Lines of the fuselage forebody and canard are shown in figure 2. To facilitate their movement to alternate vertical locations, the inlets are supported by a rear support system which maintains a gap of 1.02 centimeters (0.4 inches) for boundary layer clearance. No attempt was made to simulate a boundary layer gutter. Canard annedral angle is 20°. Canard incidence angle is changed by rotating the entire surface about the attaching pin axis. Filler blocks provide a smoothly faired forebody when the canards are removed.

Inlets

Two basic inlet shaped were investigated; one, an inlet of kidney shape, was derived from structures and aerodynamics considerations. The second, an inlet of essentially rectangular shape (two-dimensional), was selected to facilitate the design and installation of interchangeable lower cowl lips, slats, and a turning vane. A subsonic diffuser provides a smooth transition from the inlet face to a circular engine face. The centroids of the inlets are aligned with the engine face centerline to prevent distortion that is not directly related to the external flow field or inlet lip shape.

The left inlet has steady-state and dynamic pressure rakes at the simulated engine face, a flow control valve, and a flow metering nozzle. The variable vane flow control valve is located just aft of the engine face station to provide good dynamic simulation of an aircraft installation.

The right inlet is a flow-through inlet without engine face station instrumentation or mass flow control capabilities. In much of the test program, a flow field rake was installed in place of the right inlet.

Inlet locations. - The kidney-shaped inlet was tested in two locations, an upper shoulder "design" position and a lower shoulder alternate position, as indicated in figure 3. The two-dimensional inlet was tested only in the middle position, figure 3. In this position, the inlet sides are vertical.

Kidney-shaped inlet. - Lines of the kidney-shaped inlet are presented in figure 4. The lip contour consists of a 0.127 centimeter (0.050) radius tangent to a short constant area internal section. The radius is tangent to a shallow parabola at the outer surface. Internal contraction ratio from the lip highlight is small, approximately 1.04.

Two-dimensional inlets. - The basic configuration of the two-dimensional inlet is shown in figure 5(a). The inlet sharp lips are similar in contour and have the same leading edge radius as the kidney-shaped inlets. Four alternate configurations are formed by replacing the sharp lower lip (L2) of the basic configuration with alternate parts, figures 5(b) and 5(c). The alternate parts are an intermediate thickness lip (L4), the intermediate thickness lip with a slat leading edge which translates forward (L4-1), the intermediate thickness cowl lip with a slat leading edge which translates upward (L4-2), and a fat lip (L3). All the alternate lip configurations have the coordinates developed by the NASA Ames Research Center which are listed in Table 1.

Two further variations are obtained by installation of a horizontal flow turning vane. Conceptually, the vane leading edge and trailing edge deflection angles would be scheduled as a function of angle of attack for optimum inlet performance. For economy in these exploratory tests, the turning vane is of fixed geometry as shown in figure 6.

Configuration designations. - Each combination of model hardware tested is designated by a single configuration number. The configuration numbers are defined in Table II.

INSTRUMENTATION

The primary instrumentation for the model consists of a combined steady-state/transient pressure 40-probe rake assembly mounted at the engine face station of the left inlet and a flow metering nozzle. The engine face rake assembly and the flow control valve are shown in figure 7. Each total pressure probe consists of a 0.178-centimeter (0.070-inch) diameter, high frequency response transducer mounted in the center of a 0.318-centimeter (0.125-inch) outside diameter tube. A shield protects the transducer from foreign particle damage. Steady-state total pressure is sensed by the coannular pitot tube which leads to an external transducer. The flow meter is located downstream of the engine face station flow control valve. It consists of a 10-diameter

length approach section leading to venturi-type ASME calibrated meter. There are four individual static pressure orifices in the upstream section and four static pressures in the throat section of the flow metering nozzle.

Secondary instrumentation in the left inlet includes 4 wall static pressures at the engine face station and two cowl lip static pressure orifices in the kidney-shaped inlet. Locations of the left inlet pressure instrumentation are shown in figure 8.

Flow field instrumentation. - Two combined steady-state/transient total pressure probes are mounted off of the right inlet cowl as illustrated in figure 9. Additionally, the right hand inlet could be completely replaced by the flow field rake assembly also shown in figure 9. The flow field rake assembly consists of three steady-state/transient total pressure rakes which had been used as engine face station rakes for another model. These probes differ from the engine face rake probes in that the steady state pressure is sensed by an external small diameter tube whose entrance is on top and slightly aft of the transient pressure probe.

Steady-State Measuring Accuracies

With exceptions when instrumentation malfunctioned, the estimated accuracies of measuring total pressure ratio (PT/PTO), internal static pressure ratio (P/PTO), angle of attack (α), and angle of sideslip (β) are as follows.

Parameter:	PT/PTO	P/PTO	α	β
Accuracy:	$\pm$ 0.005	$\pm$0.010	$\pm$0.1°	$\pm$ 0.1°

Mass flow ratios are believed to be accurate within $\pm$0.01 during low-distortion, subcritical inlet operation. At conditions of high angle-of-attack and/or highly supercritical operation, there is evidence that the measured mass flow ratios are sometimes low, the error being in the range of 0.02. Specifically, a physically improbable reduction in the mass flow ratio with decreasing total pressure recovery is sometimes observed in the supercritical portion of the pressure recovery - mass flow ratio curves. Analysis indicates that total pressure distortion in the flow entering the metering nozzle is the probable source of these errors; and, with such distortion, the measured flow will be less than the actual mass flow.

MODEL INSTALLATION

In the first of the two test periods, the model assembly was attached directly to the tunnel sting; and, the tunnel section mechanism was used to vary angle of attack. In the second test period a pitch-yaw mechanism was located between the model and the tunnel sting (figure 1 (C)). This mechanism

permitted remote changes in angle of sideslip and an increased range of angle of attack.

STEADY-STATE DATA PRESENTATION AND DISCUSSION

Because of the large number of configurations investigated in this exploratory test program, data are presented both to show performance of a given configuration over ranges of operating conditions, and to compare performance of different configurations at a given operating condition. Additionally, curves of total pressure recovery and distortion versus mass flow ratio are presented in appendix A for each test run.

Inlet Performance Variation with Angle of Attack

Variations in total pressure recovery, distortion parameter IDT, and mass flow ratio with angle of attack are shown for configuration 1 in figures 10 through 14, for configuration 2 in figure 15, for configuration 10 in figures 16 through 19, and for configuration 11 in figure 20. In configuration 1, the kidney-shaped inlet is located on the upper fuselage shoulder aft and above the variable-incidence-angle canard. Configuration 2 differs from configuration 1 in that the canard is removed. Configuration 10 is similar to configuration 1 except that the kidney-shaped inlet is located on the fuselage lower shoulder. Configuration 11 differs from configuration 10 in that the canard is removed.

Tuft photographs showing typical patterns of flow adjacent to the fuselage are presented in figure 21 for configurations 1 and 2, and in figure 22 for configurations 10 and 11.

The variations in inlet performance characteristics with angle of attack for the two-dimensional inlet configurations 3, 4, 8, 6, 5, 7 and 9 are presented in figures 23 through 29. In all the two-dimensional inlet tests, the inlet is located in the middle position (figure 3); and, the canard is removed. Configurations 3, 4, and 8 are similar except that the bottom lip is progressively thicker (figure 5 (b)). In configuration 6, a slat formed by the leading edge section of the intermediate thickness bottom lip is translated upward and forward parallel to the sideplate leading edge. The same slat is translated forward for configuration 5. Configurations 7 and 9 are configurations 3 and 8, respectively, with the addition of a horizontal flow turning vane.

Performance of configuration 1.- At angles of attack from -8° to 16° and with positive or 0° canard deflection angles, inlet performance characteristics of configuration 1 are excellent (figures 11, 12 and 13). Performance characteristics are poorer but acceptable with a canard deflection of -10° (figure 14). An increase in angle of attack to 20° results in an appreciable reduction in pressure recovery and mass flow ratio. However, inlet/engine matching and performance level are still quite acceptable. A further increase

in angle of attack to 30° is accompanied by a drastic reduction in inlet performance to a probably unacceptable level (figure 10 (b)). Distortion is suprisingly low, probably indicating that the flow entering the inlet is uniformly poor.

A better picture of the effect of the canard and canard deflection angle is provided by figure 30. (Recall that configuration 1 with the canard removed is configuration 2). At angles of attack up to 8°, performance is similar or slightly better with the canard except for a canard deflection angle of -10° where performance is slightly lower. At angles of attack of 12°, 16°, and 20°, performance is appreciable better with the canard at canard deflection angles of 0° and above. Performance was somewhat better even with a canard deflection angle of -10°. At a 30-degree angle of attack, however, both pressure recovery and mass flow ratio were sharply lower with the canard.

The tuft photographs of figure 21 provide evidence that the canard improves inlet performance at intermediate-high angles of attack by better aligning the flow with the inlet. At higher angles of attack and canard deflection angles, wake from the canard enters the inlet, and performance drops drastically.

Performance of configuration 2. - At angles of attack of 8° and above, configuration 2 shows a continuous reduction in performance with increasing angle of attack (figure 15). The slope of pressure recovery with mass flow ratio during subcritical operation is appreciably greater than for configuration 1, and the knee in the pressure recovery-mass flow curve is less distinct. Distortion during subcritical operation at intermediate-high angles of attack is also appreciably greater than for configuration 1.

Performance of configuration 10. - The inlet is much more in line with the canard for configuration 10 than for configuration 1. Consequently, canard wake is ingested at lower angles of attack; and, inlet performance is more sensitive to canard deflection angle as shown in figures 16 through 19. The high sensitivity to both angle of attack and deflection angle would seem to preclude this configuration for an aircraft installation.

Performance of configuration 11. At low angles of attack, configuration 11 has performance characteristics similar to configuration 2. As angle of attack increases to 8° and above, however, the decrease in mass flow ratio and pressure recovery is more rapid for the lower shoulder inlet position of configuration I1 (figure 20). As illustrated by figure 31, the performance of configuration 11 (no canard) relative to configuration 10 (canard) is highly dependent on the canard deflection angle, and may be either higher or lower. Figure 22 shows the changes in the flow field near the inlet with and without a canard.

Performance of configuration 3.- The two-dimensional inlet of configuration 3 is identical in capture area and in cowl leading edge shape to the kidney-shaped inlet of configurations 2 and 11. At negative angles of attack (figure 23), performance suffers because of the scarfed face of the inlet. Performance relative to configurations 2 and 11 (figure 32) is poor at angle of attack up to 8°, similar at 12°, and superior at angles above 12° to 30°. At 30°, performance again is similar to that for configuration 2. Differences in inlet location as well as inlet shape undoubtedly contribute to the performance differences.

Performance of configuration 4.- Configuration 4 has the same inlet throat area as configuration 3, but a thicker lower lip. Consequently, the ratio of capture to throat area is greater, 1.138 as compared to 1.065. At 0.9 Mach number and low angles of attack, the throat area limits mass flow ratio (figure 24). Mass flow ratios are therefore less for configuration 4 than configuration 3 at angles of attack below 12° (figure 33). At 12°, the beneficial effects of the thicker lip offset the effect of the greater contraction ratio, and, performance is similar. At higher angles of attack, performance is better for configuration 4.

Performance of configuration 8.- The lower cowl lip thickness is even further increased for configuration 8 which has a capture-to-throat area ratio of 1.224. As illustrated by figures 25 and 33, the increased contraction ratio results in a large reduction in supercritical mass flow ratio at an angle of attack of 8°. It is only above 20° that the fat lip provides superior performance.

Performance of configuration 6.- The inlet bottom lip contour of configuration 6 is identical to that of configuration 4 when the slat is retracted. For an aircraft installation, the slat would be in its retracted position up to the angle where performance of configuration 6 is superior to that of configuration 4. Figures 26 and 33 show that performance of configuration 6 is inferior up to an angle of attack of 12°. A crossover occurs slightly above 12°, and, at higher angles configuration 6 has appreciably better performance.

Performance of configuration 5.- Configuration 5 is identical to configuration 6 except that the slat is translated forward rather than upward. At angles of attack of 12° and below configuration 4 (slat retracted) is superior in inlet performance. Above 12°, performance for configuration 6 is better (figures 27 and 33).

Performance of configuration 7.- Configuration 7 is configuration 3 with the addition of the horizontal turning vane shown in figure 6. At angles of attack of 12° and less, performance is inferior to that for configuration 3. This results partly from the reduction in throat area and partly because the vane leading edge and trailing edge delection angles were selected for high-

angle-of-attack operation. Performance of configuration 7 (figures 28 and 34) is superior at 20° and 30° and essentially equal at 40° to that of configuration 3. The lack of superiority at 40° is probably indicative of the need to optimize vane deflection angles at each angle of attack.

Performance of configuration 9.- Configuration 9 is configuration 8 (fat lip) with the addition of the horizontal turning vane. With the possible exception of the 30-degree angle of attack condition, performance is better without the turning vane (figures 29 and 34). There would seem to be no advantage in having both the fat lip and the turning vane.

Variation in inlet maximum mass flow ratio. - Figure 35 presents curves which are indicative of the maximum mass flow ratio versus angle of attack for each of the inlet configurations. The curves are qualified by the probability that the flow control valve limits flow in its most open position prior to supercritical inlet operation at extreme angles of attack. Nonetheless, the curves indicate the reduction in mass flow ratio at cruise conditions which may be incurred by configurations having improved performance at high angles of attack.

Inlet Performance Variation with Angle of Sideslip

The effect of sideslip on inlet performance is shown for configurations 1, 3 and 6 in figures 36, 37 and 38. Performance is presented for the left inlet, consequently, the inlet is on the windward side for negative sideslip angles.

Configuration 1 performance. - At an angle of attack of 4°, sideslip angles up to ± 4° have little effect on inlet performance. At ± 10°, performance is reduced but not sufficiently to be of concern to an aircraft installation. With an increase in angle of attack to 12°, there is an appreciably but probably acceptable loss in performance at sideslip angles of -4° and -10°. Note that with the canard, the windward inlet is the more sensitive to sideslip.

Configuration 3 performance. - Inlet performance is relatively insensitive to sideslip angles up to ± 10° at the test angles of attack of 4° and 12°. With this canardless configuration, there is a small performance loss with positive sideslip angles and a slight improvement with negative angles (inlet on the windward side).

Configuration 6 performance. - Sideslip effects are small for configuration 6, and trends are similar to those of configuration 3.

Inlet Performance at 1.2 Mach Number

Inasmuch as only a few runs were made at 1.2 Mach number, the data are

presented in comparison with corresponding runs at 0.9 Mach number in figure 39 and 40. Tunnel fogging was encountered in the 1.2 Mach number test; and, the accuracy of the data is questionable. Relative to the 0.9 Mach number data, total pressure recoveries are lower and by amounts greater than were expected. Maximum mass flow ratios are somewhat higher at an angle of attack of 0° (as would be expected for an inlet operating in free stream conditions), but became lower at an angle of attack 8°.

Engine Face Total Pressure Distribution

Total pressure contours at the engine face station are presented in figures 41 through 61. In these plots, the spatial average total pressure at the engine face is listed at the top of the circle defining the inside diameter of the engine-face annulus. Next is the increment in total pressure ratio units (Δ) between contour lines. Each contour line differs from the average total pressure ratio by the product of Δ and the number forming the contour line. The contour is above the average if the contour line is not underlined, and below average if the number is underlined. For example, if Δ is 0.02 and the number forming the contour line is 3, that contour line is 0.06 units above the listed average total pressure ratio. The contour formed by dots is at the average total pressure ratio. For the most part, the contour plots convey their message better than words. Therefore, the discussion is limited to general observations or unusual characteristics.

Configurations 1 and 2. - Total pressure distributions for configurations 1 and 2 are illustrated by figures 41 through 45. For configuration 2, (figure 41) the variation with angle of attack is predictable; and, the influence of the inlet shape is quite apparent. (Note that in this and in subsequent figures, Δ may vary from plot to plot.

Figure 42, showing the variation in total pressure distribution for configuration 2 at an angle of attack of 12° reveals an interesting characteristic. As total pressure increases and mass flow ratio decreases, the region of minimum total pressure moves from the upper outboard quadrant to the lower outboard quadrant.

The effects of angle of attack, mass flow ratio, and canard deflection angle on total pressure distribution for configuration 1 are depicted in figures 43, 44, and 45.

Configurations 10 and 11. - Total pressure distributions for the kidney-shaped inlet in the lower shoulder position are shown in figures 46 and 47. The very steep gradients in total pressure ratio in the bottom portions of some of the plots are perhaps misleading, and may indicate an erroneous interpretation of the data by the computer program logic. The pressure probe spacing was too large to measure or confirm such steep gradients.

Effect of inlet location. - The variation in total pressure distribution with inlet location is illustrated in figure 48 (no canard) and figure 49 (canard).

Two-dimensional inlet configurations. - Figures 50 through 58 present total pressure ratio contour plots for configurations 3, 4, 8, 6, 7, and 9 respectively. A low pressure region appears in the upper outboard quadrant at angles of attack of 20° and 30° at high mass flow ratios for configuration 3. It disappears at 40° and at lower mass flow ratios (figure 51). Similar but less pronounced characteristics are observed for configuration 8 (figures 53 and 54). Configurations 4, 6 and 5 (figures 52, 55, and 56) do not show this characteristic.

Configurations 7 and 9 (figures 57 and 58) suggest that further refinement in shape and location would make the turning vane more effective. For configuration 7 in particular, the turning vane reduces total pressure in the top sector of the inlet.

Effect of sideslip. - Changes in total pressure distribution with sideslip are illustrated in figure 59 for configuration 1, in figure 60 for configuration 3, and in figure 61 for configuration 6.

Alternate Distortion Parameters

In preceding figures, the parameter IDT has been used as a measure of engine face distortion. It has the advantage of simplicity, being the difference between the maximum and minimum measured total pressure divided by the average. It has the disadvantage that its value can be established by a single erroneous measurement. Further, it gives no indication of the magnitude or pattern of the low pressure areas, factors which are important in determining an engine's response to distortion. Alternate distortion parameters defined by an engine manufacturer are presented in figure 62 for configuration 4.

Figure 62(a) shows the variation of the circumferential distortion factor, IDC, with mass flow ratio, pressure recovery and angle of attack. The corresponding radial distortion parameter, IDR, is presented in figure 62(b). Figure 24 shows the distortion parameter IDT for the same runs. IDC increases with angle of attack much as does IDT. In contrast, IDR shows little effect of angle of attack, and varies primarily as a function of mass flow ratio.

TRANSIENT DATA

Results of limited investigations of the transient pressures in the inlet and in the external flow field at the inlet face station are presented in figures 63 through 70. All the data presented are for inlet operation at the test point nearest the critical point.

Turbulence Measurements

Turbulence is defined in this discussion as the variation of a pressure about its mean (steady-state) value. Two measurements of turbulence are used, the root-mean-square value of the pressure oscillation (RMS), and the power spectral density of the pressure oscillations (PSD). In both measurements, the pressure has been divided by free stream total pressure to make the value dimensionless. The RMS value covers the same frequency range, 1024 Hz., as the PSD plots.

Configurations 1 and 2.- Steady-state data are presented in figure 63 to assist in interpreting the transient data. The essentially constant total pressures of flow field probes 58 and 59 suggest that the canard wake passes below the inlet at angles of attack below 16°. With a further increase in angle of attack to 16°, the bottom probe is immersed in the canard wake at a canard deflection angle of 5°. With no canard deflection, the lower probe becomes immersed in the canard wake at an angle of attack between 16° and 20°. The reduced engine face total pressure recoveries with the negative canard deflection angle probably reflect sharp-lip-separation losses, the canard having an adverse effect on the flow field alignment with the inlet.

The data of figure 64(a) were measured at pressure probe 180 with the external flow field rake (figure 9) rotated up 23° to correspond to the upper shoulder inlet location. At angles of attack of 12° and above, RMS increases almost linearly with angle of attack with the canard at a deflection angle of 0°. With the canard removed, RMS is constant up to an angle of attack of 30°. The slight increase at 40° may be due to flow separation over the probe lip. With the canard and at an angle of attack of 30°, the PSD curve shows a slight peak near 380 Hz. There is no sharp peak indicating a canard vortex-shedding frequency. Figure 64(b) shows turbulence variation with angle of attack at probe 158. Data were obtained with the canard at different deflection angles and with it removed. RMS is low and constant with angle of attack with the canard removed. RMS increases with canard deflection angle and angle of attack. Power decreases only slightly with frequency; and, there are no discrete peaks.

Configurations 10 and 11.- The turbulence variation with angle of attack at engine face probe 129 is shown in figure 65 for configurations 10 and 11. At an angle of attack of 0°, turbulence is less with the canard removed. From 4° through 16°, turbulence is higher with the canard removed. At 20°, turbulence is slightly lower with the canard removed. The probable explanation for this behavior is that the canard improves alignment of the flow with the inlet at the intermediate angles of attack, and thereby reduces turbulence due to sharp-lip separation. At extreme angles of attack with the canard removed, the turbulence-generating separation and reattachment of flow about the lower lip is reduced because of the degree of separation. At high angles of attack with the canard, turbulence probably increases with angle of attack because of a combination of three things, 1) increasing ingestion of the canard wake, 2) increasing turbulence in the canard wake, and 3) increasing sharp-lip separation. At low angles of attack the PSD curves are quite flat with and

without the canard. At 12°, 16°, and 20° with the canard removed, there are two small peaks in the PSD curves, the second peak being at approximately twice the frequency of the first peak. The frequency at which the peaks occur increases as the angle of attack increases. With the canard, there is a slight peaking followed by a continuous reduction in the PSD curve at 16° and 20°. The frequency for this peaking, in contrast to that without a canard, decreases with increasing angle of attack. Figure 66 illustrates the variation in RMS from engine face probe to probe for configuration 11 tested over a range of angles of attack. The probe locations are shown in figure 8. Each RMS trace shows the same characteristic variation with angle of attack, but turbulence is less for the probes adjacent to the duct wall.

Two-dimensional inlet configurations.- The effect of lip configuration on turbulence at engine face probe 123 is shown in figure 67. The data are consistent with the steady-state results in that turbulence becomes progressively lower and steady-state performance higher going from configuration 3 (sharp-lip) to configuration 4 (intermediate lip) to configuration 8 (fat lip) to configuration 6 (slat in high position). The PSD curves are relatively flat at low angles of attack. At 30°, there is a greater variation in power with frequency. There is a peak at 390 Hz. for configuration 3, a plateau from 10 to 60 Hz. for configuration 4, and a plateau from 10 to 90 Hz. for configuration 8. Power decreases continuously with frequency for configuration 6, but with the slope being much steeper at frequencies below 30 Hz.

Instantaneous Total Pressure Distortion

The "DYNADEC" program (reference 1) was used by the Flight Dynamics Laboratory of the United States Air Force to obtain peak values of instantaneous distortion for a portion of the test runs. Peak instantaneous values of the circumferential distortion parameter, IDC, and the radial distortion parameter, IDR, are shown as a function of angle of attack in figure 68 for configurations 1 and 2. (Similar data for configurations 10 and 11 are presented in reference 2.) Instantaneous distortion increases even more sharply than steady-state distortion with canard wake ingestion. At a canard deflection angle 0°, for example, the ratio of instantaneous distortion to steady-state distortion varies with angle of attack as follows:

α	IDC_i/IDC_s	IDR_i/IDR_s
8°	1.66	1.37
16°	1.75	1.71
20°	4.07	4.57.

Instantaneous engine face total pressure distribution plots are compared with steady-state plots in figures 69 and 70. The times for the instantaneous contour plots were selected at random. Inlet operation is slightly subcritical for these points. Consequently, the figures emphasize the turbulence associated with the configuration and the external flow field. The test point of figure 69 is for a configuration and angle of attack resulting in low turbulence, while the test point of figure 70 is for a configuration and angle of attack of high turbulence. Not surprisingly, the instantaneous values of IDC and IDR differ from the

steady-state values far less for the lower turbulence test condition.

CONCLUDING REMARKS

None of the inlet configurations tested is superior over the entire range of test conditions. Which configuration is superior depends on the aircraft configuration, the required range of flight speeds, and the required range of angles of attack and angles of sideslip. For those configurations tested, tolerance to sideslip was excellent without a canard, and acceptable with the canard and inlet location of configuration 1. Three of the configurations appear most promising and merit further development and test. These are configurations 1, 6 and 8.

The test data for configuration 1 show that excellent performance can be obtained for an inlet located aft of a canard up to the limiting conditions when an appreciable amount of canard wake is ingested by the inlet. At angles of attack from -10° to 20° and angles of sideslip from -10° to 10°, performance was equal to or better than that obtained without a canard. At intermediate high angles of attack, the canard serves to better align the external flow with the inlet and thereby reduces sharp lip separation. When an appreciable amount of canard wake is ingested, there is a sharp drop in inlet steady-state performance, and dynamic distortion increases to a probably unacceptable level. The practicality of this configuration therefore depends on the required angle-of-attack range.

Configuration 10, wherein the inlet is located aft but more nearly in line with the canard than in configuration 1, is considered unacceptable. Excessive canard wake is ingested at relatively low angles of attack and canard deflection angles.

Configurations 6 and 8 are the best of the two-dimensional inlet configurations tested. Configuration 6, with the slat lip translated upward, has steady-state and transient performance characteristics equal to or better than any of the configurations at high angles of attack; and, the slat would be retracted during low-angle-of-attack operation. Although experimental data is lacking, it is reasonable to assume that the scarfed face and the reasonably thick lower lip would result in low spillage drags inasmuch as spillage would tend to occur over the lower lip. The large difference in high-angle-of-attack performance between configurations 5 and 6 suggest that more improvements could be obtained for a more optimum slat position and shape.

Configuration 8 provides good high-angle-of-attack characteristics, but has a low maximum mass flow ratio at low angles of attack. Further, its drag would be high at supersonic flight speeds. It feasibility depends directly on the development of a mechanism wherein the lip is fat only at

high angles of attack and reverts to a thin lip at other flight conditions.

The horizontal turning vane of configurations 7 and 9 would seem to have no advantage over the slat lip of configuration 6 or the fat lip of configuration 8. Performance could undoubtedly be improved by optimizing the leading-edge and trailing-edge deflection angles of the vane. However, performance at nominal operating conditions would always be penalized by the vane drag. The vane also introduces a potential icing problem.

There is a suggestion in some of the engine face total pressure distribution plots that a vortex shed by the fuselage forebody at high angles of attack is ingested by the inlets. Unfortunately, the presence and path of such a vortex can not be confirmed by the flow field rakes because 1) the steady-state probes were shielded by the dynamic probes at high angles of attack, and 2) there were several failures of transducers in transient pressure probes. Ingestion of such a vortex would limit the performance improvements that could be obtained at high angles of attack by changes in the cowl lip contour.

Los Angeles Aircraft Division
Rockwell International
Los Angeles, California, October 31, 1976

APPENDIX A

INLET PERFORMANCE FOR INDIVIDUAL TEST RUNS

The configuration, mach number, angle of attack, and angle of sideslip for each of the test runs are listed in table III along with the figure in which the curves of pressure recovery and distortion versus mass flow ratio are presented.

In some of the curves presented in this appendix, there is a reduction in the mass flow ratio as operation becomes increasingly supercritical. As mentioned in the discussion of measurement accuracies, total pressure distortion in the flow entering the metering nozzle will give erroneous measurements. With such distortion, the measured flow will be less than the actual flow. It is believed that the actual supercritical mass flow ratio is equal to or greater than the maximum measured value during each of the test runs.

In a few runs, most notably that of figure 76(m), the pressure recovery-mass-flow ratio curve shows a discontinuity not unlike that between the started and unstarted portions of the curve for a mixed compression inlet operating at supersonic speeds. No reason has been found to question this data.

REFERENCES

1. Marous, J. J.; and Sedlock, D.: Dynamic Data Editing and Computing System (DYNADEC), Air Force Flight Dynamics Laboratory, Flight Mechanics Division.

2. Mace, J.: Analysis of Rockwell International 0.25 Scale Inlet/Canard Interaction Test Data, TM 74-189 AFFDL/FXM, Air Force Flight Dynamics Laboratory, October 1974.

TABLE I. - COORDINATES FOR COWL LIPS L3 AND L4

X/T	YI/T	YO/T
0.010	0.125	0.022
0.029	0.207	0.056
0.058	0.267	0.079
0.087	0.304	0.098
0.116	0.337	0.112
0.175	0.387	0.126
0.233	0.435	0.135
0.350	0.522	0.145
0.466	0.599	0.152
0.583	0.668	0.155
0.699	0.732	0.159
0.874	0.817	0.163
0.991	0.865	0.165
1.166	0.925	0.166
1.399	0.970	0.166
1.865	1.000	0.166

TABLE II. - CONFIGURATION DESIGNATIONS

CONFIGURATION	INLET LOCATION	INLET SHAPE	BOTTOM LIP	TURNING VANE	CANARD
1	upper-shoulder	kidney	L1	no	yes
2	upper-shoulder	2-dimensional	L1	no	no
3	middle	2-dimensional	L2	no	no
4	middle	2-dimensional	L4	no	no
5	middle	2-dimensional	L4-1	no	no
6	middle	2-dimensional	L4-2	no	no
7	middle	2-dimensional	L2	yes	no
8	middle	2-dimensional	L3	no	no
9	middle	2-dimensional	L3	yes	no
10	lower-shoulder	kidney	L1	no	yes
11	lower-shoulder	kidney	L1	no	no

TABLE III. - TEST RUNS

CONFIGURATION	MACH NO.	β (DEGREES)	α (DEGREES)	FIGURE
1, $\delta = 0^{\circ}$	0.9	0	-8	71(a)
1, $\delta = 0^{\circ}$	0.9	0	-4	71(b)
1, $\delta = 0^{\circ}$	0.9	0	0	71(c)
1, $\delta = 0^{\circ}$	0.9	0	4	71(d)
1, $\delta = 0^{\circ}$	0.9	0	8	71(e)
1, $\delta = 0^{\circ}$	0.9	0	12	71(f)
1, $\delta = 0^{\circ}$	0.9	0	16	71(g)
1, $\delta = 0^{\circ}$	0.9	0	20	71(h)
1, $\delta = 0^{\circ}$	0.9	0	30	71(i)
1, $\delta = 0^{\circ}$	0.9	-2	4	71(j)
1, $\delta = 0^{\circ}$	0.9	-4	4	71(k)
1, $\delta = 0^{\circ}$	0.9	-4	12	71(l)
1, $\delta = 0^{\circ}$	0.9	-10	4	71(m)
1, $\delta = 0^{\circ}$	0.9	-10	12	71(n)
1, $\delta = 0^{\circ}$	0.9	2	4	71(o)
1, $\delta = 0^{\circ}$	0.9	4	4	71(p)
1, $\delta = 0^{\circ}$	0.9	4	12	71(q)
1, $\delta = 0^{\circ}$	0.9	10	4	71(r)
1, $\delta = 0^{\circ}$	0.9	10	12	71(s)
1, $\delta = 0^{\circ}$	1.2	0	0	71(t)
1, $\delta = 0^{\circ}$	1.2	0	4	71(u)
1, $\delta = 0^{\circ}$	1.2	0	8	71(v)
1, $\delta = 5^{\circ}$	0.9	0	0	72(a)
1, $\delta = 5^{\circ}$	0.9	0	4	72(b)
1, $\delta = 5^{\circ}$	0.9	0	8	72(c)
1, $\delta = 5^{\circ}$	0.9	0	12	72(d)
1, $\delta = 5^{\circ}$	0.9	0	16	72(e)
1, $\delta = 10^{\circ}$	0.9	0	0	73(a)
1, $\delta = 10^{\circ}$	0.9	0	4	73(b)
1, $\delta = 10^{\circ}$	0.9	0	8	73(c)
1, $\delta = 10^{\circ}$	0.9	0	12	73(d)
1, $\delta = 15^{\circ}$	0.9	0	0	74(a)
1, $\delta = 15^{\circ}$	0.9	0	4	74(b)
1, $\delta = 15^{\circ}$	0.9	0	8	74(c)
1, $\delta = -10^{\circ}$	0.9	0	0	75(a)
1, $\delta = -10^{\circ}$	0.9	0	4	75(b)
1, $\delta = -10^{\circ}$	0.9	0	8	75(c)
1, $\delta = -10^{\circ}$	0.9	0	12	75(d)
1, $\delta = -10^{\circ}$	0.9	0	16	75(e)
1, $\delta = -10^{\circ}$	0.9	0	20	75(f)

TABLE III - TEST RUNS Continued.

CONFIGURATION	MACH NO.	β (DEGREES)	α (DEGREES)	FIGURE
2,	0.9	0	-8	76(a)
2,	0.9	0	-4	76(b)
2,	0.9	0	0	76(c)
2,	0.9	0	2	76(d)
2,	0.9	0	4	76(e)
2,	0.9	0	6	76(f)
2,	0.9	0	8	76(g)
2,	0.9	0	10	76(h)
2,	0.9	0	12	76(i)
2,	0.9	0	14	76(j)
2,	0.9	0	16	76(k)
2,	0.9	0	20	76(l)
2,	0.9	0	30	76(m)
2,	0.9	0	40	76(n)
2,	1.2	0	0	76(o)
2,	1.2	0	4	76(p)
2,	1.2	0	8	76(q)
3,	0.9	0	-8	77(a)
3,	0.9	0	-4	77(b)
3,	0.9	0	0	77(c)
3,	0.9	0	4	77(d)
3,	0.9	0	8	77(e)
3,	0.9	0	12	77(f)
3,	0.9	0	20	77(g)
3,	0.9	0	30	77(h)
3,	0.9	0	40	77(i)
3,	0.9	-4	4	77(j)
3,	0.9	1	12	77(k)
3,	0.9	-10	4	77(l)
3,	0.9	4	4	77(m)
3,	0.9	1	12	77(n)
3,	0.9	10	4	77(o)
4	0.9	0	0	78(a)
4	0.9	0	4	78(b)
4	0.9	0	8	78(c)
4	0.9	0	12	78(d)
4	0.9	0	20	78(e)
4	0.9	0	30	78(f)
4	0.9	0	40	78(g)

TABLE III - TEST RUNS Continued.

CONFIGURATION	MACH NO.	β DEGREES)	α (DEGREES)	FIGURE
5	0.9	0	8	79(a)
5	0.9	0	12	79(b)
5	0.9	0	20	79(c)
5	0.9	0	30	79(d)
5	0.9	0	40	79(e)
6	0.9	0	8	80(a)
6	0.9	0	12	80(b)
6	0.9	0	20	80(c)
6	0.9	0	30	80(d)
6	0.9	0	40	80(e)
6	0.9	-4	12	80(f)
6	0.9	-10	12	80(g)
6	0.9	4	12	80(h)
6	0.9	10	12	80(i)
7	0.9	0	8	81(a)
7	0.9	0	12	81(b)
7	0.9	0	20	81(c)
7	0.9	0	30	81(d)
7	0.9	0	40	81(e)
7	0.9	-4	12	81(f)
7	0.9	-10	12	81(g)
8	0.9	0	8	82(a)
8	0.9	0	12	82(b)
8	0.9	0	20	82(c)
8	0.9	0	30	82(d)
8	0.9	0	40	82(e)
8	0.9	-4	12	82(f)
8	0.9	-10	12	82(g)
9	0.9	0	8	83(a)
9	0.9	0	12	83(b)
9	0.9	0	20	83(c)
9	0.9	0	30	83(d)
9	0.9	0	40	83(e)
9	0.9	-4	12	83(f)
9	0.9	-10	12	83(g)
10, $\delta=0^{\circ}$	0.9	0	-8	84(a)
10, $\delta=0^{\circ}$	0.9	0	-4	84(b)
10, $\delta=0^{\circ}$	0.9	0	0	84(c)
10, $\delta=0^{\circ}$	0.9	0	4	84(d)
10, $\delta=0^{\circ}$	0.9	0	8	84(e)
10, $\delta=0^{\circ}$	0.9	0	12	84(f)

TABLE III - TEST RUNS Concluded.

CONFIGURATION	MACH NO.	β(DEGREES)	α(DEGREES)	FIGURE
10 , $\delta=0^{\circ}$	0.9	0	16	84(g)
10 , $\delta=0^{\circ}$	0.9	0	20	84(h)
10 , $\delta=10^{\circ}$	0.9	0	-8	85(a)
10 , $\delta=10^{\circ}$	0.9	0	-4	85(b)
10 , $\delta=10^{\circ}$	0.9	0	0	85(c)
10 , $\delta=10^{\circ}$	0.9	0	4	85(d)
10 , $\delta=10^{\circ}$	0.9	0	8	85(e)
10 , $\delta=10^{\circ}$	0.9	0	12	85(f)
10 , $\delta=10^{\circ}$	0.9	0	16	85(g)
10 , $\delta=15^{\circ}$	0.9	0	0	86(a)
10 , $\delta=15^{\circ}$	0.9	0	4	86(b)
10 , $\delta=15^{\circ}$	0.9	0	8	86(c)
10 , $\delta=15^{\circ}$	0.9	0	10	86(d)
10 , $\delta=15^{\circ}$	0.9	0	12	86(e)
10 , $\delta=-10^{\circ}$	0.9	0	-8	87(a)
10 , $\delta=-10^{\circ}$	0.9	0	0	87(b)
10 , $\delta=-10^{\circ}$	0.9	0	4	87(c)
10 , $\delta=-10^{\circ}$	0.9	0	8	87(d)
10 , $\delta=-10^{\circ}$	0.9	0	12	87(e)
10 , $\delta=-10^{\circ}$	0.9	0	16	87(f)
10 , $\delta=-10^{\circ}$	0.9	0	20	87(g)
11	0.9	0	-8	88(a)
11	0.9	0	-4	88(b)
11	0.9	0	0	88(c)
11	0.9	0	4	88(d)
11	0.9	0	8	88(e)
11	0.9	0	12	88(f)
11	0.9	0	16	88(g)
11	0.9	0	20	88(h)

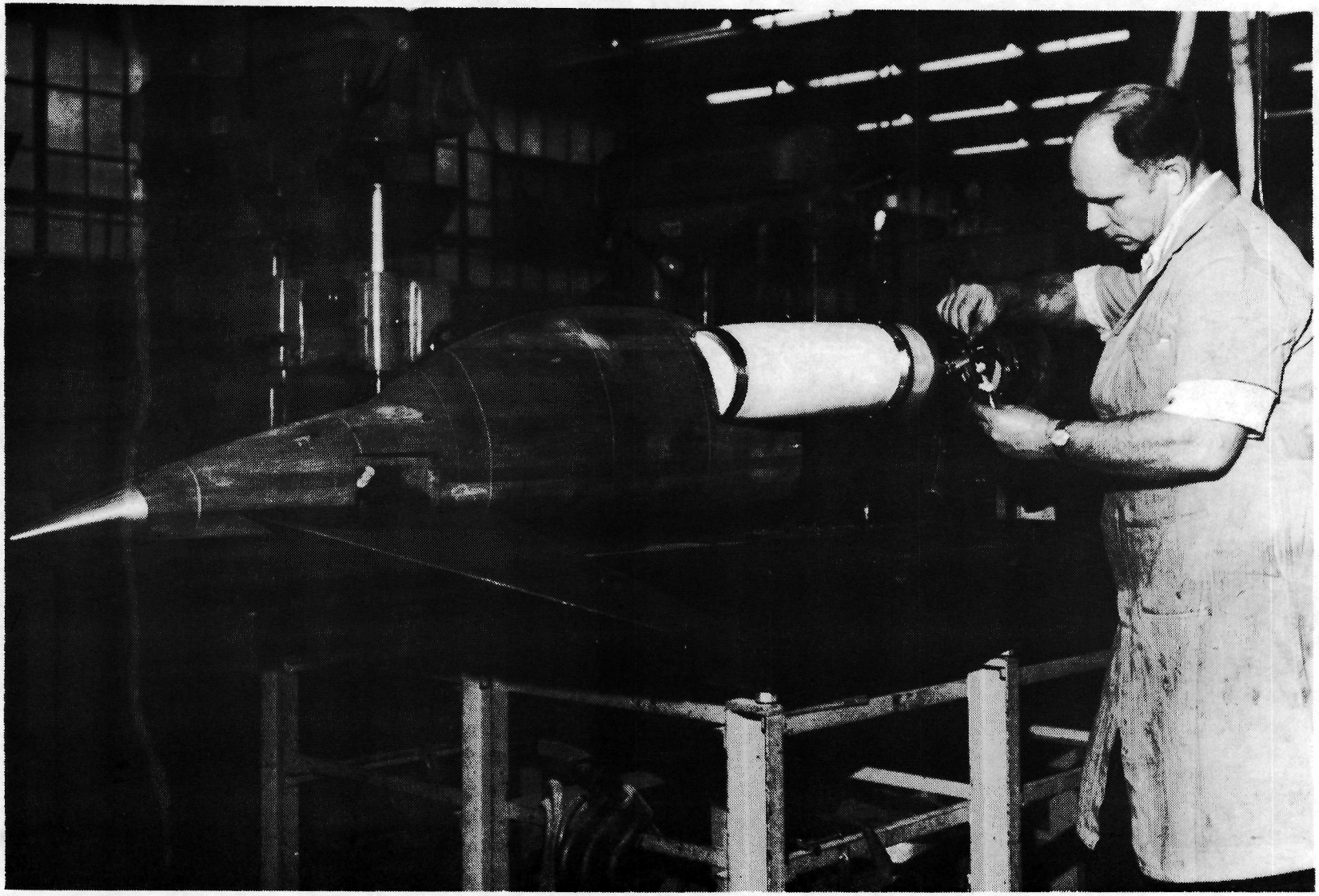

Figure 1. - Model and test installation.

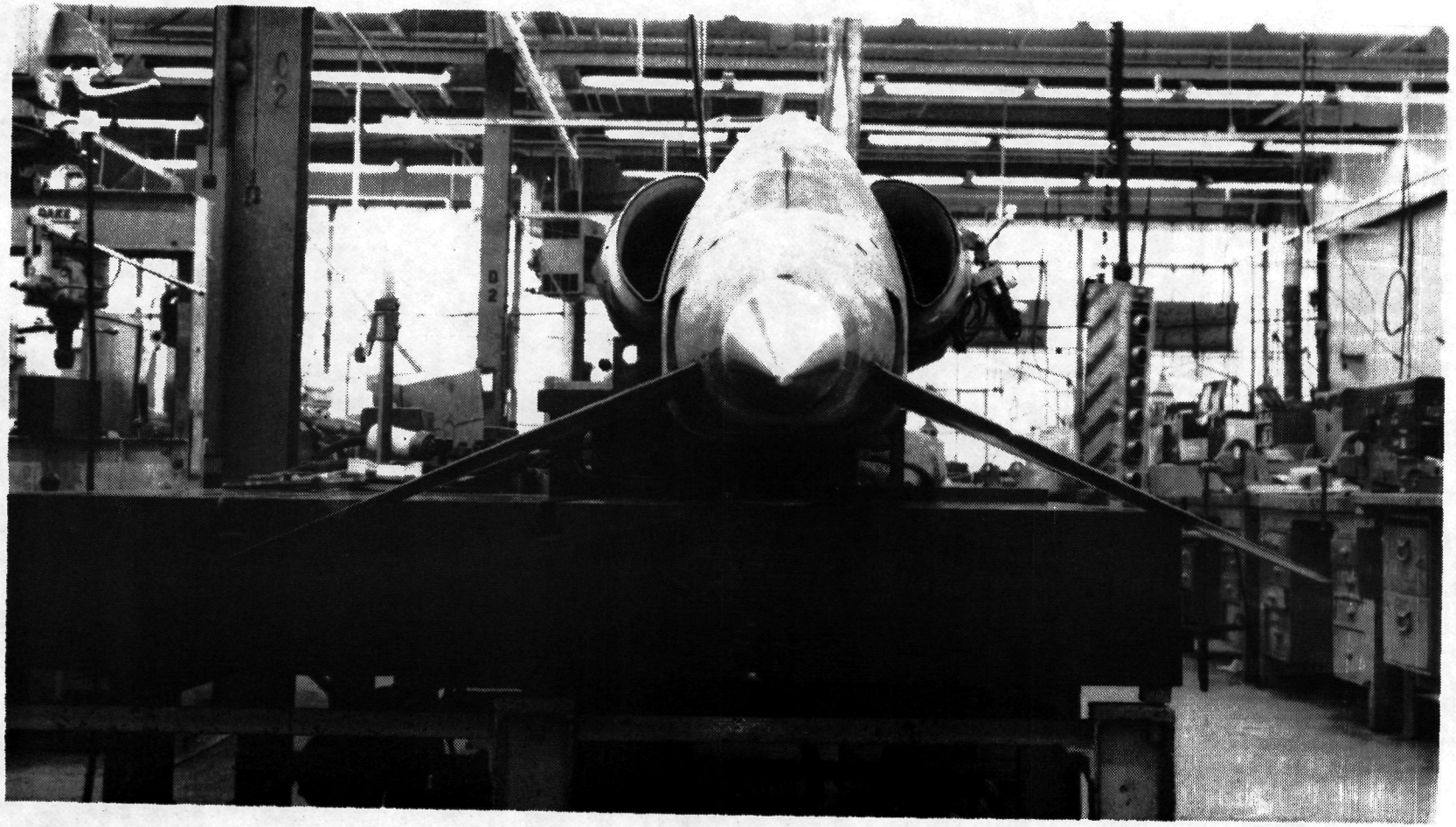

Figure 1. - Continued.

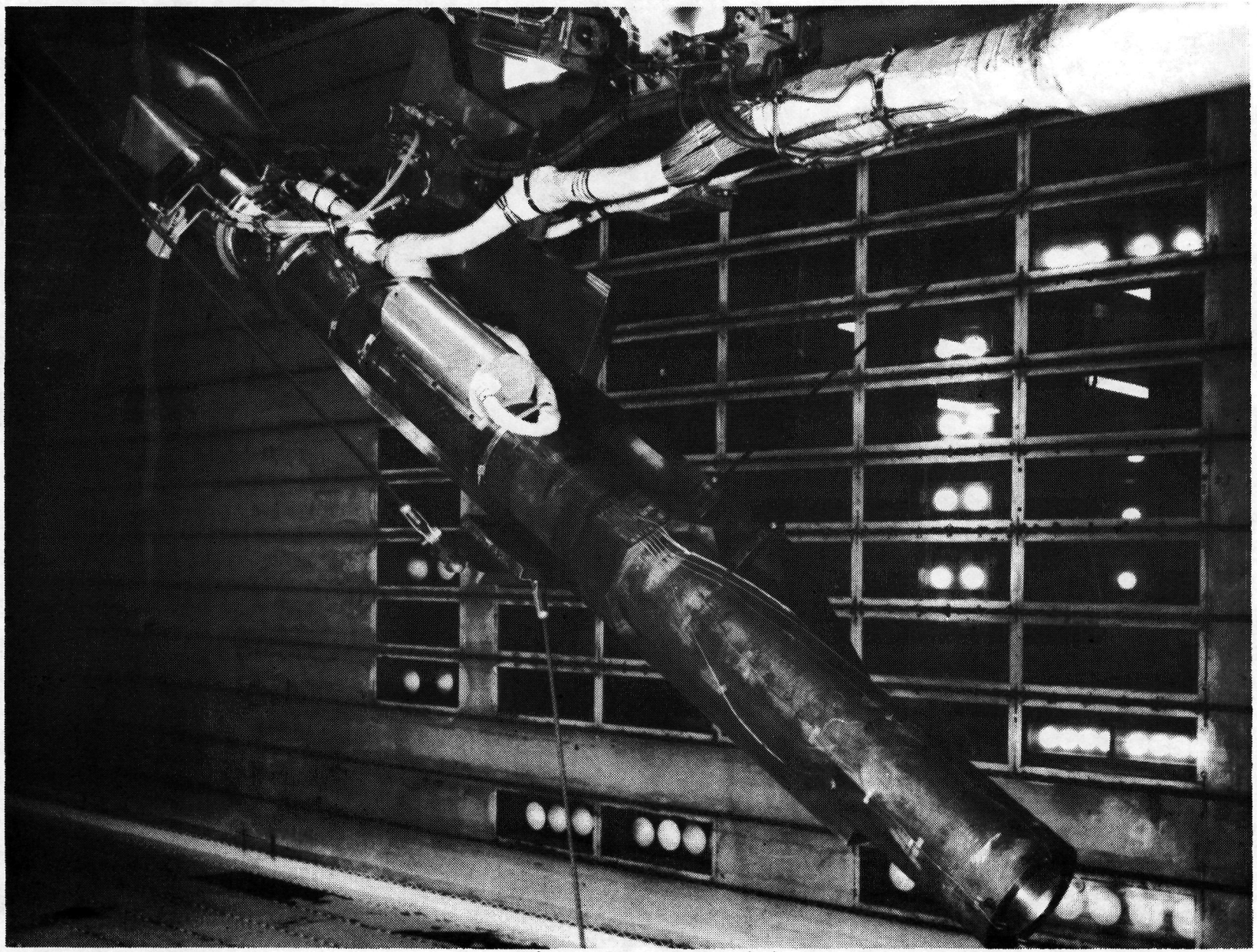

Figure 1. - Concluded.

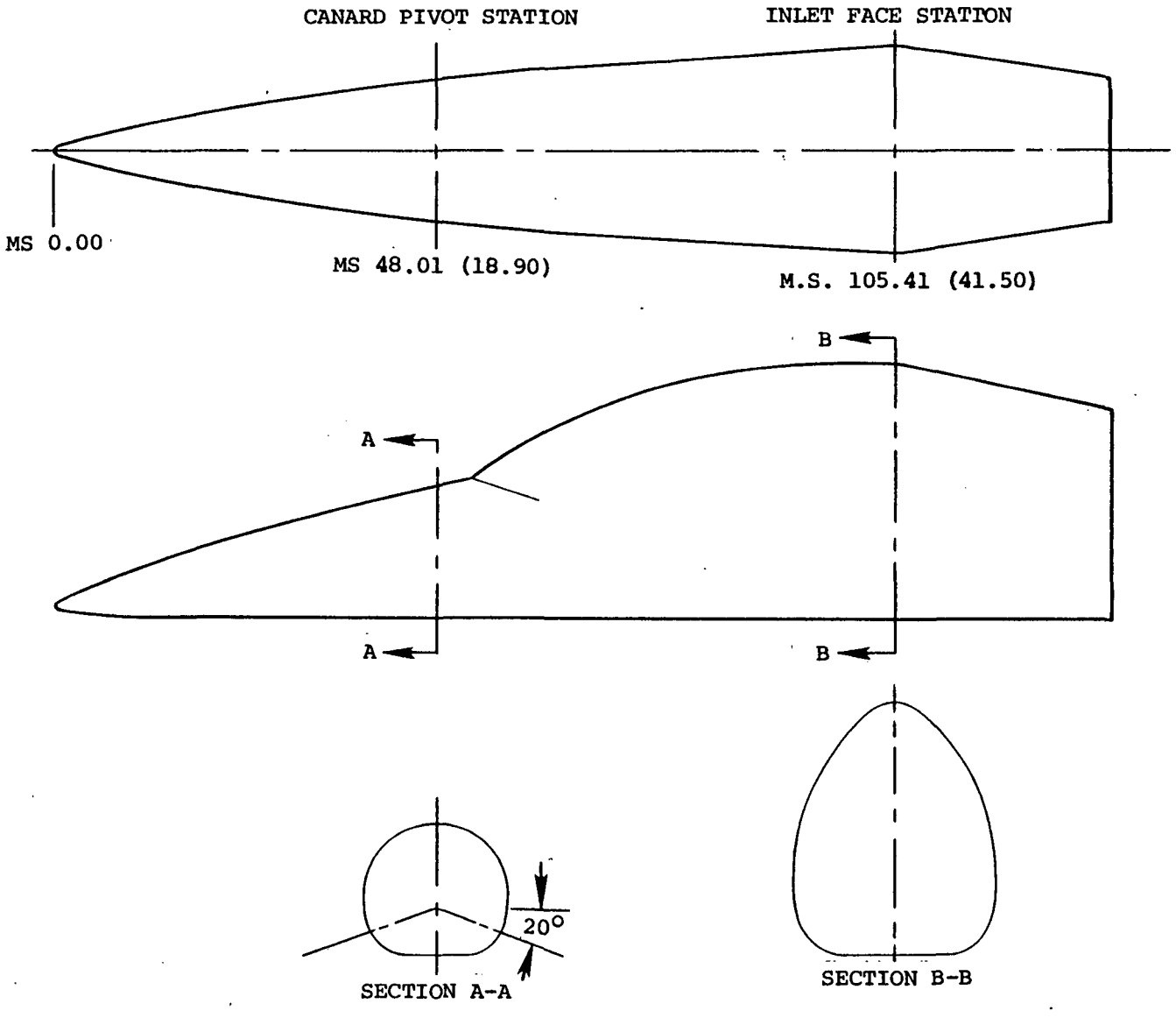

(a) fuselage forebody

Figure 2. - Fuselage forebody and canard.

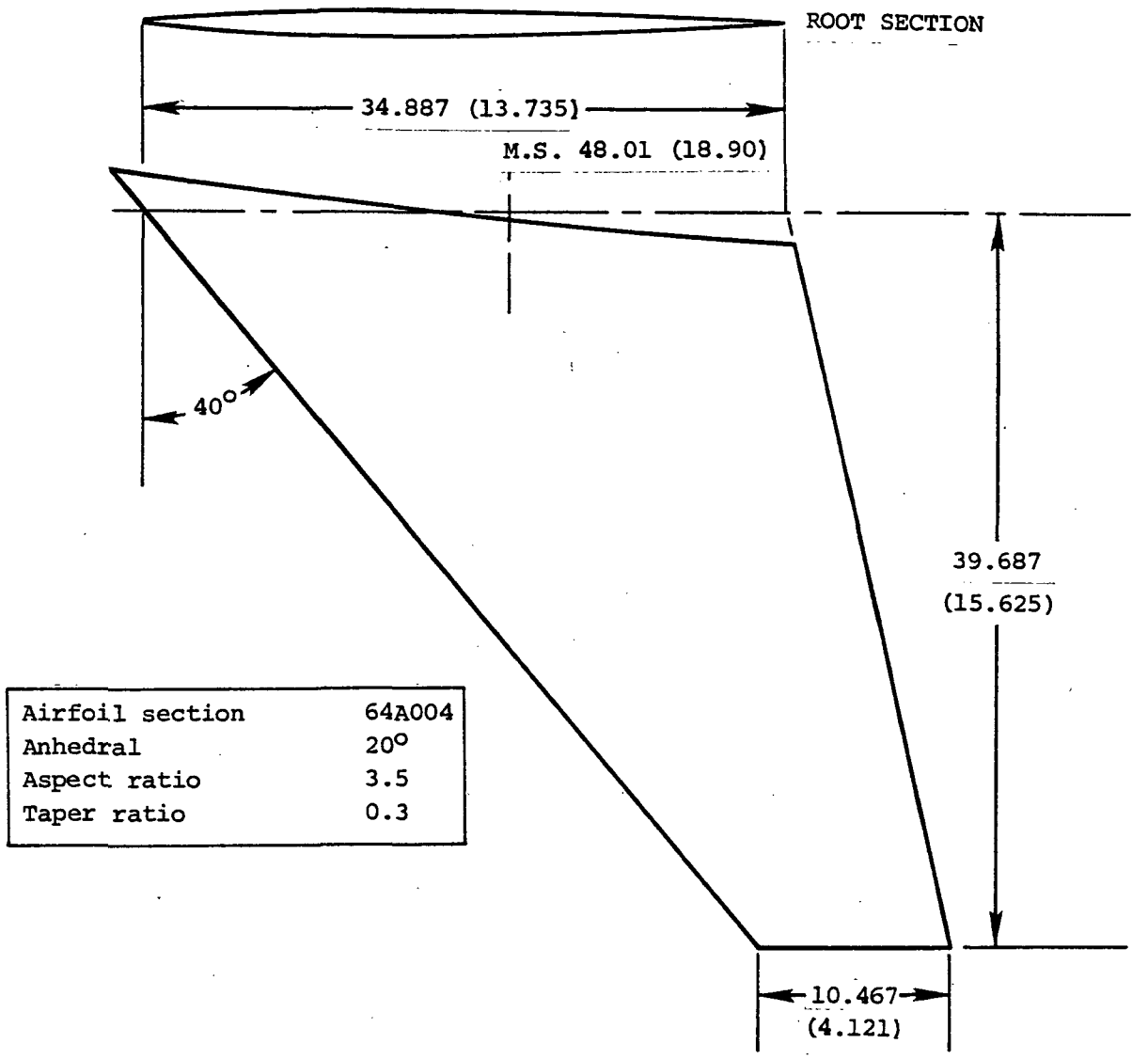

(b) canard

Figure 2. - concluded.

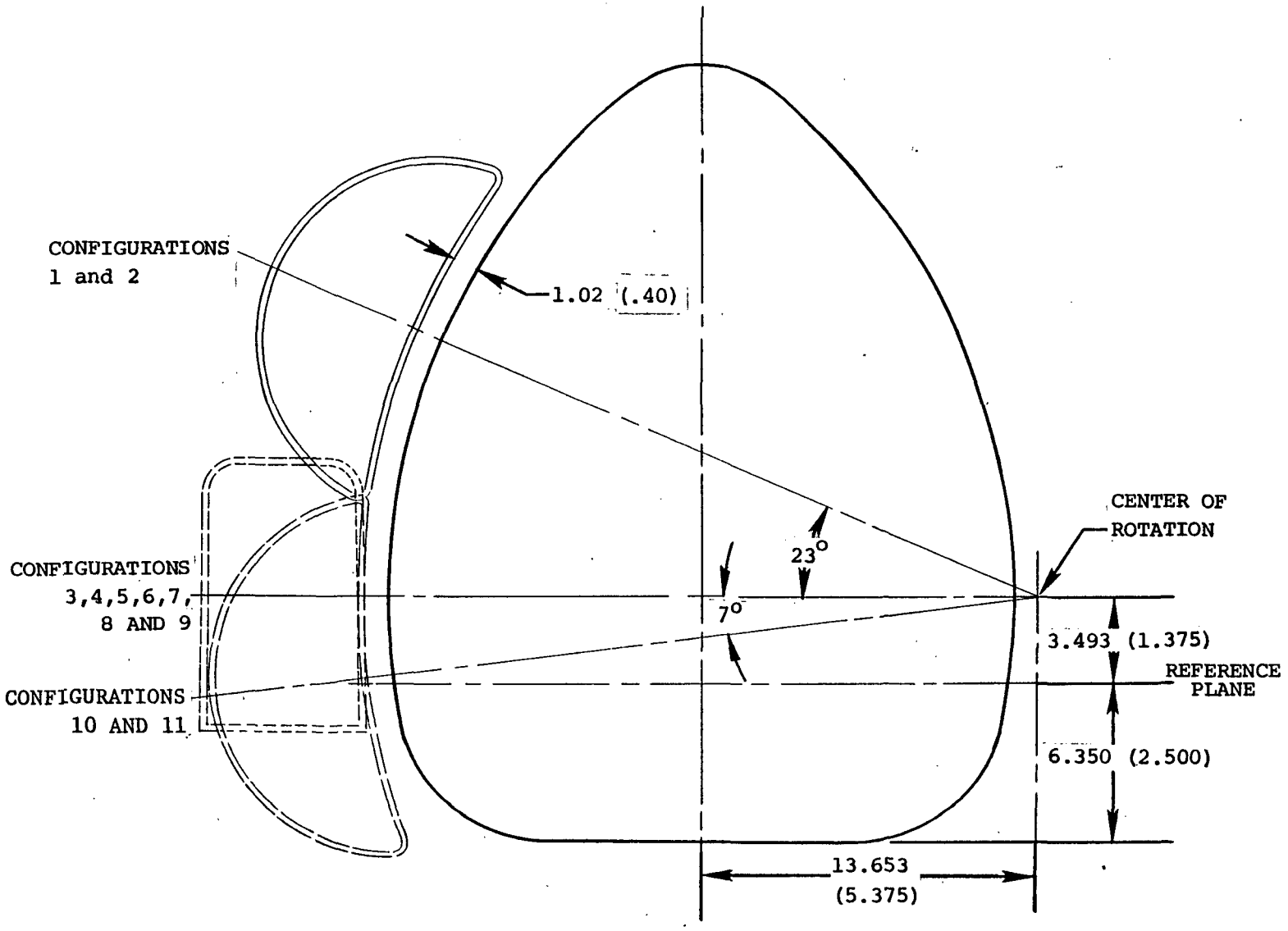

Figure 3. - Inlet locations.

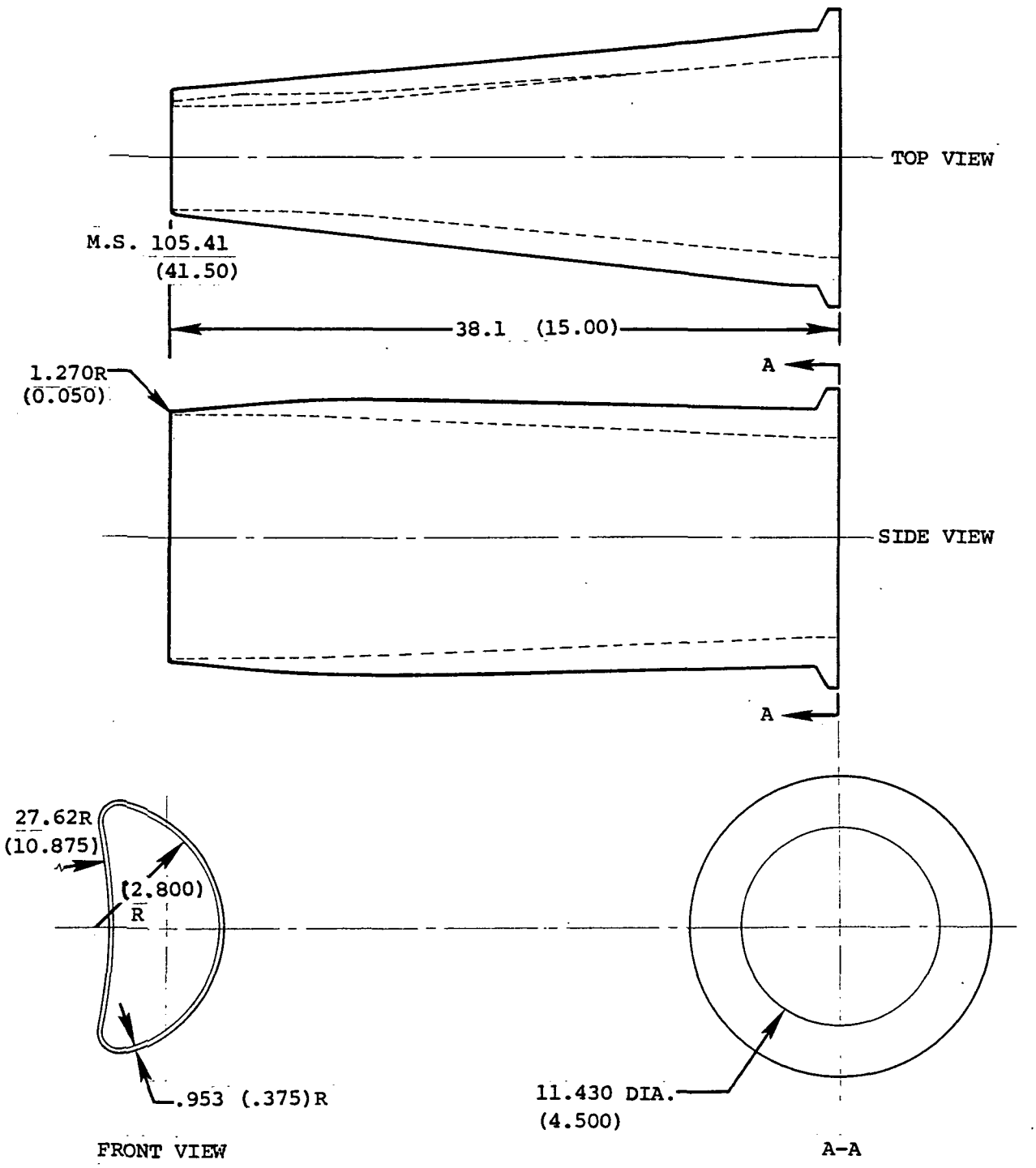

Figure 4. - Kidney-shaped inlet lines

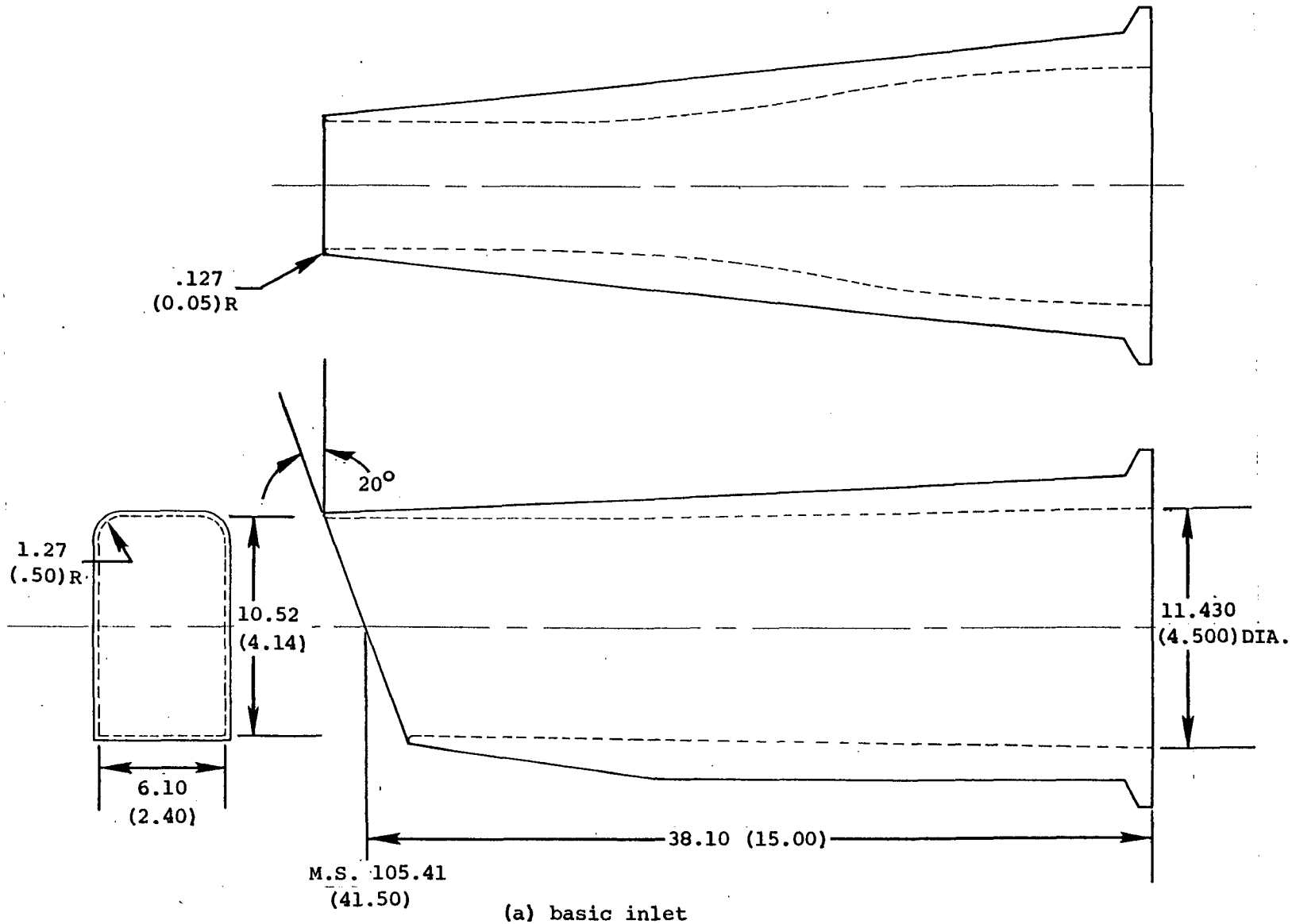

(a) basic inlet

Figure 5. - Two-dimensional inlet lines and lip contours

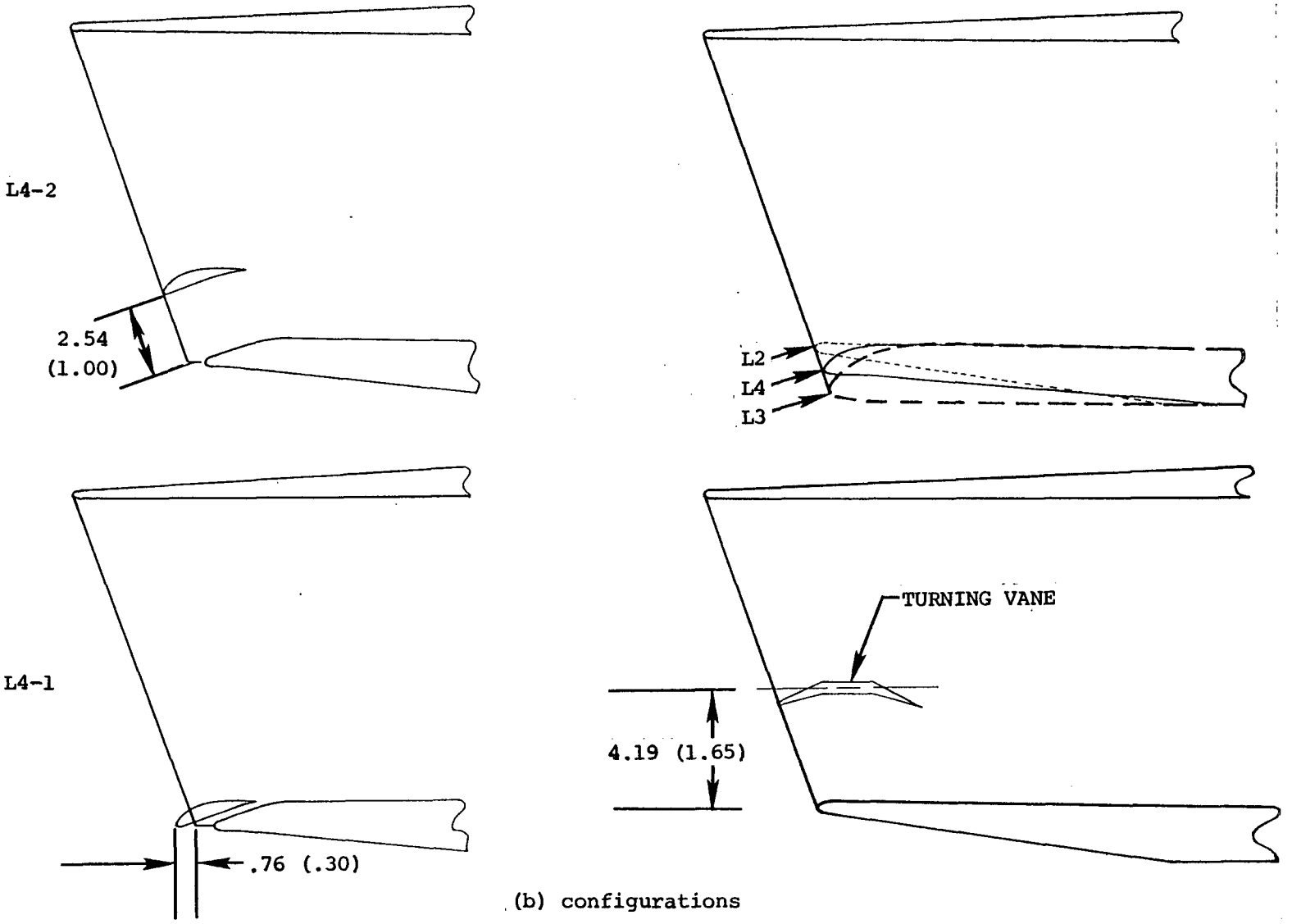

(b) configurations

Figure 5. - Two-dimensional inlet lines and lip contours.

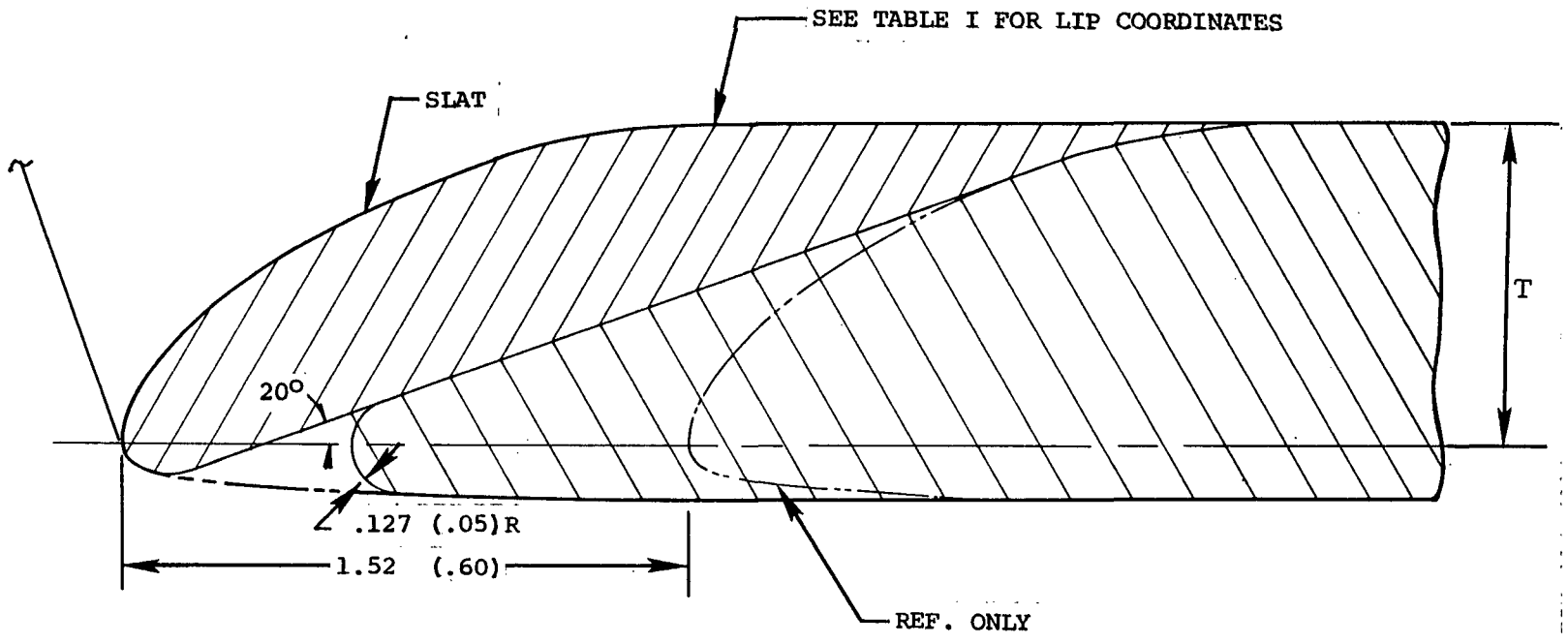

(c) slat lip

Figure 5. - Two dimensional inlet lines and lip contours.

TURNING VANE

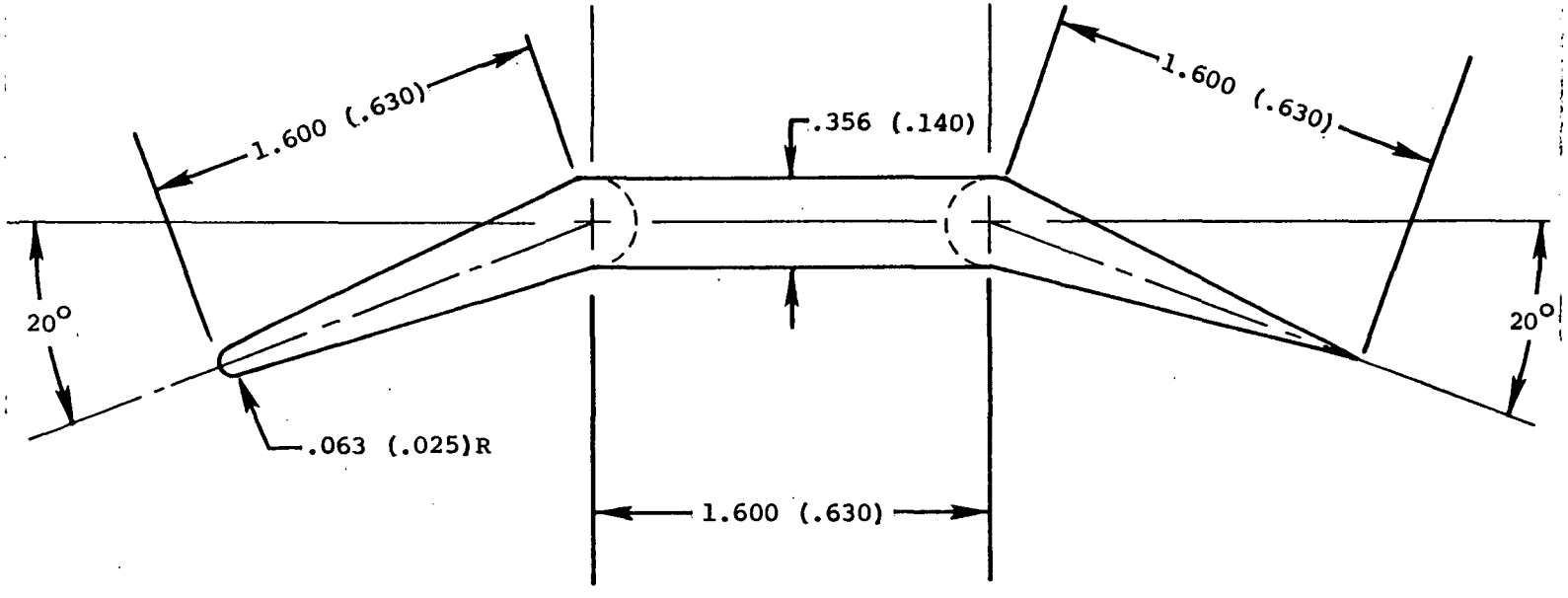

Figure 6. - Turning vane configuration.

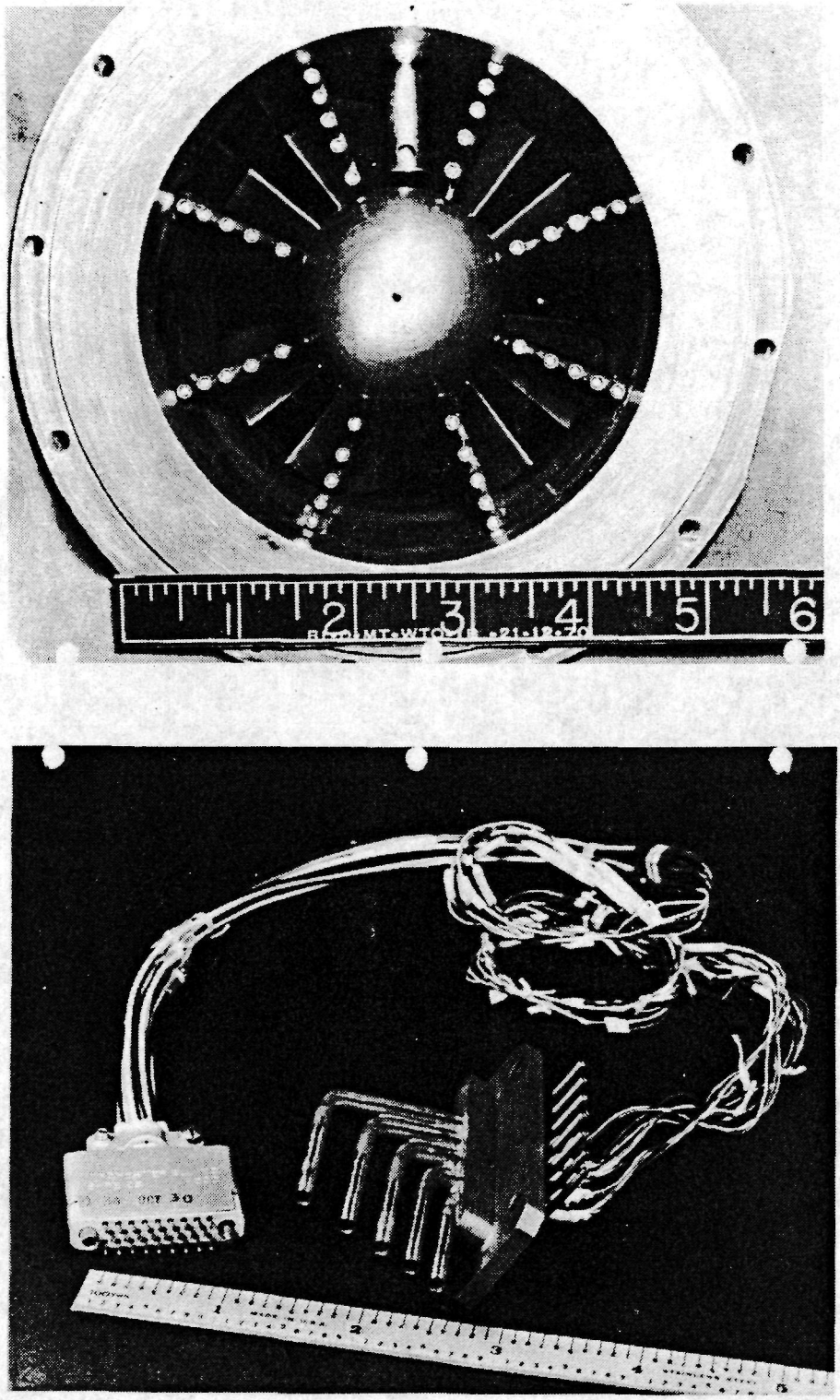

Figure 7.- Engine face rake assembly and flow control valve

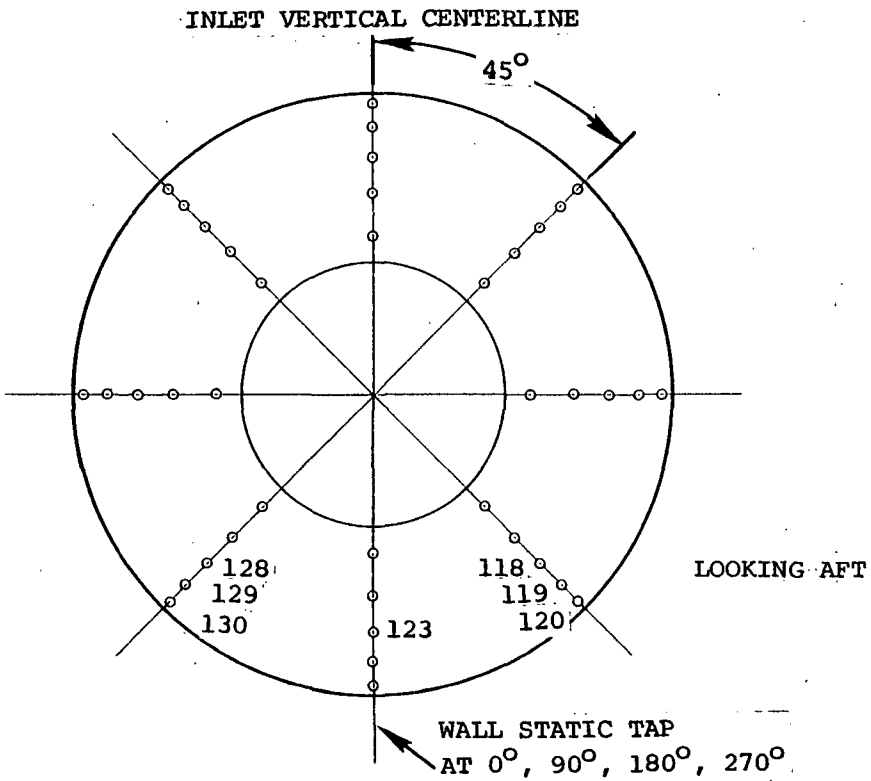

INNER RADIUS	2.494 (.982)
RING 1	2.977 (1.172)
RING 2	3.762 (1.481)
RING 3	4.409 (1.736)
RING 4	4.973 (1.958)
RING 5	5.479 (2.157)
OUTER RADIUS	5.715 (2.250)

NOTE:
Probe locations are rotated clockwise 45° for two-dimensional inlet tests

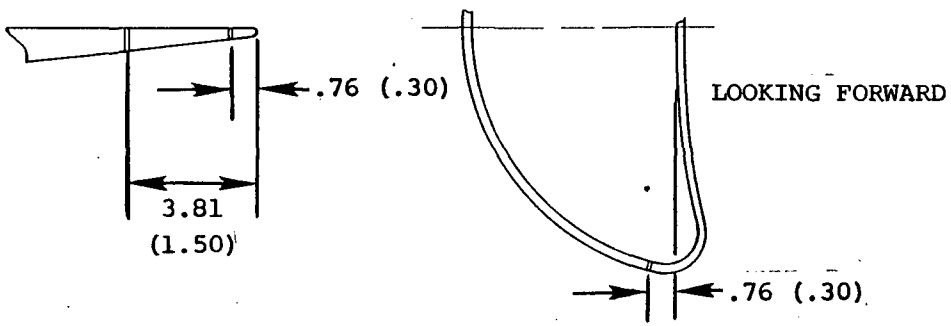

Figure 8. - Left inlet instrumentation.

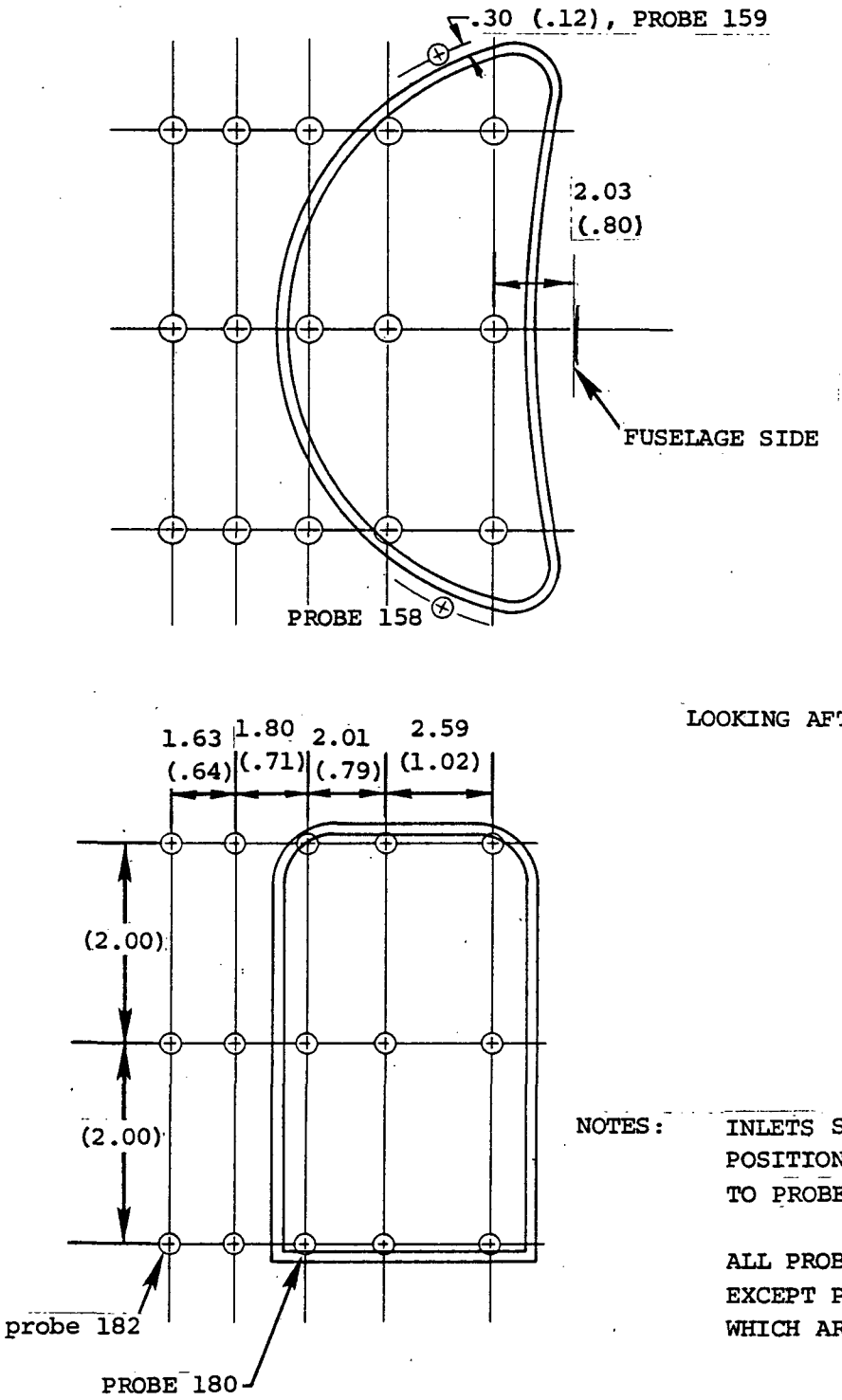

Figure 9. - Flow field instrumentation

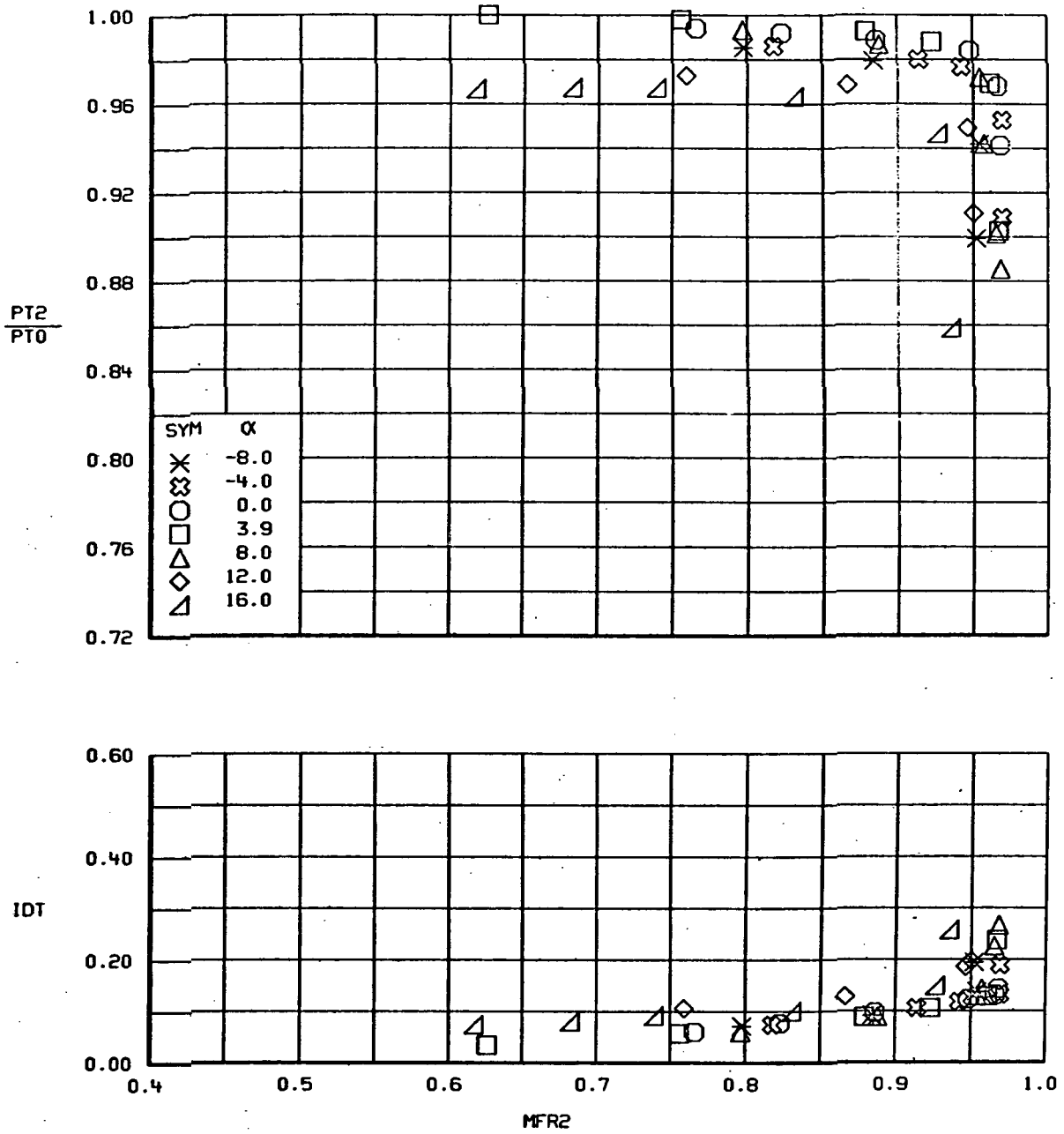

(a)

FIGURE 10.- VARIATION IN INLET PERFORMANCE WITH ANGLE OF ATTACK CONFIGURATION 1, $\delta=0°$, M=0.9, $\beta=0°$

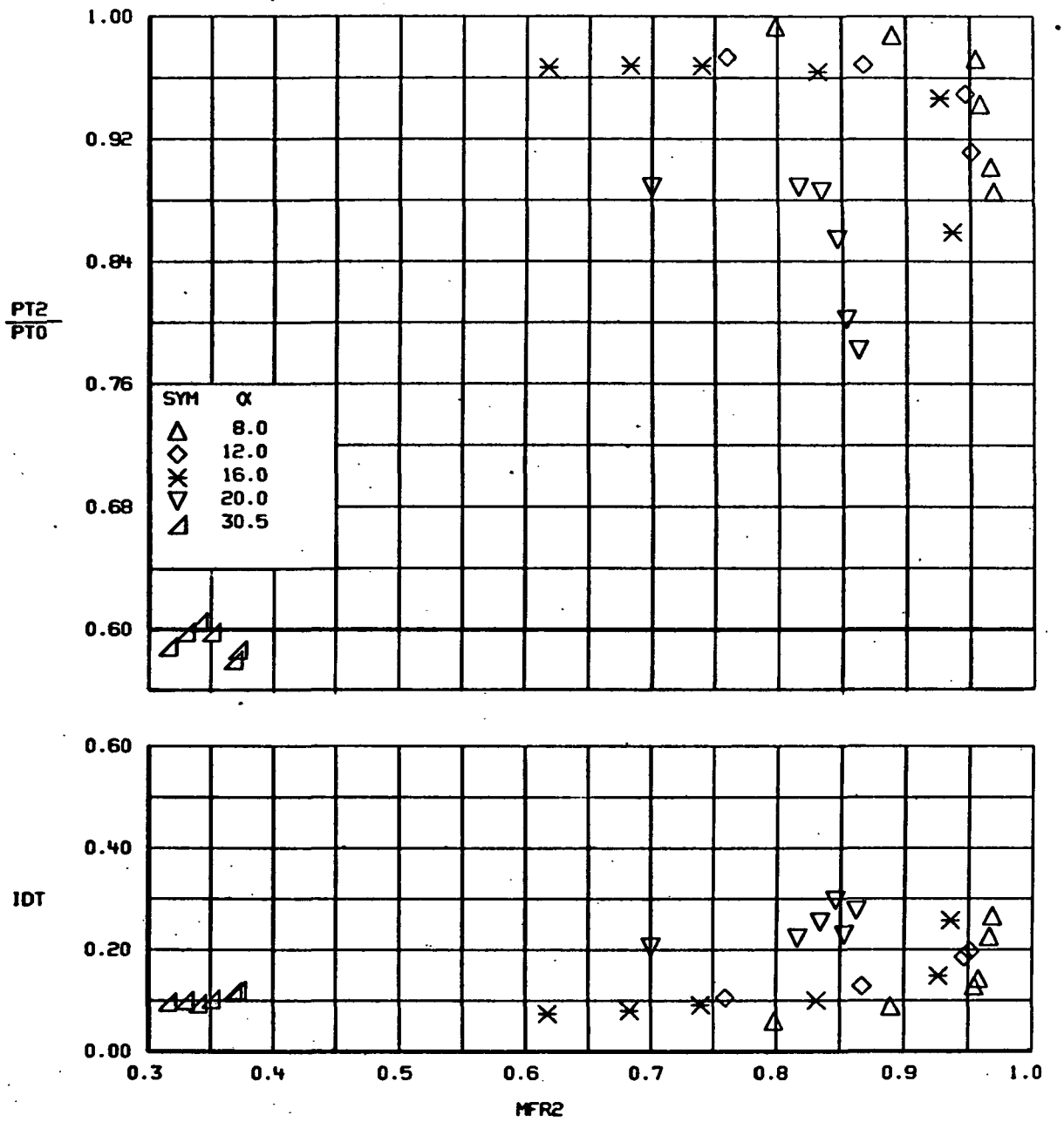

(b)

FIGURE 10.–Concluded.

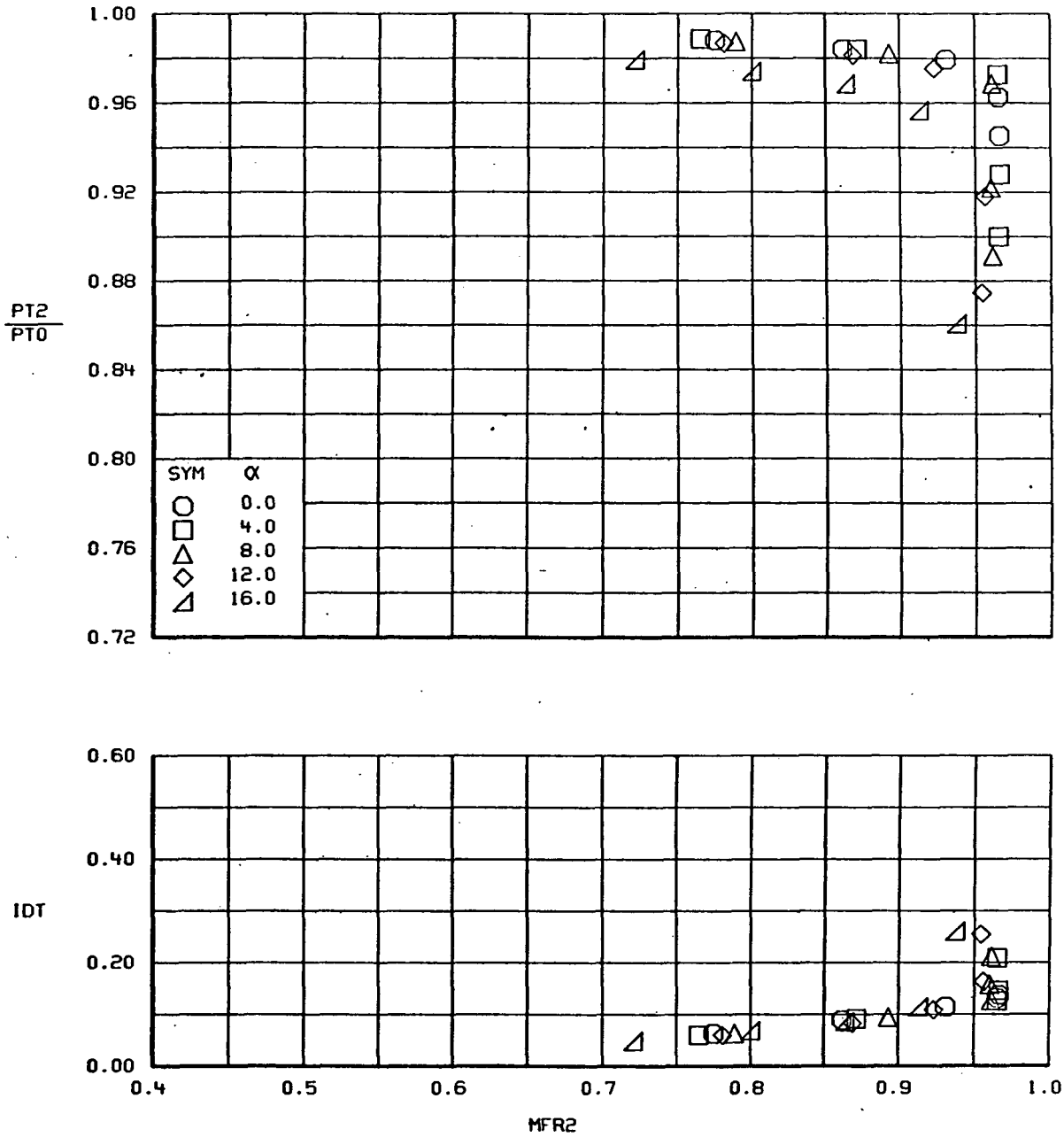

FIGURE 11.- VARIATION IN INLET PERFORMANCE WITH ANGLE OF ATTACK
CONFIGURATION 1, δ=5°, M=0.9, β=0°

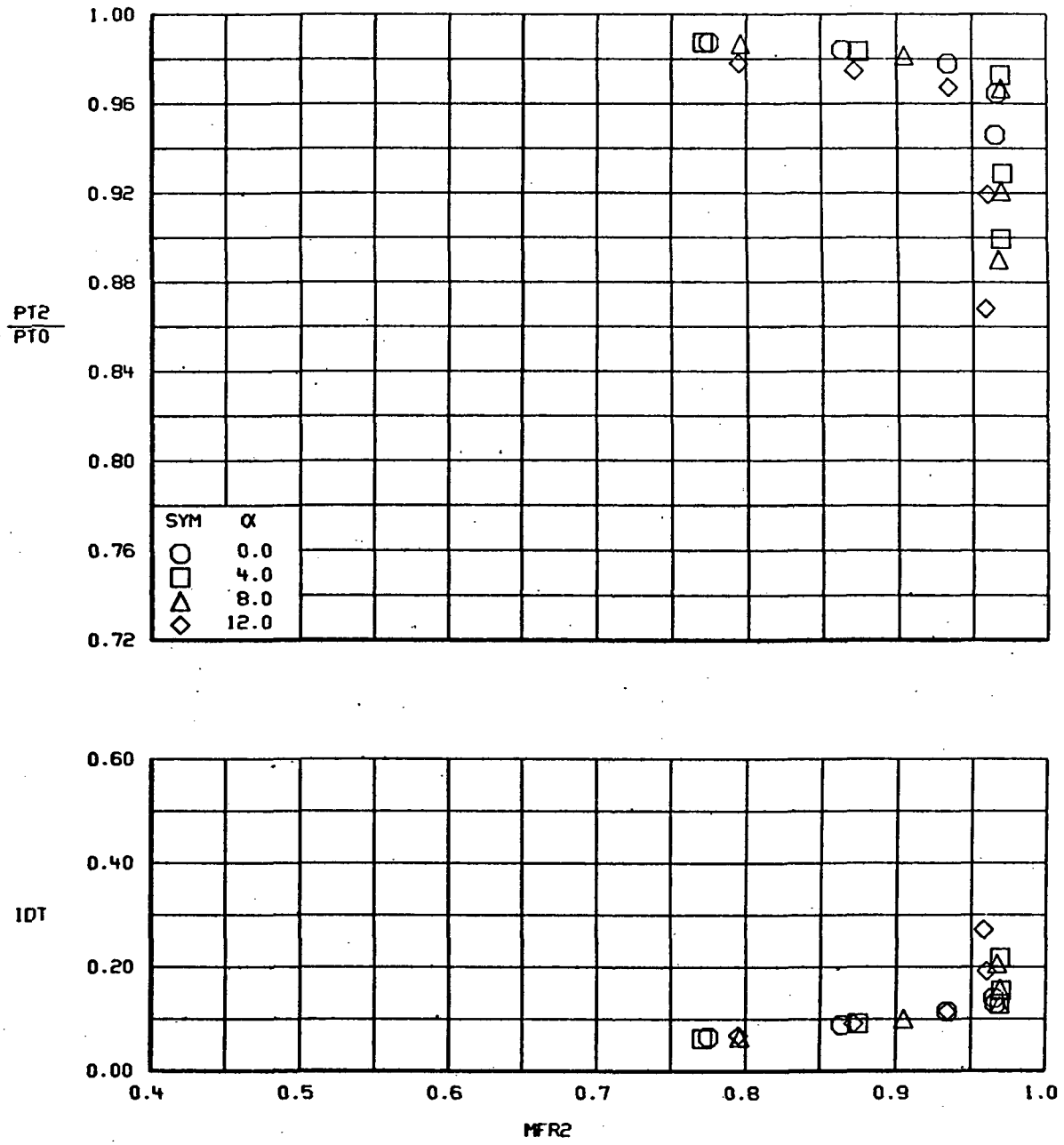

FIGURE 12.- VARIATION IN INLET PERFORMANCE WITH ANGLE OF ATTACK
CONFIGURATION 1, δ=10°, M=0.9, β=0°

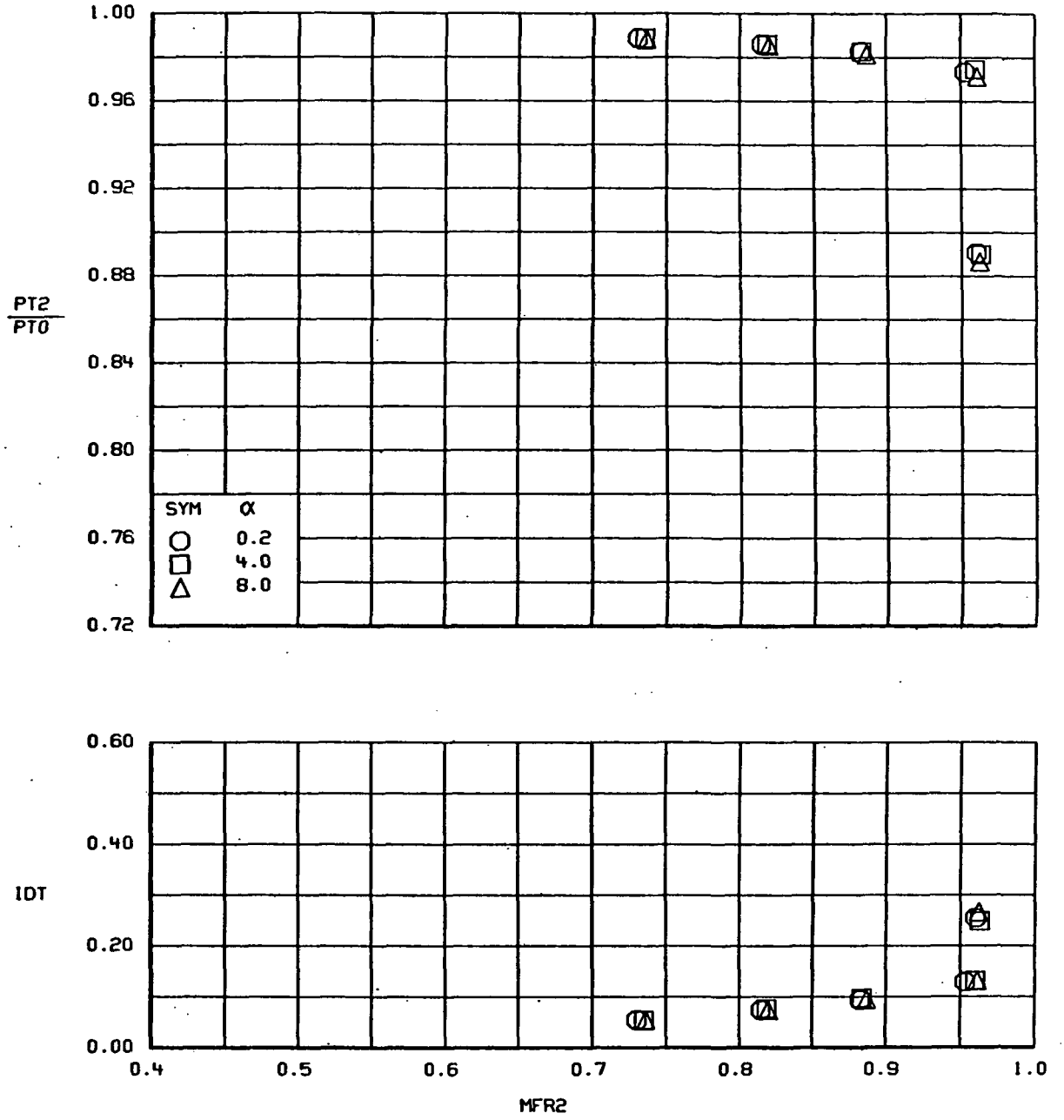

FIGURE 13.- VARIATION IN INLET PERFORMANCE WITH ANGLE OF ATTACK
CONFIGURATION 1, δ=15°, M=0.9, β=0°

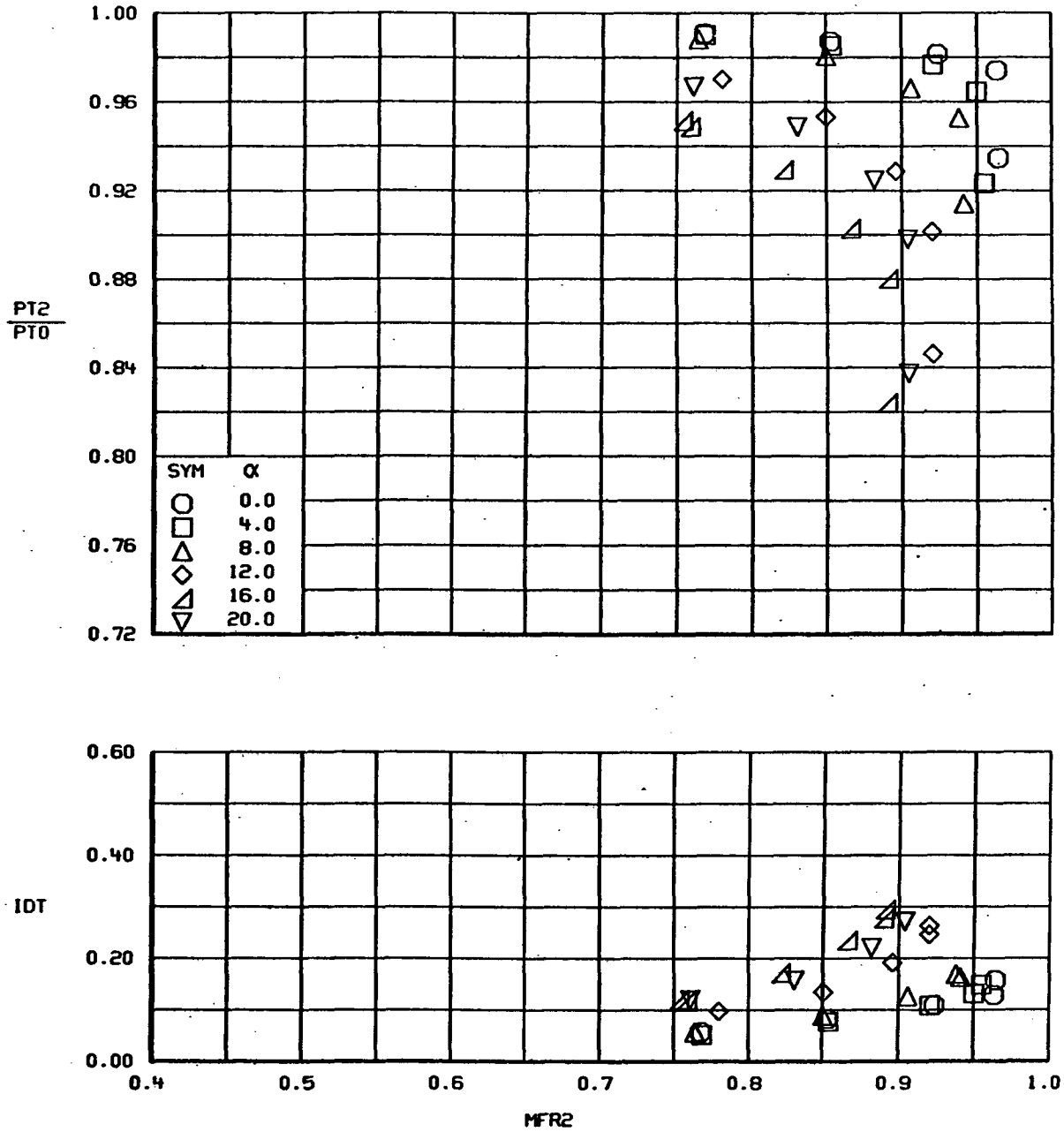

FIGURE 14.-VARIATION IN INLET PERFORMANCE WITH ANGLE OF ATTACK
CONFIGURATION 1, δ=-10°, M=0.9, β=0°

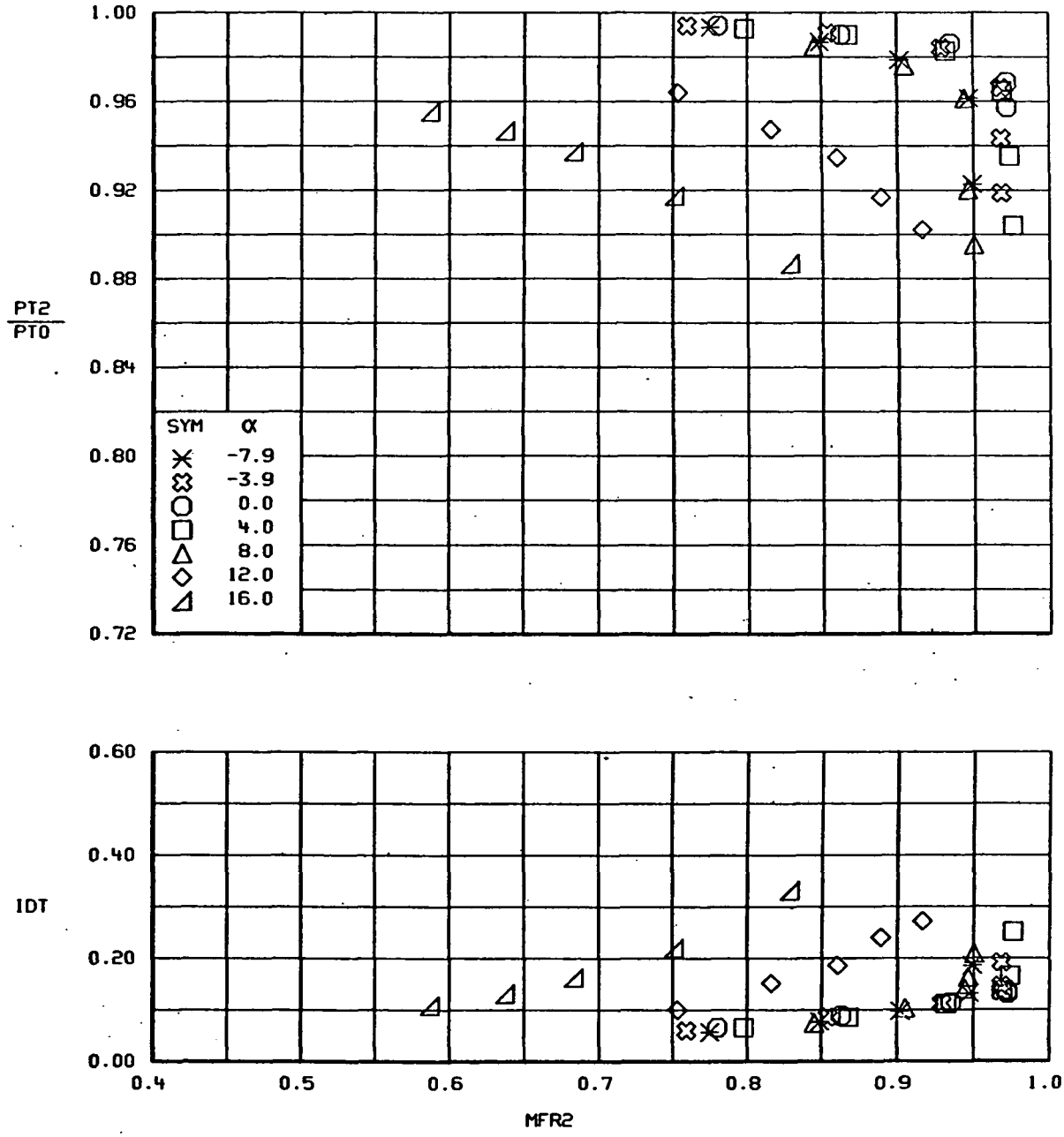

(a)

FIGURE 15.- VARIATION IN INLET PERFORMANCE WITH ANGLE OF ATTACK CONFIGURATION 2, M=0.9, $\beta=0^{\circ}$

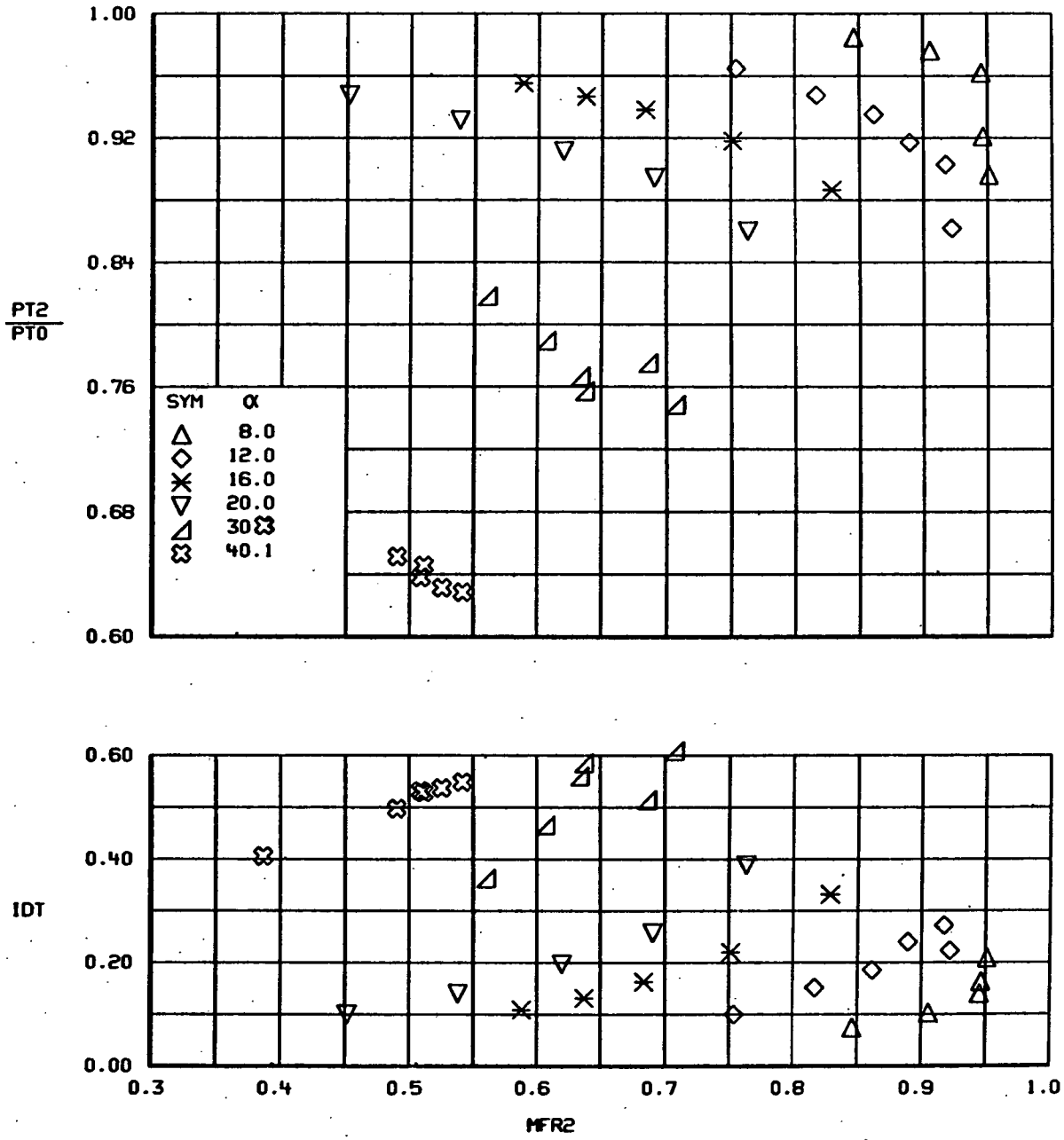

(b)

FIGURE 15.-Concluded.

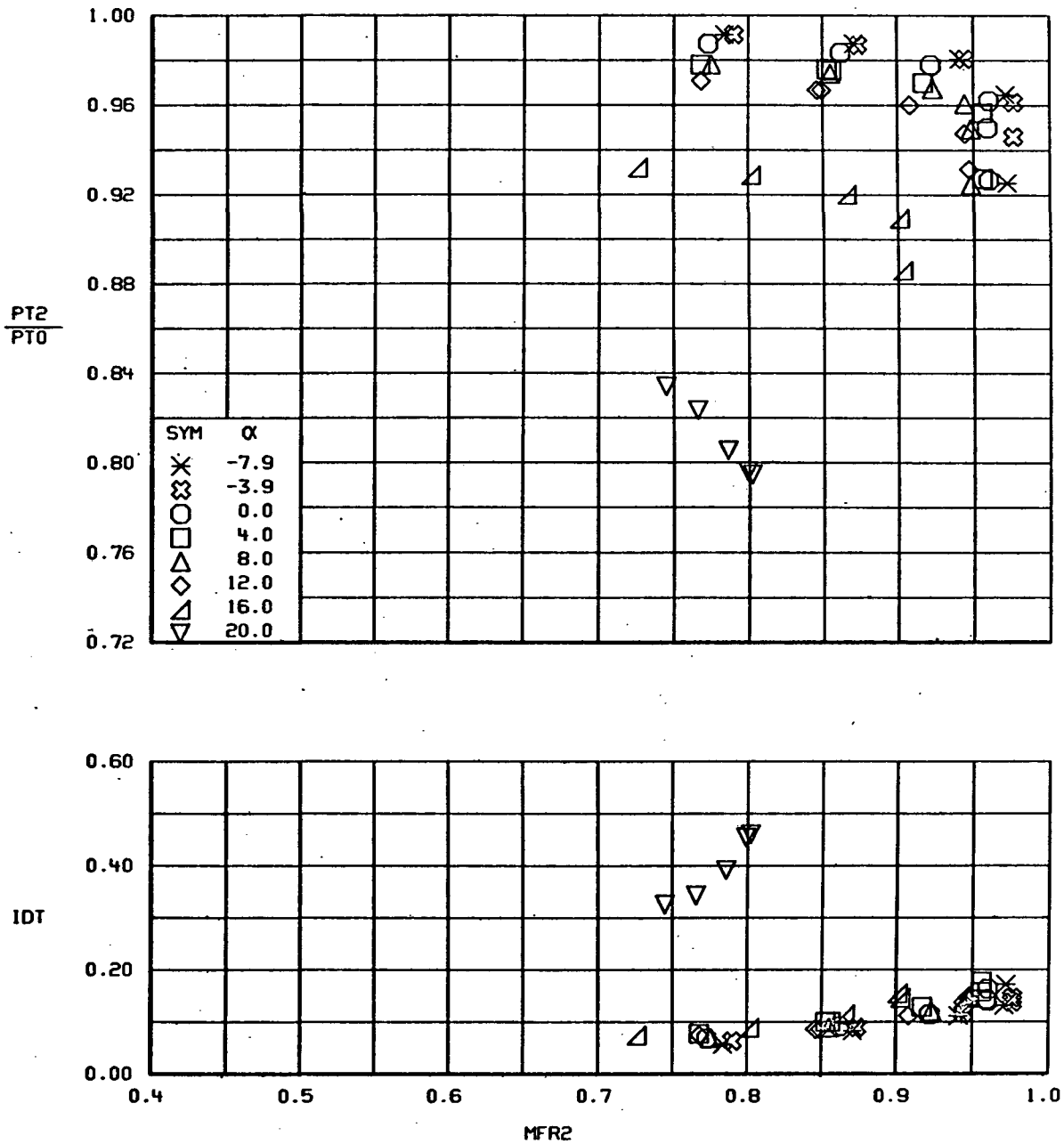

FIGURE 16.- VARIATION IN INLET PERFORMANCE WITH ANGLE OF ATTACK
CONFIGURATION 10.δ=0°, M=0.9, β=0

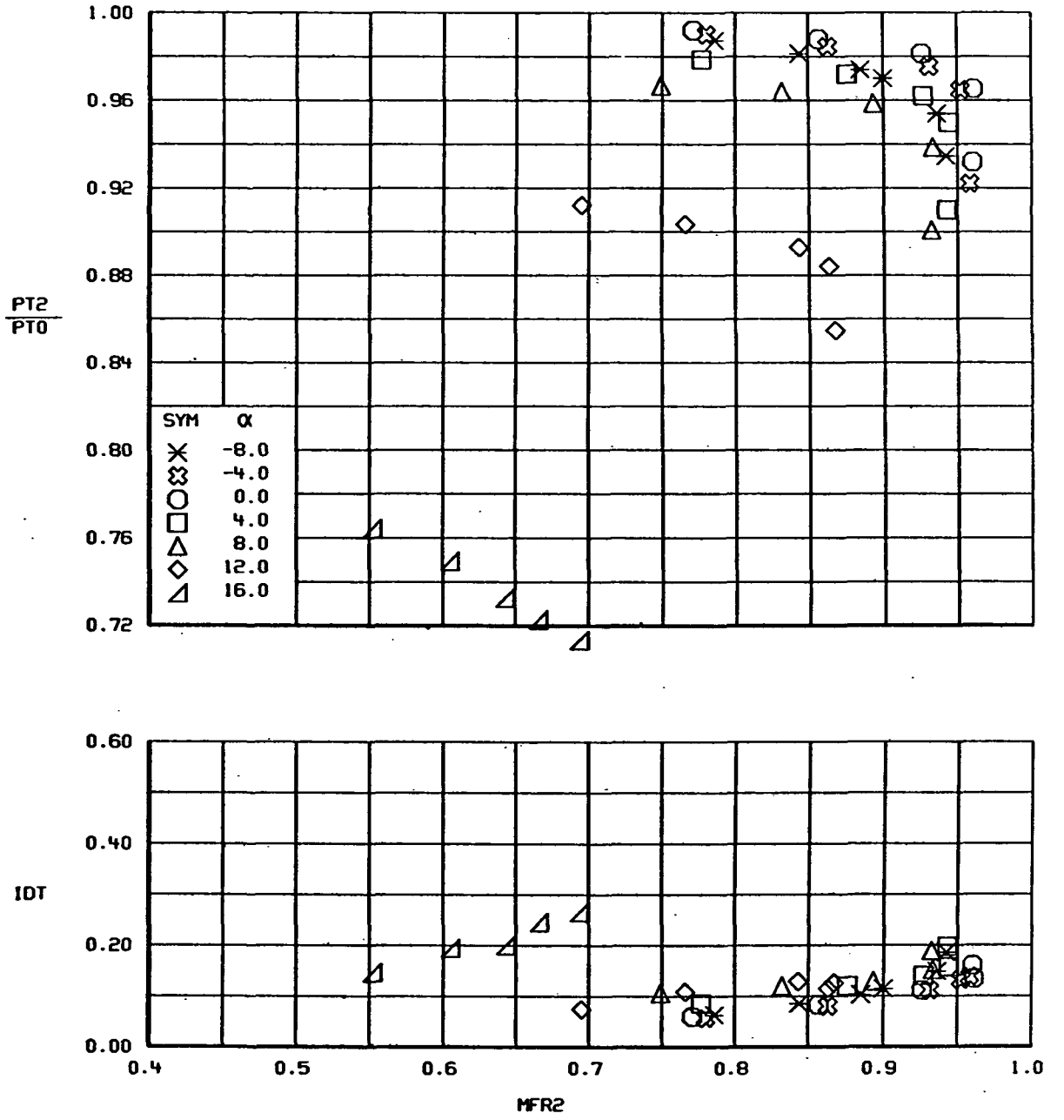

FIGURE 17.- VARIATION IN INLET PERFORMANCE WITH ANGLE OF ATTACK
CONFIGURATION 10, δ=10°, M=0.9, β=0°

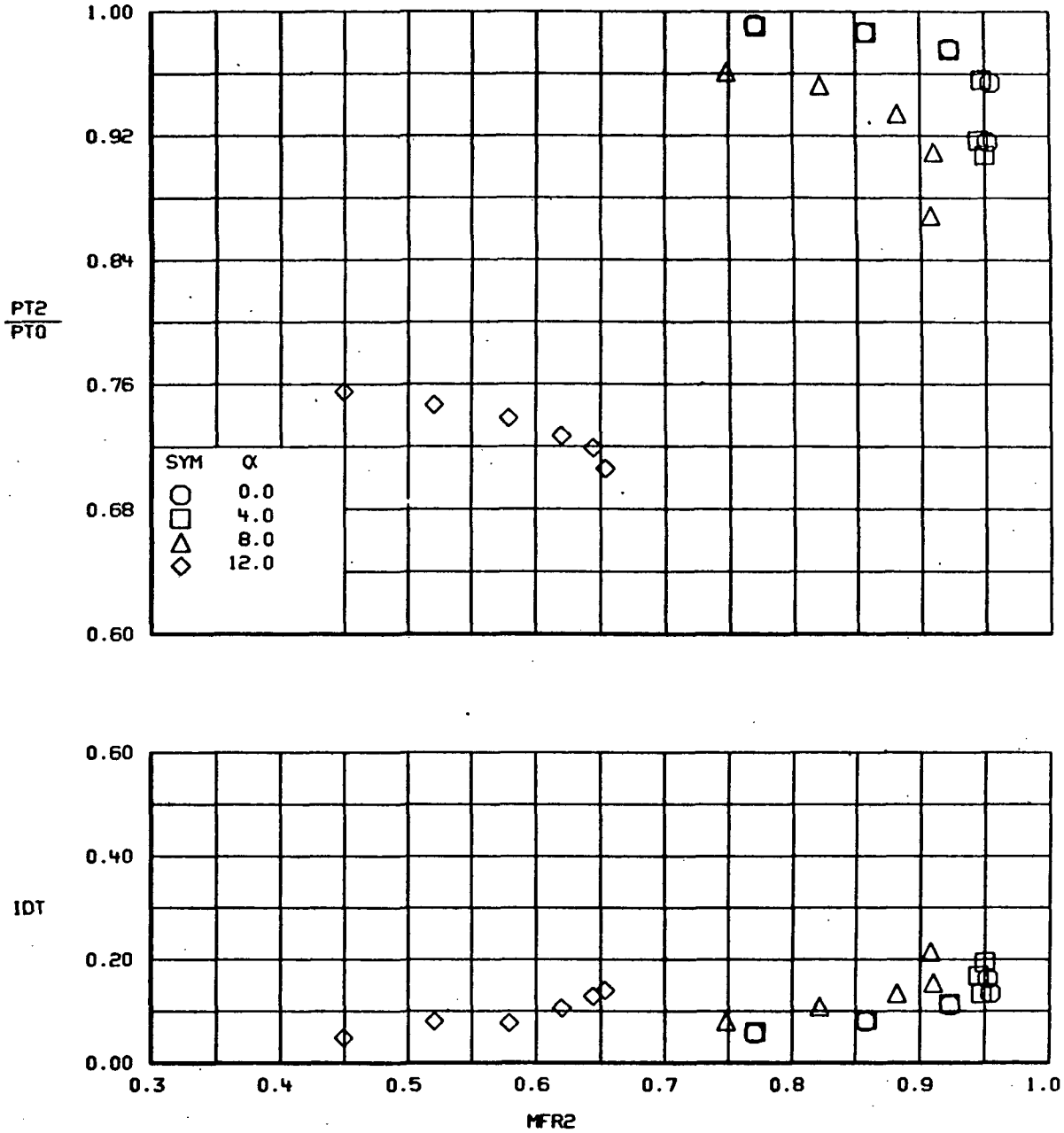

FIGURE 18.- VARIATION IN INLET PERFORMANCE WITH ANGLE OF ATTACK
CONFIGURATION 10, δ=15°, M=0.9, β=0°

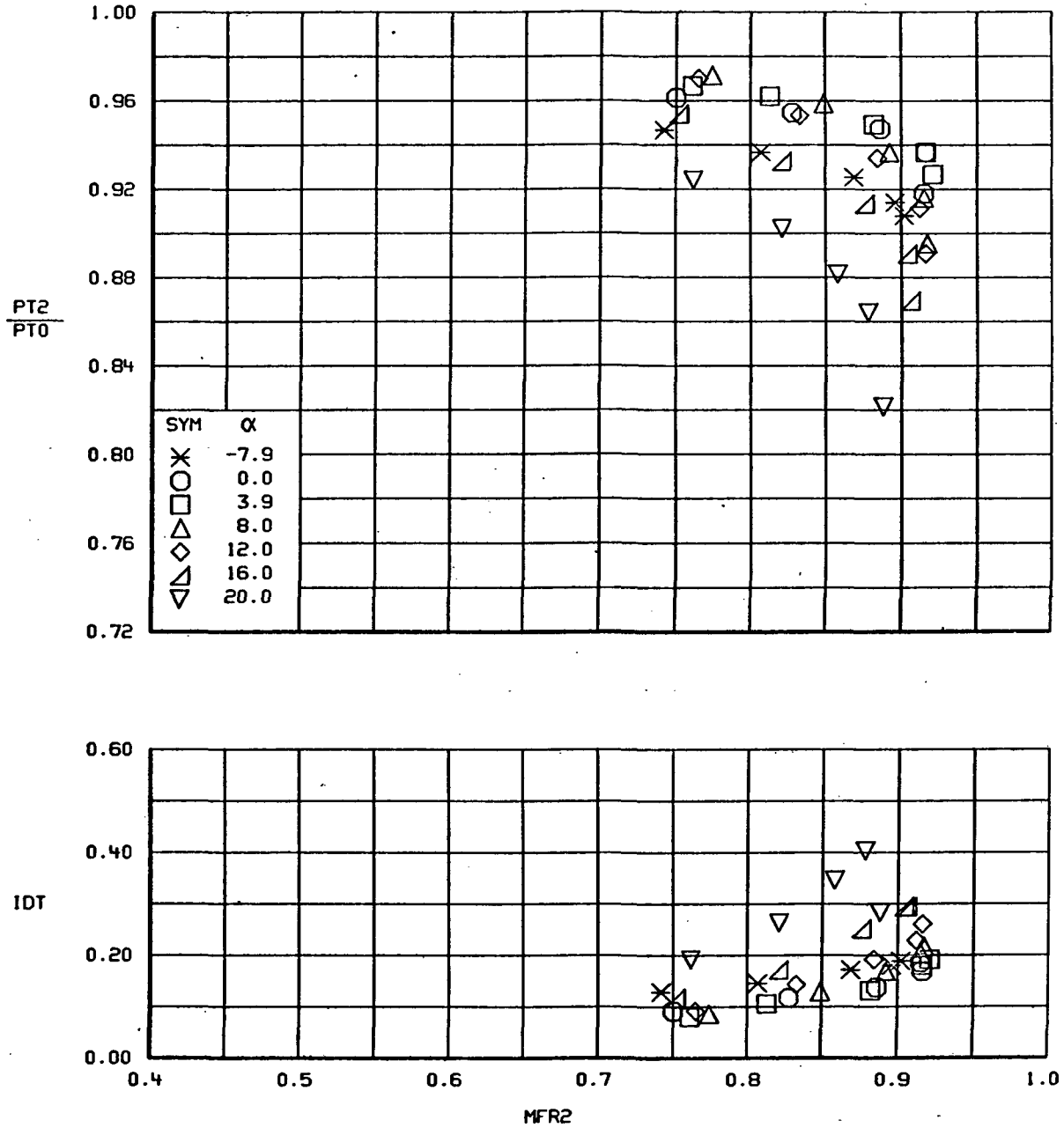

FIGURE 19.—VARIATION IN INLET PERFORMANCE WITH ANGLE OF ATTACK
CONFIGURATION 10, δ=10°, M=0.9, β=0°

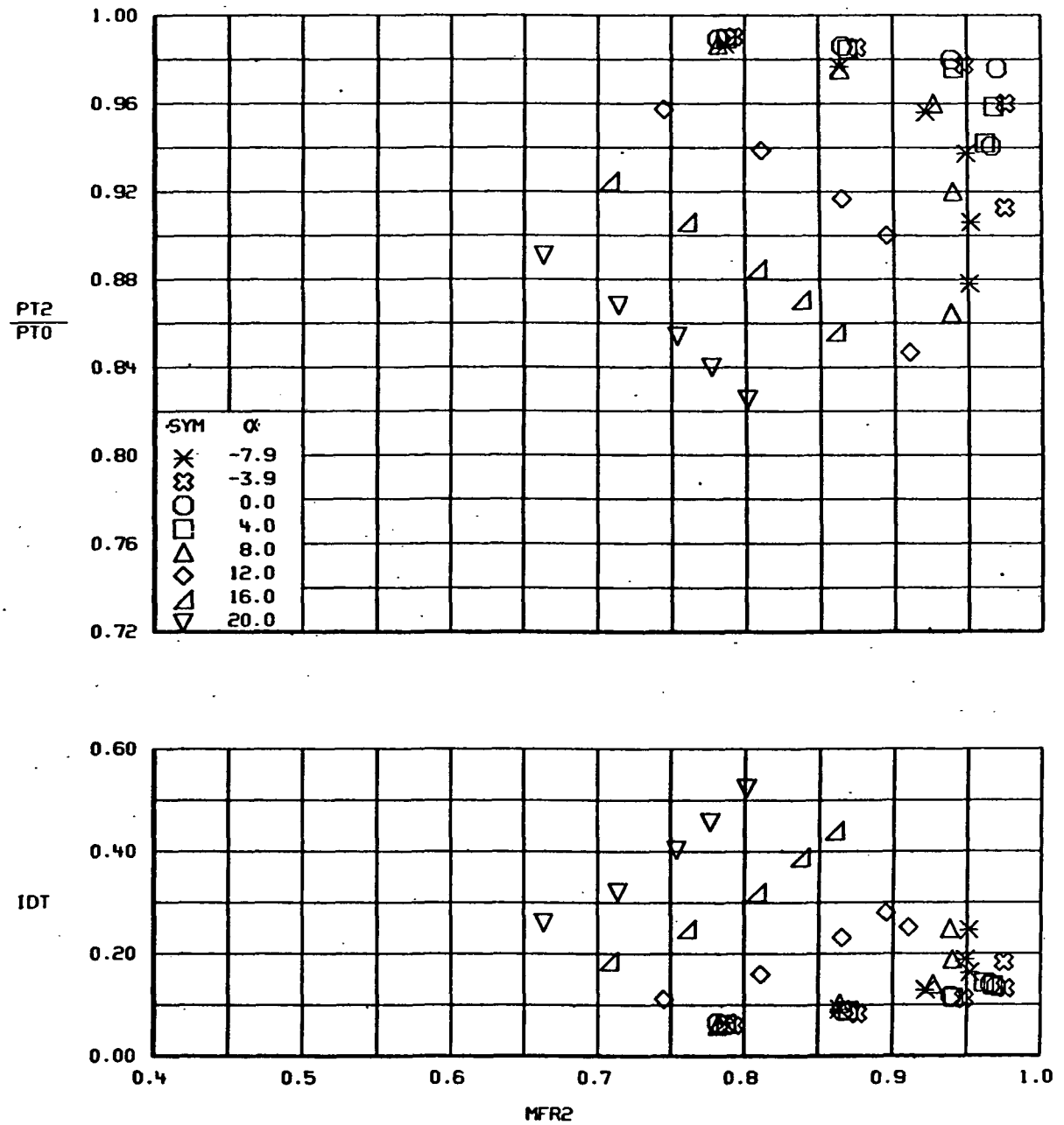

FIGURE 20.- VARIATION IN INLET PERFORMANCE WITH ANGLE OF ATTACK
CONFIGURATION 11, M=0.9, β=0°

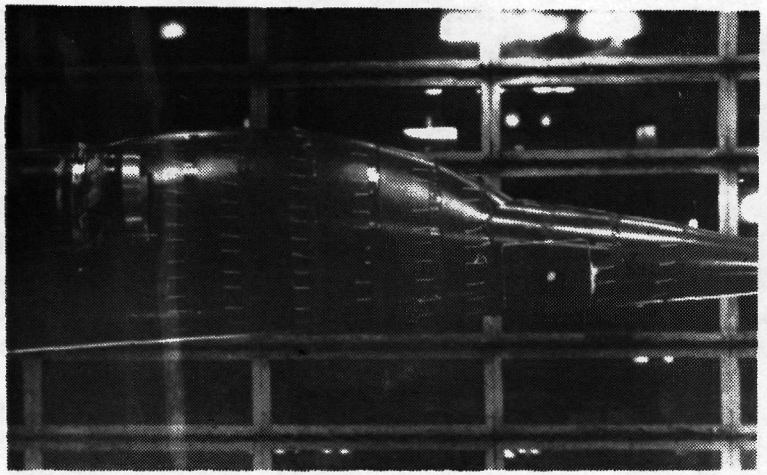

No canard
α = 4°

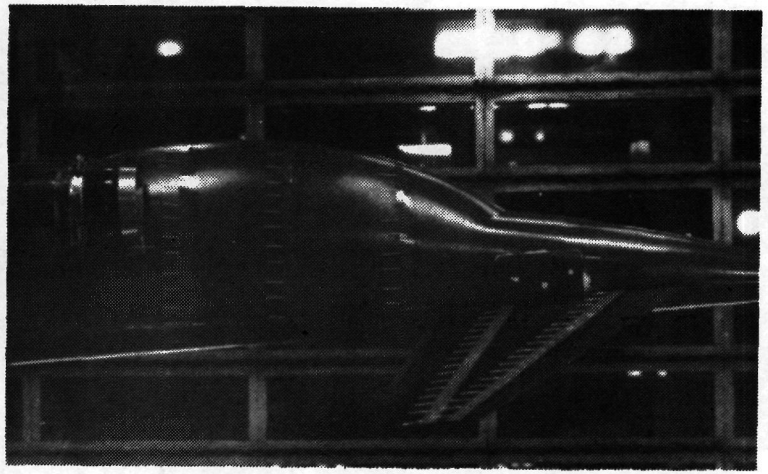

δ = 0°
α = 4°

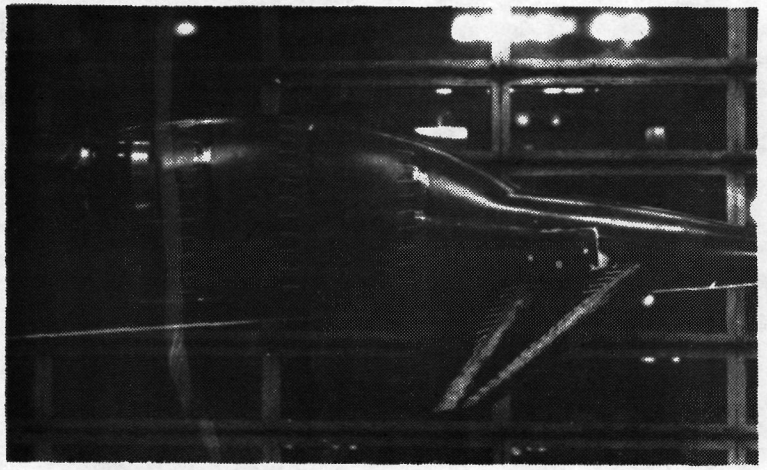

δ = 5°
α = 4°

δ = 15°
α = 16°

Figure 21. - Tuft patterns, configurations 1 and 2, M = 0.9, β = 0°.

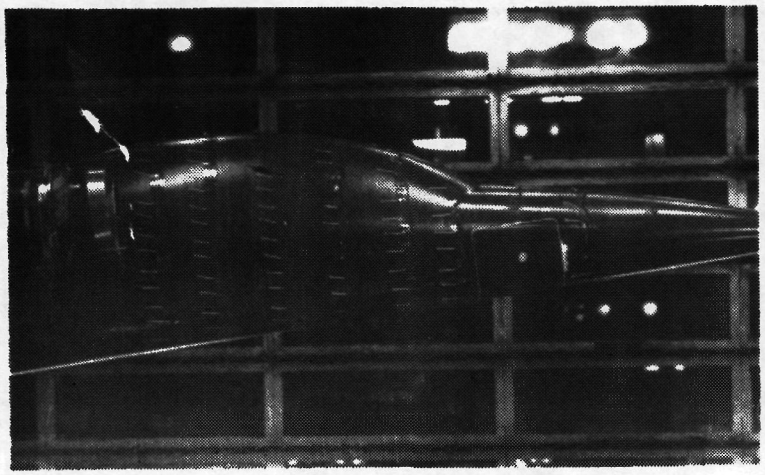

No canard
α = 8°

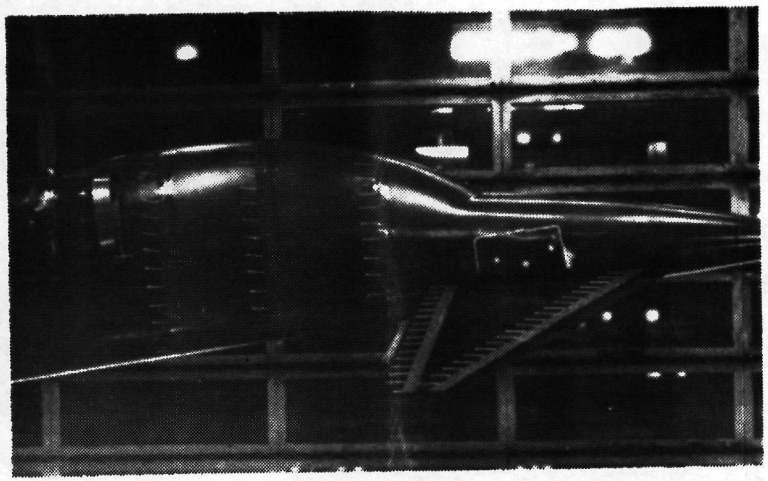

δ = -10°
α = 8°

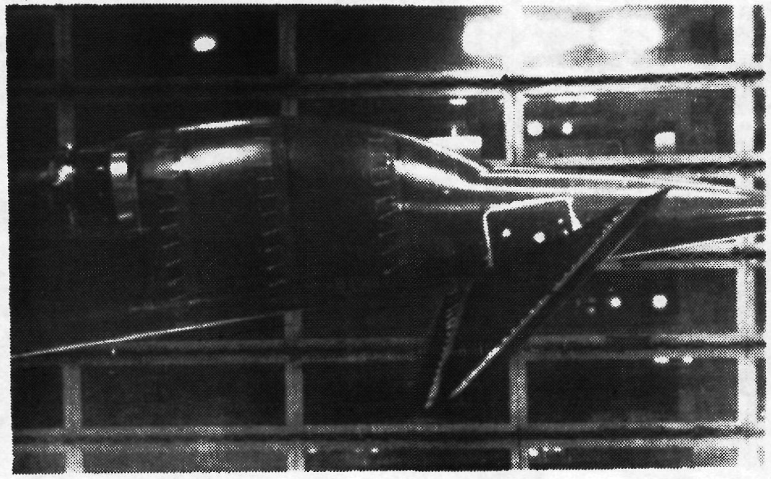

δ = 15°
α = 8°

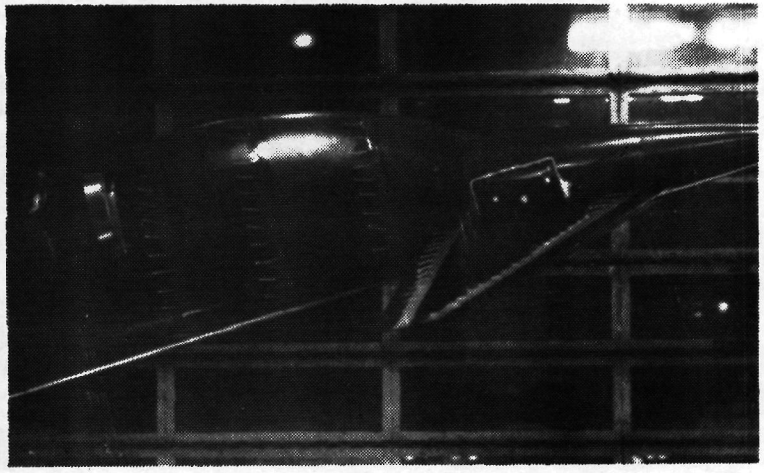

δ = -10°
α = 16°

Figure 21. - Concluded.

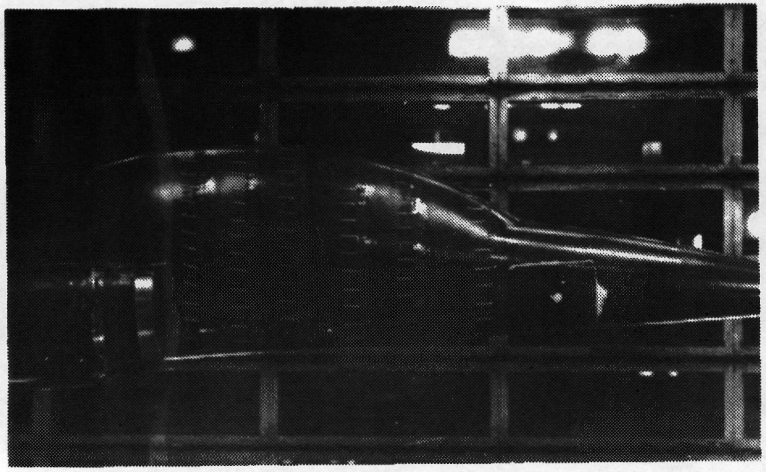

No canard
α = 4°

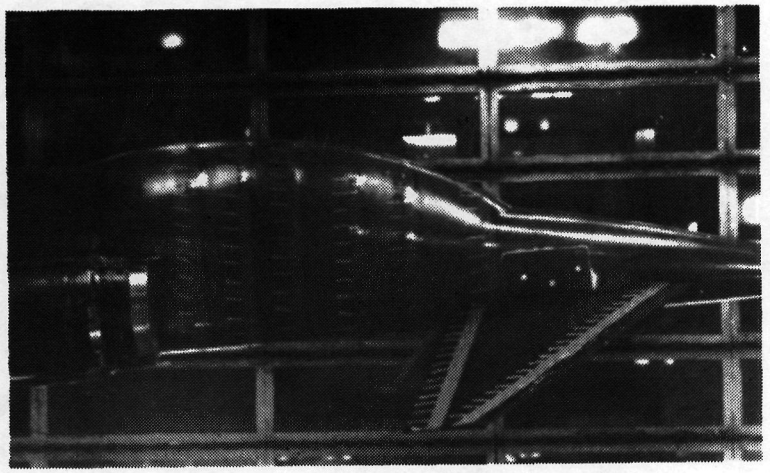

δ = 0°
α = 4°

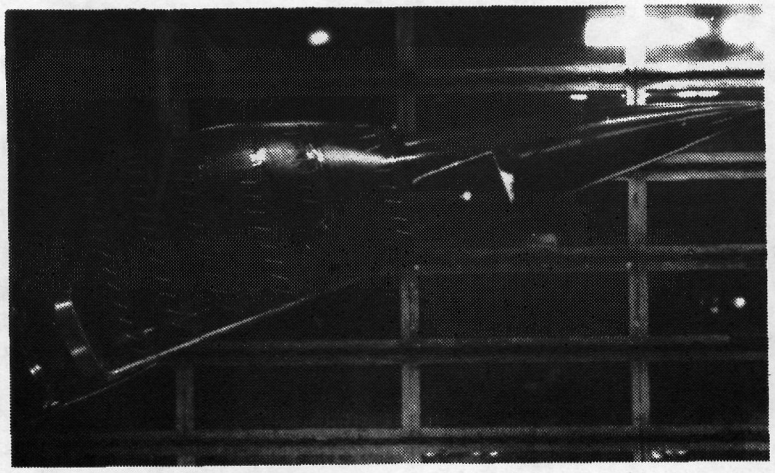

No canard
α = 20°

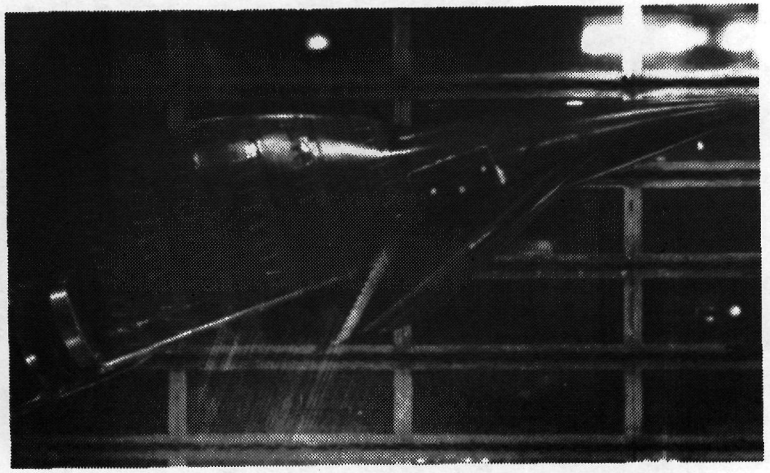

δ = 0°
α = 20°

Figure 22. - Tuft patterns, configurations 10 and 11, M = 0.9, β = 0°.

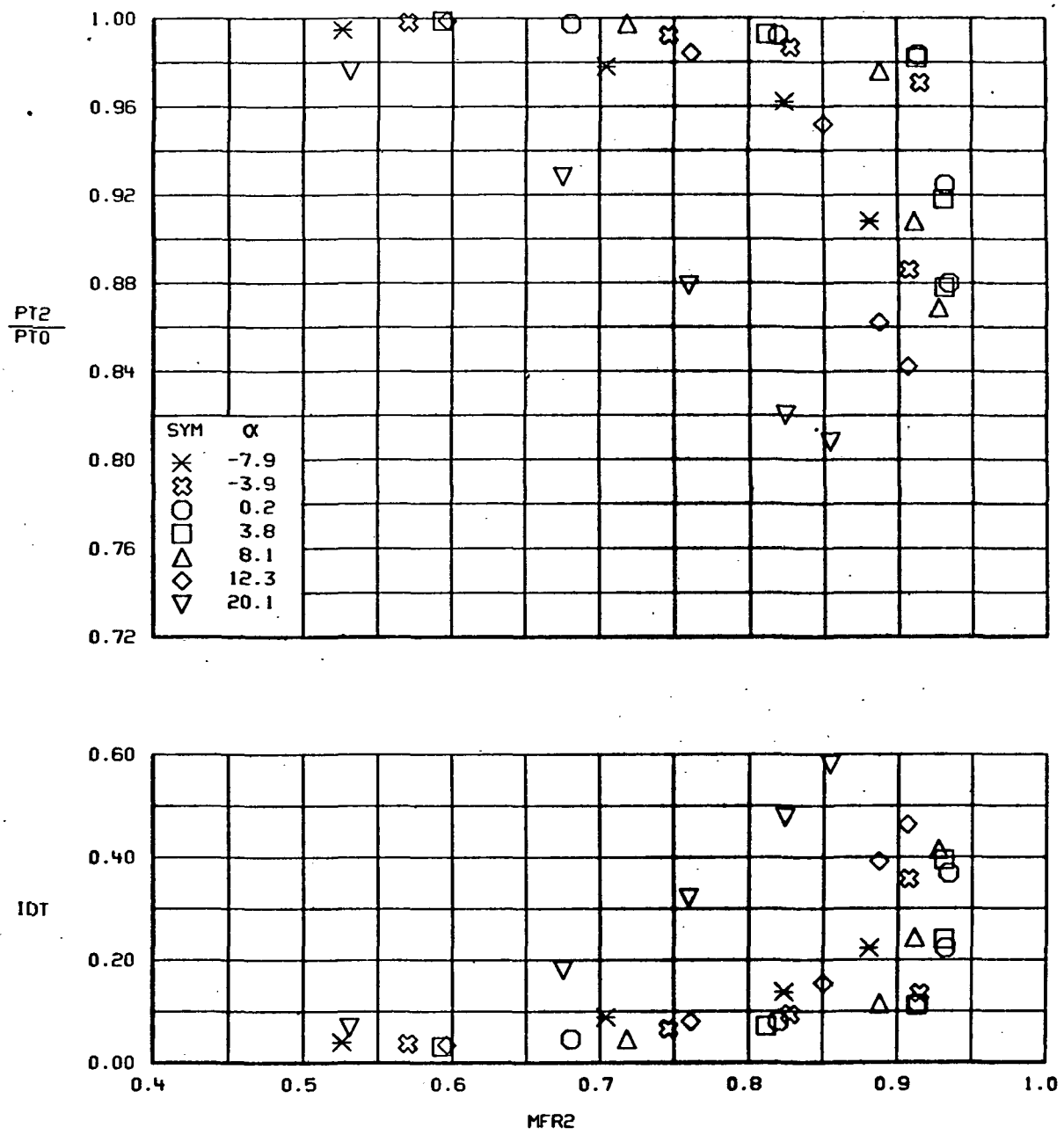

(a)

FIGURE 23.- VARIATION IN INLET PERFORMANCE WITH ANGLE OF ATTACK CONFIGURATION 3, M=0.9, β=0°

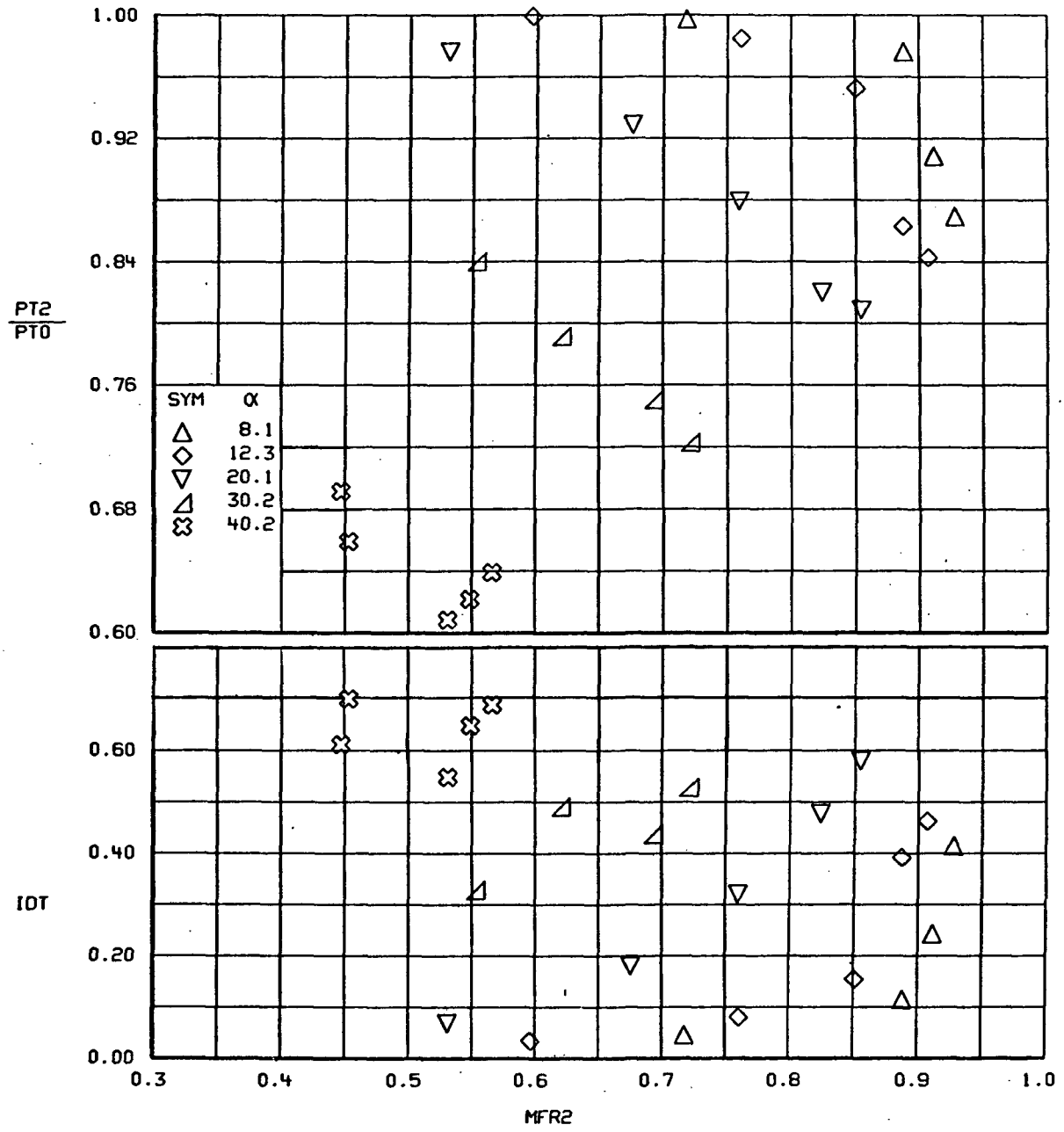

(b)

FIGURE 23.-Concluded.

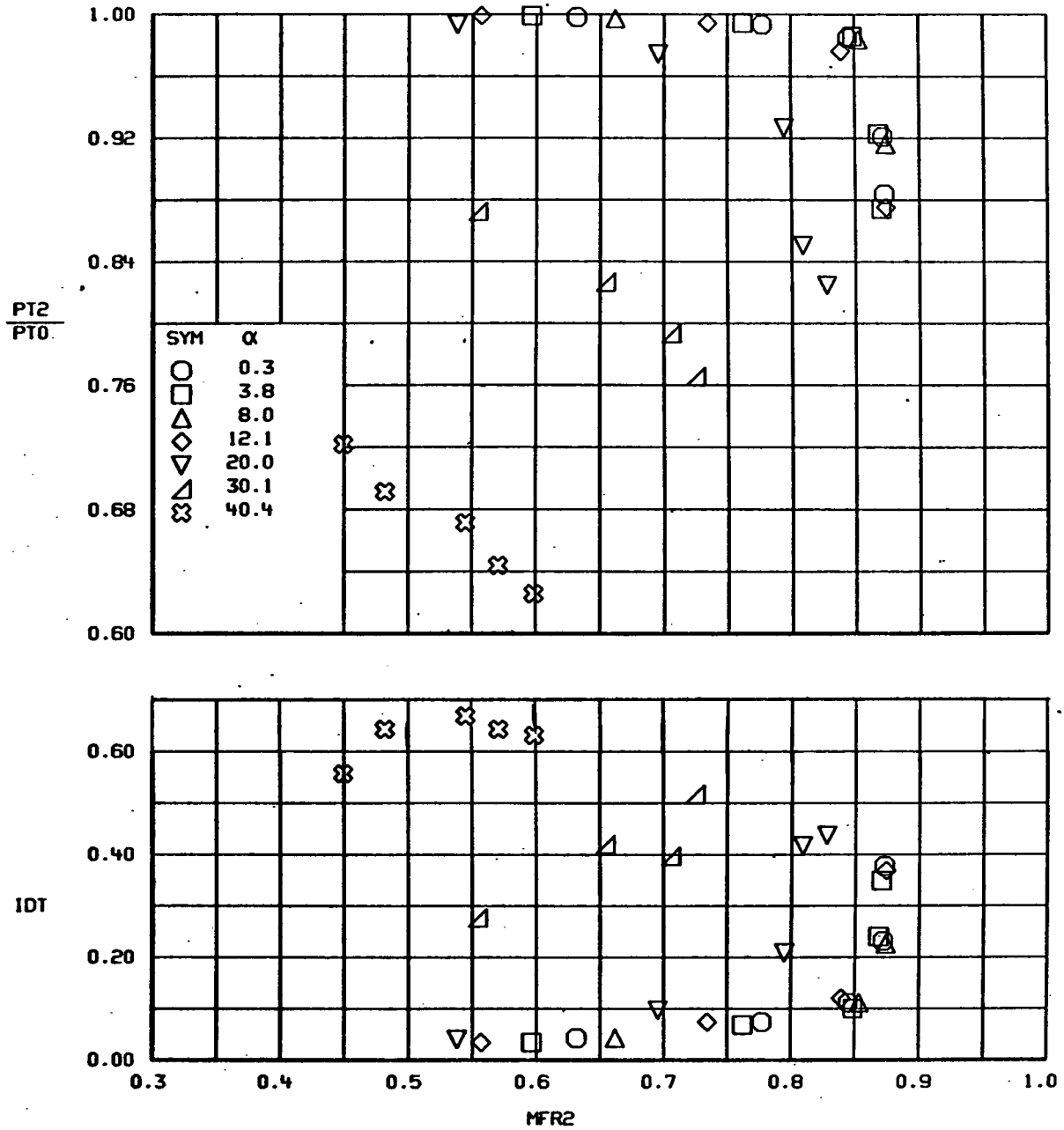

FIGURE 24.-VARIATION IN INLET PERFORMANCE WITH ANGLE OF ATTACK CONFIGURATION 4, M=0.9, β=0

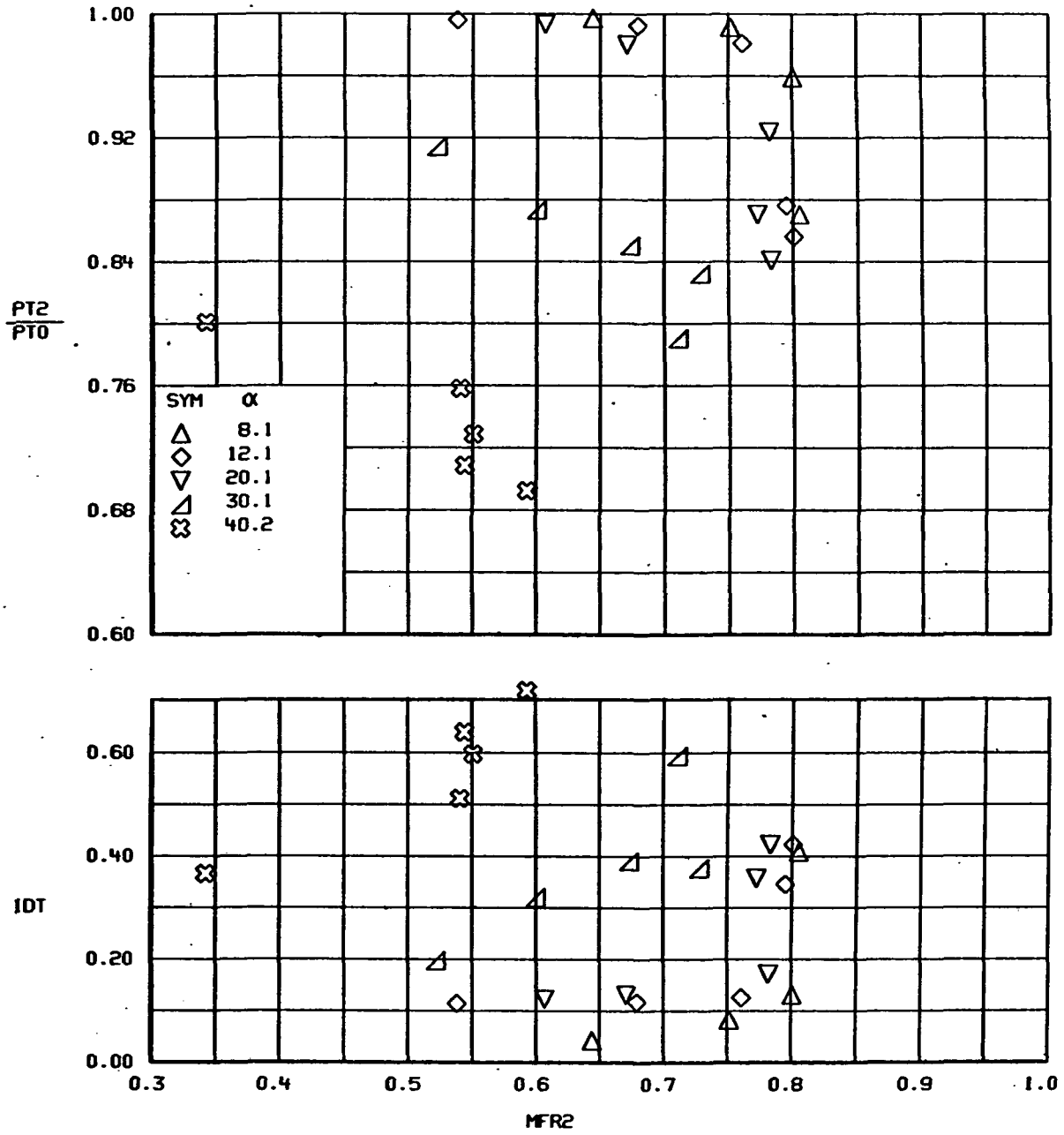

FIGURE 25.- VARIATION IN INLET PERFORMANCE WITH ANGLE OF ATTACK
CONFIGURATION 8, M=0.9, β=0°

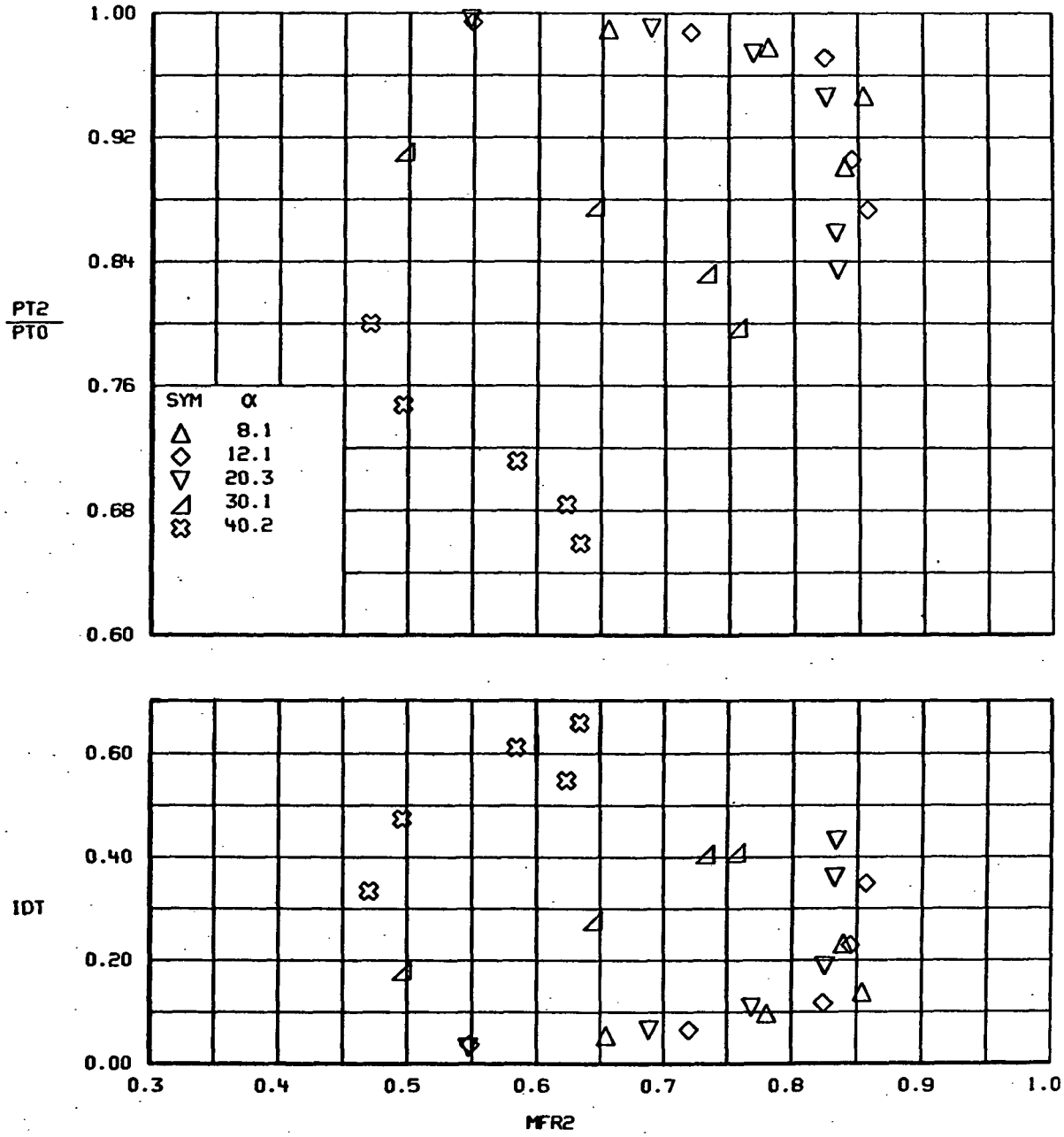

FIGURE 26.- VARIATION IN INLET PERFORMANCE WITH ANGLE OF ATTACK
CONFIGURATION 6, M=0.9, β=0°

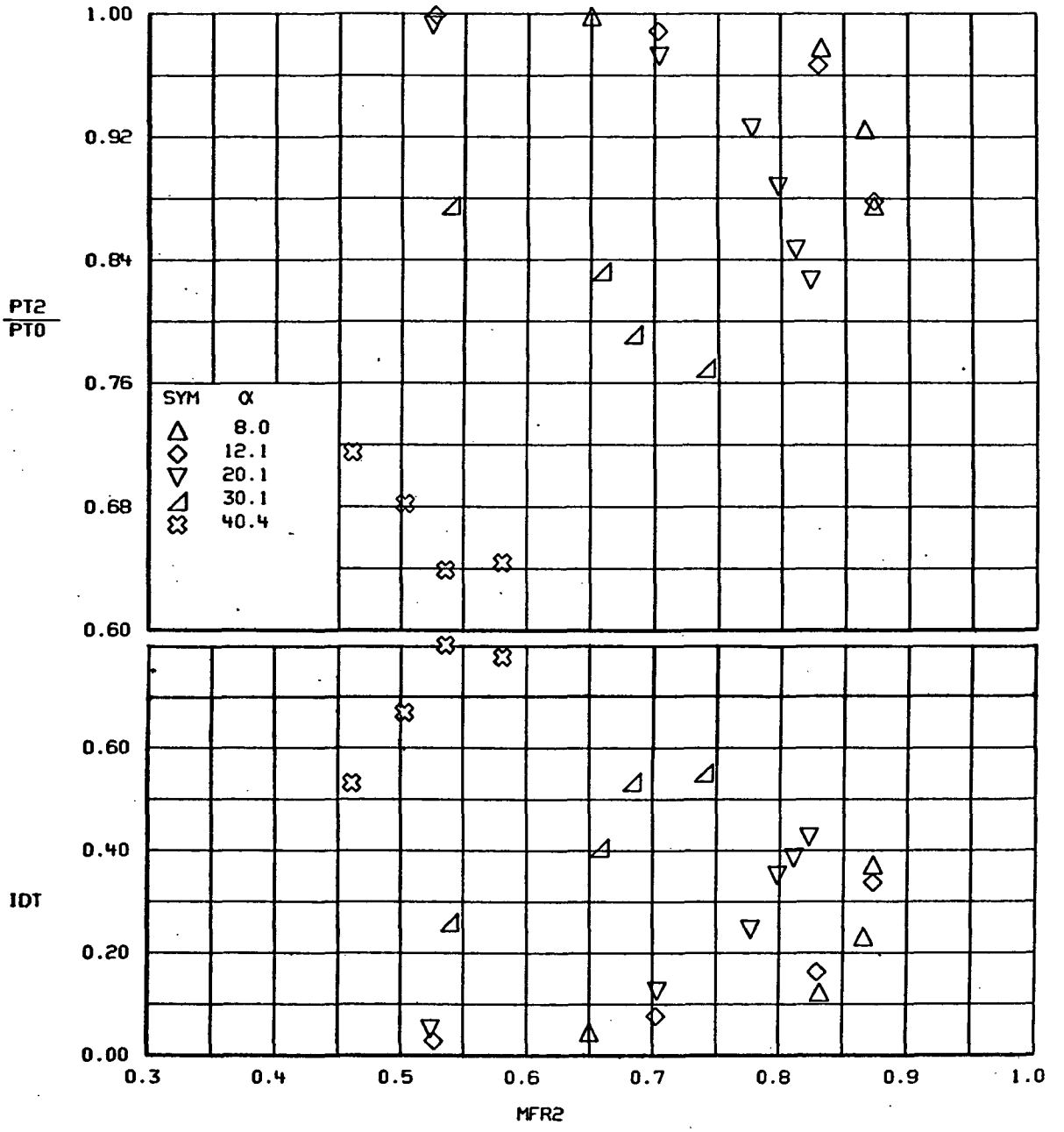

FIGURE 27.- VARIATION IN INLET PERFORMANCE WITH ANGLE OF ATTACK
CONFIGURATION 5, M=0.9, β=0°

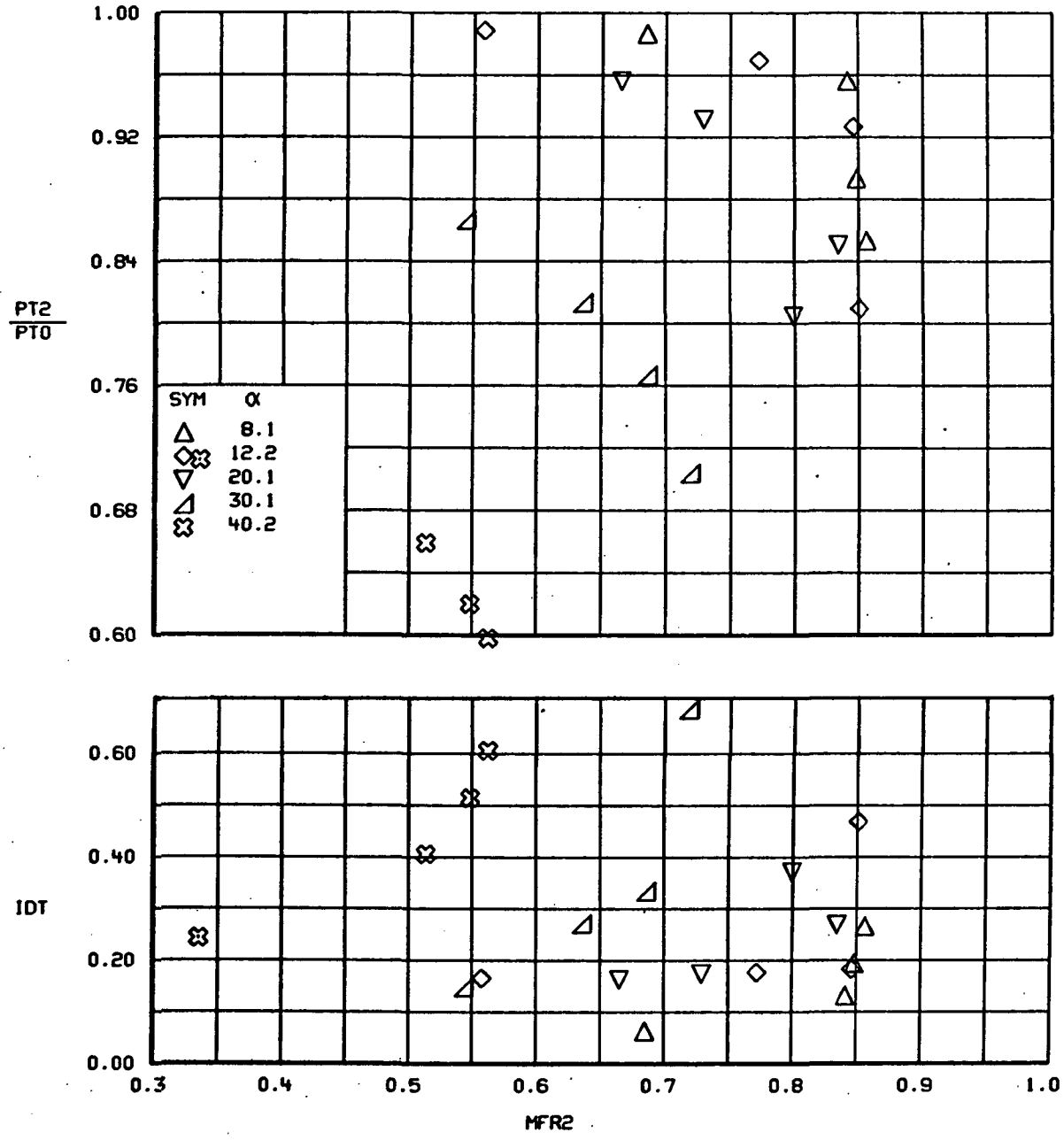

FIGURE 28.-VARIATION IN INLET PERFORMANCE WITH ANGLE OF ATTACK CONFIGURATION 7, M=0.9, β=0

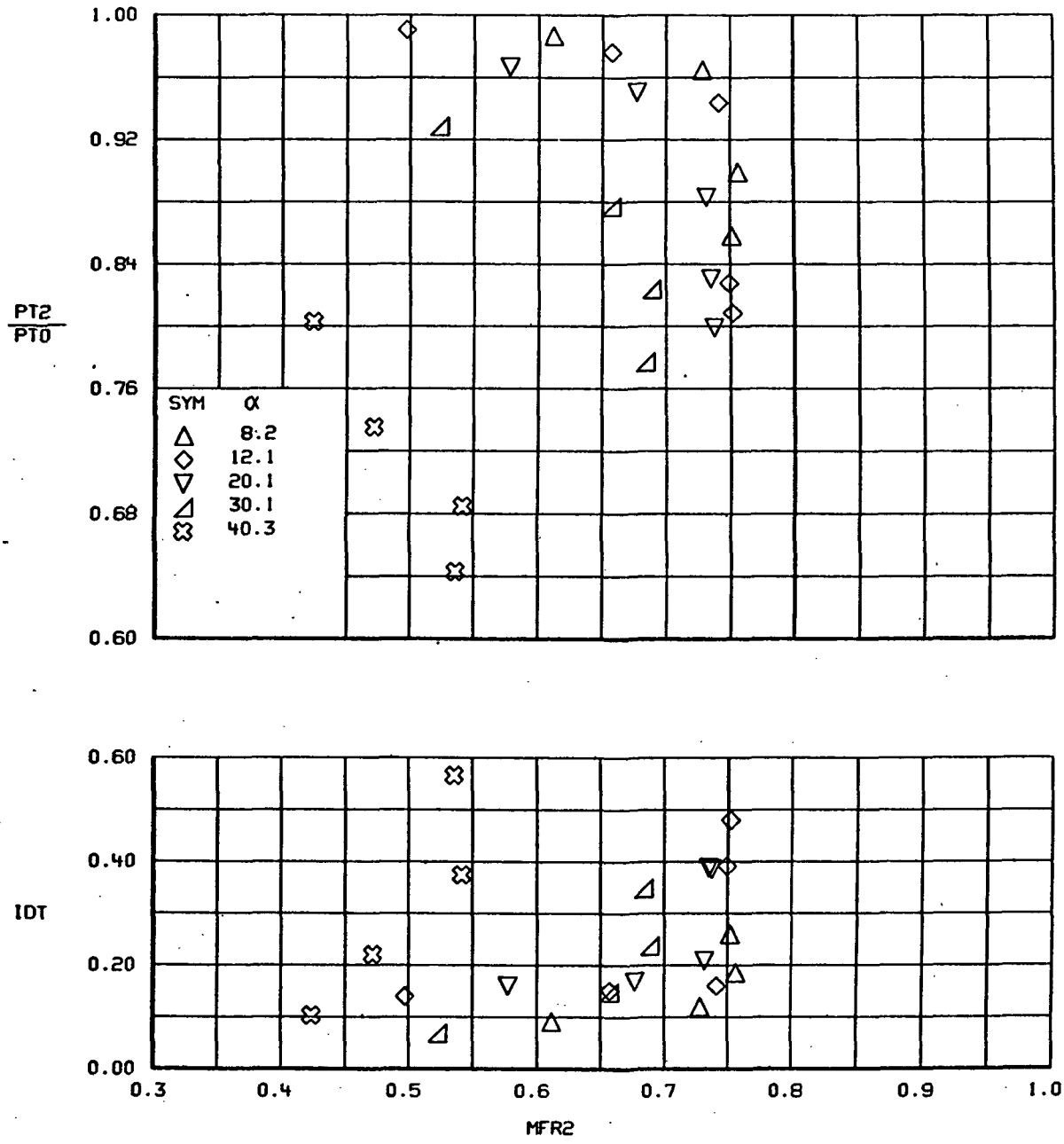

FIGURE 29.- VARIATION IN INLET PERFORMANCE WITH ANGLE OF ATTACK
CONFIGURATION 9, M=0.9, β=0°

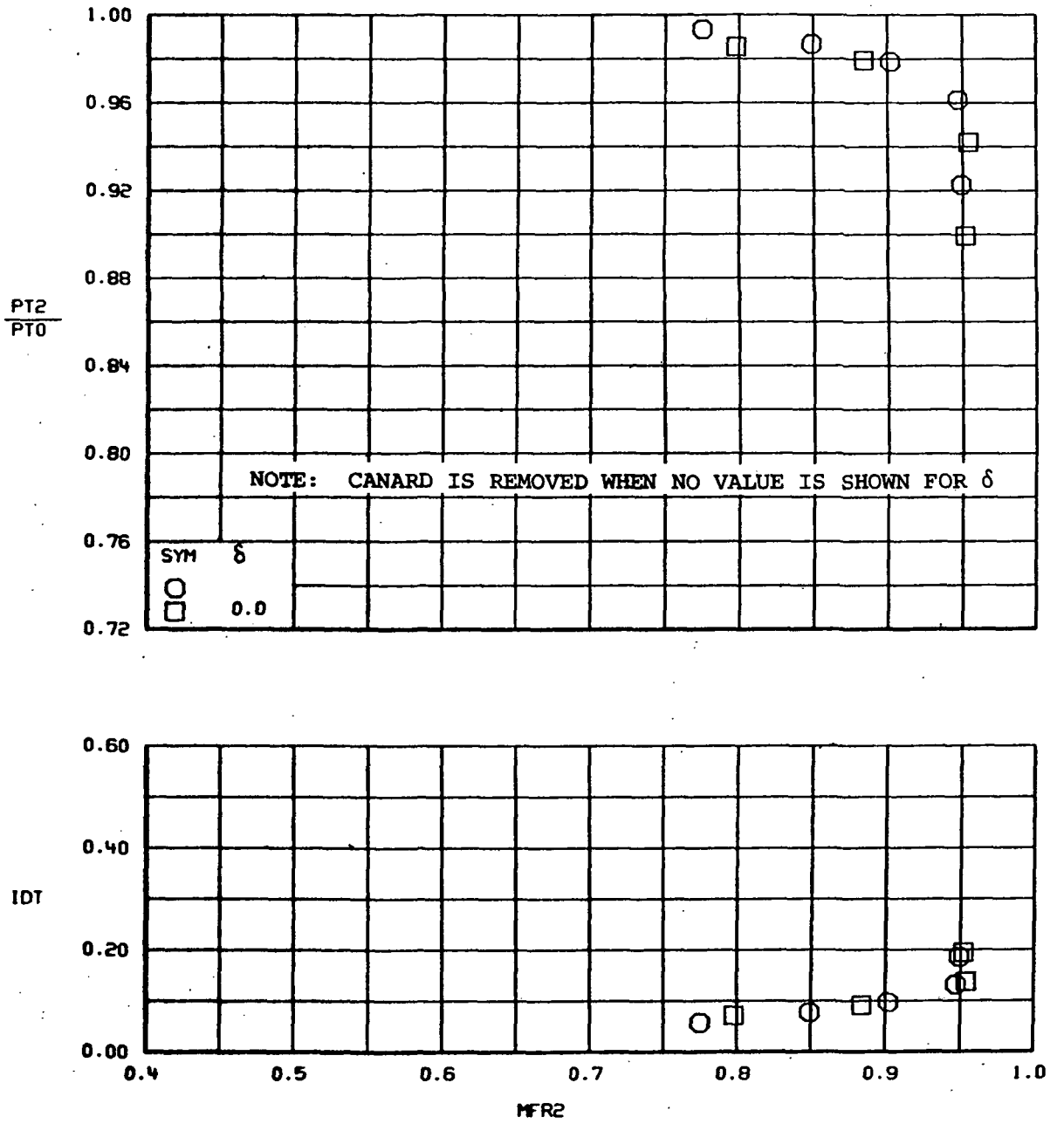

(a) $\alpha=-8^{\circ}$

FIGURE 30.- EFFECT OF A CANARD ON INLET PERFORMANCE, CONFIGURATION 1 M=0.9, $\beta=0^{\circ}$.

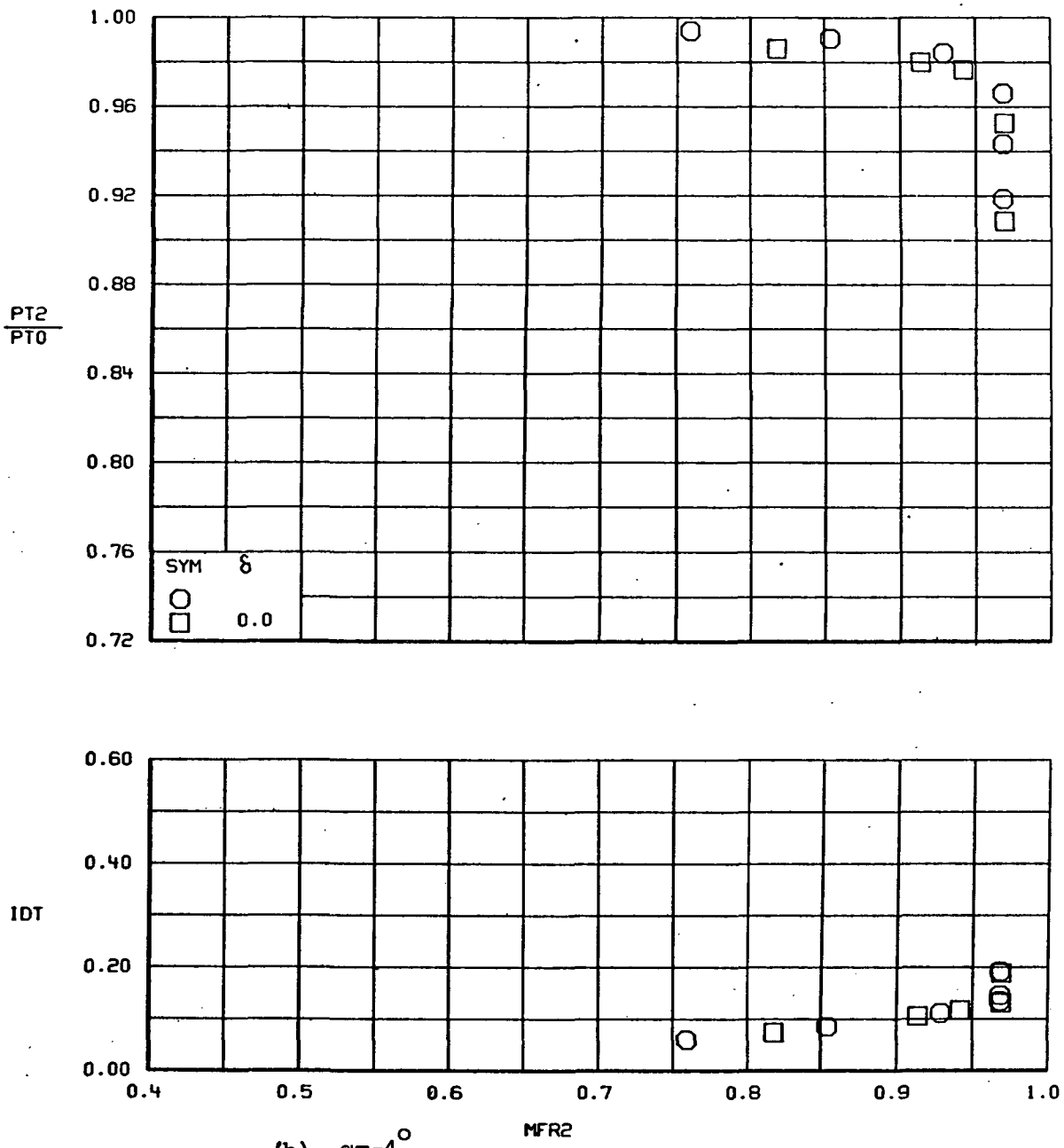

(b) $\alpha=-4^{o}$

FIGURE 30.-CONTINUED.

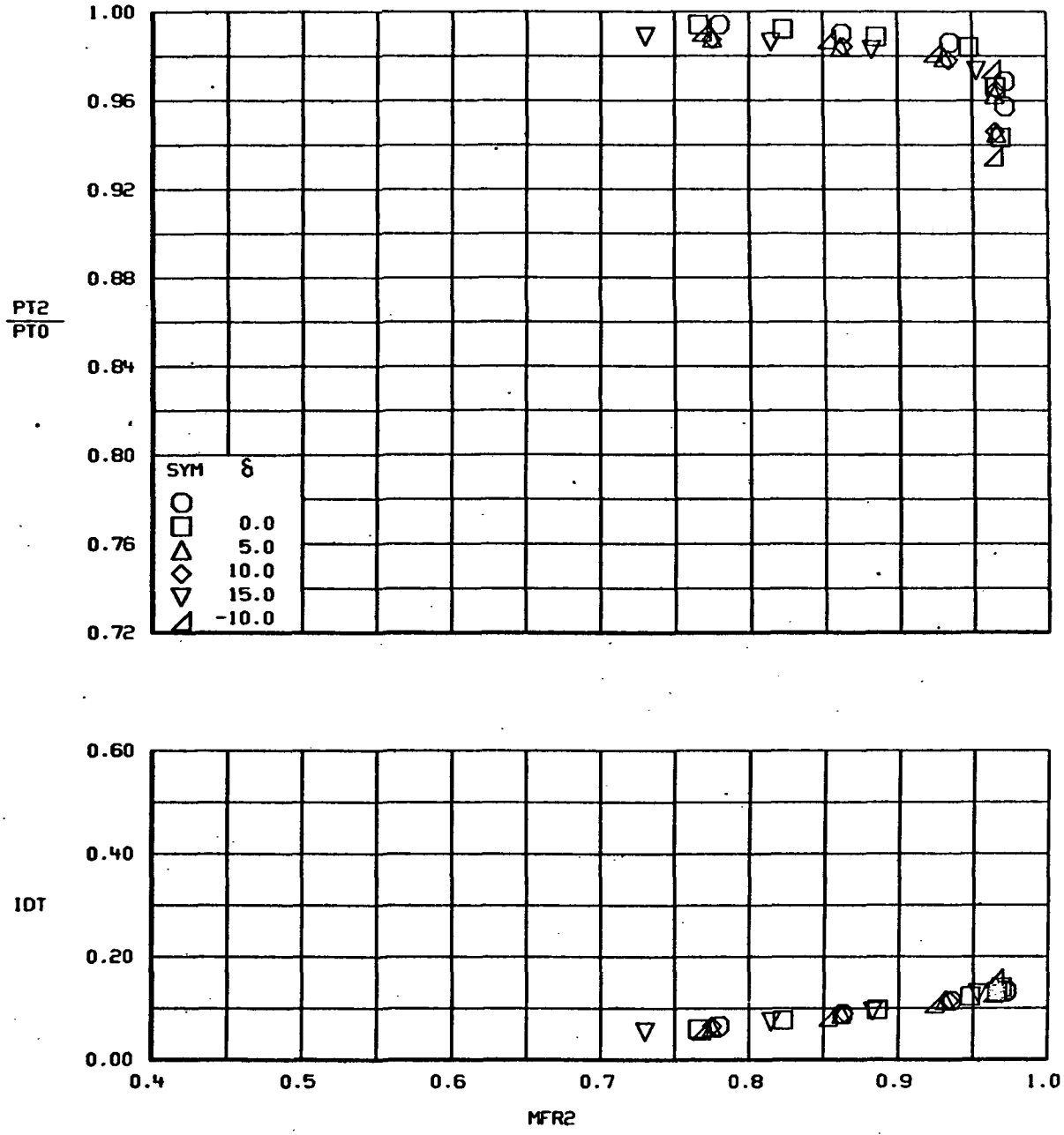

(c) $\alpha=0°$

FIGURE 30.-CONTINUED.

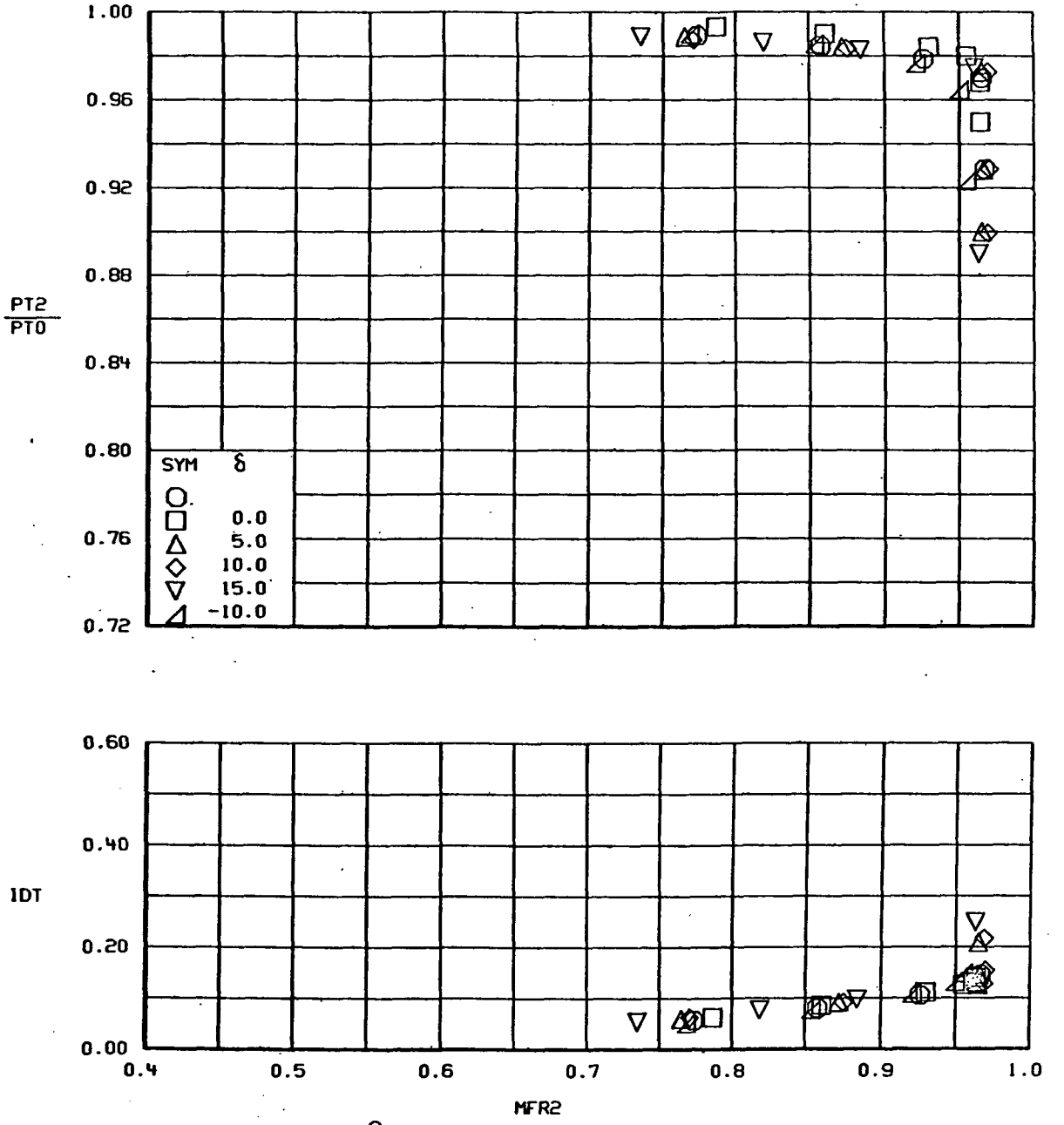

(d) $\alpha=4^{\circ}$

FIGURE 30.-CONTINUED.

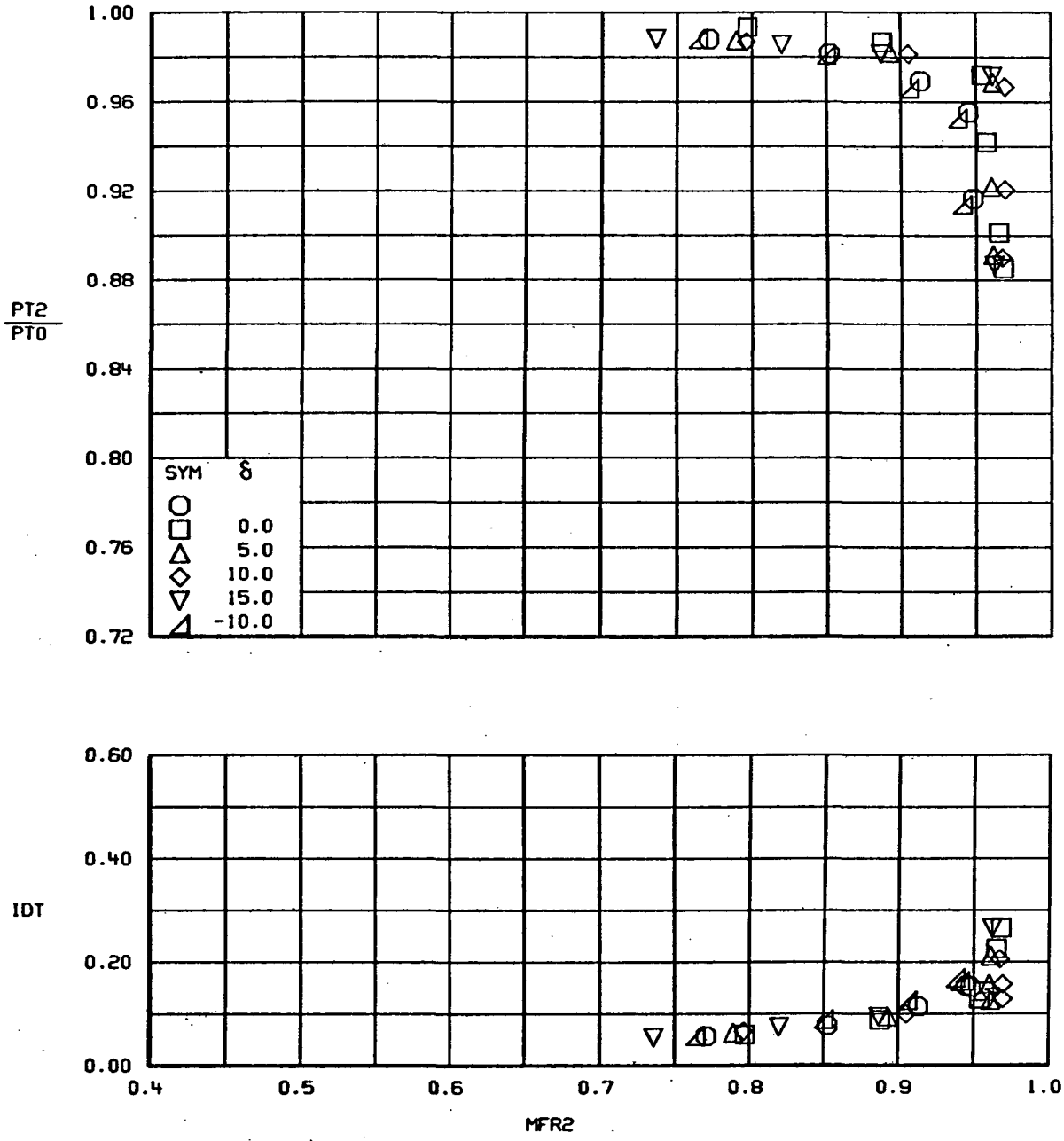

(e) α=8°

FIGURE 30.-CONTINUED.

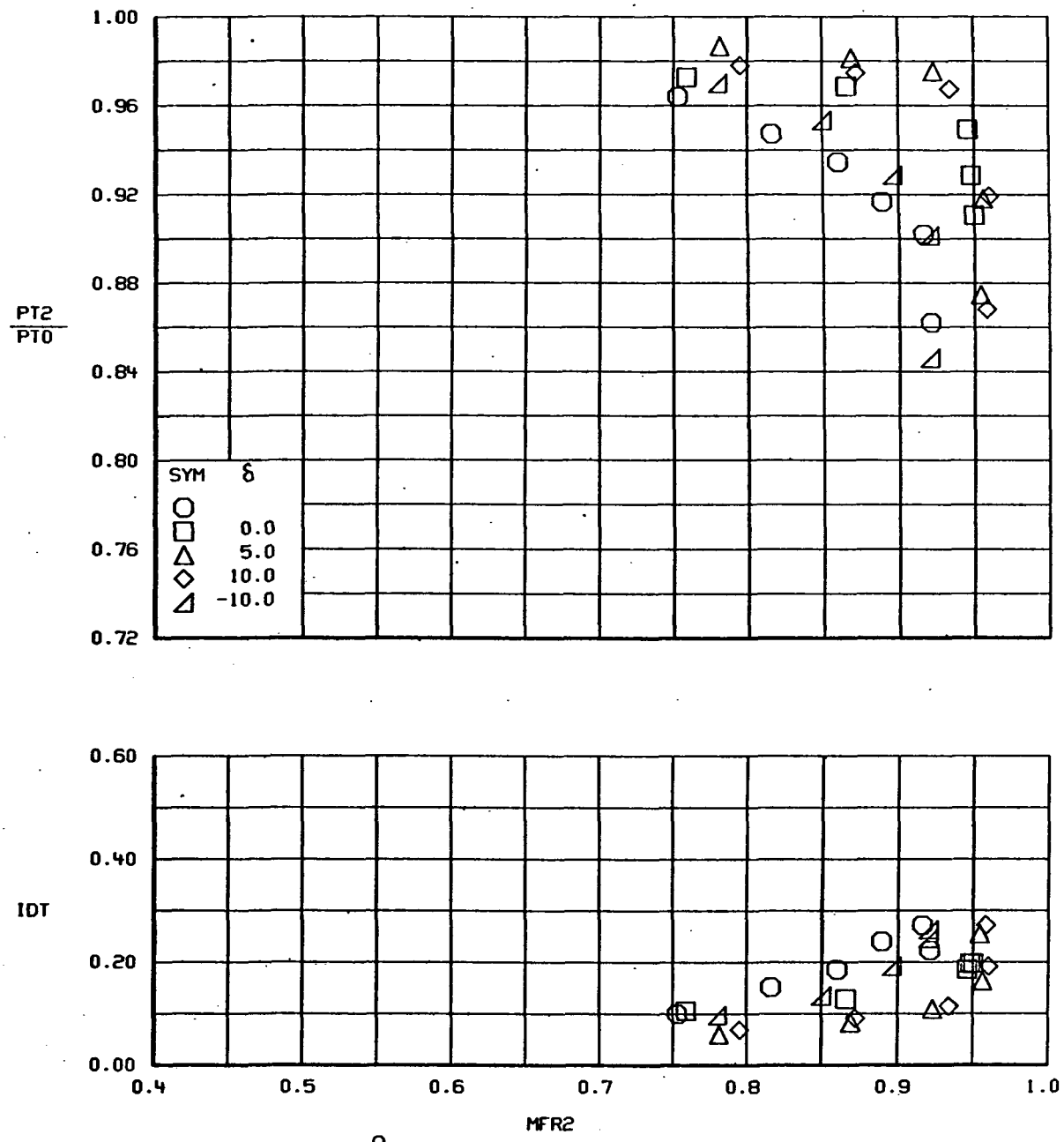

(f) $\alpha=12^{\circ}$

FIGURE 30.-CONTINUED.

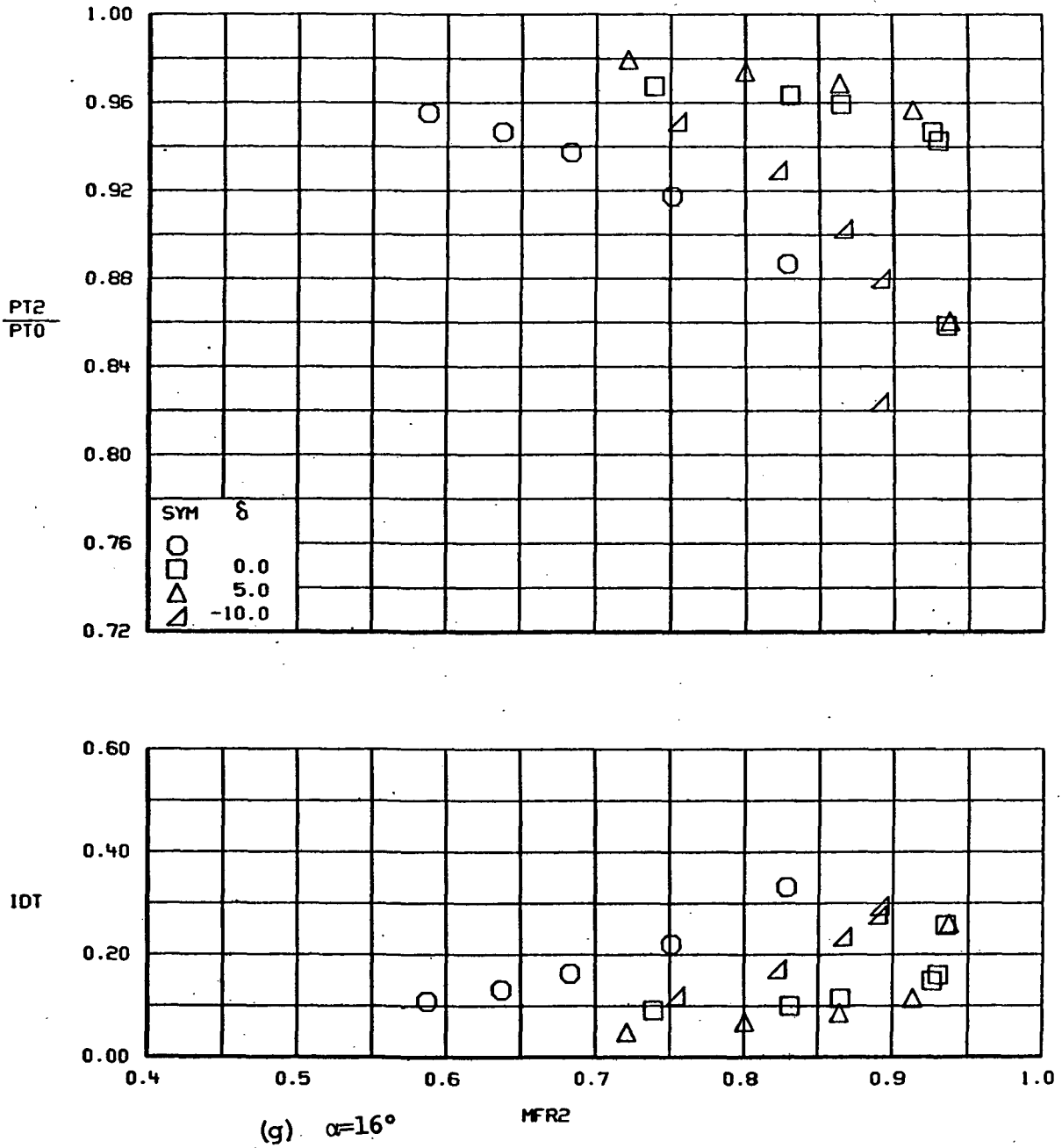

(g) α=16°

FIGURE 30.-CONTINUED.

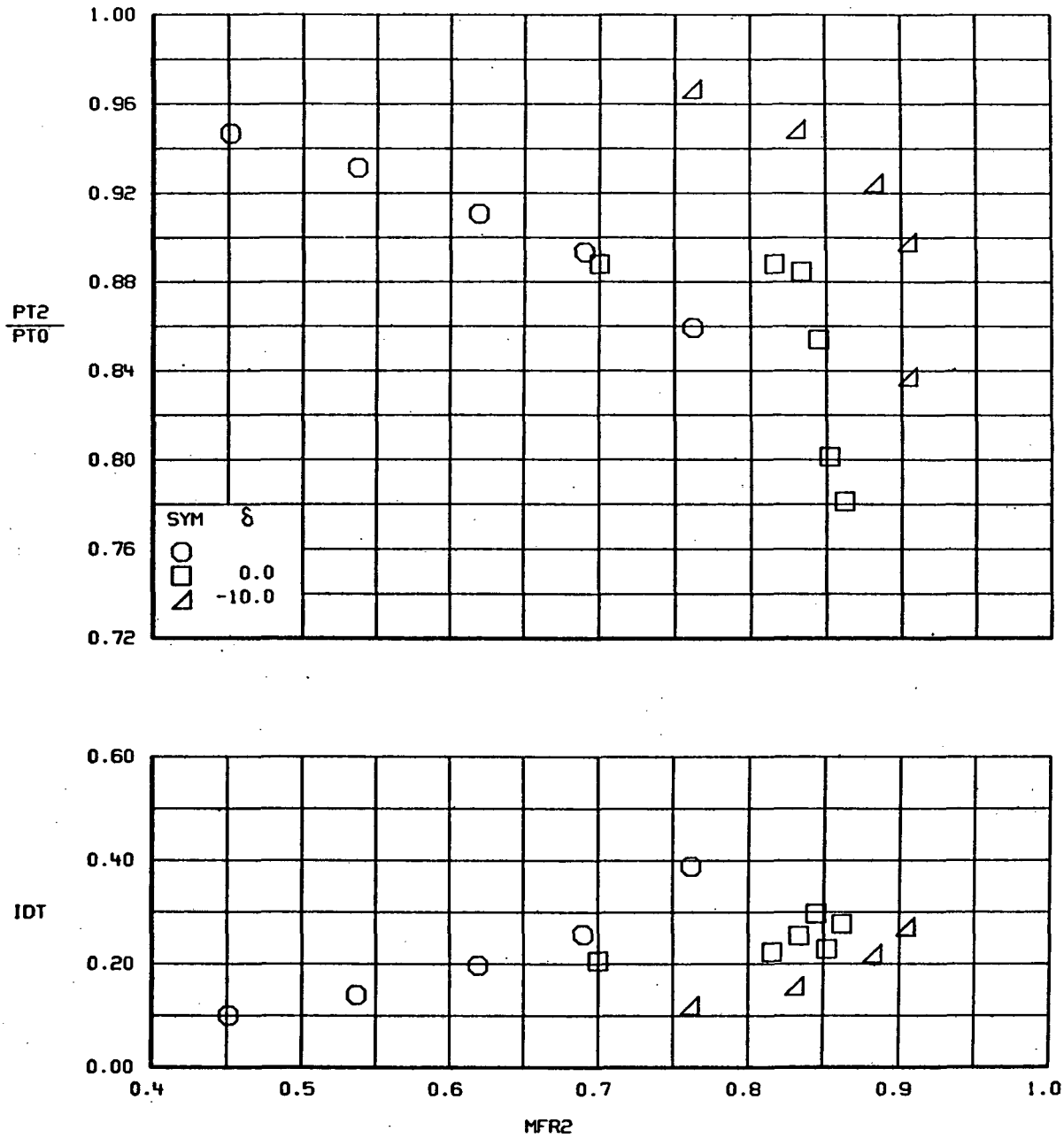

(h) α=20°

FIGURE 30.-CONTINUED.

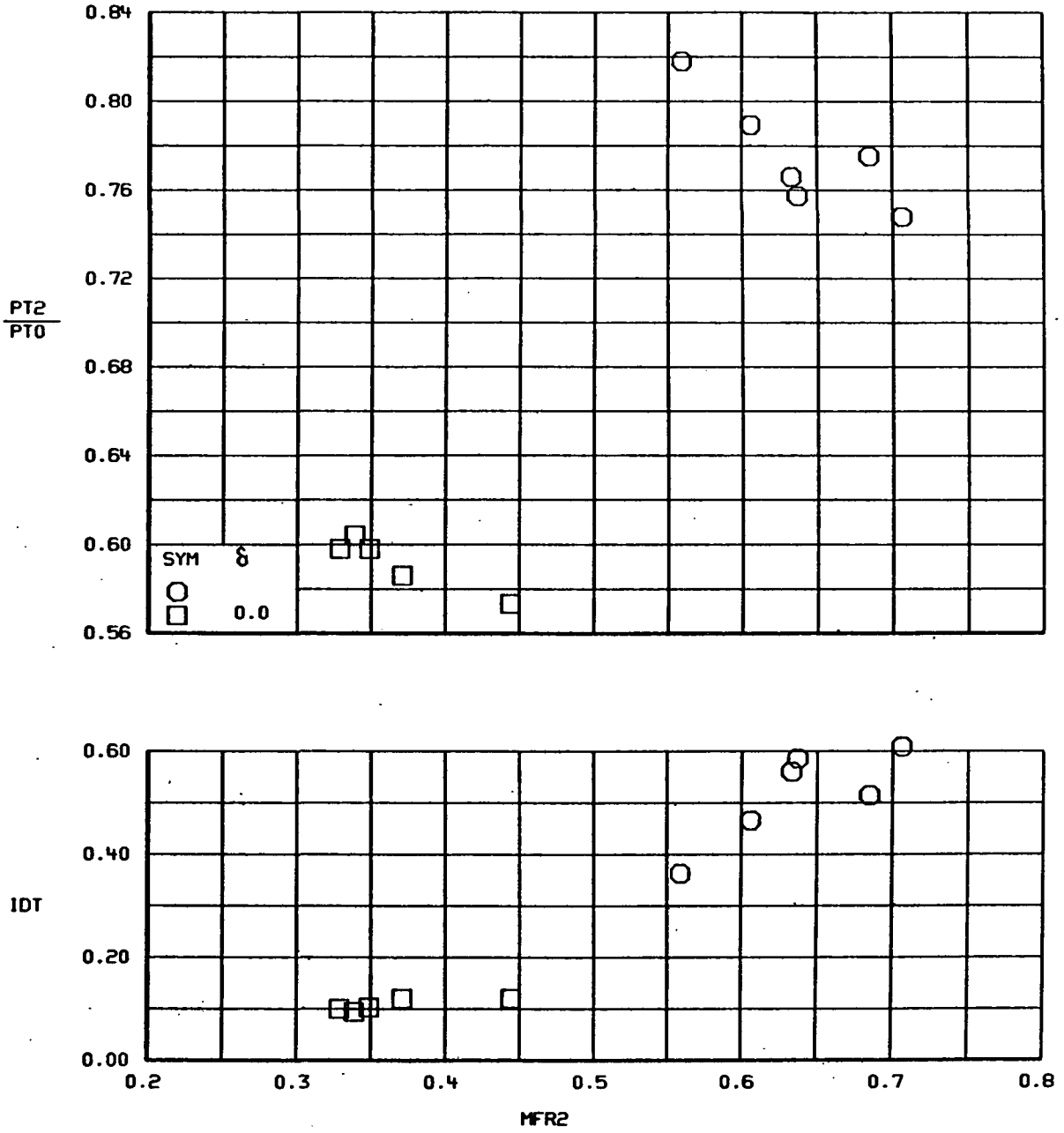

(i) $\alpha=30°$

FIGURE 30.-CONCLUDED.

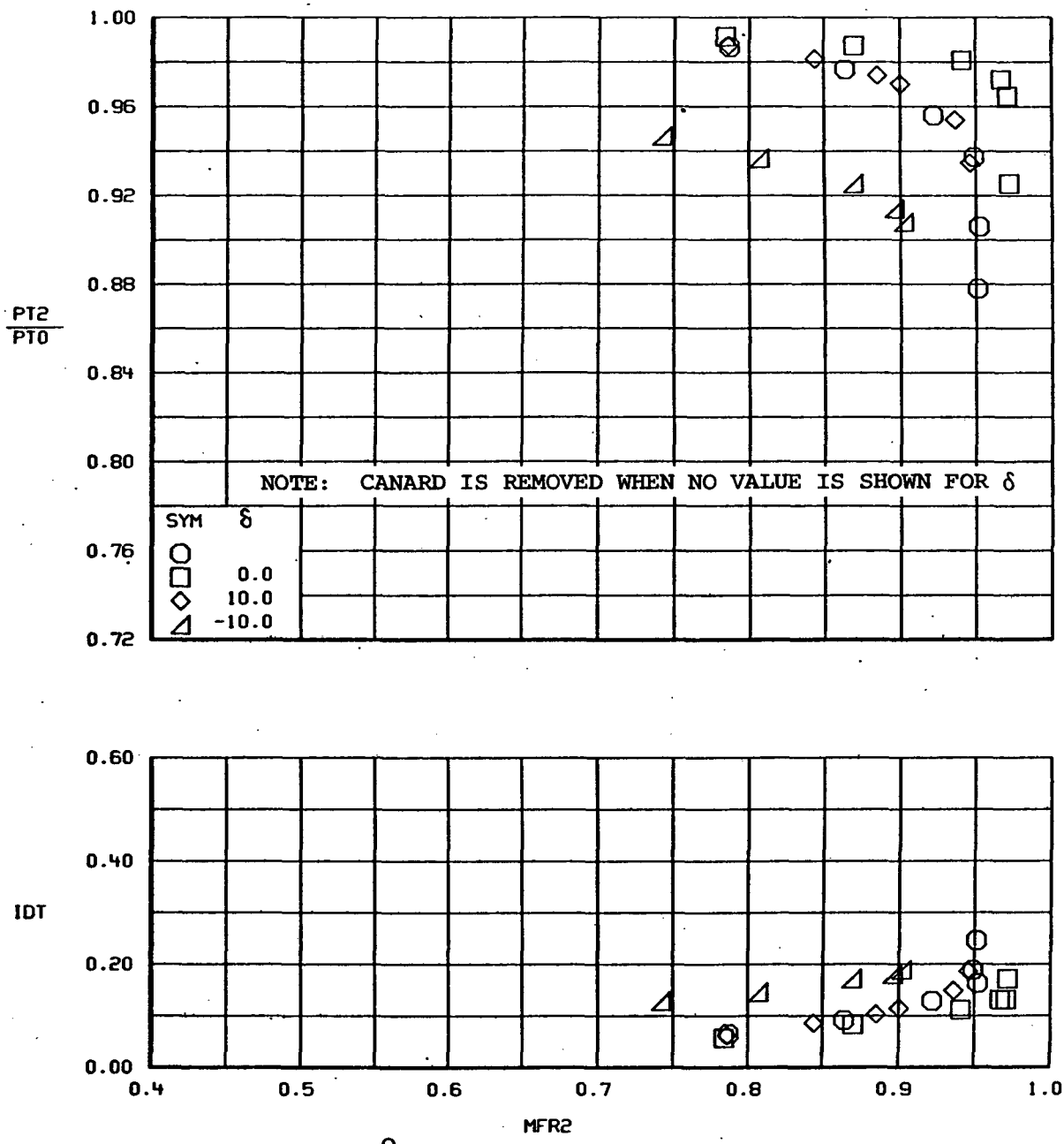

(a) $\alpha = -8^{\circ}$

FIGURE 31.- EFFECT OF A CANARD ON INLET PERFORMANCE, CONFIGURATION 10
M=0.9, $\beta=0^{\circ}$

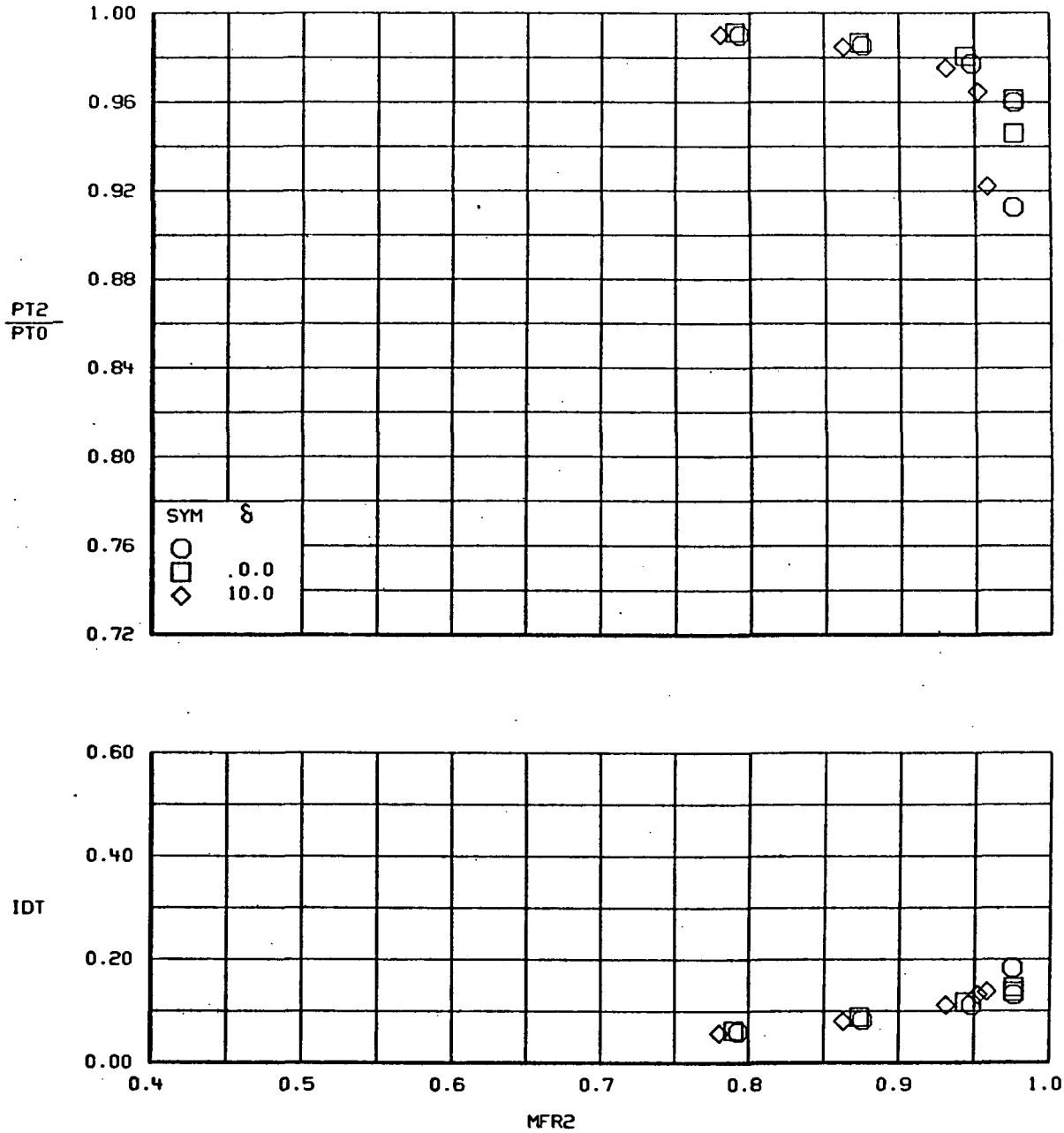

(b) $\alpha = -4^{\circ}$

FIGURE 31.-CONTINUED.

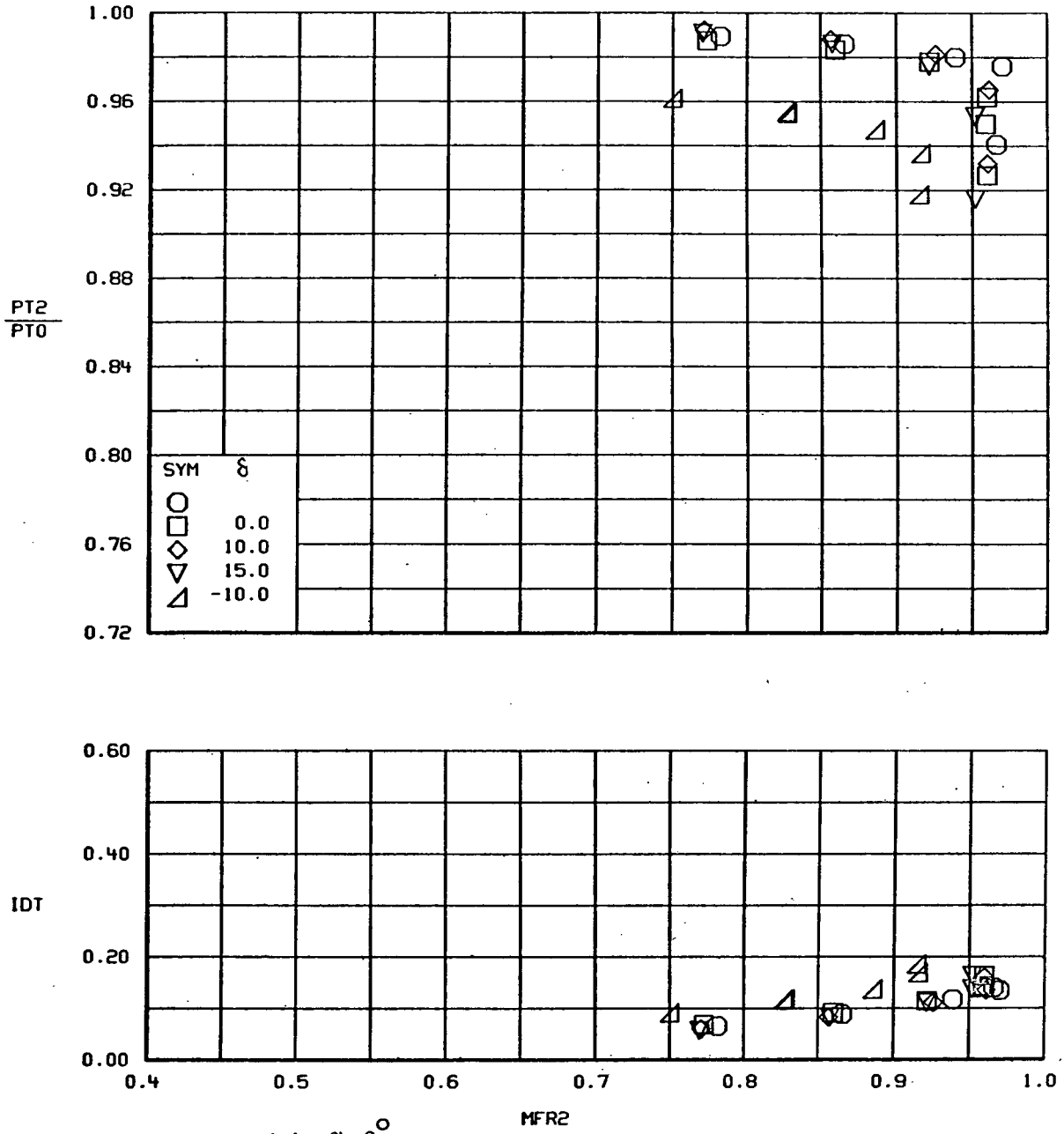

(c) $\alpha = 0^{\circ}$

FIGURE 31.-CONTINUED.

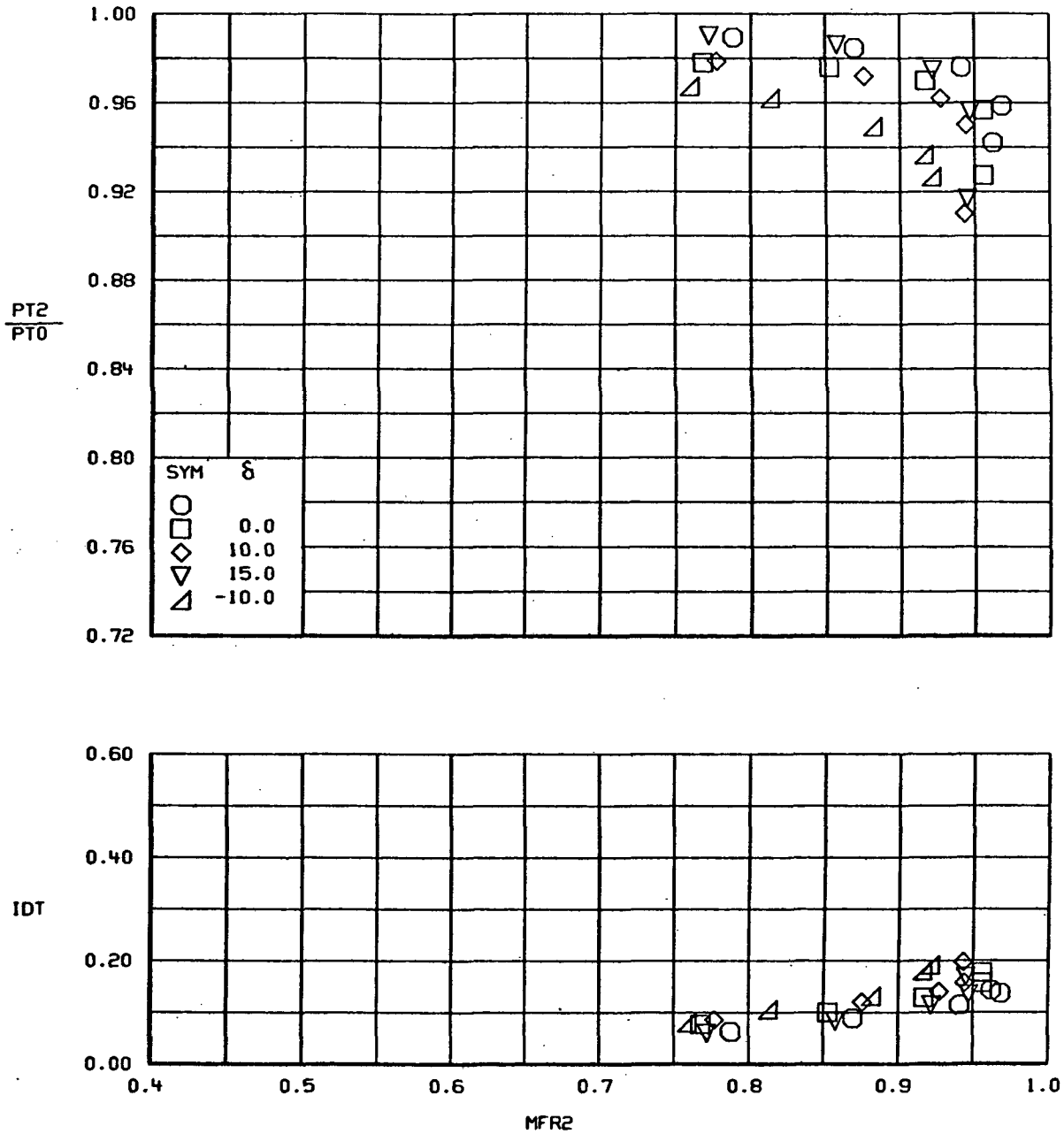

(d) $\alpha=4^{\circ}$

FIGURE 31.-CONTINUED.

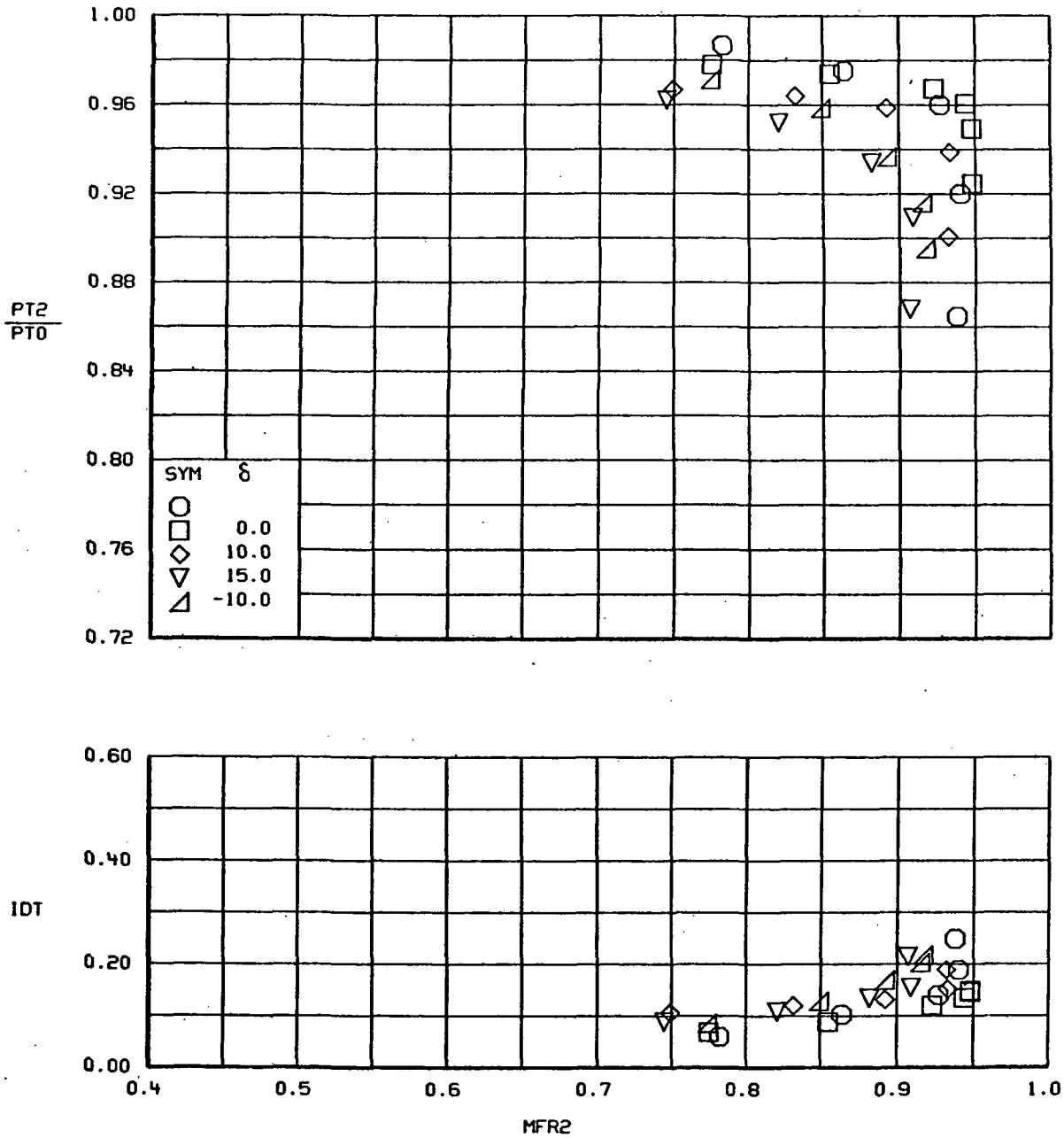

(e) α=8°

FIGURE 31.-CONTINUED.

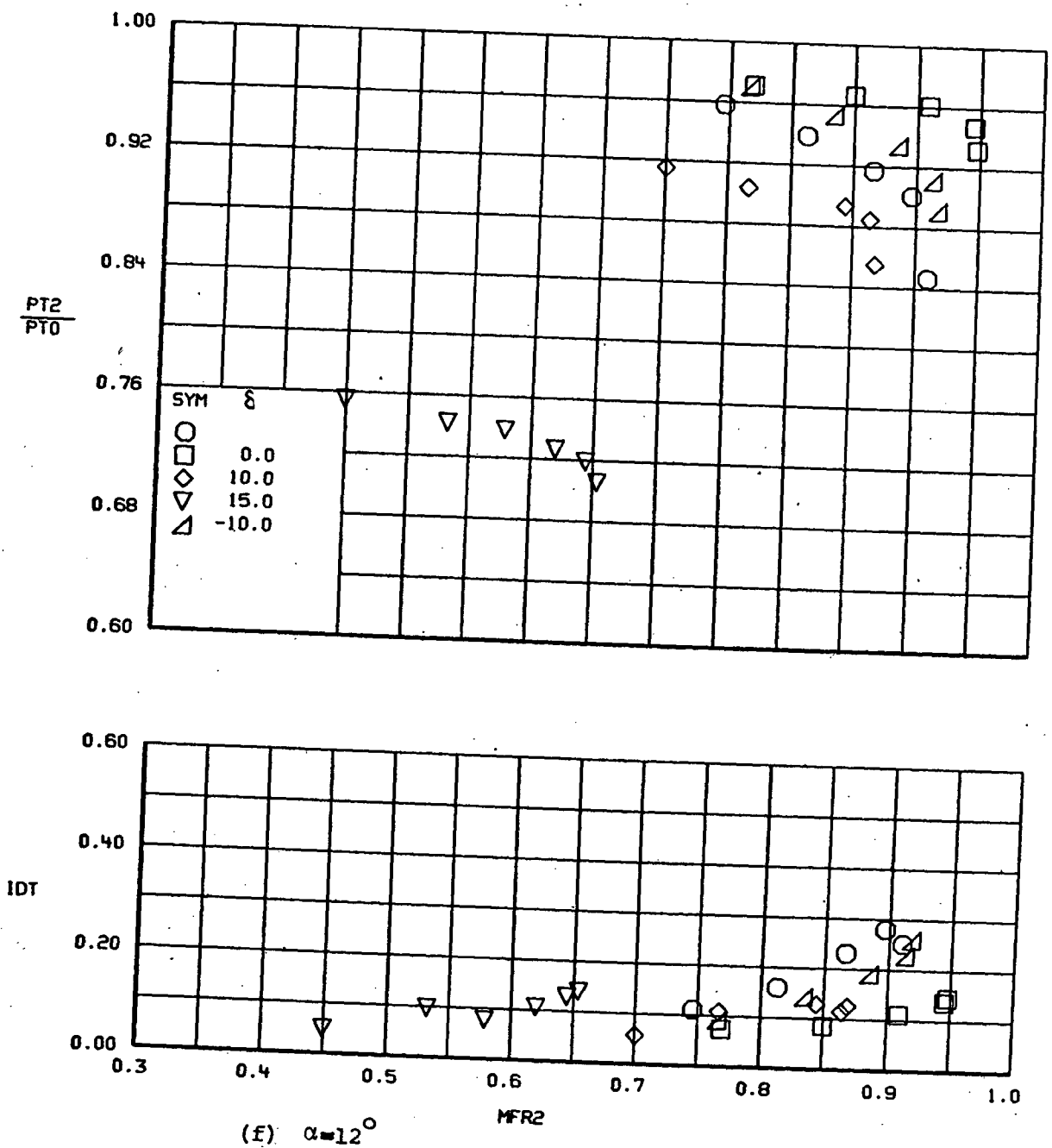

(f) $\alpha = 12^{\circ}$

FIGURE 31.-CONTINUED..

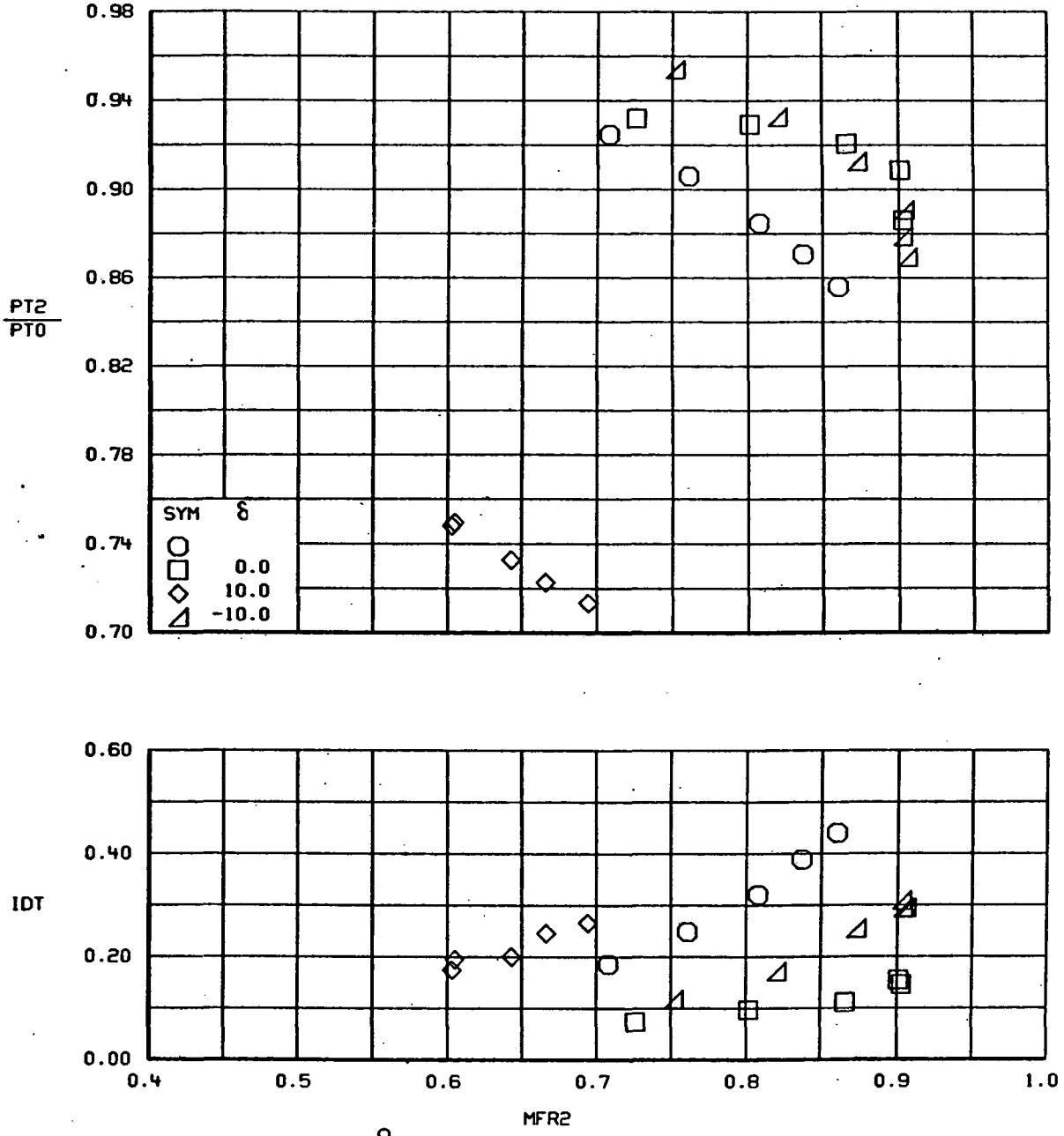

(g) $\alpha=16^{\circ}$

FIGURE 31.-CONTINUED.

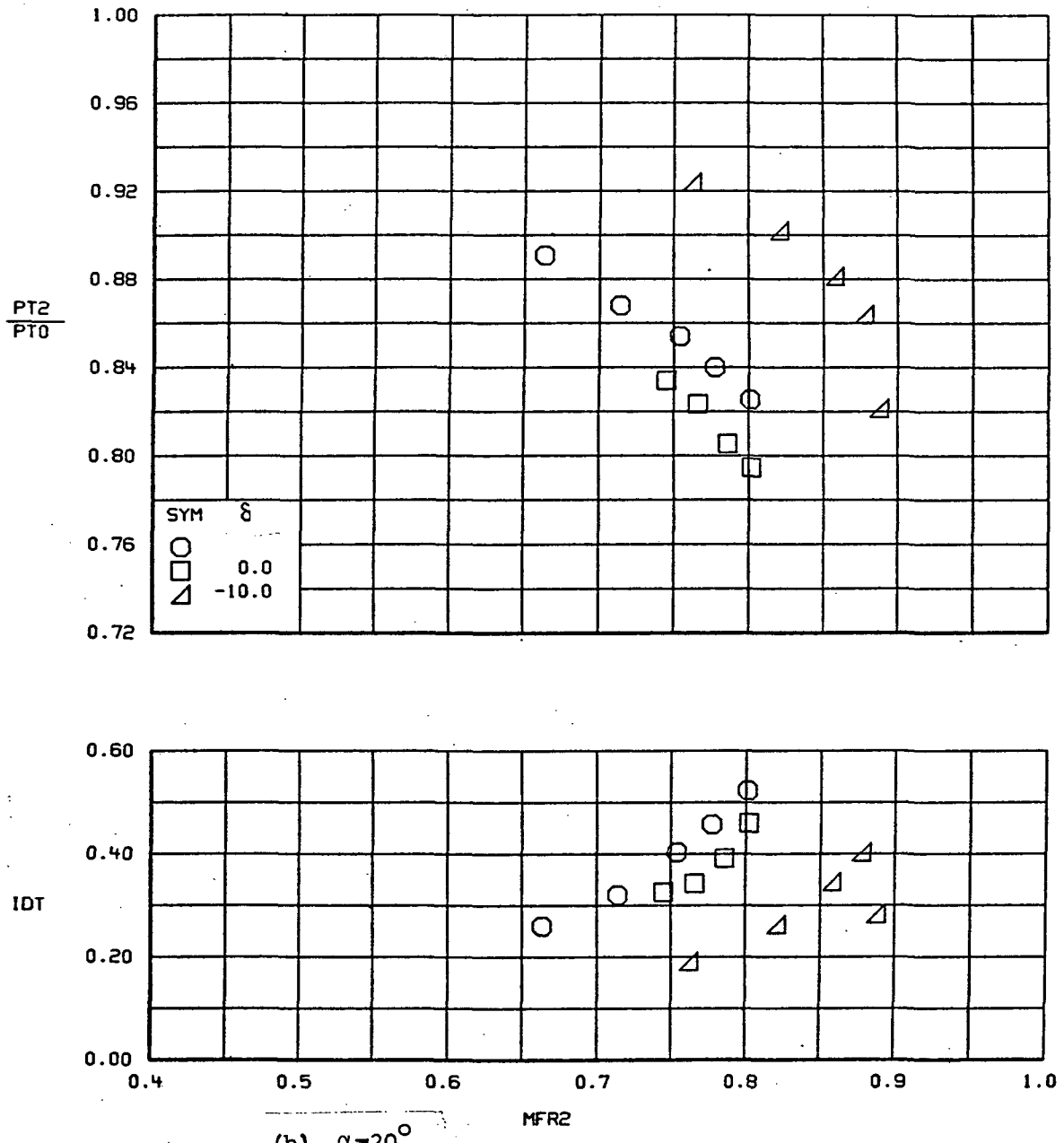

(h) $\alpha=20^{\circ}$

FIGURE 31.-CONCLUDED.

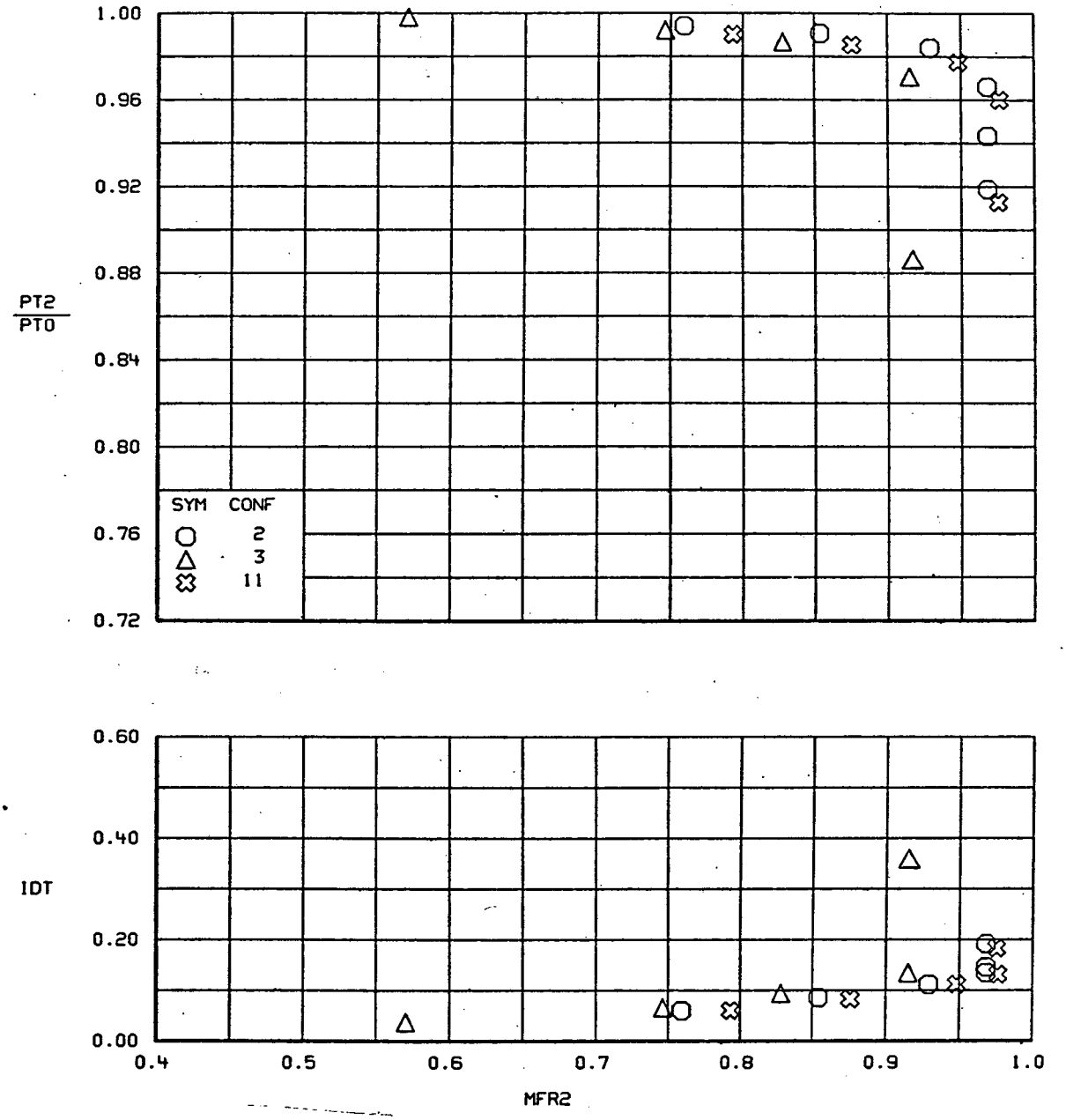

(a) $\alpha=-4°$

FIGURE 32.-PERFORMANCE VARIATION WITH INLET LOCATION AND SHAPE
$M=0.9$, $\beta=0°$

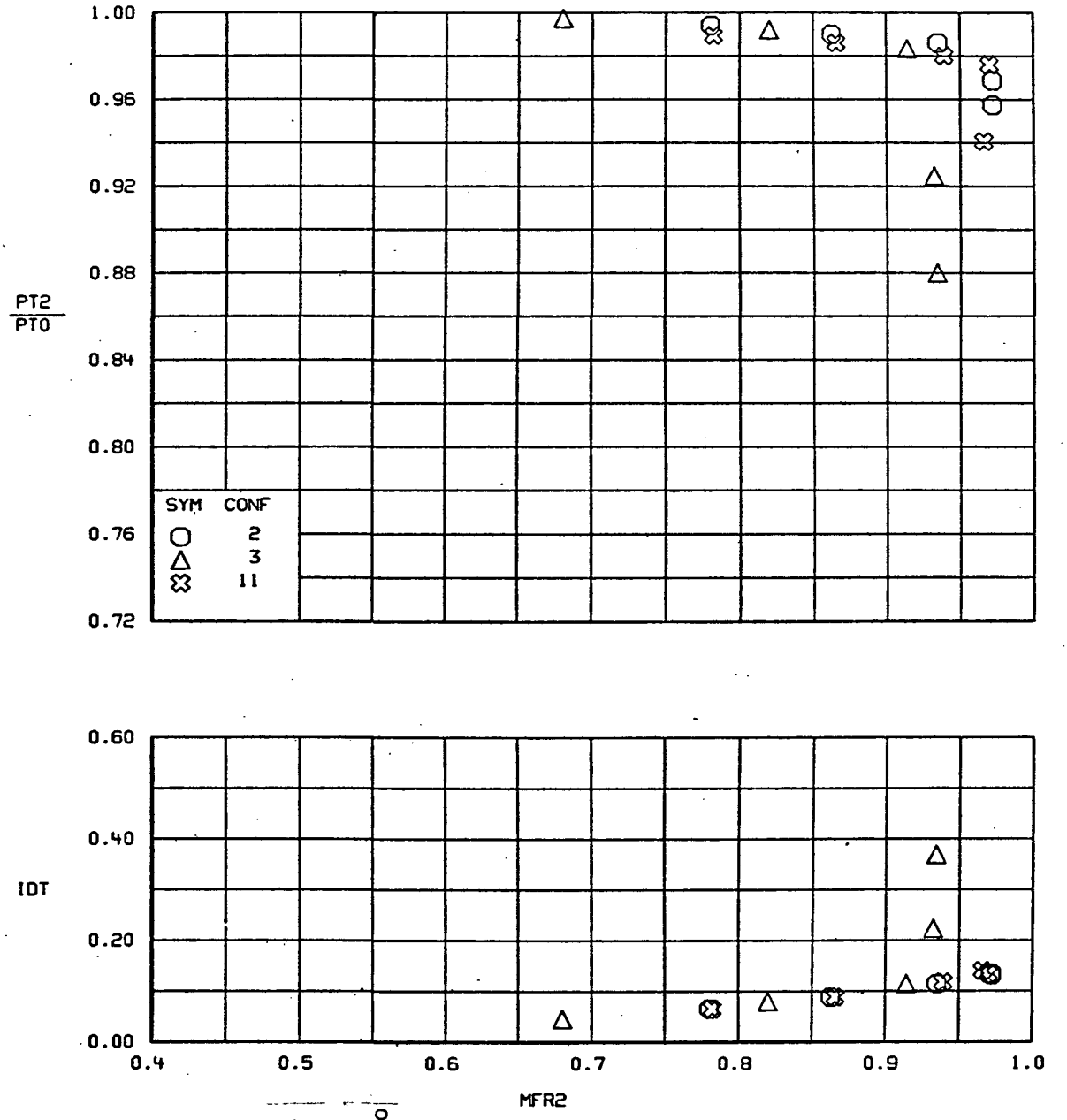

(b) $\alpha=0^{\circ}$

FIGURE 32.-CONTINUED.

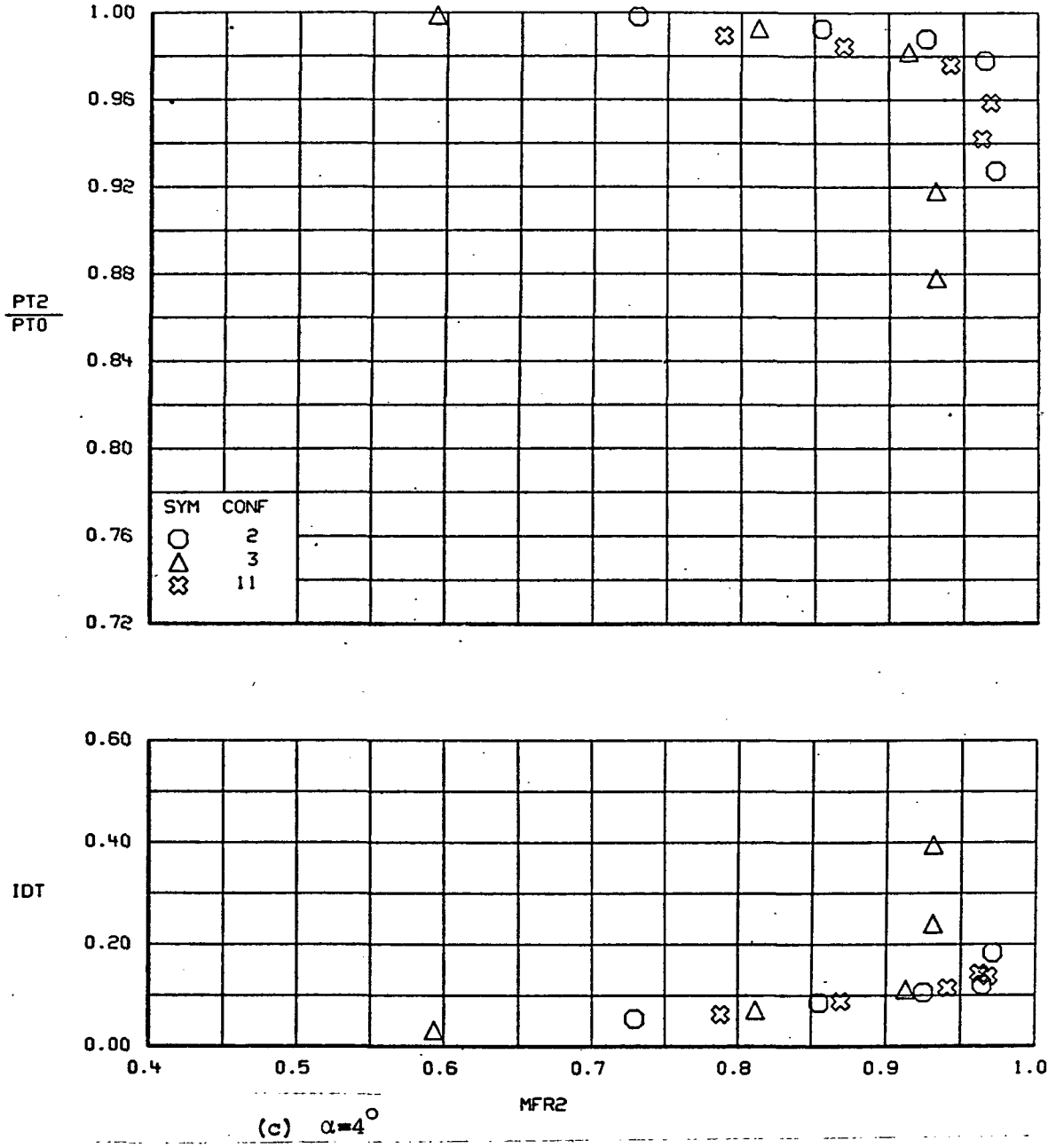

(c) $\alpha=4^{\circ}$

FIGURE 32.-CONTINUED.

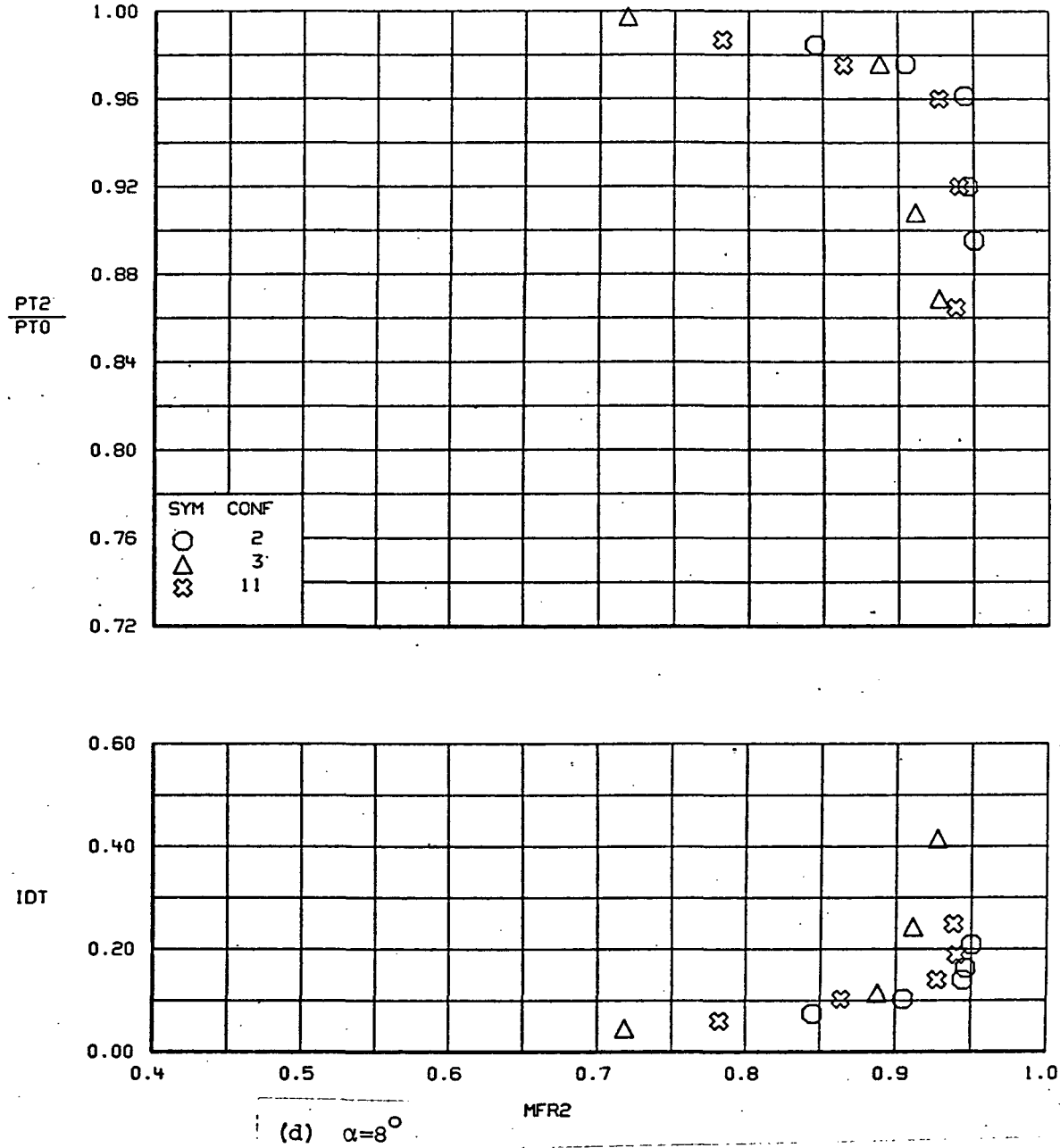

(d) $\alpha=8^{\circ}$

FIGURE 32.-CONTINUED.

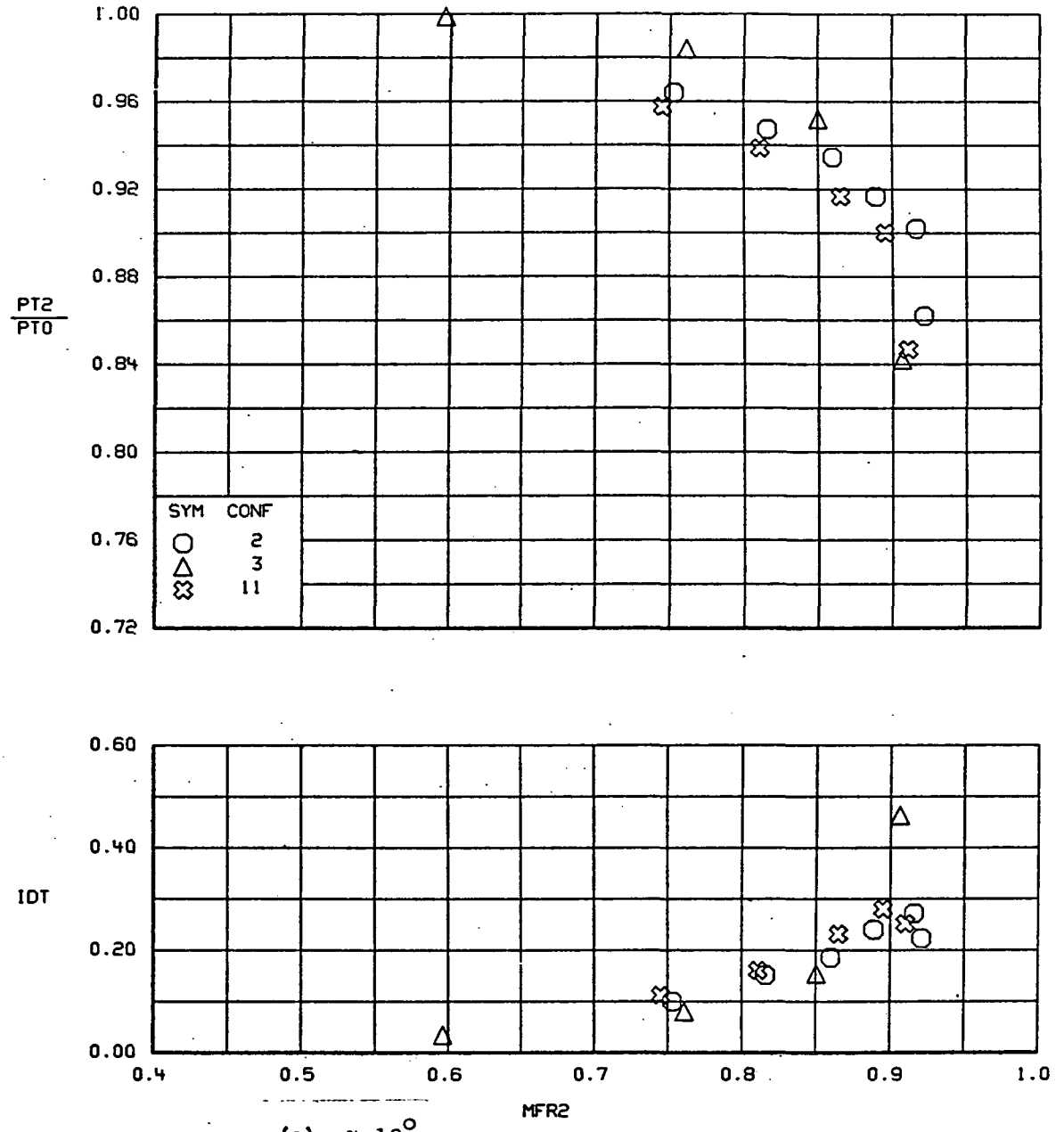

(e) $\alpha=12^{\circ}$

FIGURE 32.-CONTINUED.

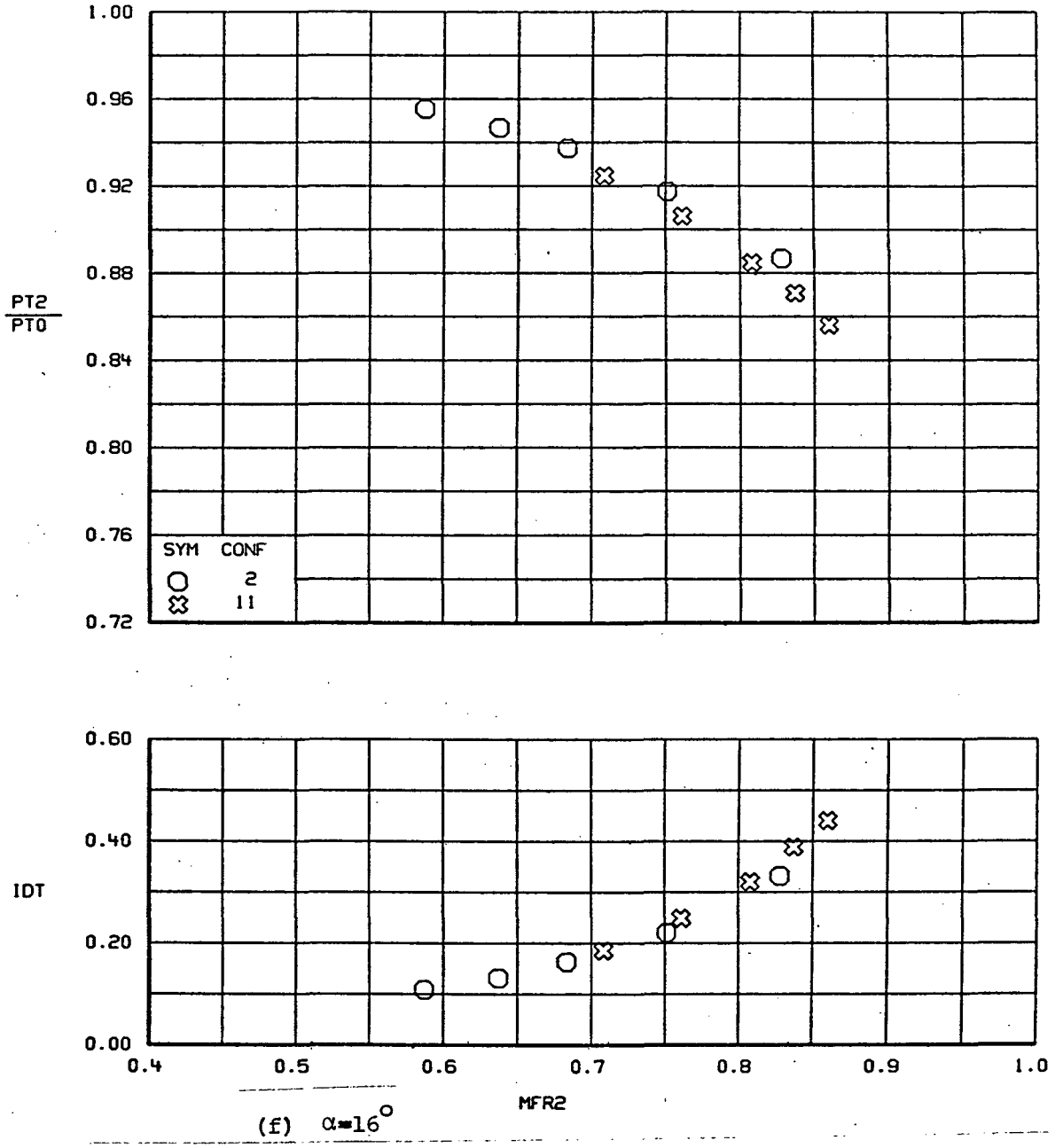

(f) $\alpha=16^{\circ}$

FIGURE 32.-CONTINUED.

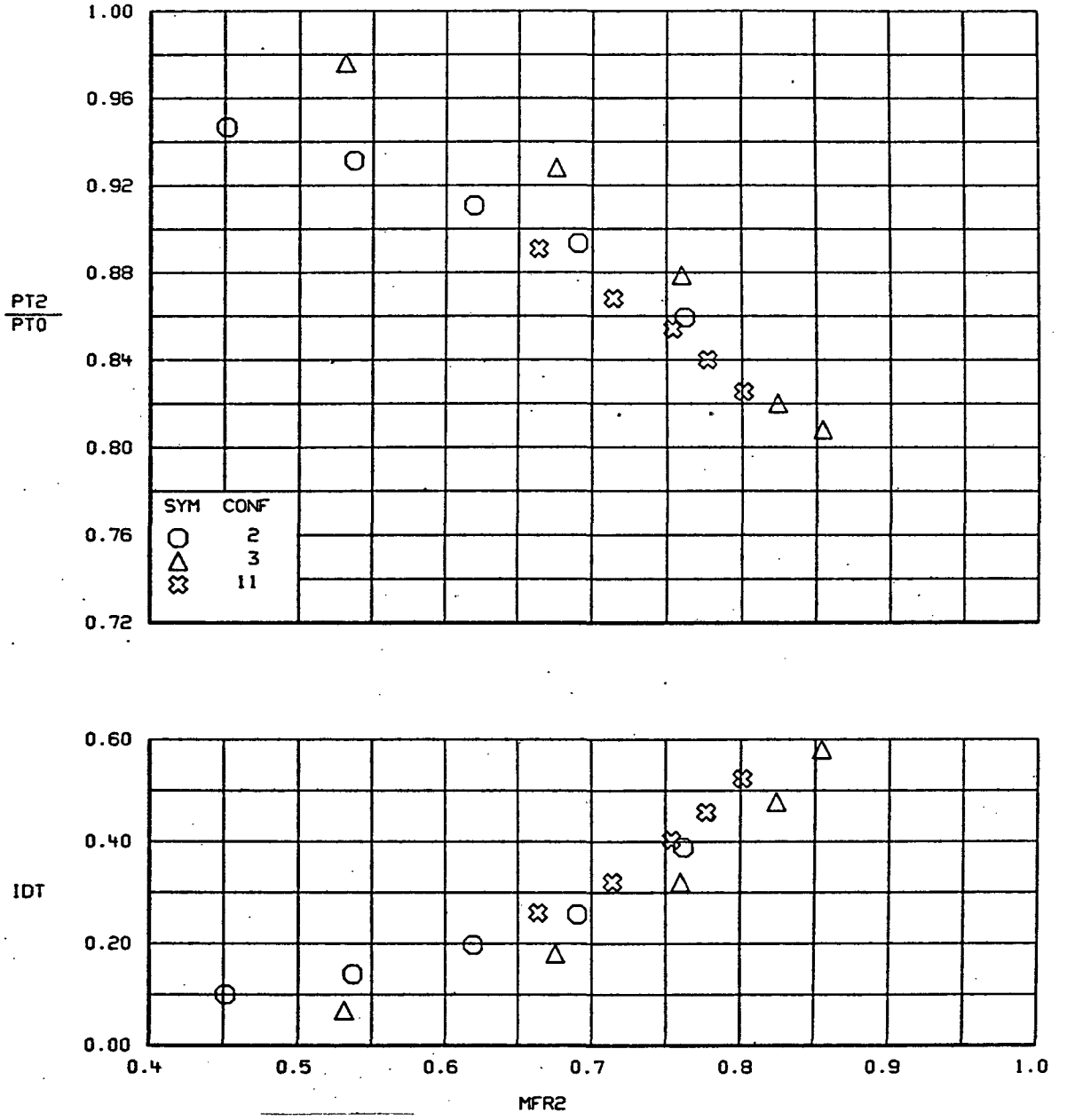

(g) α=20°

FIGURE 32.-CONTINUED.

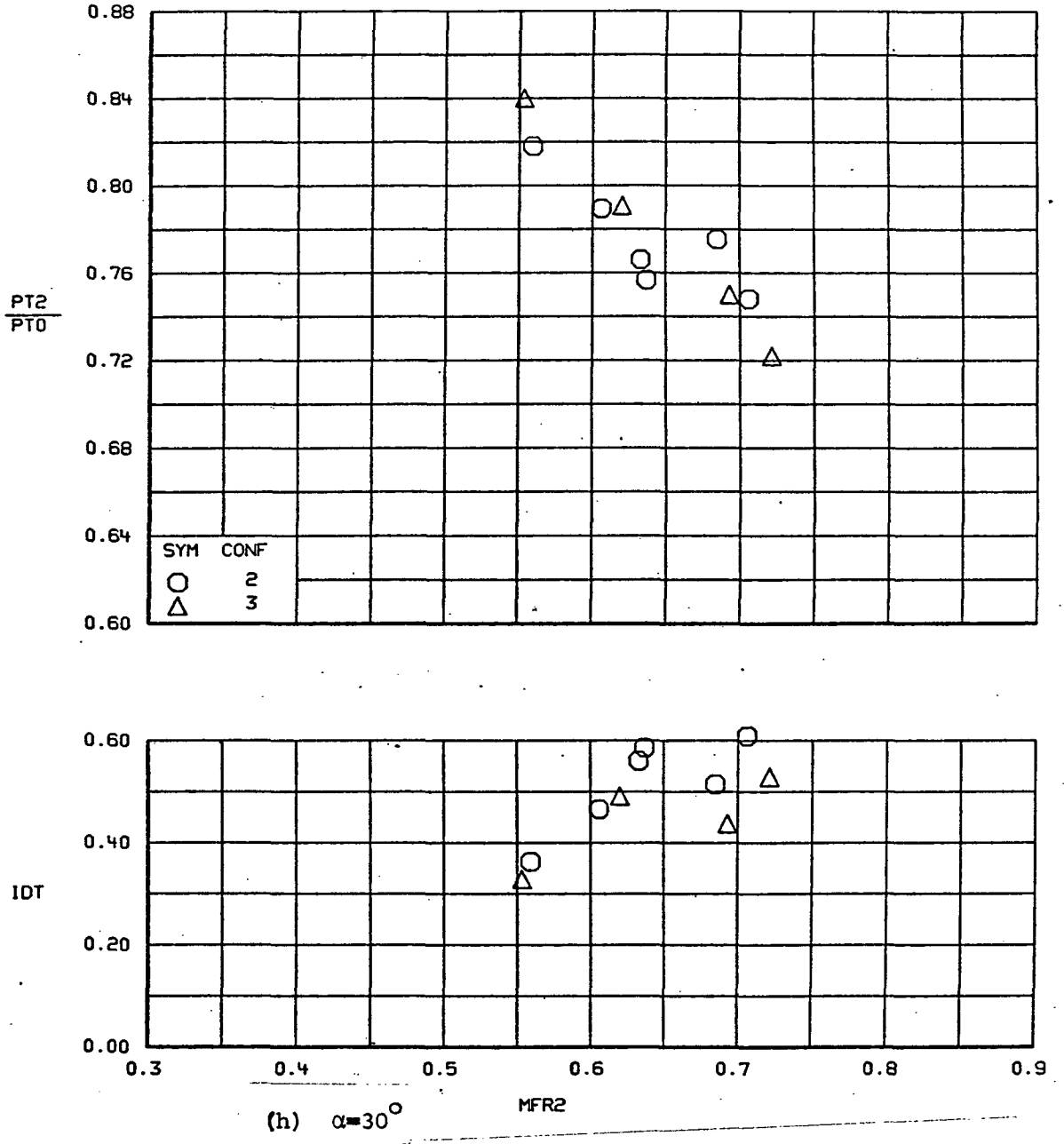

(h) $\alpha=30^{\circ}$

FIGURE 32.-CONCLUDED.

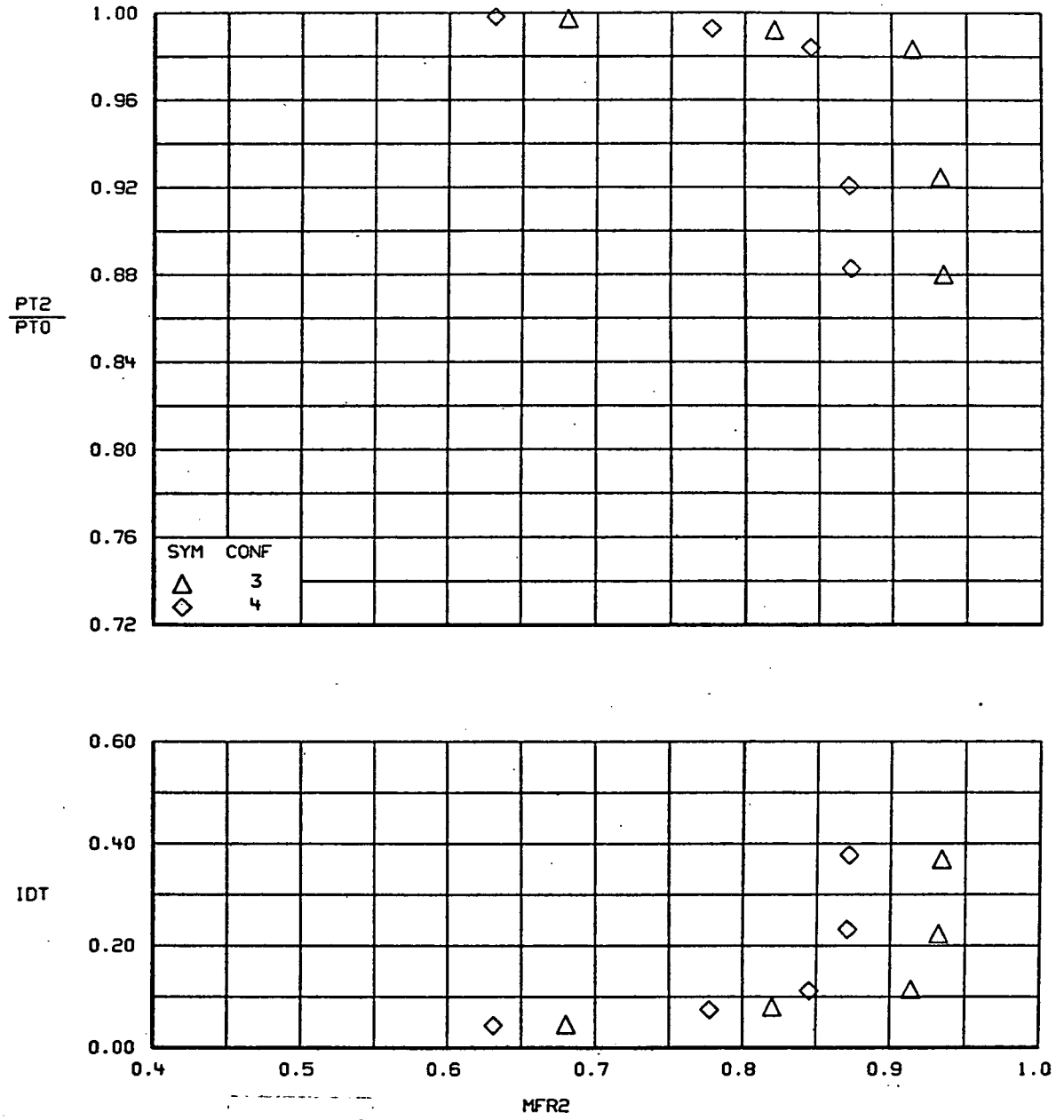

(a) $\alpha=0^{\circ}$

FIGURE 33.- VARIATION IN TWO-DIMENSIONAL INLET PERFORMANCE WITH BOTTOM LIP CONFIGURATION M=0.9, $\beta=0^{\circ}$

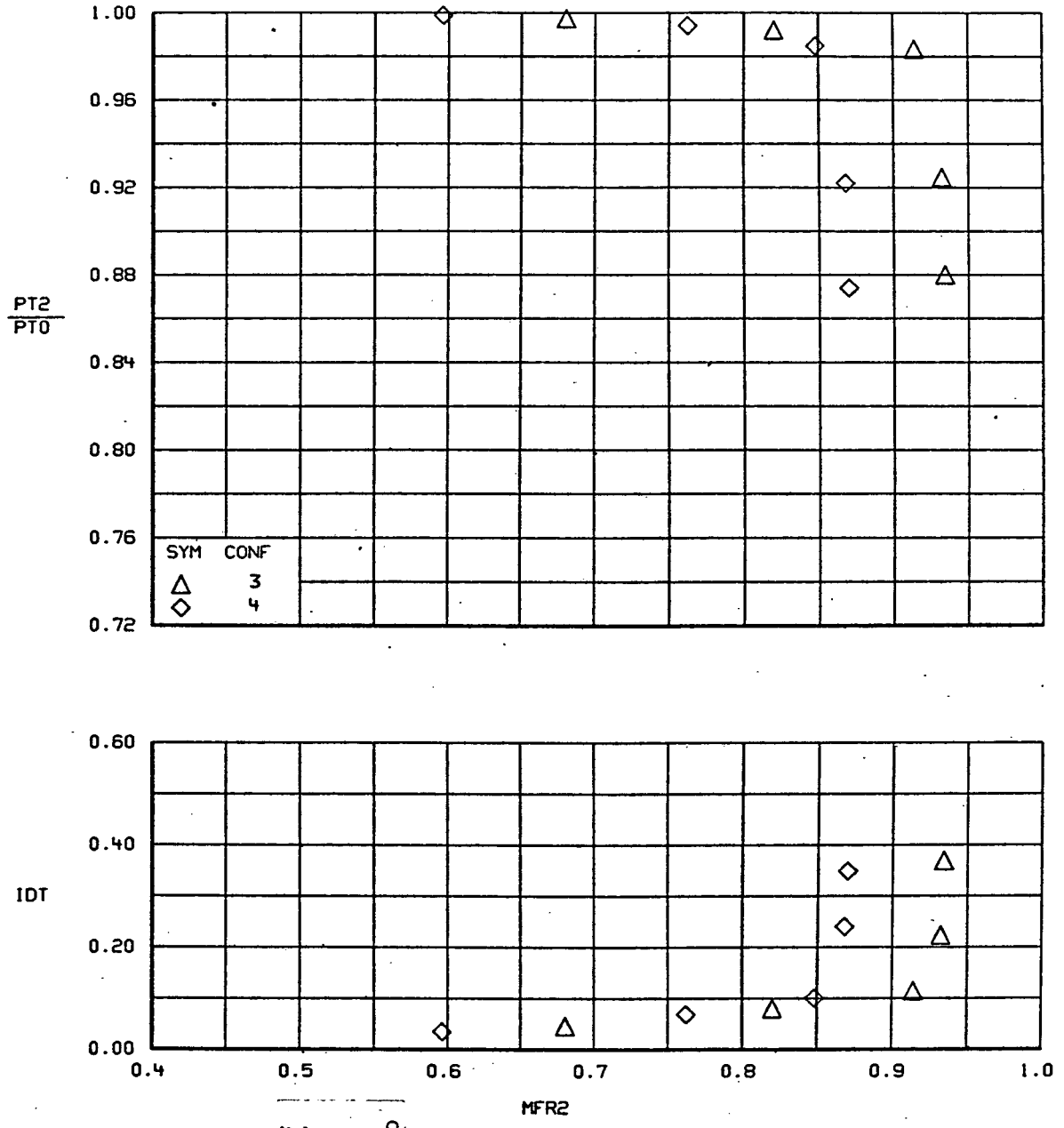

(b) $\alpha=4^{\circ}$

FIGURE 33.-CONTINUED.

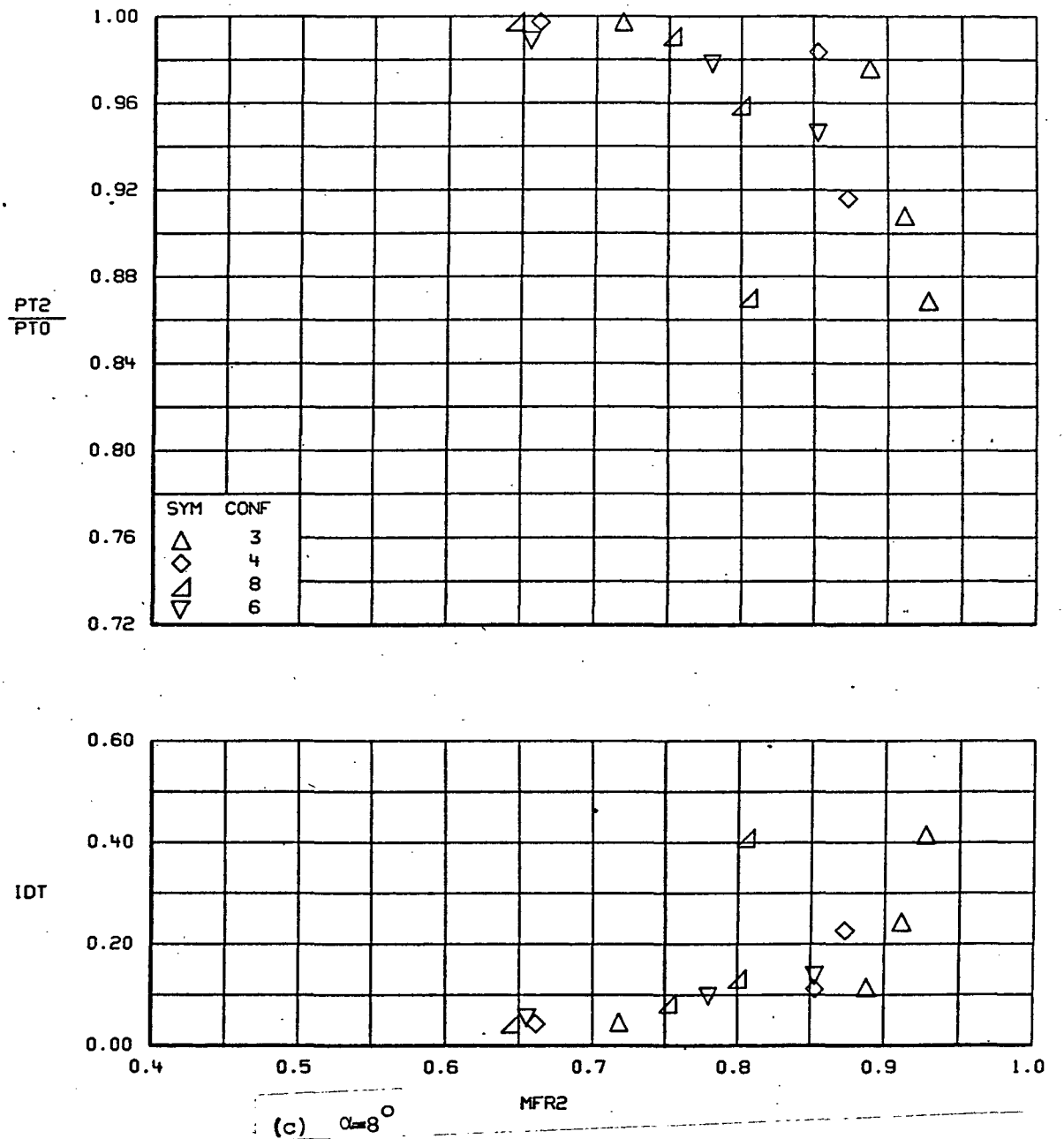

(c) $\alpha = 8^{\circ}$

FIGURE 33.-CONTINUED.

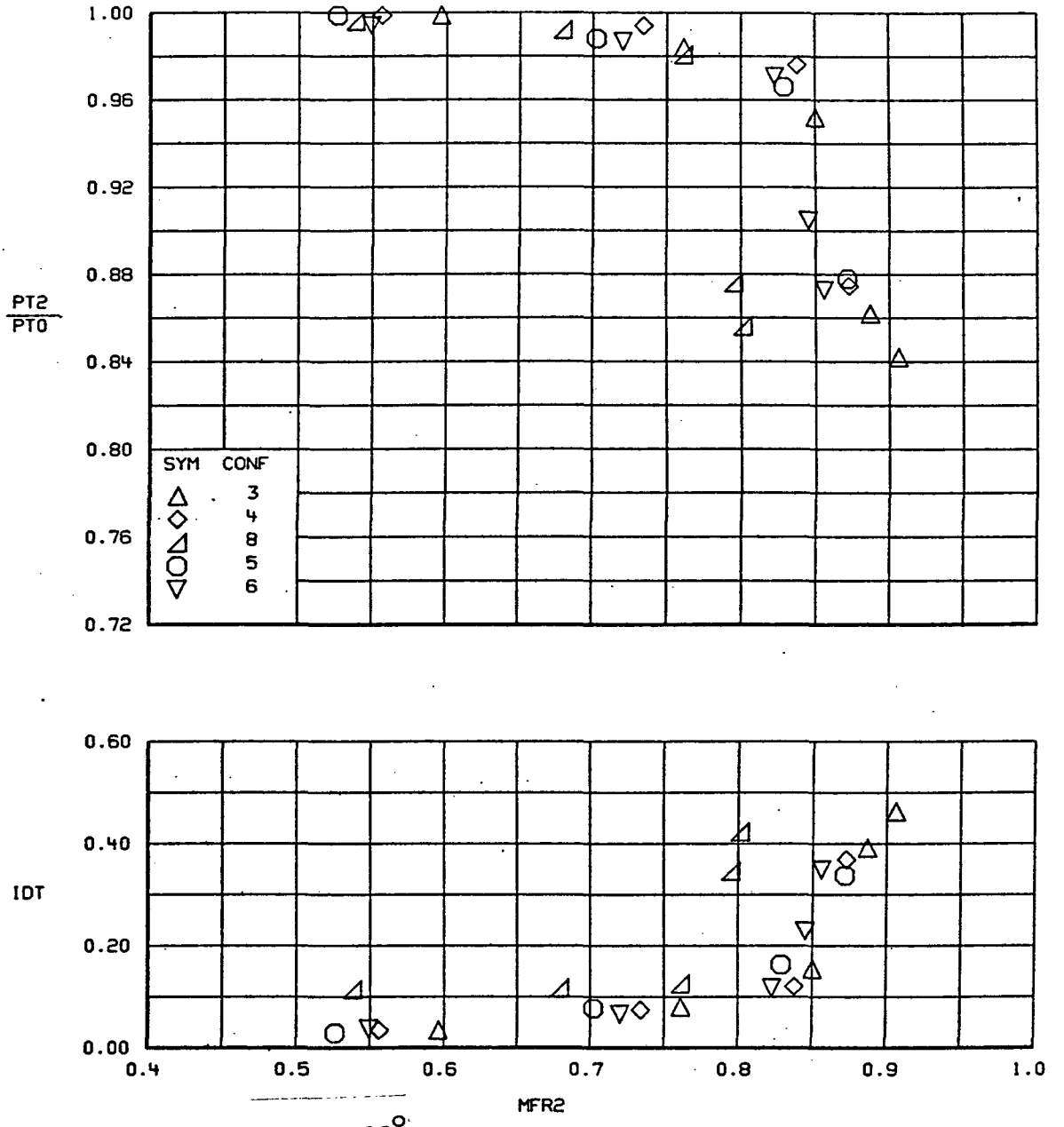

(d) $\alpha=12^{\circ}$

FIGURE 33.- CONTINUED.

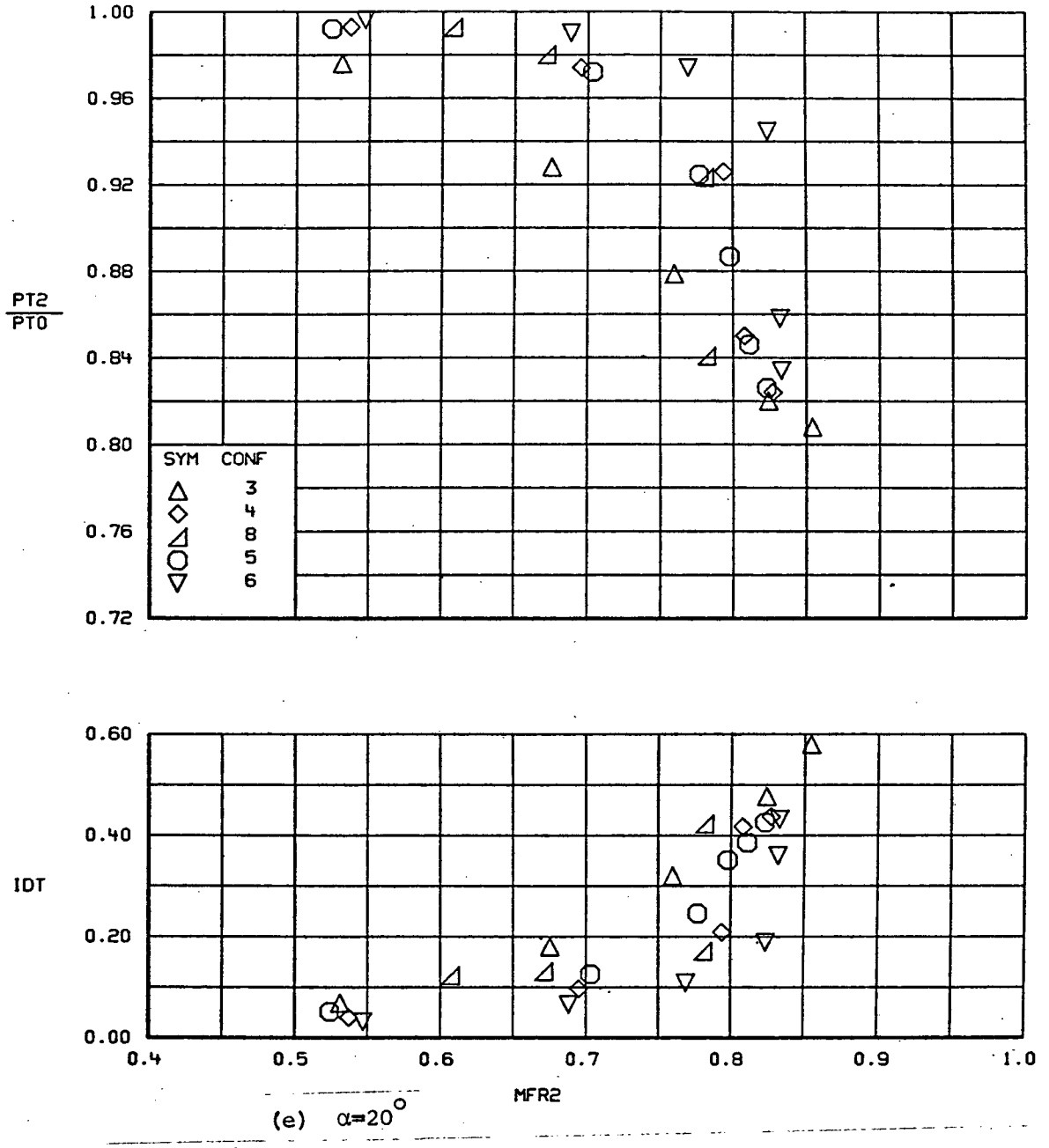

(e) $\alpha=20^{\circ}$

FIGURE 33.-CONTINUED.

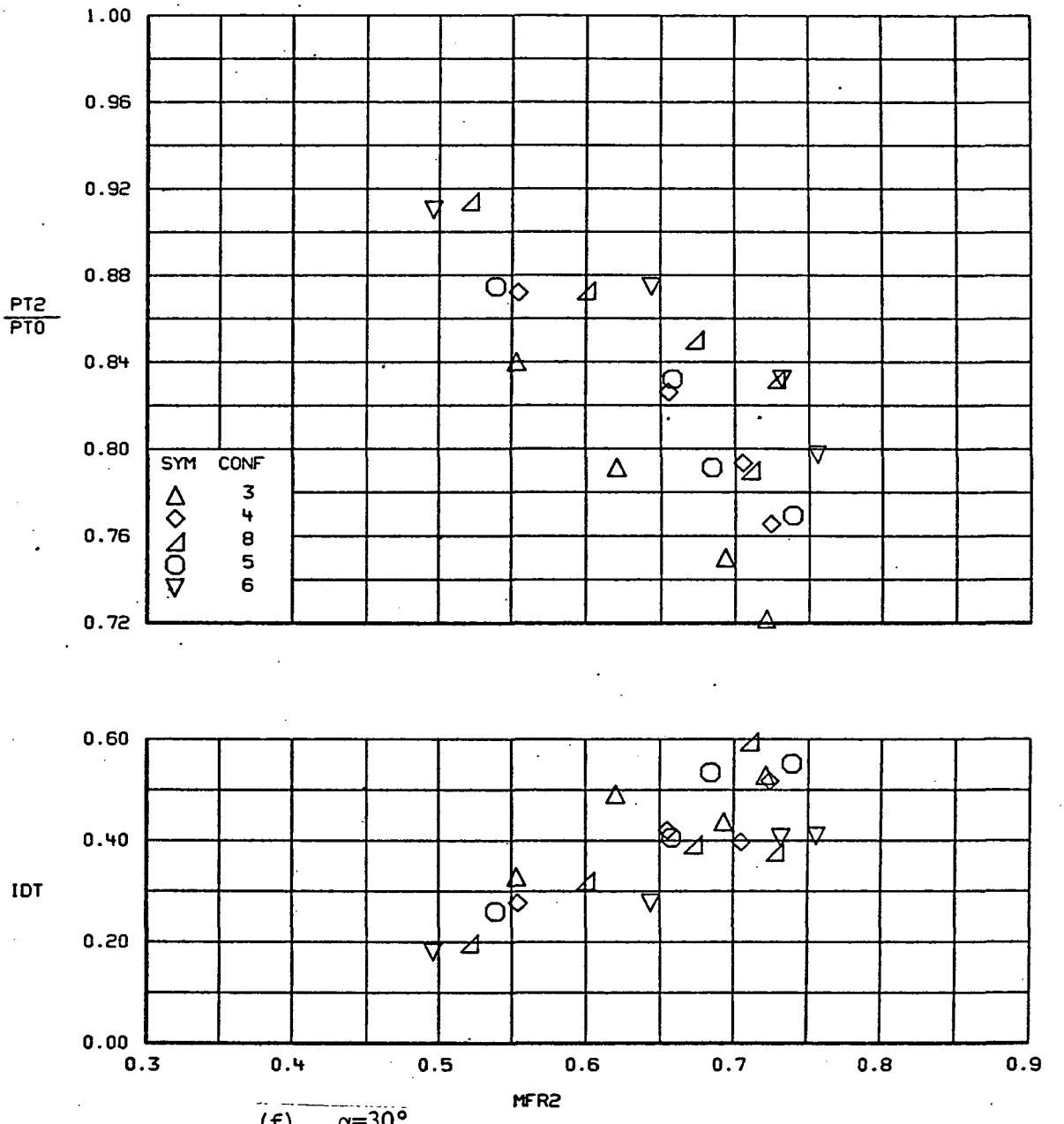

(f) α=30°

FIGURE 33.-CONTINUED.

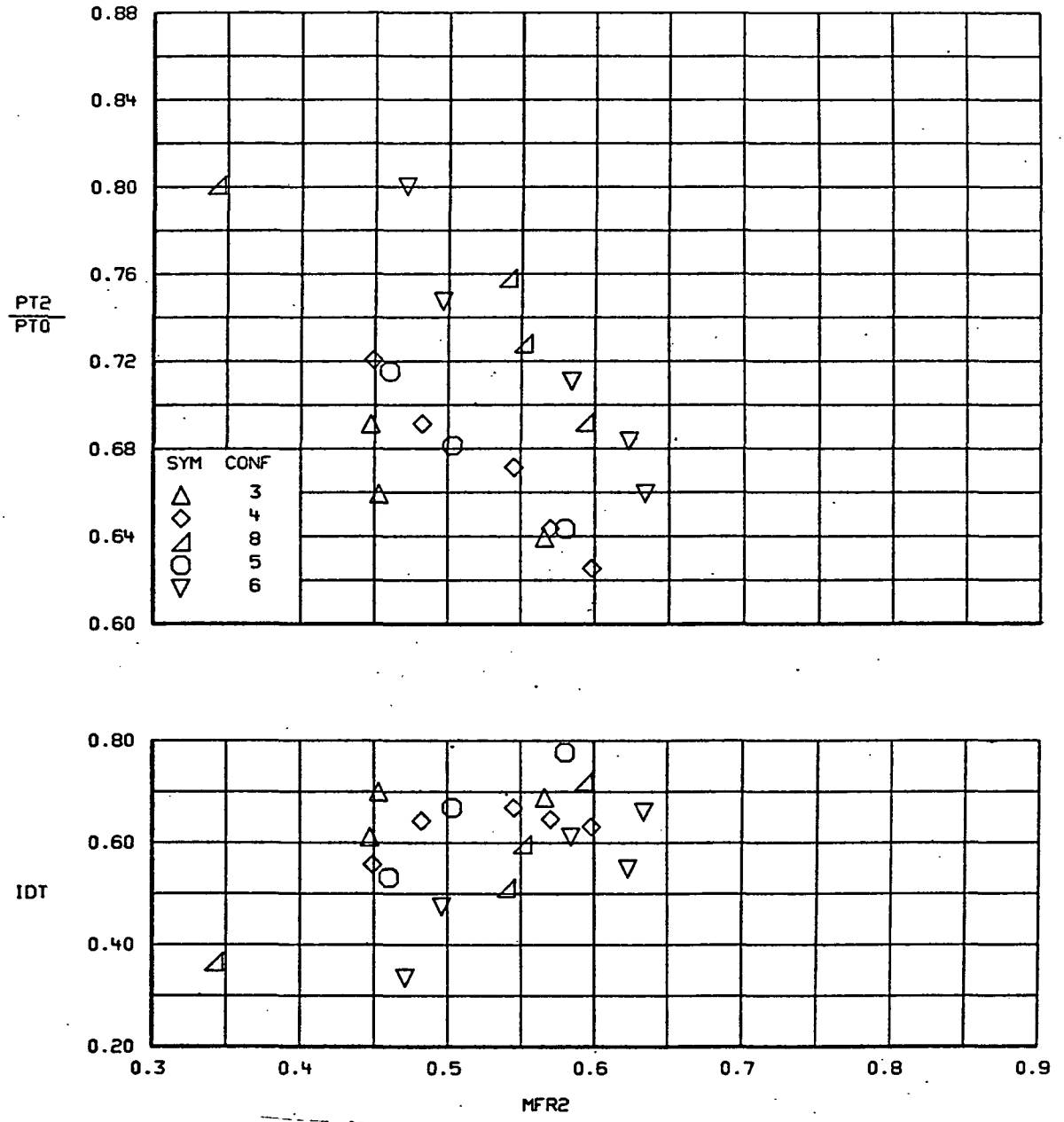

(g) α=40°

FIGURE 33.-CONCLUDED.

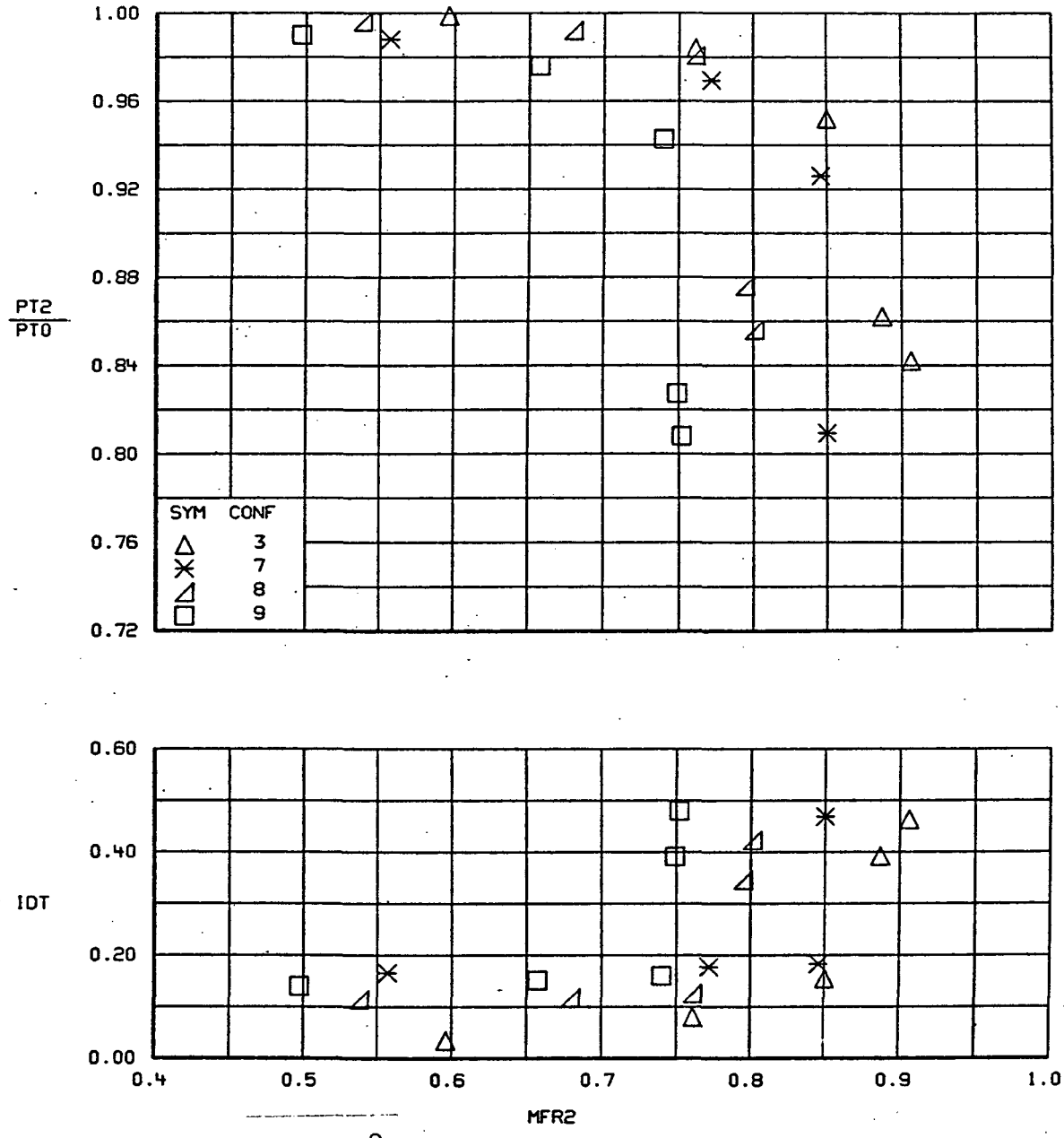

(a) $\alpha=12^{\circ}$

FIGURE 34.- EFFECT OF A TURNING VANE ON INLET PERFORMANCE
$M=0.9$, $\beta=0^{\circ}$

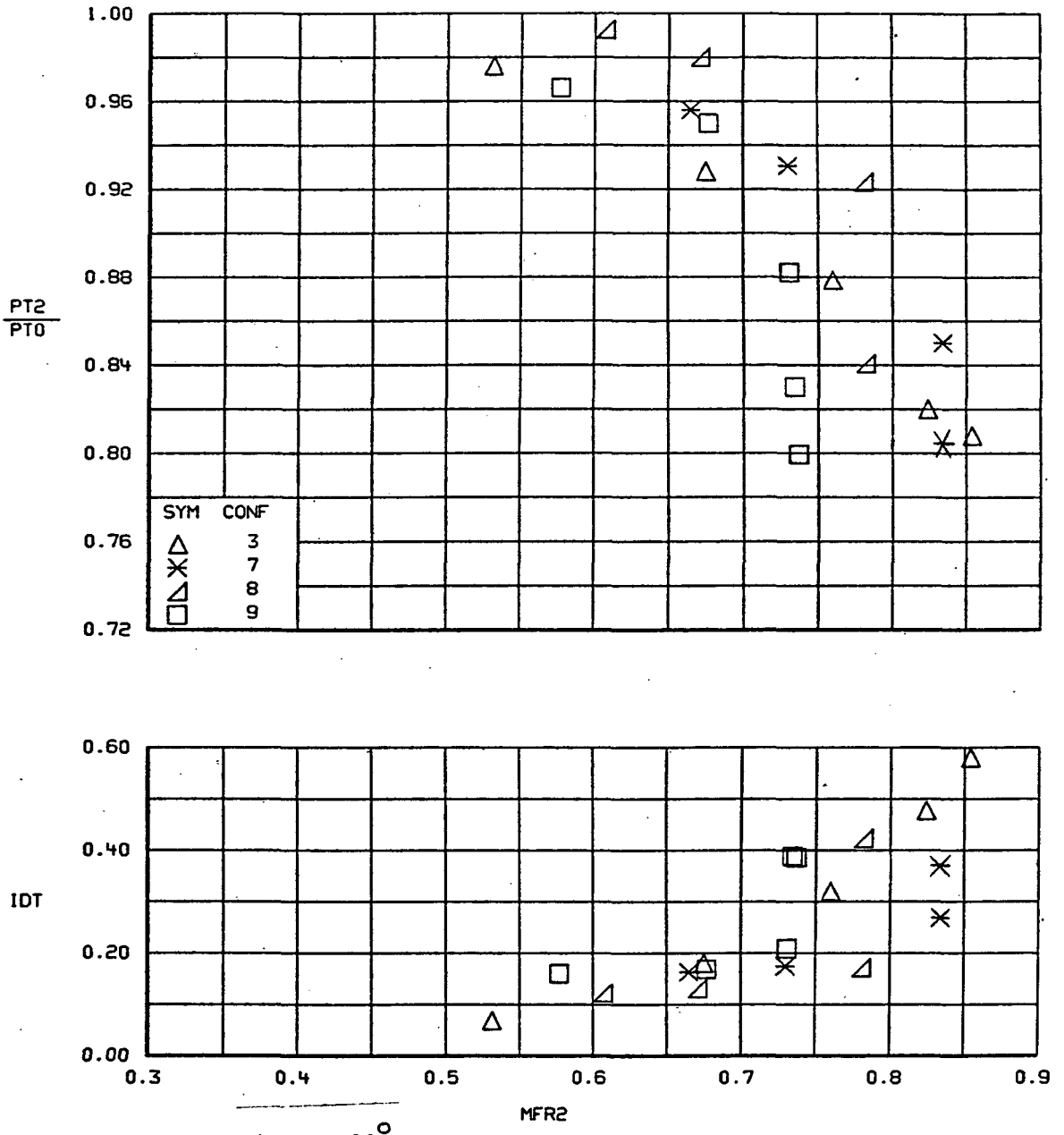

(b) $\alpha=20^{\circ}$

FIGURE 34.-CONTINUED.

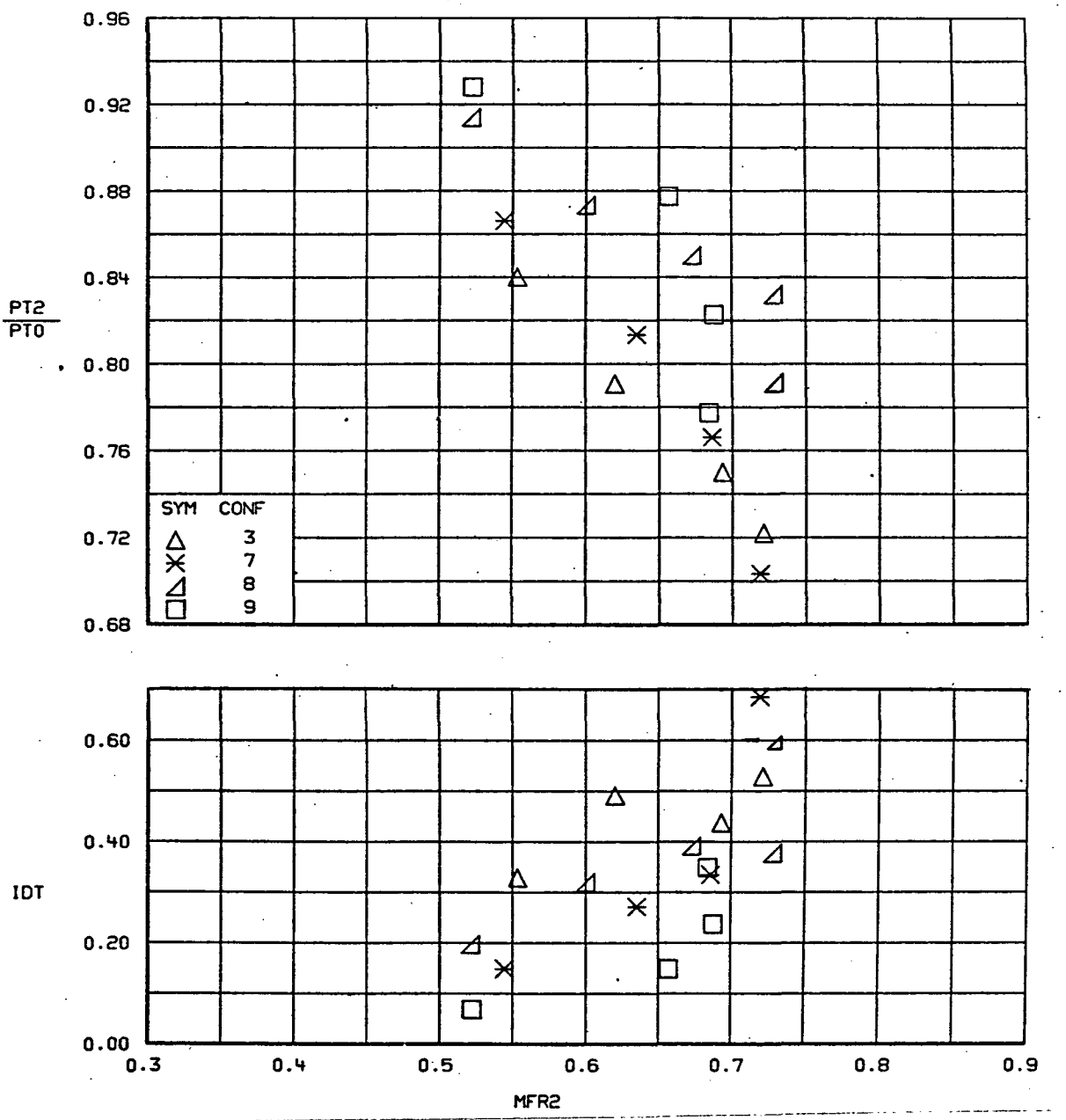

(c) $\alpha=30°$

FIGURE 34.-CONTINUED.

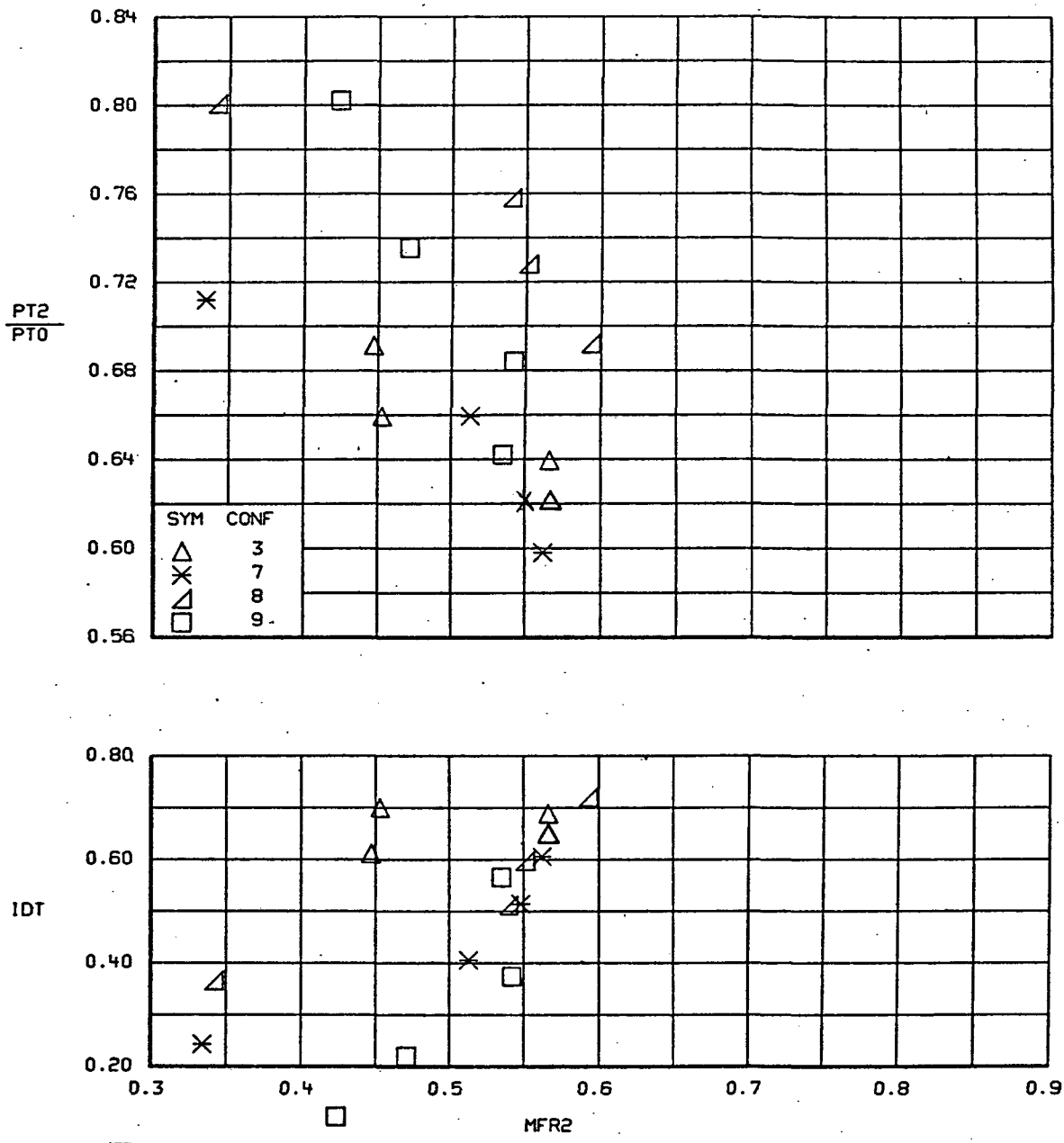

(d) α=40°

FIGURE 34.-CONCLUDED

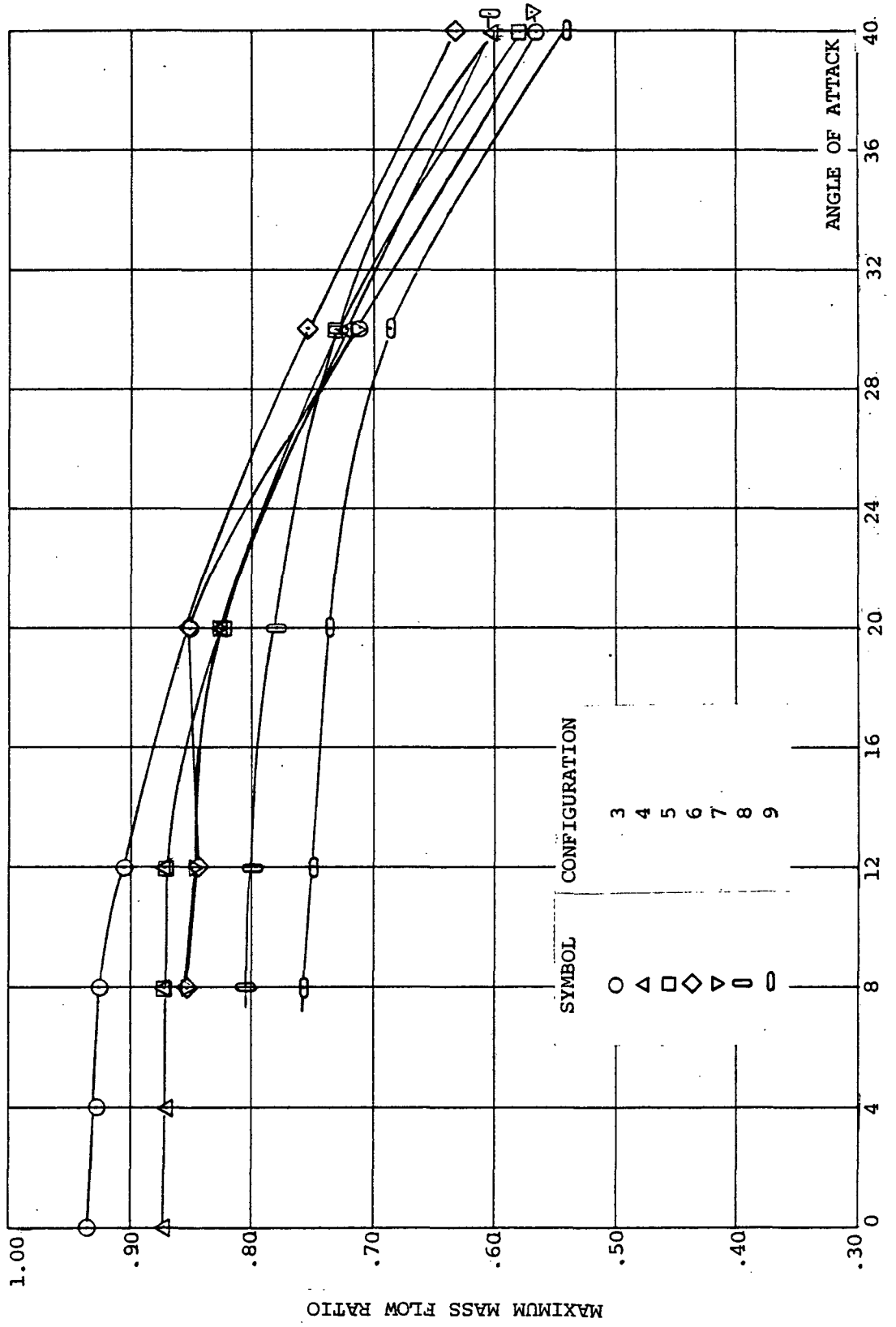

Figure 35.- Variation in maximum mass flow ratio with configuration.

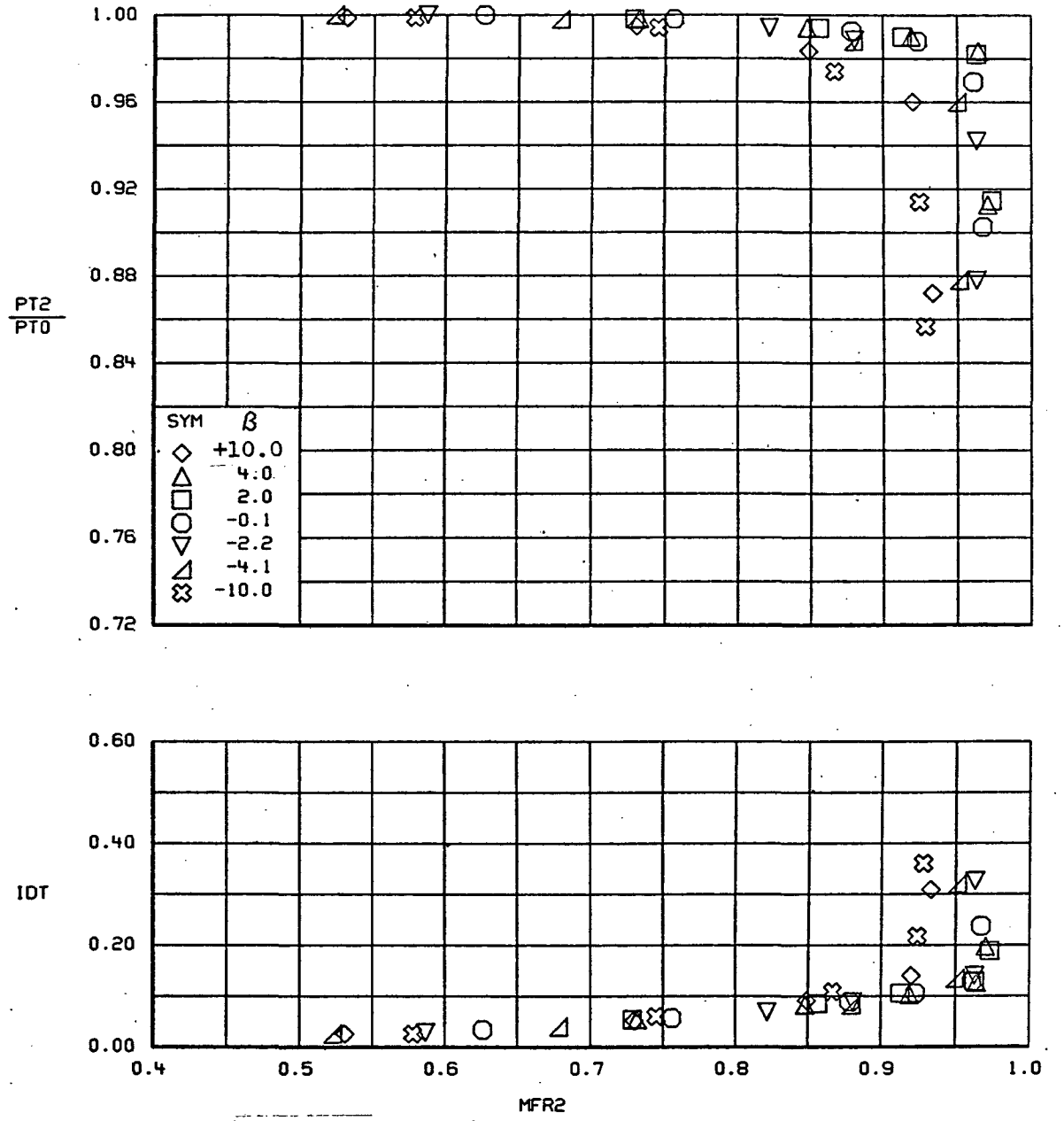

(a) α=4°

FIGURE 36.–VARIATION IN INLET PERFORMANCE WITH SIDESLIP CONFIGURATION 1, δ=0°, M=0.9

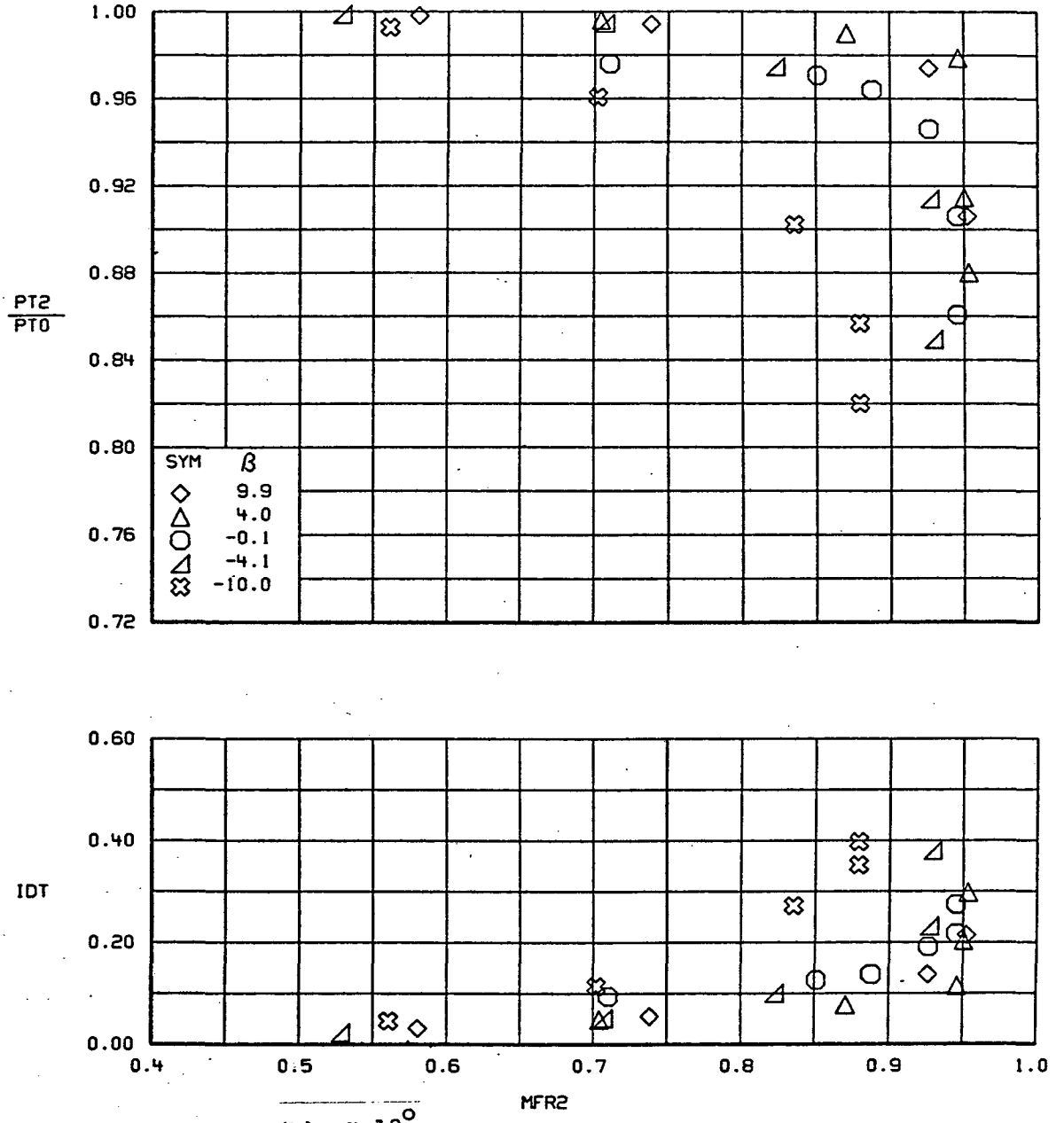

(b) $\alpha=12^{\circ}$

FIGURE 36.-CONCLUDED.

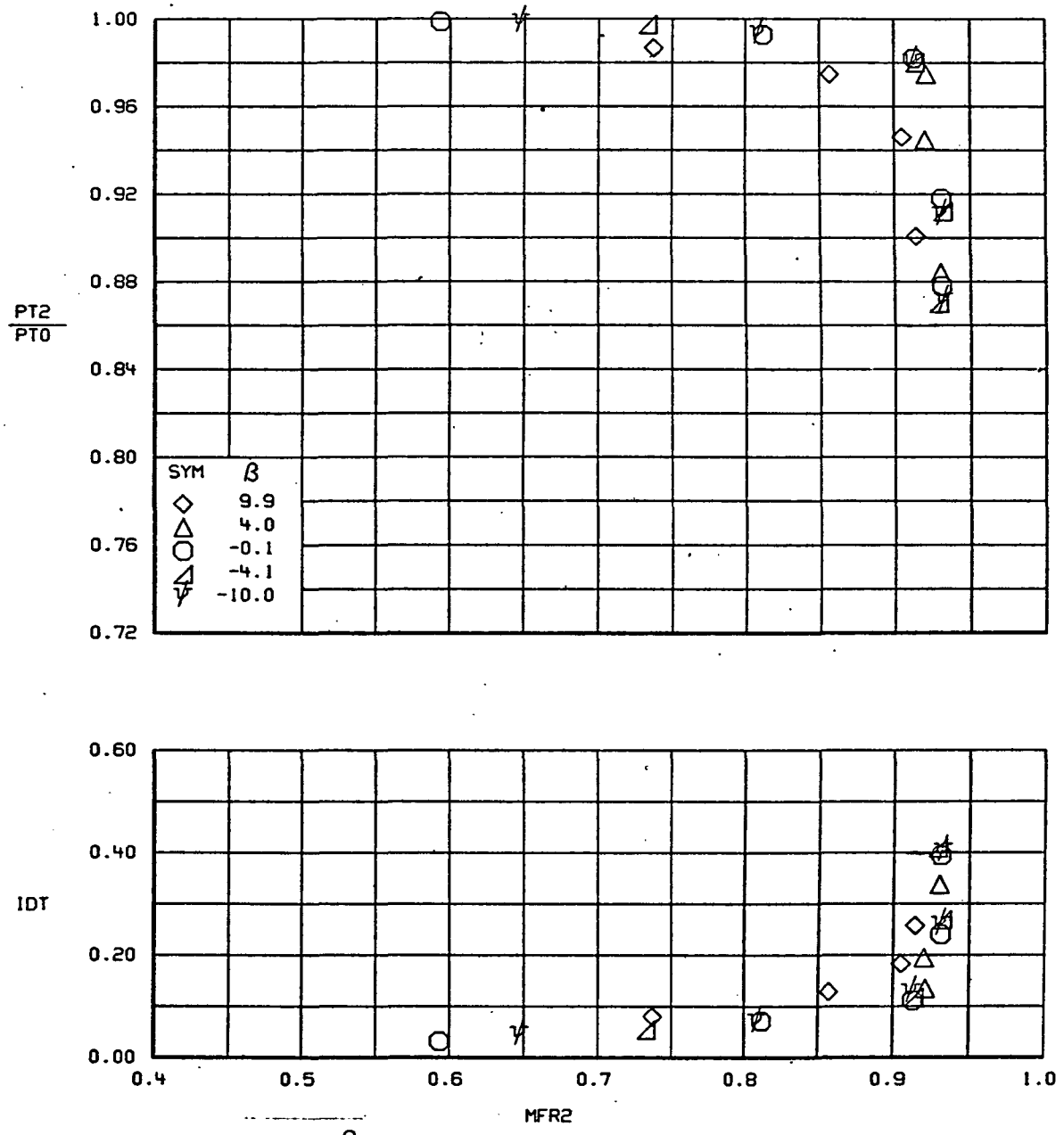

(a) $\alpha=4^{\circ}$

FIGURE 37.-VARIATION IN INLET PERFORMANCE WITH SIDESLIP CONFIGURATION 3, M=0.9.

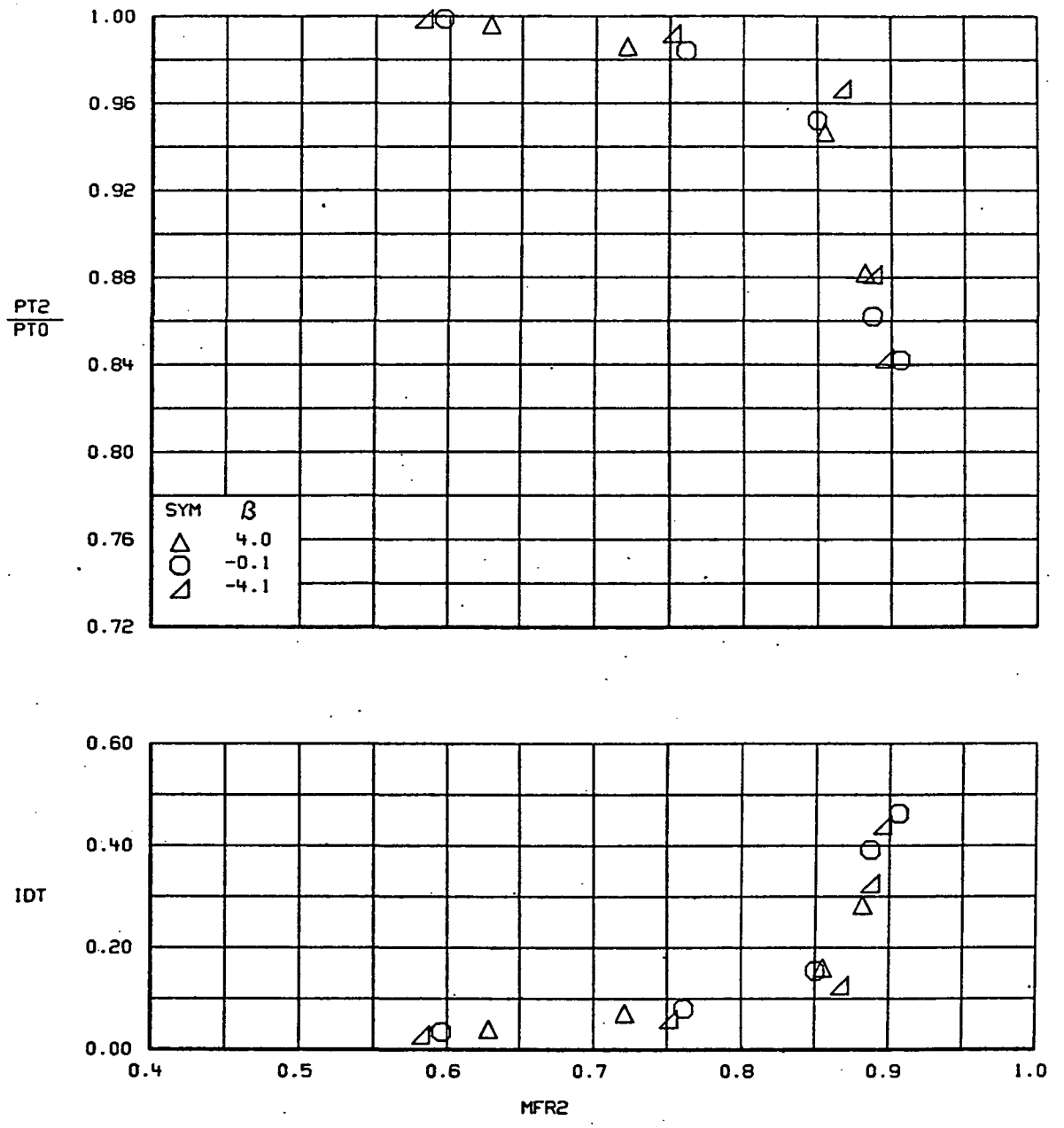

(b) α=12°

FIGURE 37.-CONCLUDED.

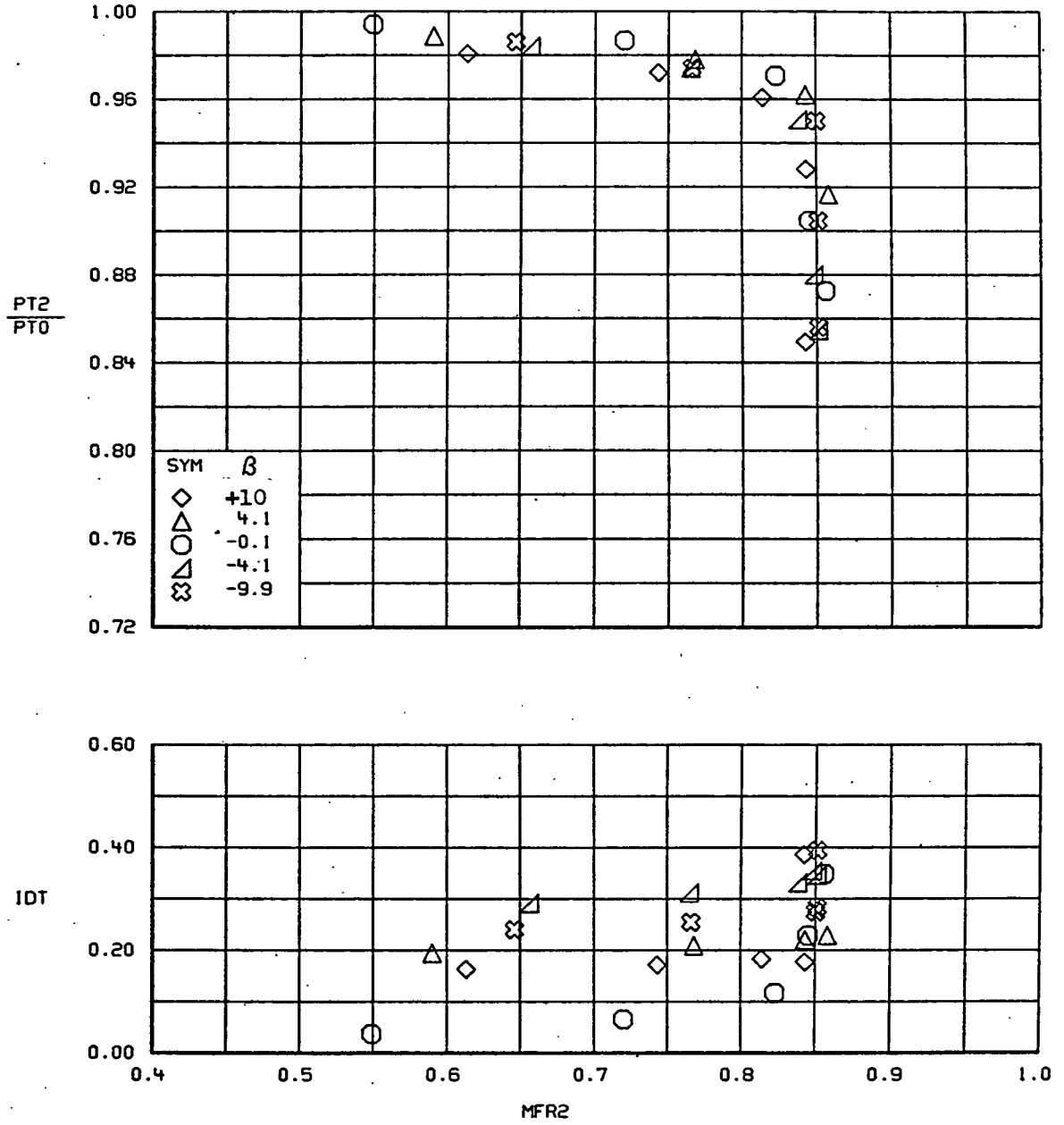

FIGURE 38.- VARIATION IN INLET PERFORMANCE WITH SIDESLIP
CONFIGURATION 6, M=0.9, $\alpha=12^{\circ}$

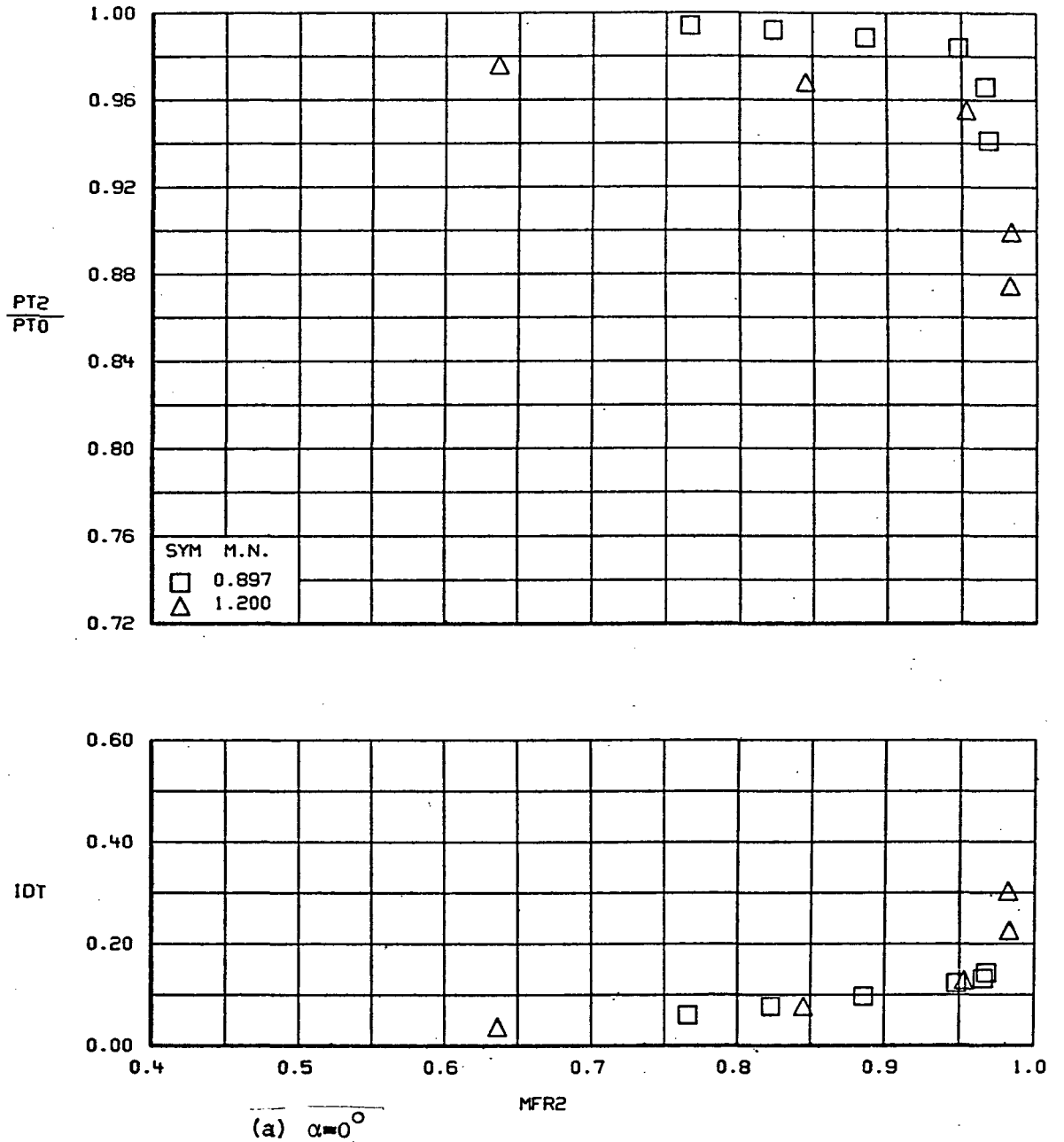

(a) $\alpha=0^{\circ}$

FIGURE 39.- INLET PERFORMANCE VARIATION WITH MACH NUMBER
CONFIGURATION 1, $\delta=0°$, $\beta=0°$

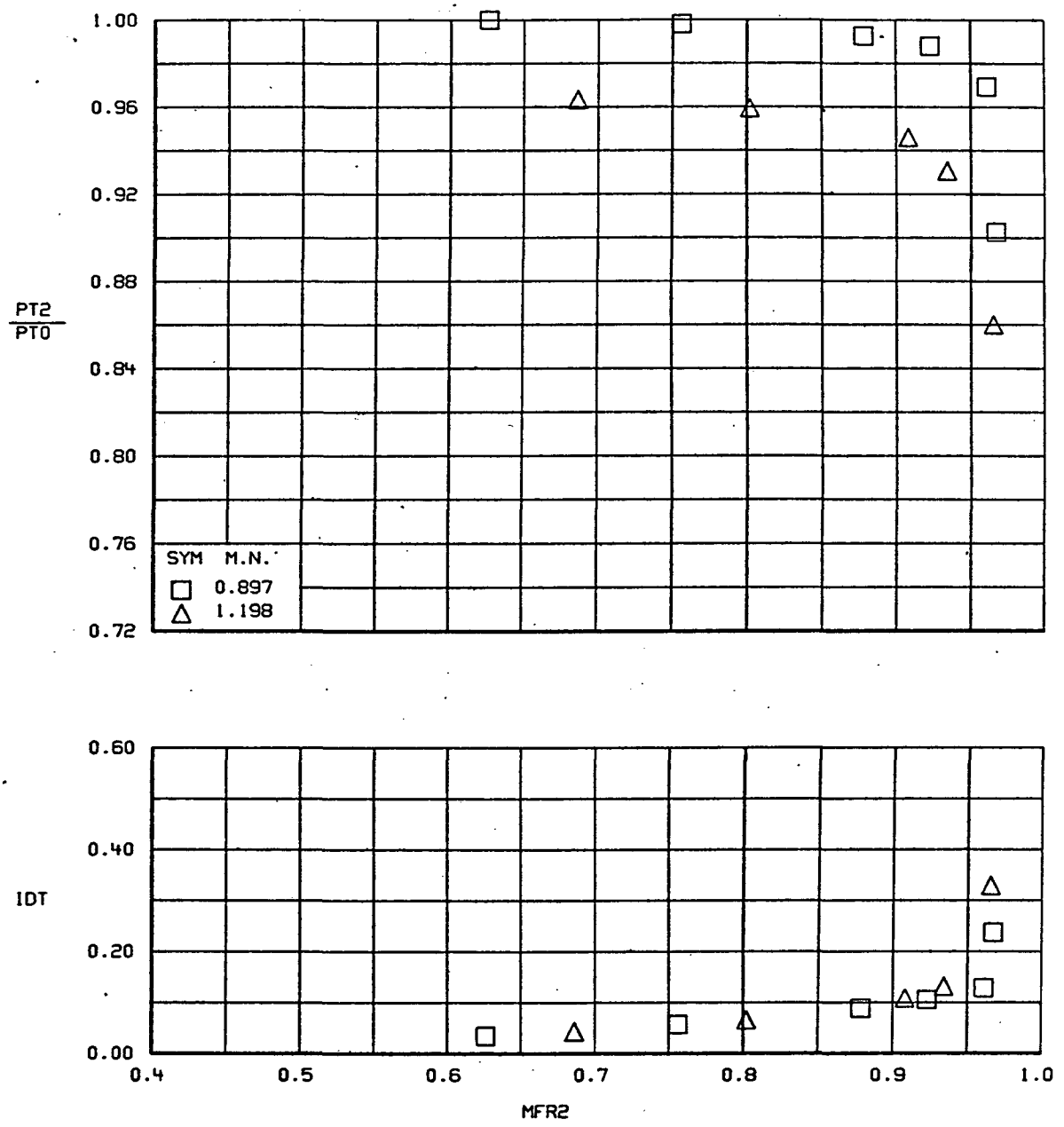

(b) α=4°

FIGURE 39.-CONTINUED.

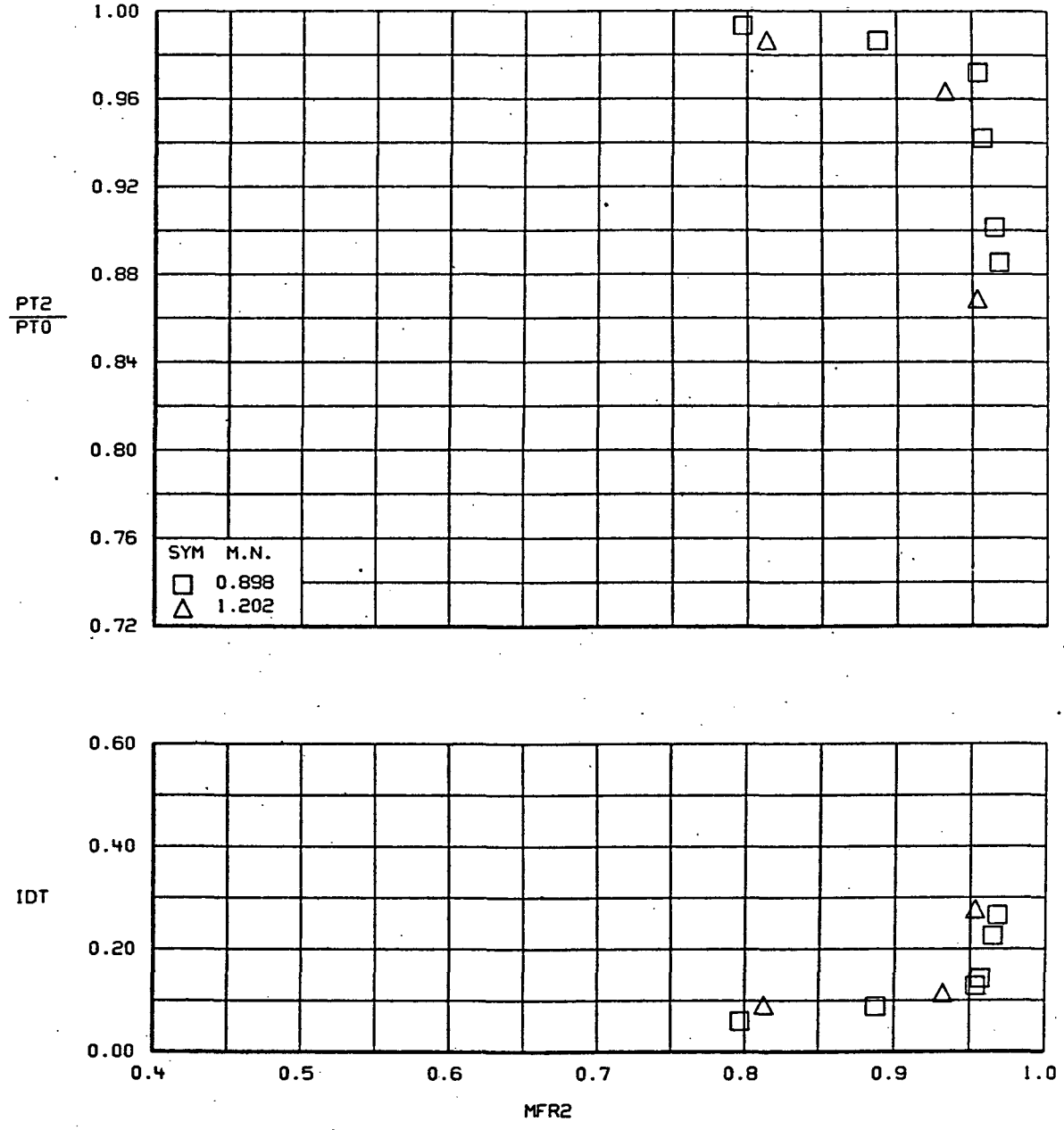

(c) α=8°

FIGURE 39.-CONCLUDED.

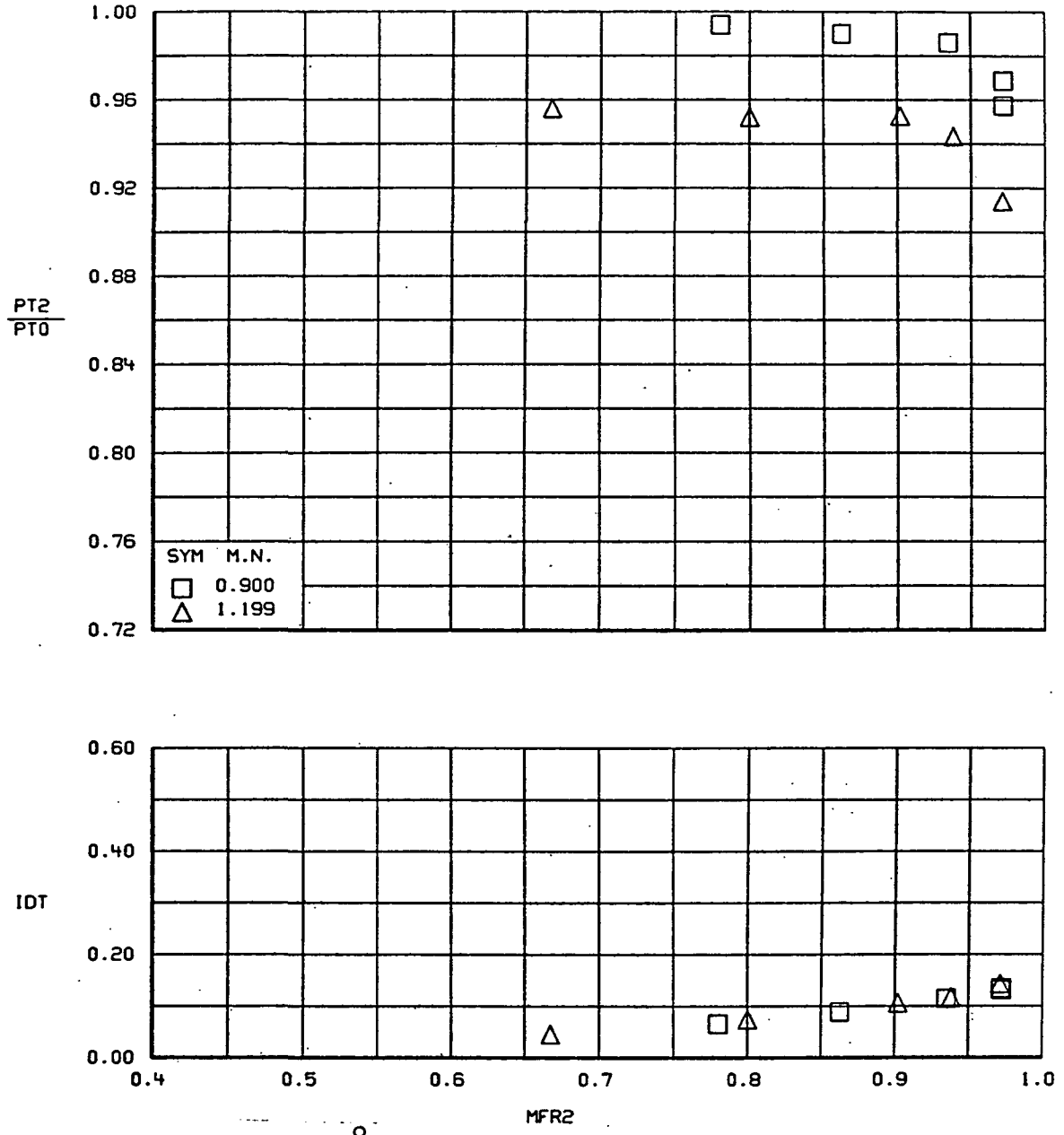

(a) $\alpha=0^{\circ}$

FIGURE 40.- INLET PERFORMANCE VARIATION WITH MACH NUMBER CONFIGURATION 2, M=0.9, $\beta=0^{\circ}$

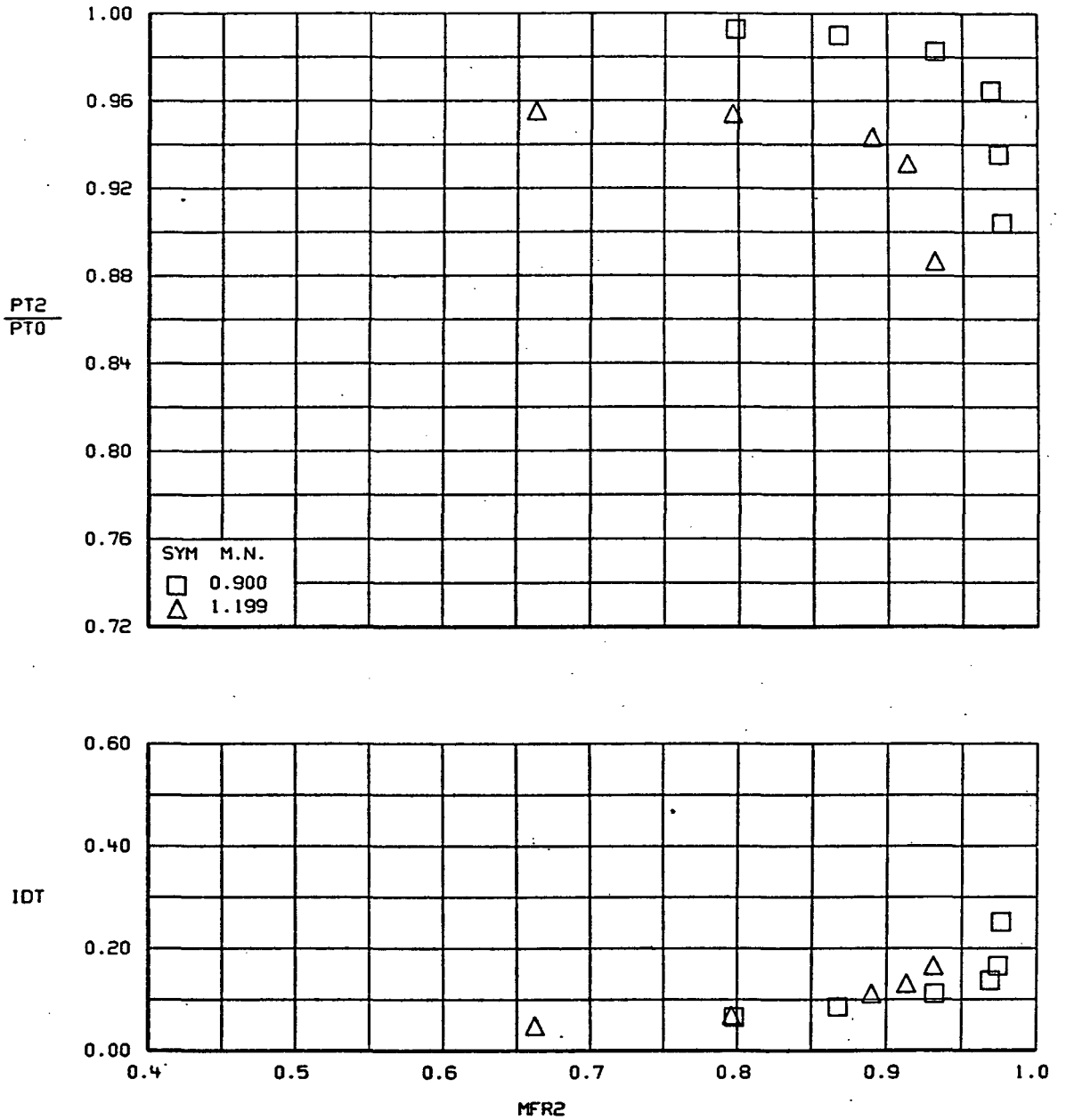

(b) $\alpha=4°$

FIGURE 40.-CONTINUED.

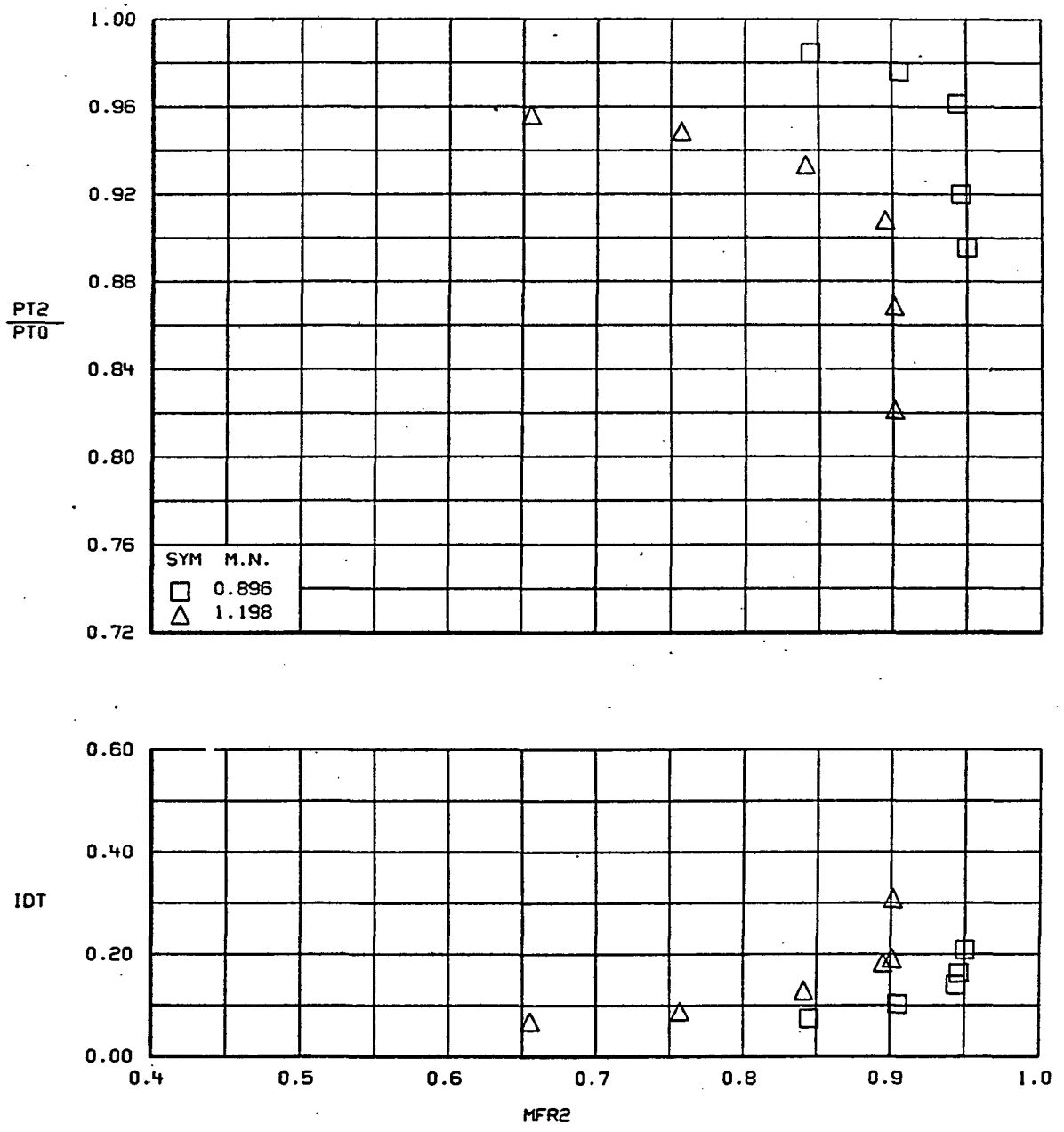

(c) α=8°

FIGURE 40.-CONCLUDED.

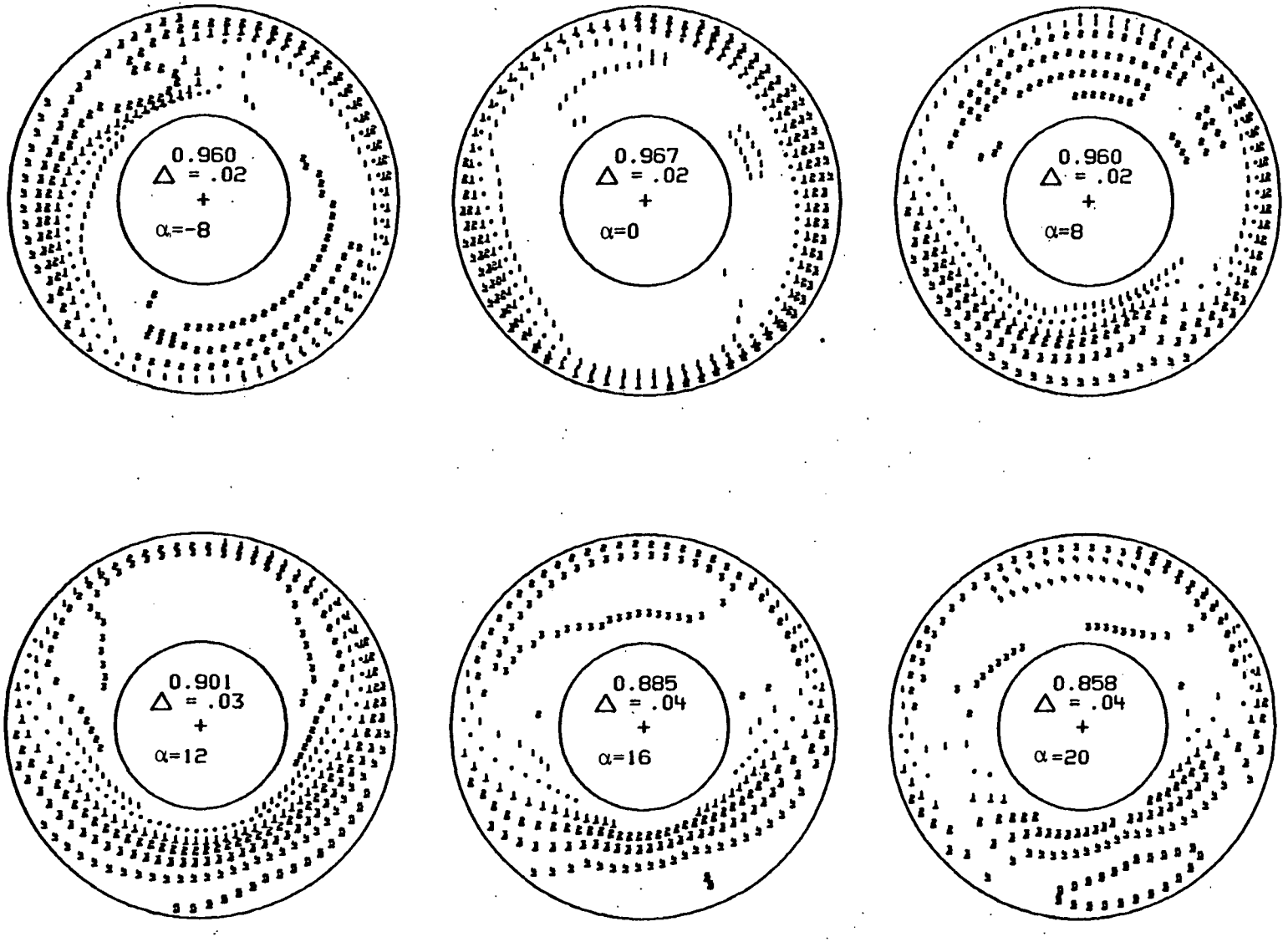

(A)

FIGURE 41.- VARIATION IN ENGINE FACE TOTAL PRESSURE DISTRIBUTION WITH ANGLE OF ATTACK, CONFIGURATION 2, M=0.9, β=0°

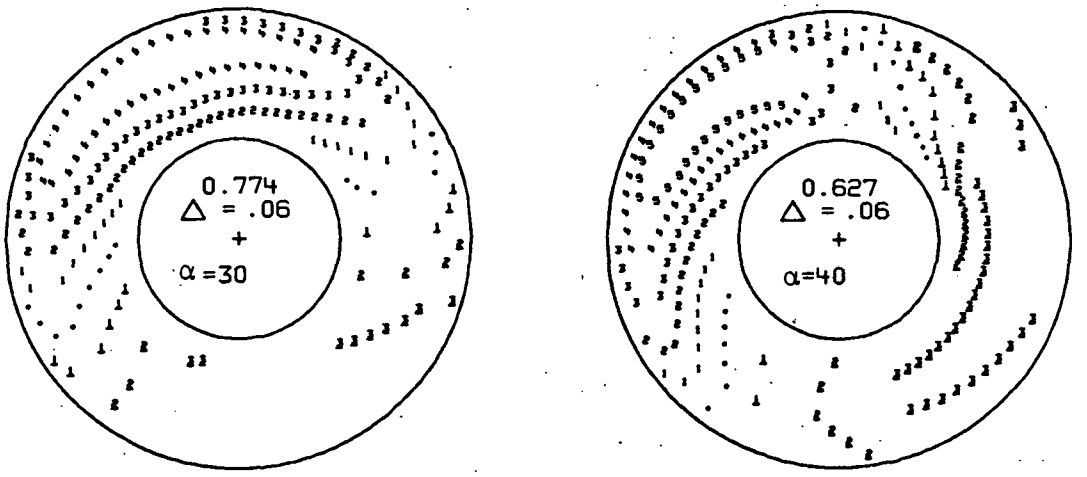

(B)

FIGURE 41.- CONCLUDED

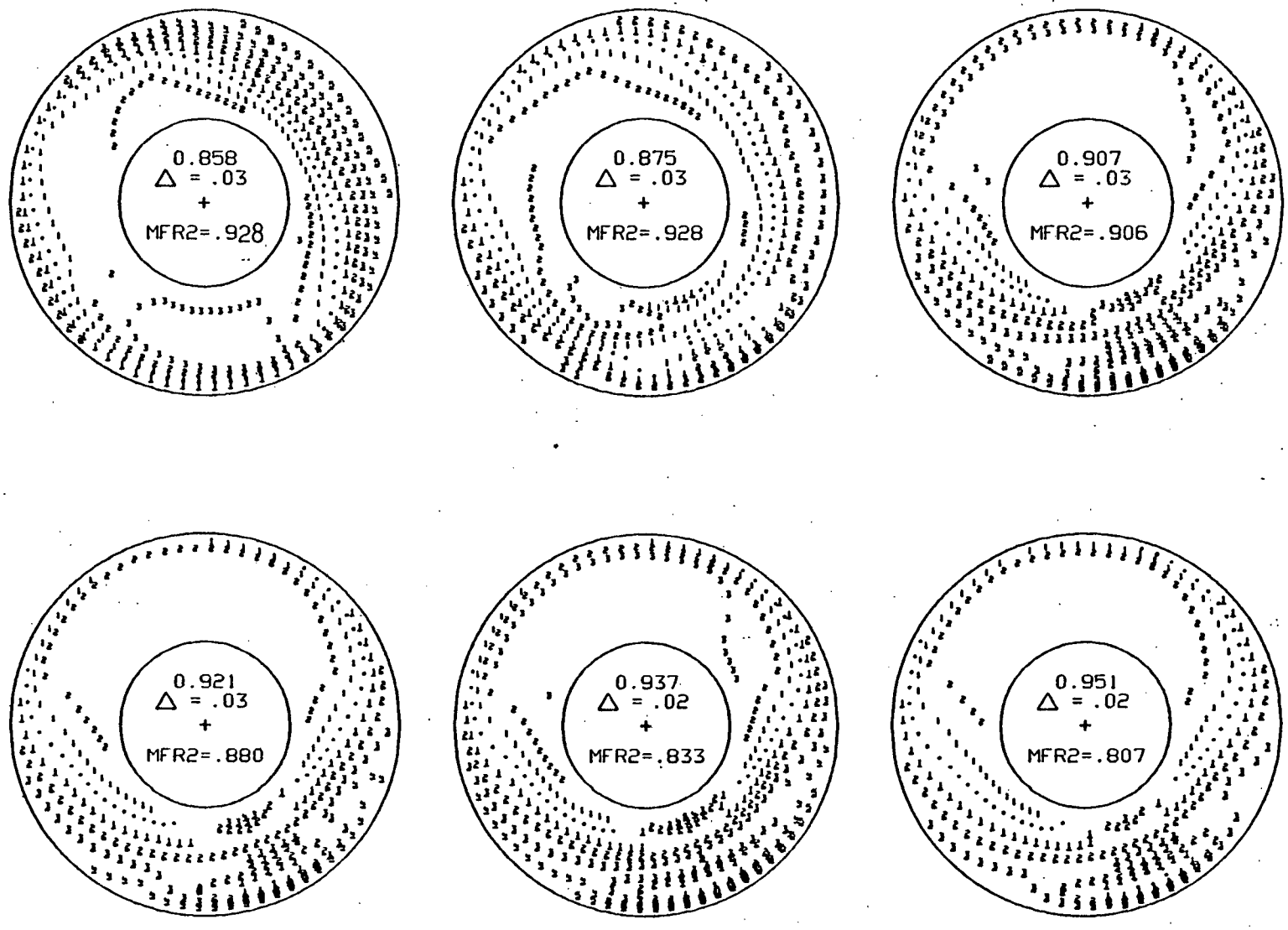

(A) α=12

FIGURE 42.-VARIATION IN ENGINE FACE TOTAL PRESSURE DISTRIBUTION WITH MASS FLOW RATIO, CONFIGURATION 2, M=0.9, β=0°

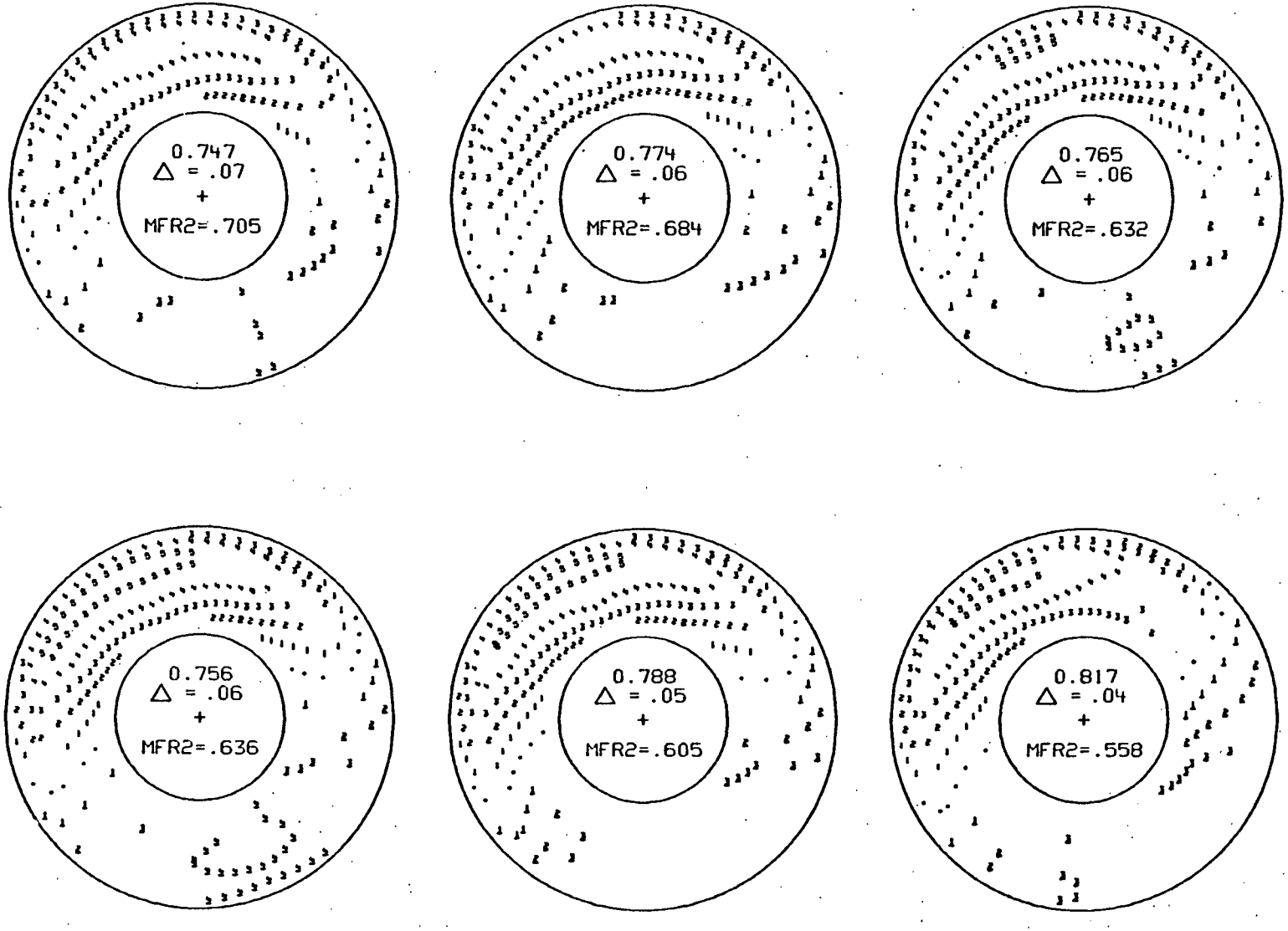

(B) α=30

FIGURE 42.- CONCLUDED

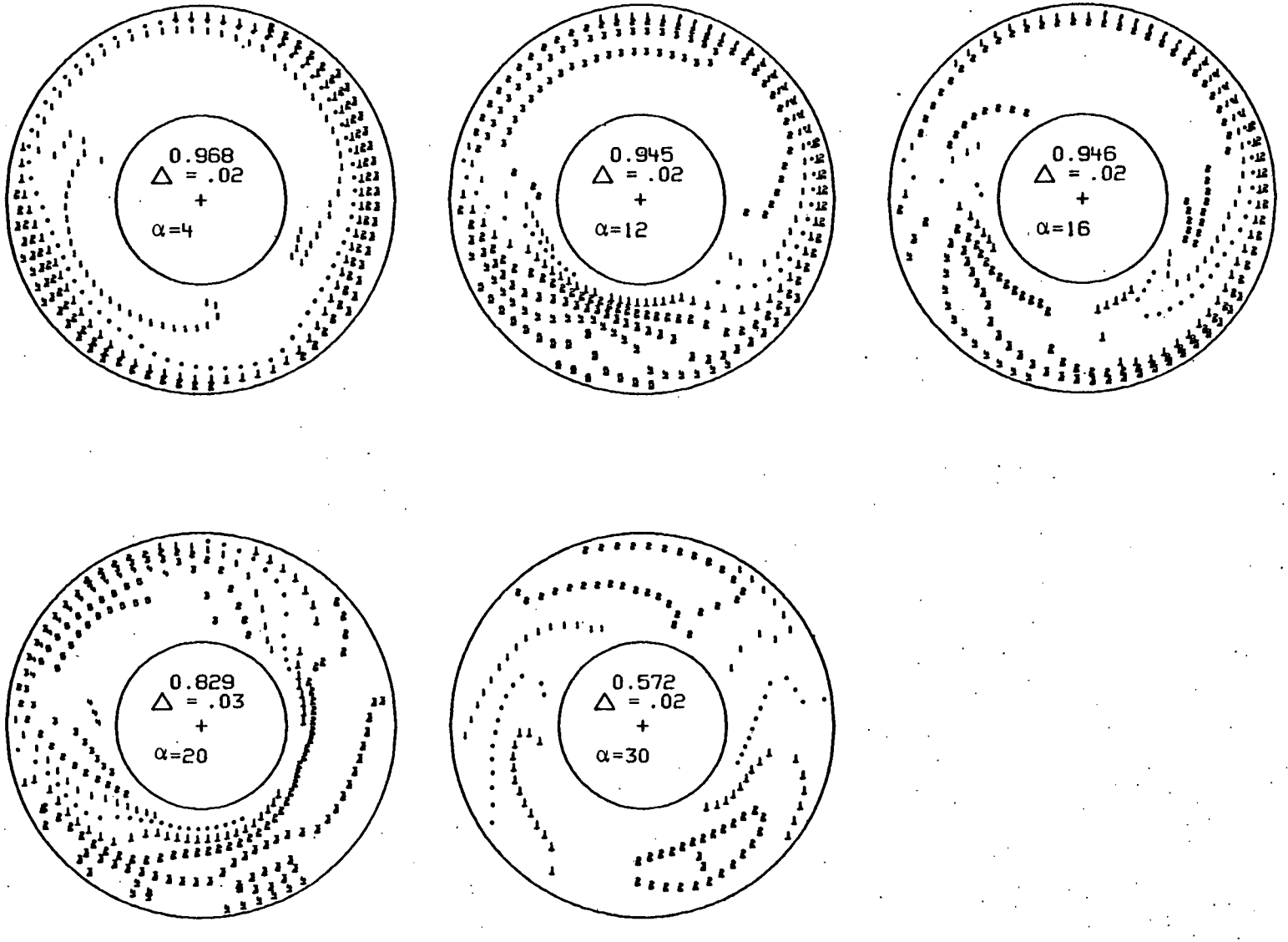

FIGURE 43.- VARIATION IN ENGINE FACE TOTAL PRESSURE DISTRIBUTION WITH ANGLE OF ATTACK, CONFIGURATION 1, $\delta=0^{\circ}$, $M=0.9$, $\beta=0^{\circ}$

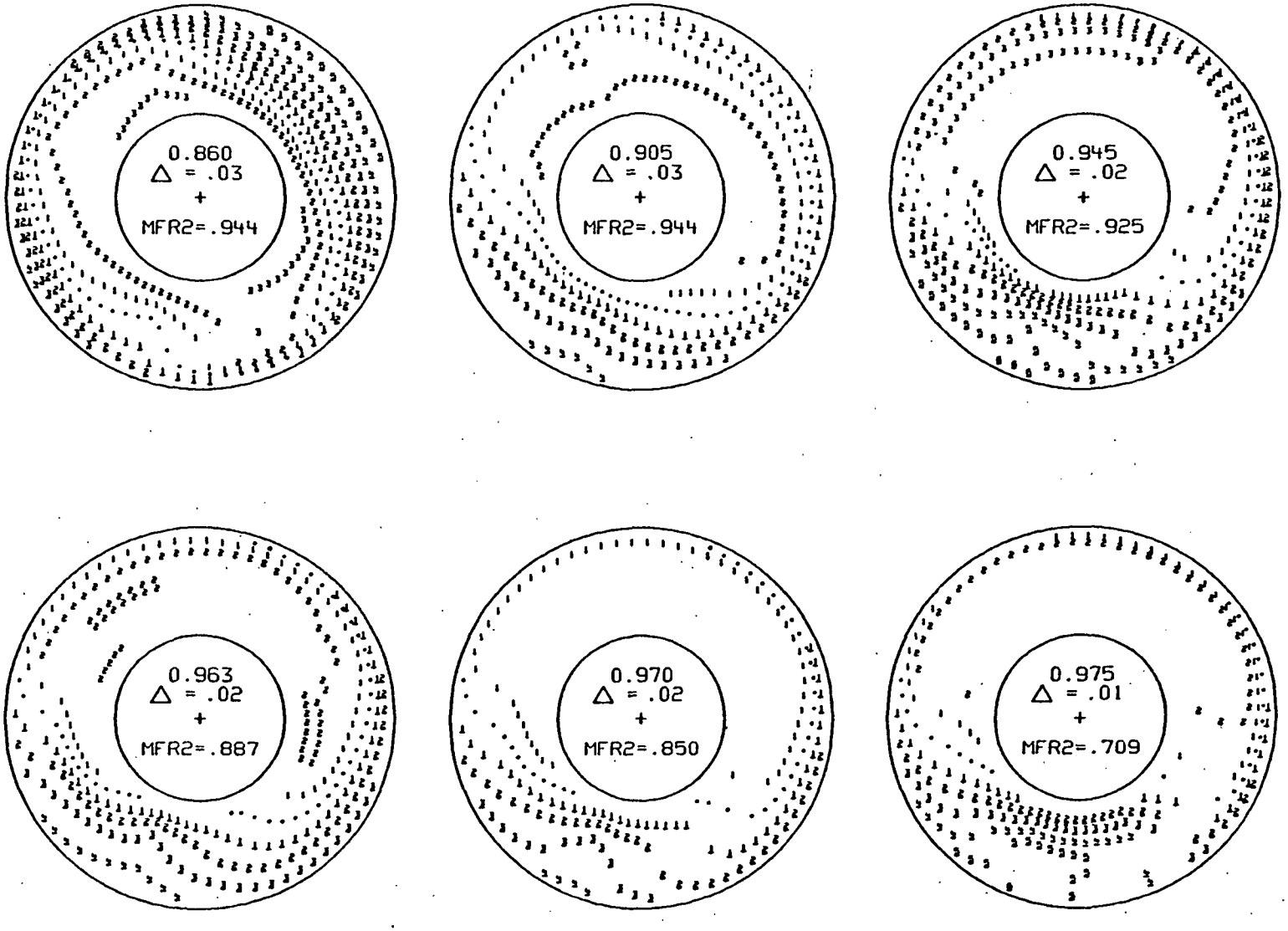

(A) $\alpha = 12$

FIGURE 44.-VARIATION IN ENGINE FACE TOTAL PRESSURE DISTRIBUTION WITH MASS FLOW RATIO, CONFIGURATION 1, $\delta = 0^{\circ}$, M-00.9, $\beta = 0^{\circ}$

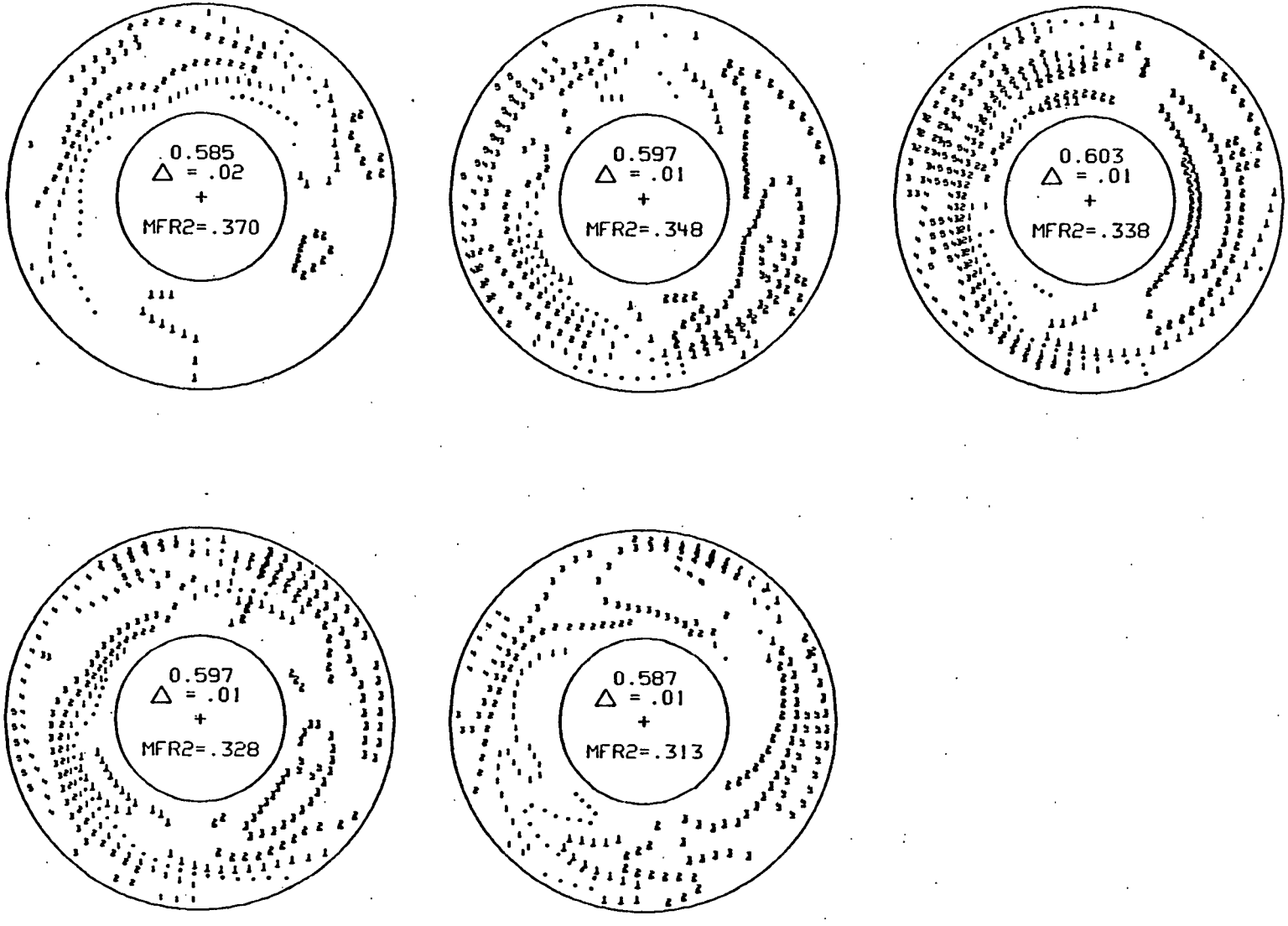

(B) α=30

FIGURE 44.- CONCLUDED

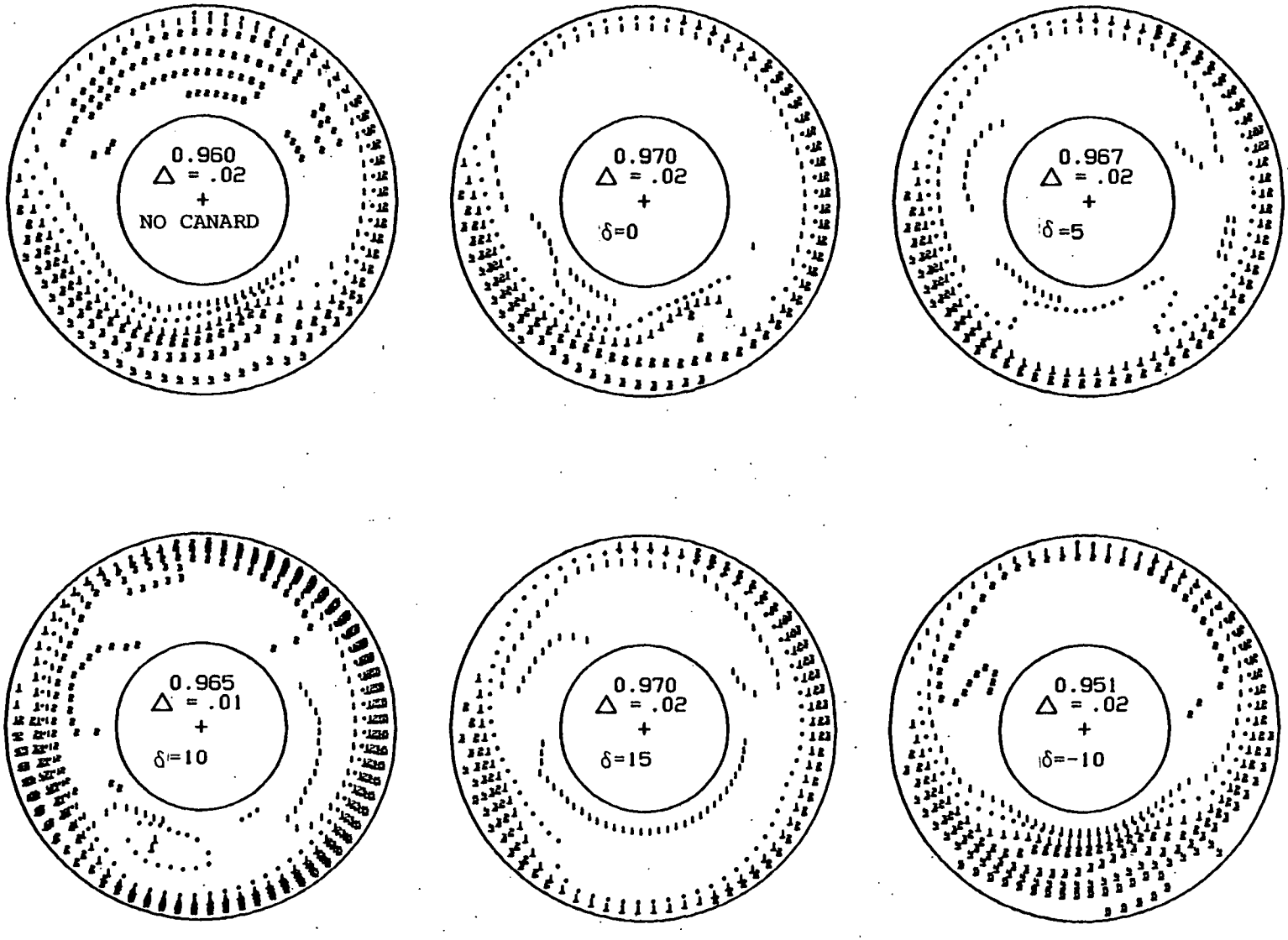

(A) α=8

FIGURE 45.-EFFECT OF A CANARD ON ENGINE FACE TOTAL PRESSURE DISTRIBUTION, CONFIGURATION 1, M=0.9, $\beta=0^{\circ}$

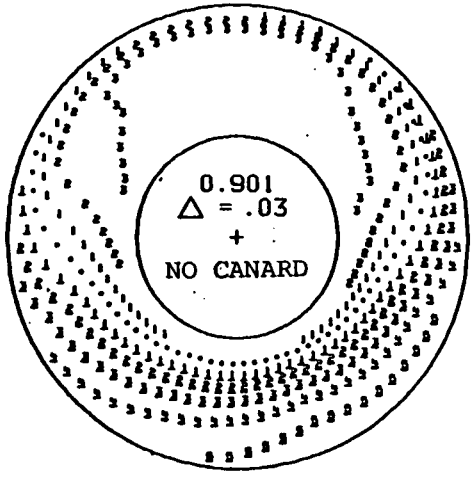

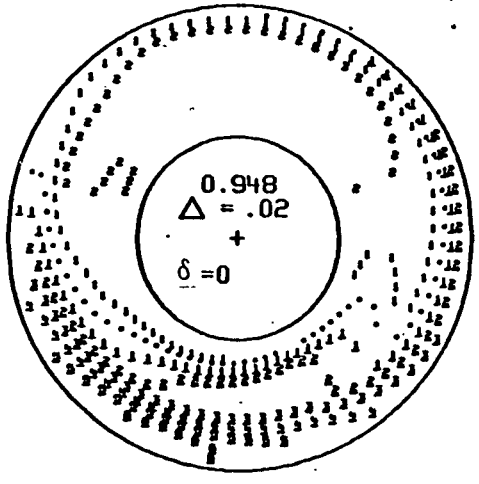

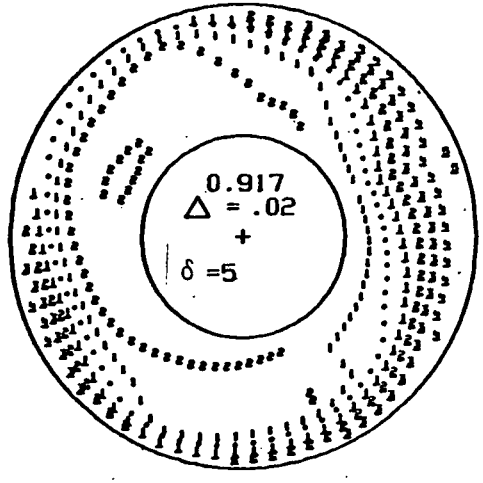

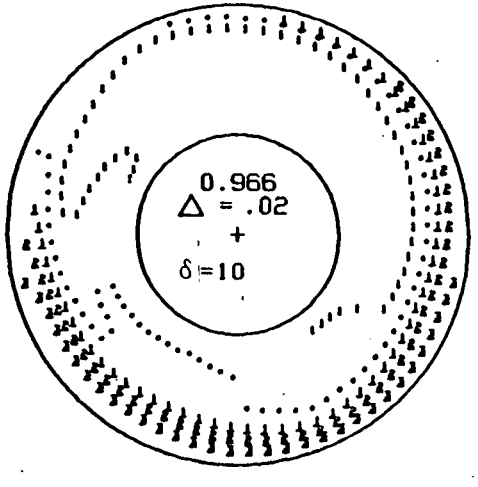

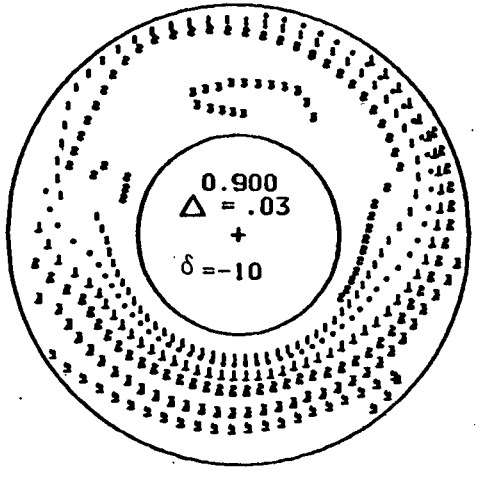

(B) α=12

FIGURE 45.- CONTINUED

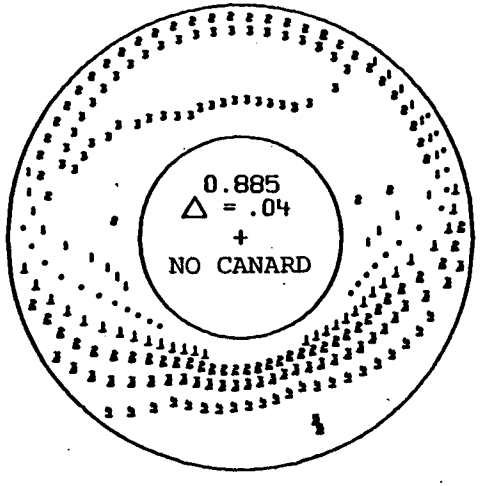

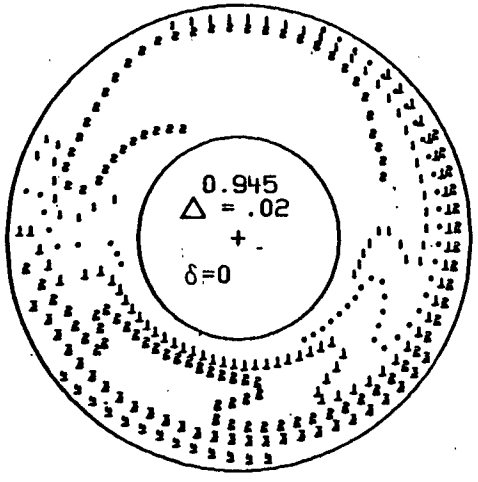

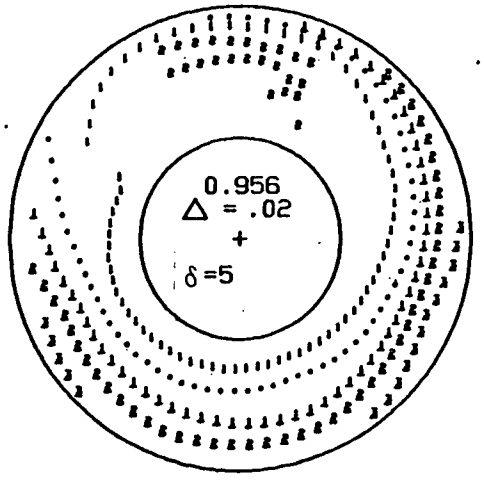

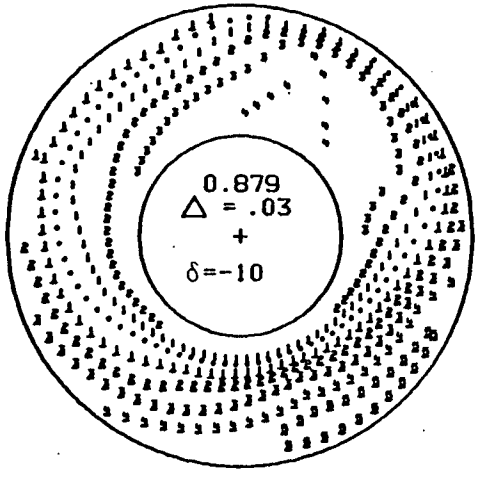

(C) $\alpha=16^{\circ}$

FIGURE 45.- CONTINUED

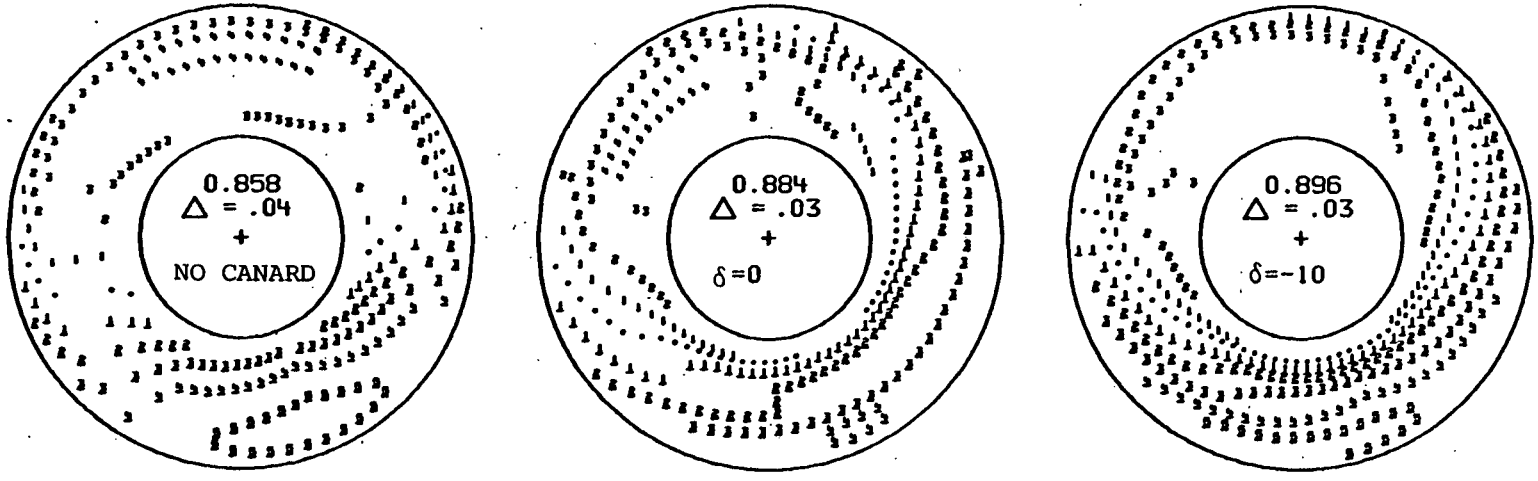

(D) $\alpha=20^{\circ}$

FIGURE 45.- CONCLUDED

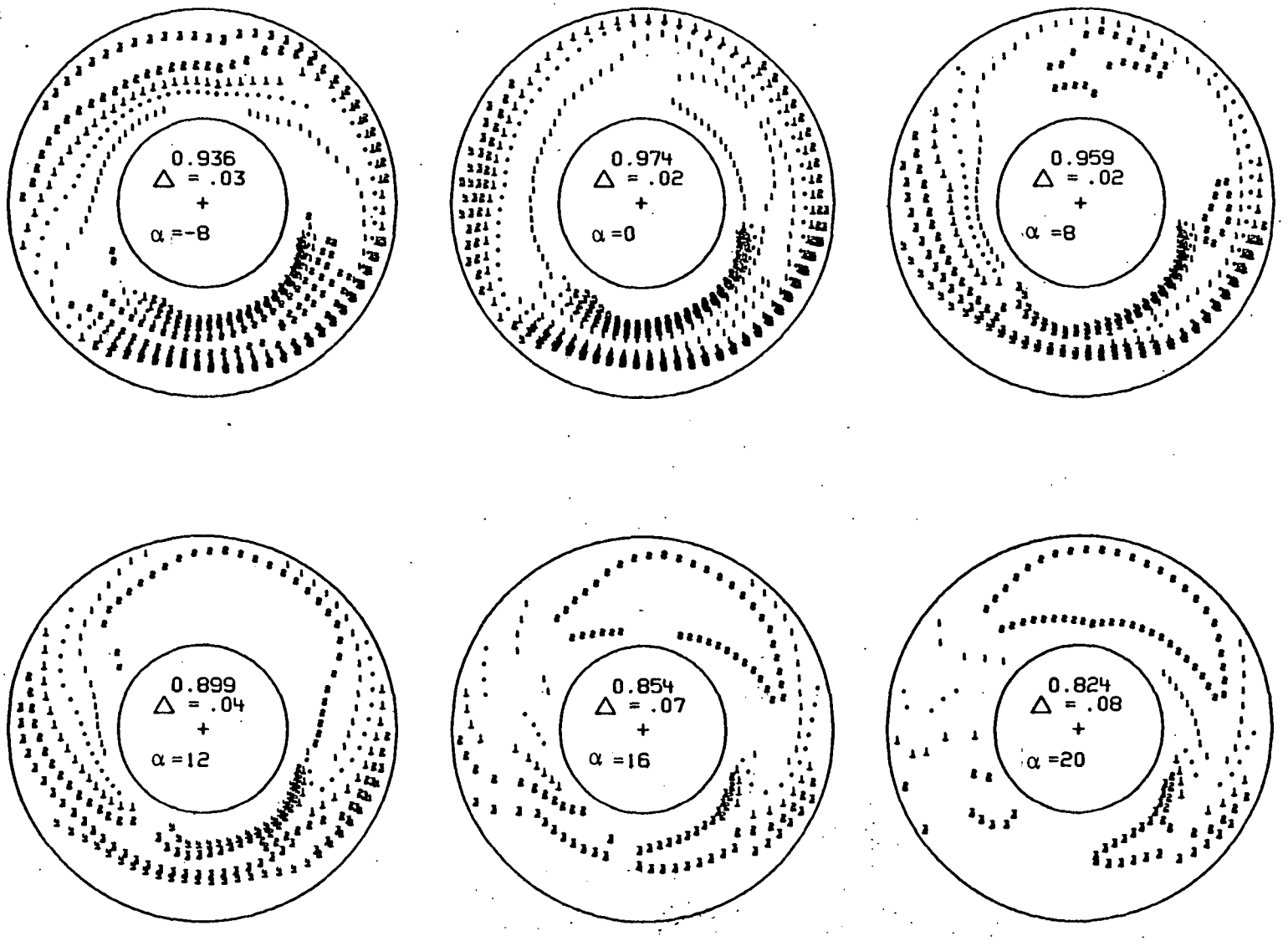

FIGURE 46.- VARIATION IN ENGINE FACE TOTAL PRESSURE DISTRIBUTION WITH ANGLE OF ATTACK, CONFIGURATION 11, M=0.9, $\beta=0^{o}$

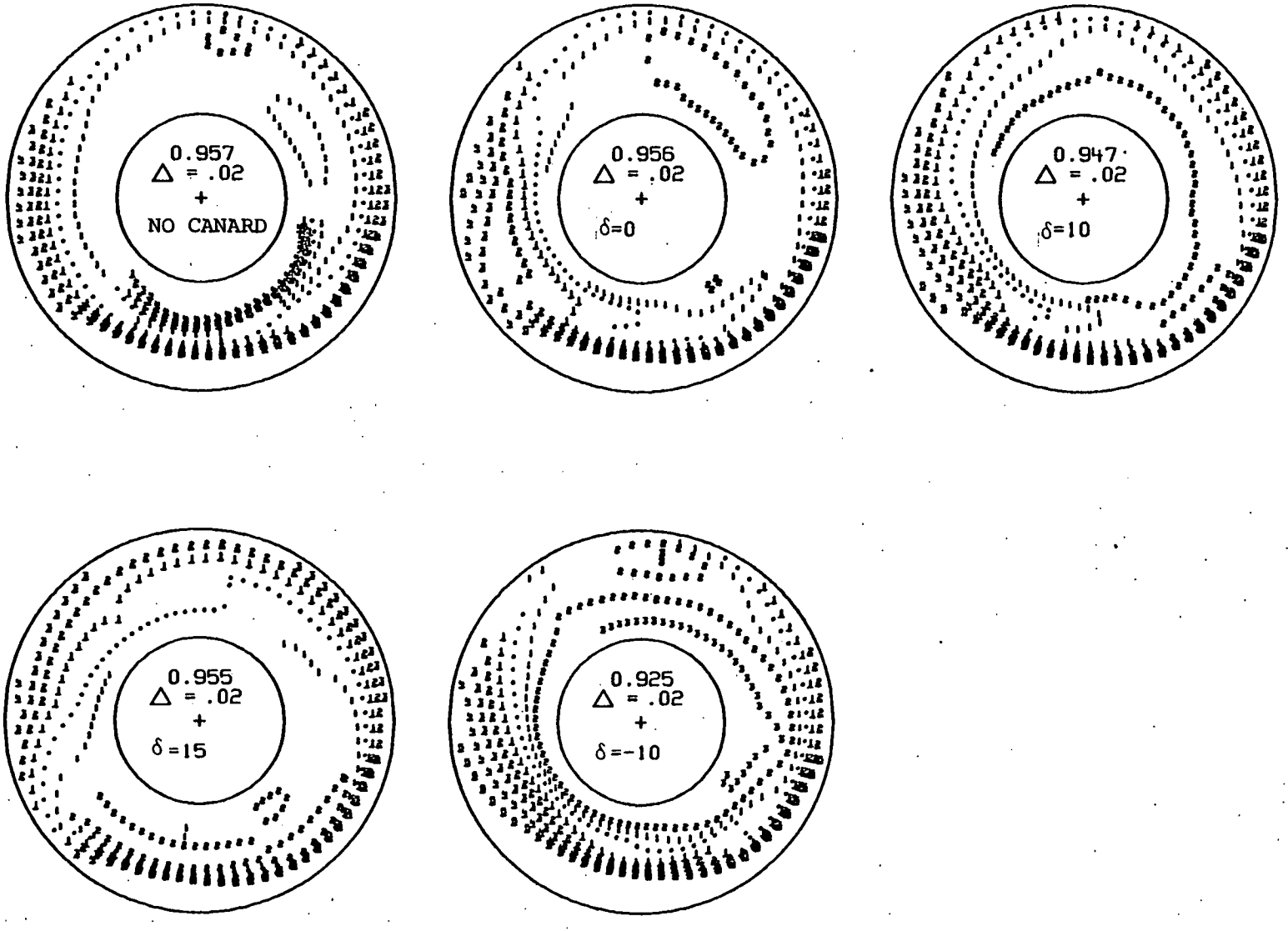

(A) $\alpha = 4$

FIGURE 47.- EFFECT OF A CANARD ON ENGINE FACE TOTAL PRESSURE DISTRIBUTION, CONFIGURATION 10, M=0.9, $\beta = 0$.

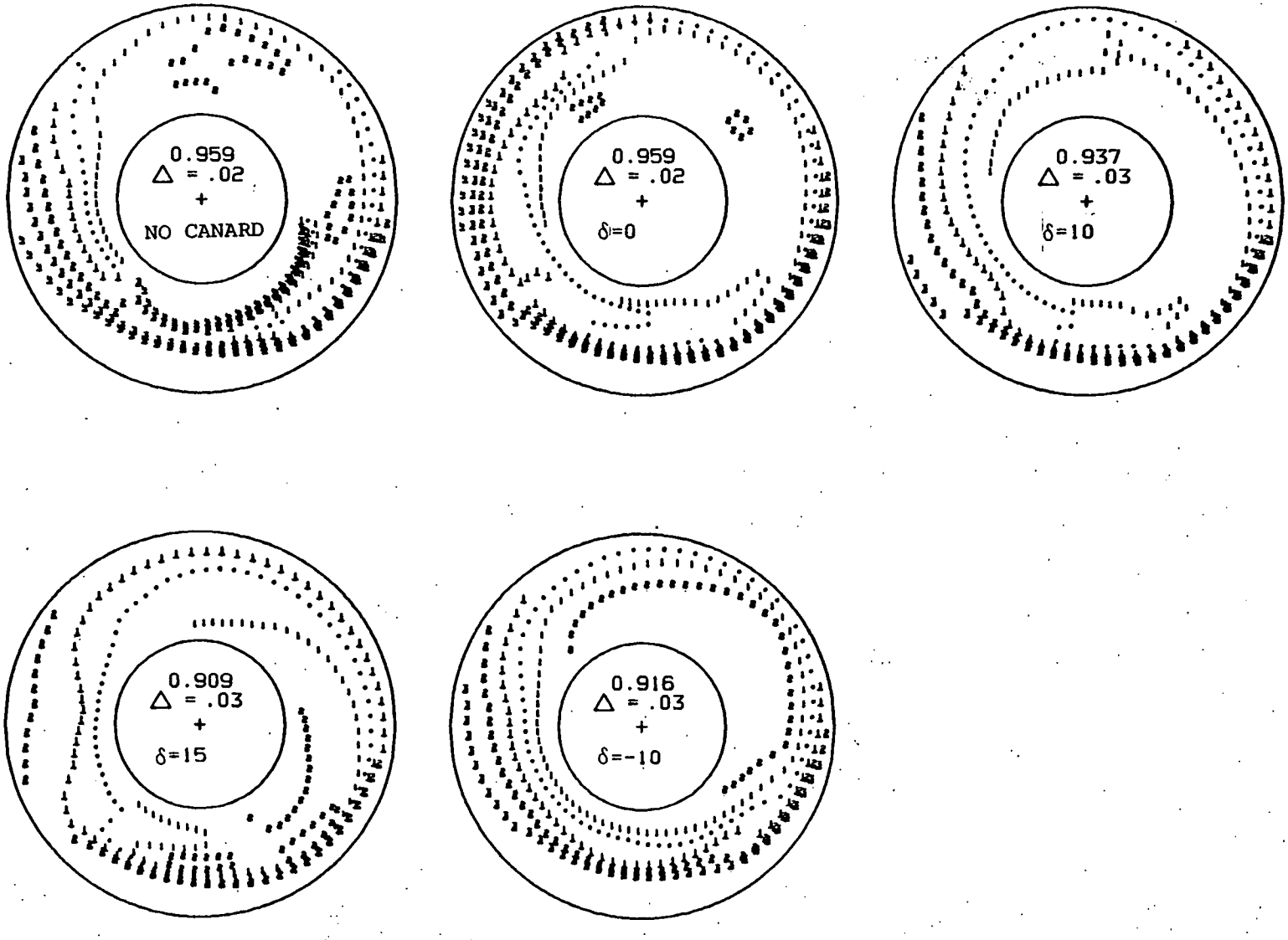

(B). $\alpha = 8$

FIGURE 47. - CONTINUED

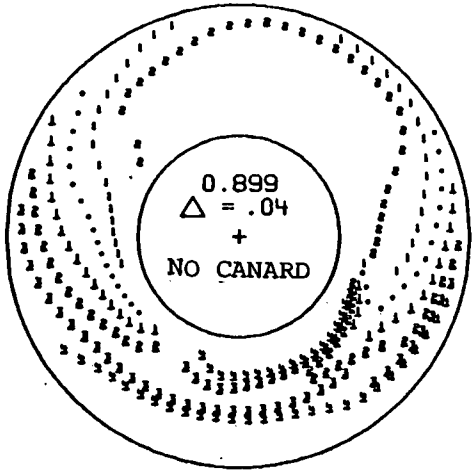

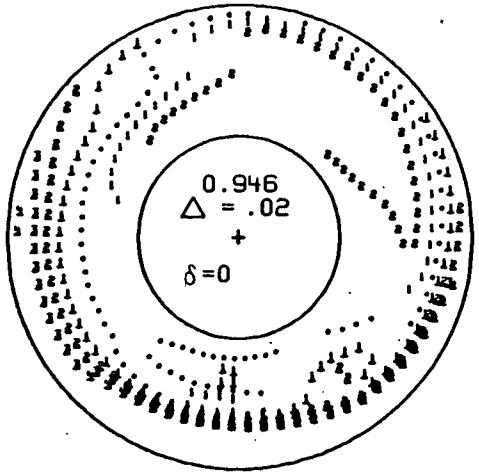

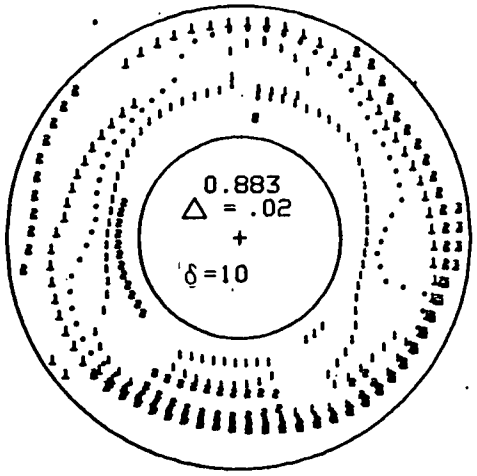

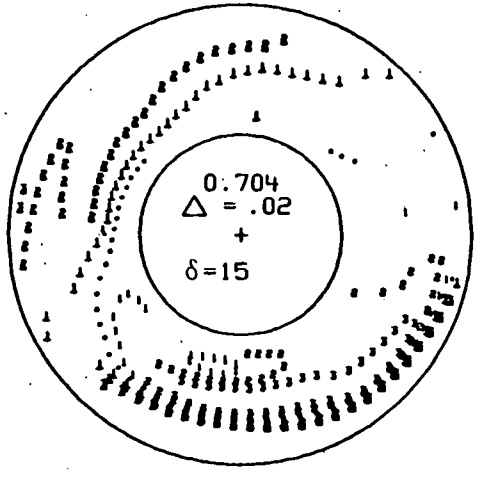

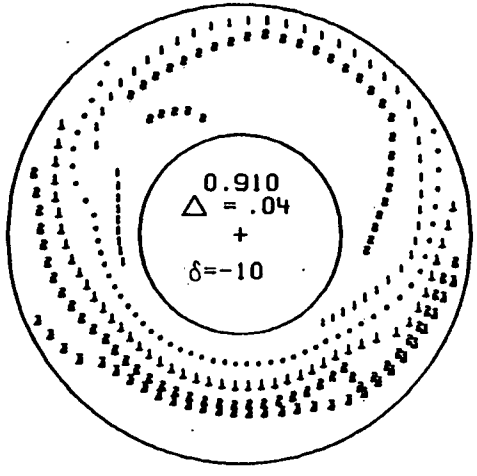

(C) α =12

FIGURE 47.- CONTINUED

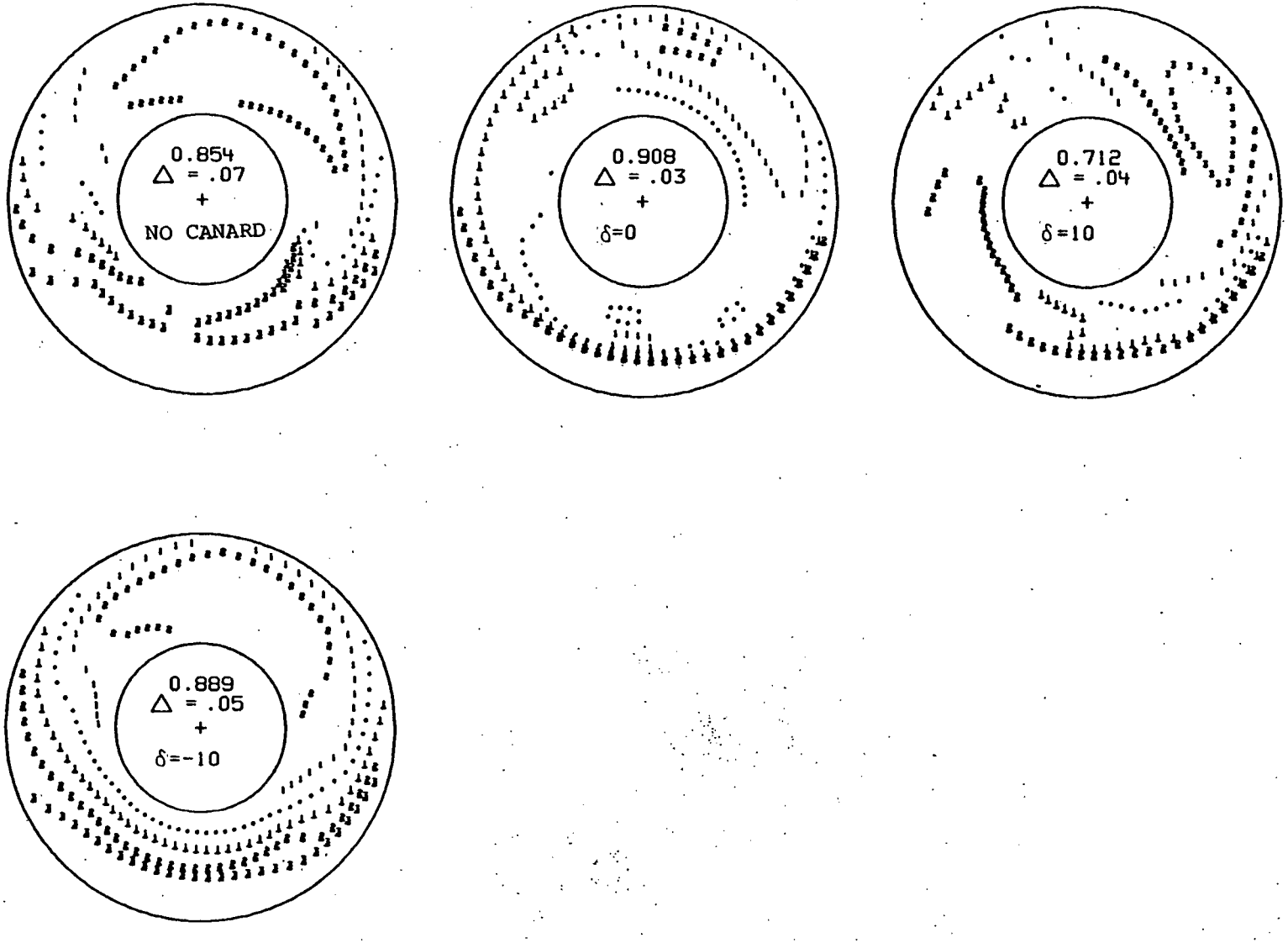

(D) α=16

FIGURE 47.-CONTINUED

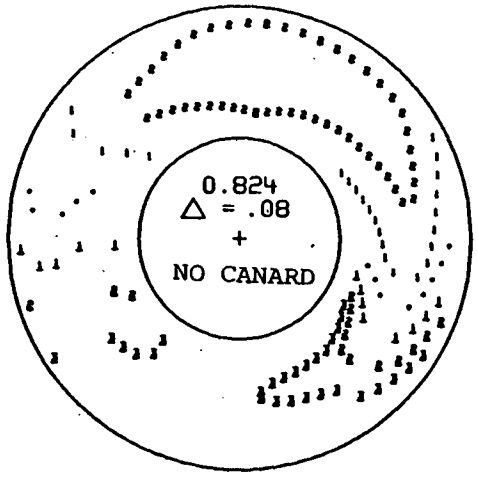

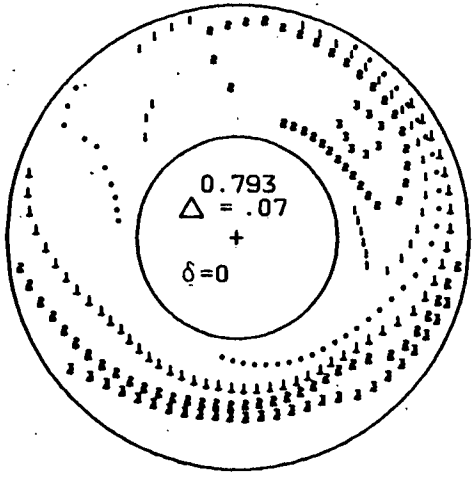

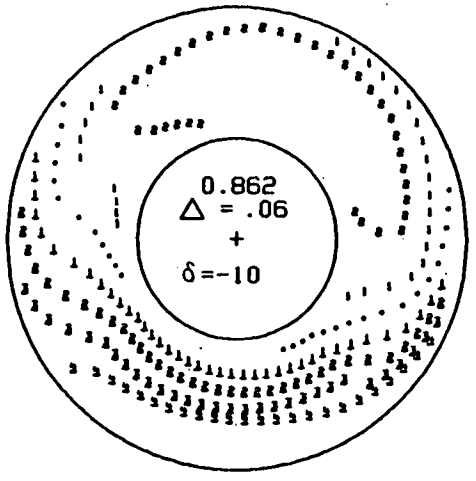

(E) α=20

FIGURE 47.- CONCLUDED

UPPER SHOULDER (CONFIGURATION 2)

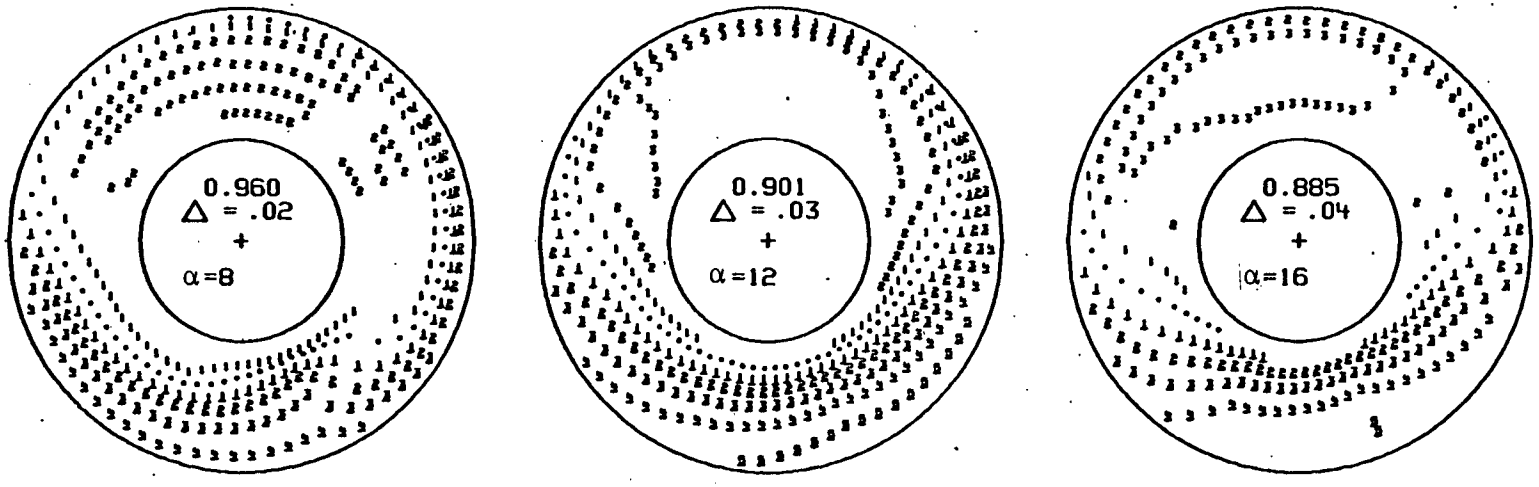

LOWER SHOULDER (CONFIGURATION 11)

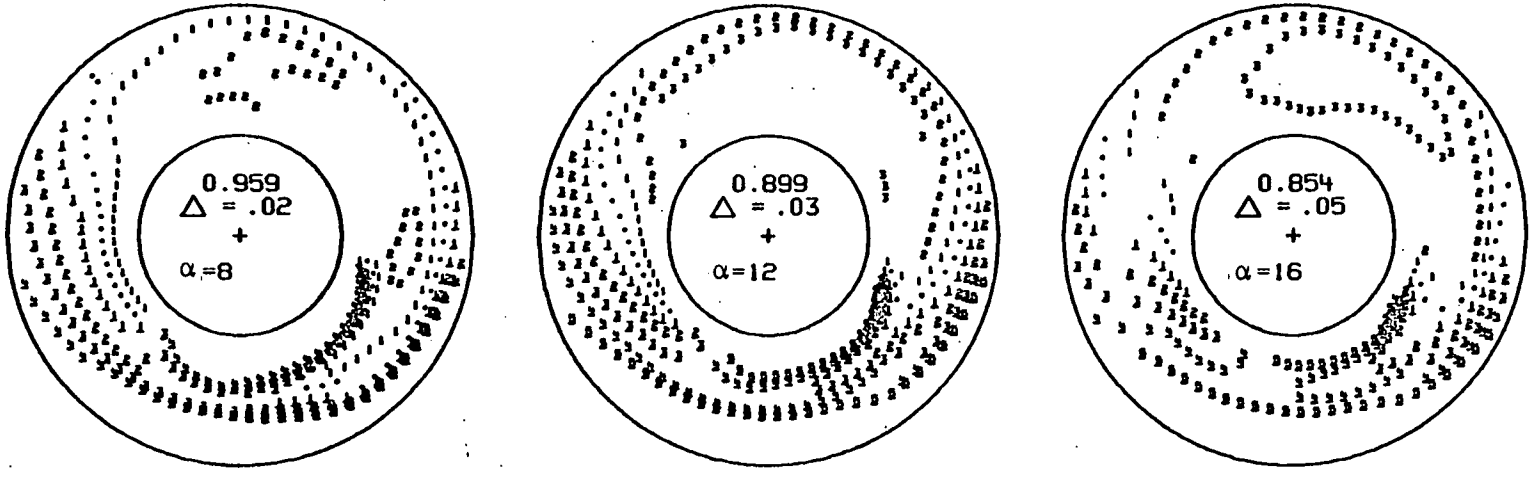

FIGURE 48.- VARIATION IN ENGINE FACE TOTAL PRESSURE DISTRIBUTION WITH INLET LOCATION, KIDNEY-SHAPED INLET, NO CANARD, M=0.9, β=0°

UPPER SHOULDER (CONFIGURATION 1)

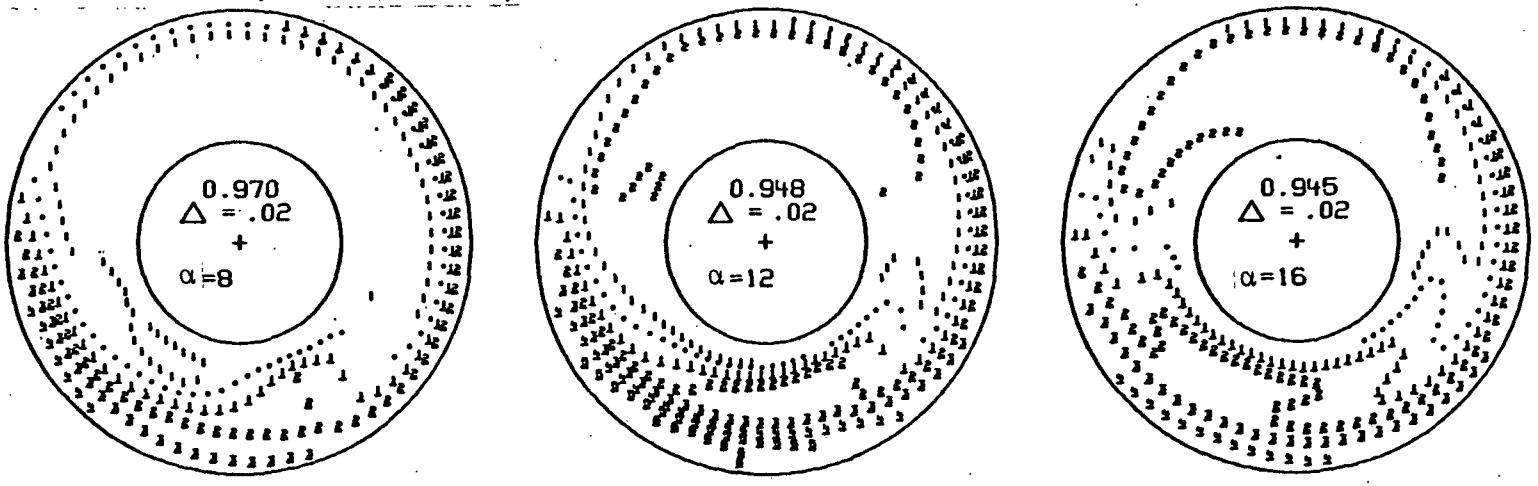

LOWER SHOULDER (CONFIGURATION 10)

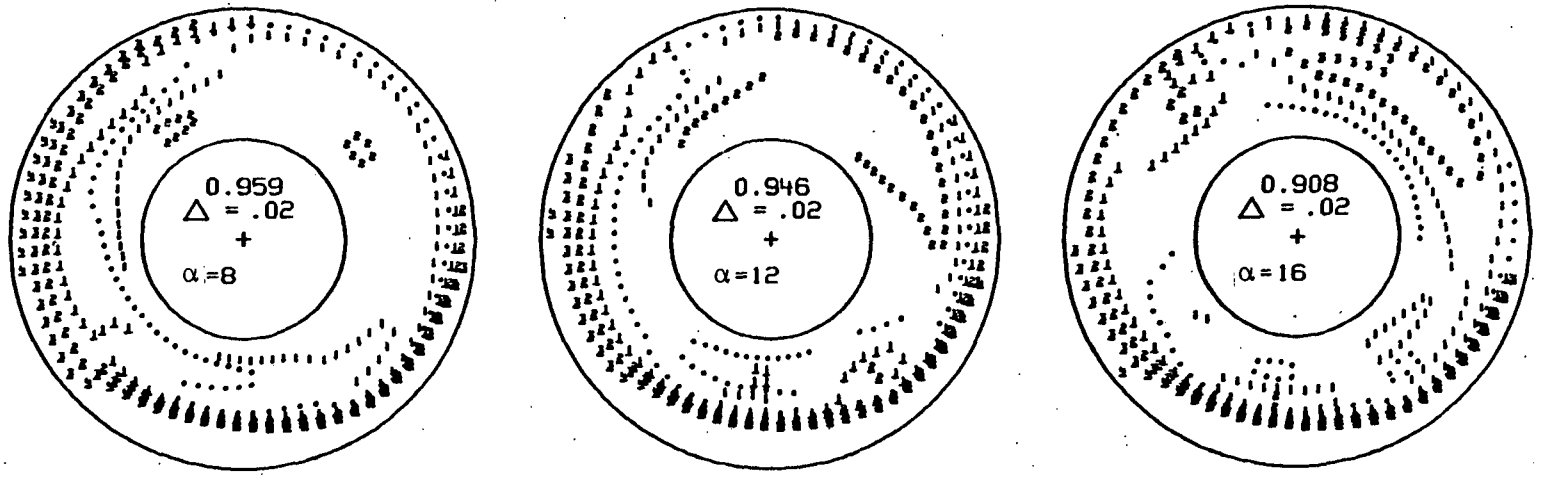

FIGURE 49.-VARIATION IN ENGINE FACE TOTAL PRESSURE DISTRIBUTION WITH INLET LOCATION, KIDNEY-SHAPED INLET, $\delta=0°$, $M=0.9$, $\beta=0°$

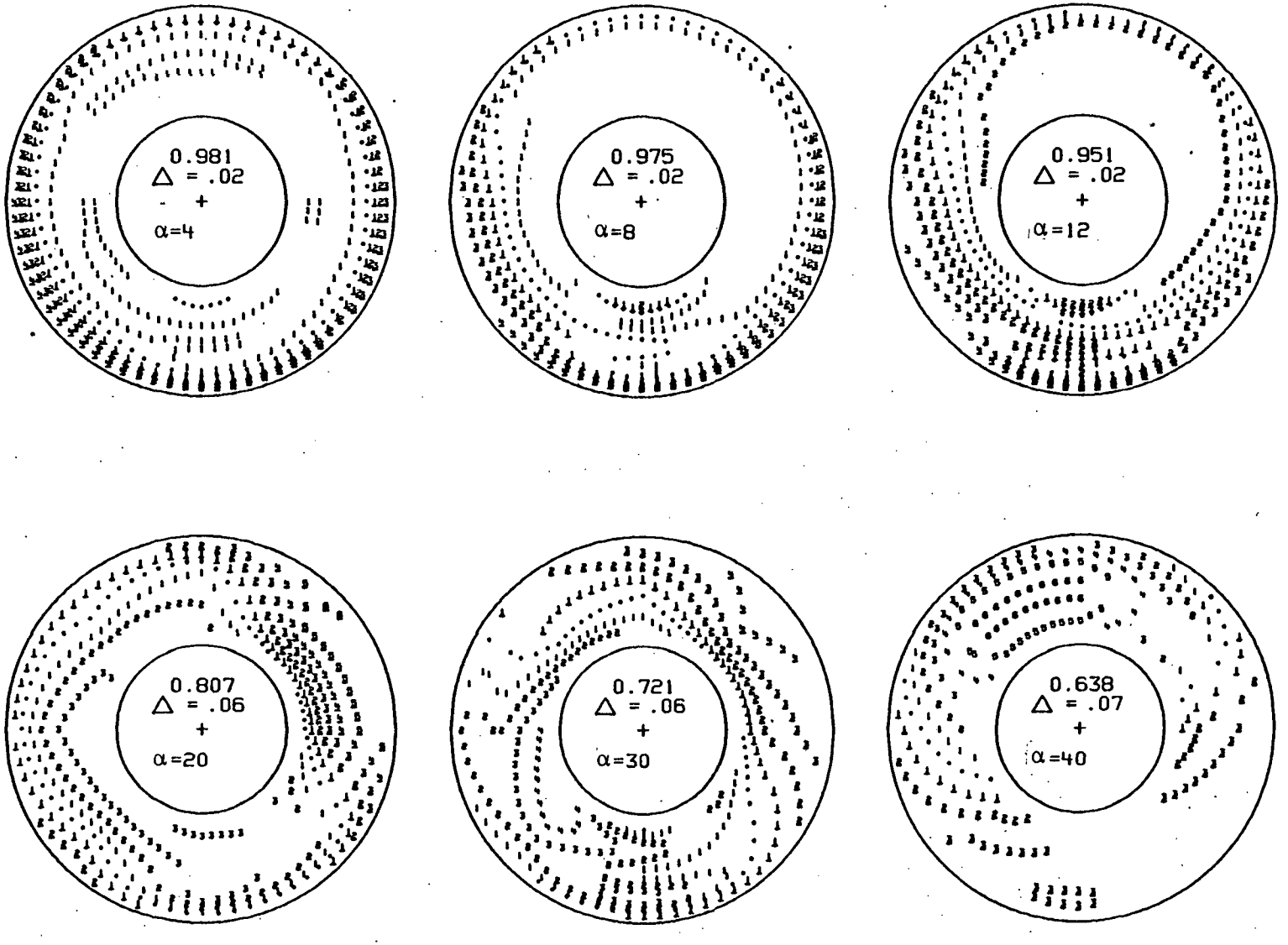

(A)

FIGURE 50.- VARIATION IN ENGINE FACE TOTAL PRESSURE DISTRIBUTION WITH ANGLE OF ATTACK, CONFIGURATION 3, M=0.9, $\beta=0^{o}$

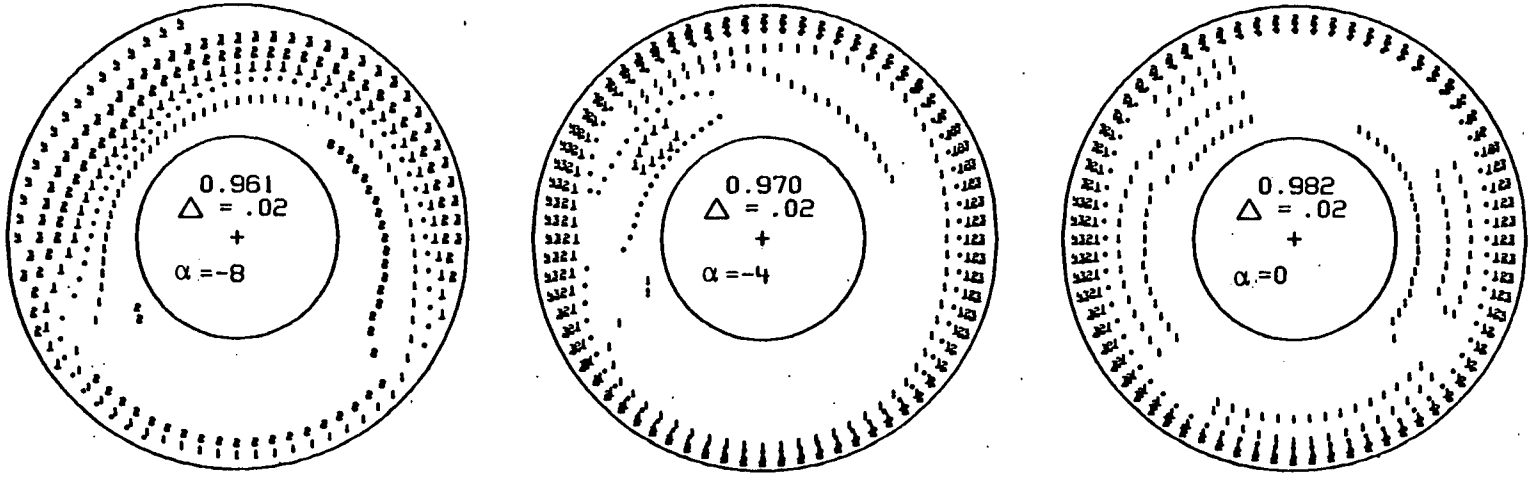

(B)

FIGURE 50.- CONCLUDED

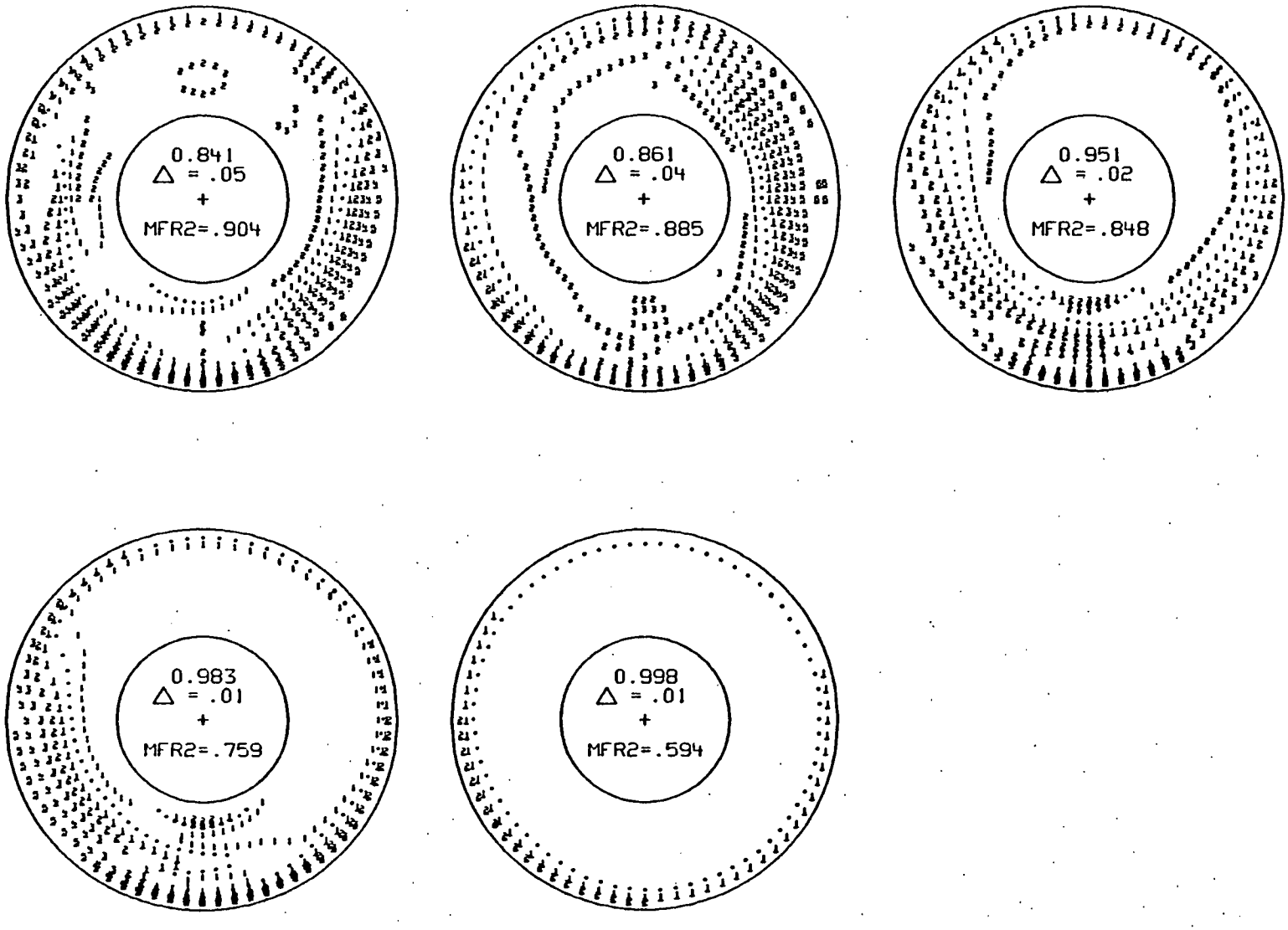

(A) $\alpha=12^{\circ}$

FIGURE 51.- VARIATION IN ENGINE FACE TOTAL PRESSURE DISTRIBUTION WITH MASS FLOW RATIO, CONFIGURATION 3, M=0.9, $\beta=0^{\circ}$

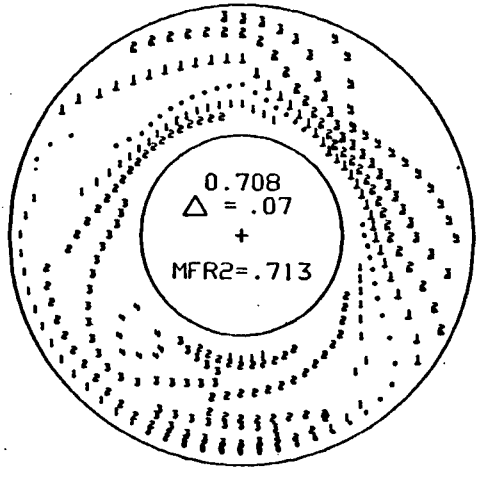

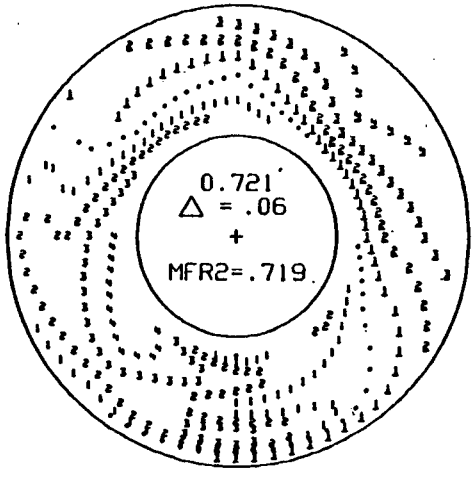

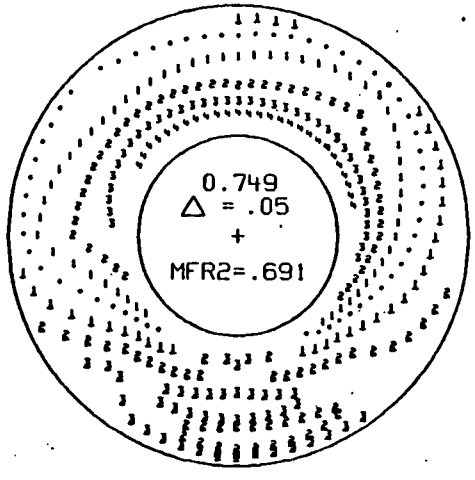

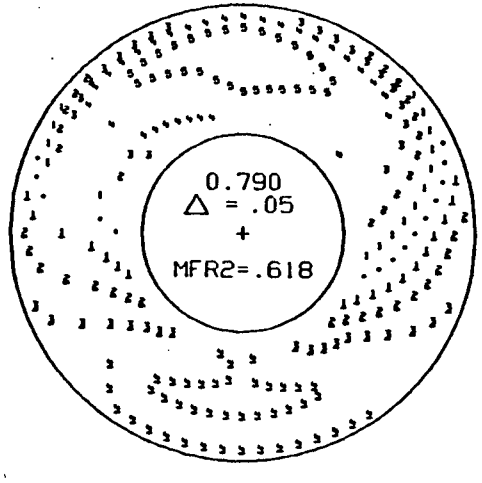

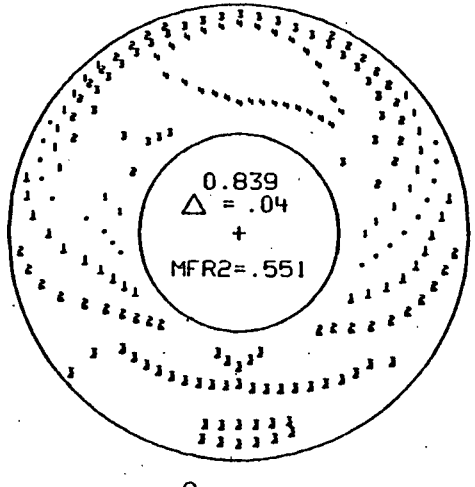

(C) $\alpha = 30^{\circ}$

FIGURE 51.- CONTINUED

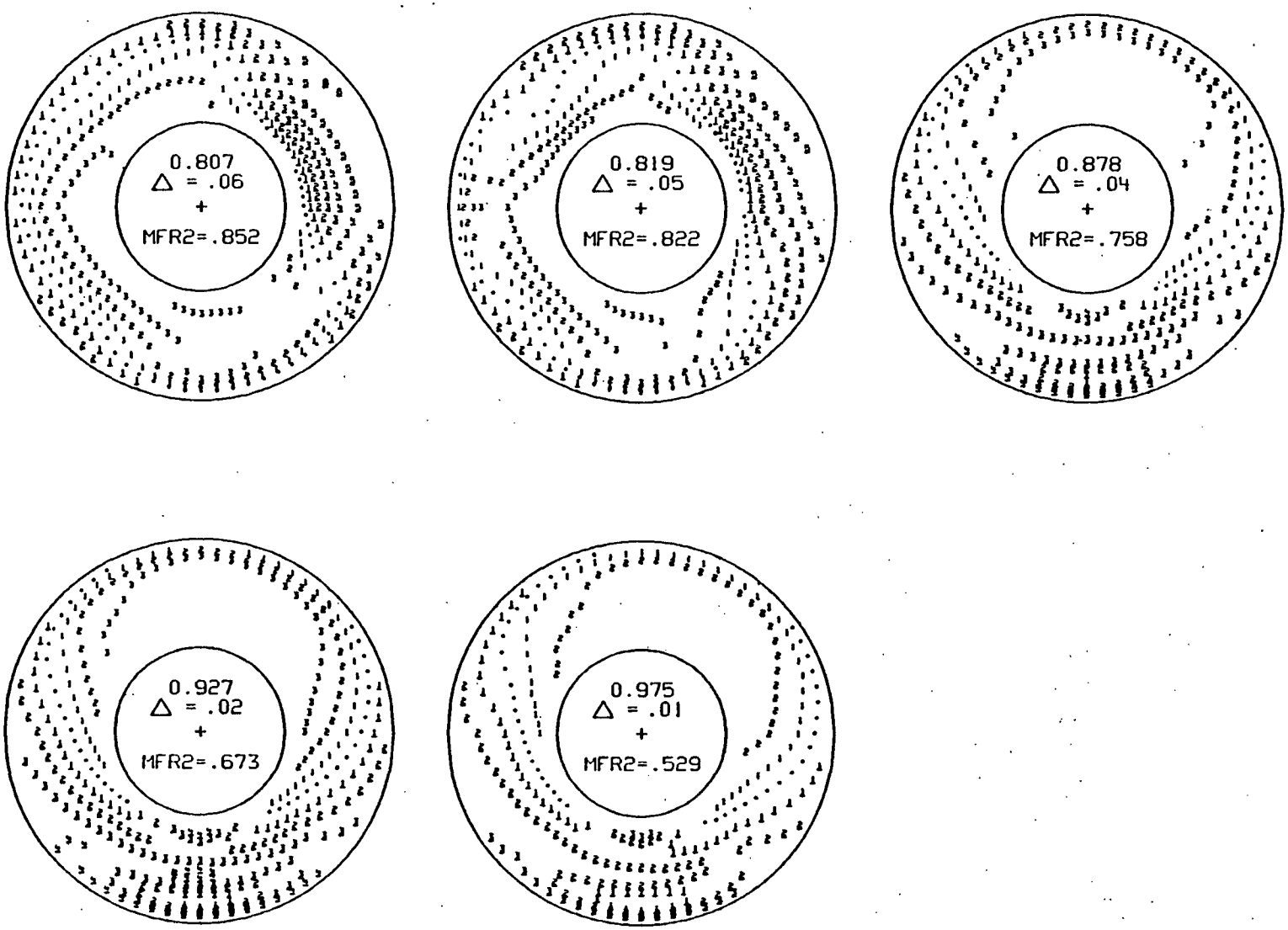

(B) $\alpha=20°$

FIGURE 51.-CONTINUED

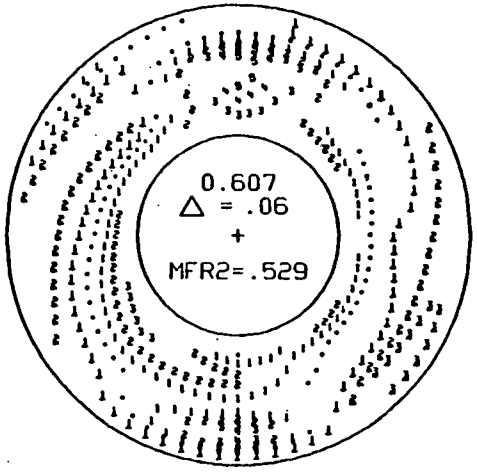

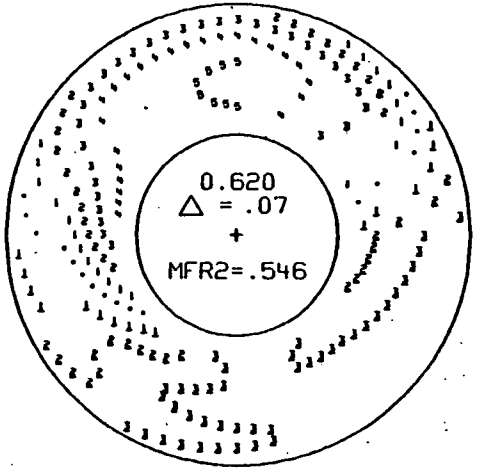

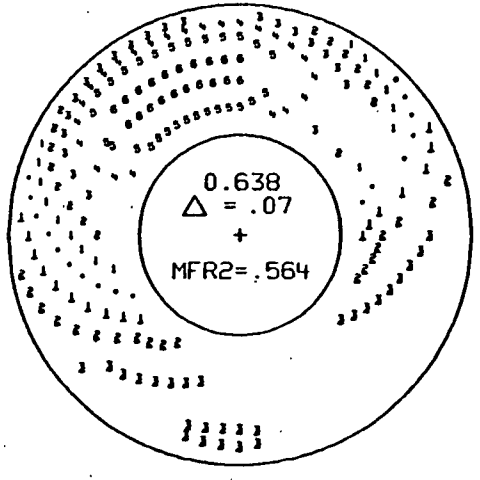

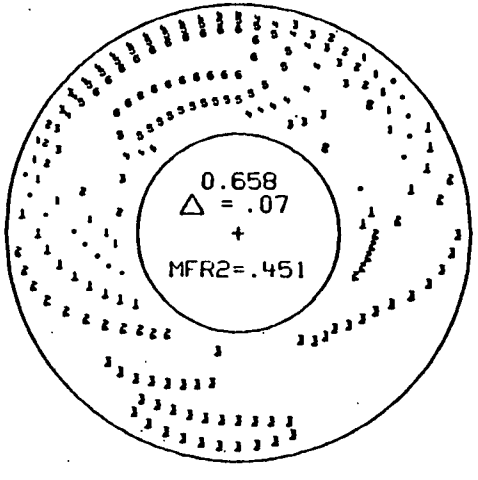

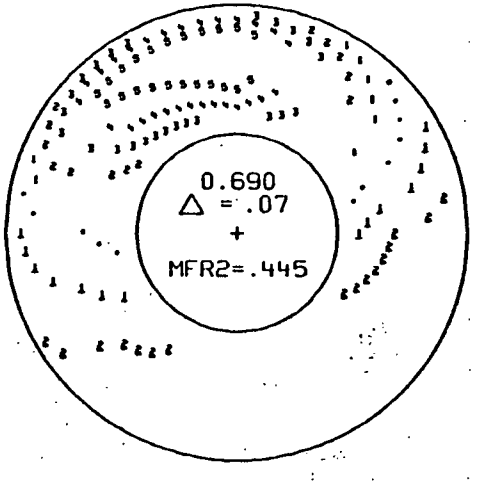

(D) α=40°

FIGURE 51.-CONCLUDED

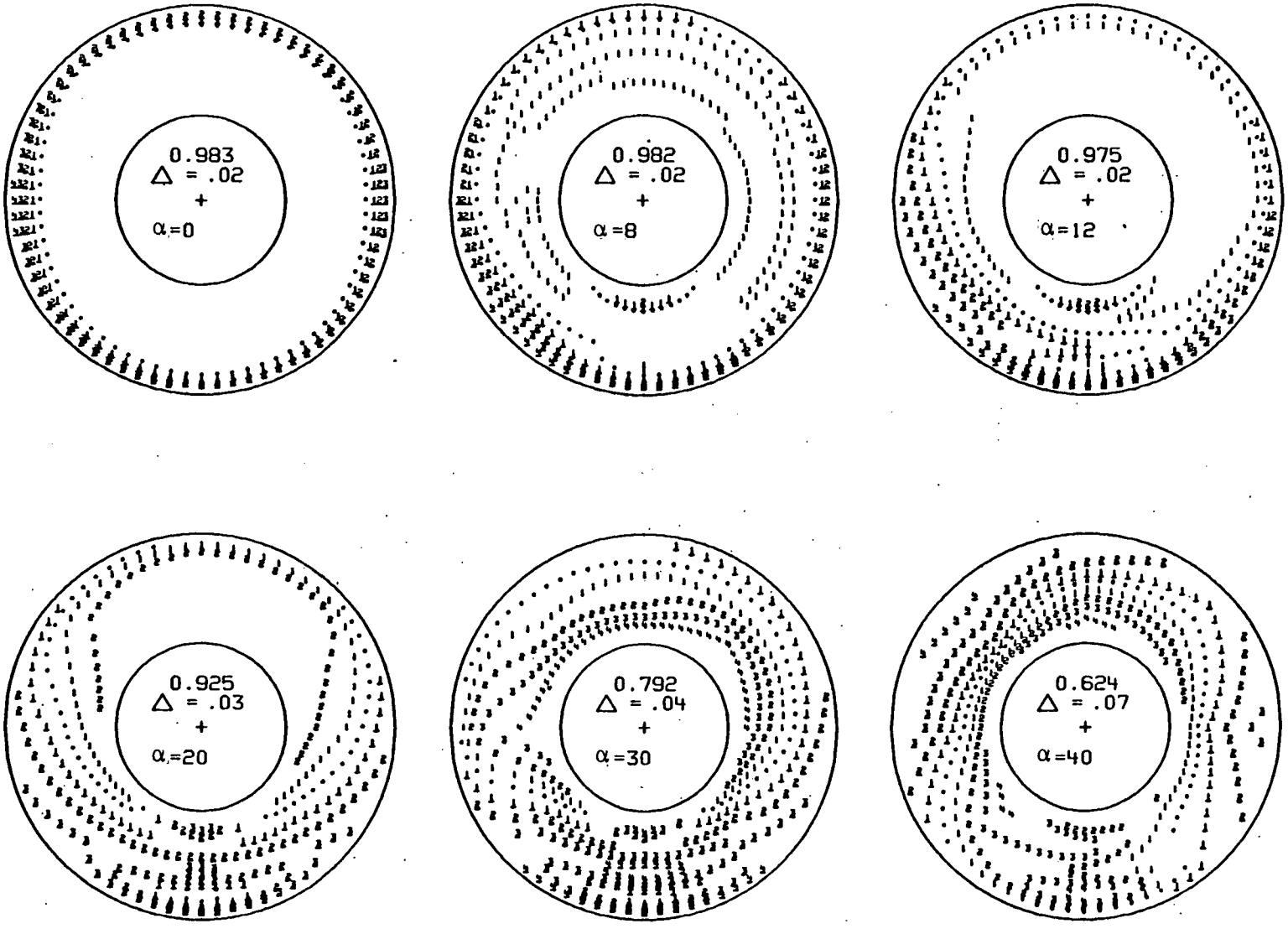

FIGURE 52.-VARIATION IN ENGINE FACE TOTAL PRESSURE DISTRIBUTION WITH ANGLE OF ATTACK, CONFIGURATION 4, M=0.9, $\beta=0^{\circ}$

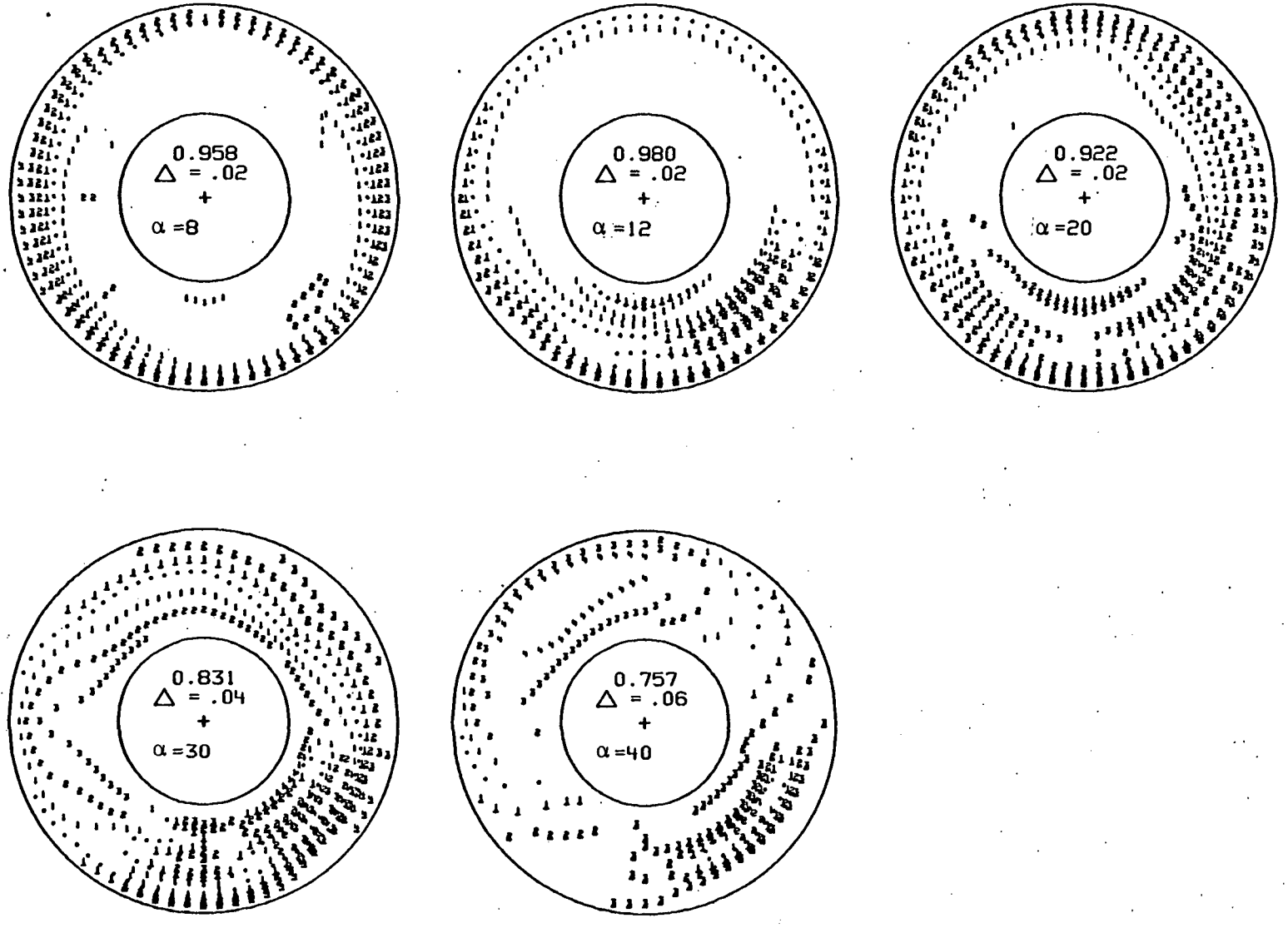

FIGURE 53.-VARIATION IN ENGINE FACE TOTAL PRESSURE DISTRIBUTION WITH ANGLE OF ATTACK, CONFIGURATION 8, M=0.9, $\beta=0^{o}$

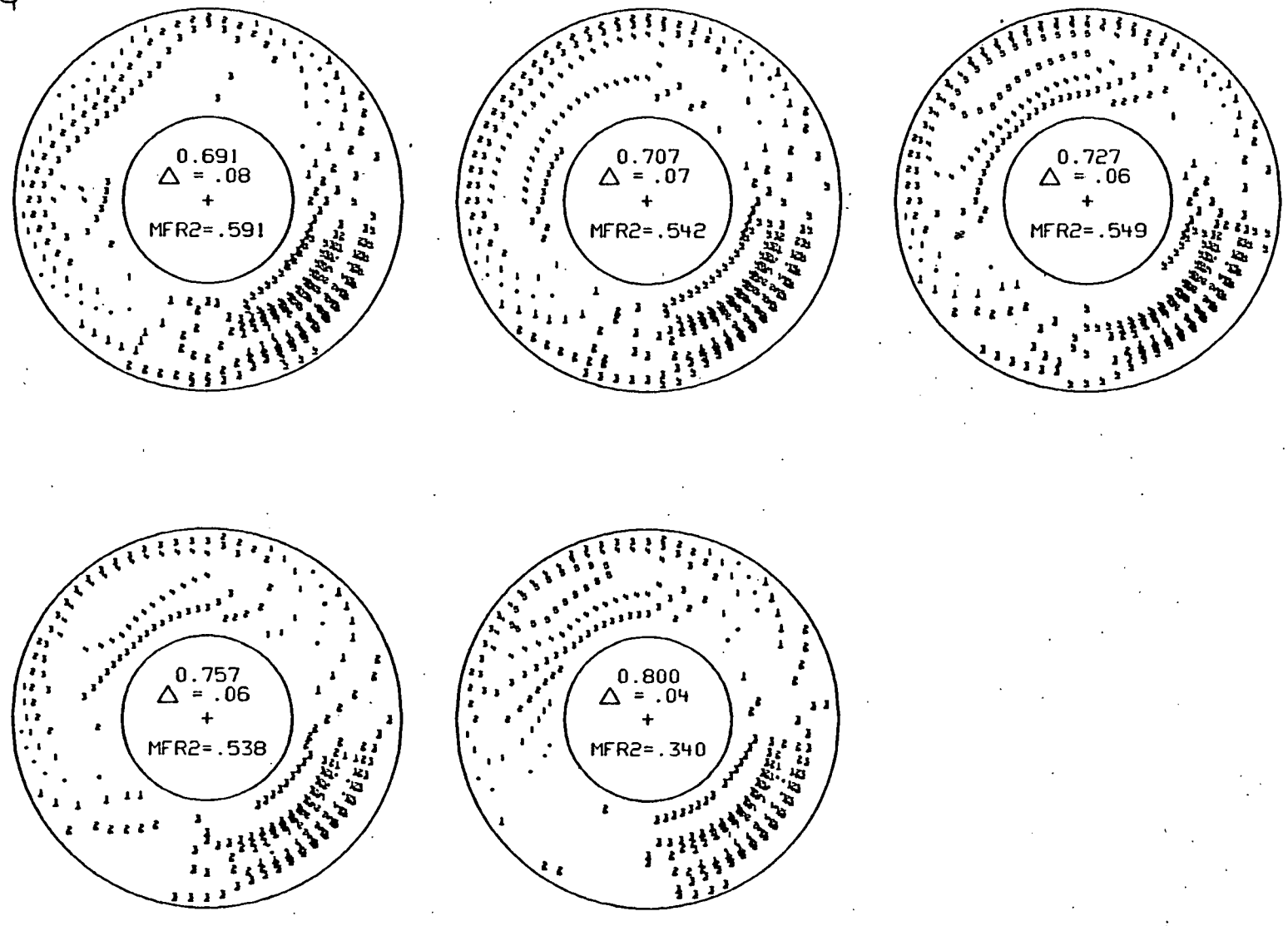

FIGURE 54.-VARIATION IN ENGINE FACE TOTAL PRESSURE DISTRIBUTION WITH MASS FLOW RATIO, CONFIGURATION 8, M=0.9, β=0°, α=40°.

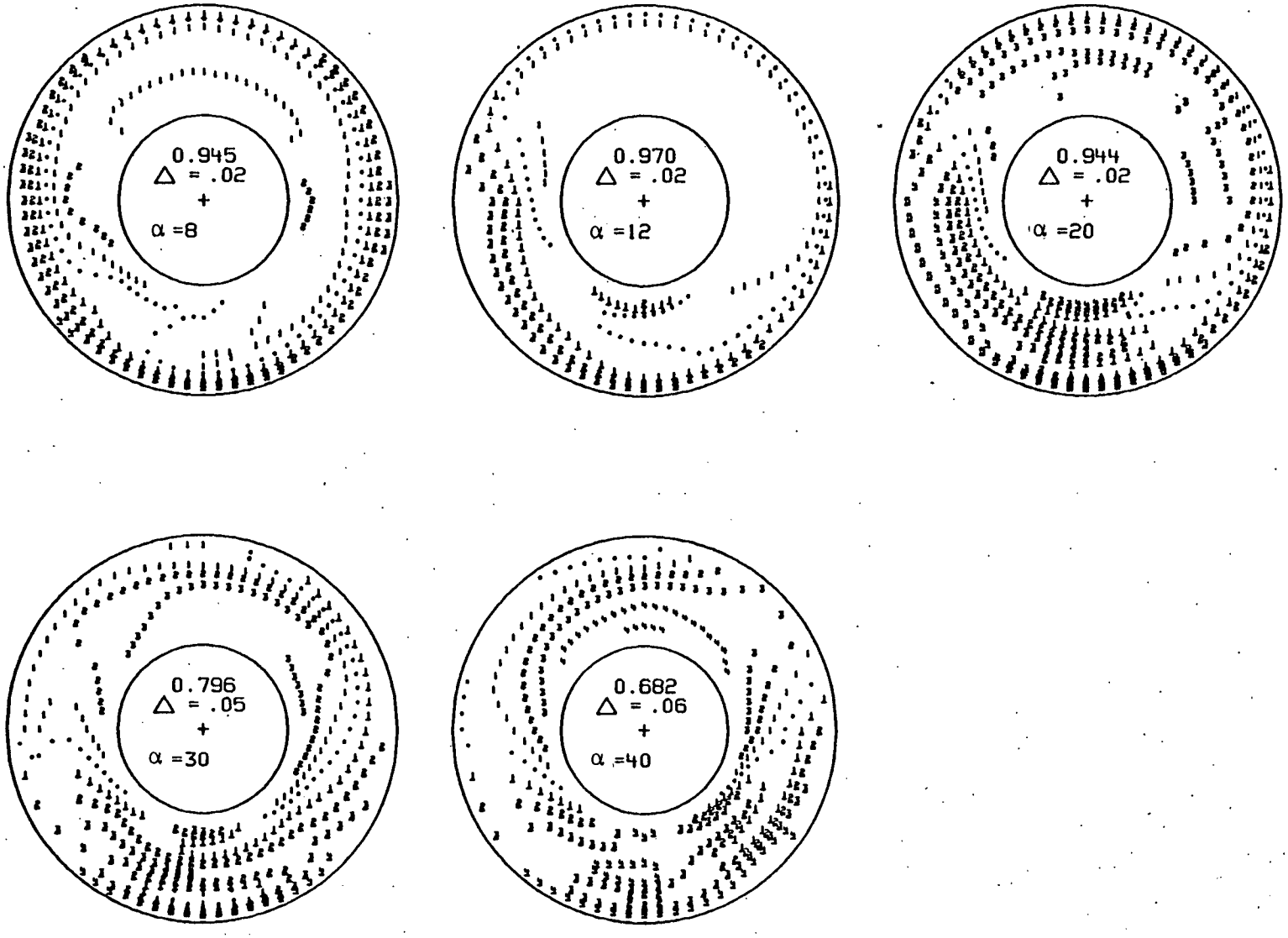

FIGURE 55.-VARIATION IN ENGINE FACE TOTAL PRESSURE RATIO DISTRIBUTION WITH ANGLE OF ATTACK, CONFIGURATION 6, M=0.9, $\beta=0^{\circ}$

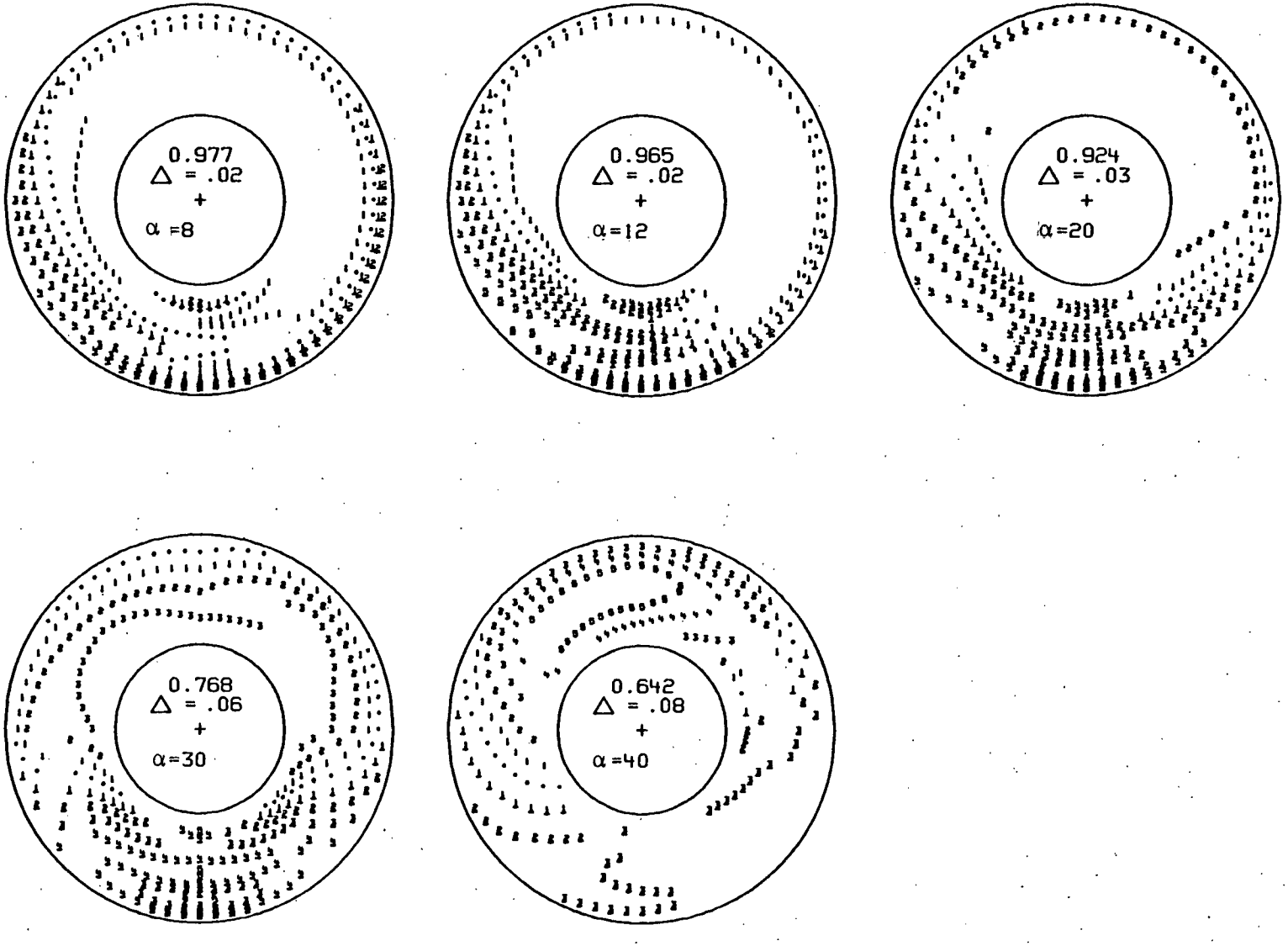

FIGURE 56.-VARIATION IN ENGINE FACE TOTAL PRESSURE DISTRIBUTION WITH ANGLE OF ATTACK, CONFIGURATION 5, M=0.9, $\beta=0^{\circ}$

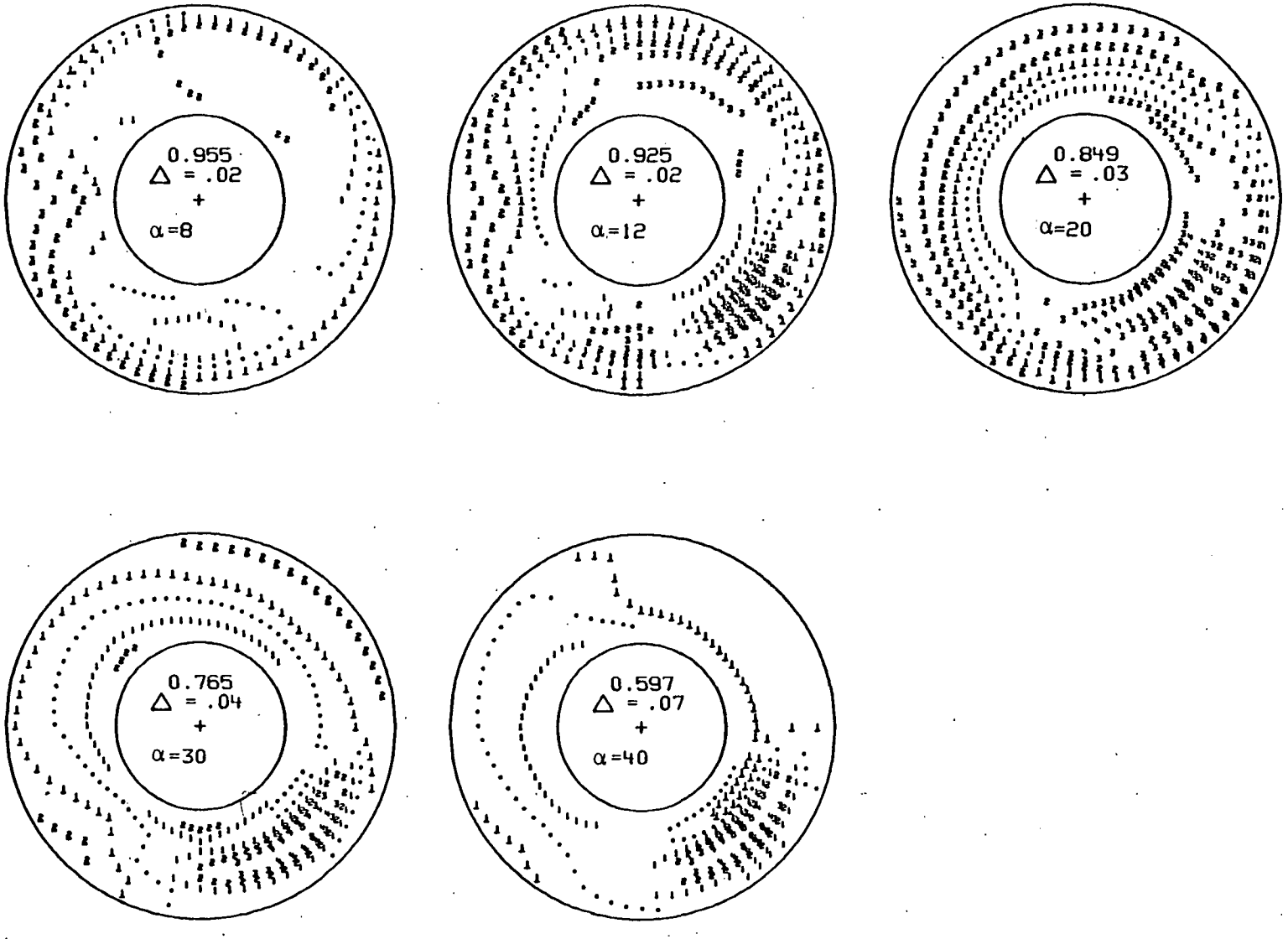

FIGURE 57.-VARIATION IN ENGINE FACE TOTAL PRESSURE DISTRIBUTION WITH ANGLE OF ATTACK, CONFIGURATION 7, M=0.9, $\beta = 0^{\circ}$

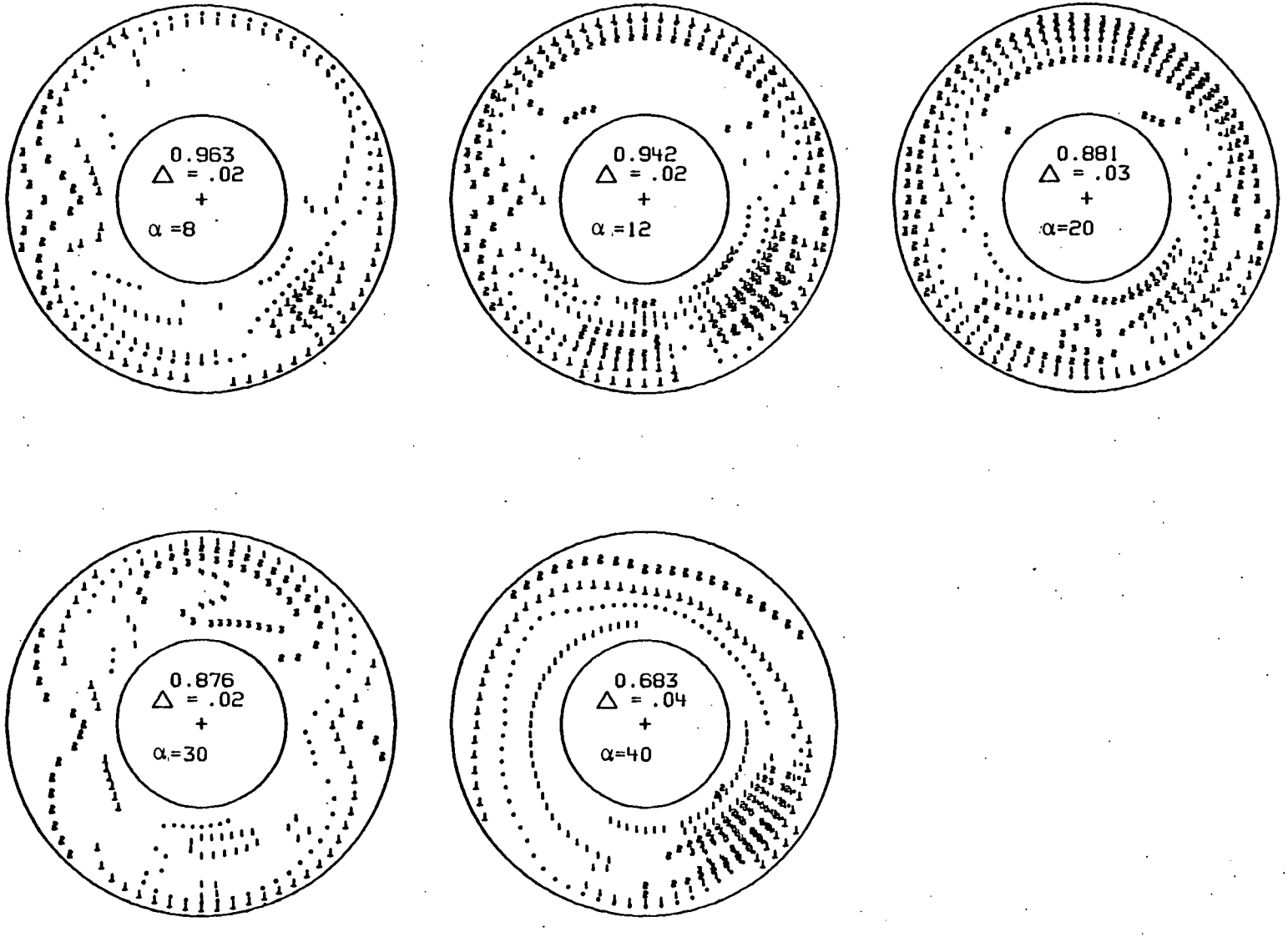

FIGURE 58.-VARIATION IN ENGINE FACE TOTAL PRESSURE DISTRIBUTION WITH ANGLE OF ATTACK, CONFIGURATION 9, M=0.9, $\beta=0^{\circ}$

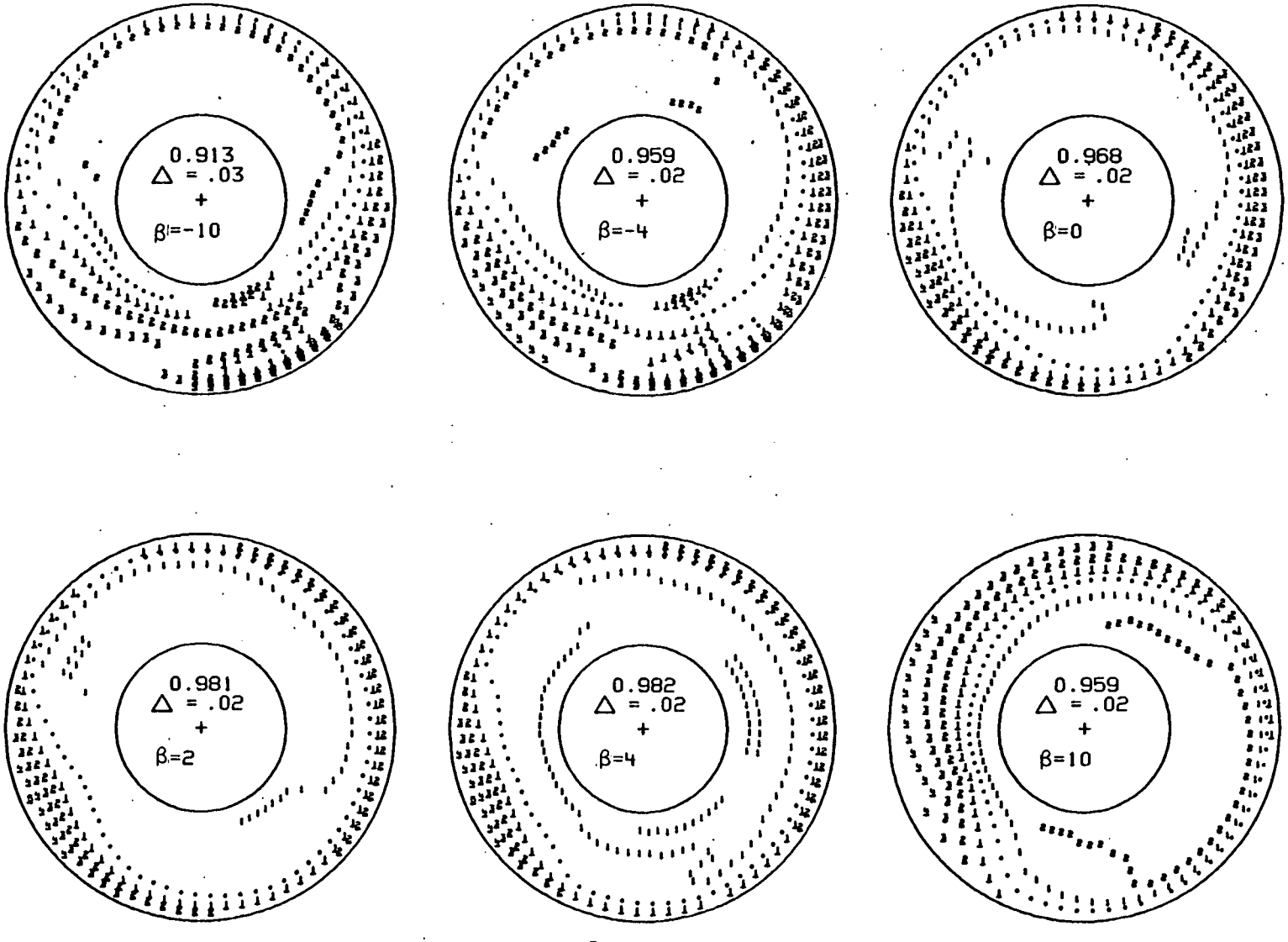

(A) $\alpha = 4^{\circ}$

FIGURE 59.-VARIATION IN ENGINE FACE TOTAL PRESSURE DISTRIBUTION WITH ANGLE OF SIDESLIP, CONFIGURATION 1, $\delta=0°$, M=0.9, $\beta=0°$

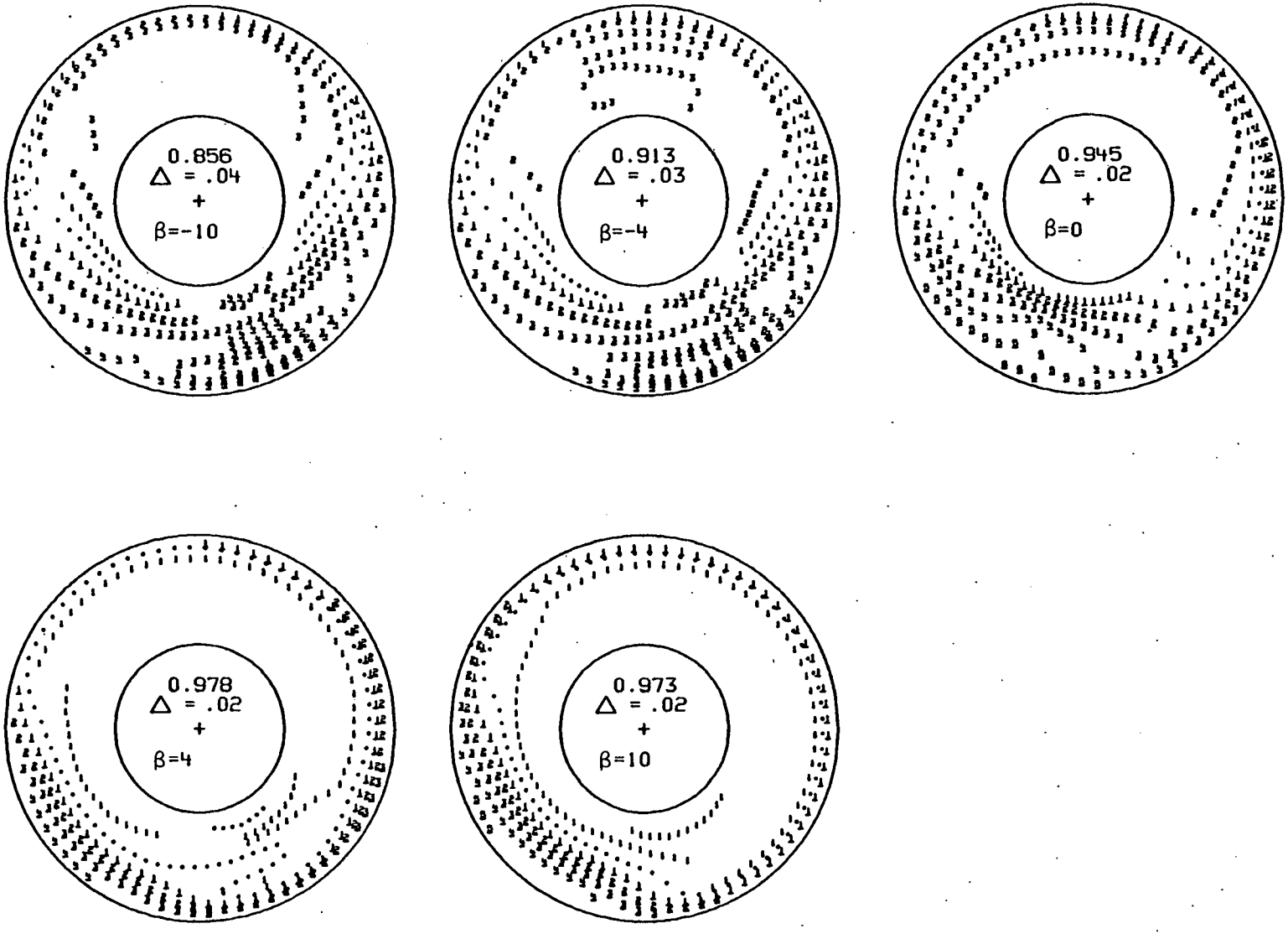

(B) α=12°

FIGURE 59.-CONCLUDED

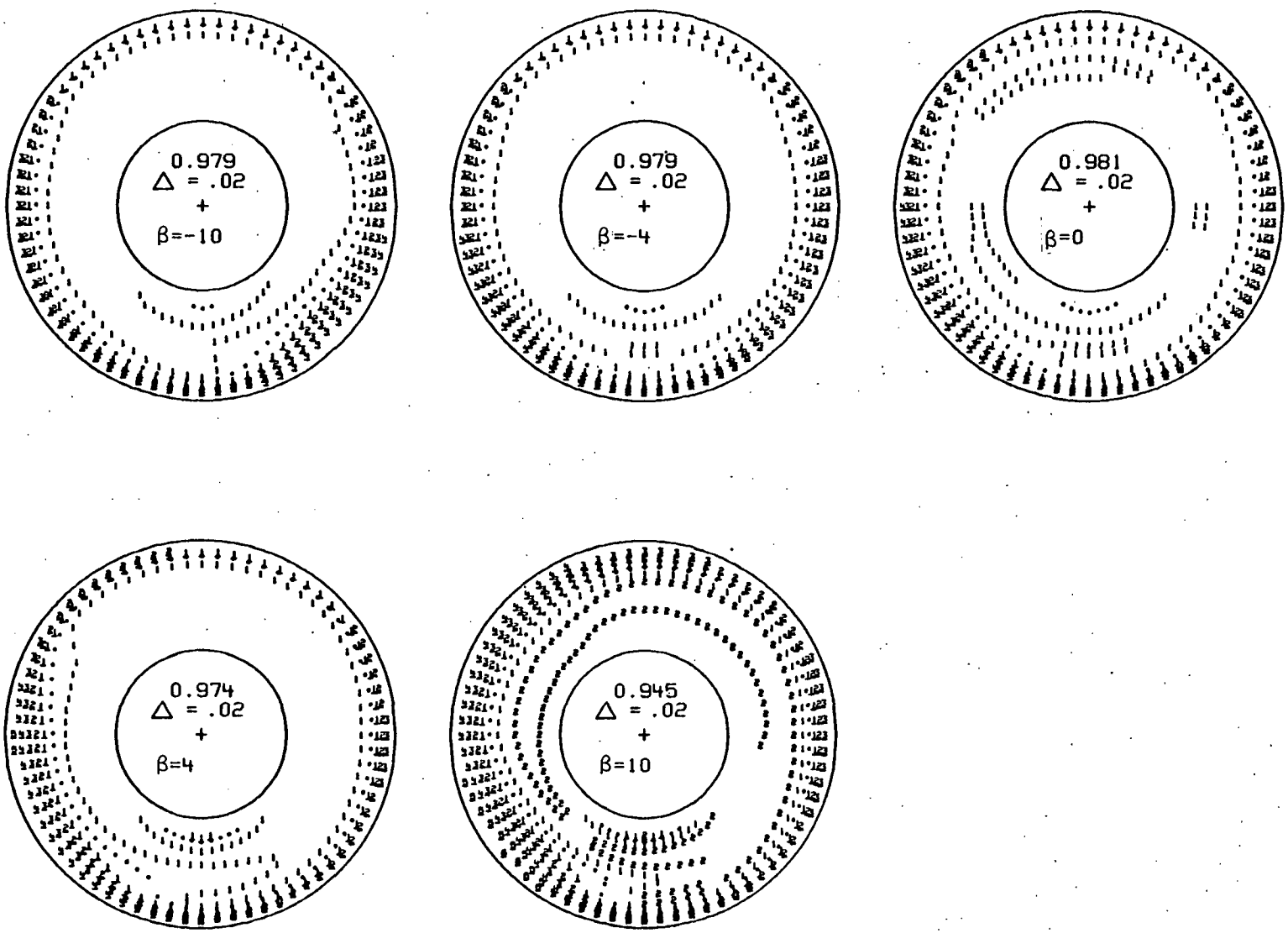

(A) $\alpha = 4^{\circ}$

FIGURE 60.- VARIATION IN ENGINE FACE TOTAL PRESSURE DISTRIBUTION WITH ANGLE OF SIDESLIP, CONFIGURATION 3, M=0.9, $\beta = 0^{\circ}$

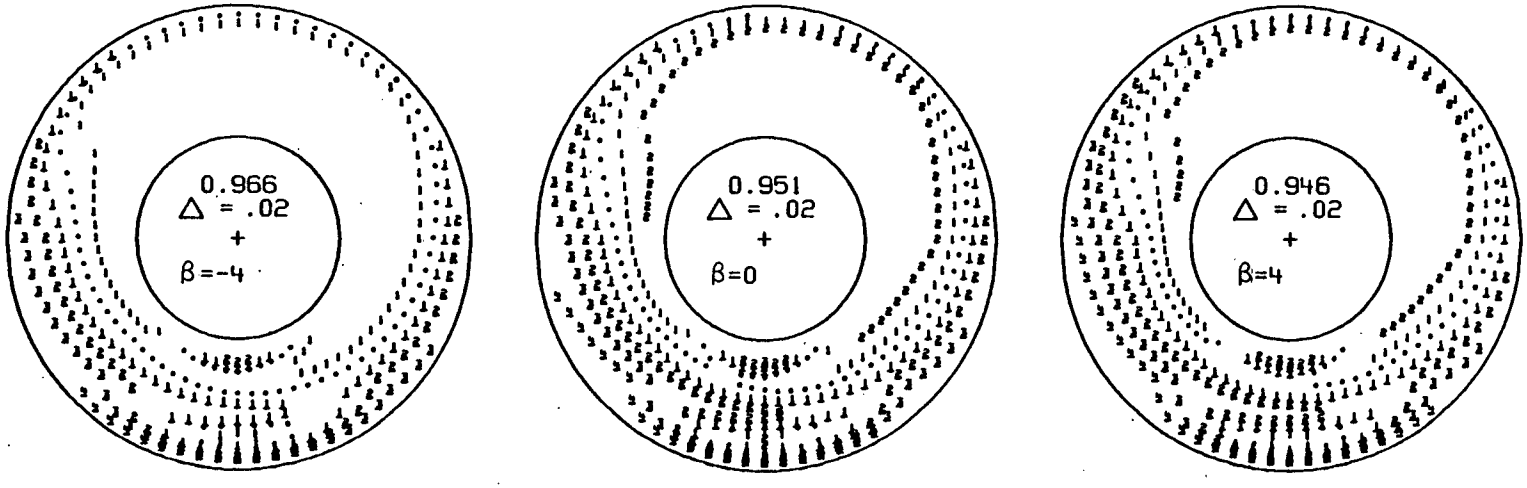

(B) $\alpha = 12^{\circ}$

Figure 60.-Concluded.

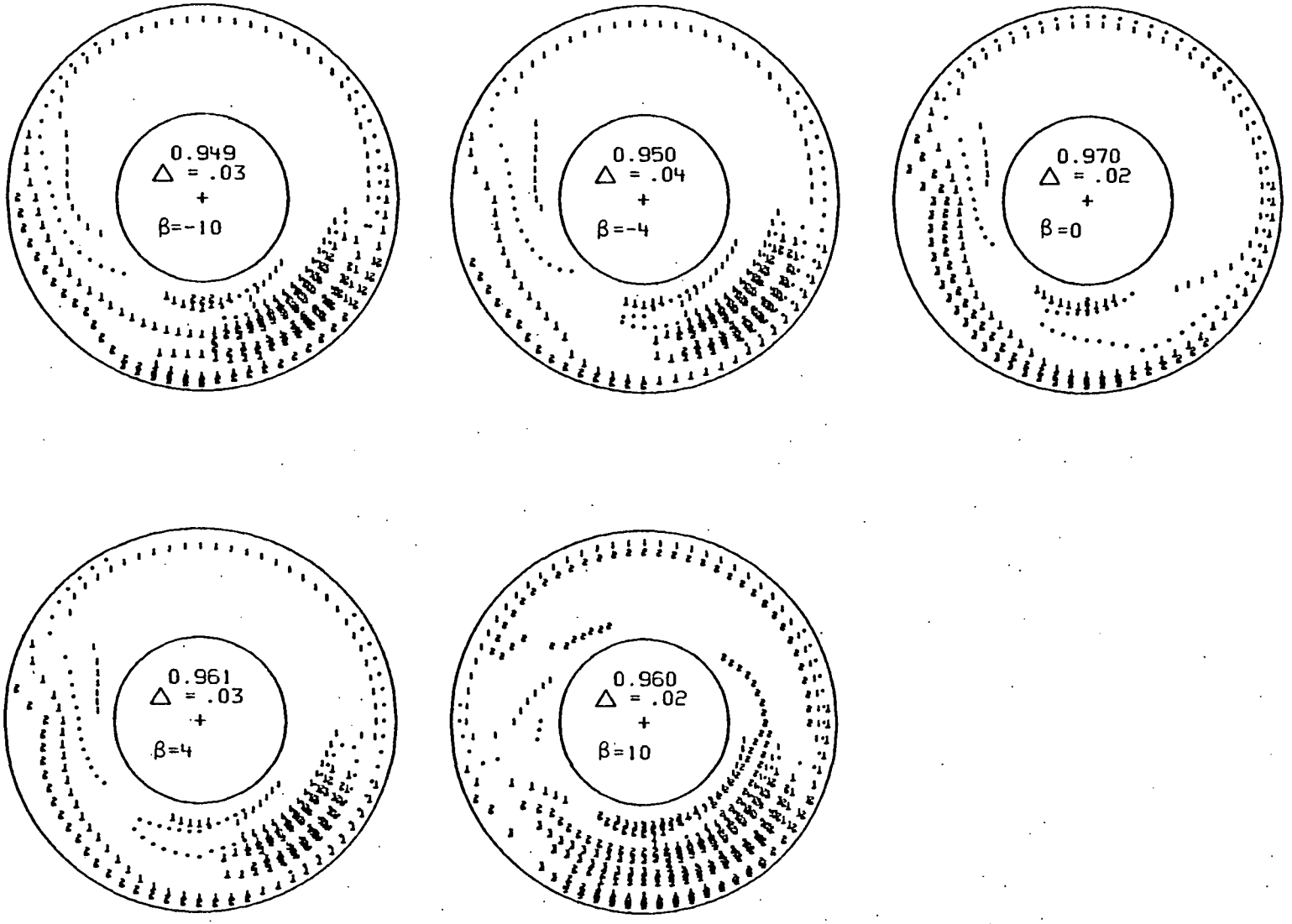

FIGURE 61.-VARIATION IN ENGINE FACE TOTAL PRESSURE DISTRIBUTION WITH ANGLE OF SIDESLIP, CONFIGURATION 6, M=0.9, β=0°, α=12°.

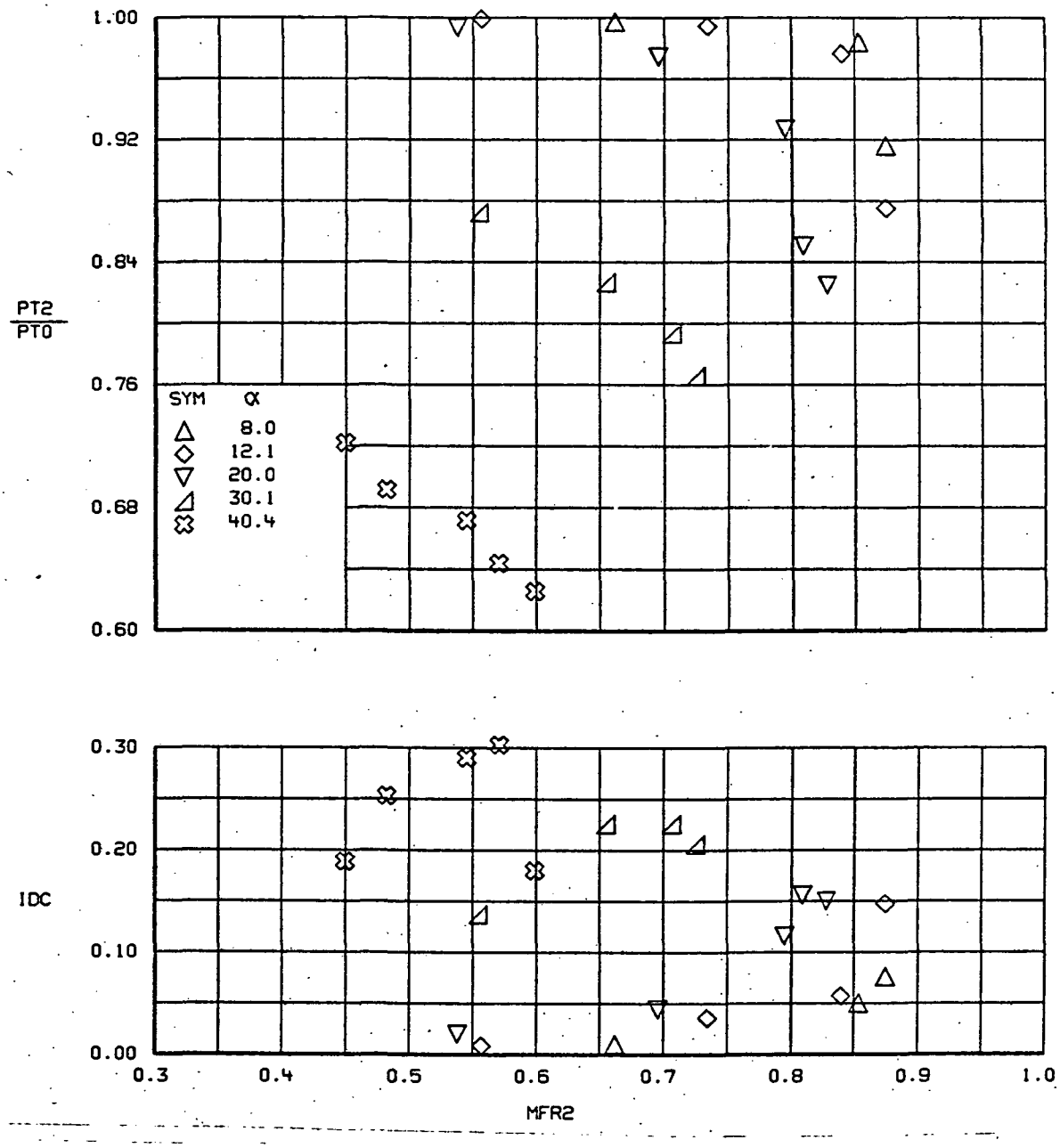

(a) IDC

Figure 62.-Variation in circumferential and radial distortion parameters with angle of attack, configuration 4, M=0.9, β=0°.

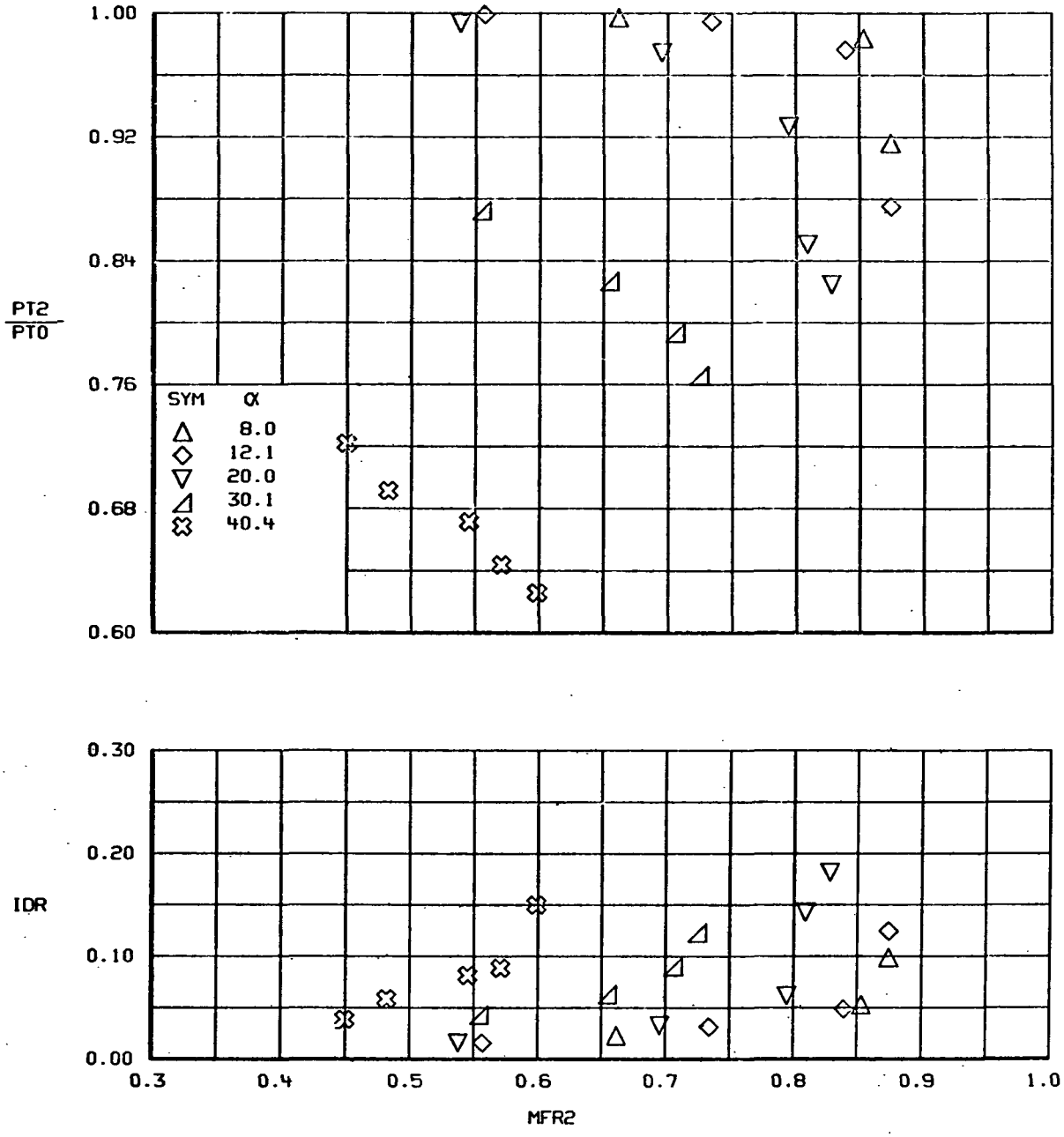

(b) IDR

Figure 62.-Concluded.

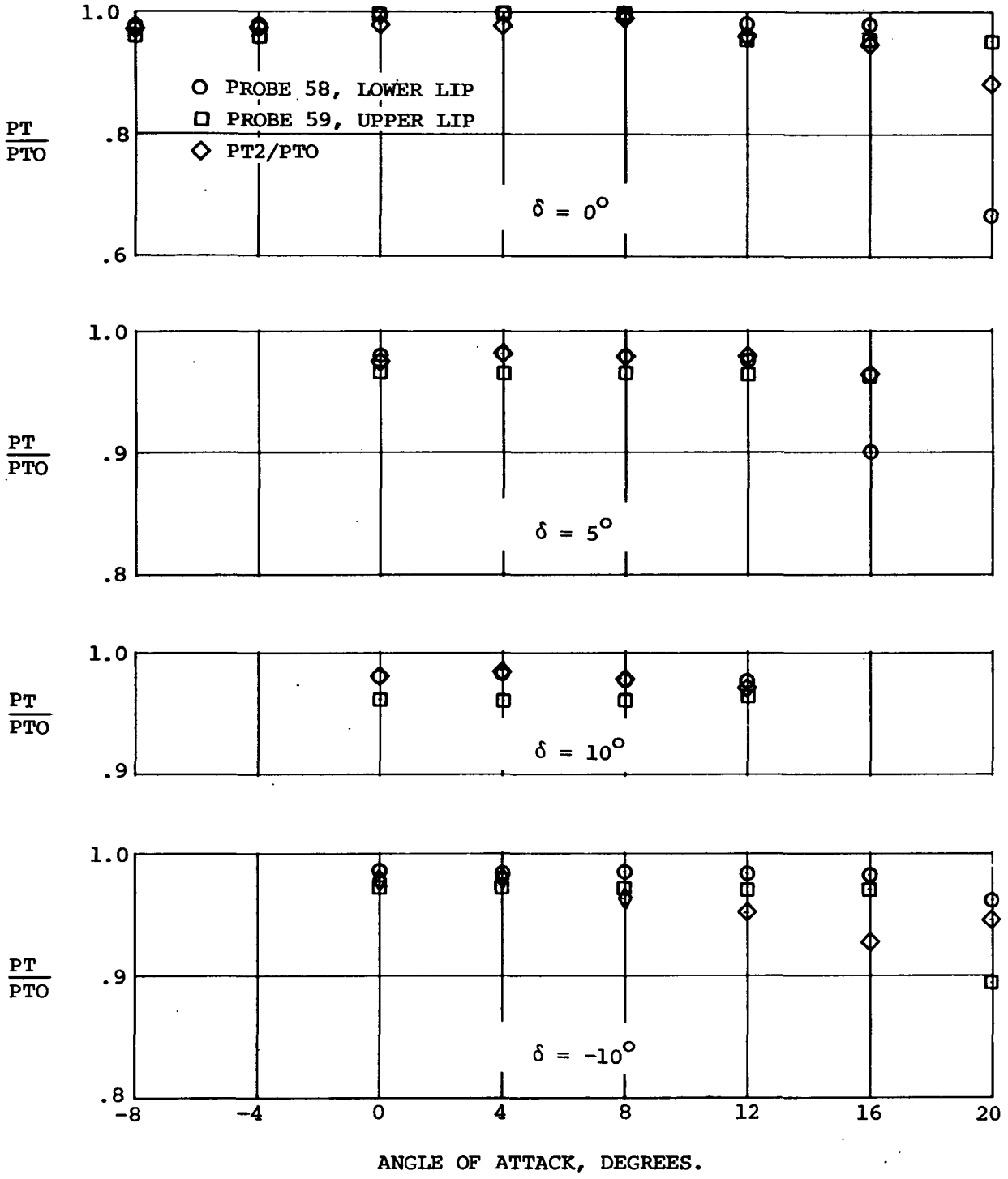

Figure 63.- Canard deflection and angle of attack effects on inlet and inlet flow field, inlet in upper position, M=0.9, $\beta=0^{\circ}$.

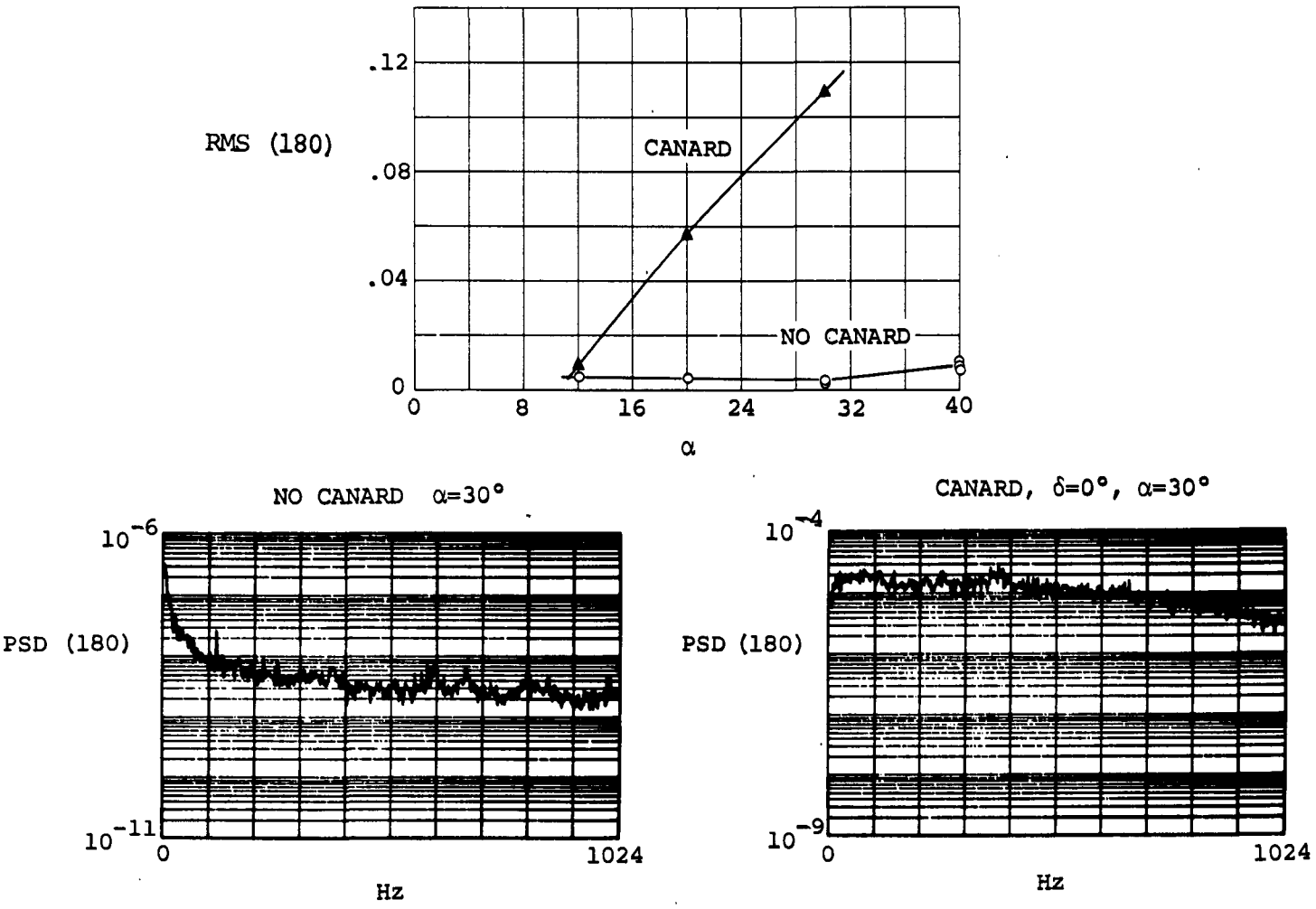

(a)

Figure 64.- Effect of canard and angle of attack on flow field turbulence, inlet in upper position, M=0.9, β=0°.

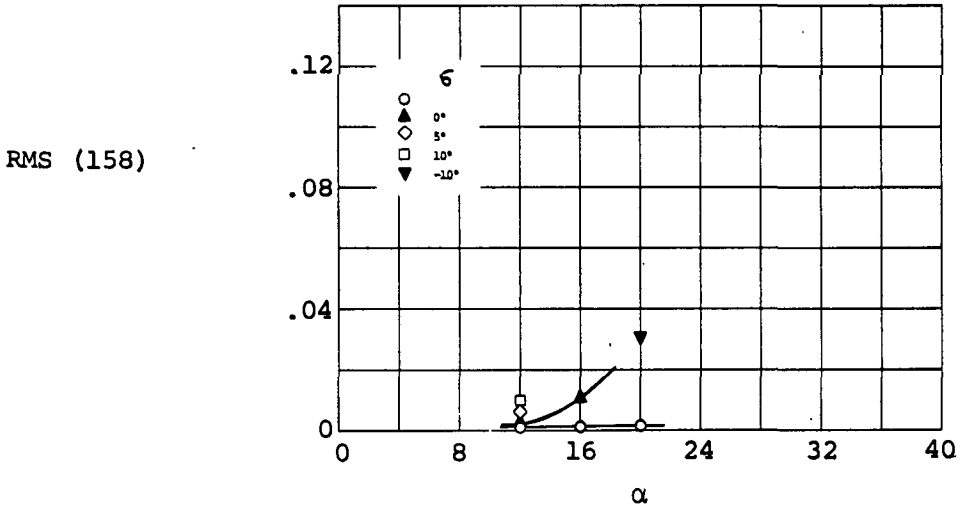

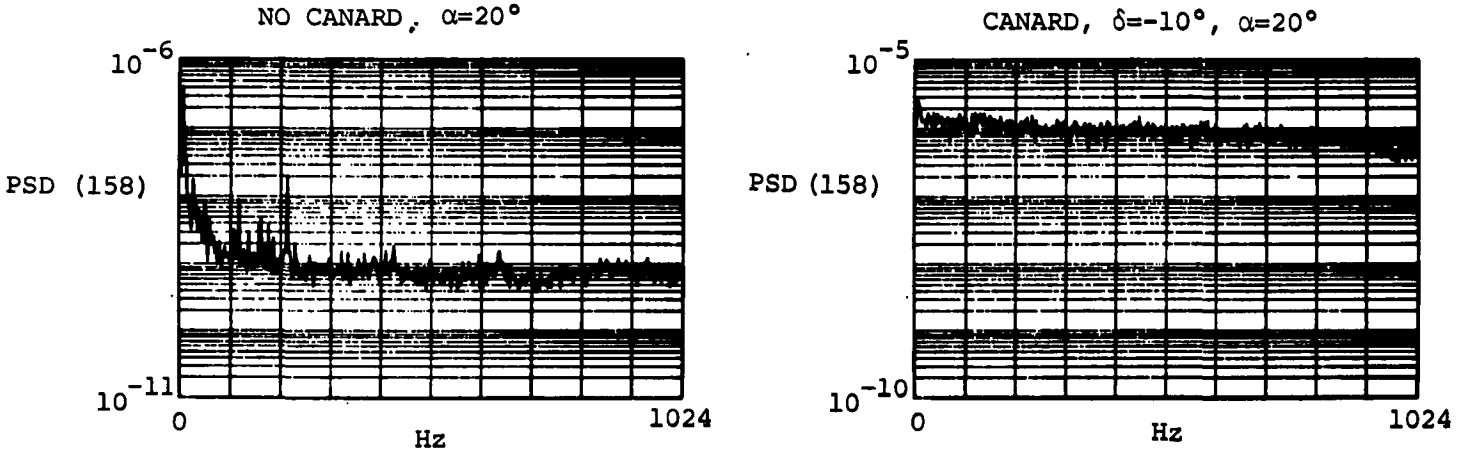

(b)

Figure 64.- Concluded

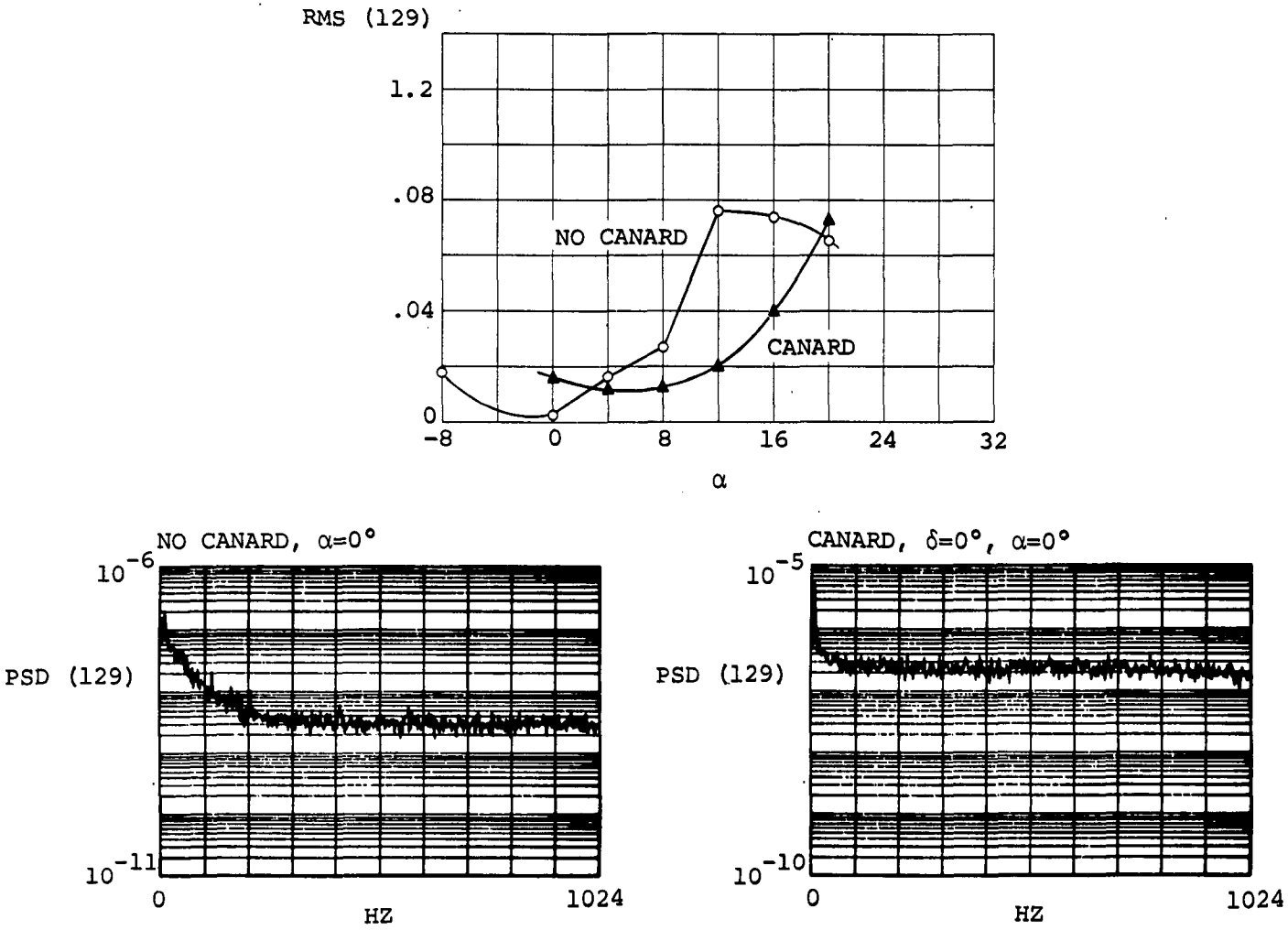

(a)

Figure 65.- Effect of canard and angle of attack on turbulence, engine face probe 129, inlet in lower position, M=0.9, β=0°.

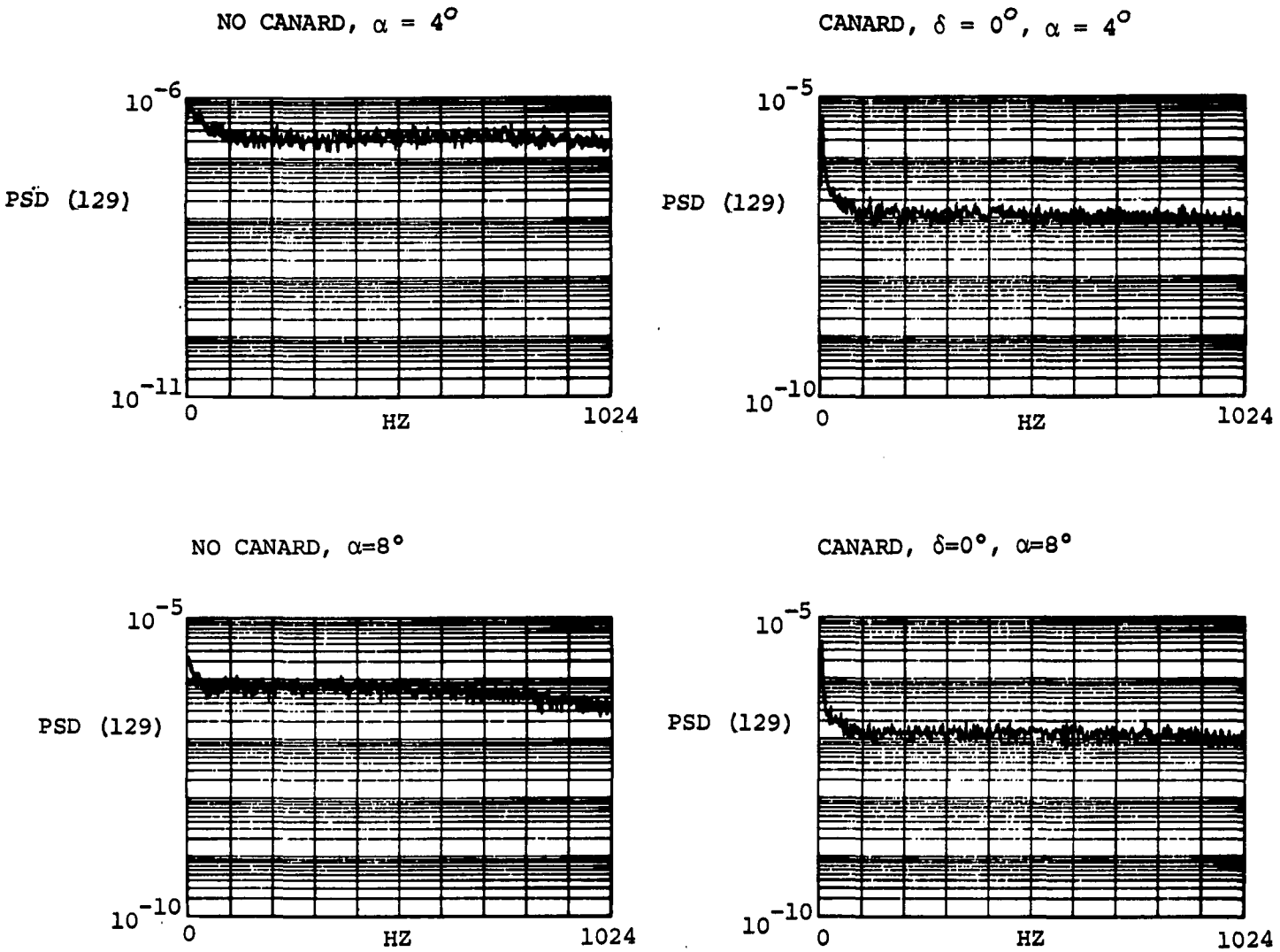

(b)

Figure 65.- Continued.

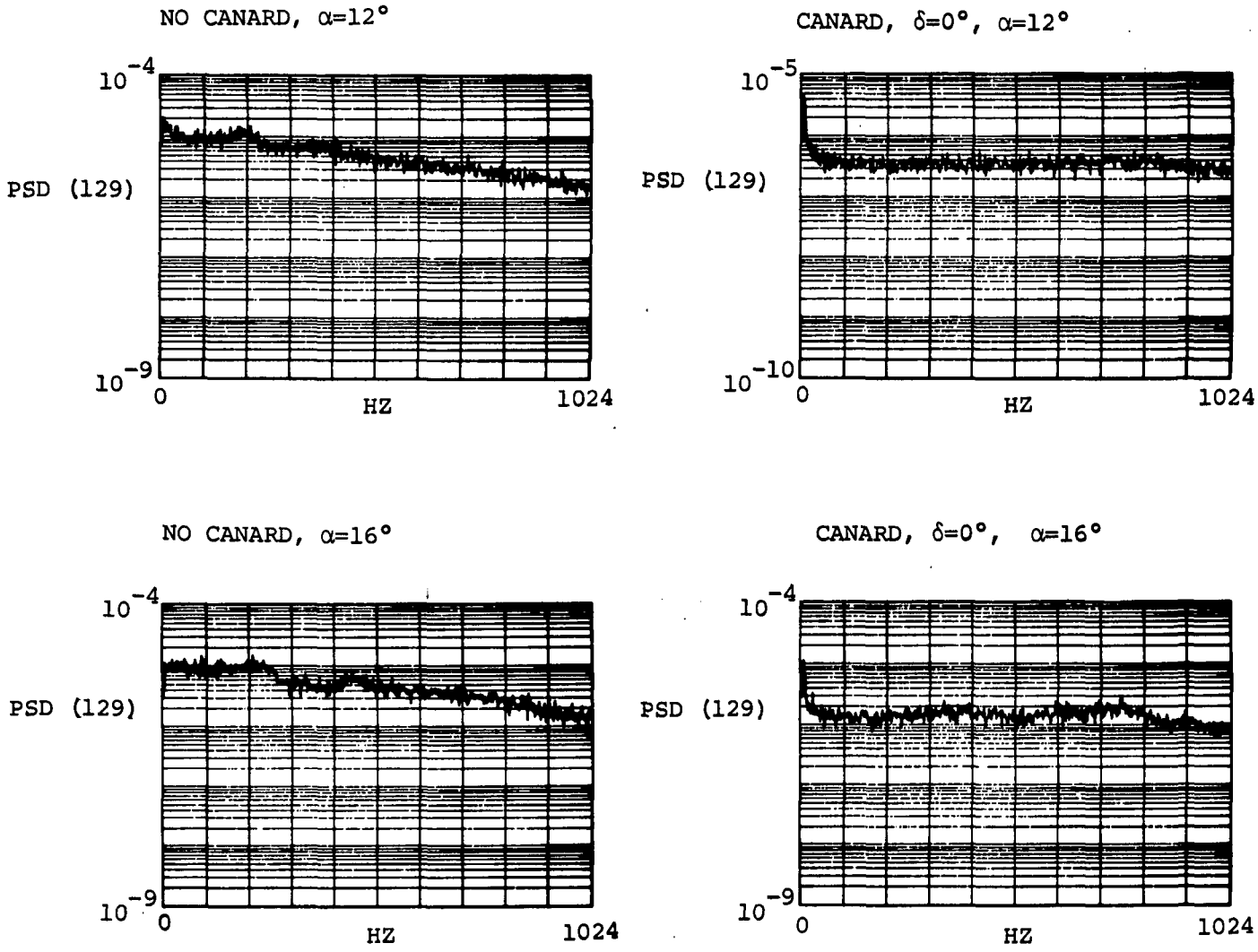

(c)

Figure 65.- Continued.

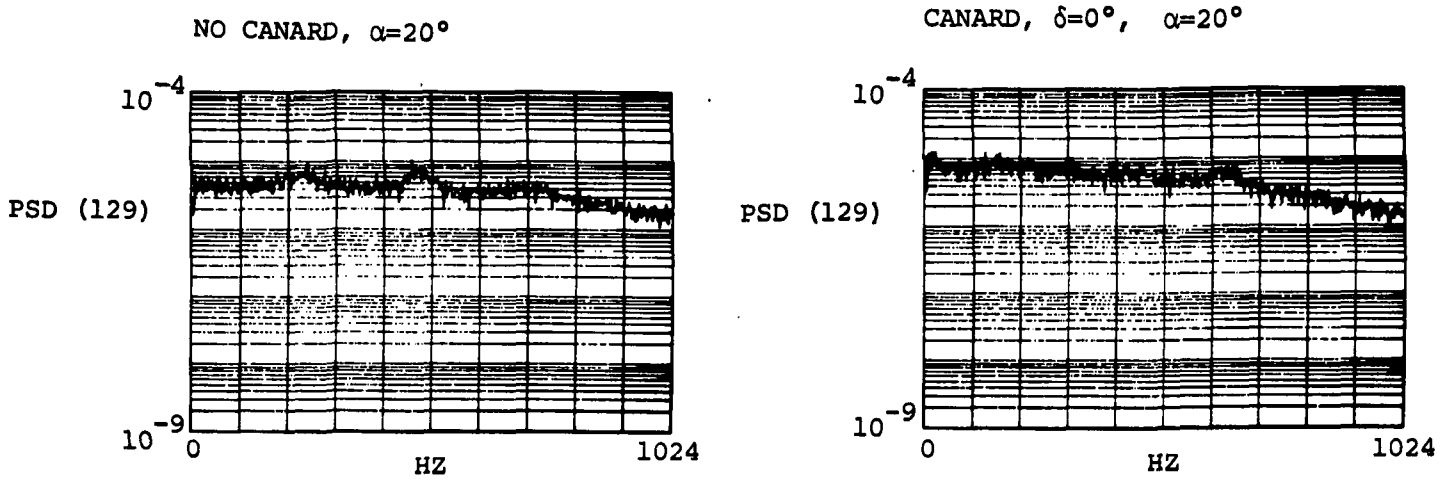

(d)

Figure 65.- Concluded.

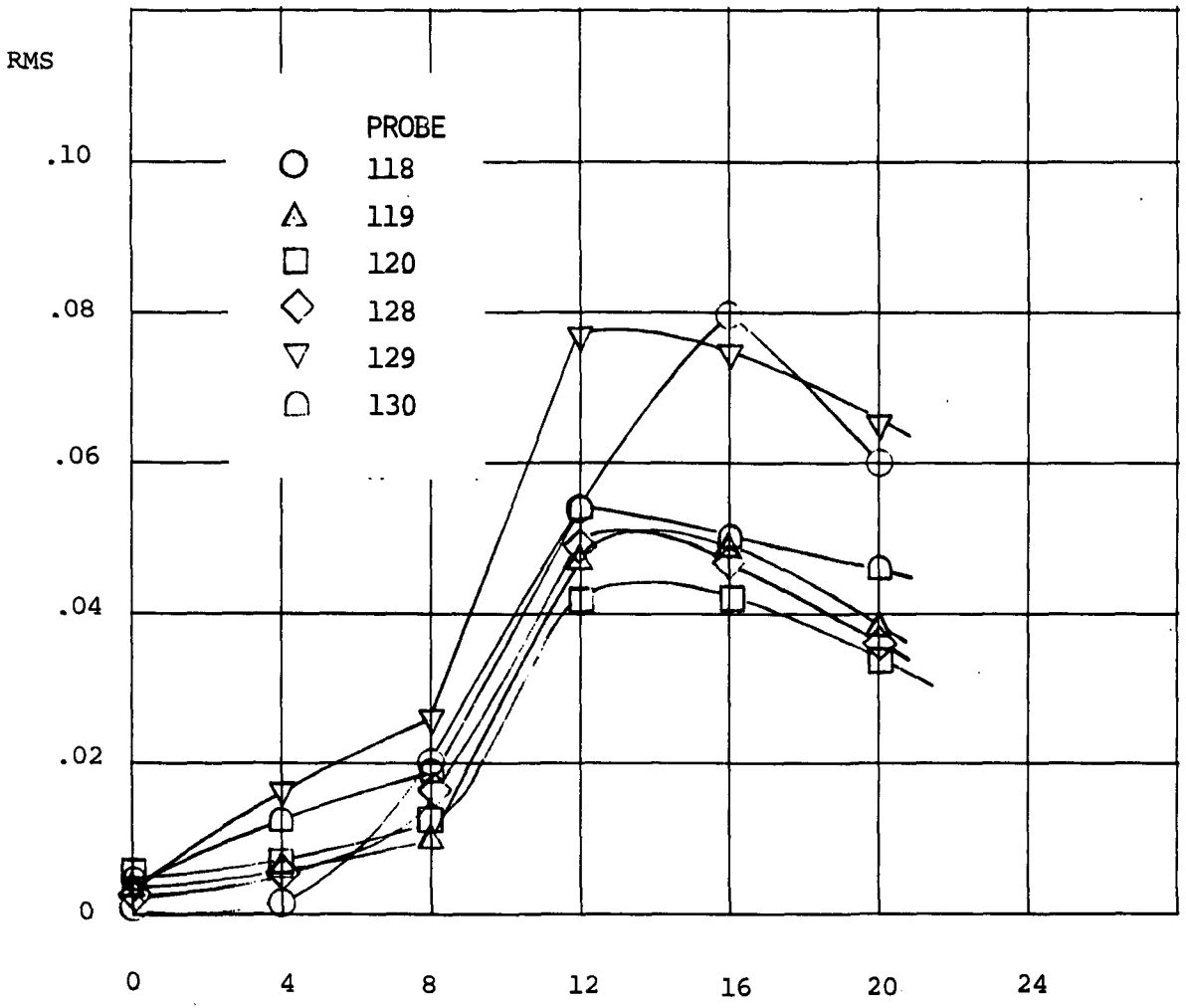

Figure 66.-Effect of angle of attack on engine face turbulence, configuration 11, M=0.9, β=0°

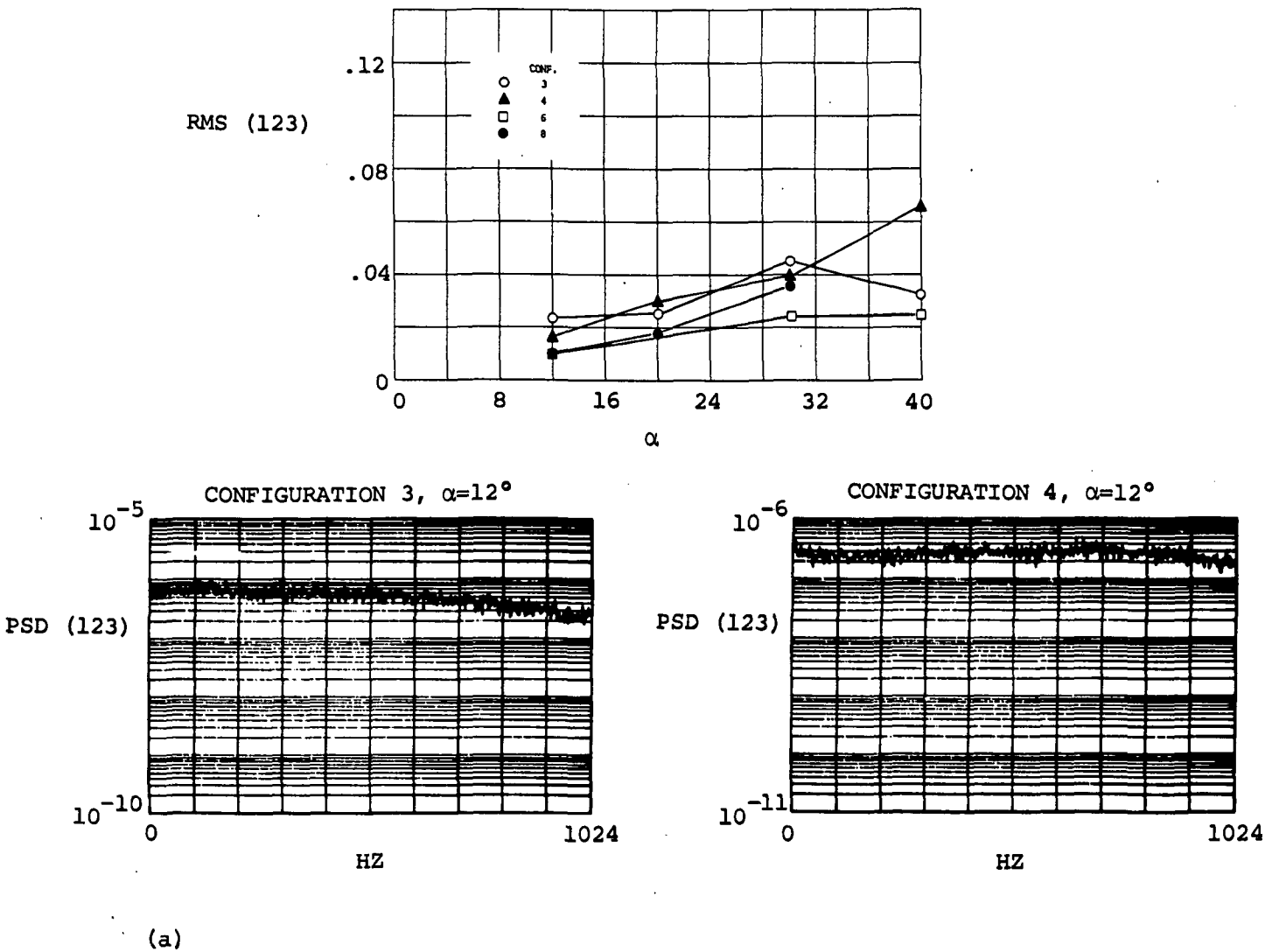

(a)

Figure 67.- Effect of lip configuration and angle of attack on engine face turbulence, probe 123, two-dimensional inlet, M=0.9, β=0°.

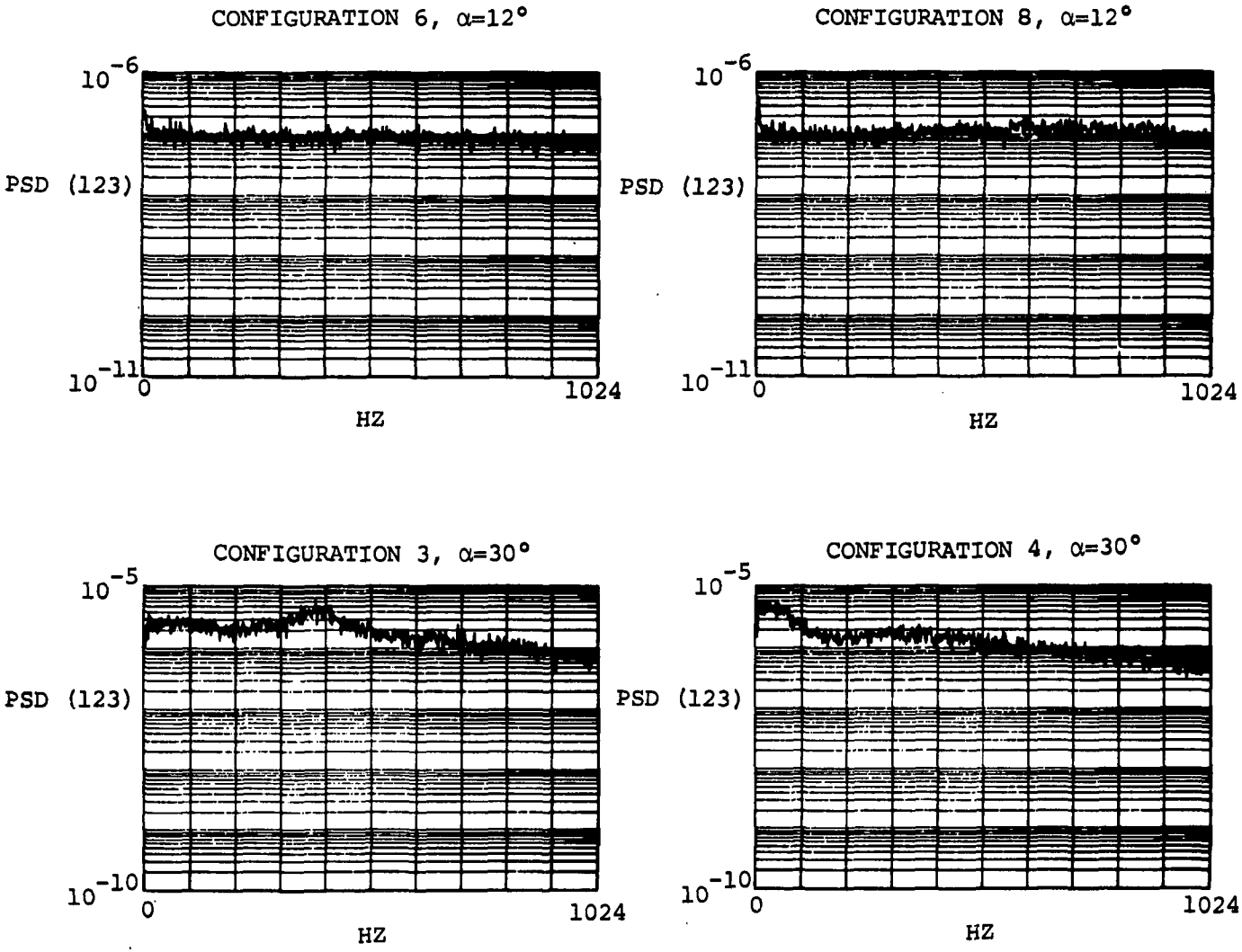

(b)

Figure 67.- Continued.

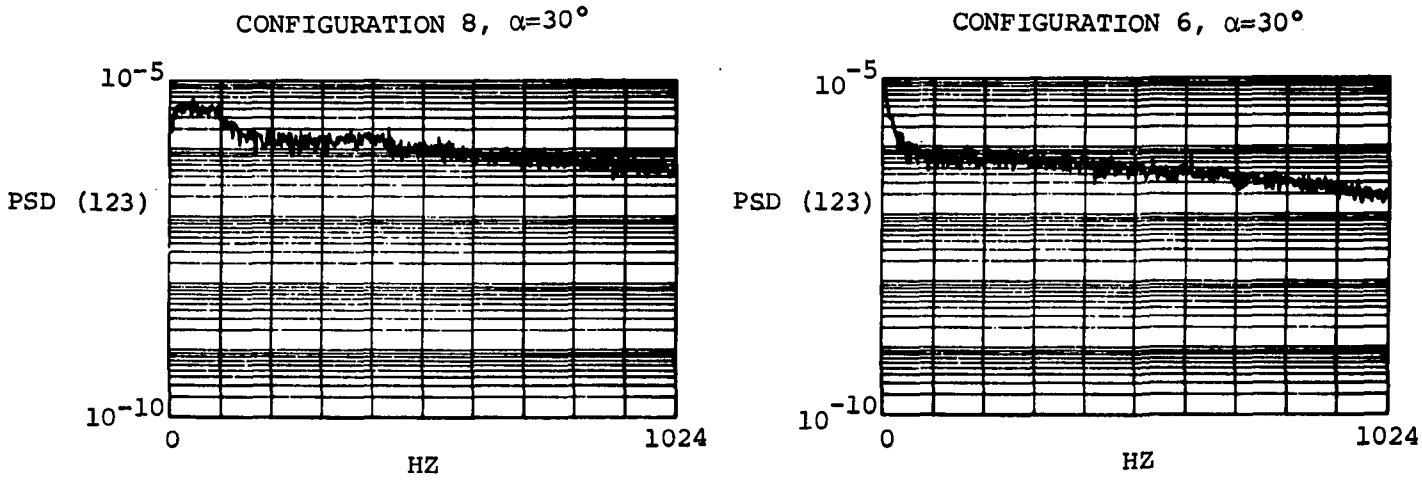

(c)

Figure 67.-Concluded.

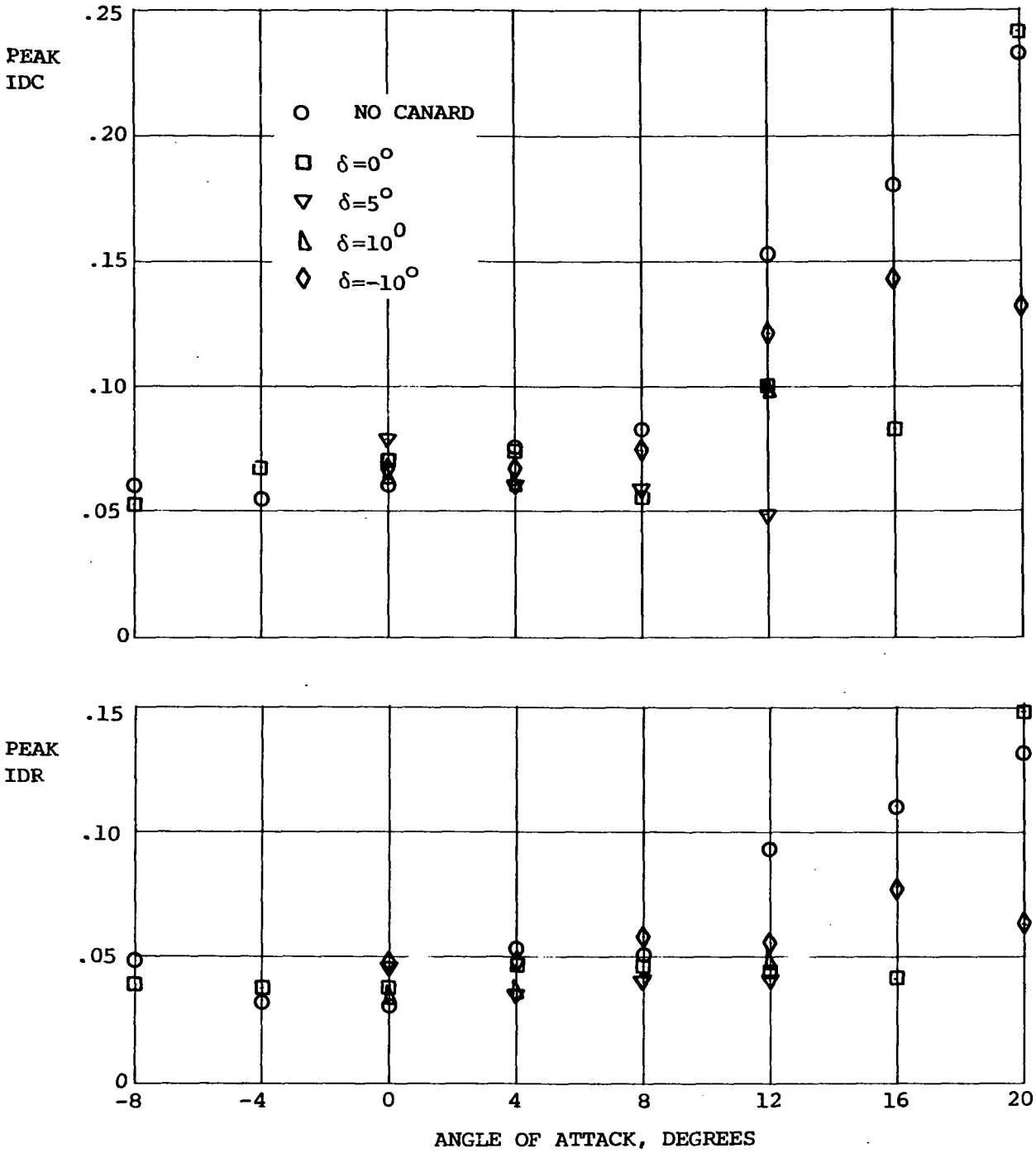

Figure 68.- Variation in peak instantaneous distortion with angle of attack, configurations 1 and 2, M=0.9, $\beta=0^{\circ}$

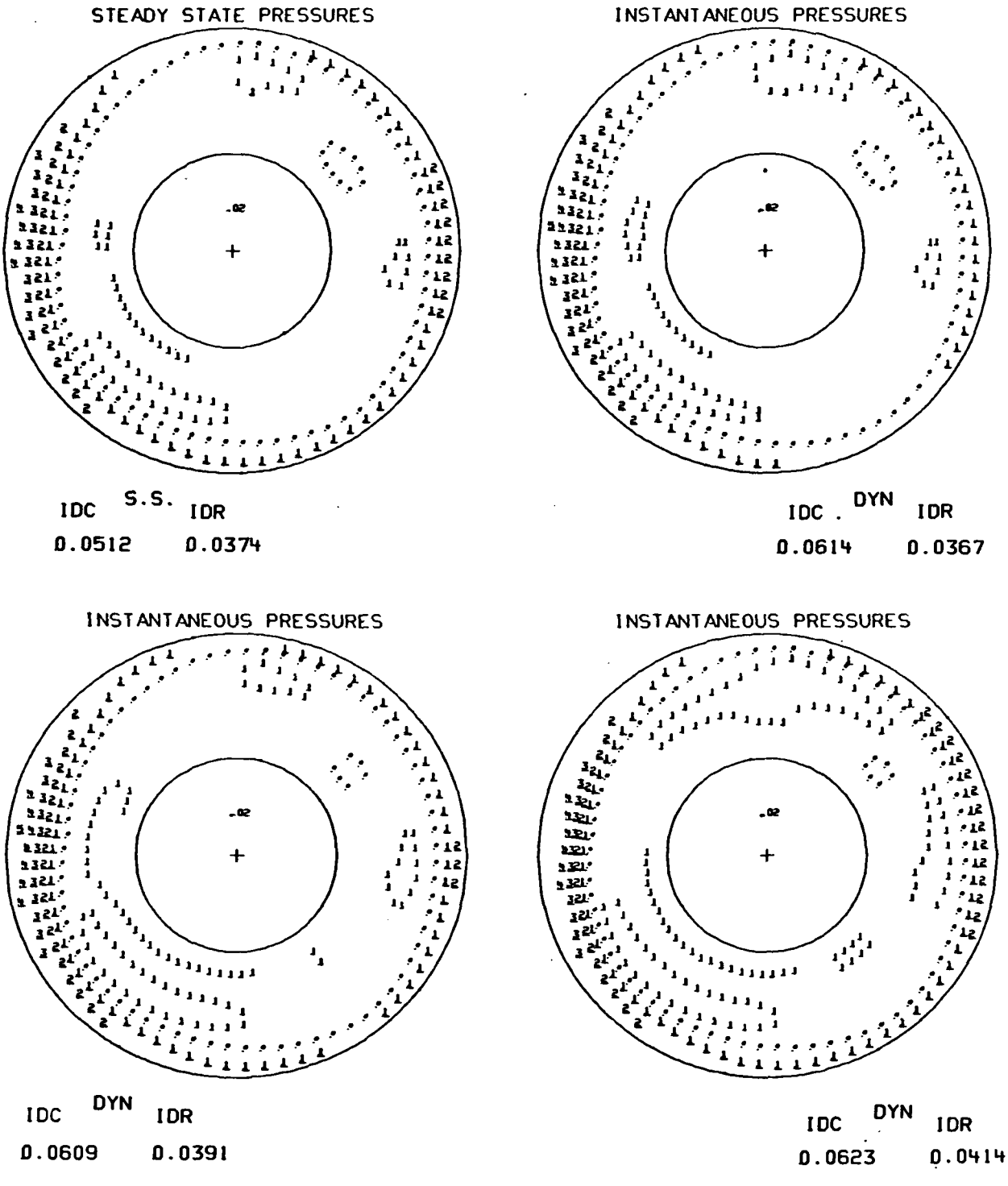

Figure 69. - Instanteous total pressure distortion configuration 11, $\alpha = 0$, $M = 0.9$, $\beta = 0^{\circ}$

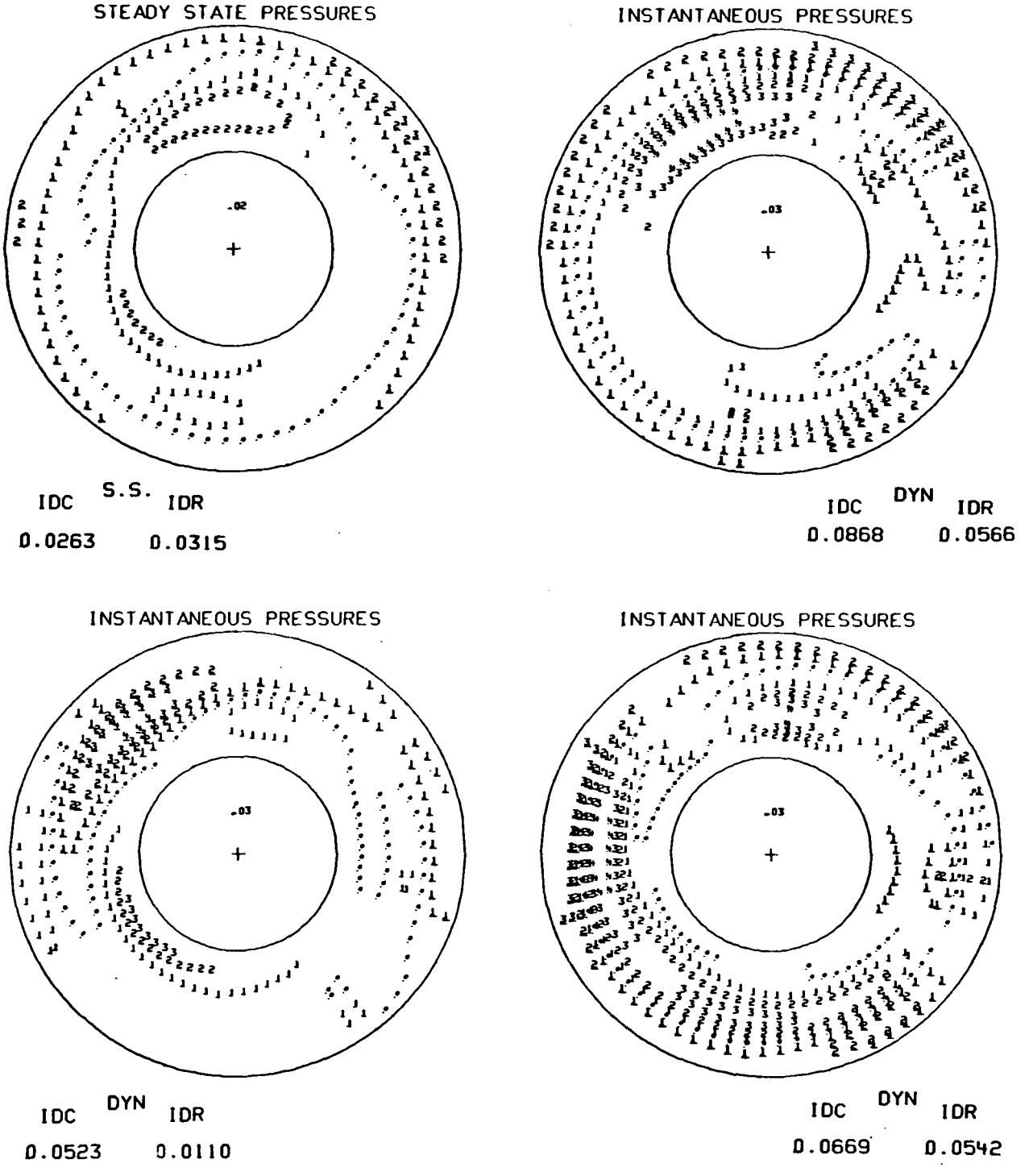

Figure 70. - Instanteous total pressure distortion configuration 10, $\delta = 10^{o}$, $\alpha = 12^{o}$, M = 0.9, $\beta = 0^{o}$

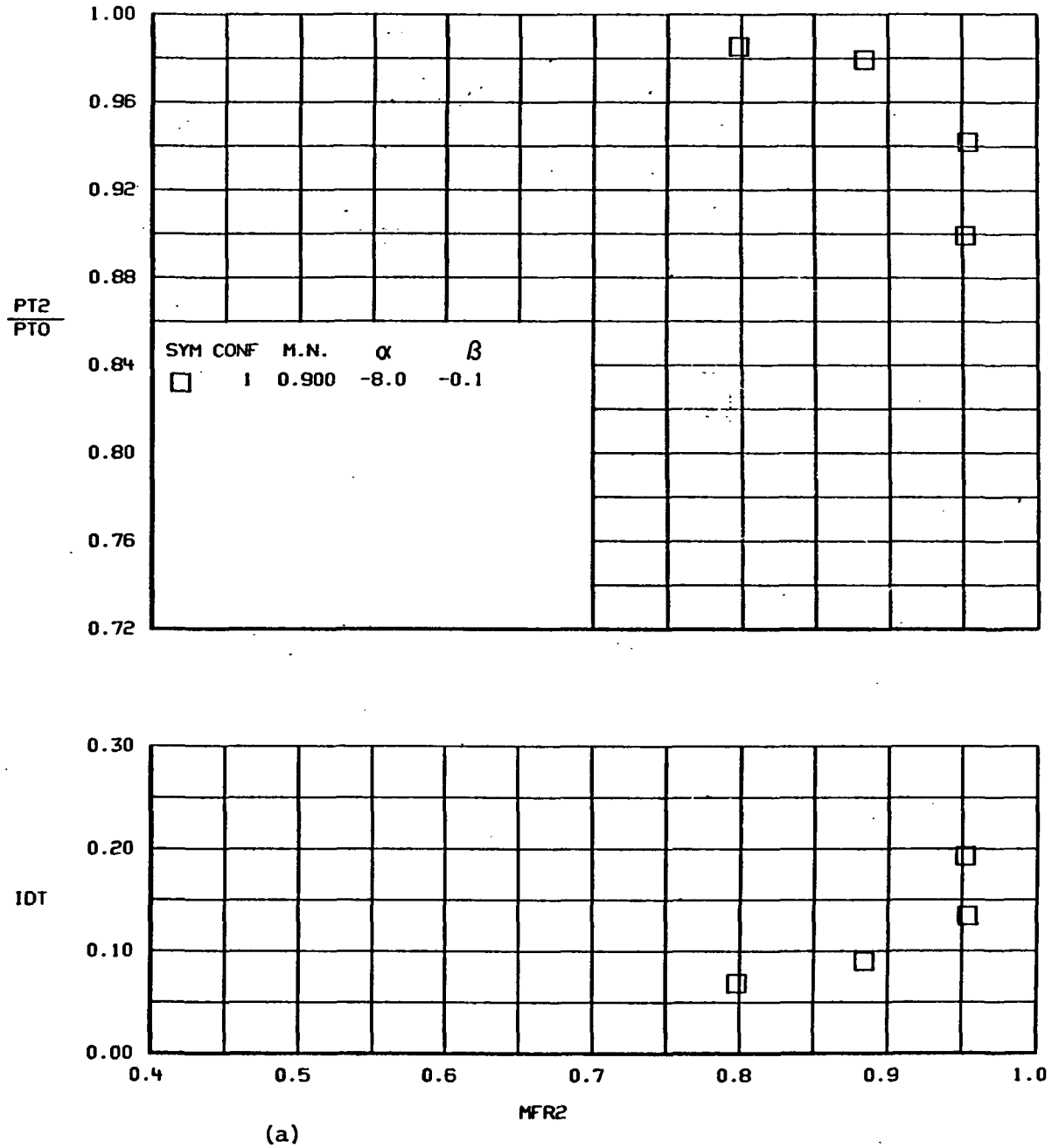

(a)

FIGURE 71.- TOTAL PRESSURE RECOVERY AND DISTORTION VERSUS MASS FLOW RATIO
Configuration 1, $\delta=0^{o}$.

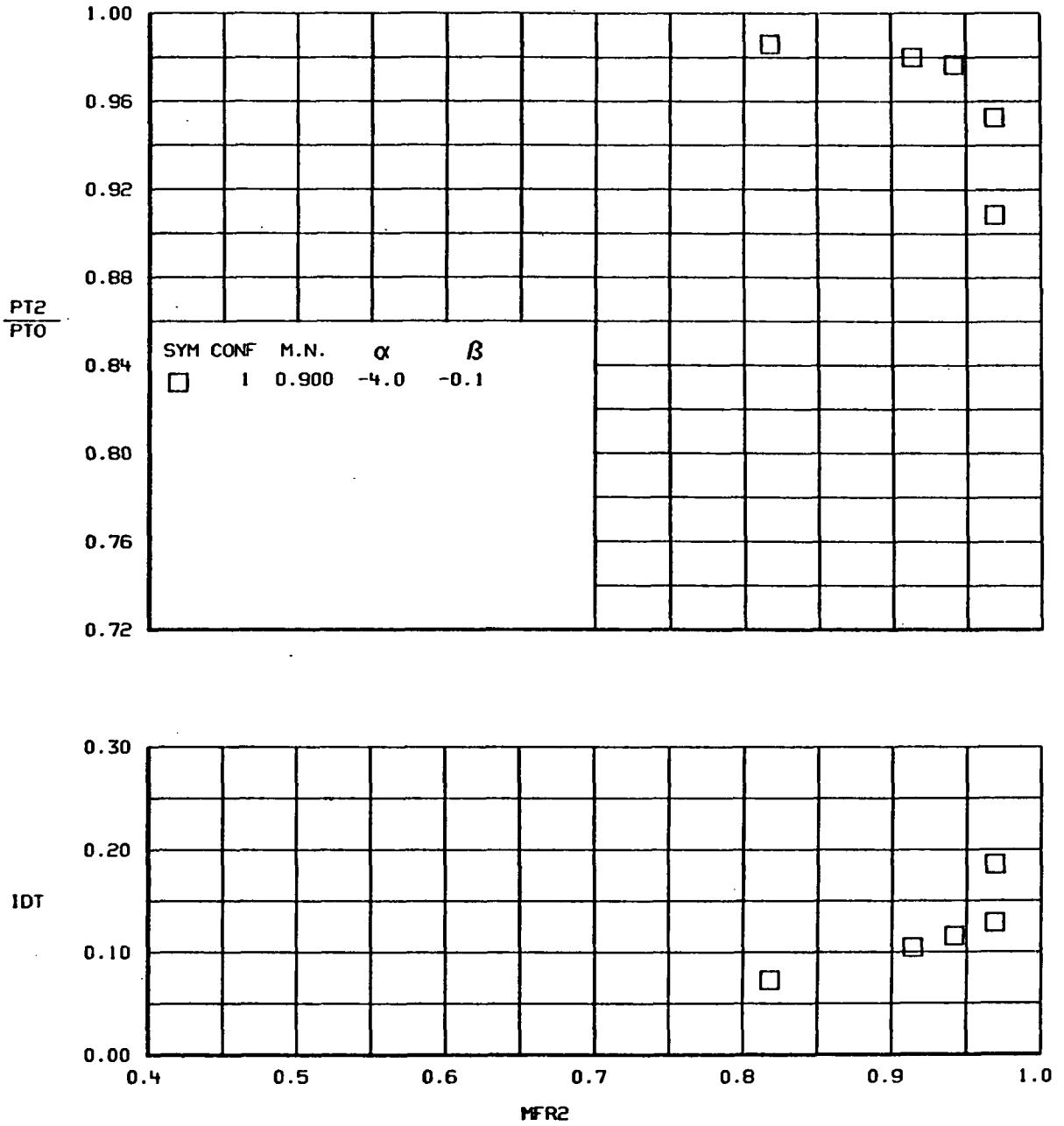

(b)

Figure 71.-Continued

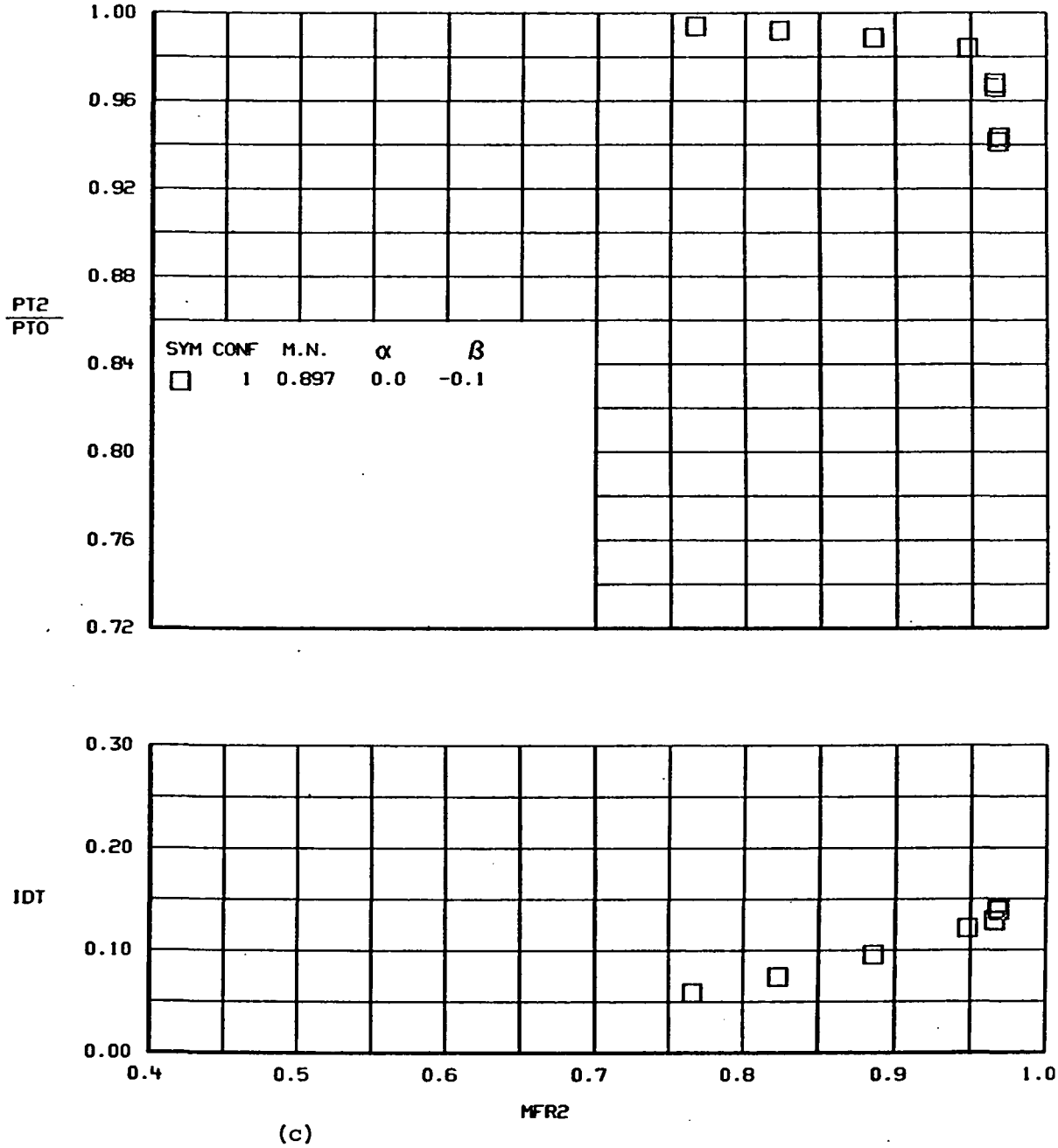

(c)

Figure 71.-Continued.

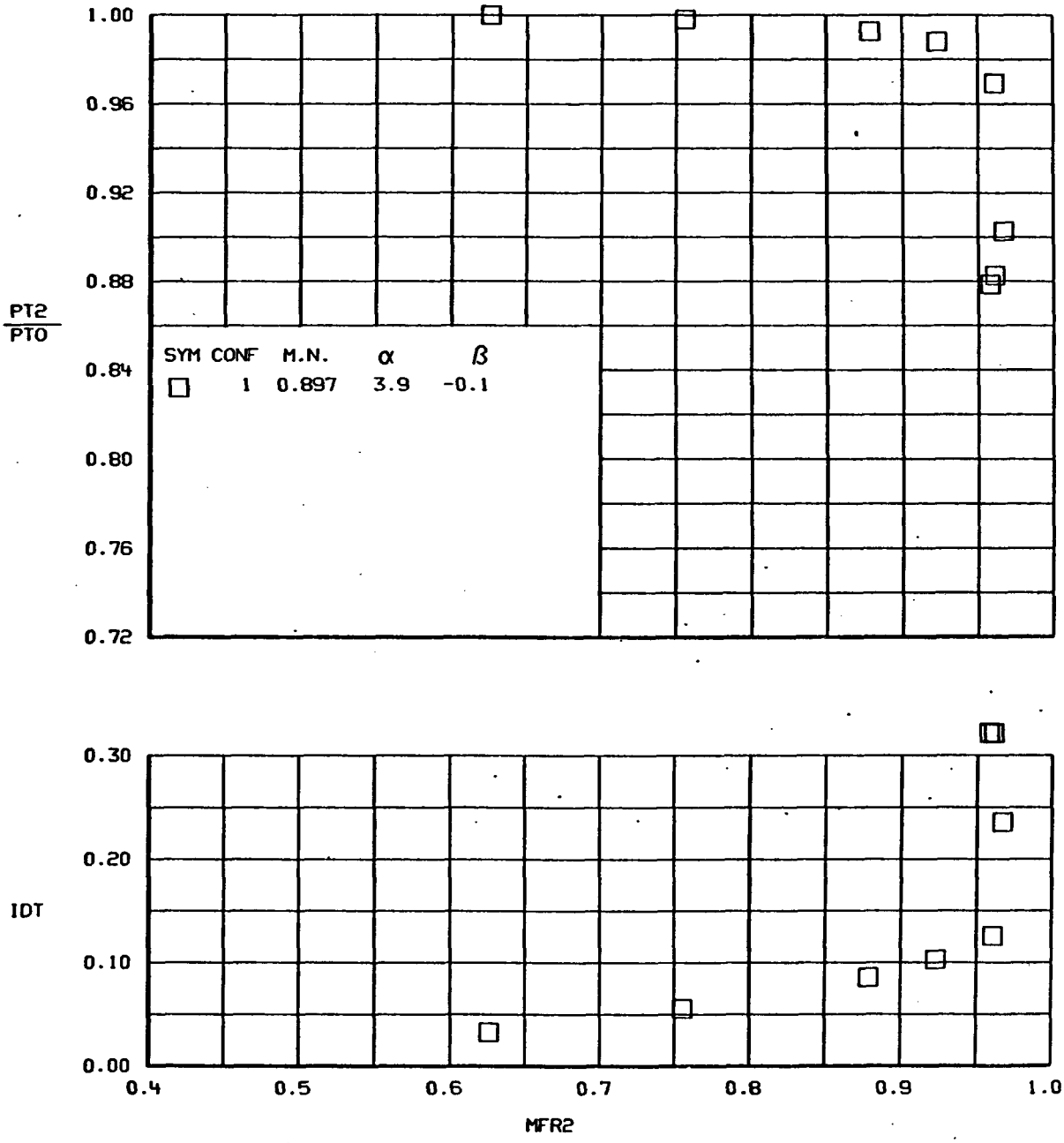

(d)

Figure 71.-Continued.

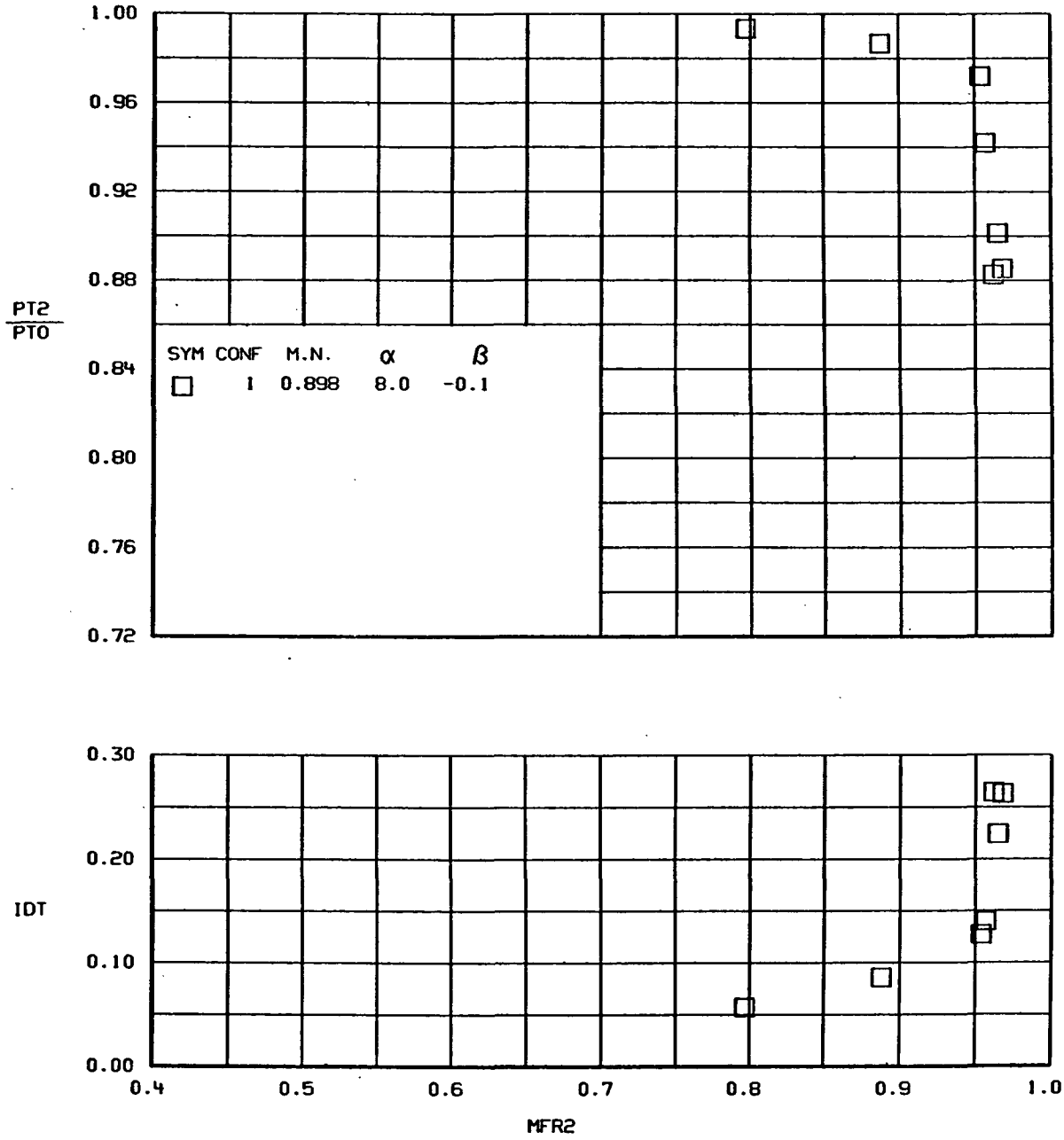

(e)

Figure 71.-Continued

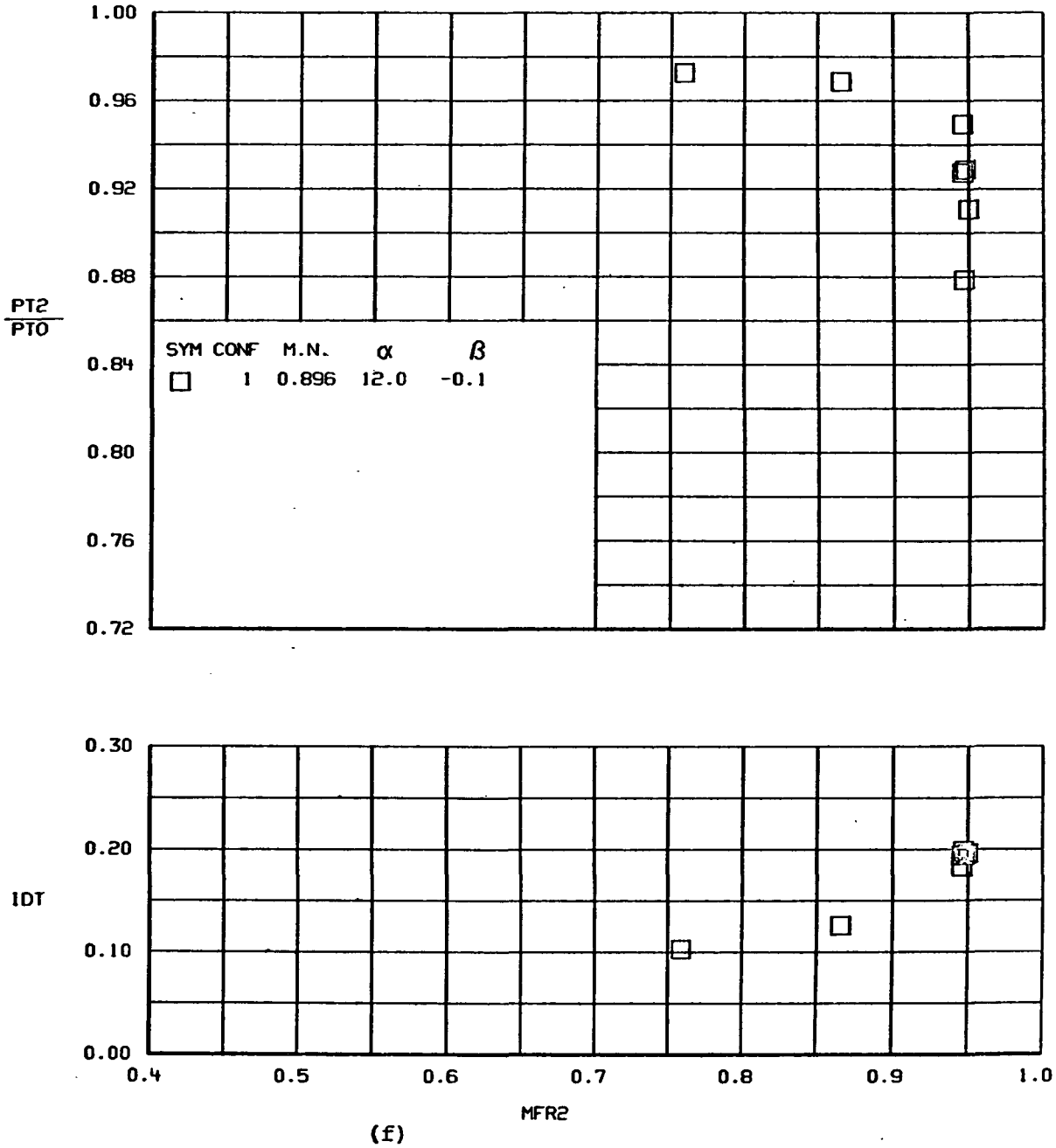

(f)

Figure 71.-Continued

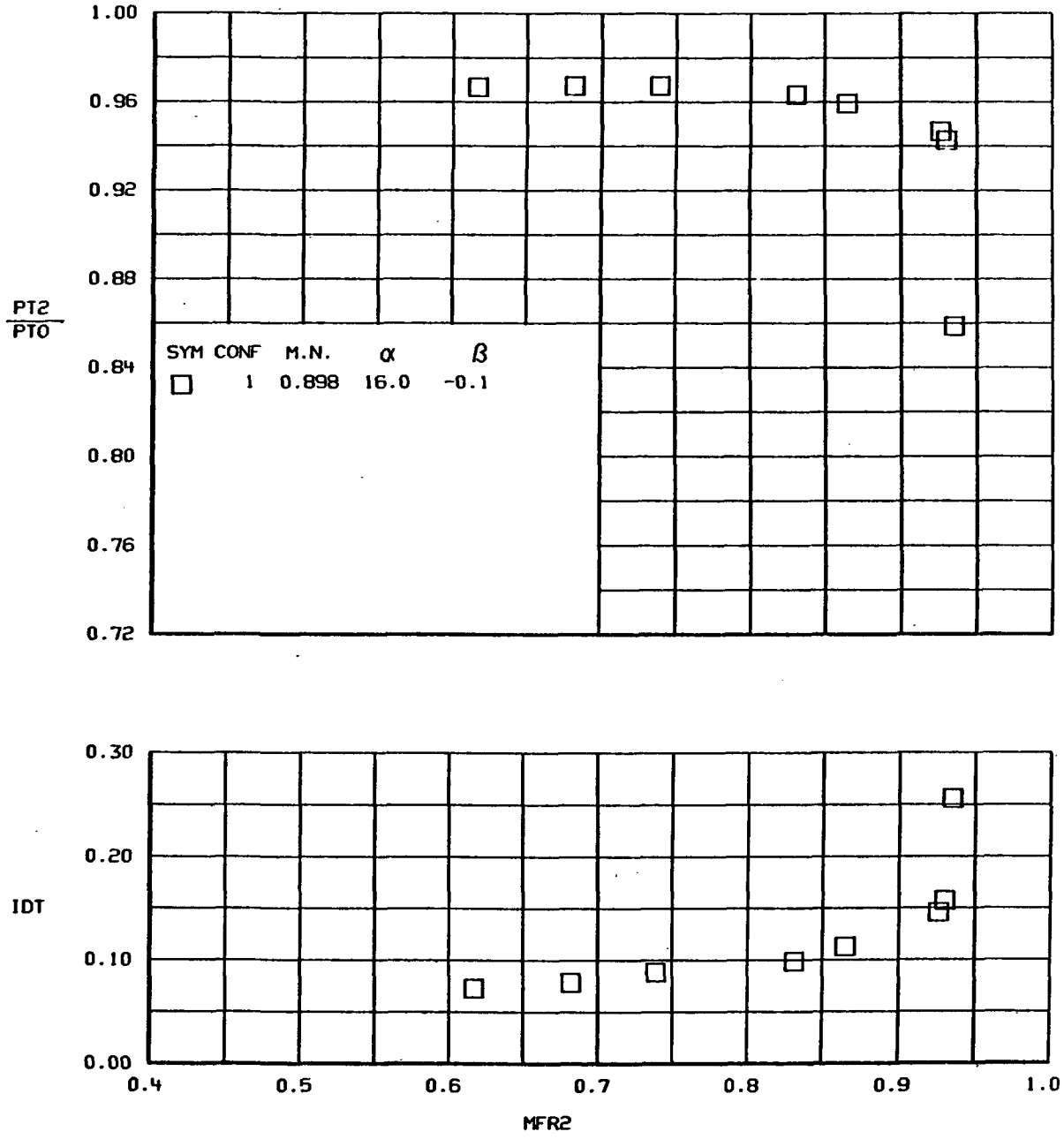

(g)

Figure 71.-Continued.

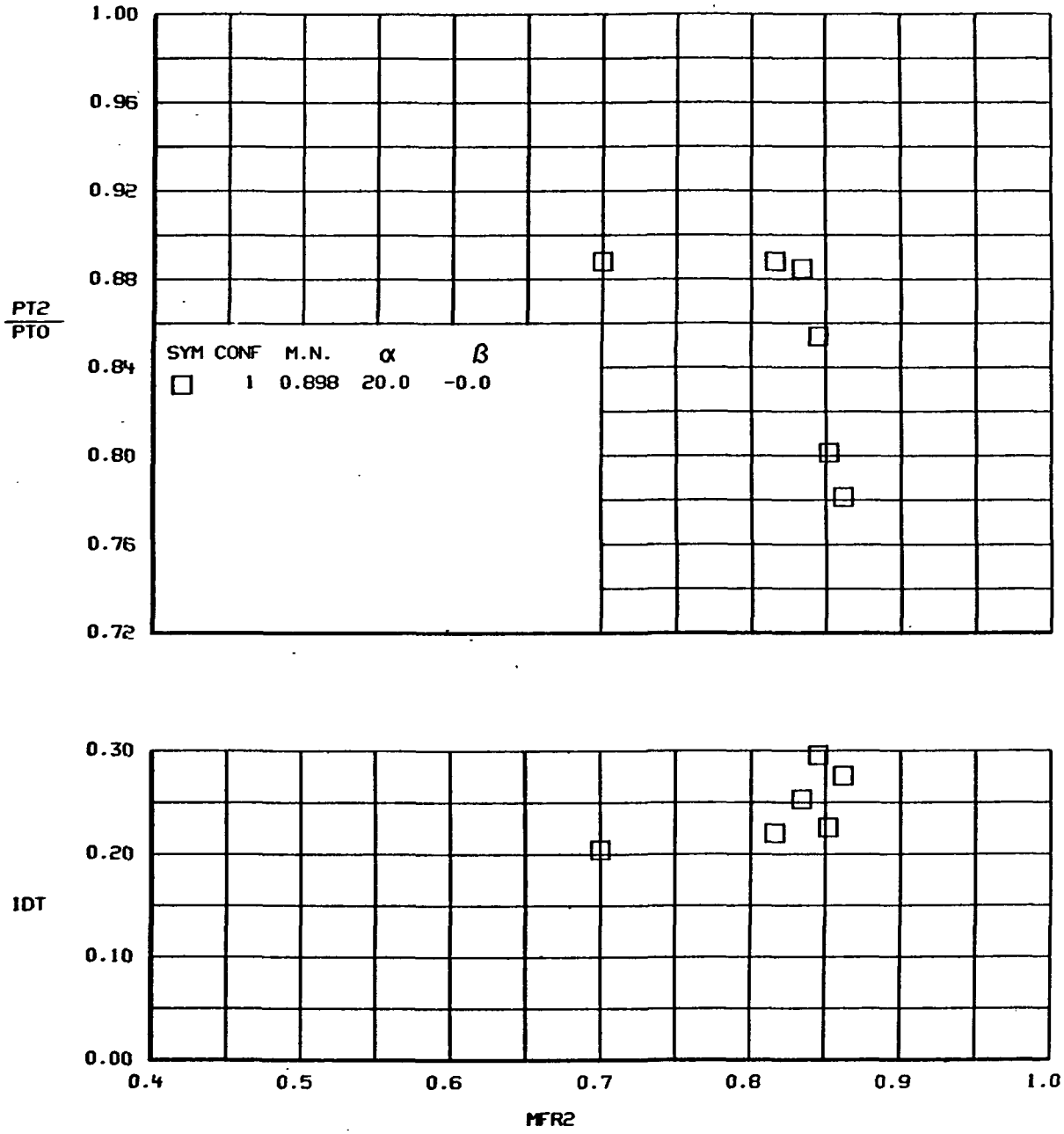

(h)

Figure 71.-Continued.

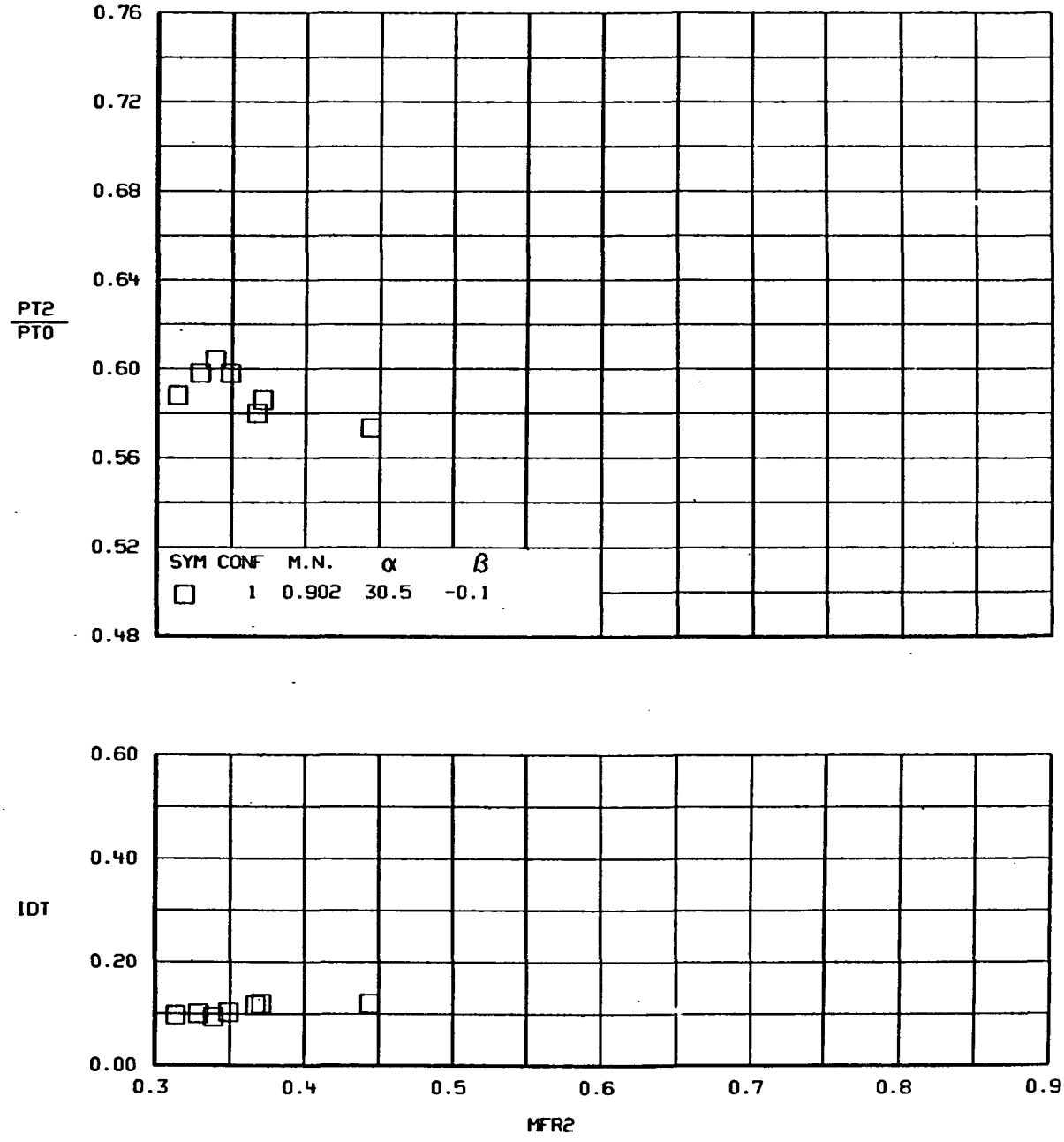

(i)

Figure 71.-Continued.

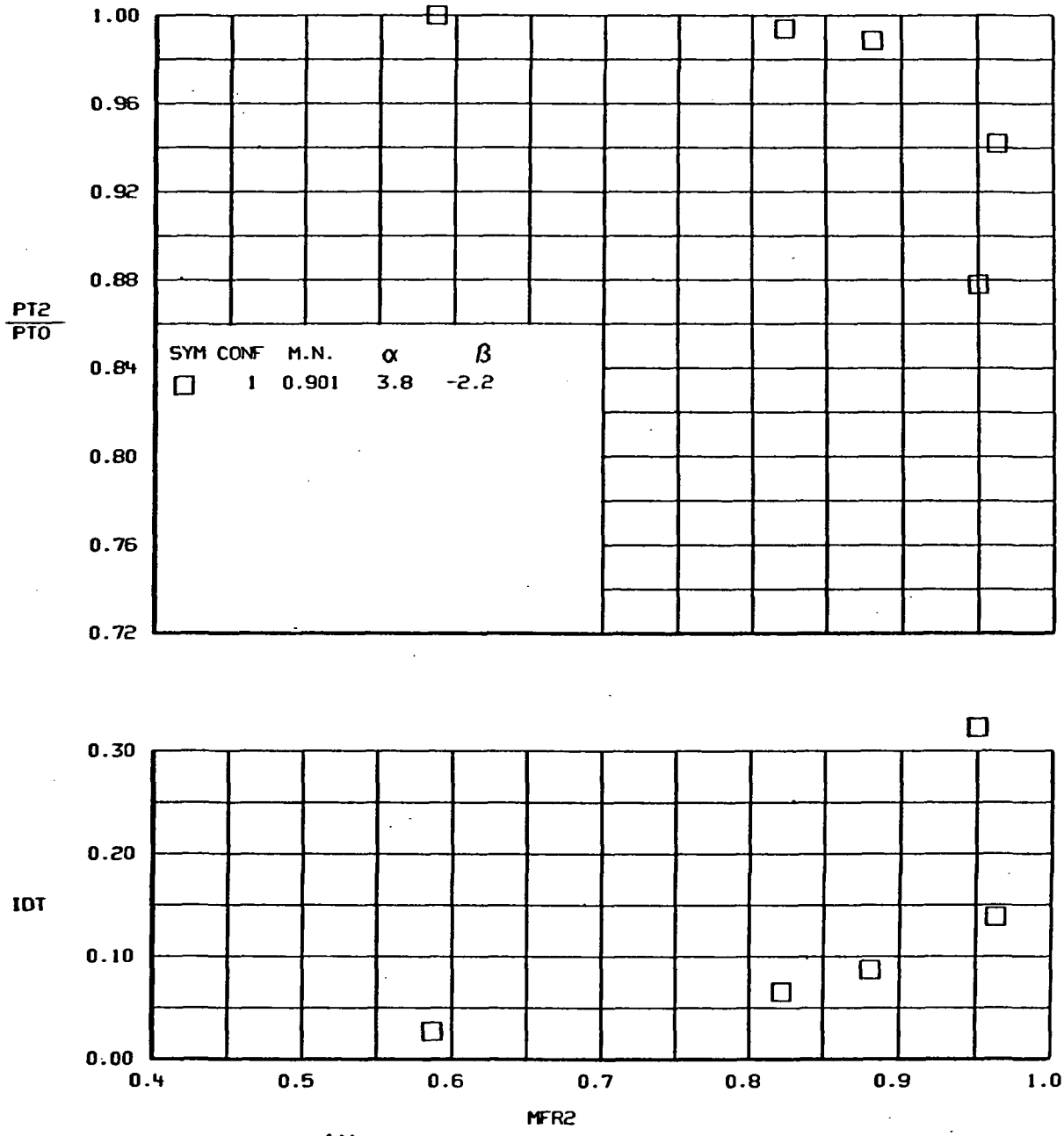

(j)

Figure 71.-Continued.

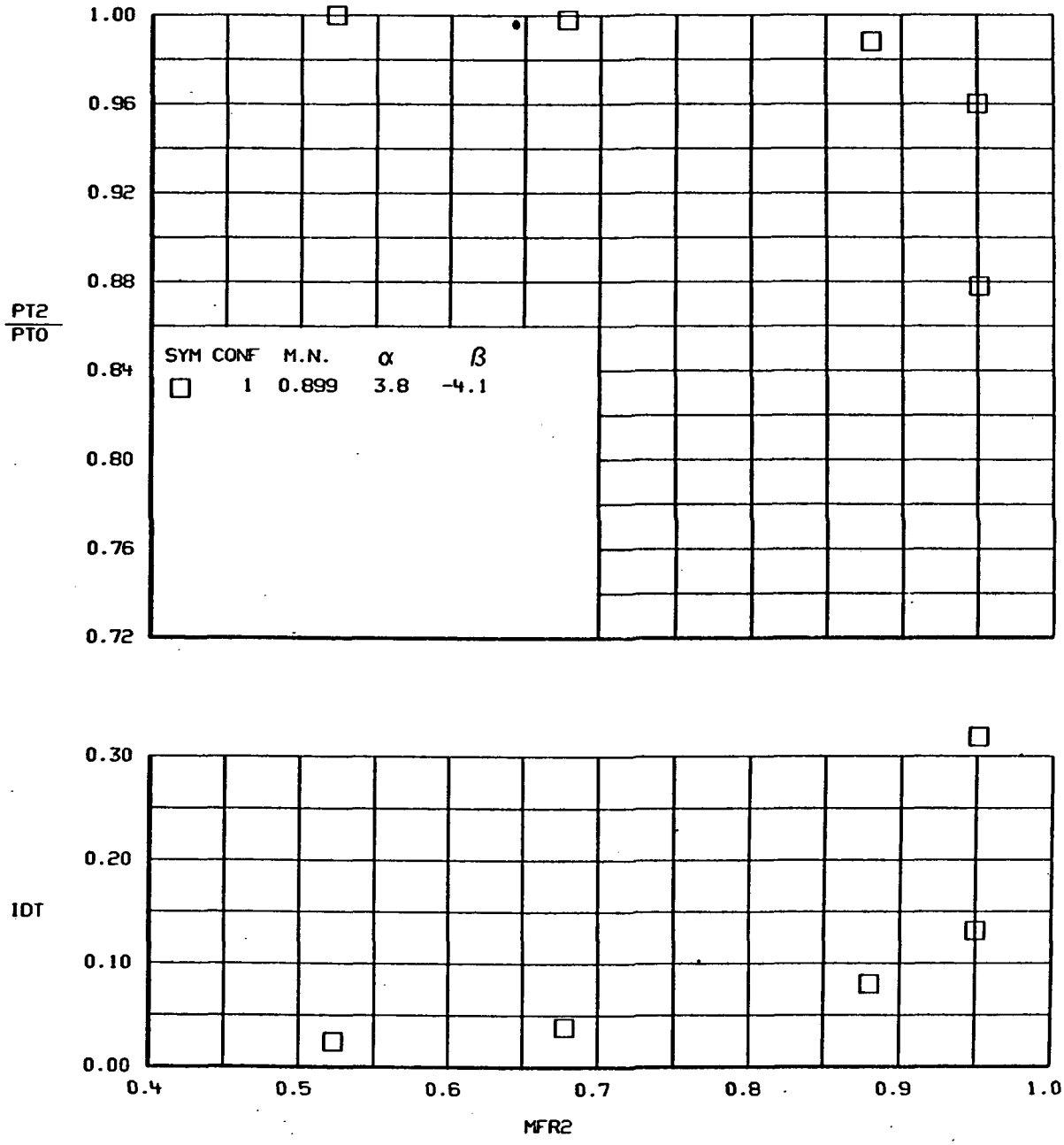

(k)

Figure 71.-Continued.

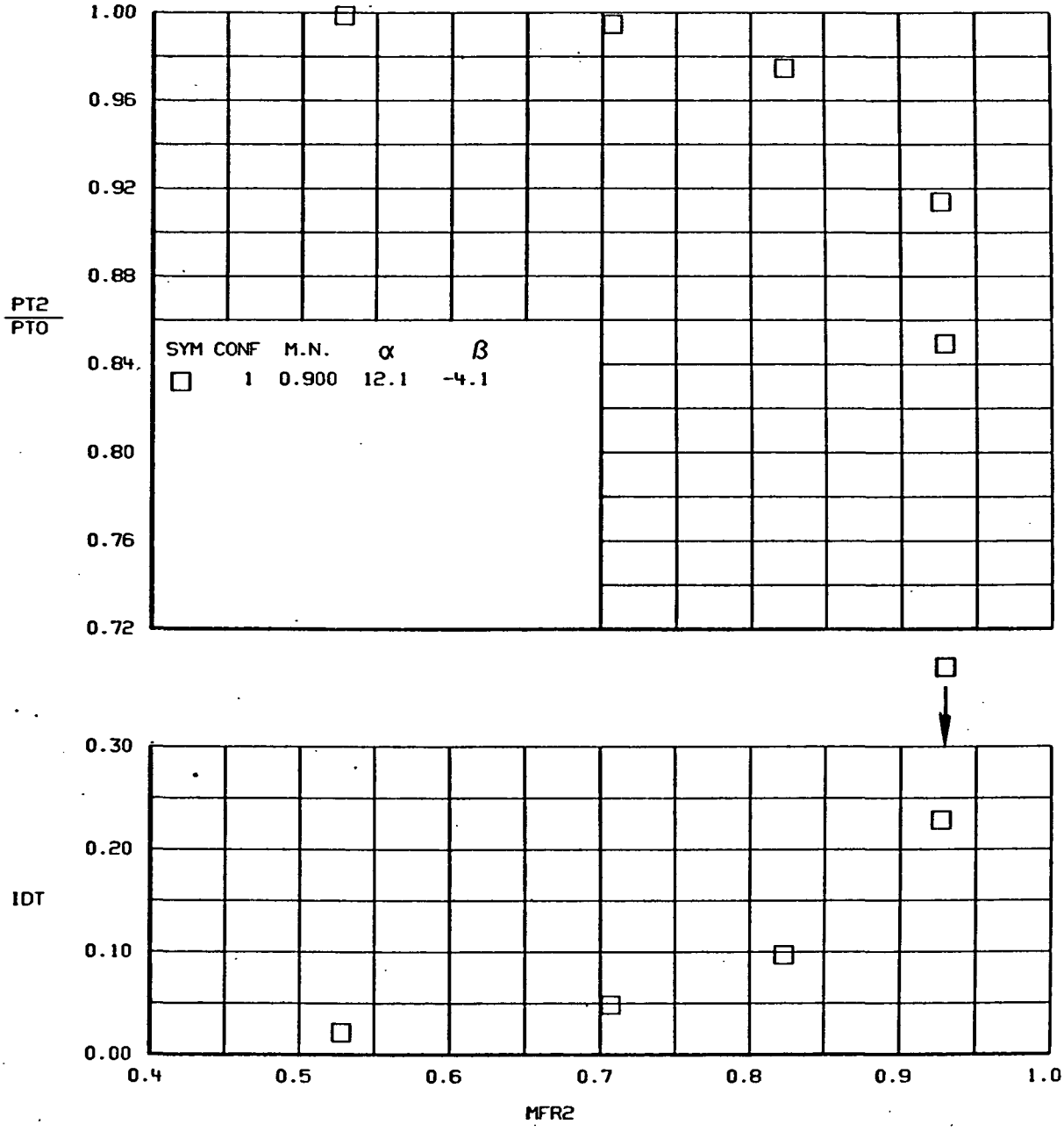

(1)

Figure 71.-Continued.

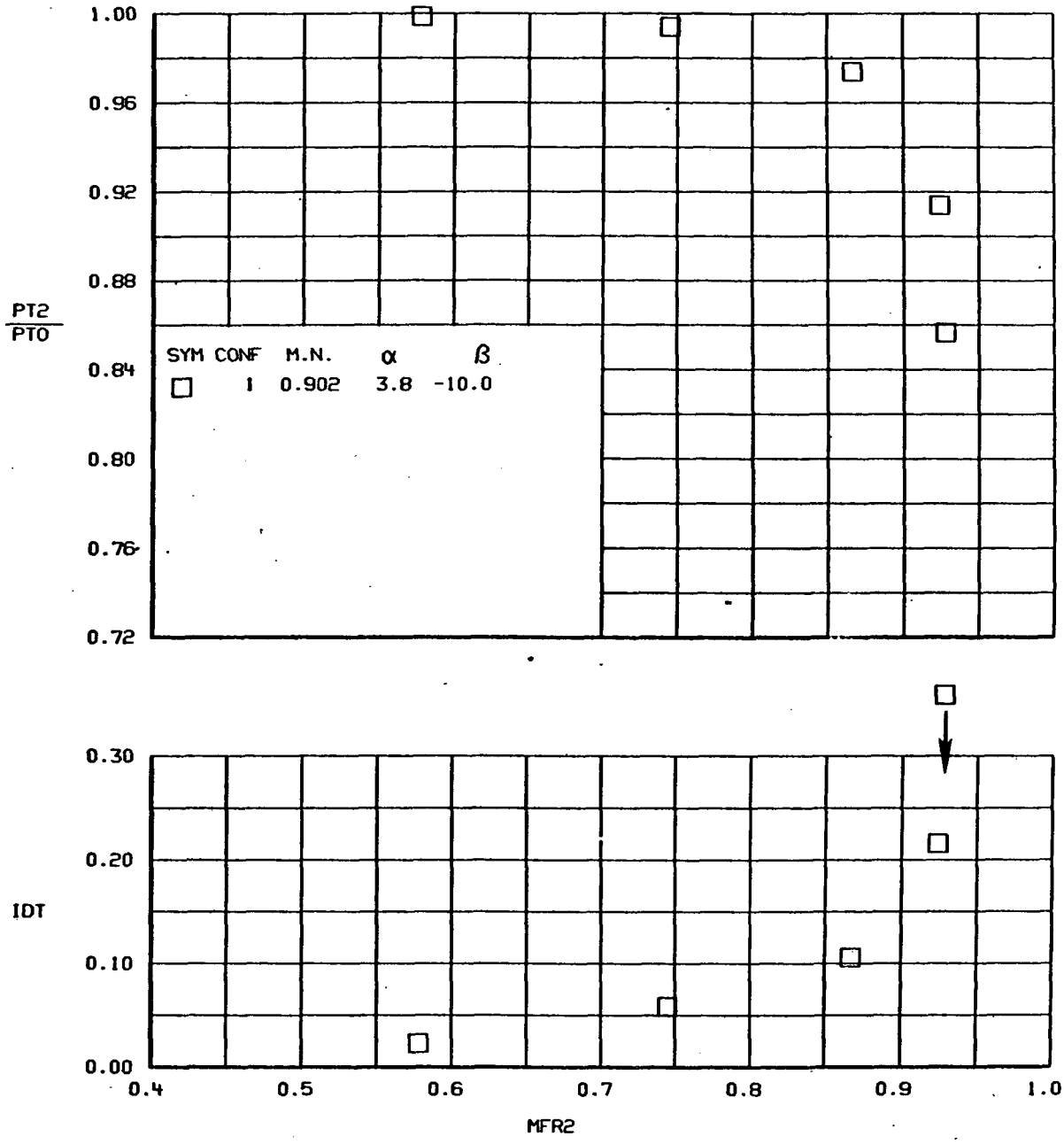

Figure 71.-Continued.

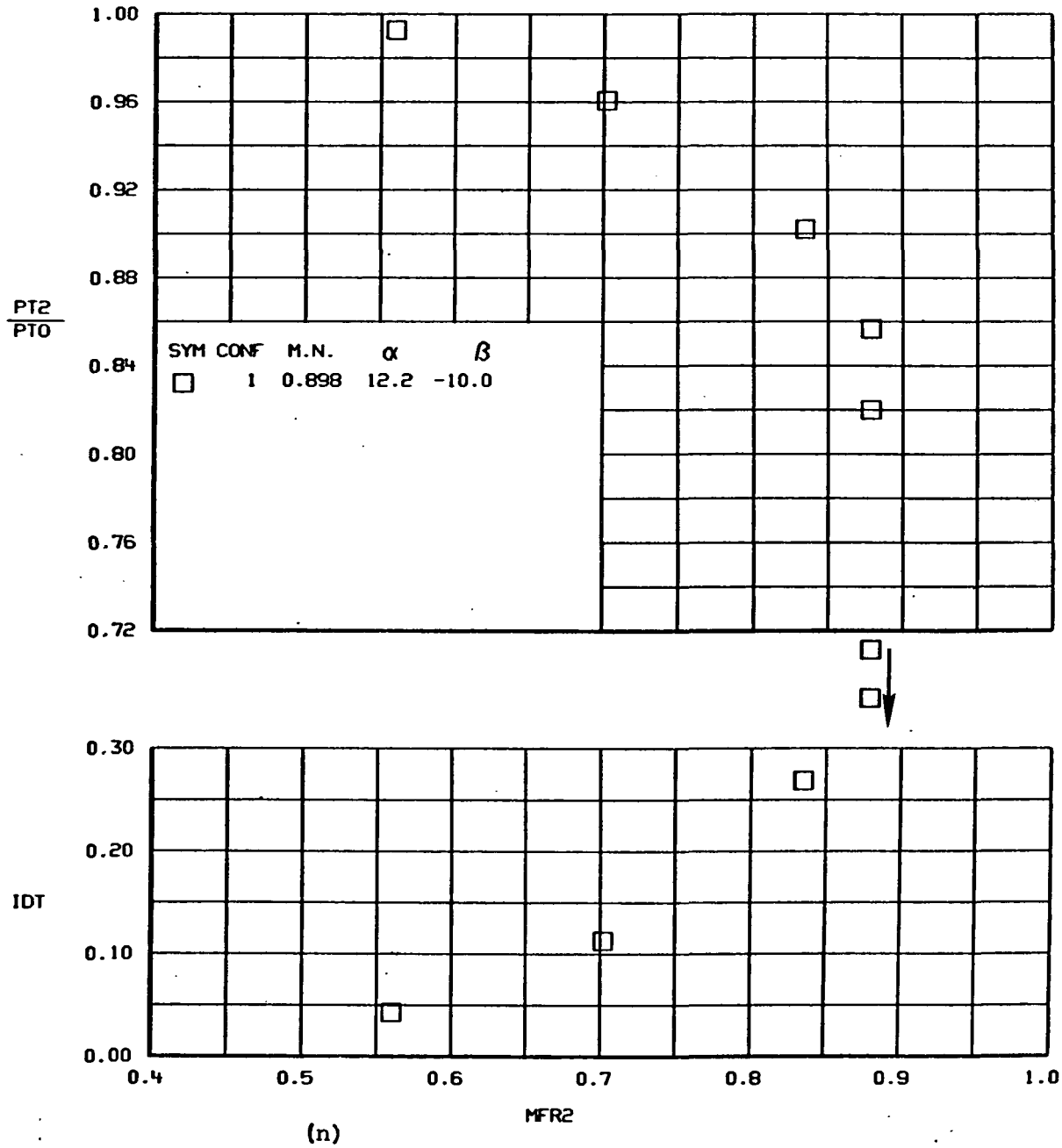

(n)

Figure 71.-Continued.

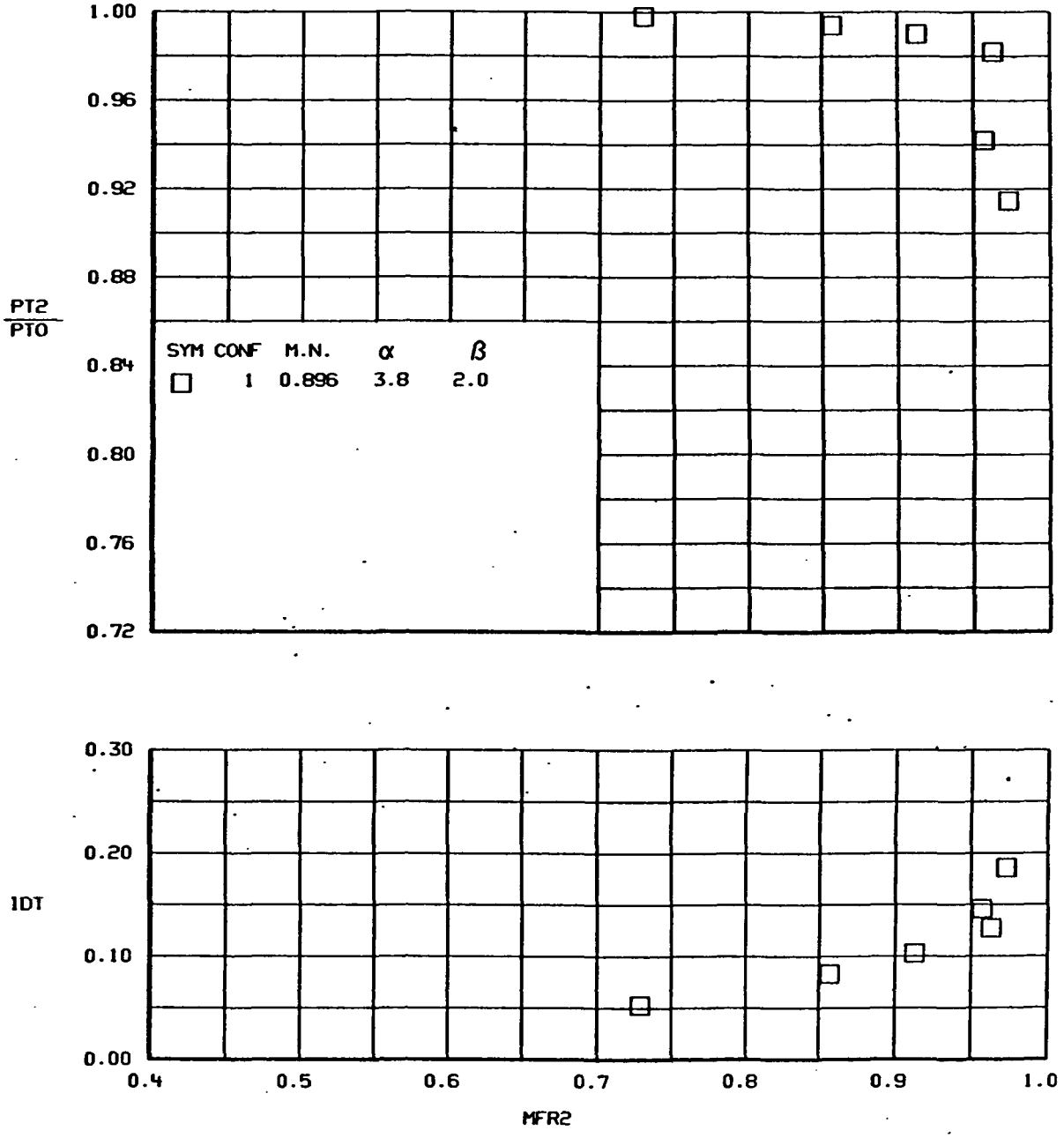

(o)

Figure 71.-Continued.

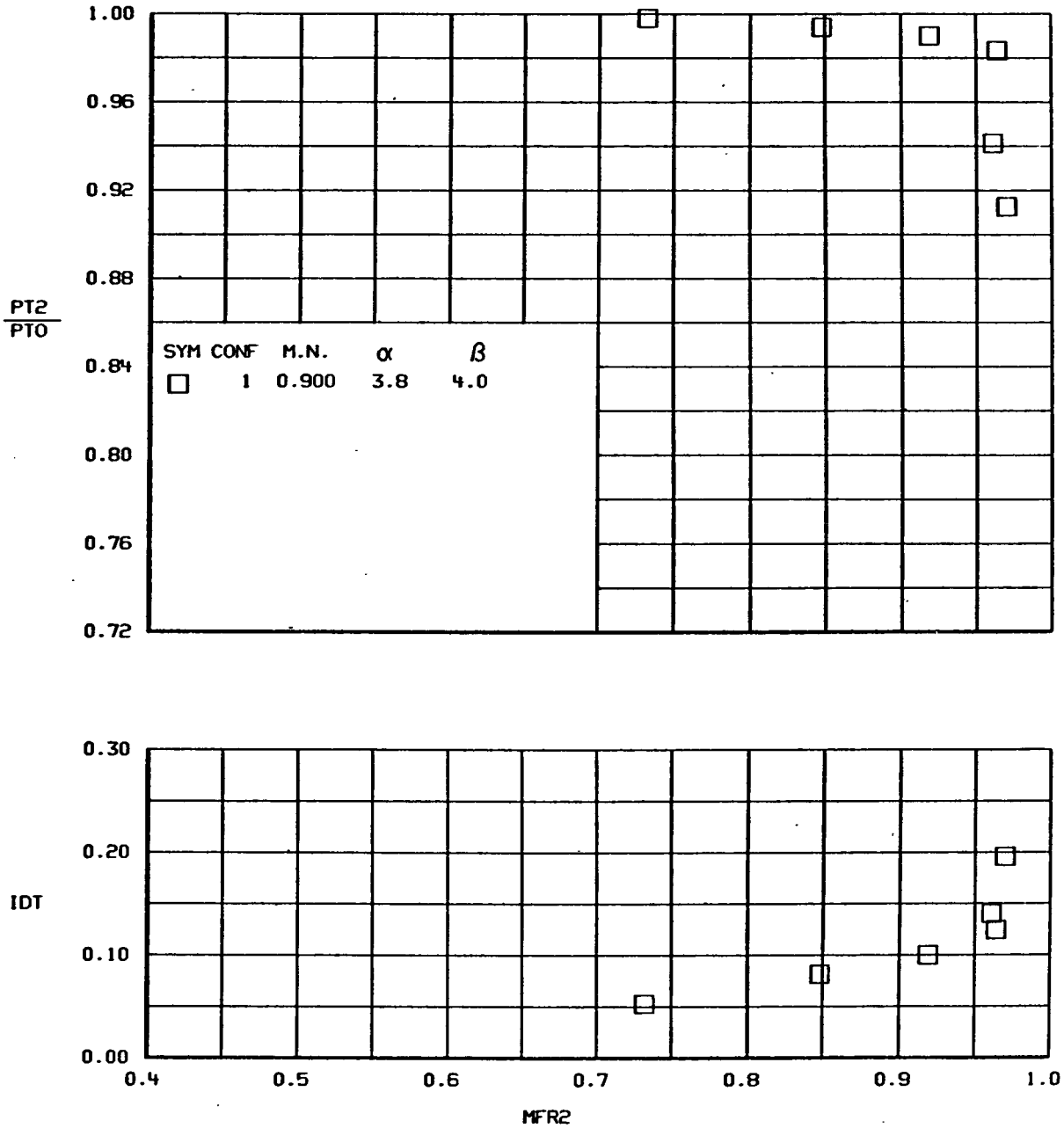

(p)

Figure 71.-Continued.

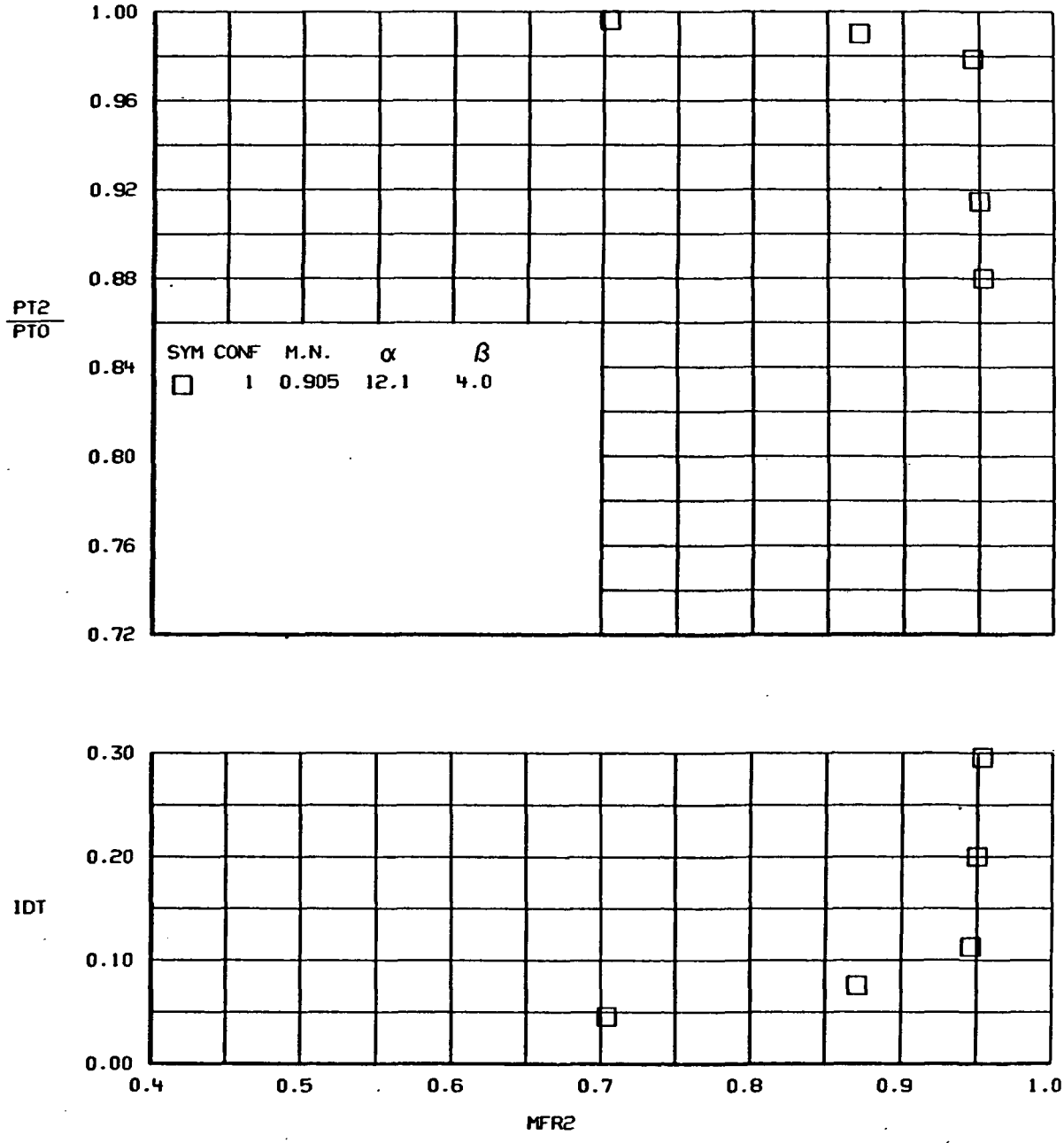

(q)

Figure 71.-Continued.

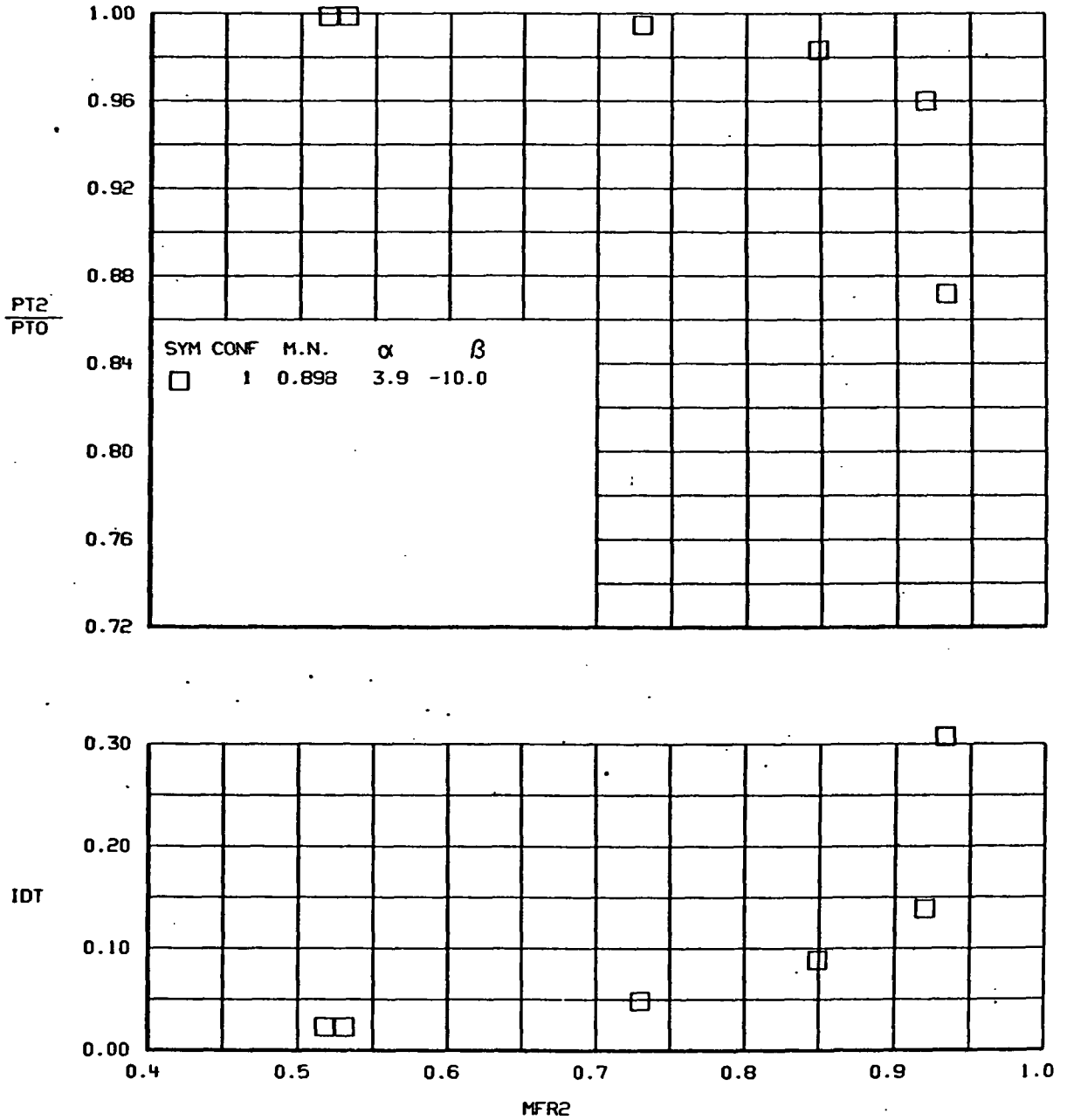

(r)

Figure 71.-Continued.

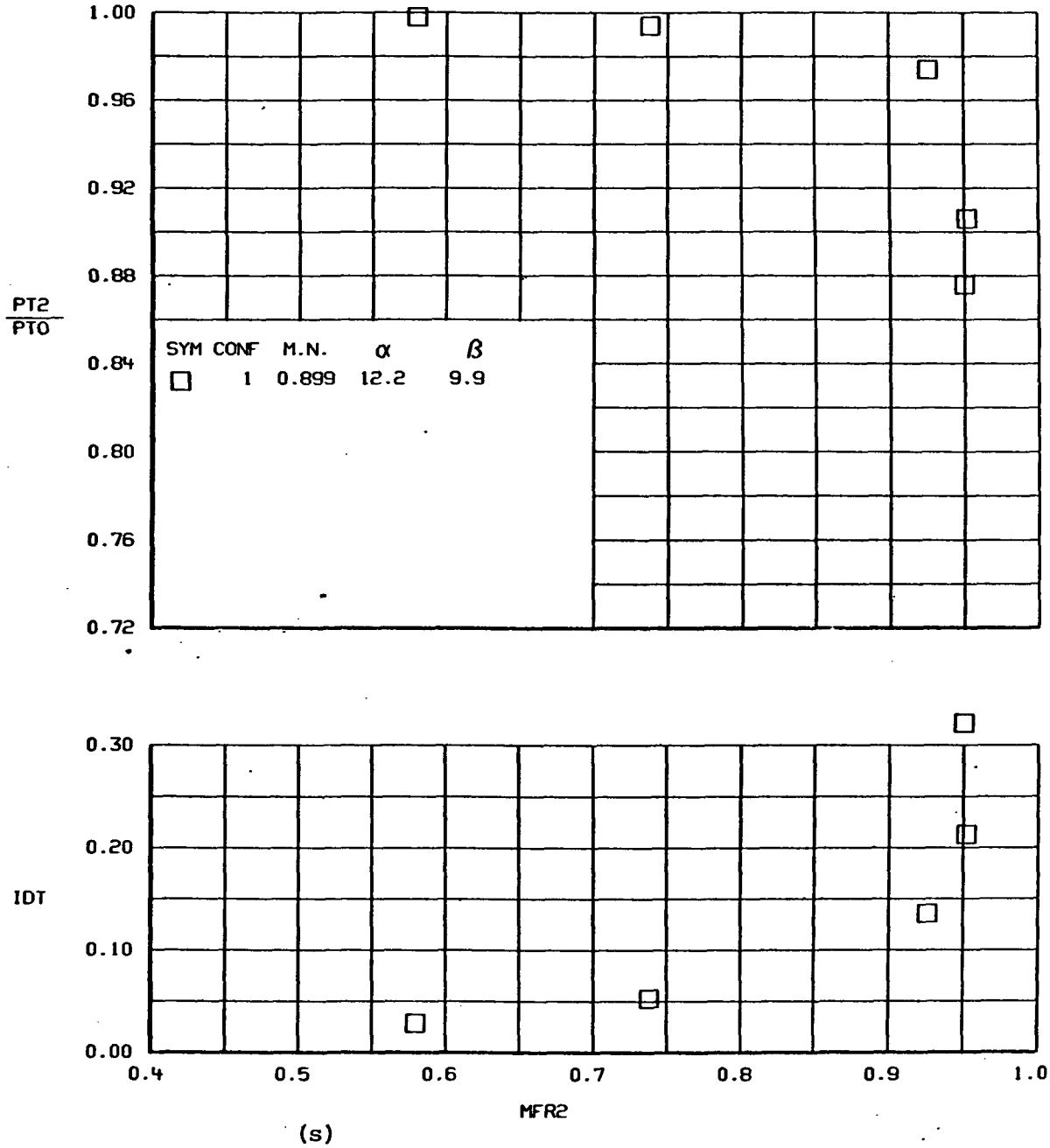

Figure 71.-Continued.

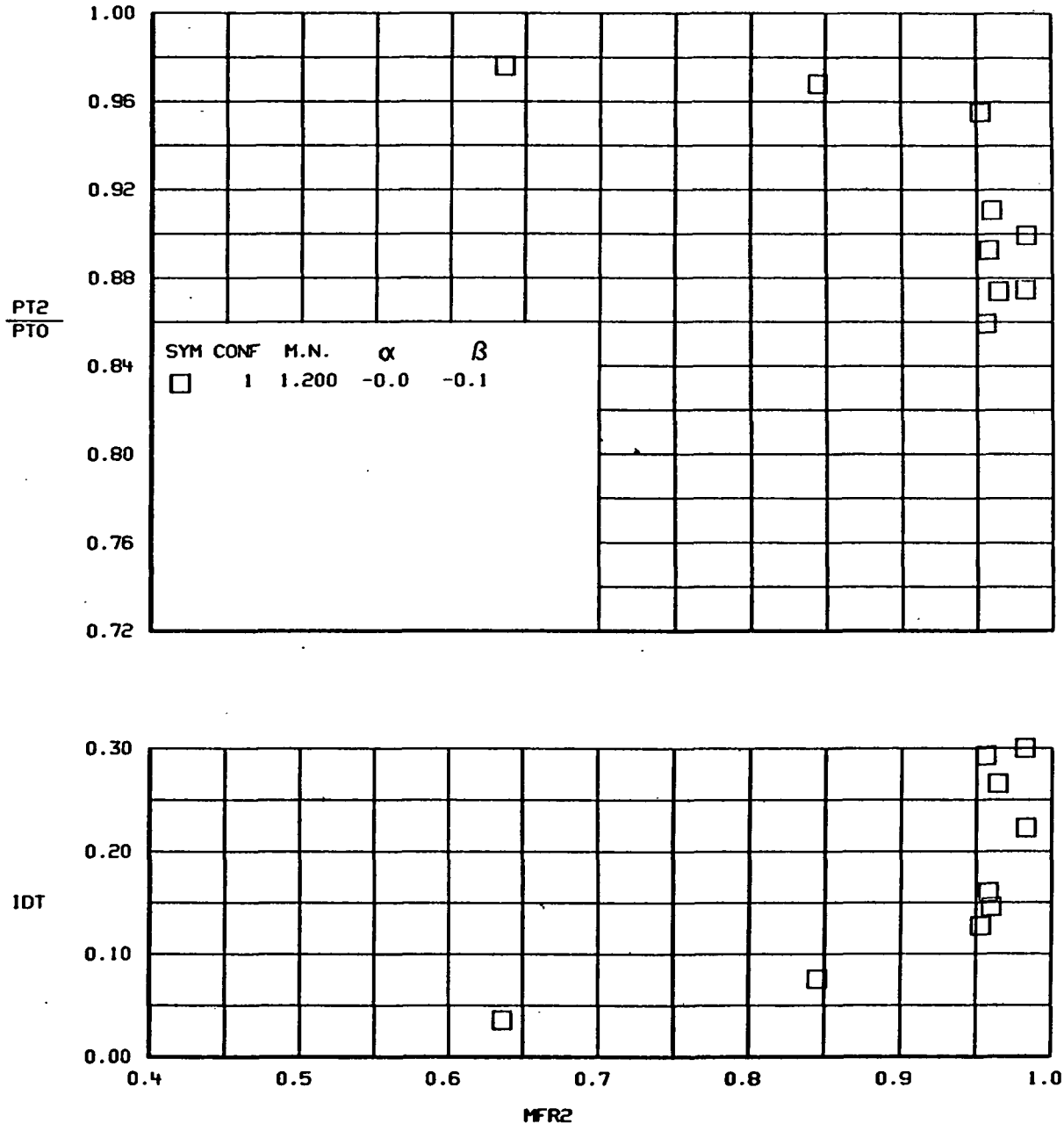

(t)

Figure 71.-Continued.

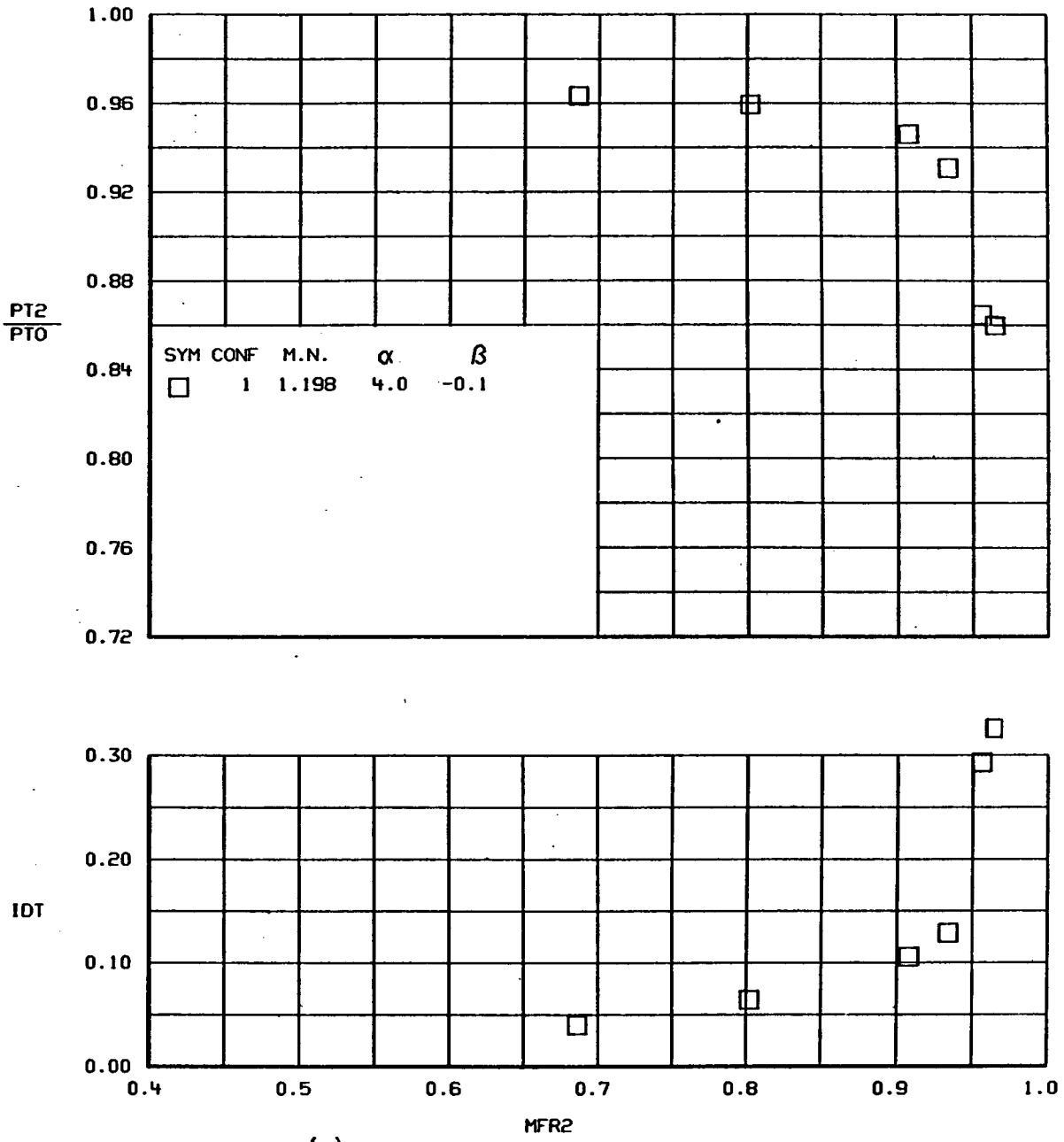

(u)

Figure 71.-Continued.

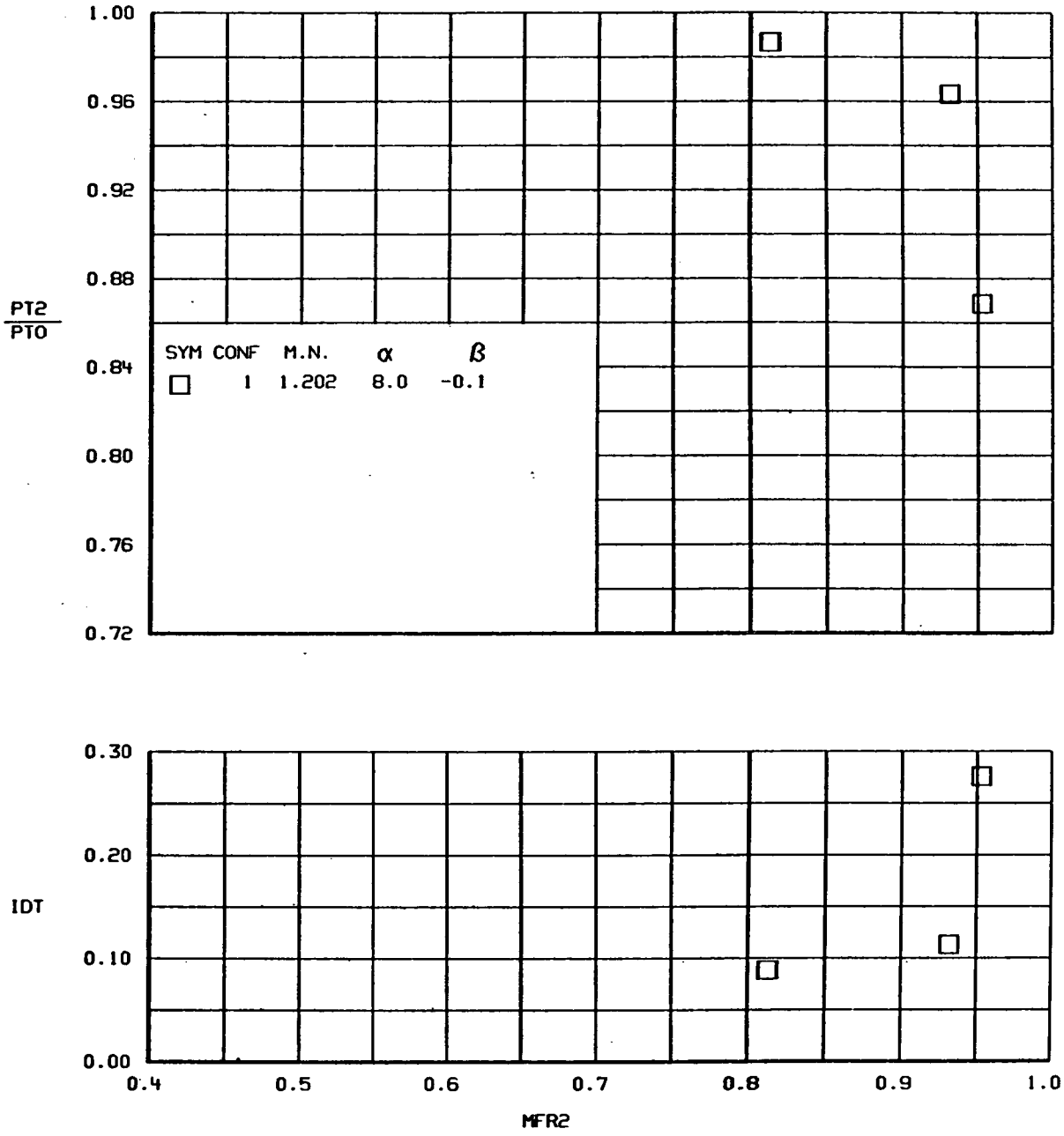

(v)

Figure 71.-Concluded.

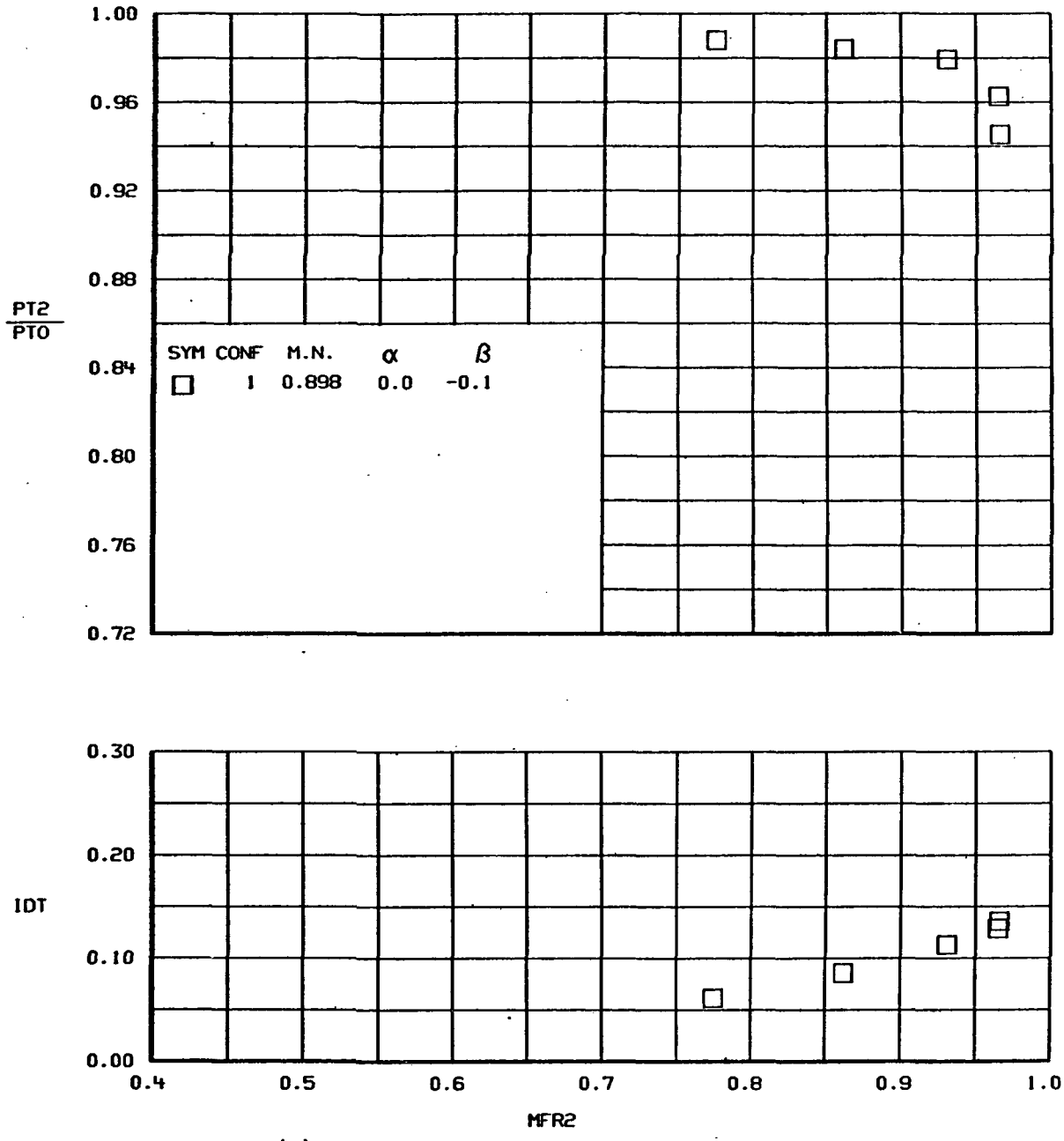

(a)

Figure 72.- TOTAL PRESSURE RECOVERY AND DISTORTION VERSUS MASS FLOW RATIO Configuration 1, δ=5°.

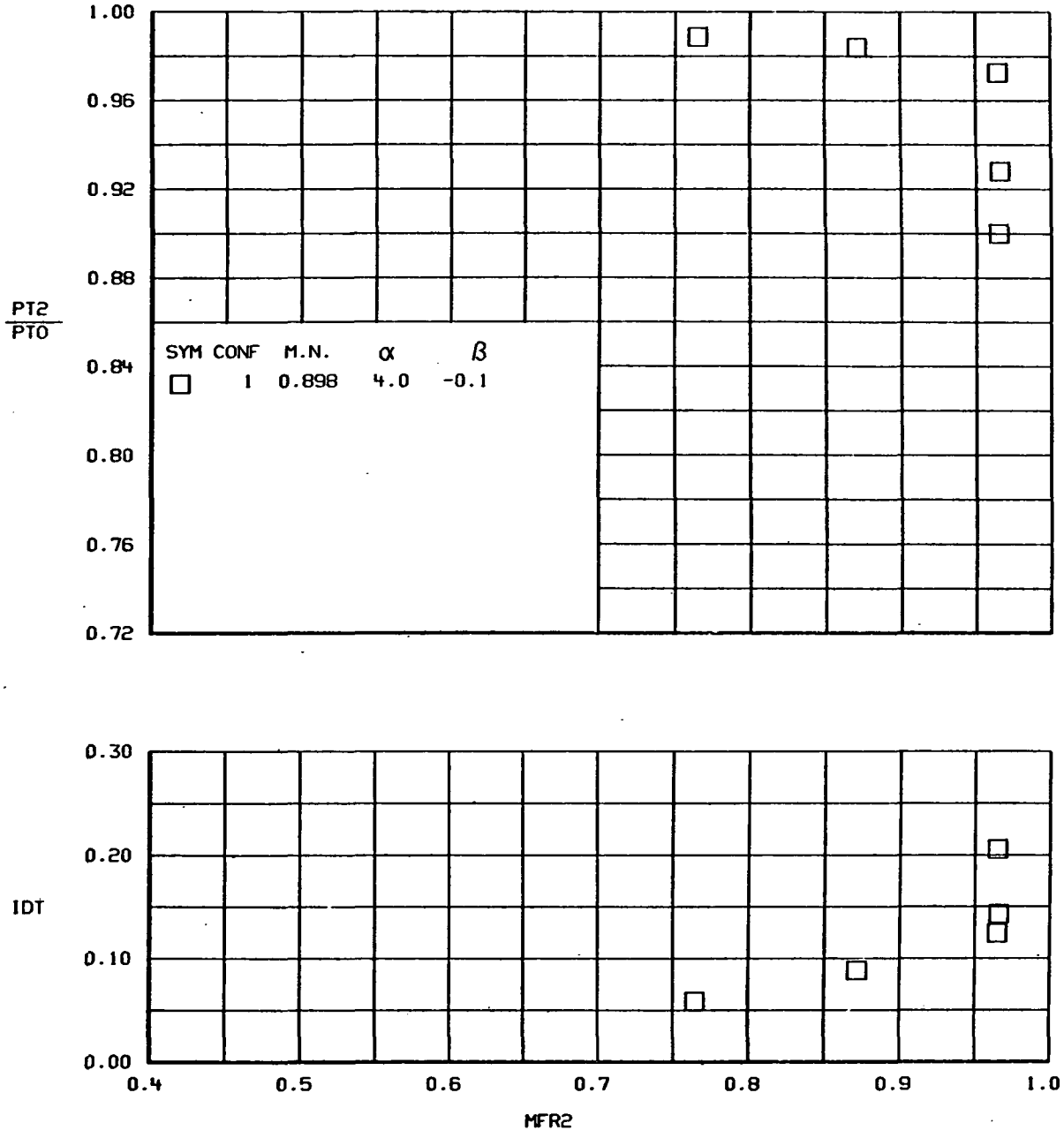

(b)

Figure 72.-Continued.

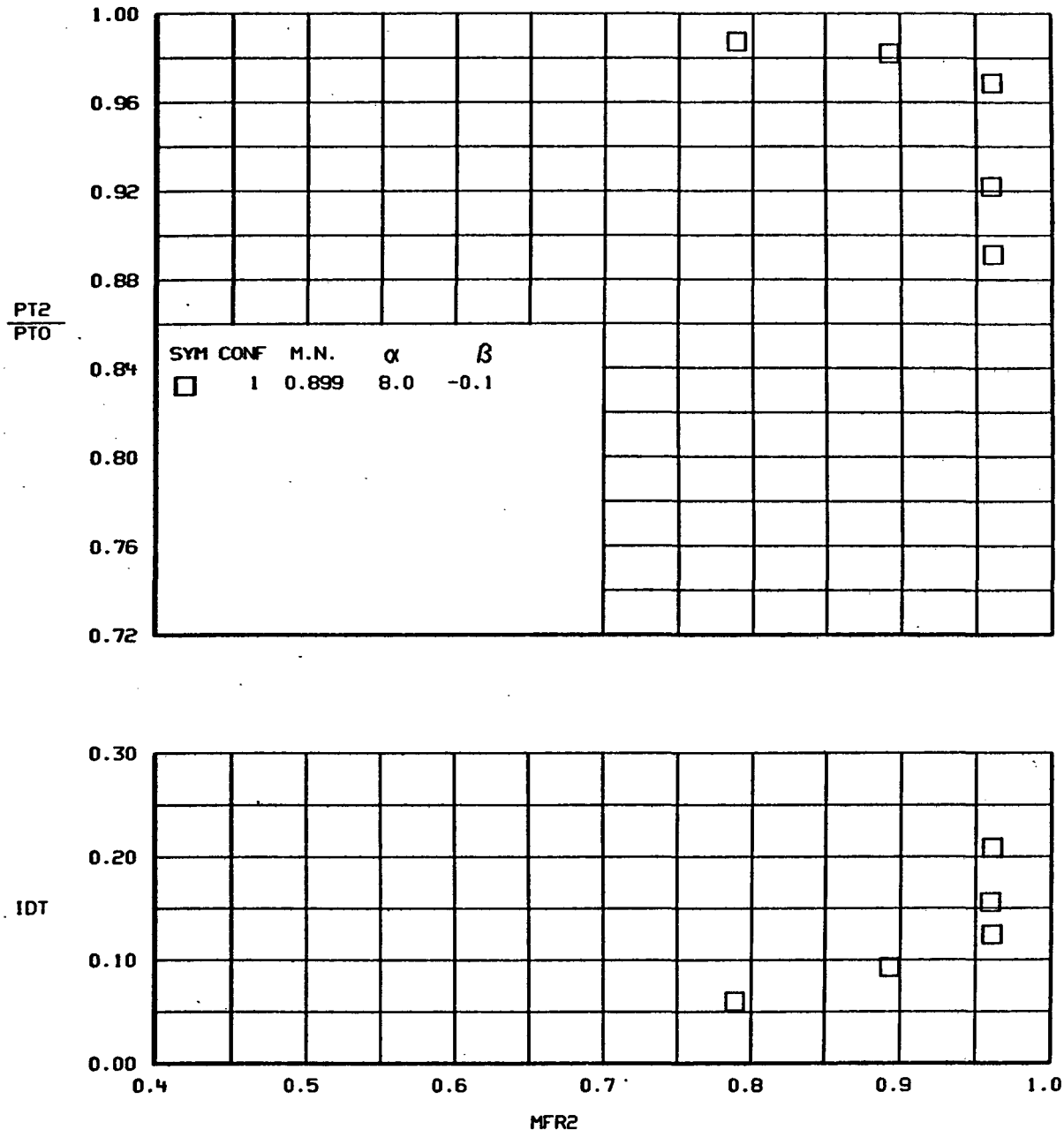

(c)

Figure 72.-Continued.

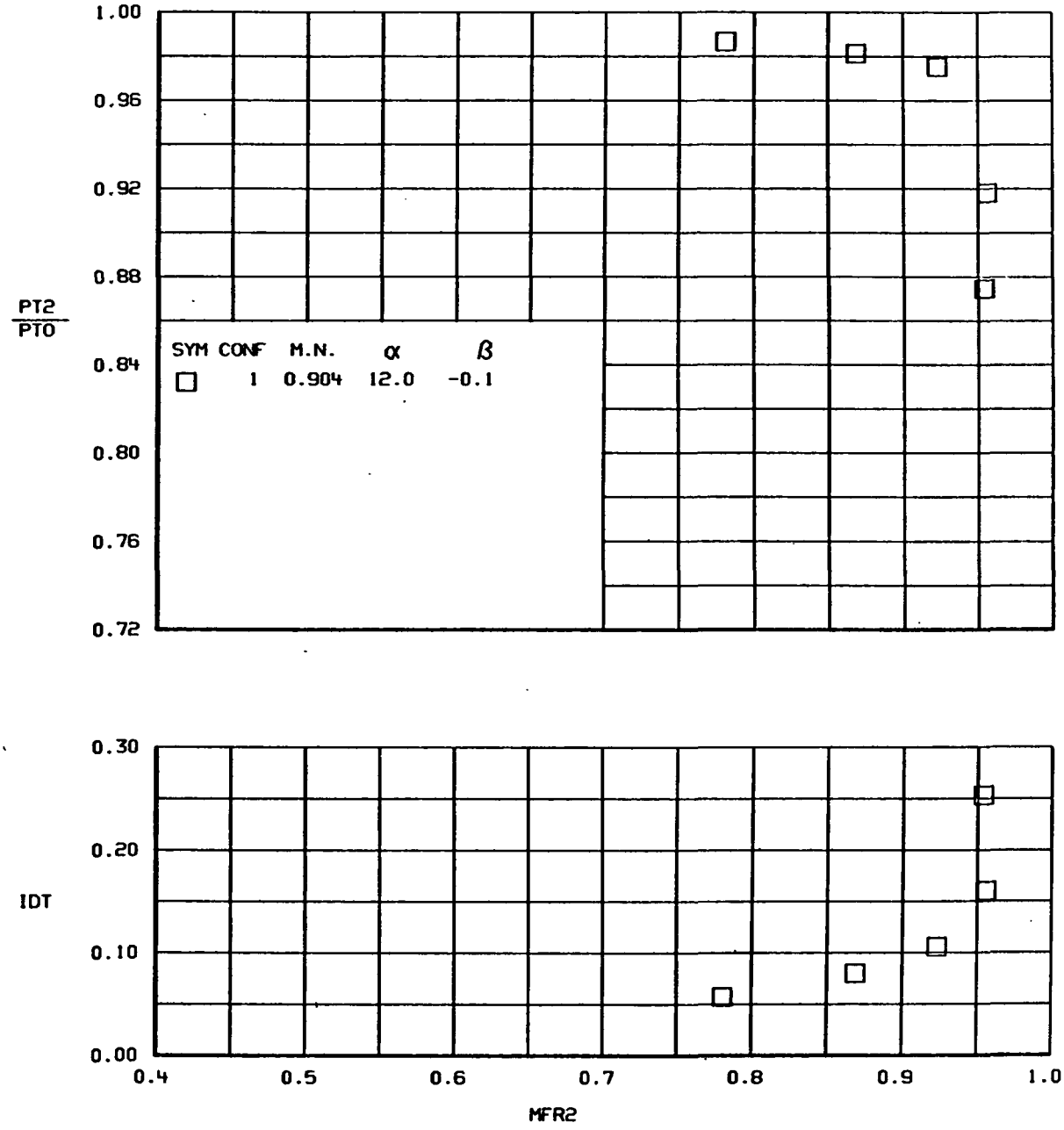

(d)

Figure 72.-Continued.

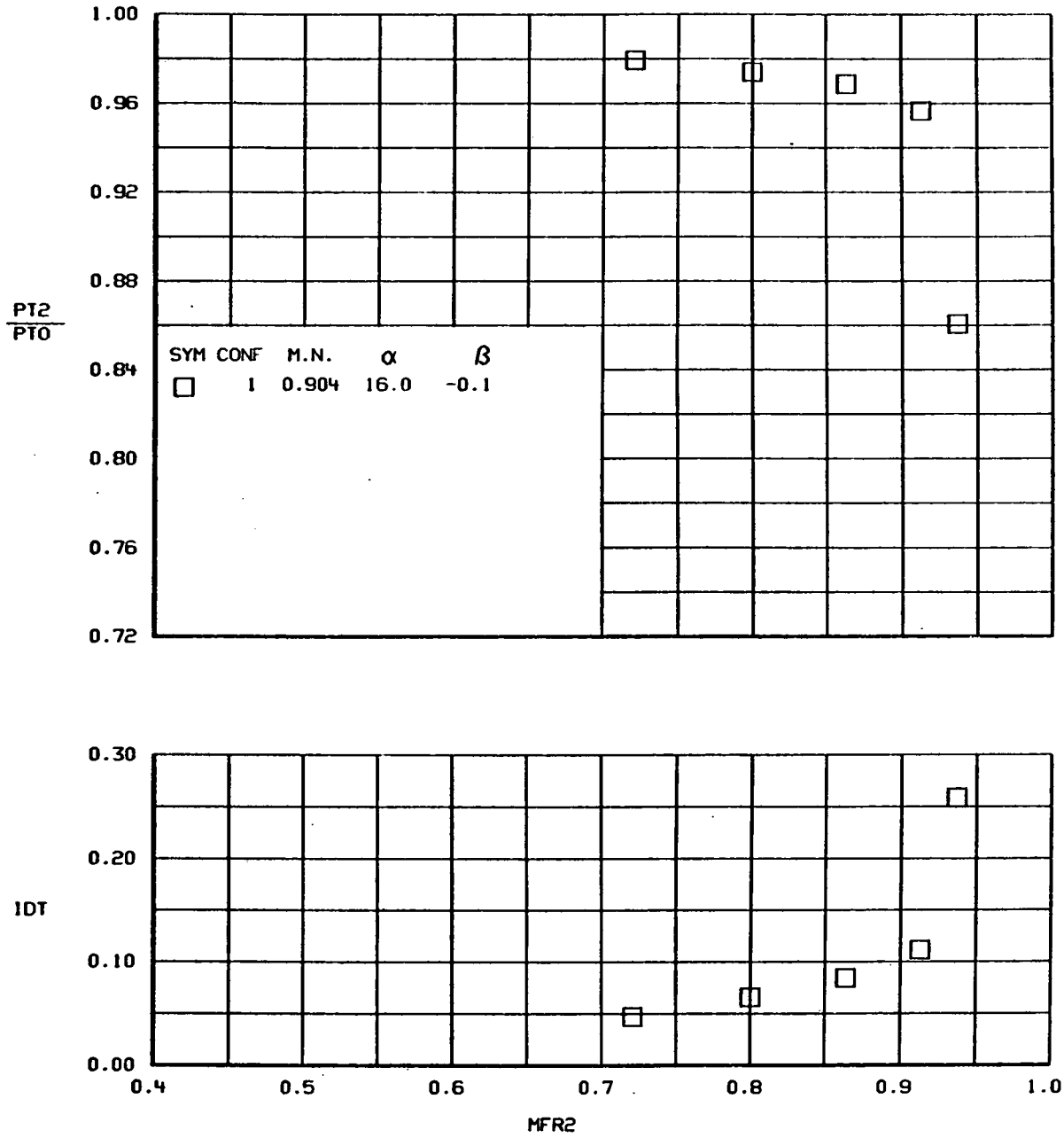

(e)

Figure 72.-Concluded.

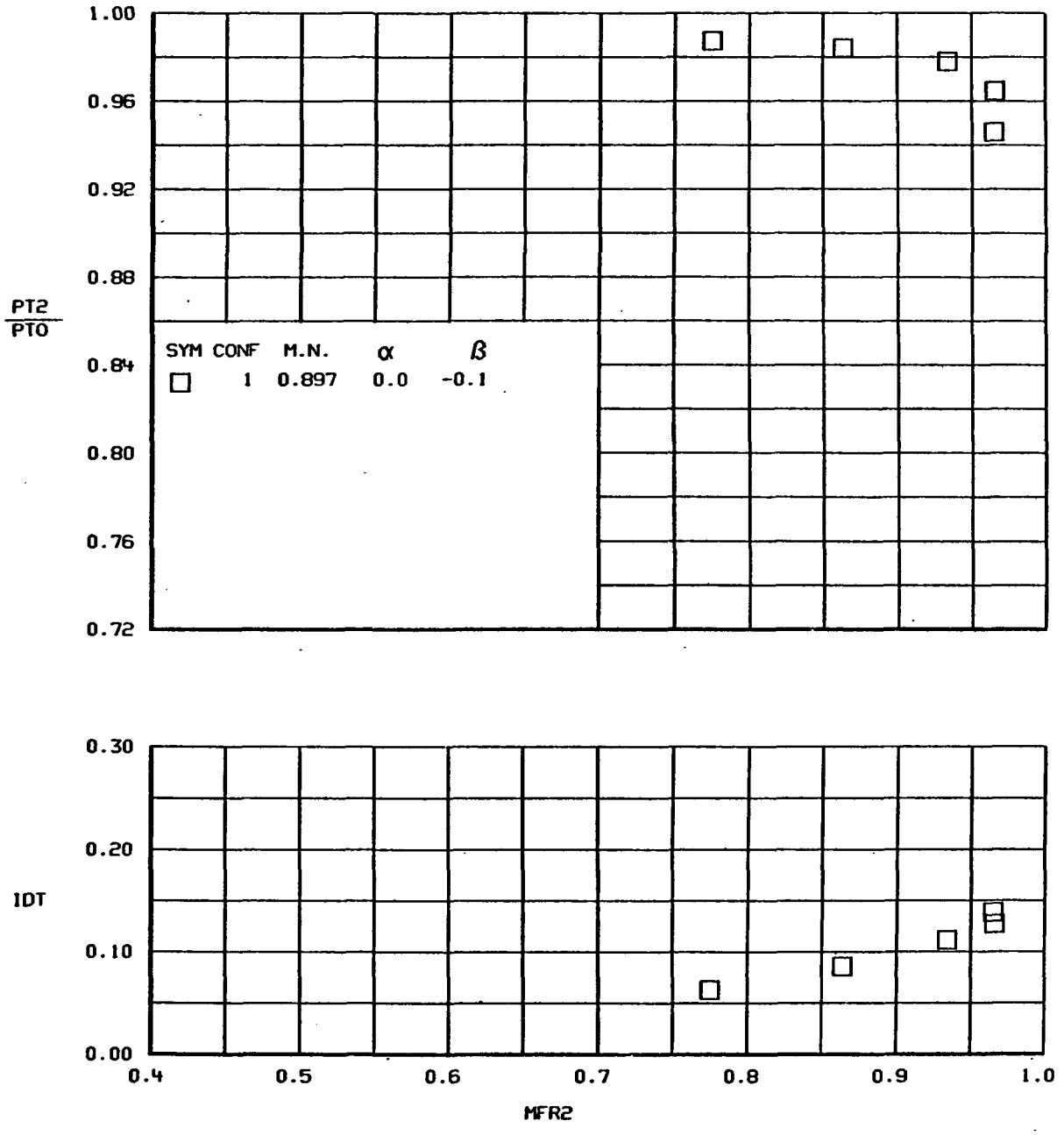

(a)

Figure 73.- TOTAL PRESSURE RECOVERY AND DISTORTION VERSUS MASS FLOW RATIO Configuration 1, $\delta=10^{o}$.

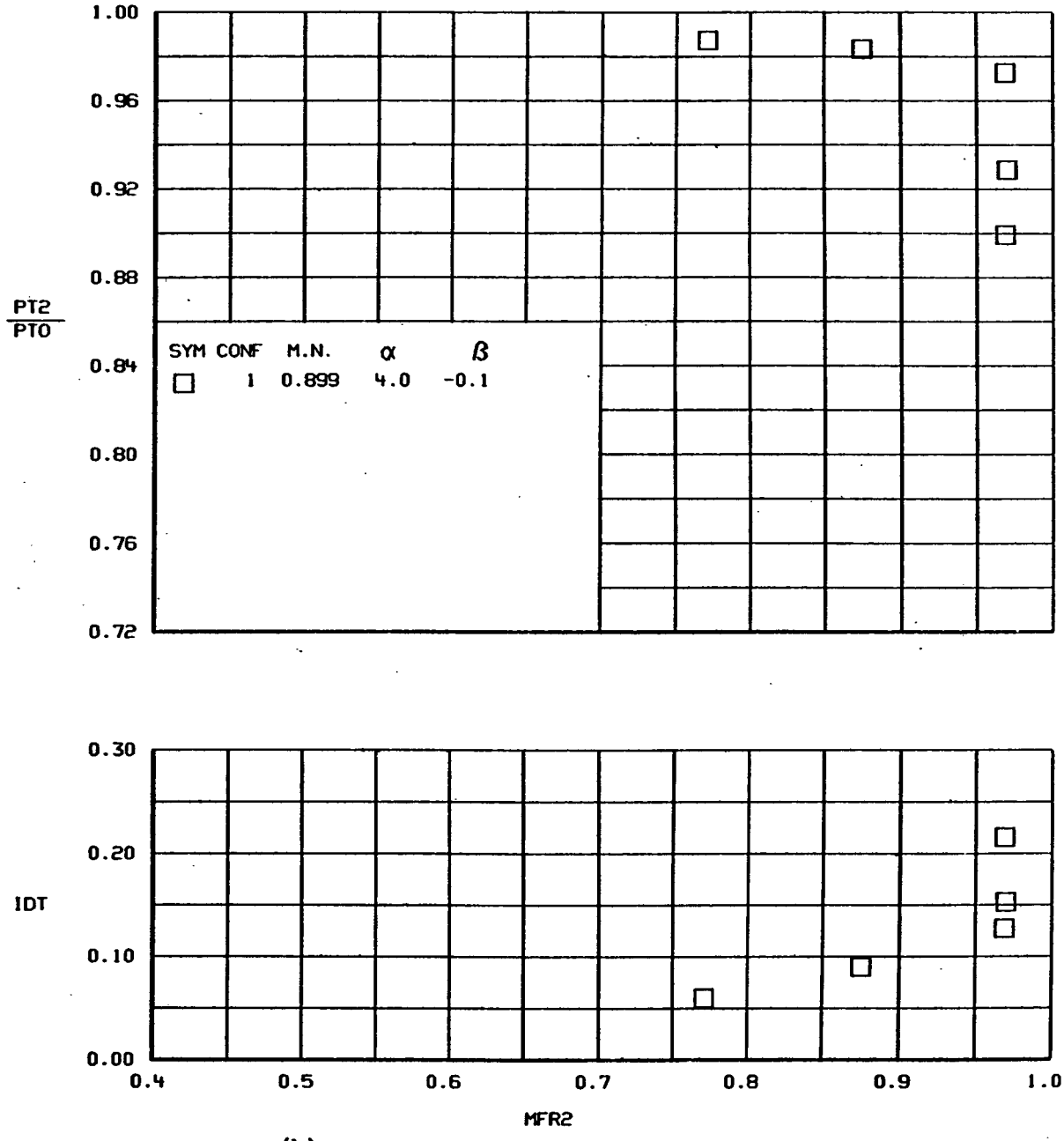

(b)

Figure 73.-Continued.

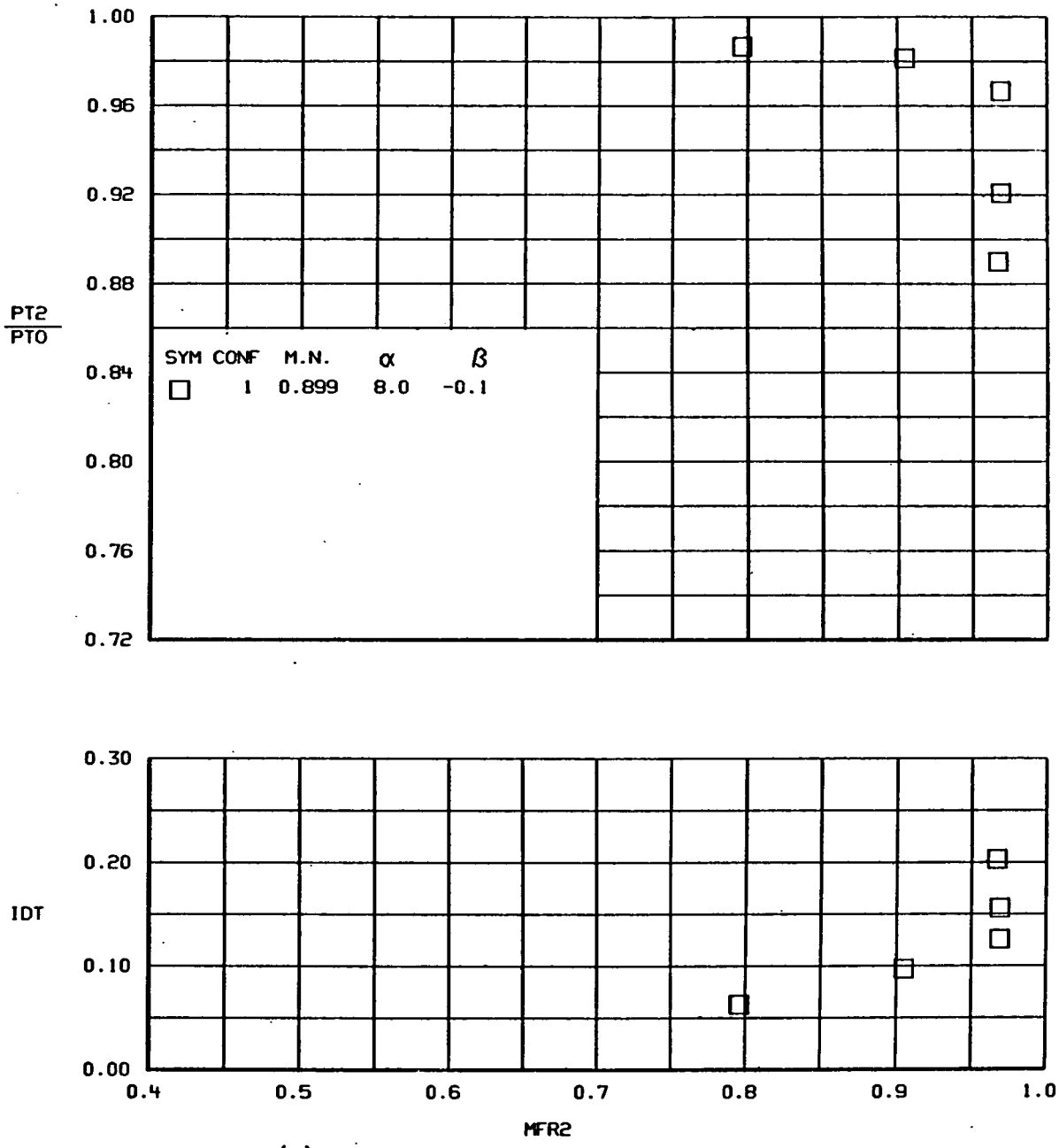

(c)

Figure 73.-Continued.

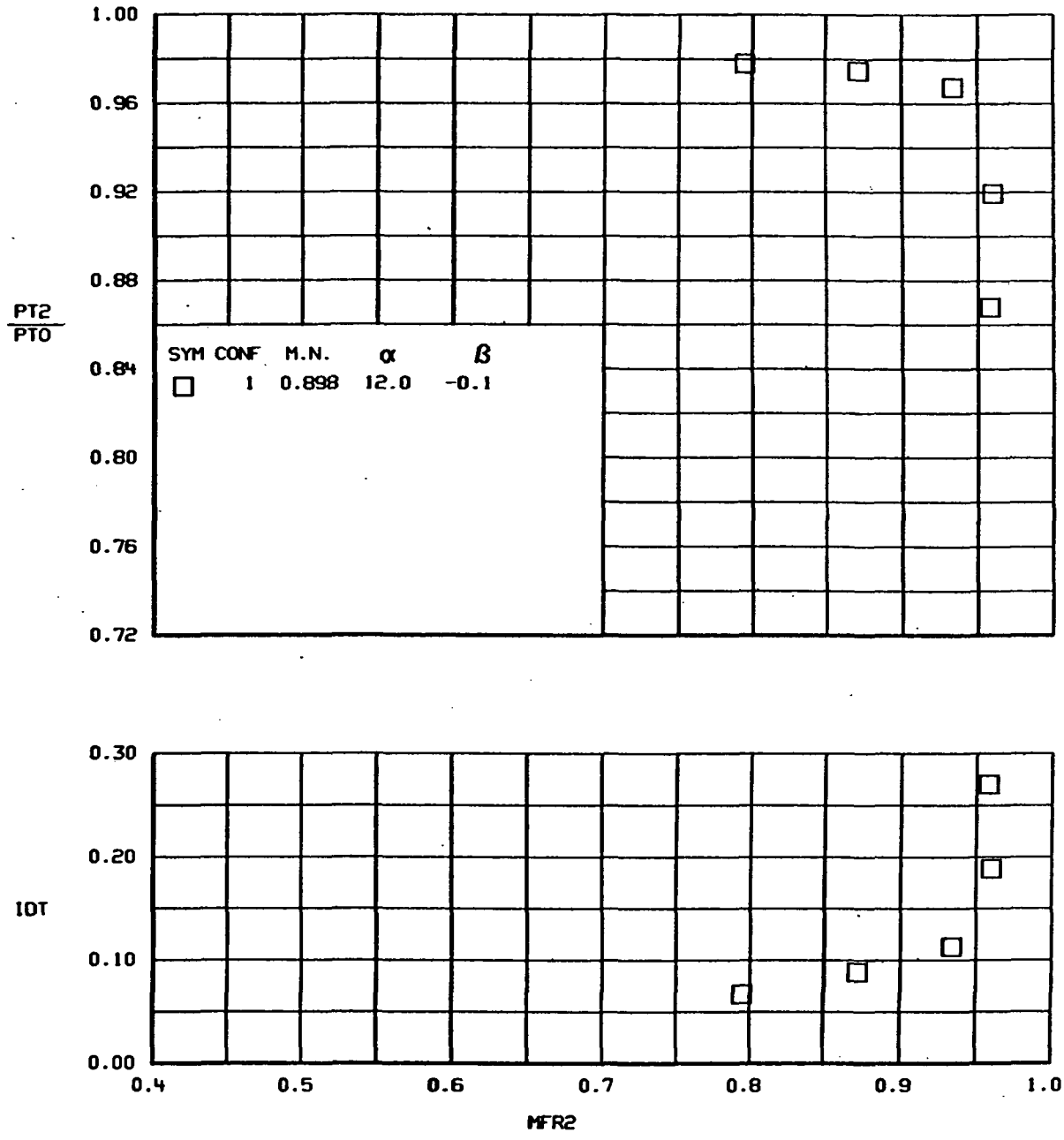

(d)

Figure 73.-Concluded.

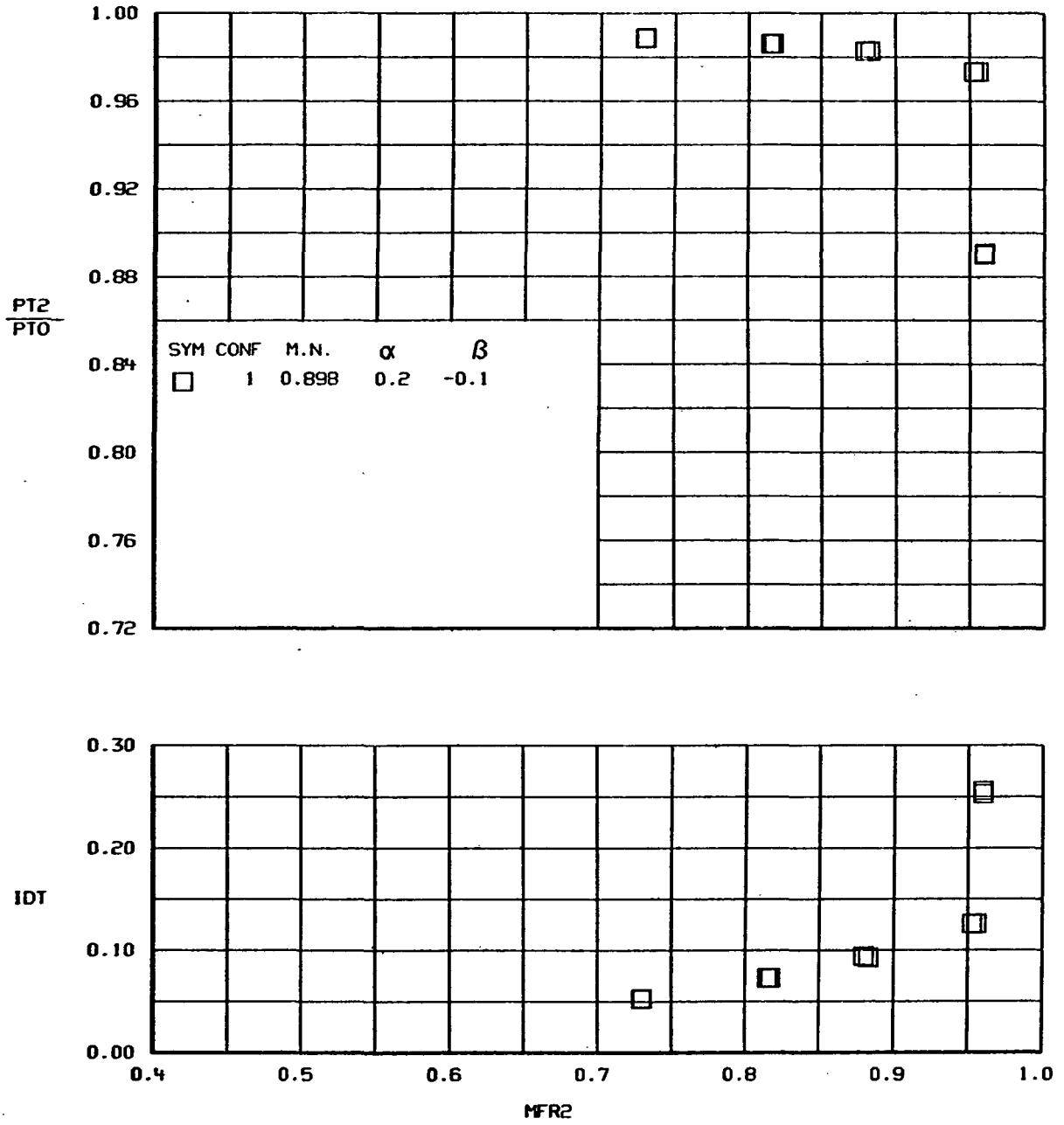

(a)

Figure 74.- TOTAL PRESSURE RECOVERY AND DISTORTION VERSUS MASS FLOW RATIO Configuration 1, $\delta=15^{o}$.

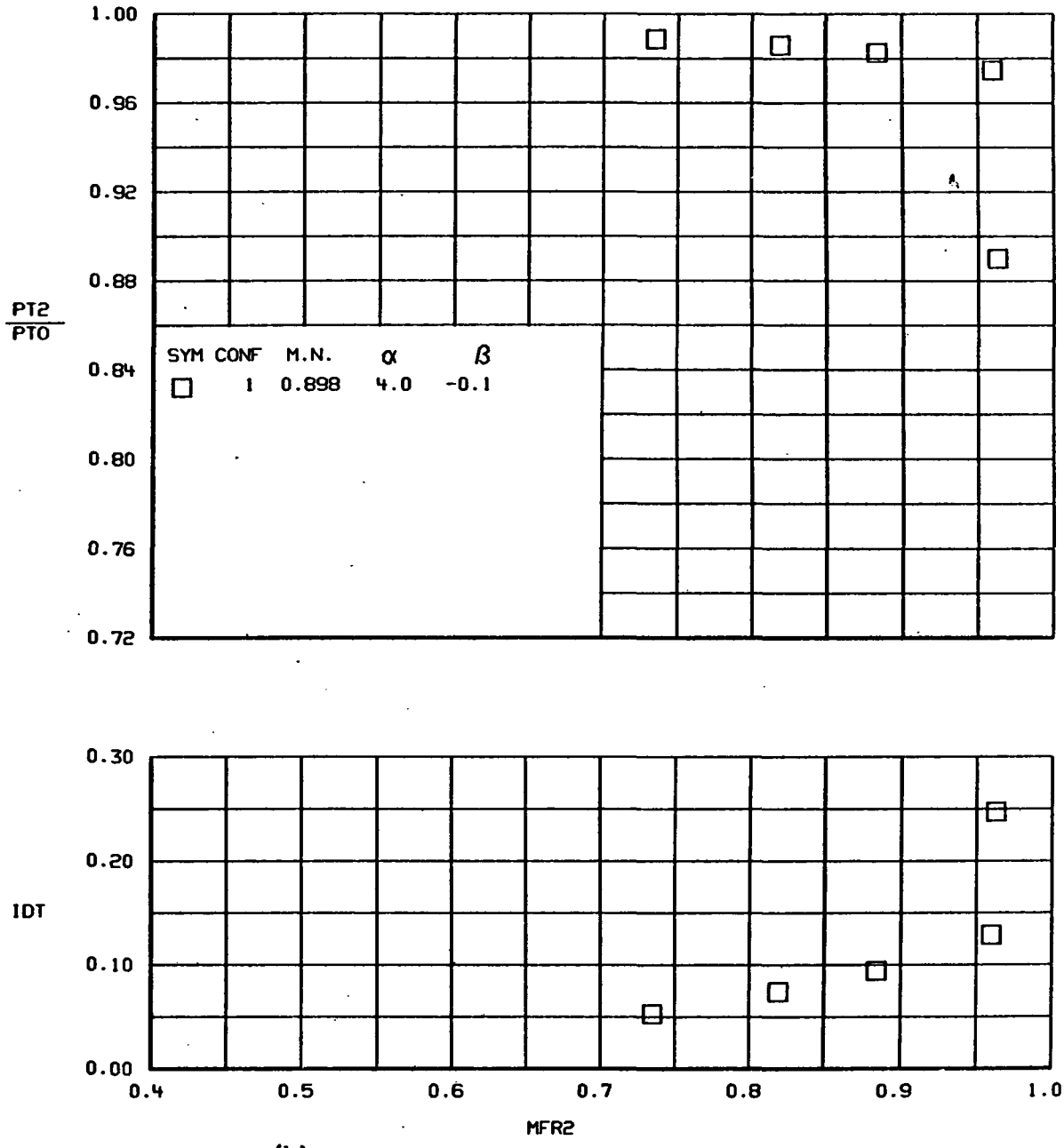

(b)

Figure 74.-Continued.

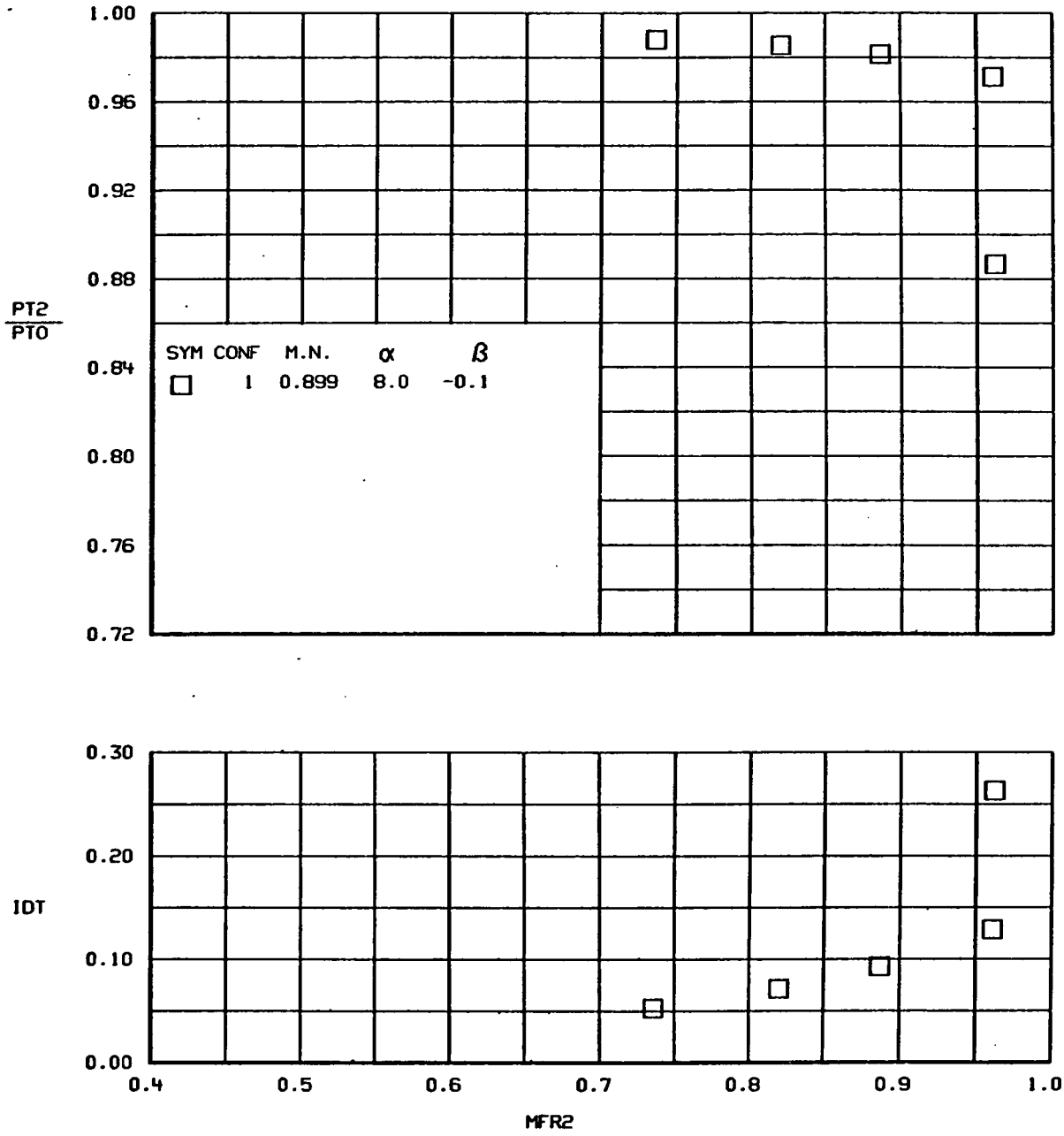

(c)

Figure 74.-Concluded.

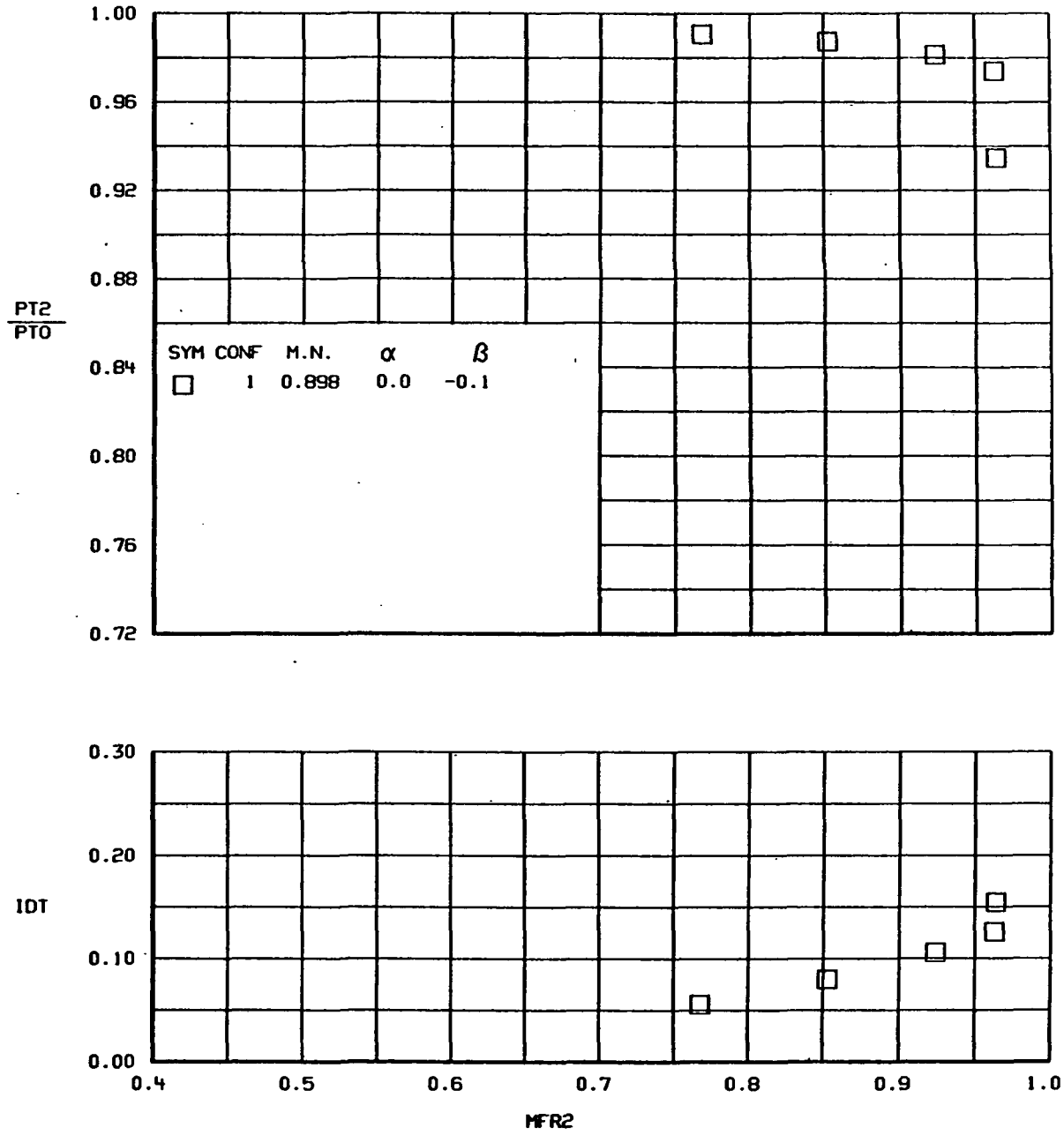

(a)

Figure 75.- TOTAL PRESSURE RECOVERY AND DISTORTION VERSUS MASS FLOW RATIO Configuration 1, $\delta = -10^{\circ}$.

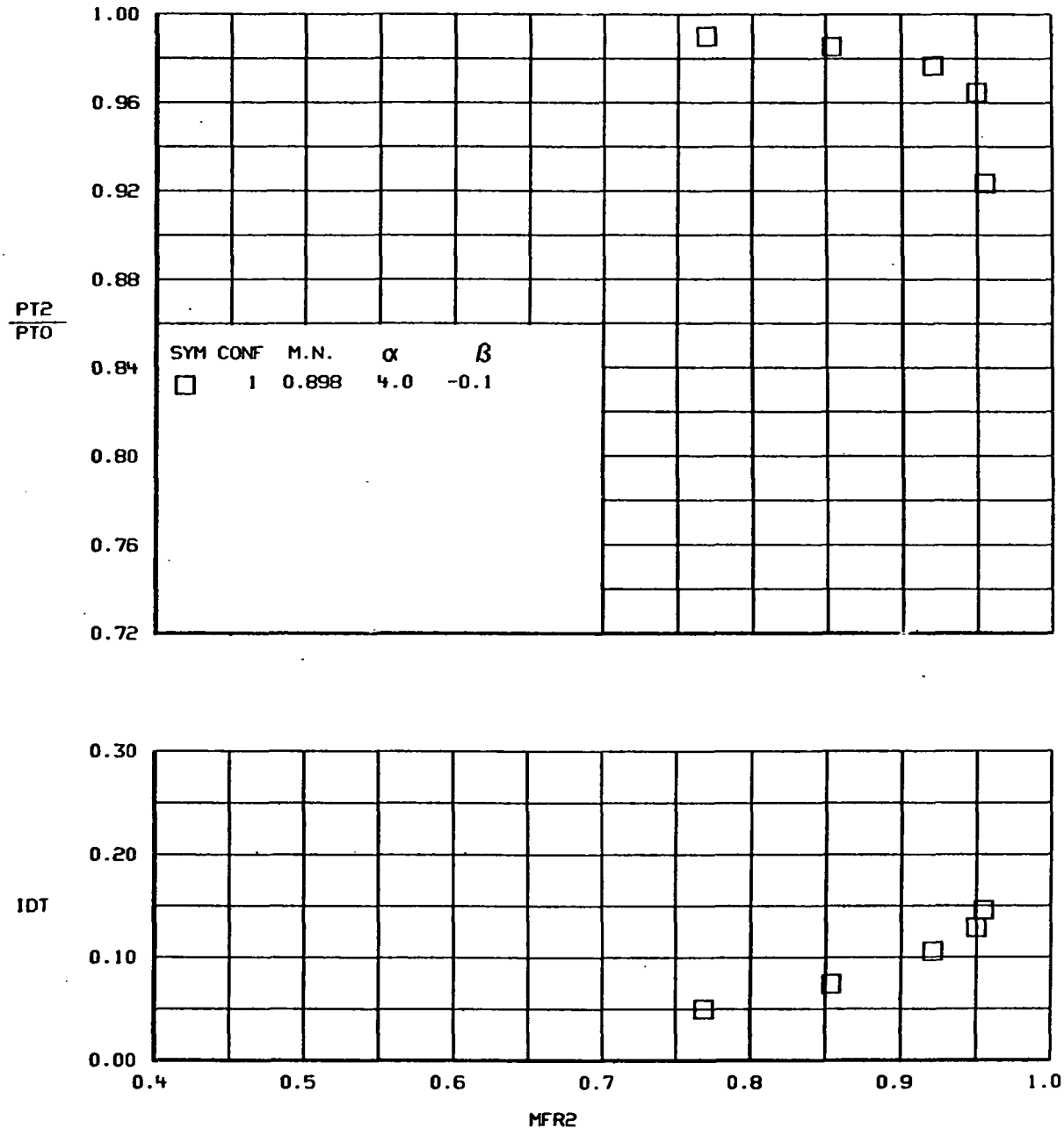

(b)

Figure 75.-Continued.

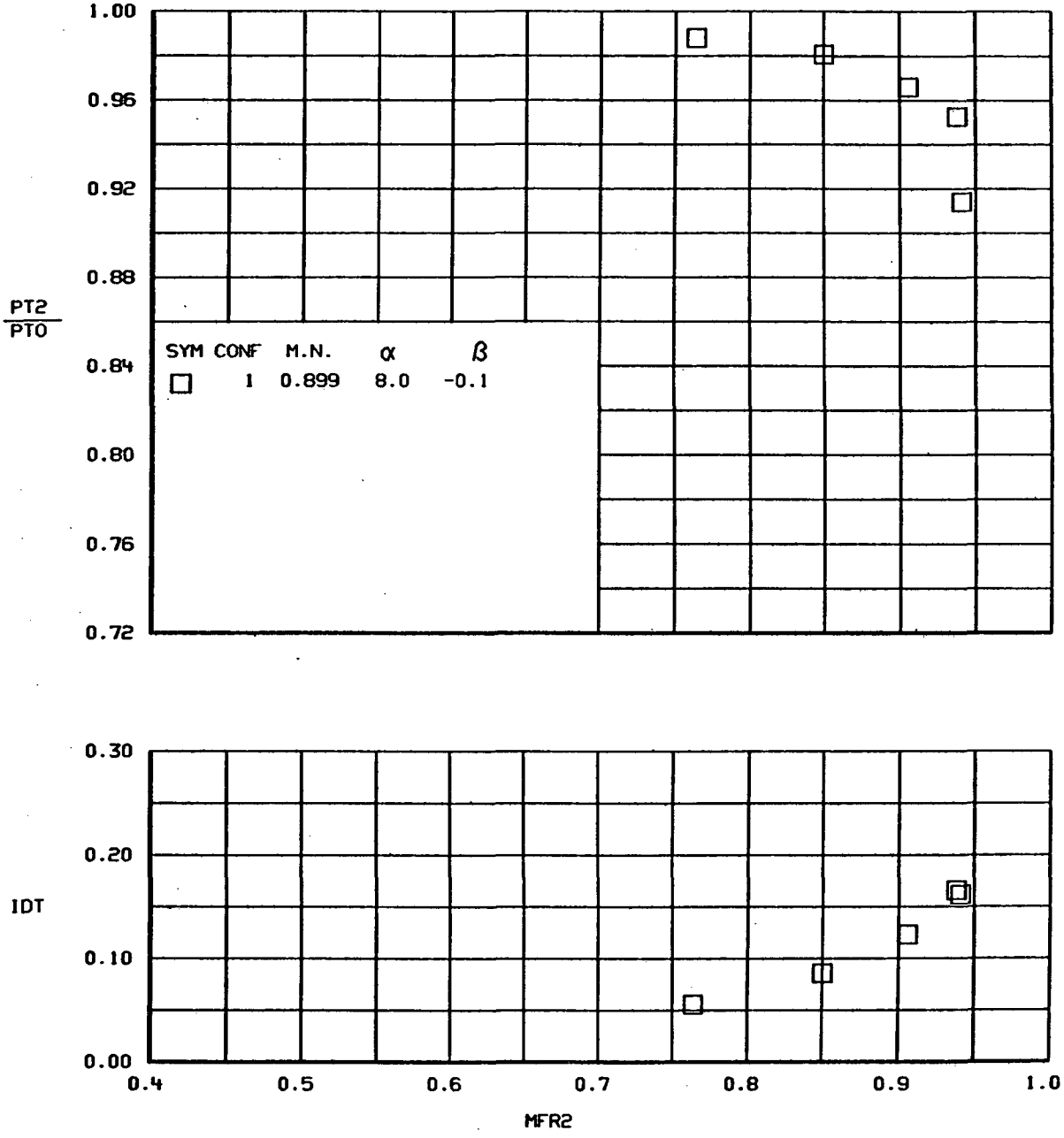

(c)

Figure 75.-Continued.

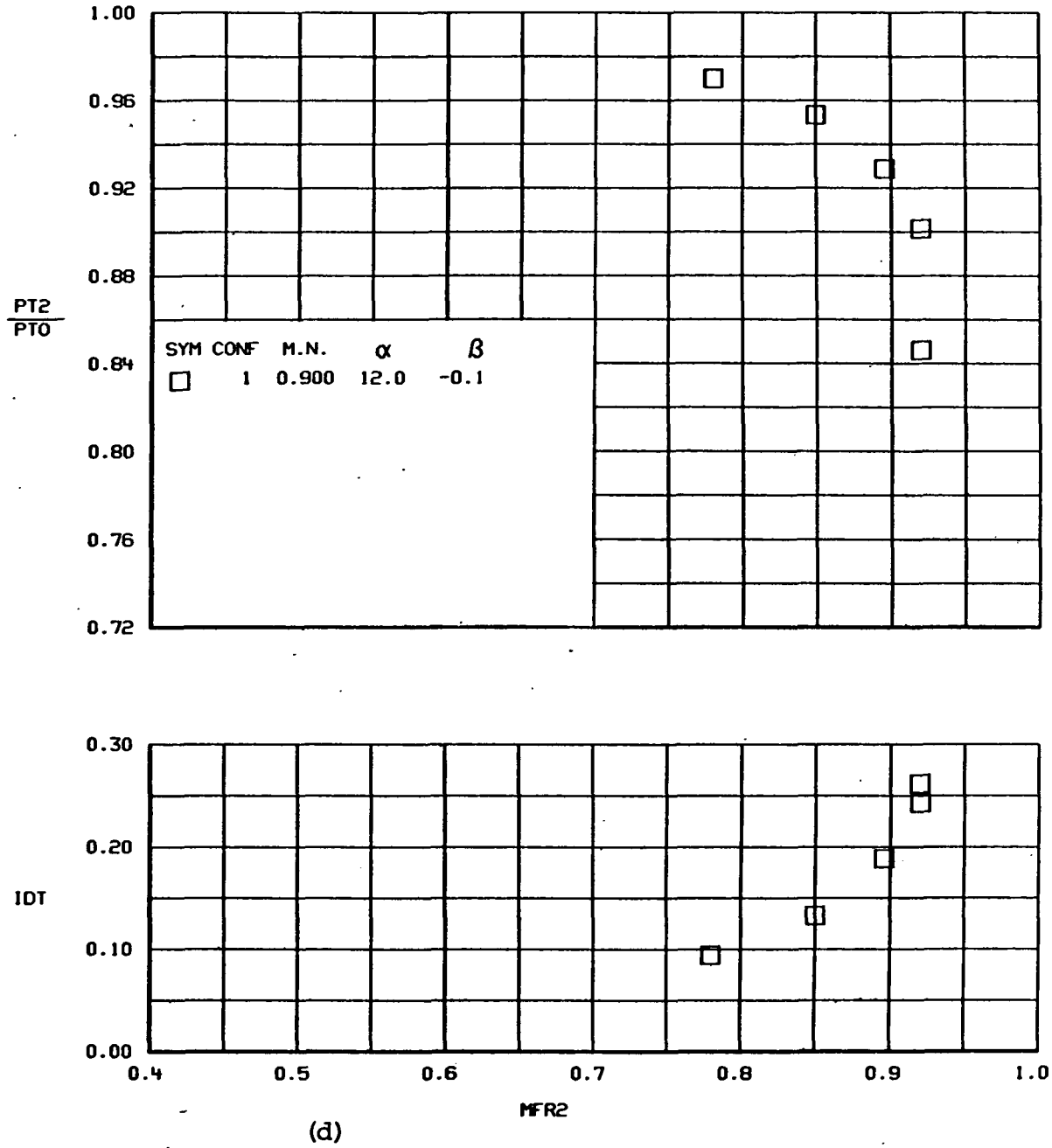

(d)

Figure 75.-Continued.

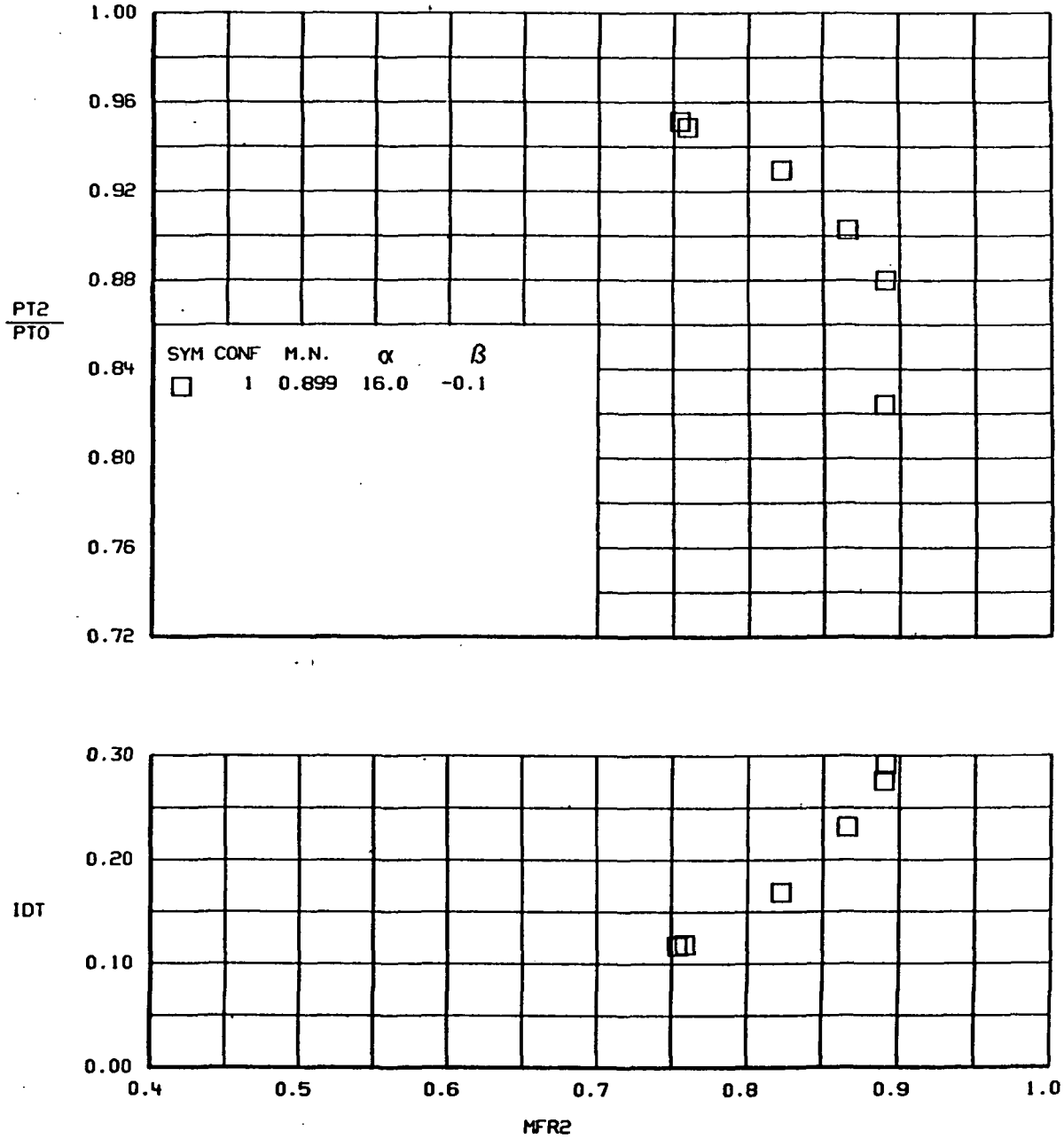

(e)

Figure 75.-Continued.

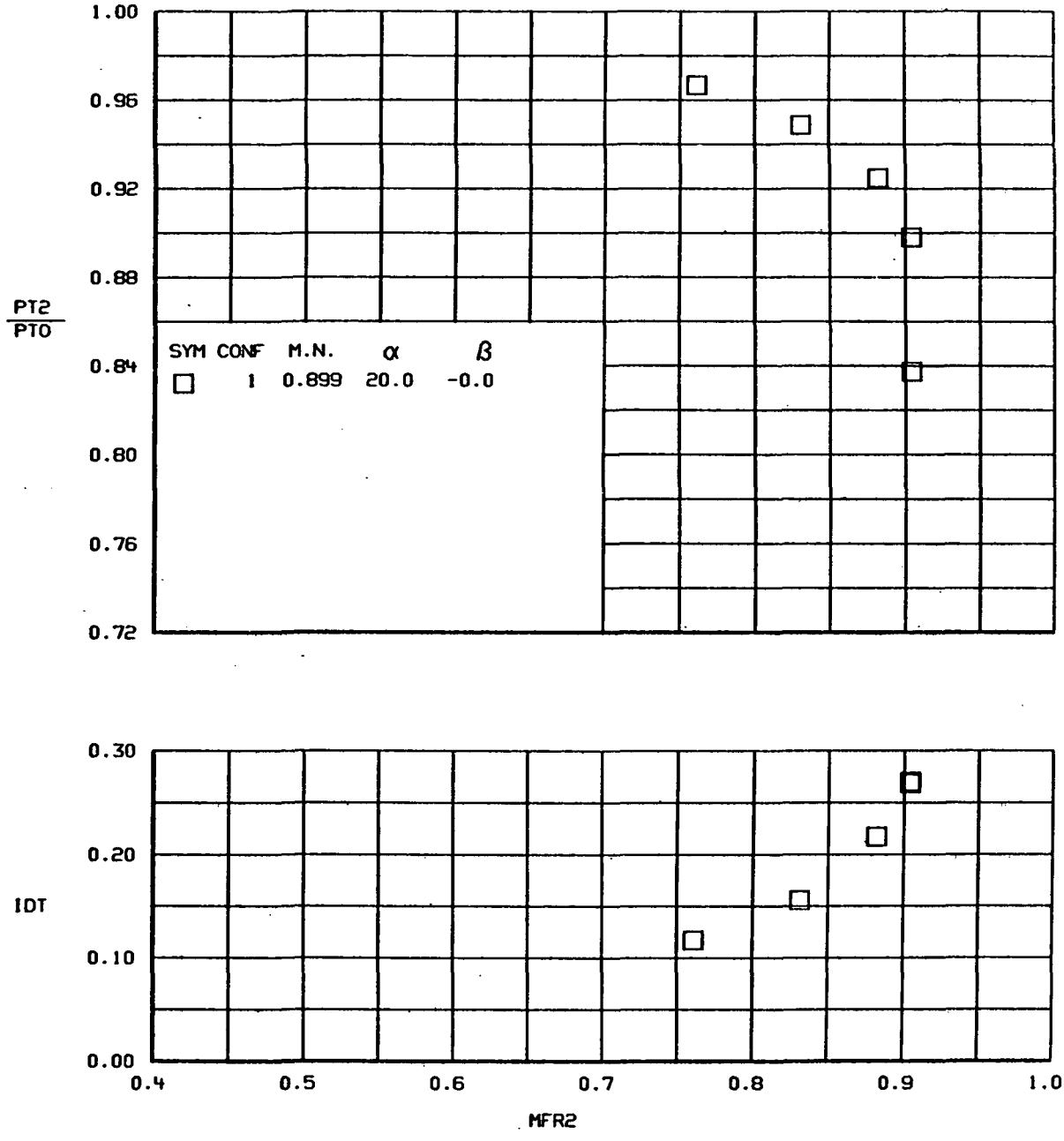

(f)

Figure 75.-Concluded.

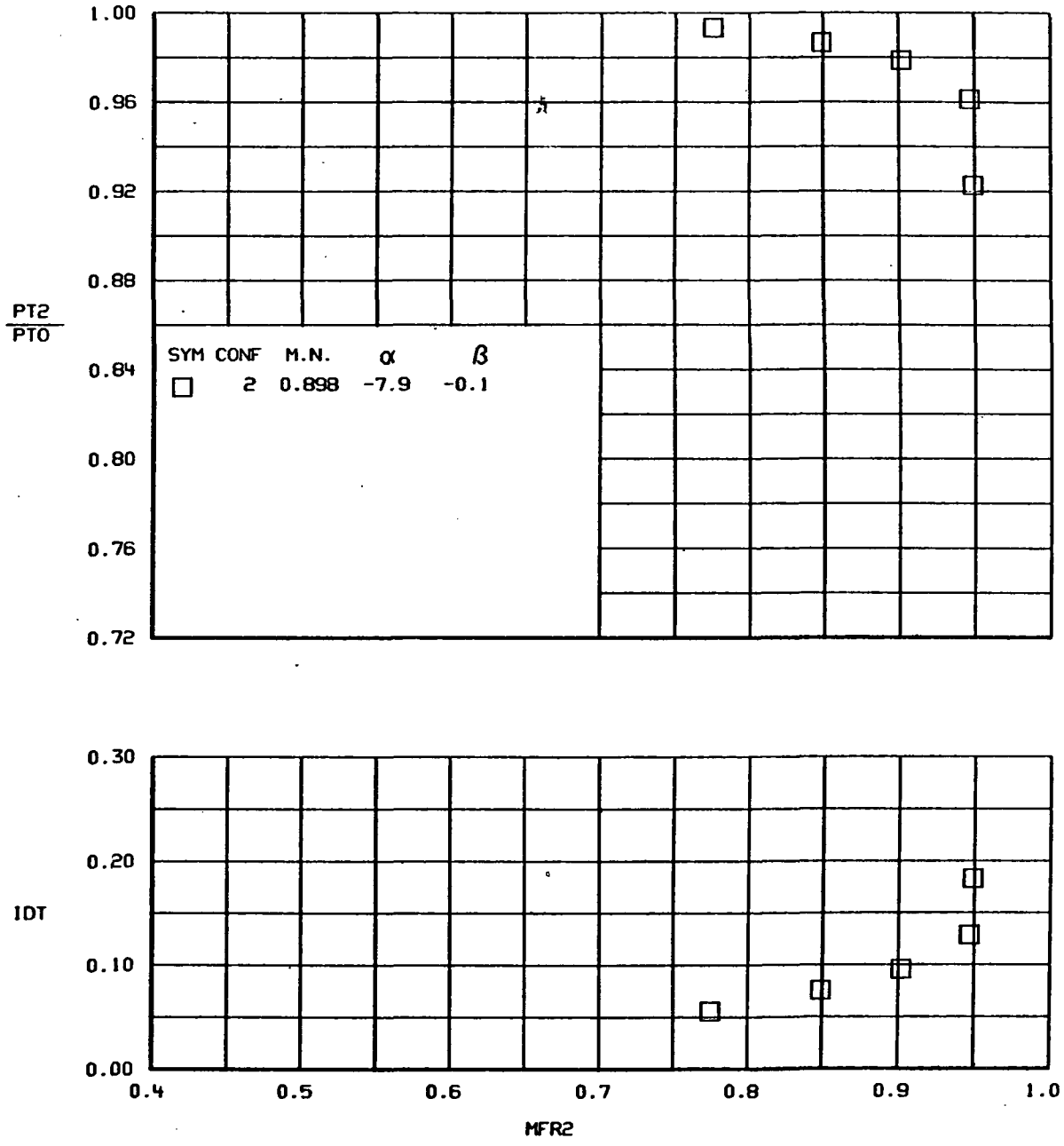

(a)

Figure 76.- TOTAL PRESSURE RECOVERY AND DISTORTION VERSUS MASS FLOW RATIO Configuration 2.

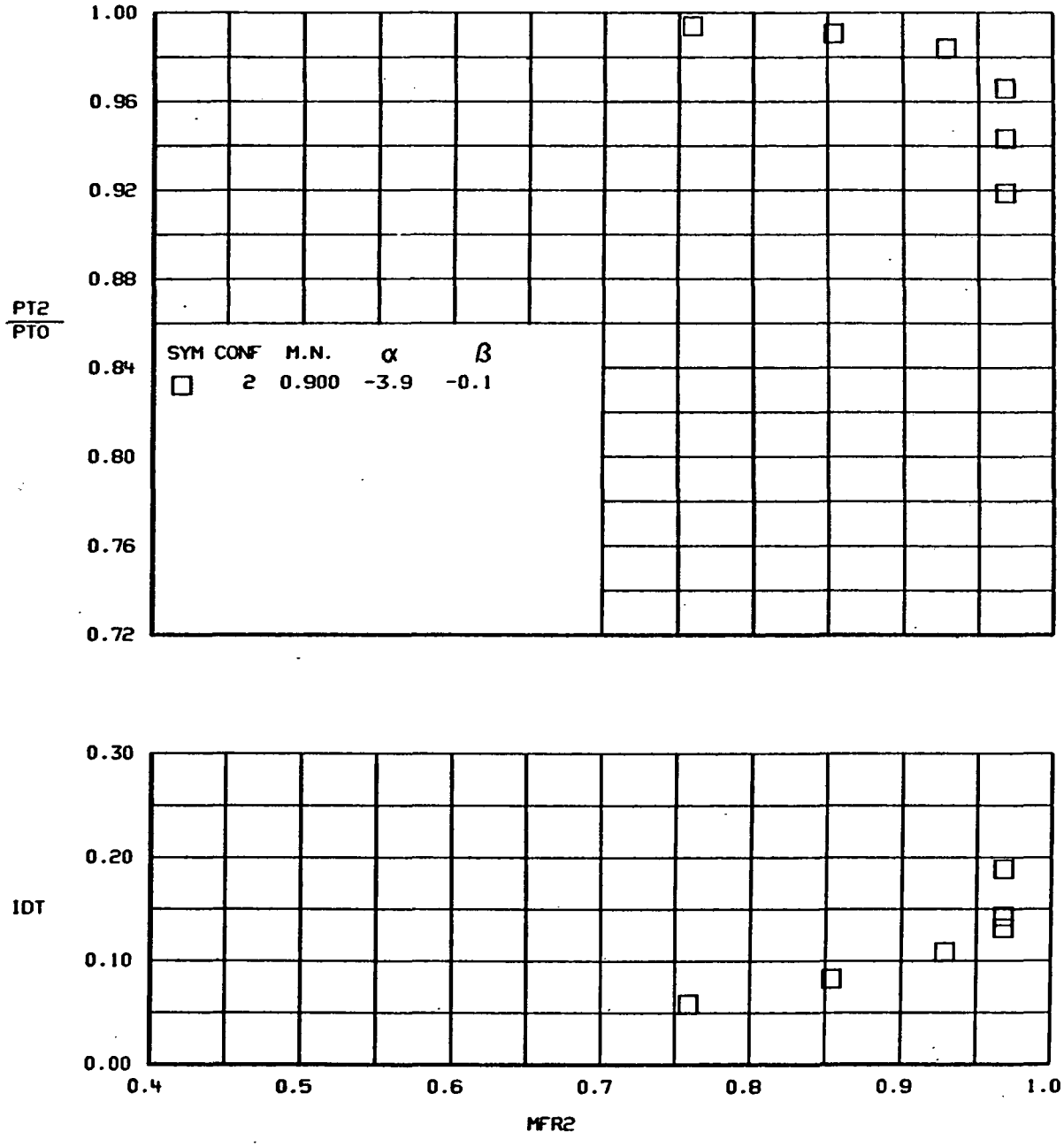

(b)

Figure 76.-Continued.

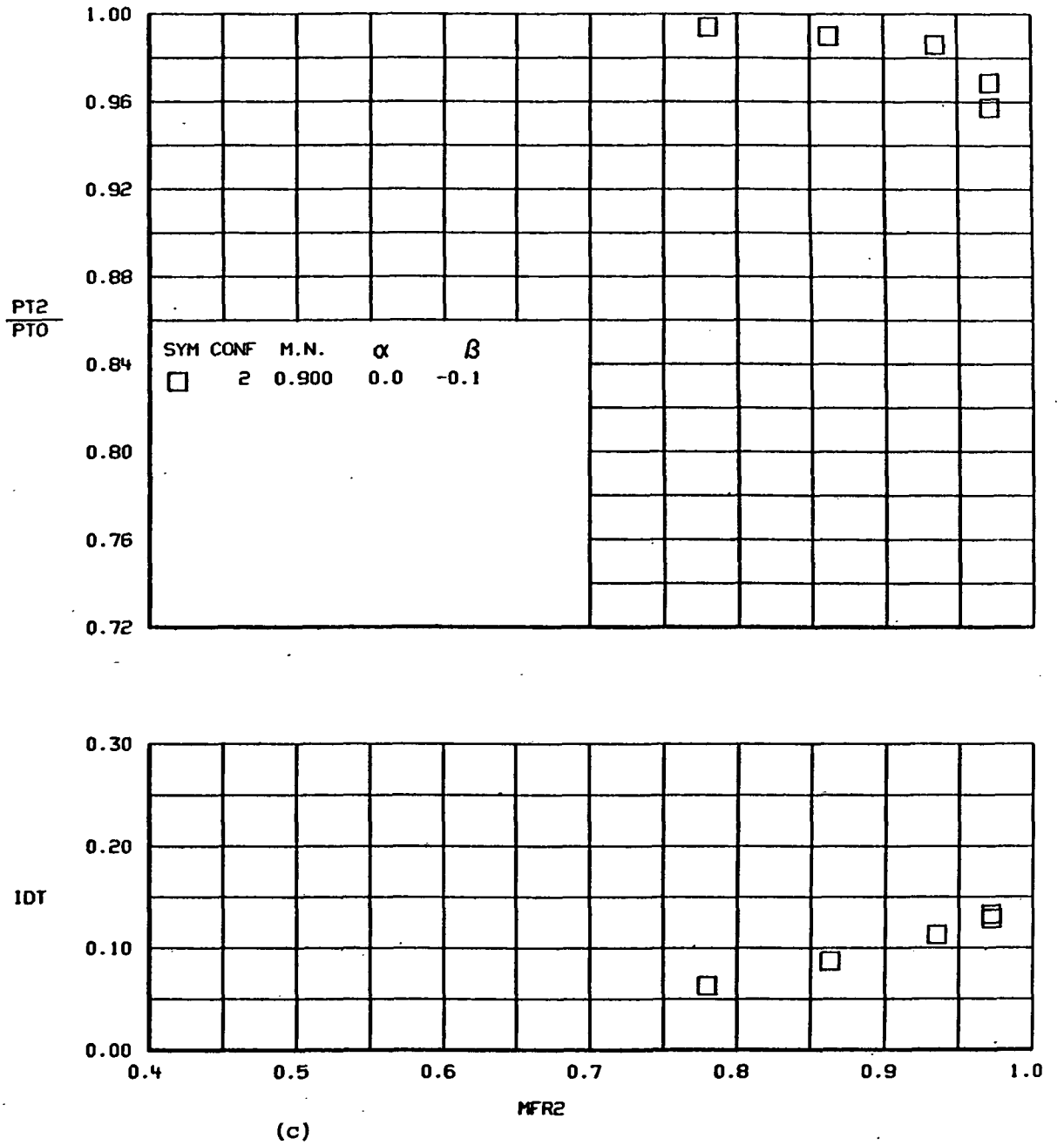

(c)

Figure 76.-Continued.

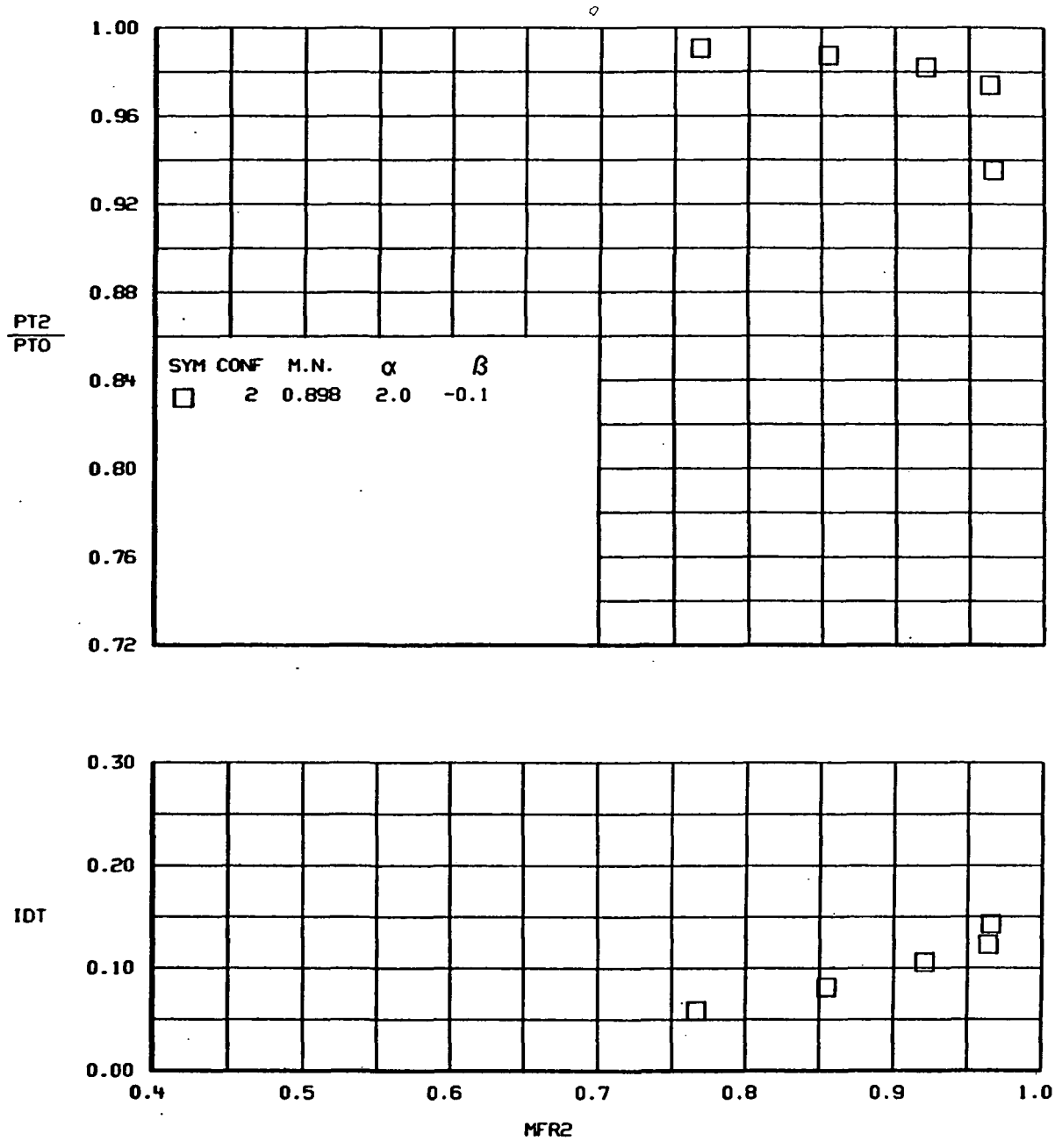

(d)

Figure 76.-Continued.

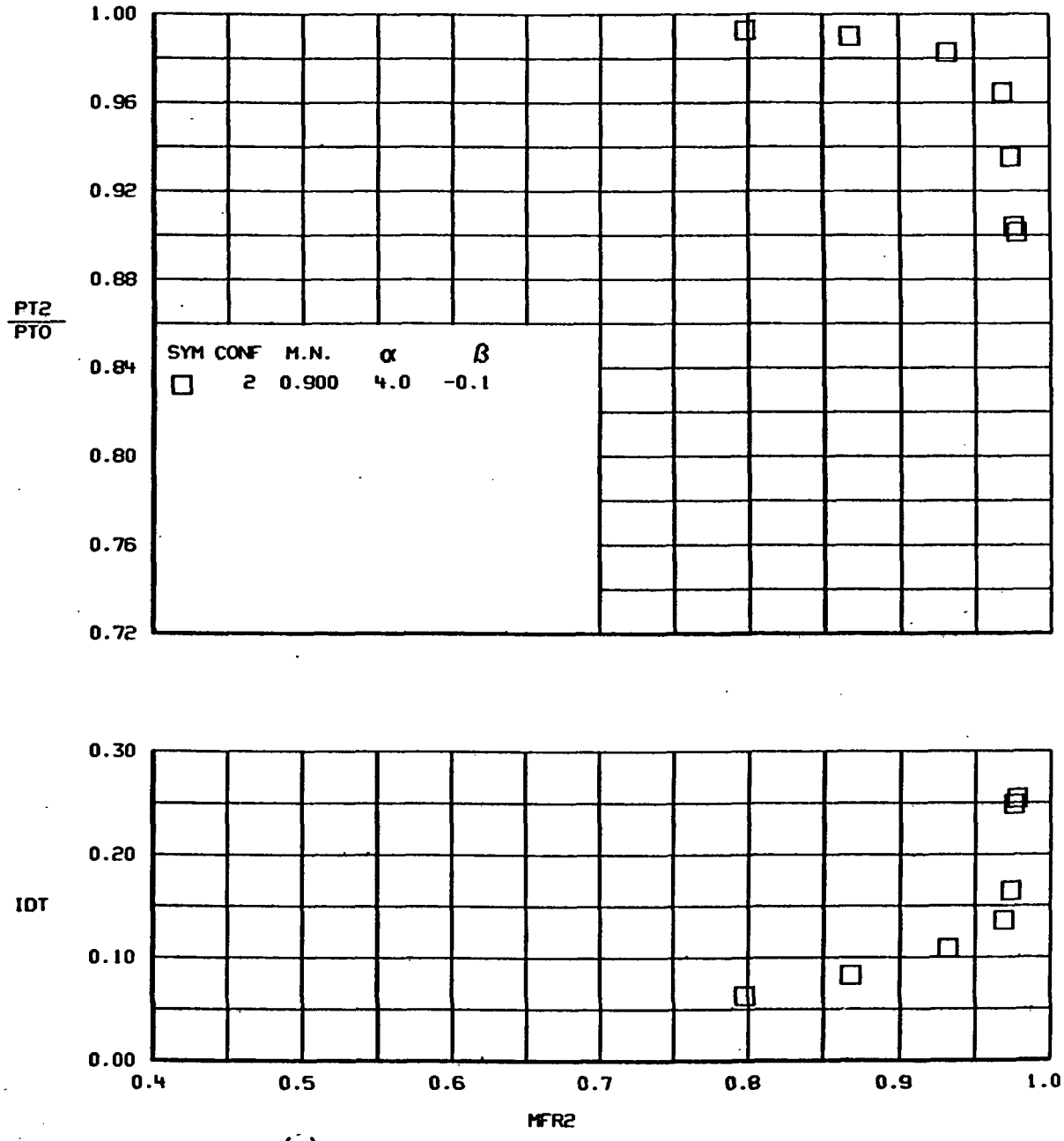

(e)

Figure 76.-Continued.

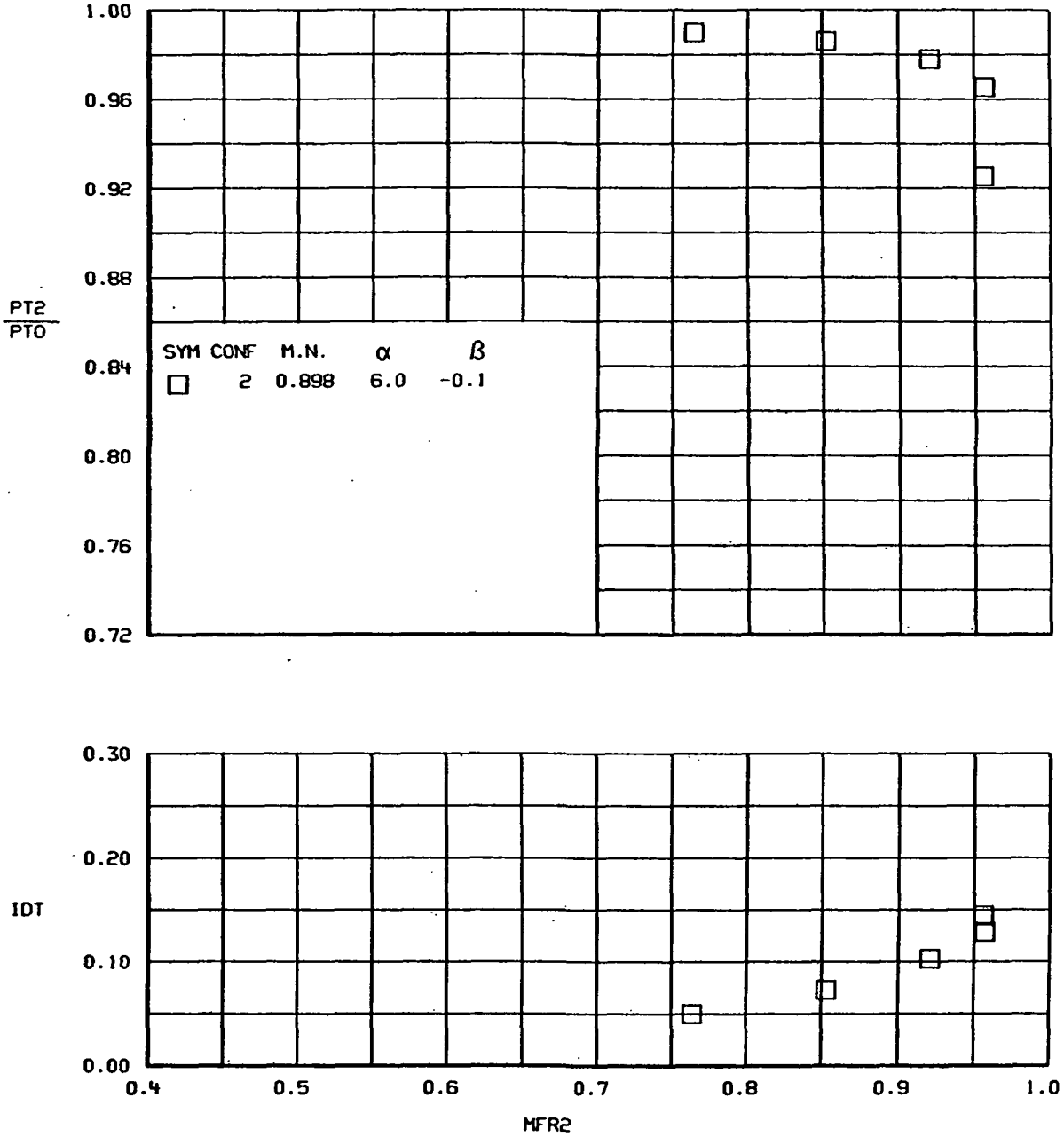

(f)

Figure 76.-Continued.

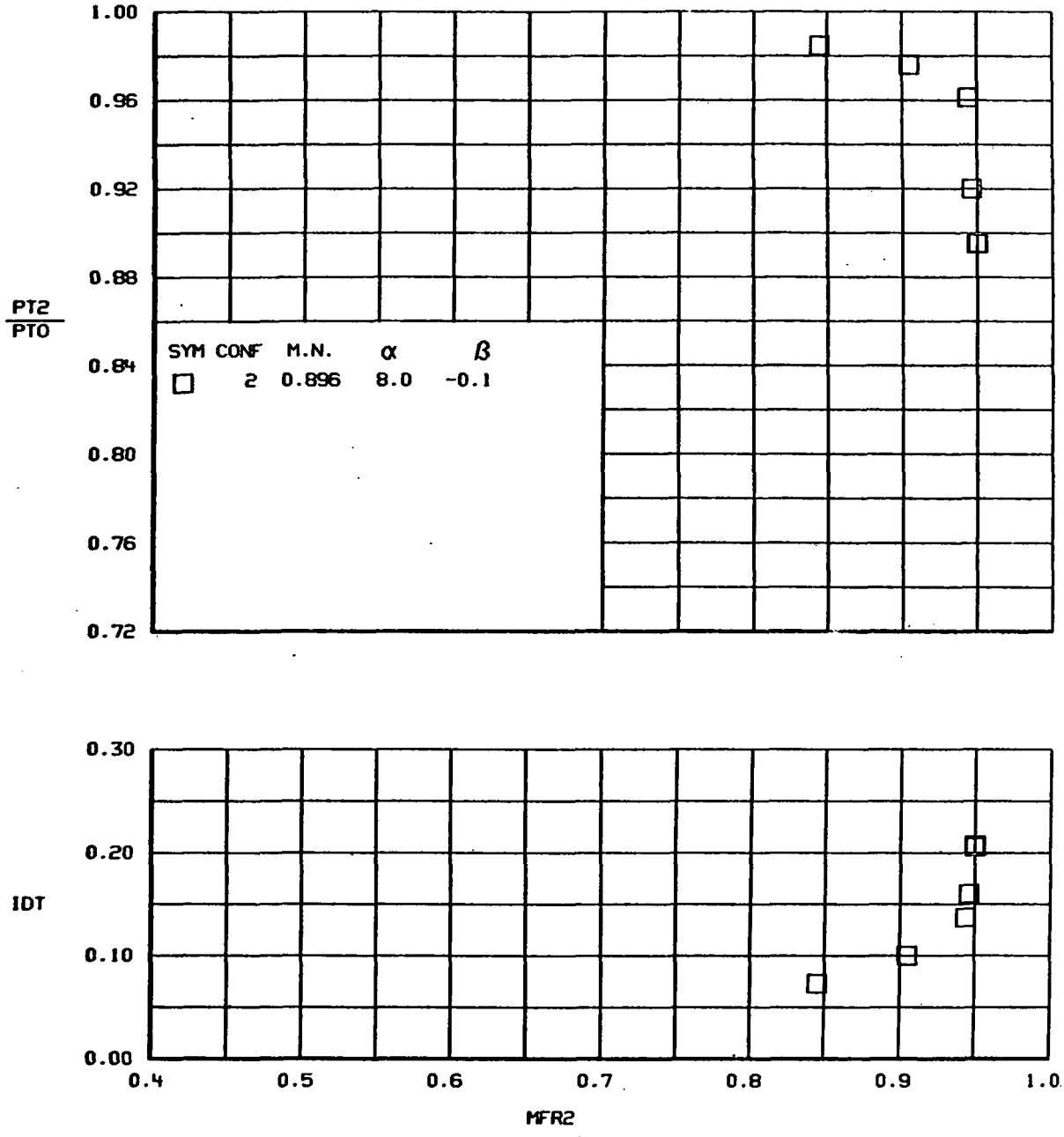

(g)

Figure 76.-Continued.

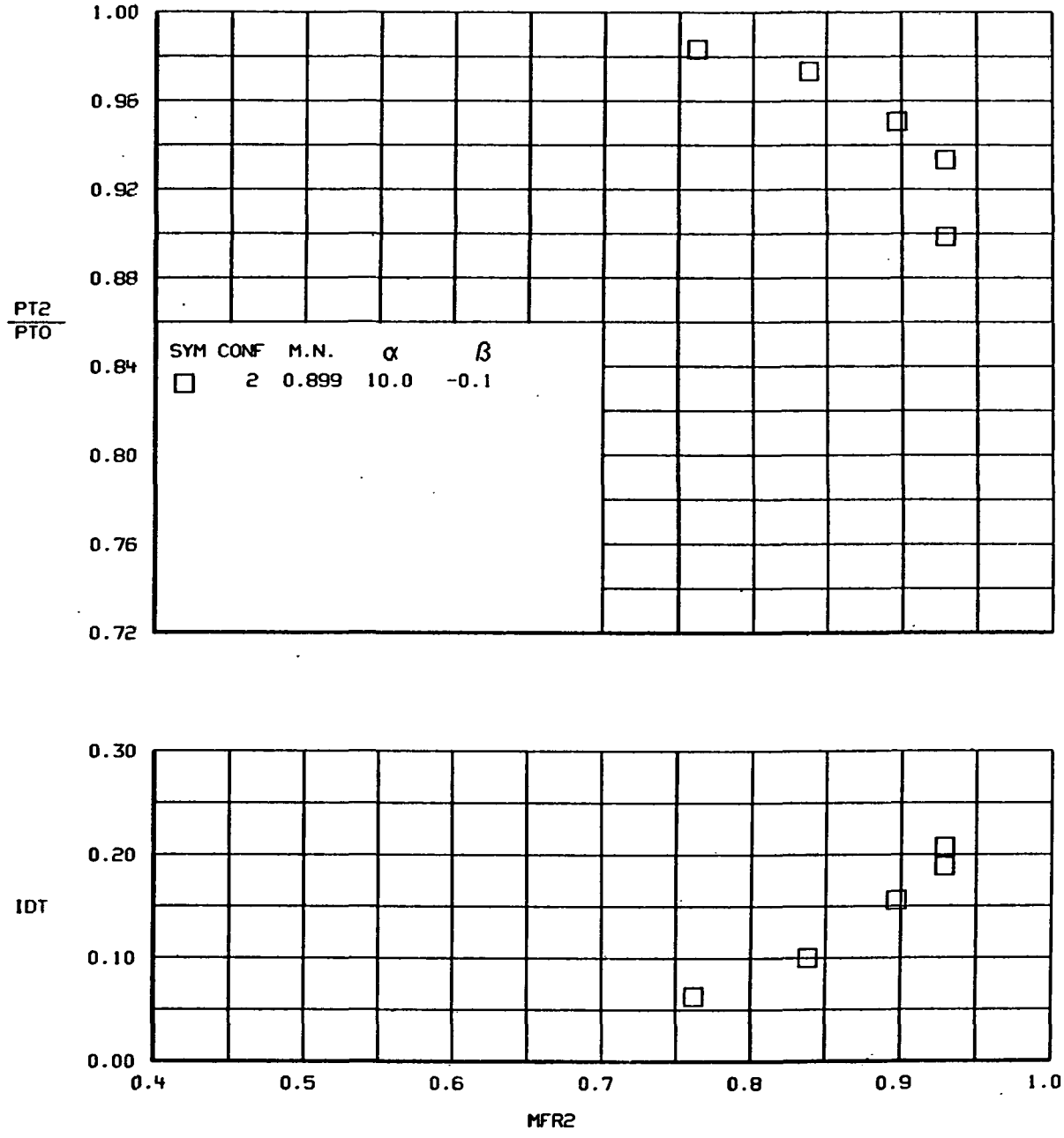

(h)

Figure 76.-Continued.

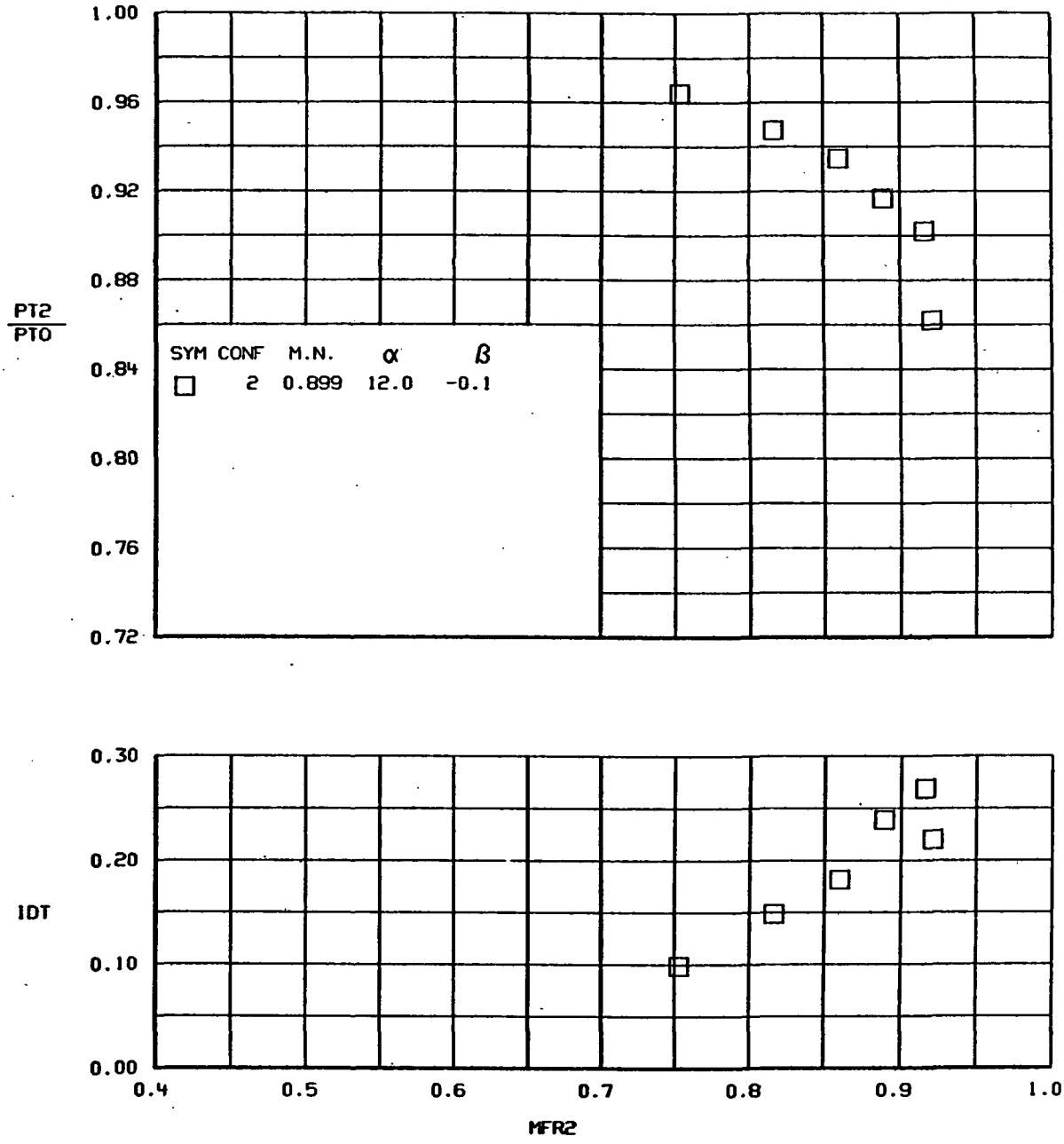

(i)

Figure 76.-Continued.

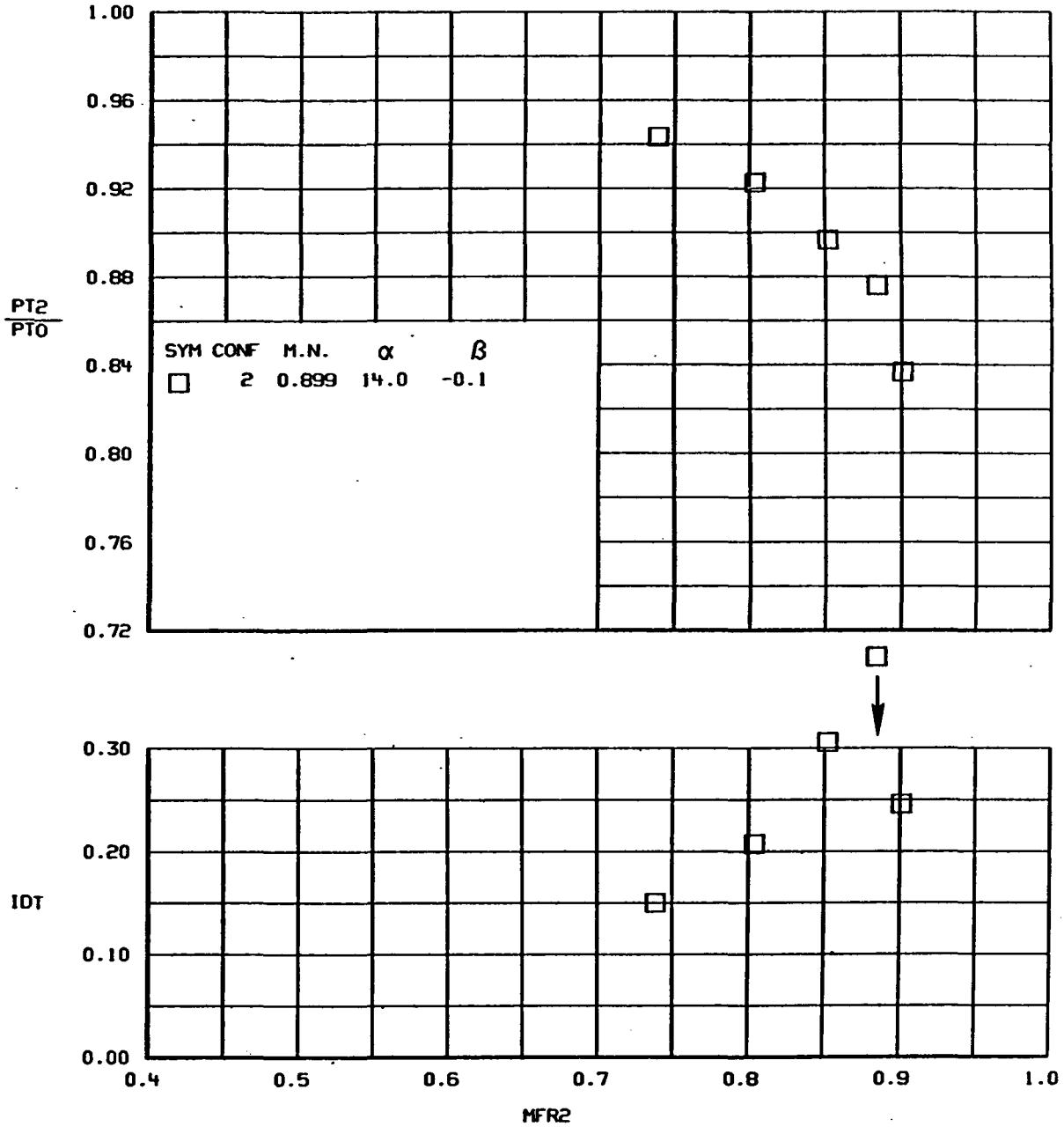

(j)

Figure 76.-Continued.

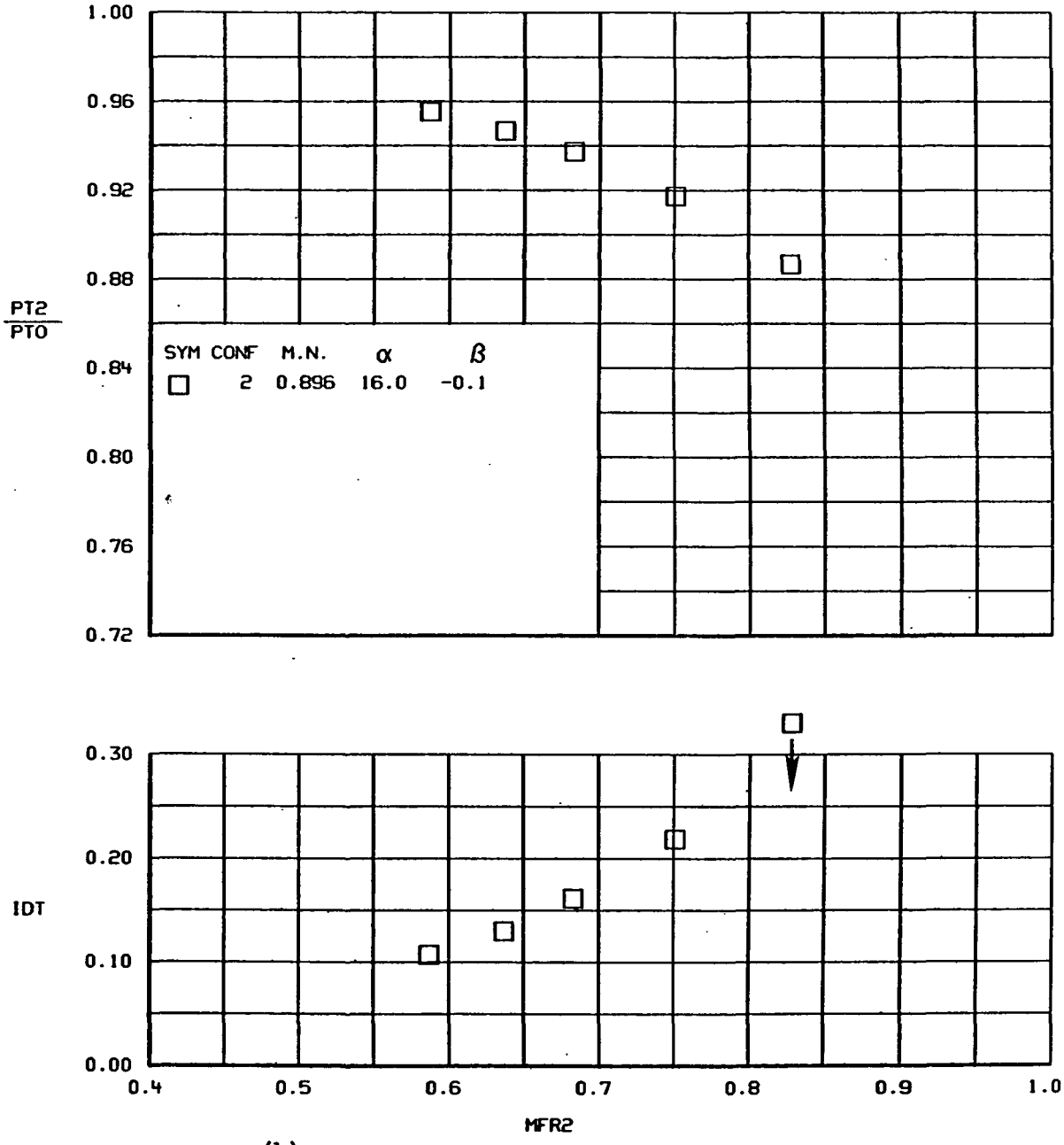

(k)

Figure 76.-Continued.

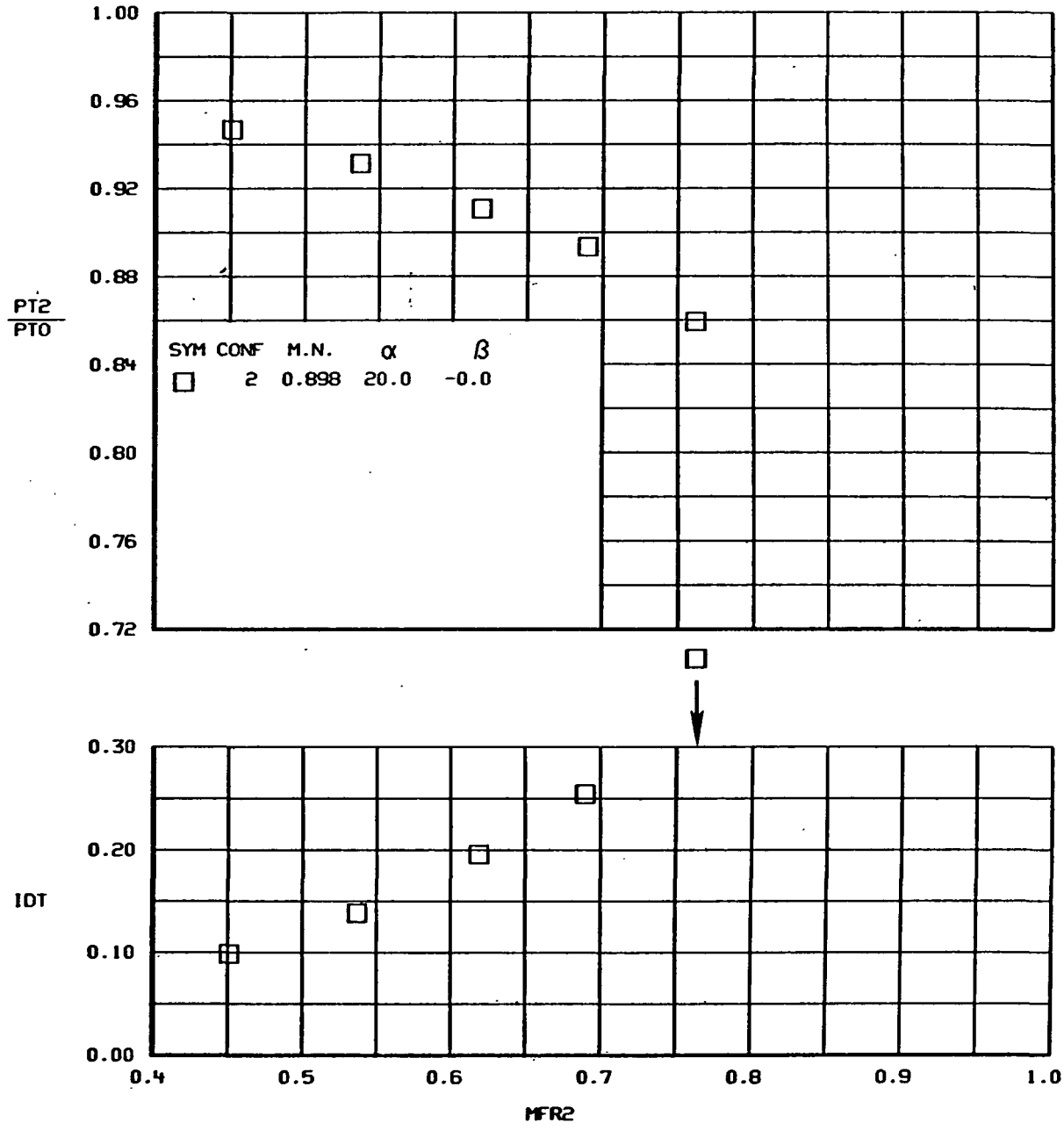

(1)

Figure 76.-Continued.

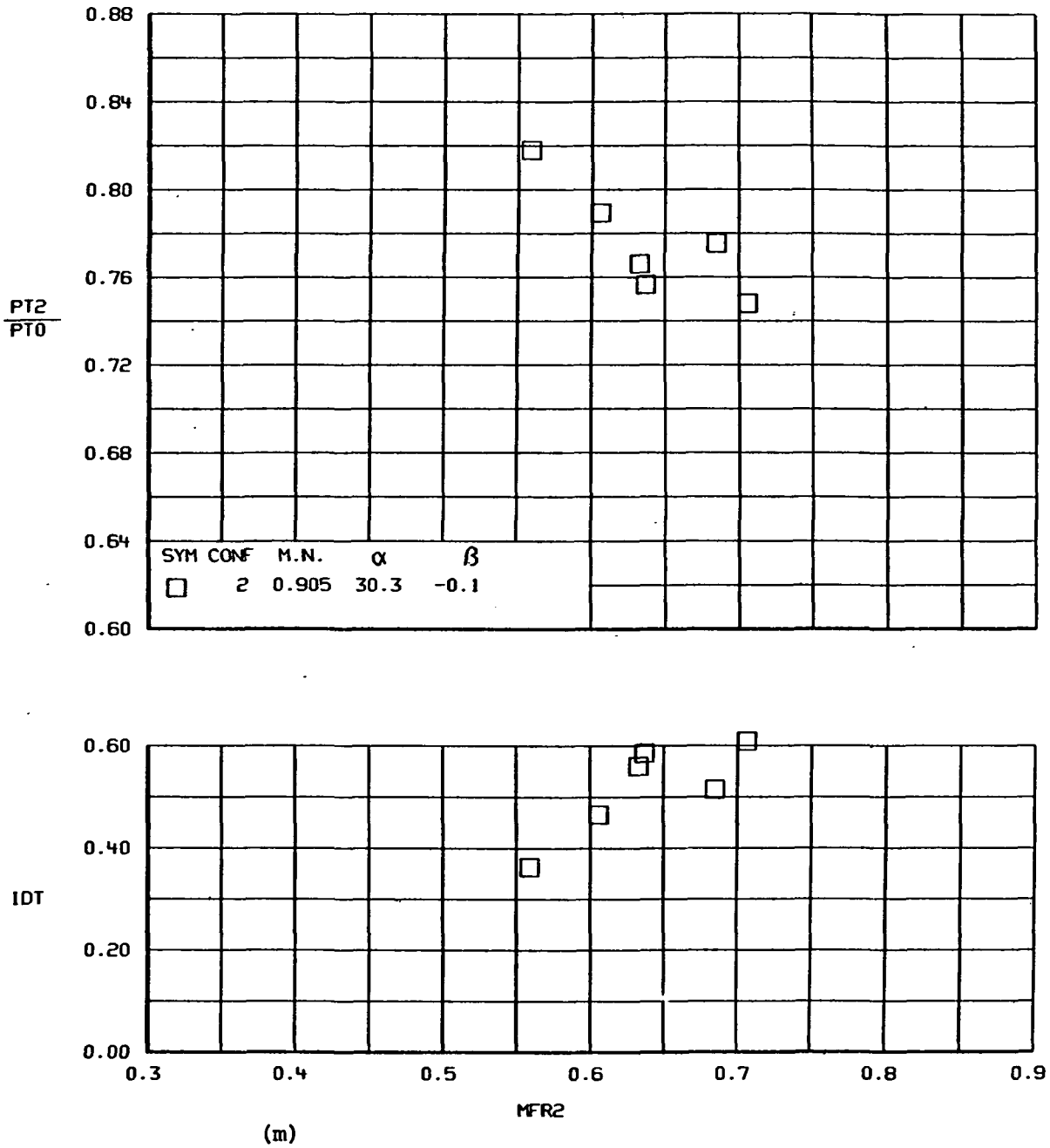

Figure 76.-Continued.

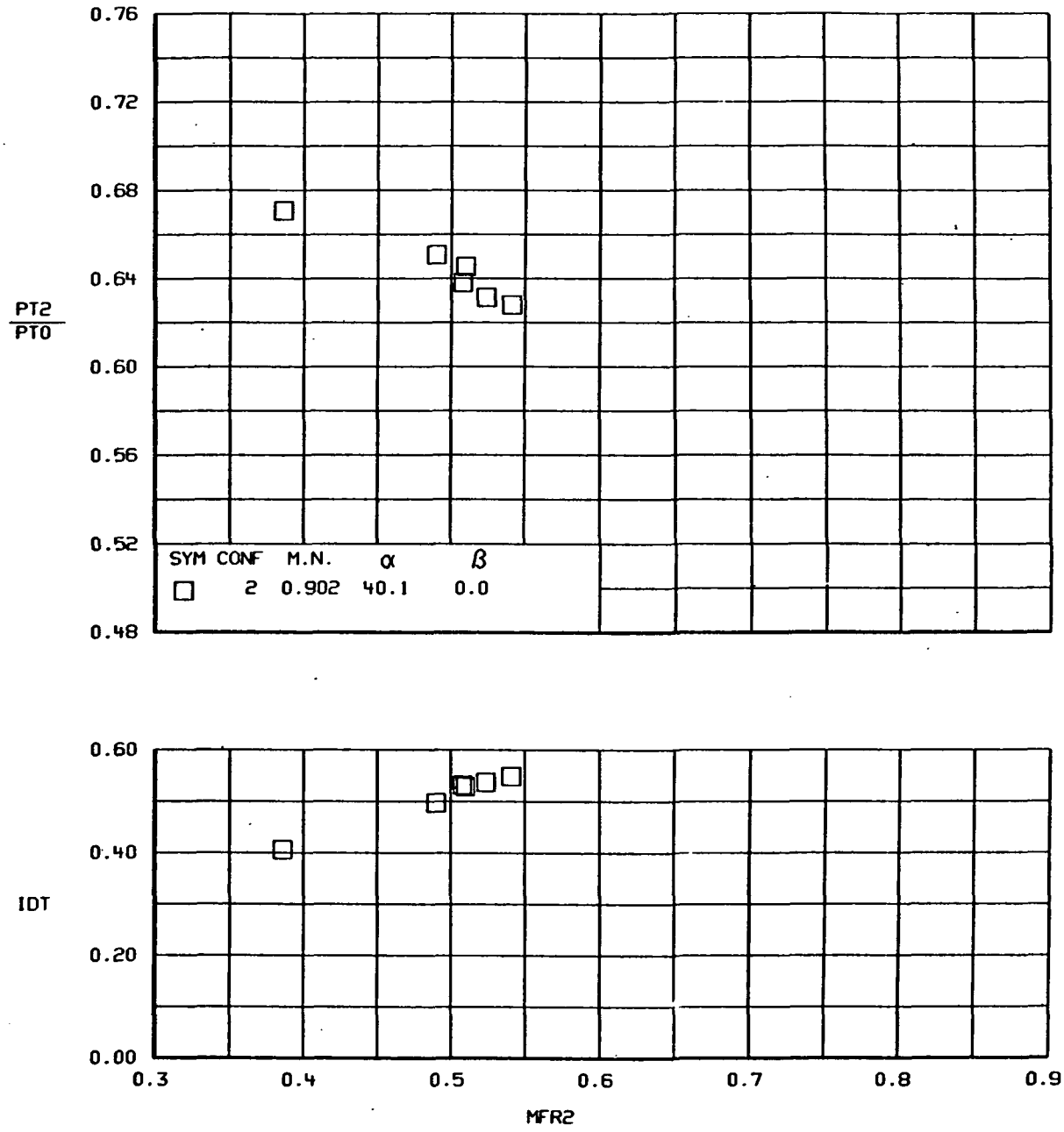

(n)

Figure 76.-Continued.

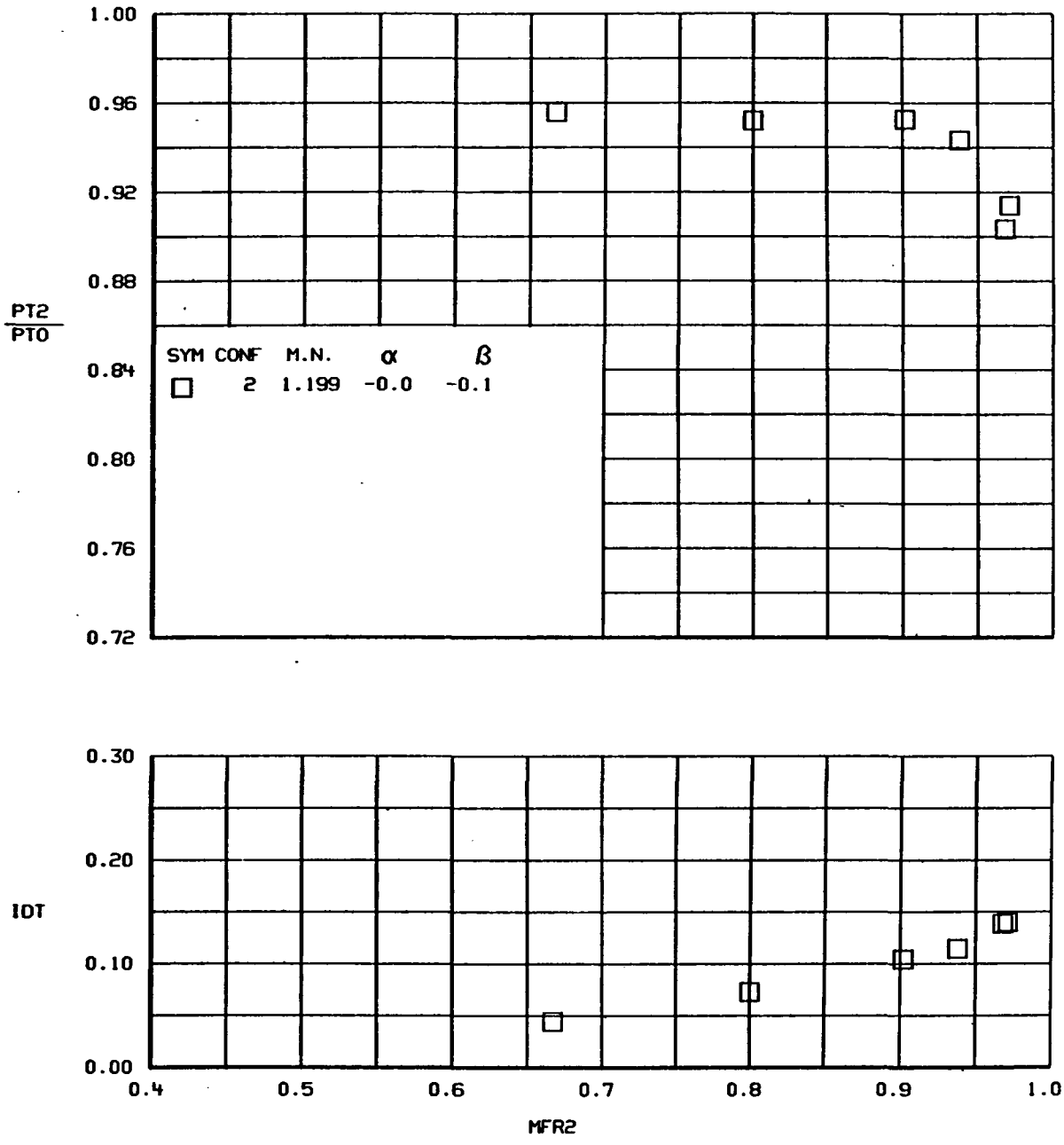

(o)

Figure 76.-Continued.

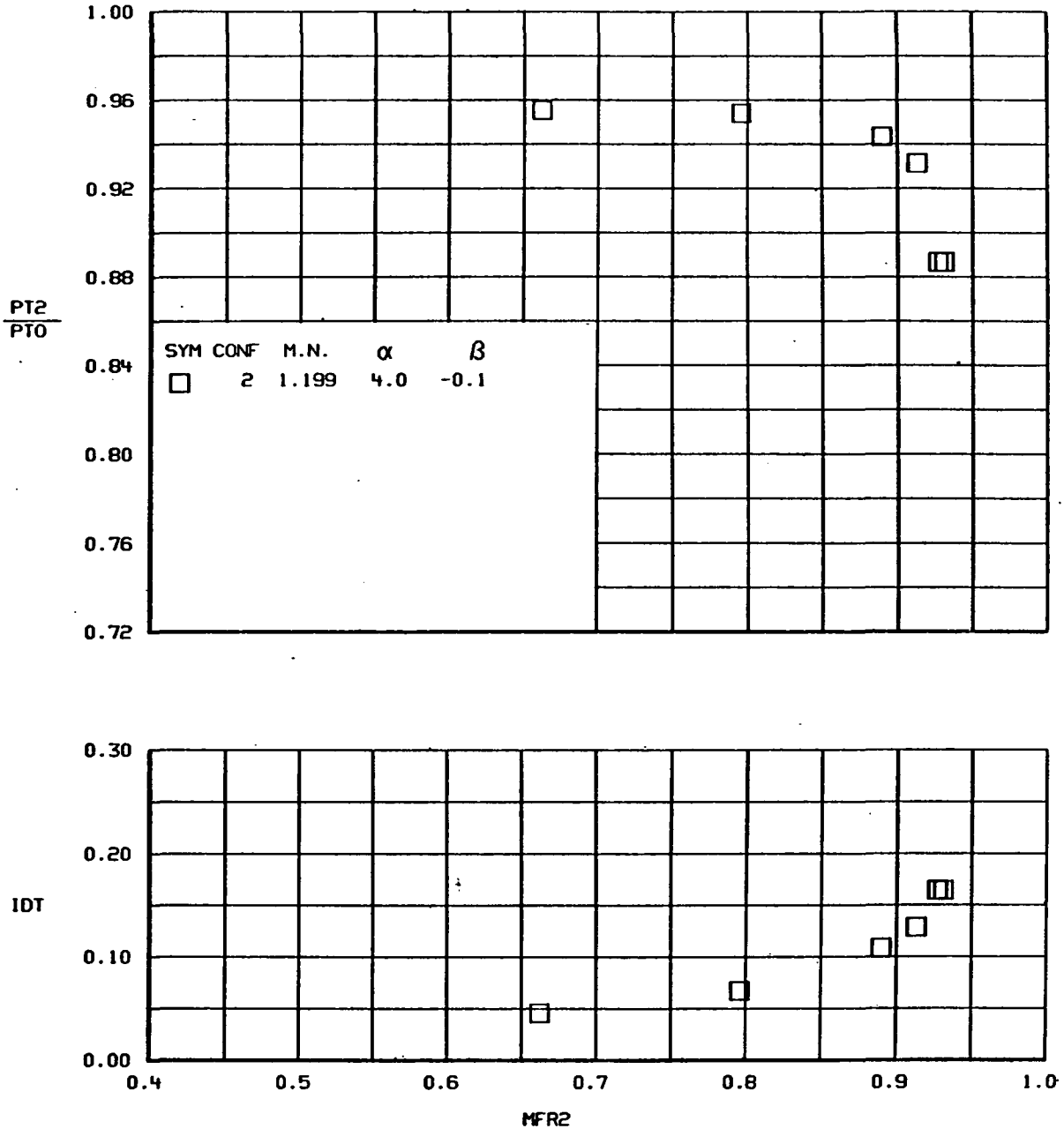

(p)

Figure 76.-Continued.

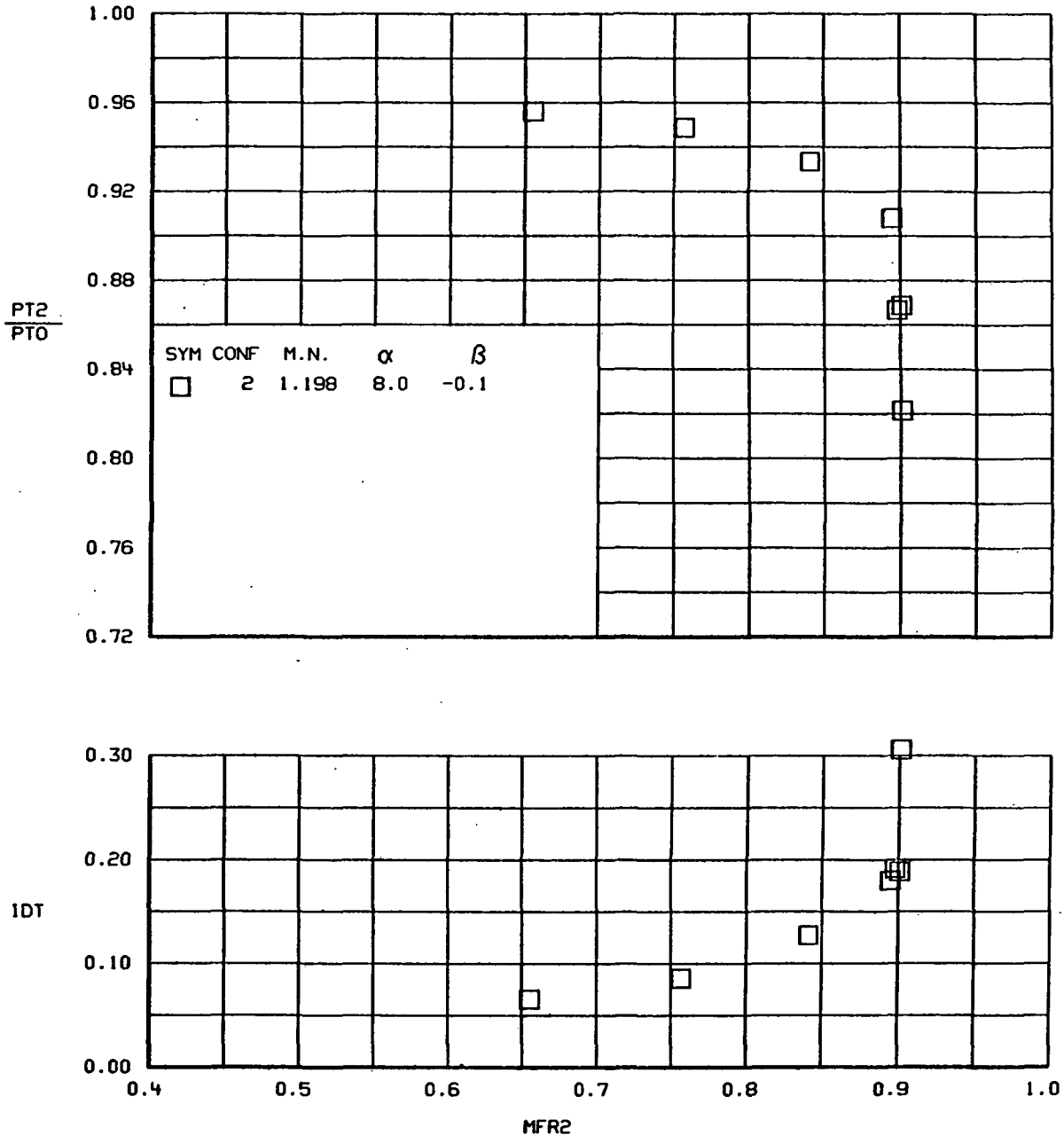

(q)

Figure 76.-Concluded.

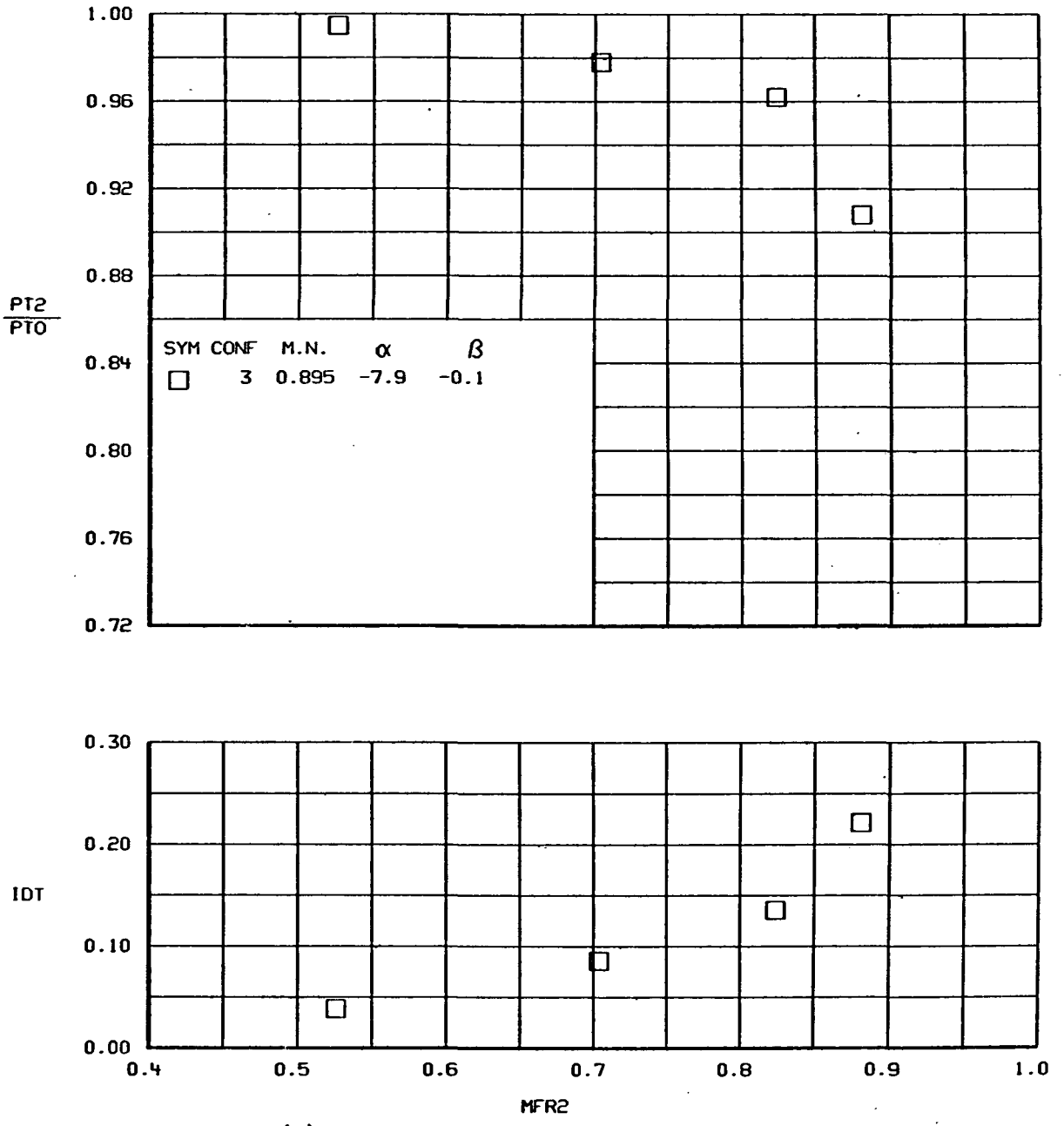

(a)

Figure 77.- TOTAL PRESSURE RECOVERY AND DISTORTION VERSUS MASS FLOW RATIO. Configuration 3.

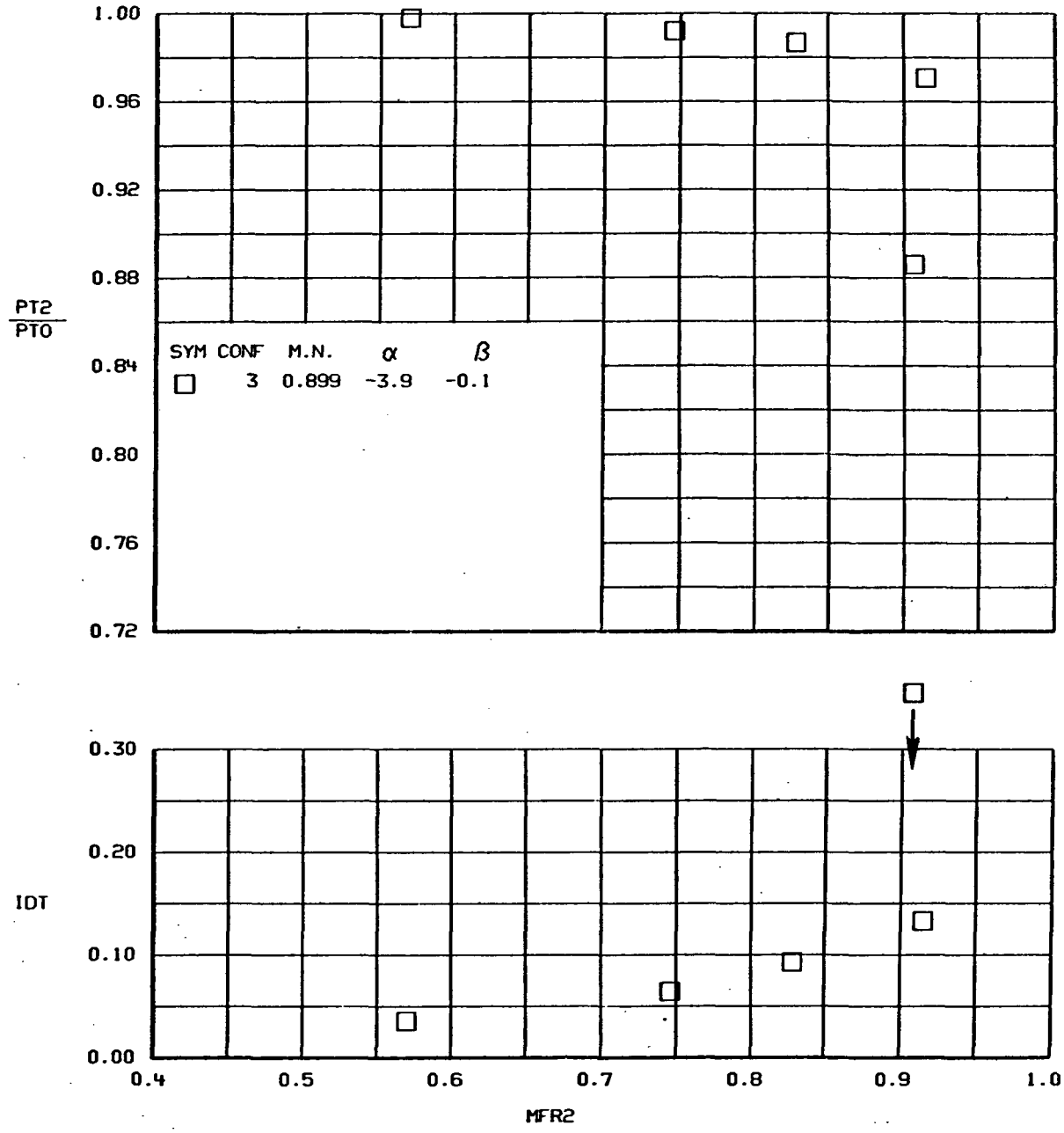

(b)

Figure 77.-Continued.

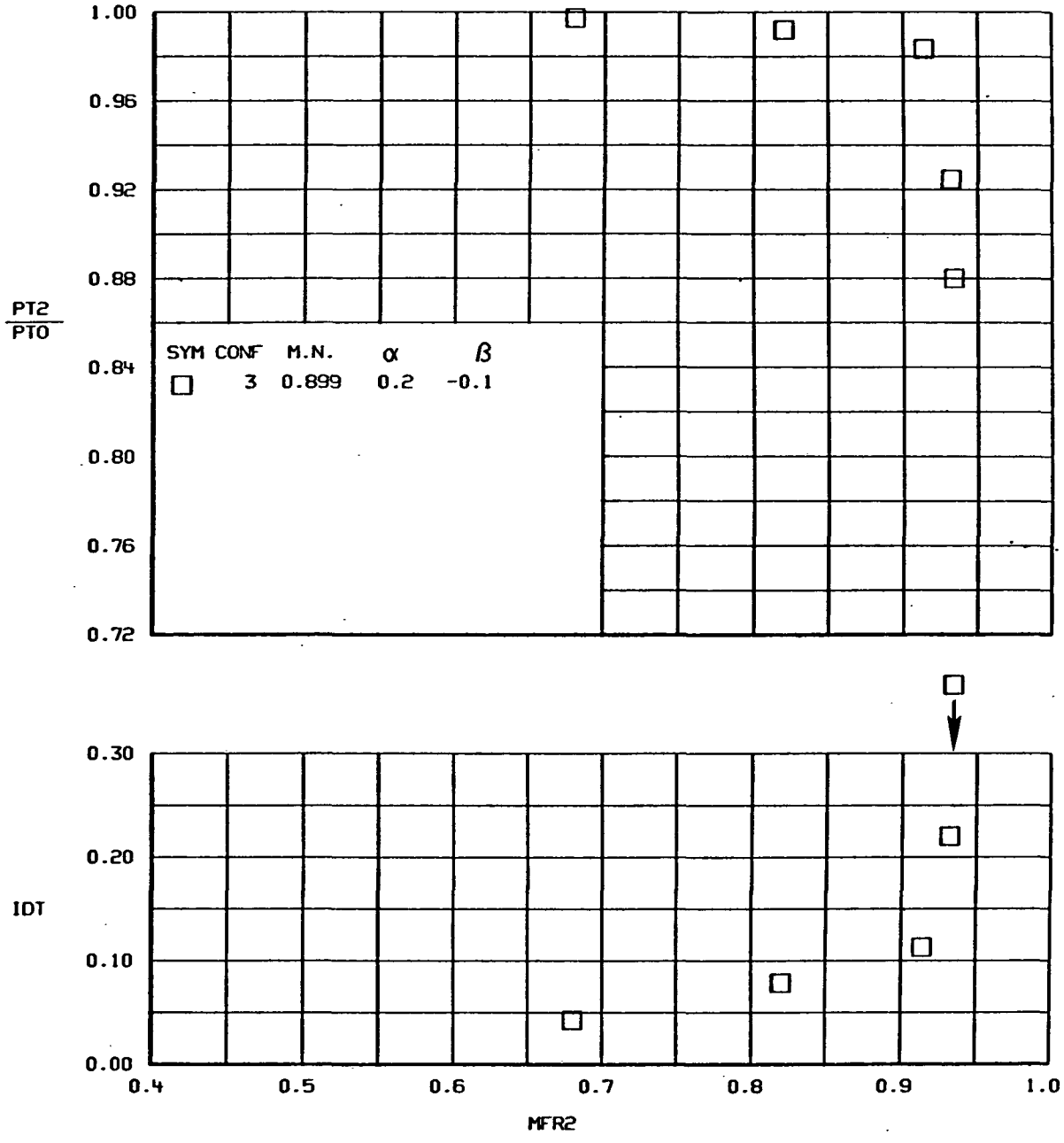

(c)

Figure 77.-Continued.

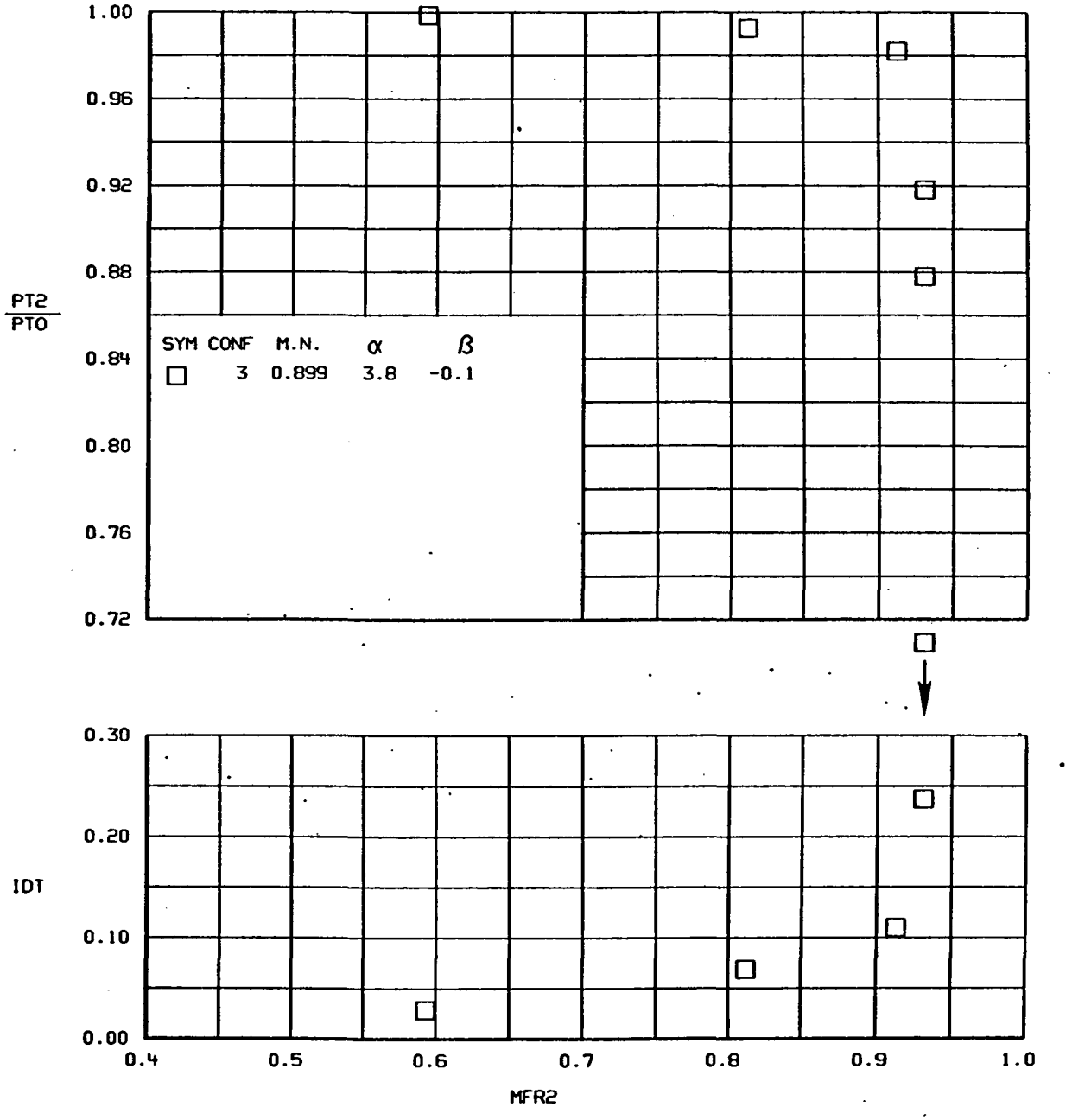

(d)

Figure 77.-Continued.

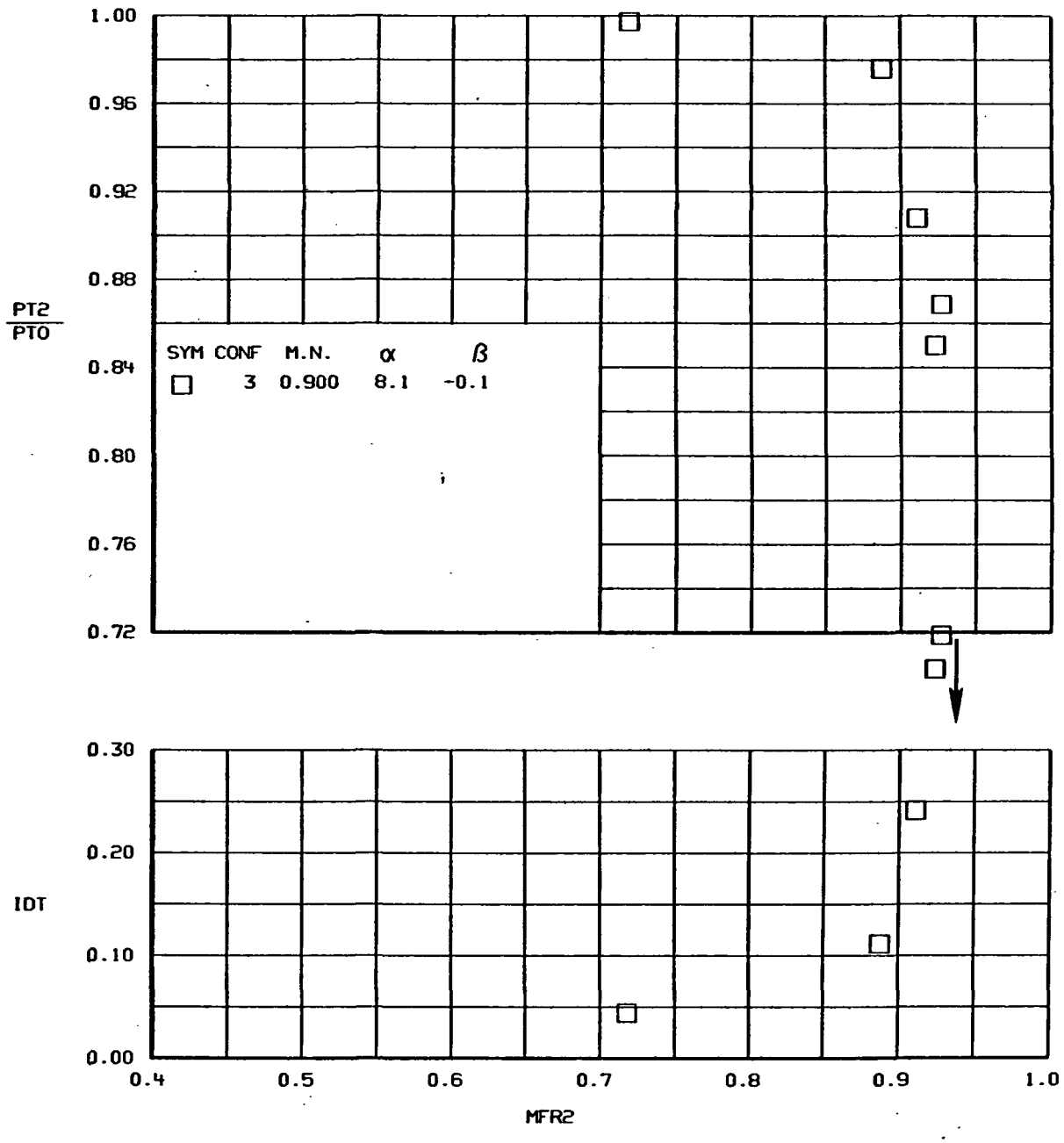

(e)

Figure 77.-Continued.

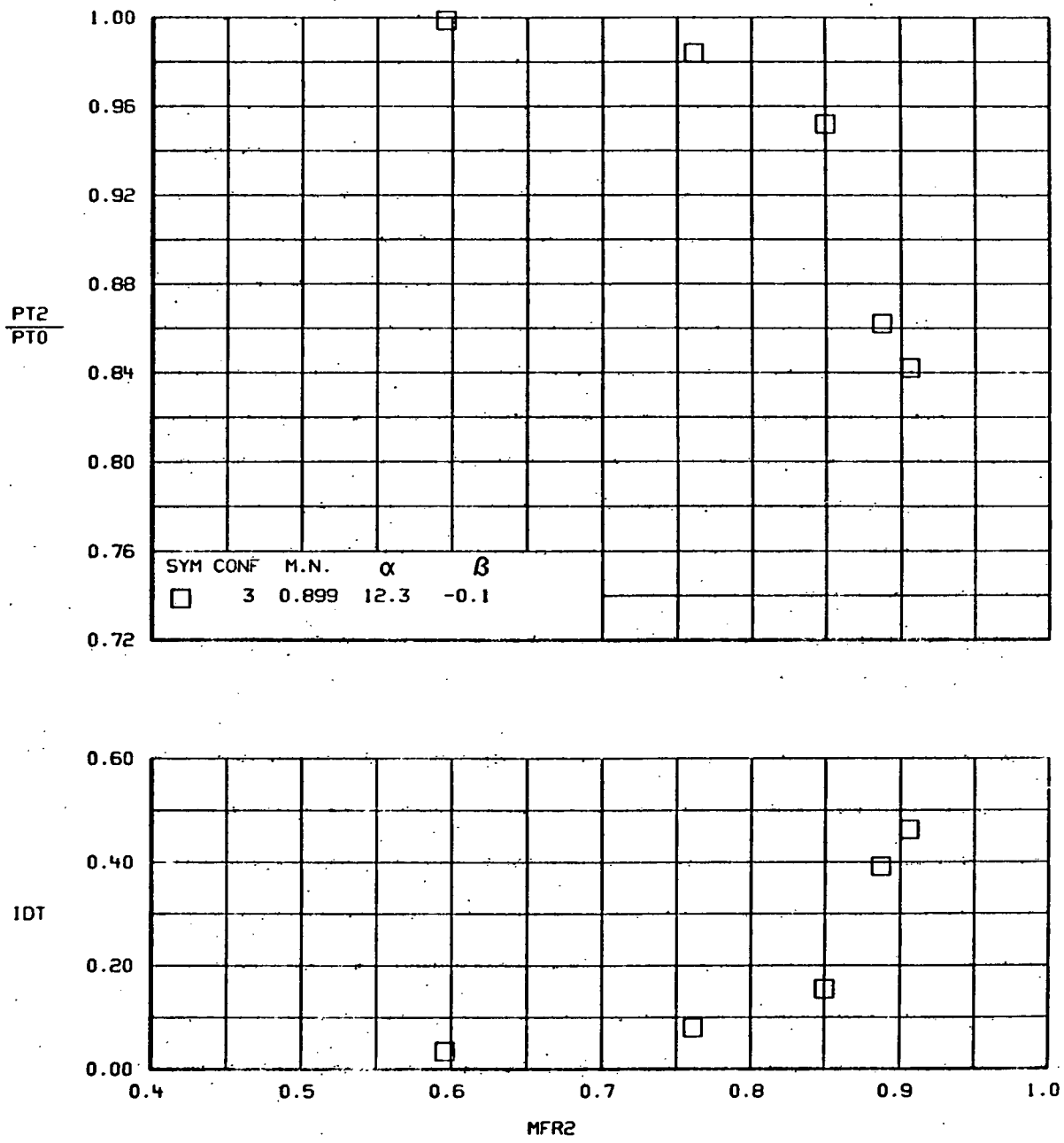

(F)

FIGURE 77.-CONTINUED.

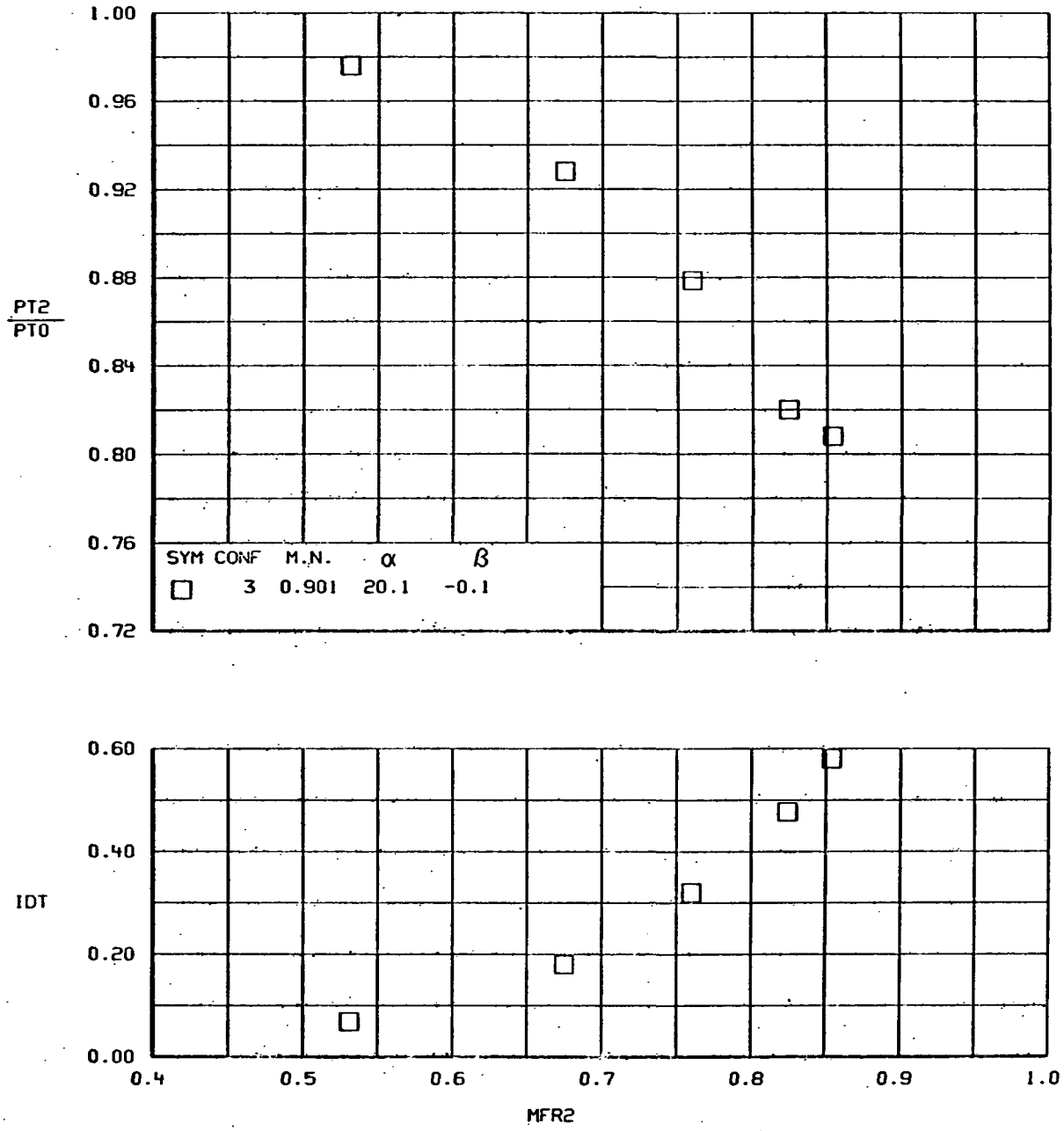

(G)

FIGURE 77.-CONTINUED.

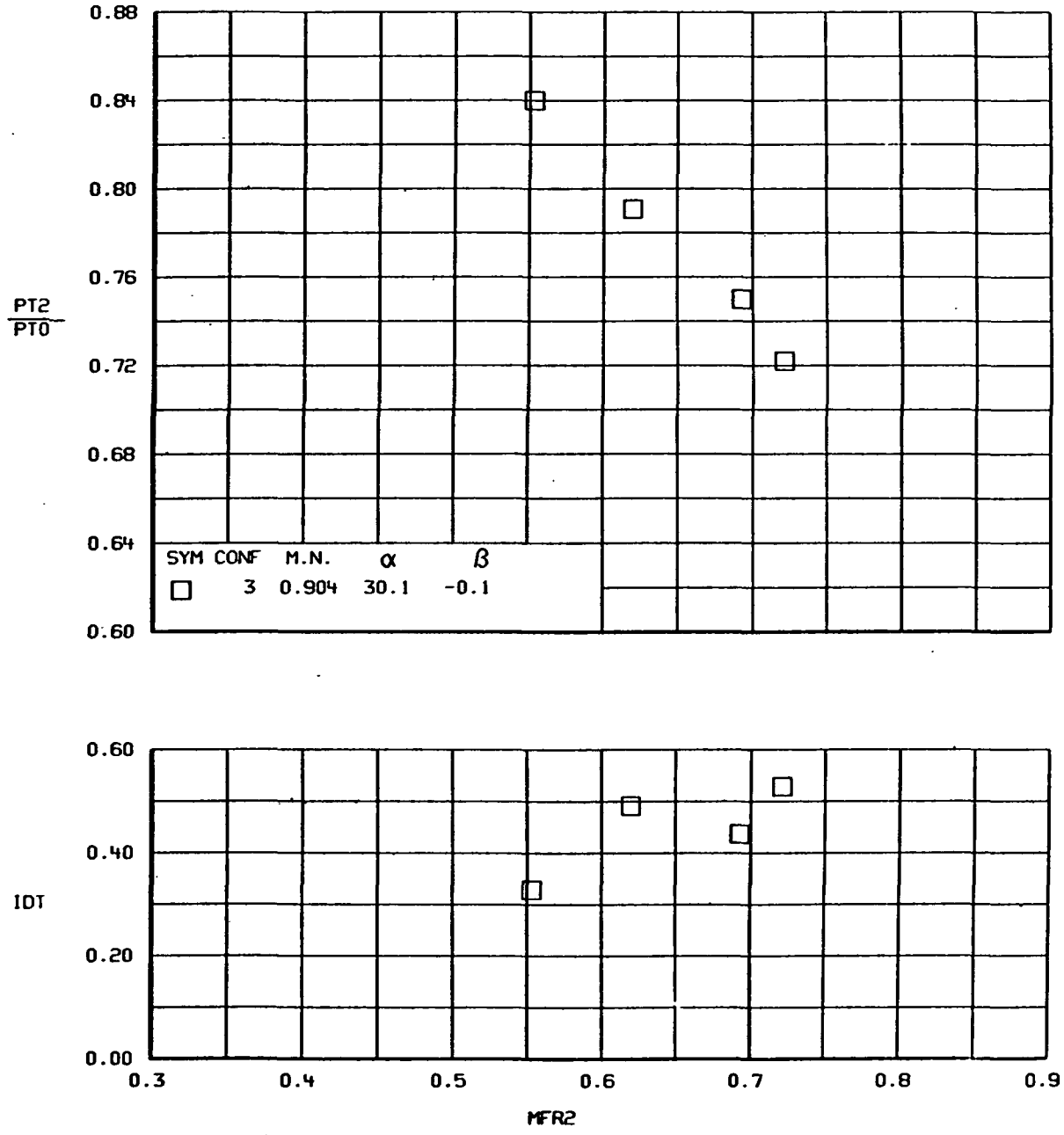

(h)

Figure 77.-Continued.

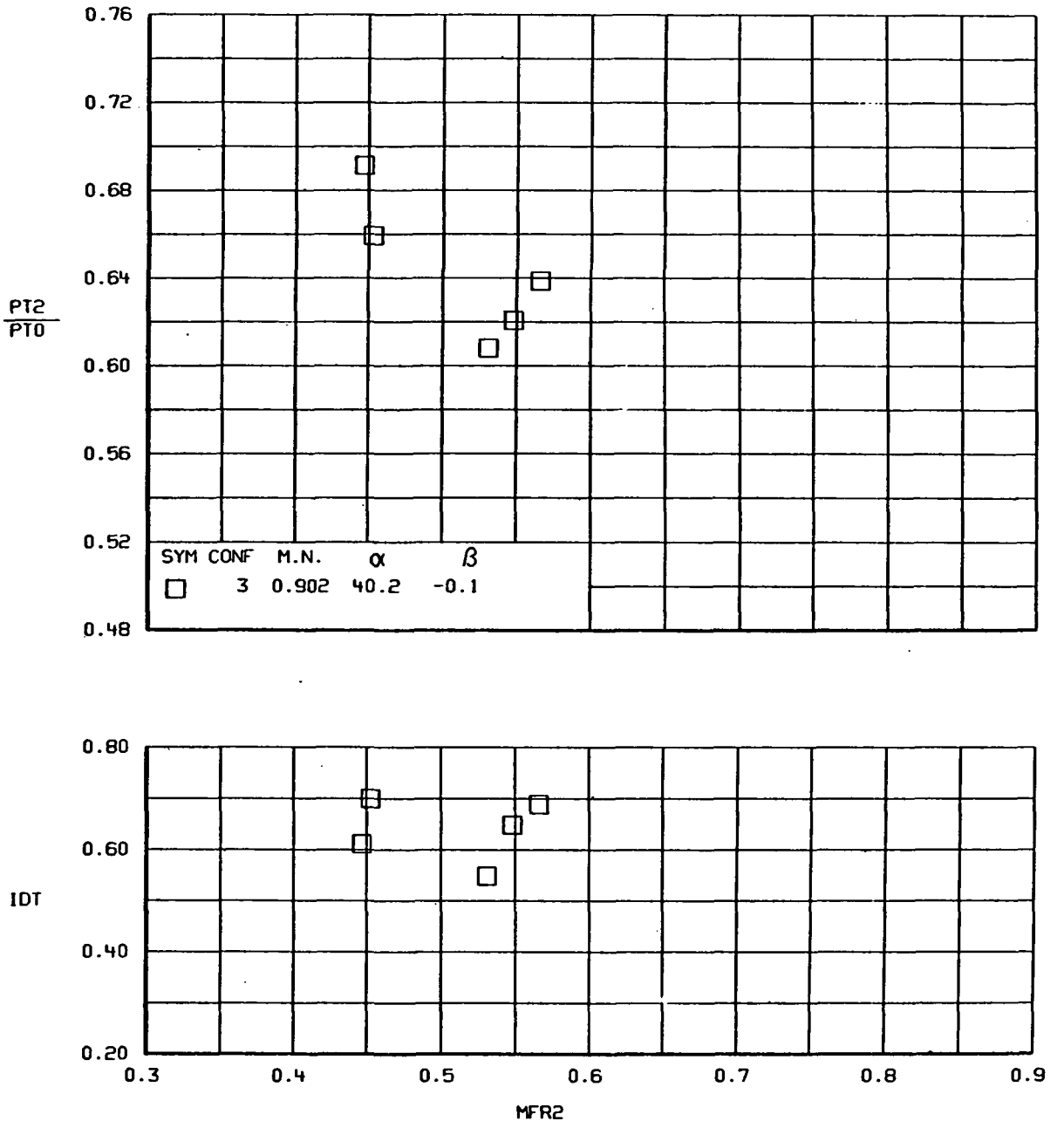

(i)

Figure 77.-Continued.

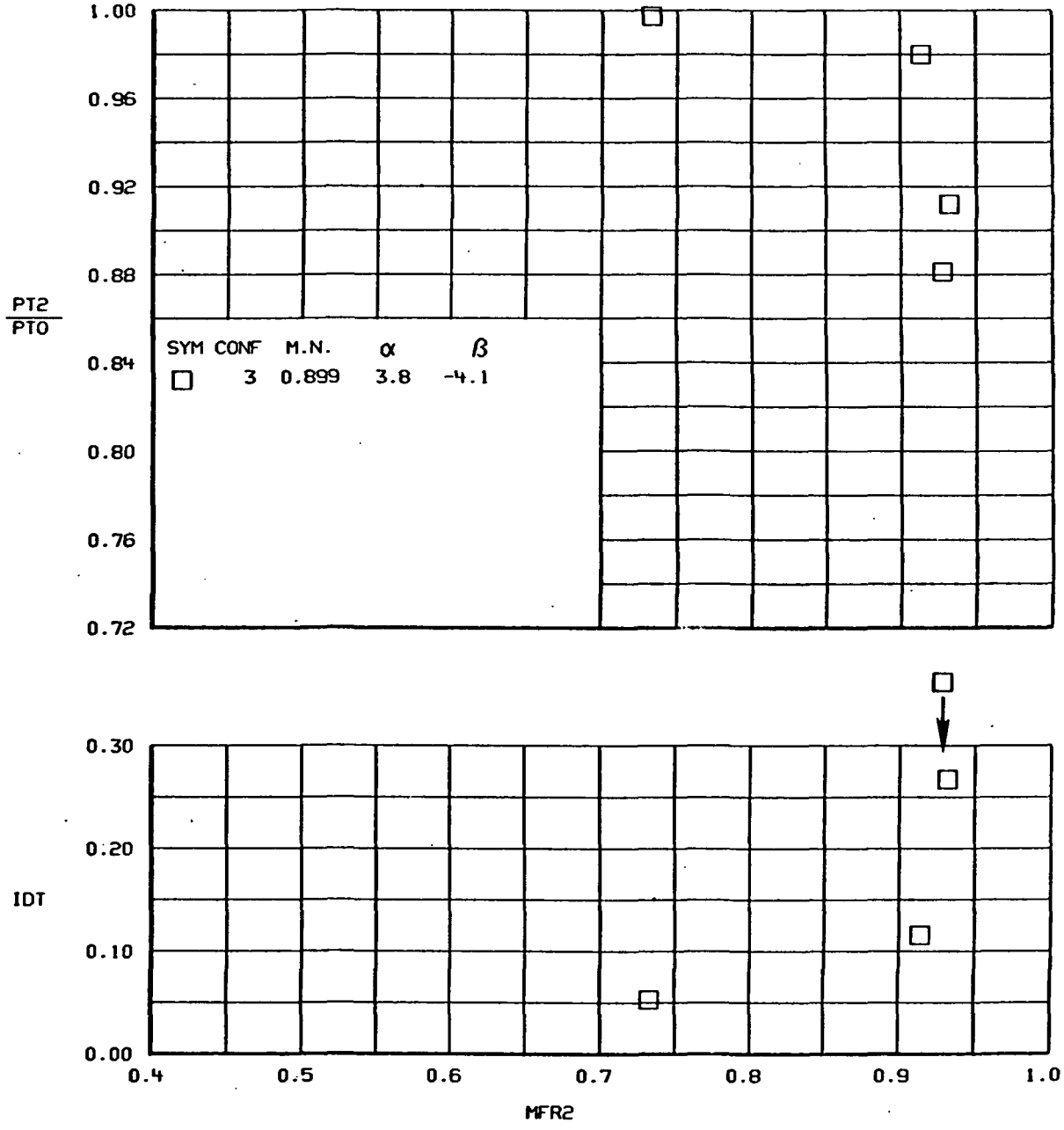

(j)

Figure 77-Continued.

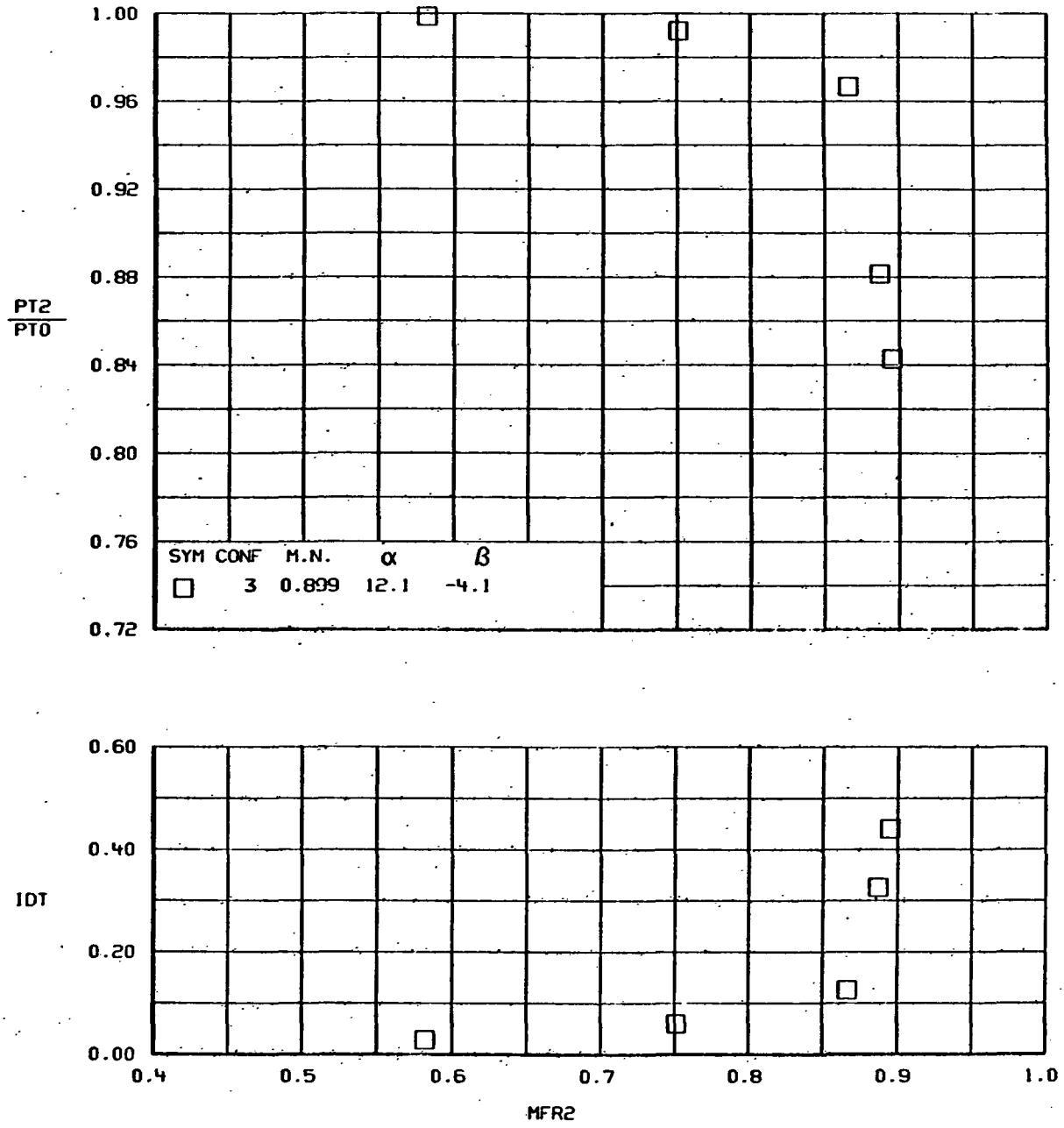

(K)

FIGURE 77.-CONTINUED.

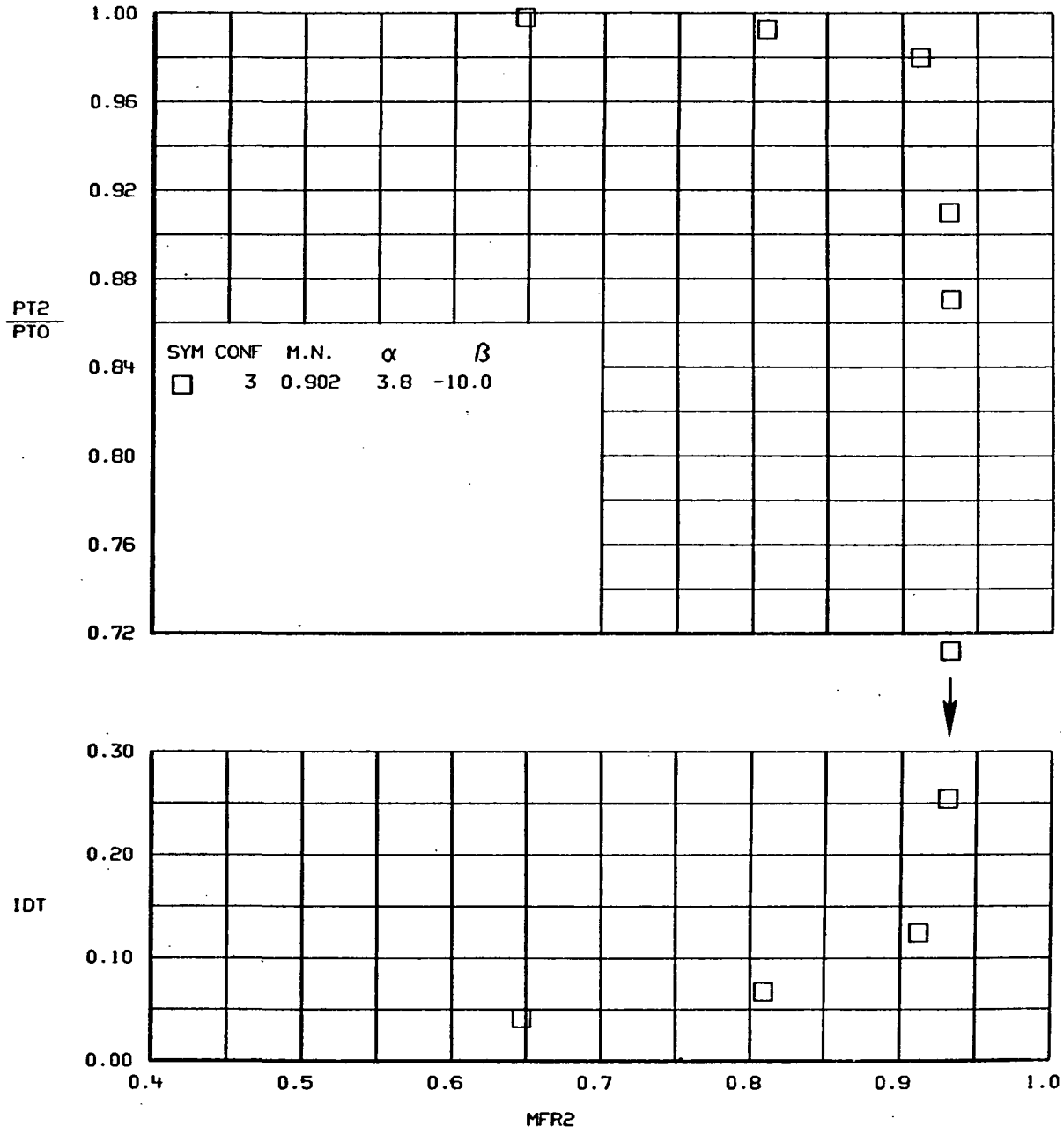

(l)

Figure 77-Continued.

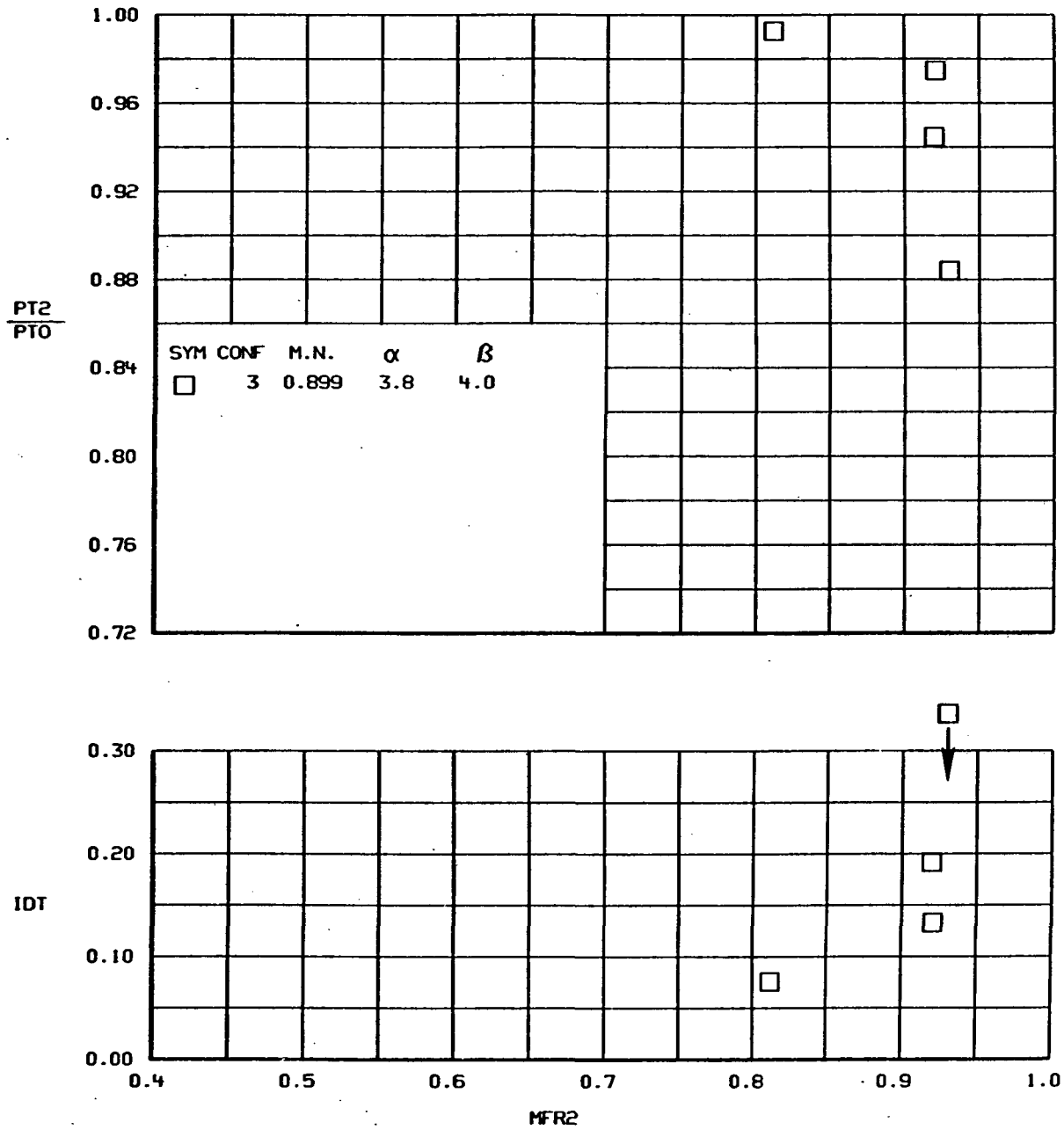

(m)

Figure 77-Continued.

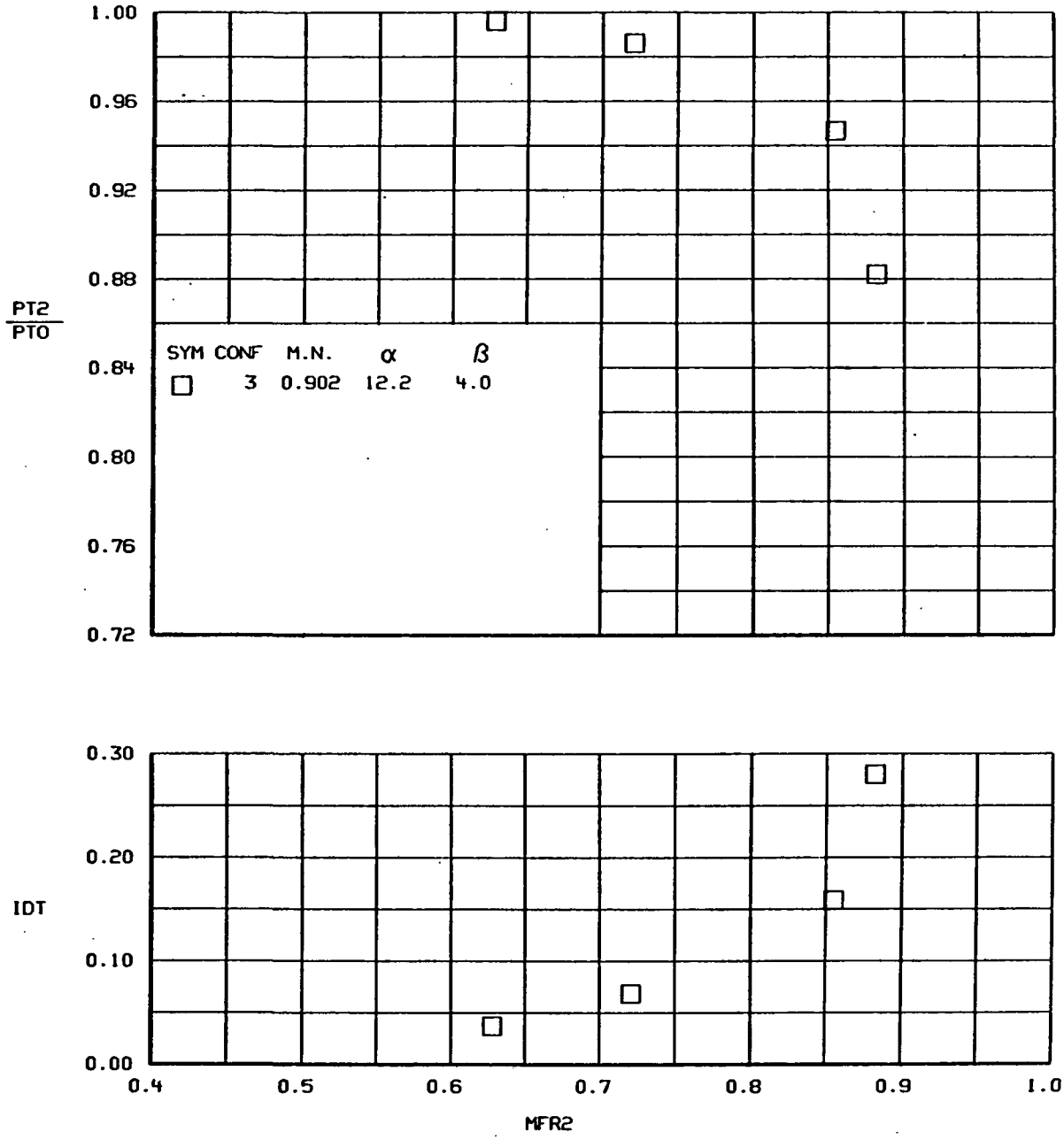

(n)

Figure 77-Continued.

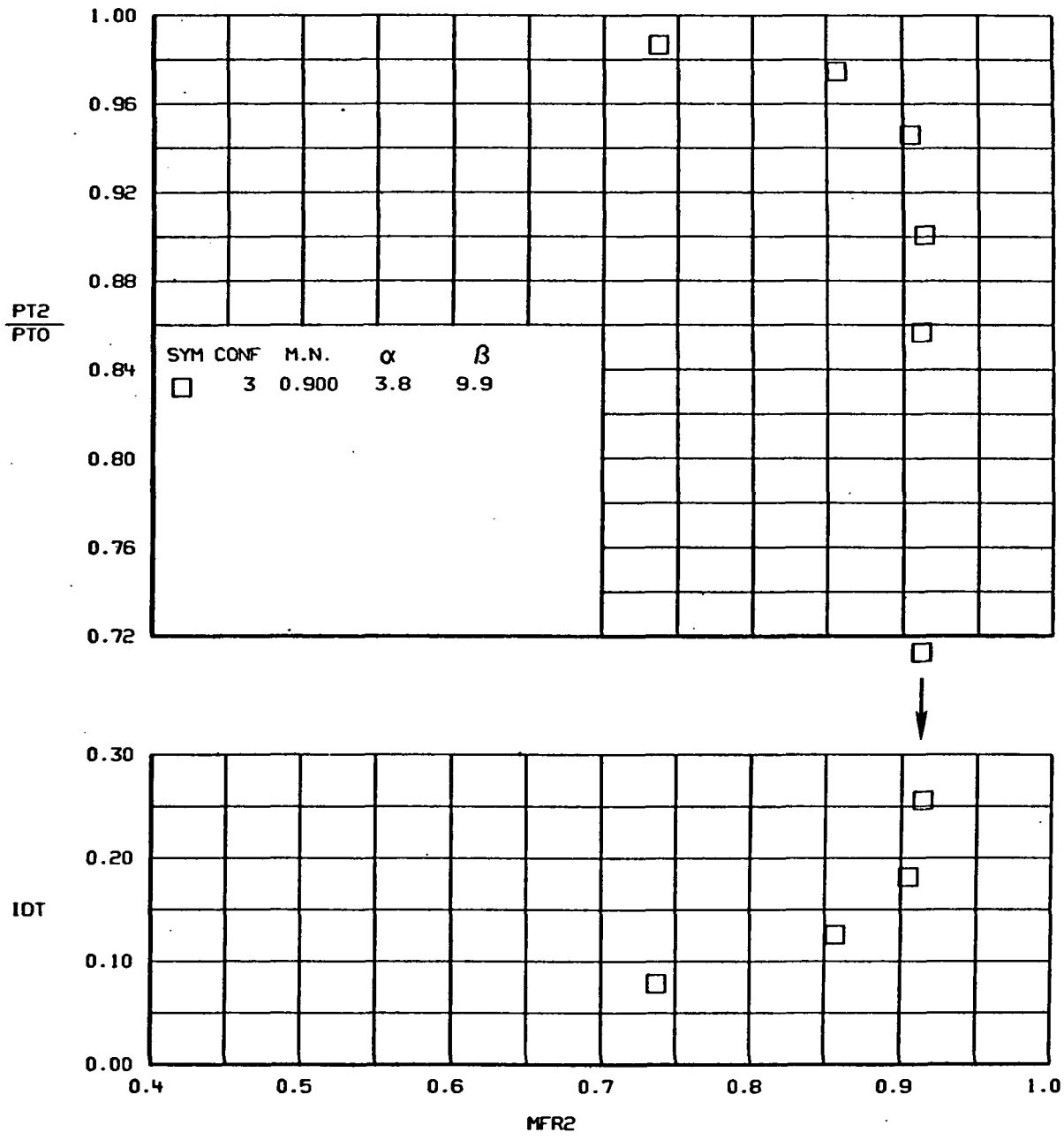

(o)

Figure 77-Concluded.

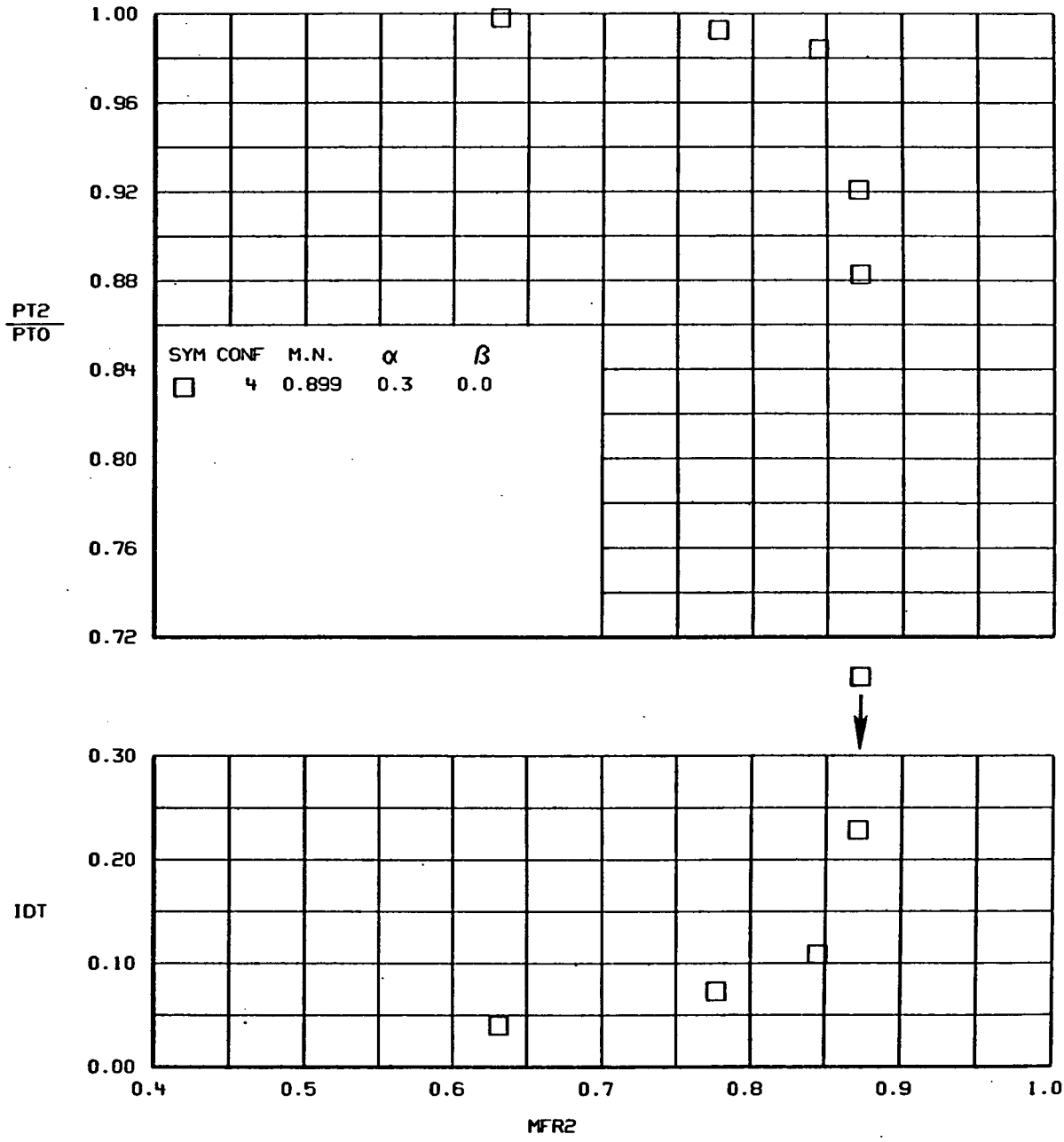

(a)

Figure 78.- TOTAL PRESSURE RECOVERY AND DISTORTION VERSUS MASS FLOW RATIO Configuration 4.

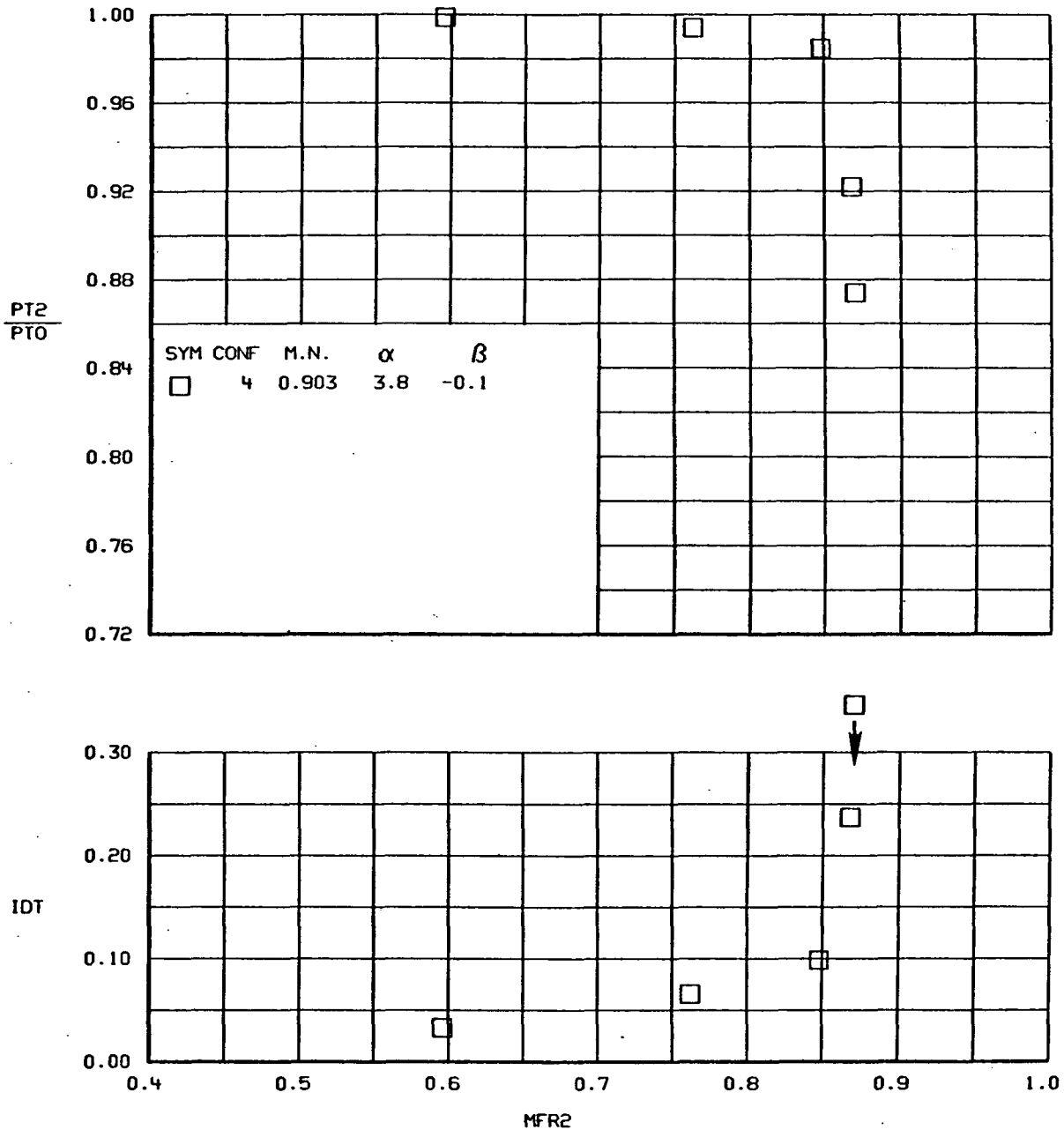

(b)

Figure 78.-Continued.

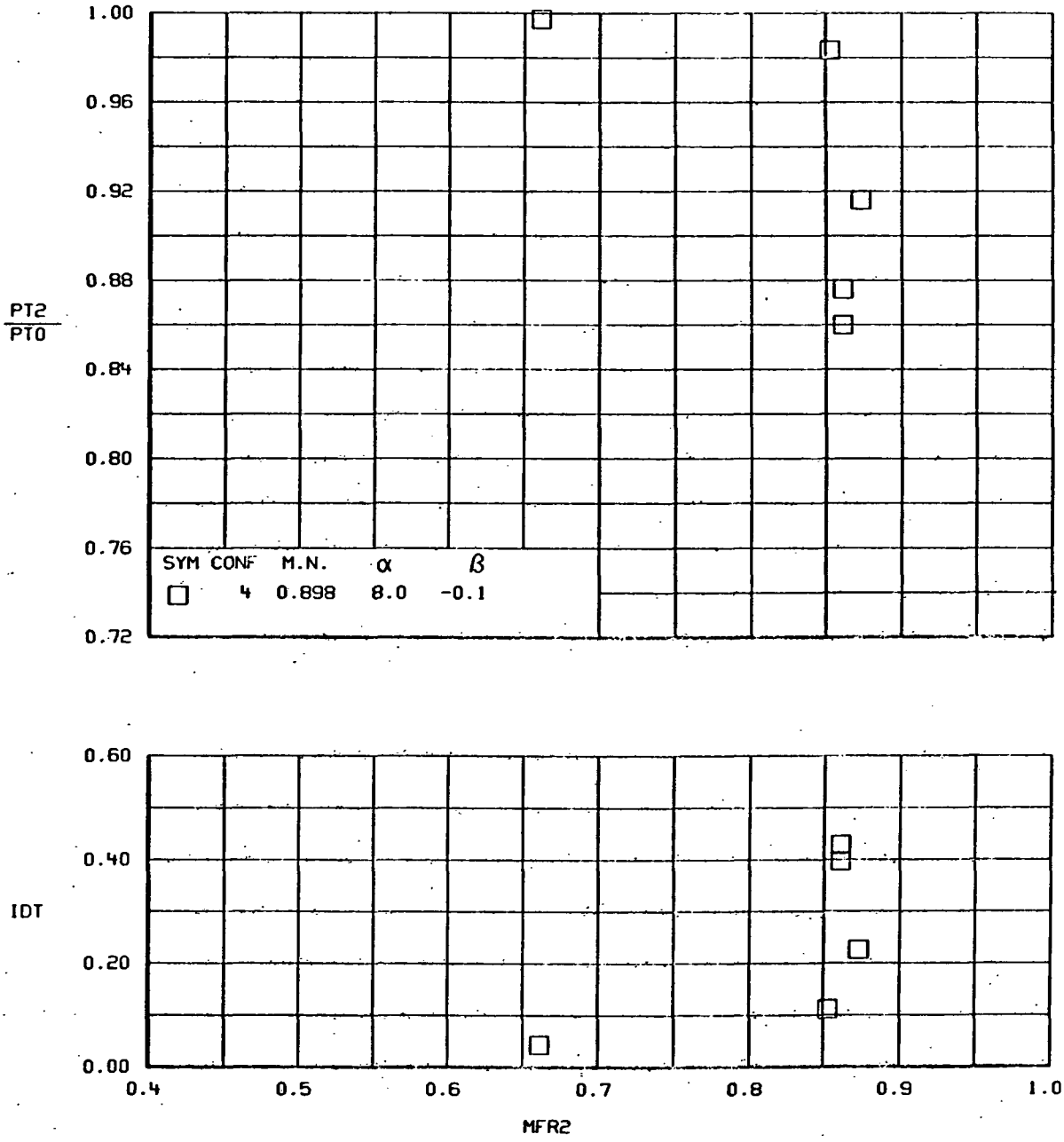

(C)
FIGURE 78.-CONTINUED.

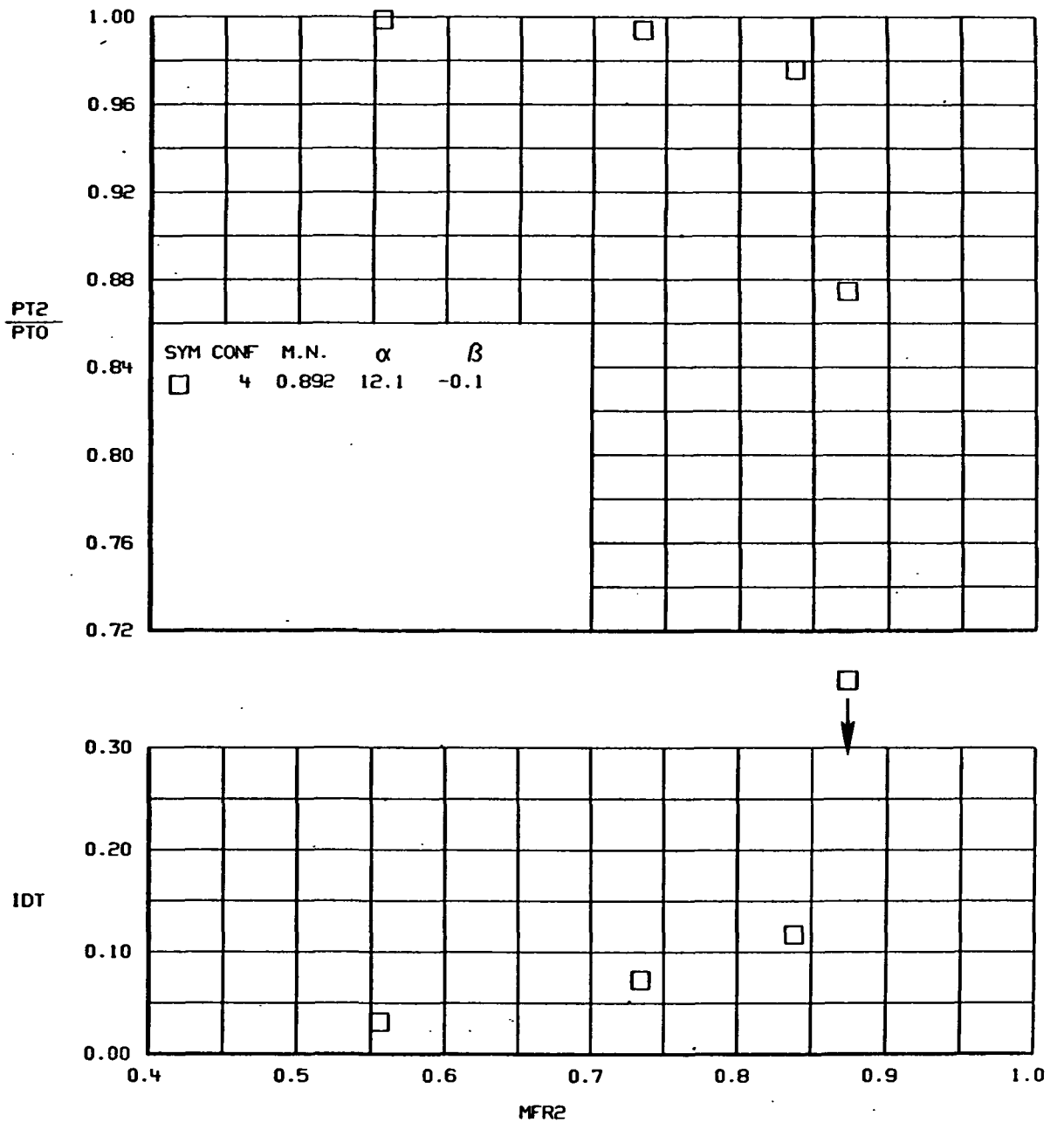

(d)

Figure 78.-Continued.

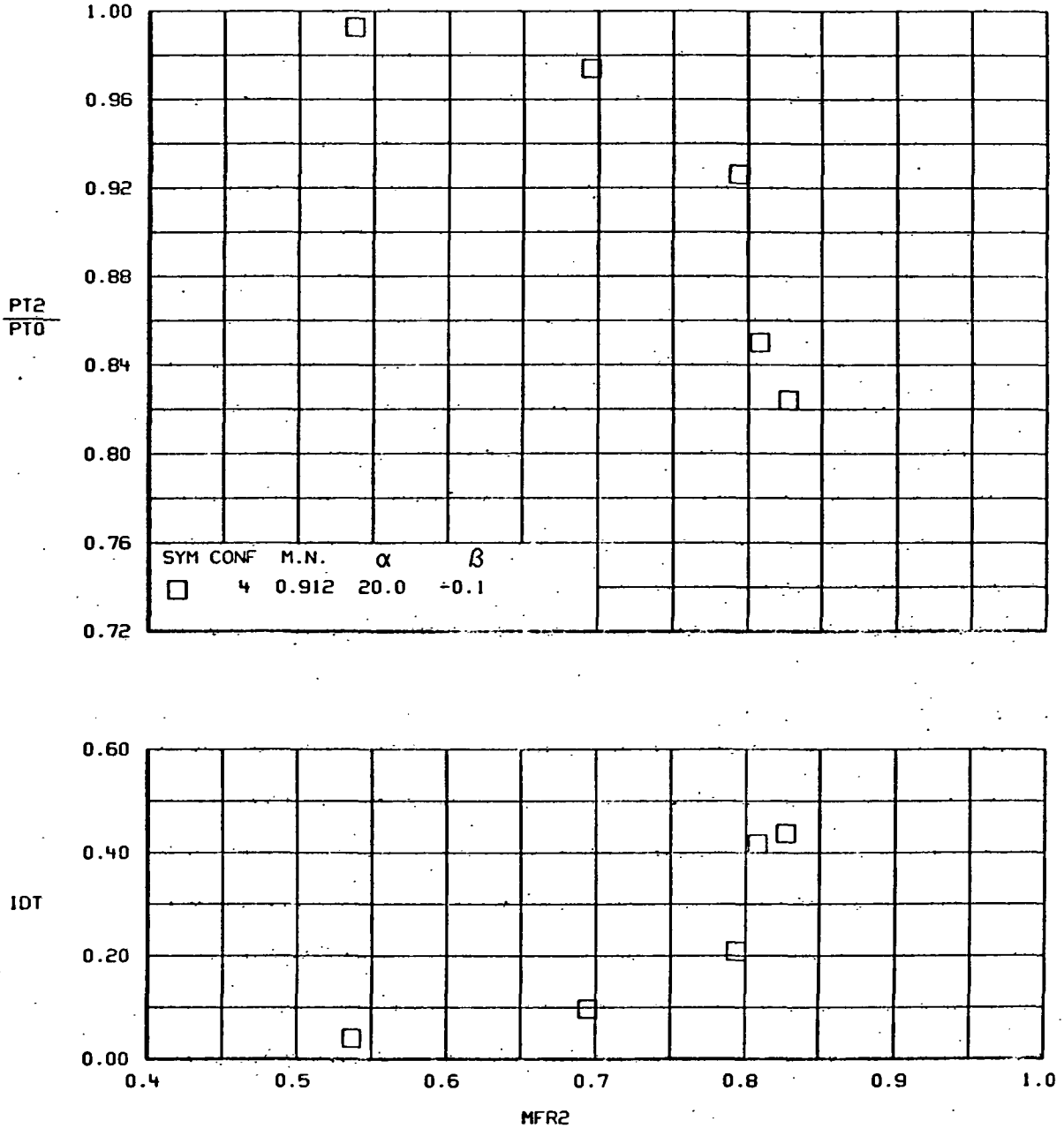

(E)
FIGURE 78.-CONTINUED.

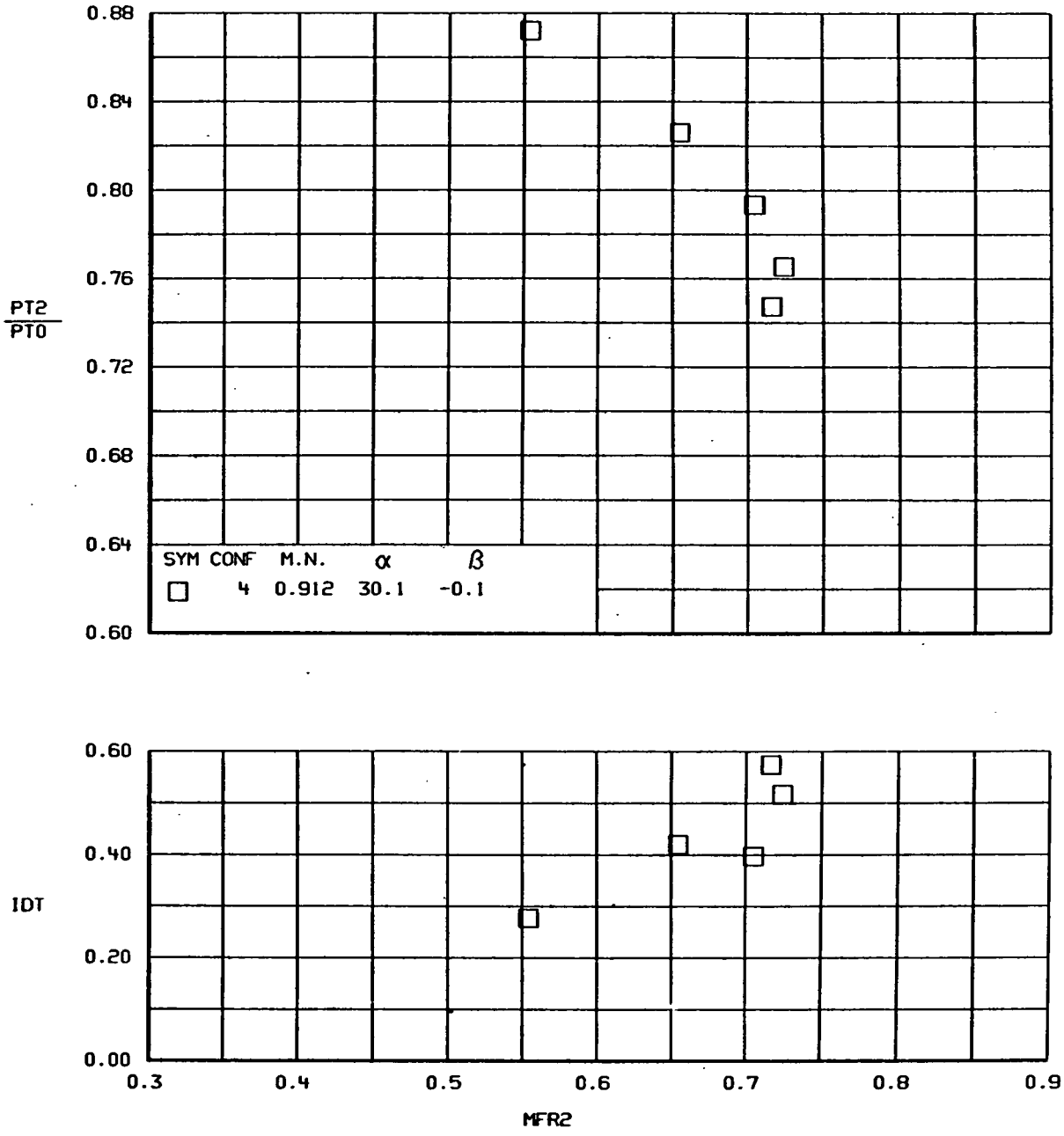

(f)

Figure 78.-Continued.

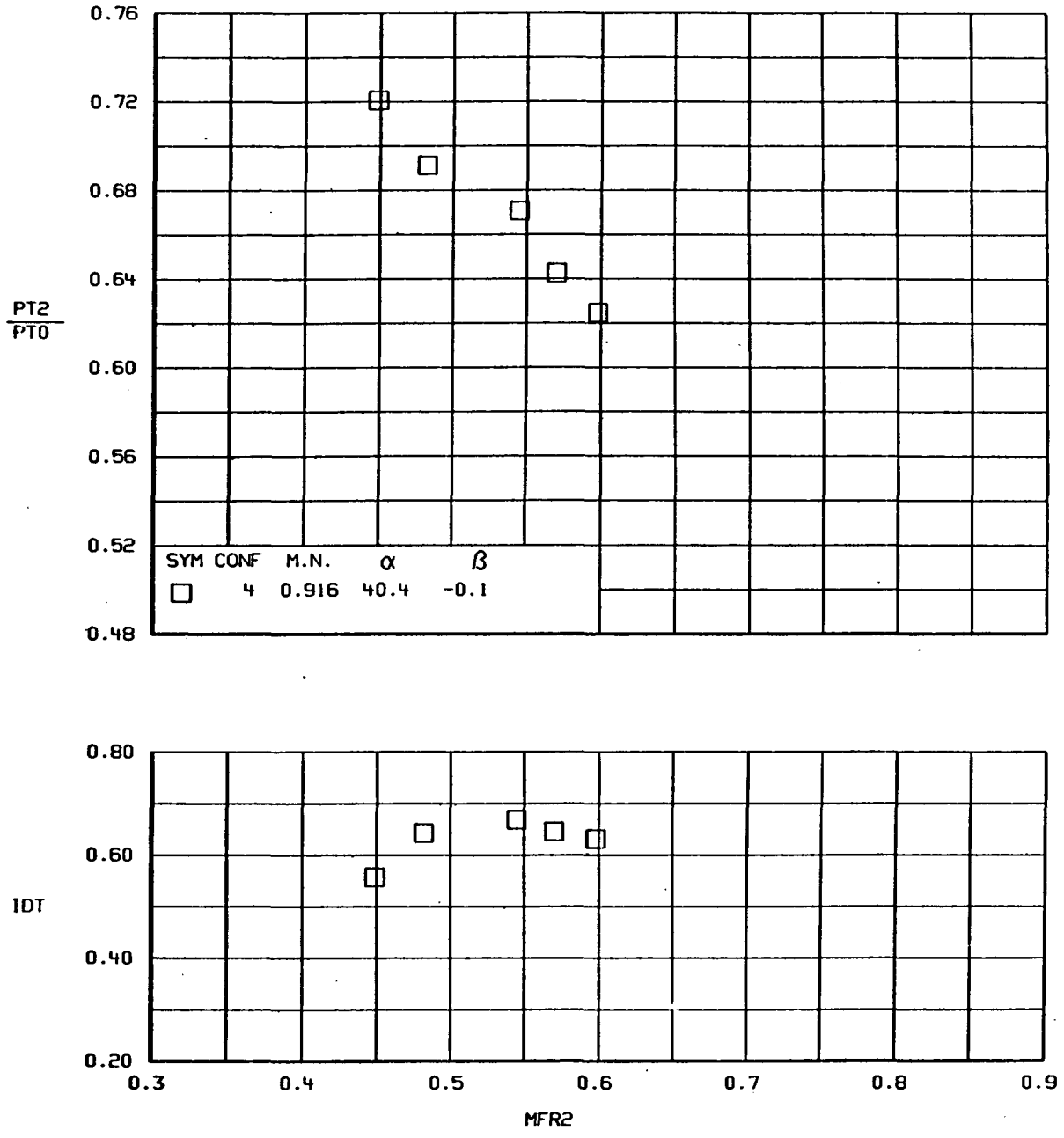

(g)

Figure 78.-Concluded.

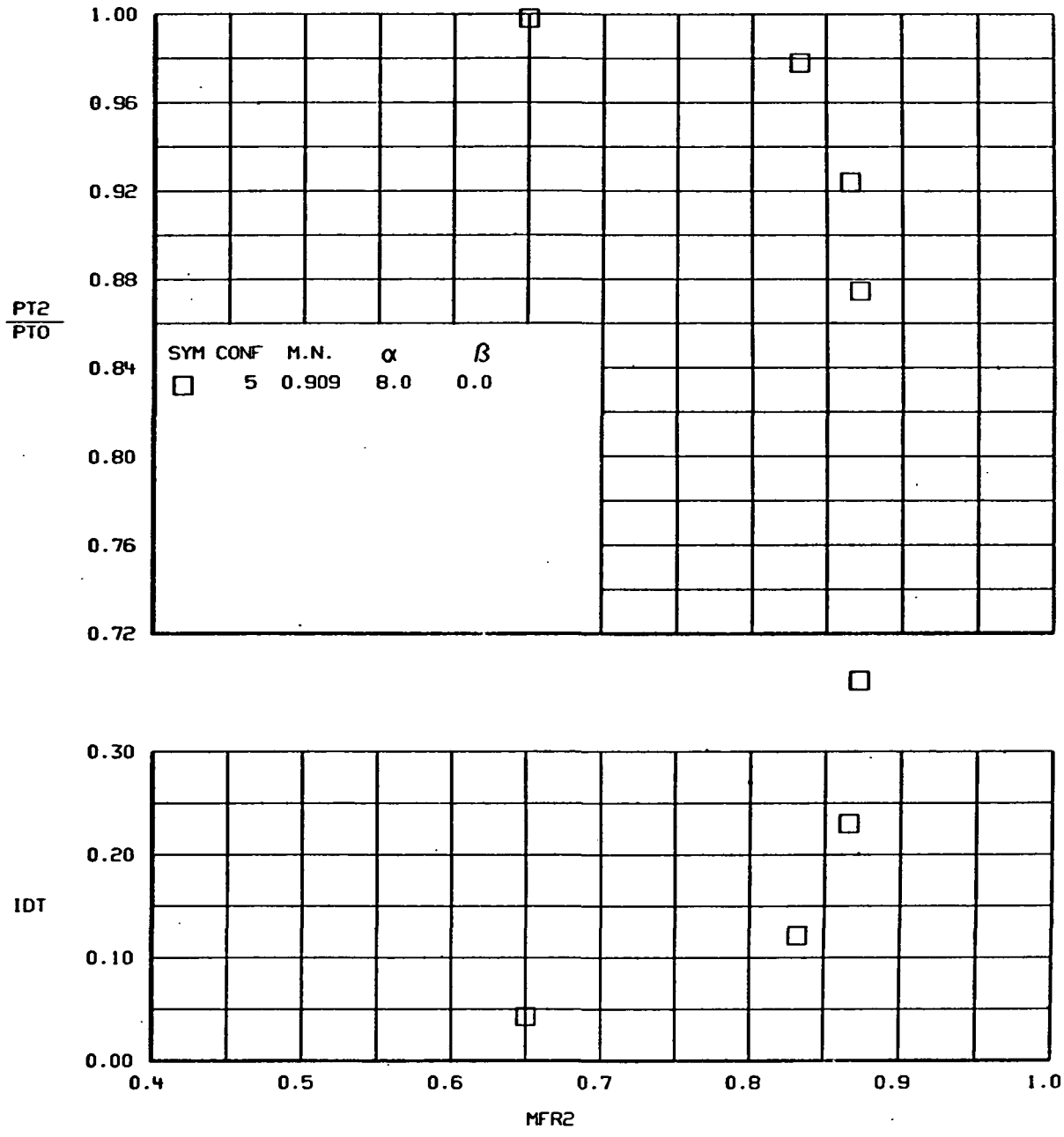

(a)

Figure 79.- TOTAL PRESSURE RECOVERY AND DISTORTION VERSUS MASS FLOW RATIO Configuration 5.

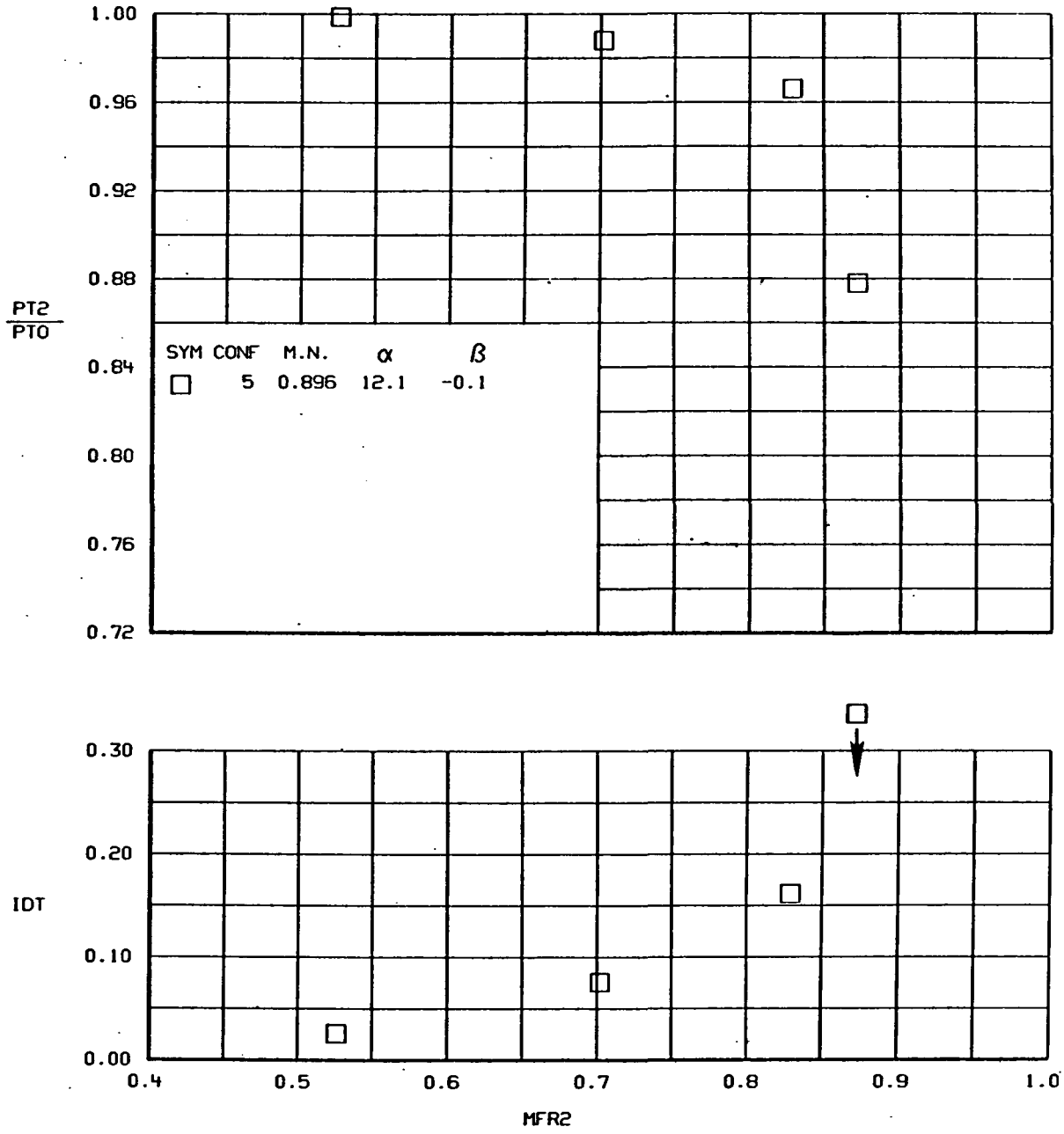

(b)

Figure 79.-Continued.

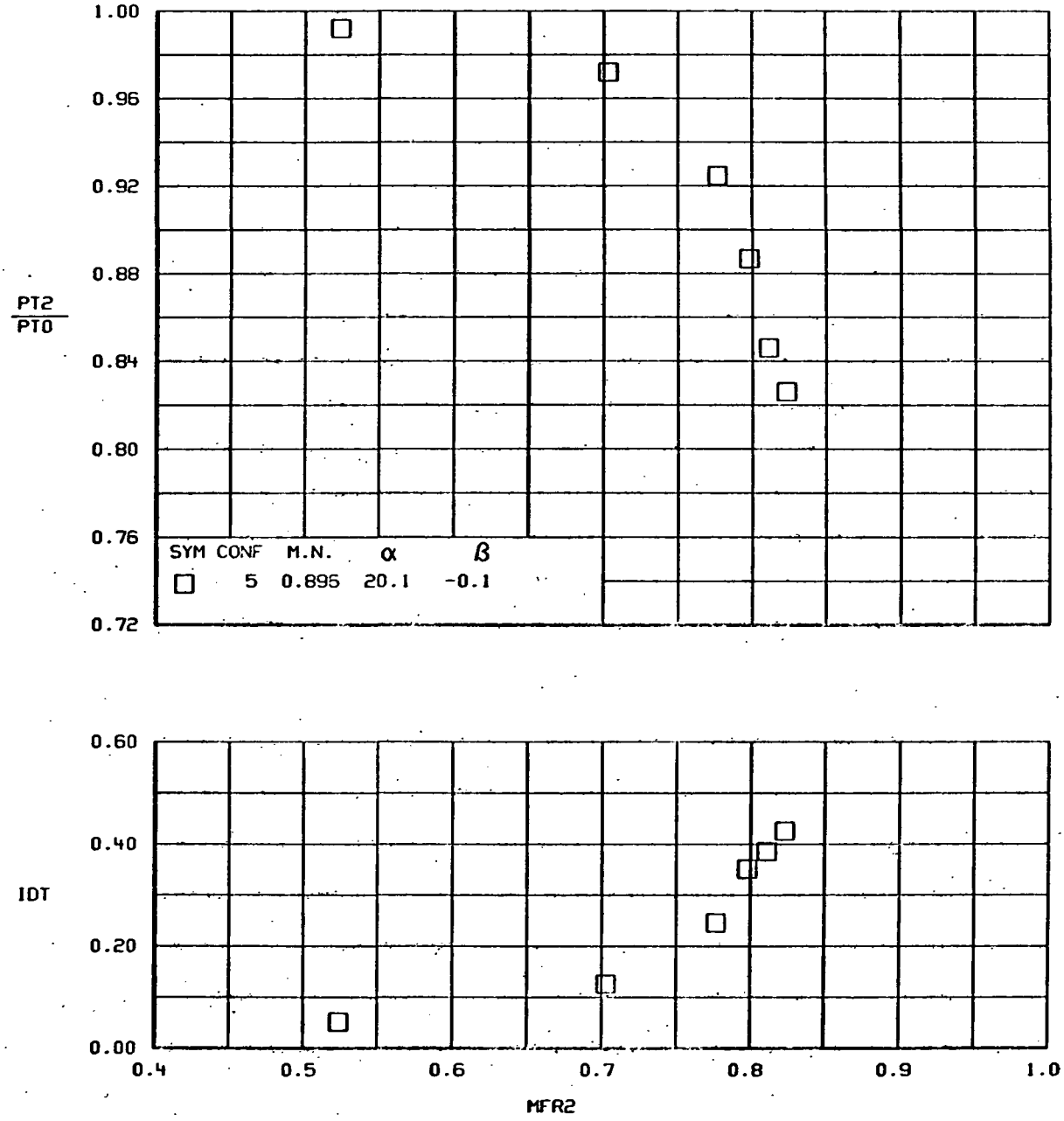

(C)

FIGURE 79.-CONTINUED.

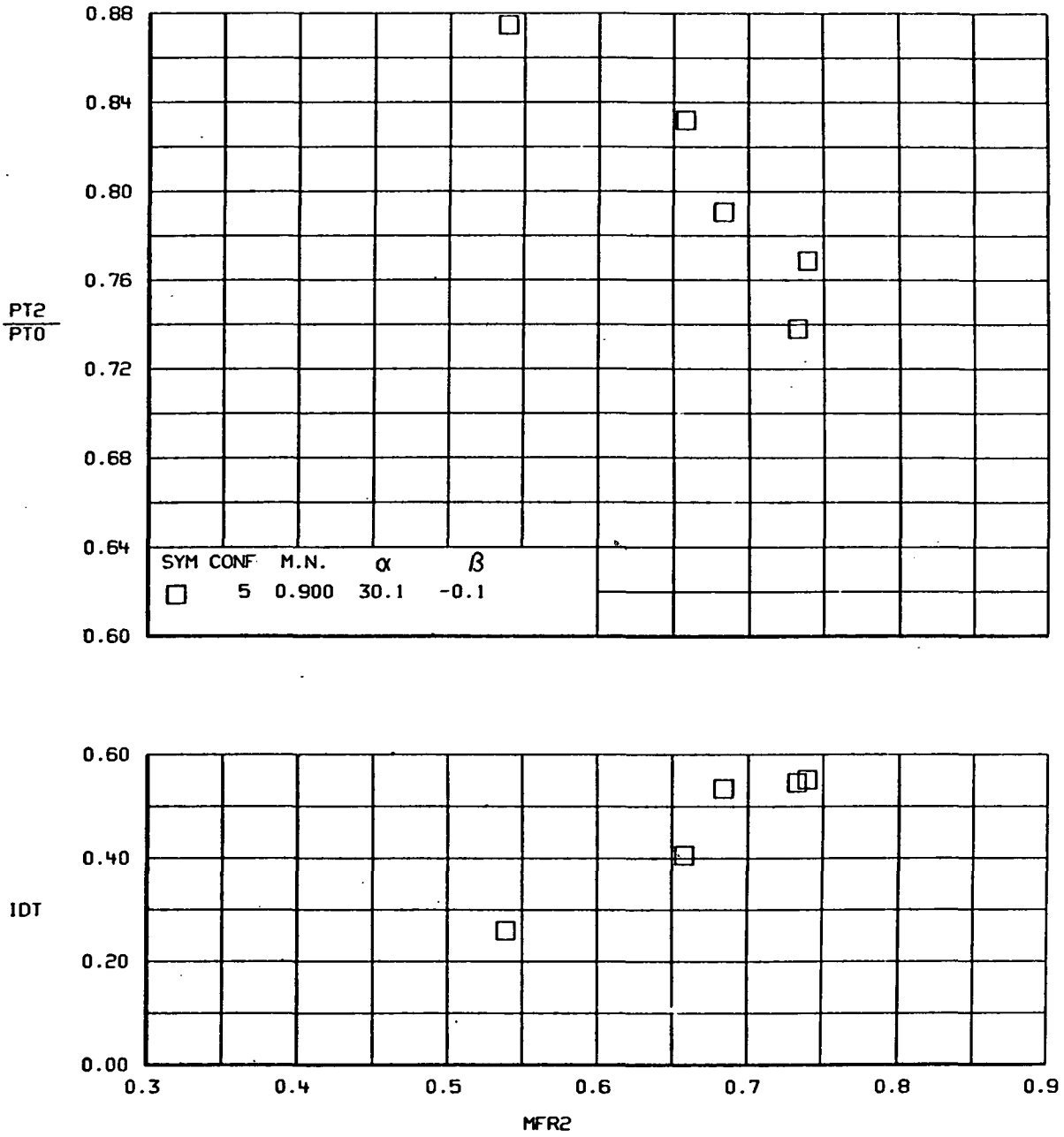

(d)

Figure 79.-Continued.

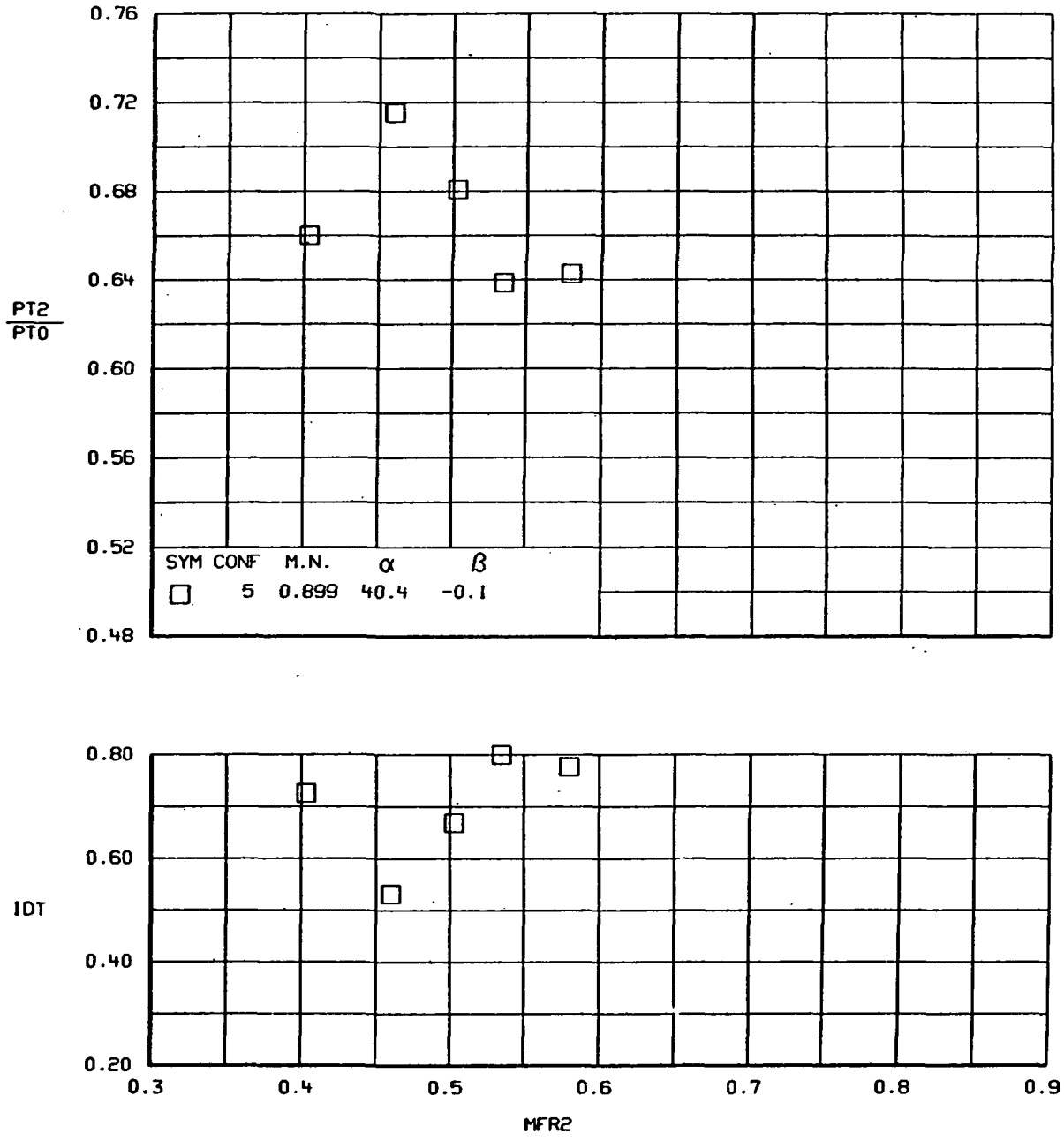

(e)

Figure 79.-Concluded.

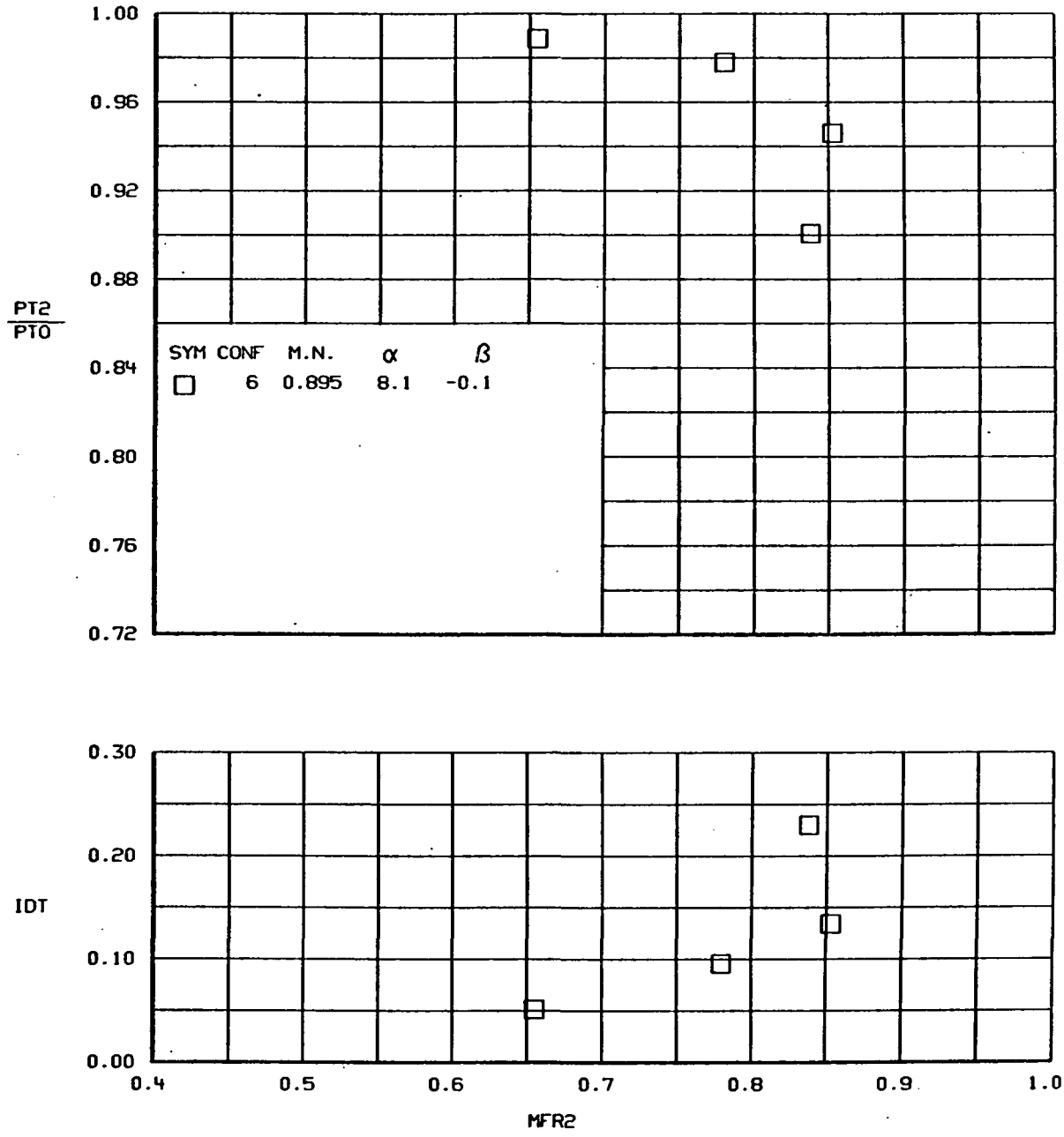

(a)

Figure 80.- TOTAL PRESSURE RECOVERY AND DISTORTION VERSUS MASS FLOW RATIO Configuration 6.

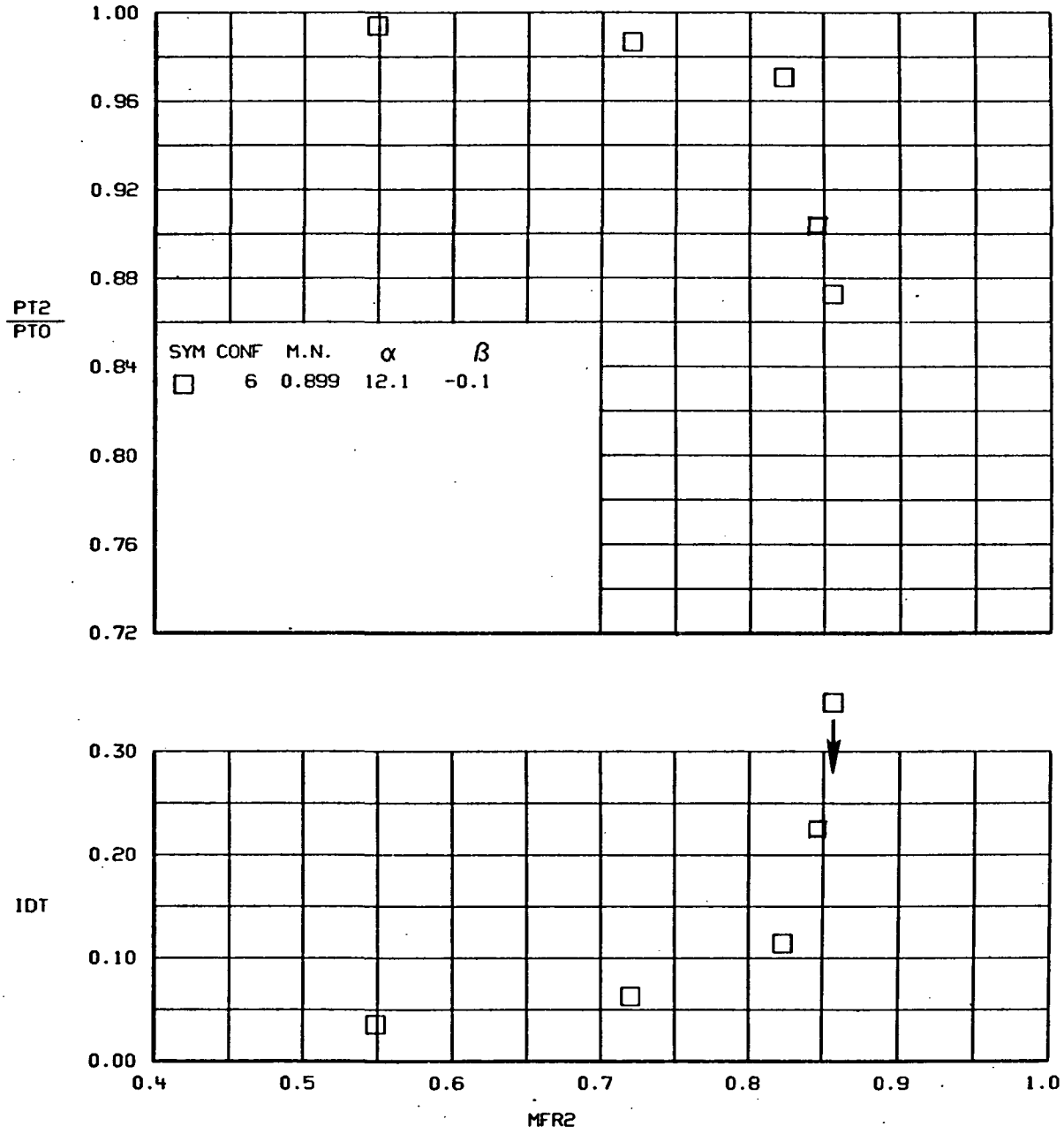

(b)

Figure 80.-Continued.

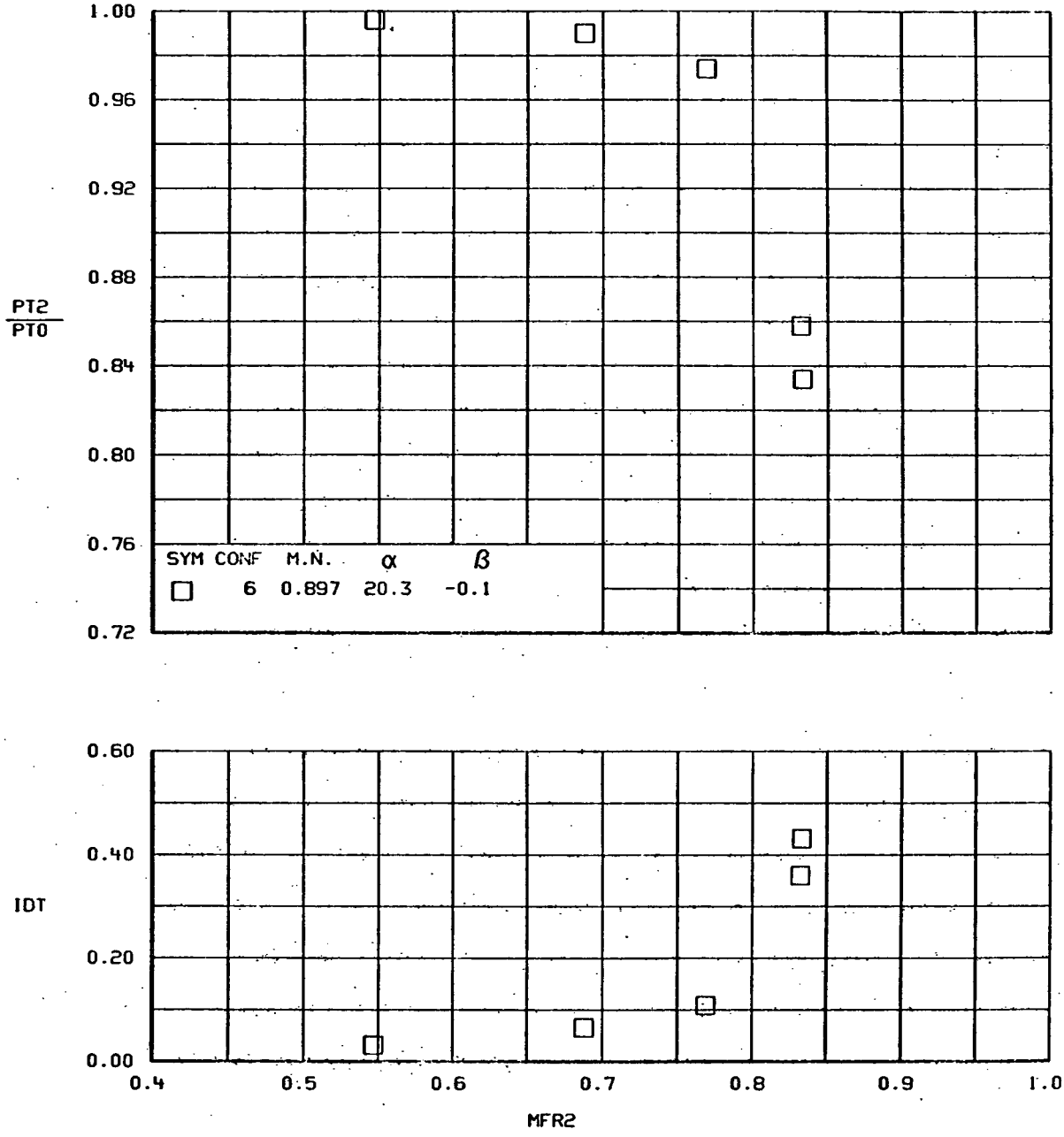

(C)
FIGURE 80.-CONTINUED.

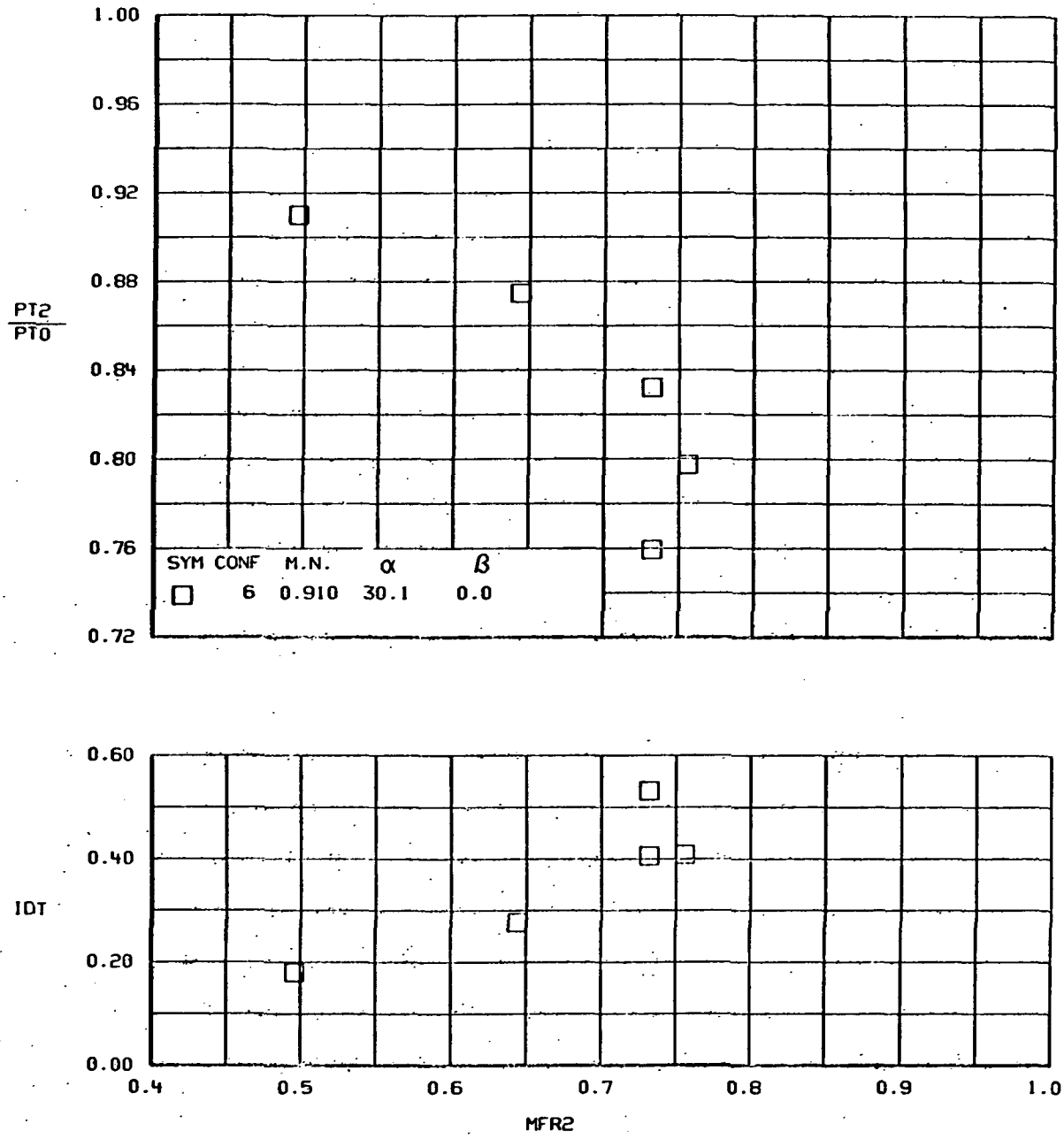

(D)
FIGURE 80.-CONTINUED.

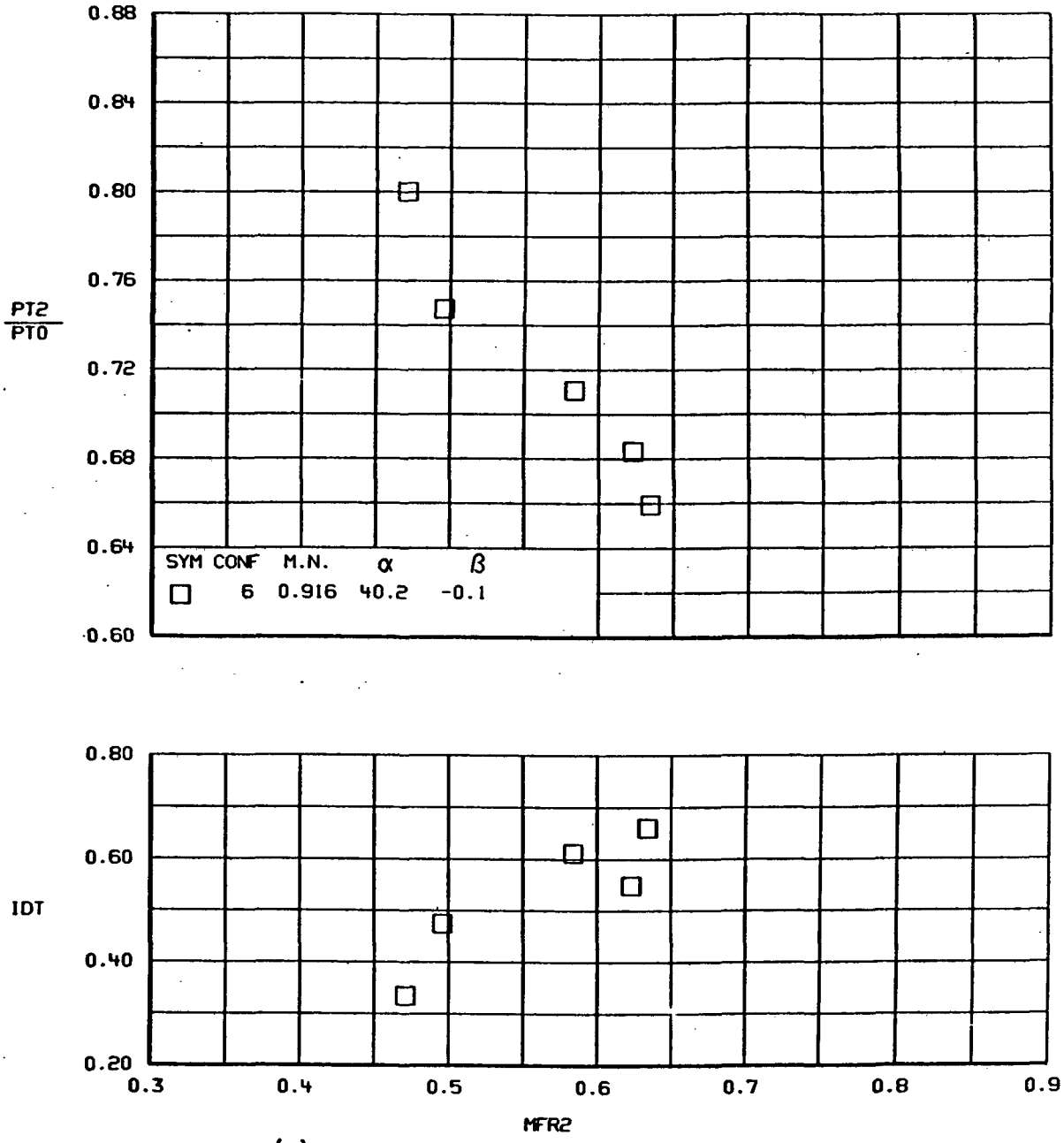

(e)

Figure 80.-Continued.

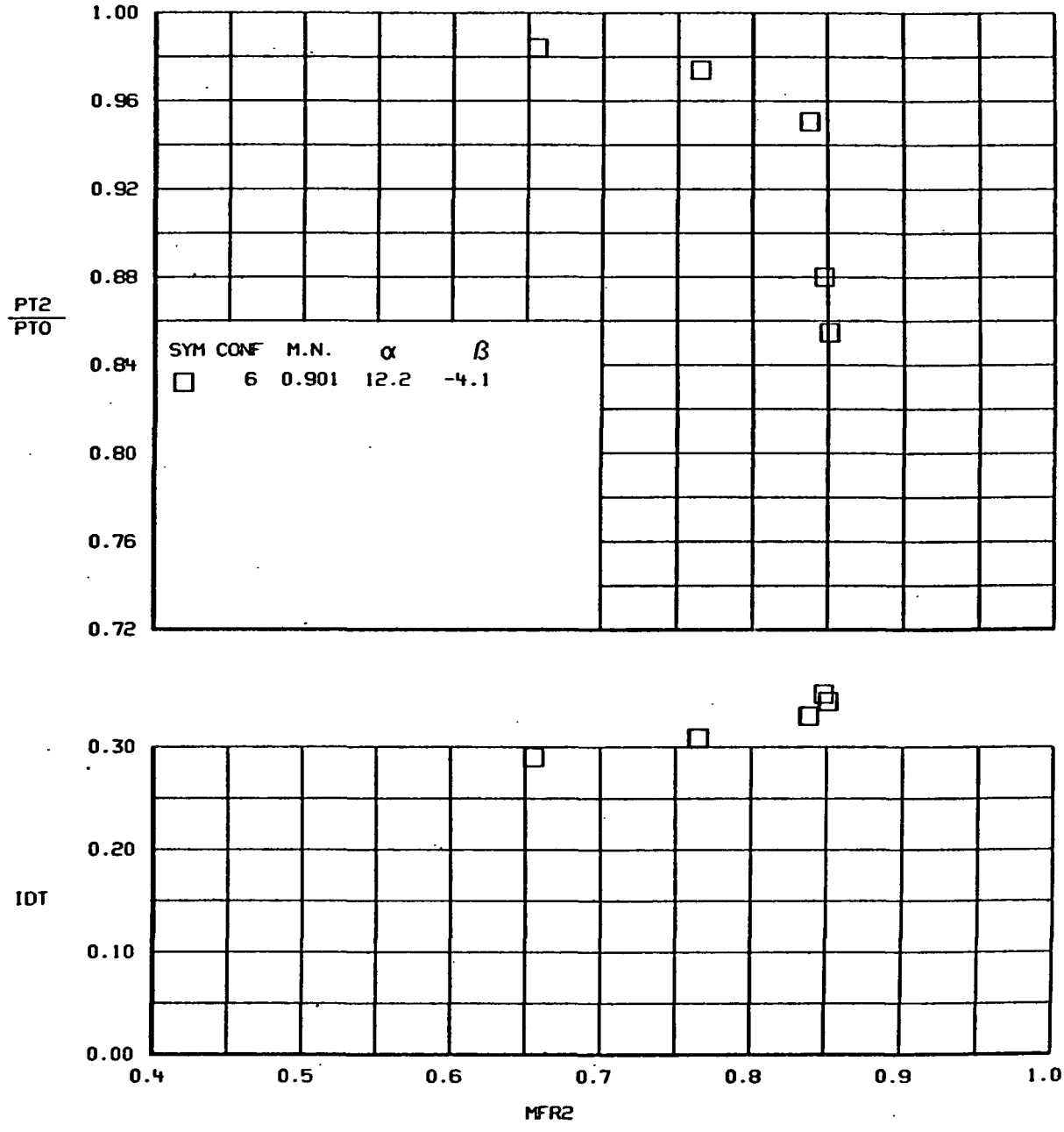

(f)

Figure 80.-Continued.

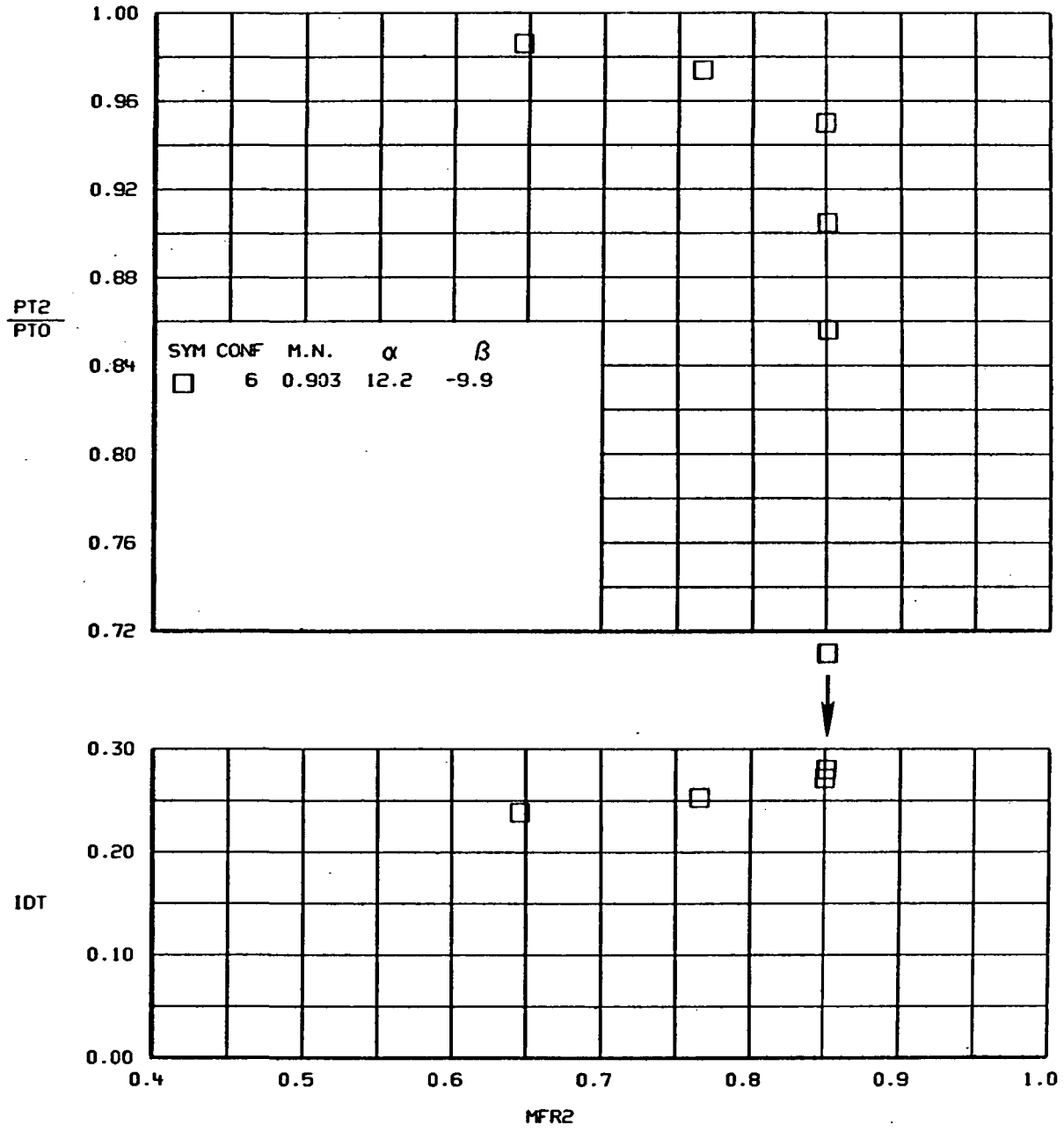

(g)

Figure 80.-Continued.

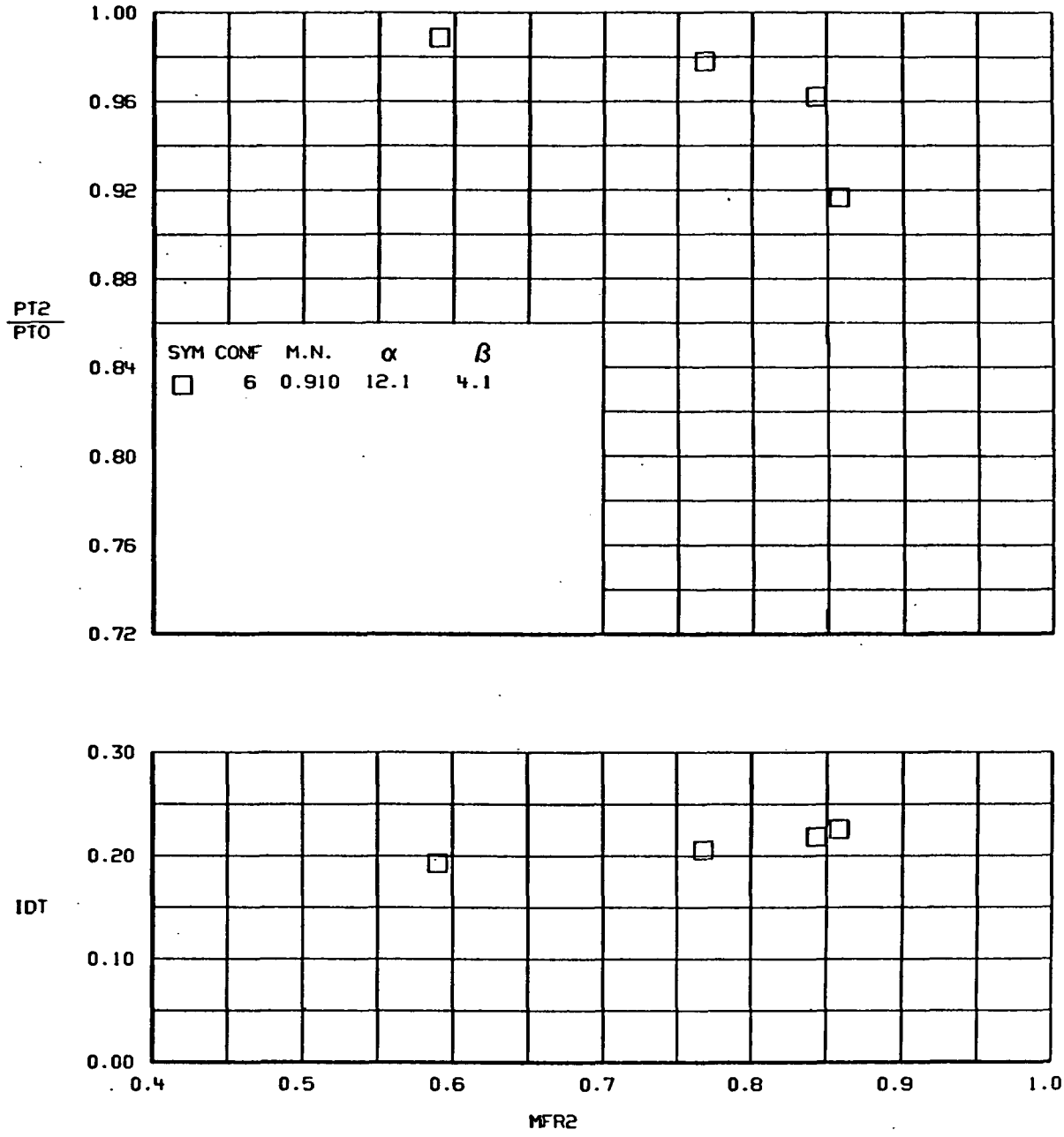

(h)

Figure 80.-Continued.

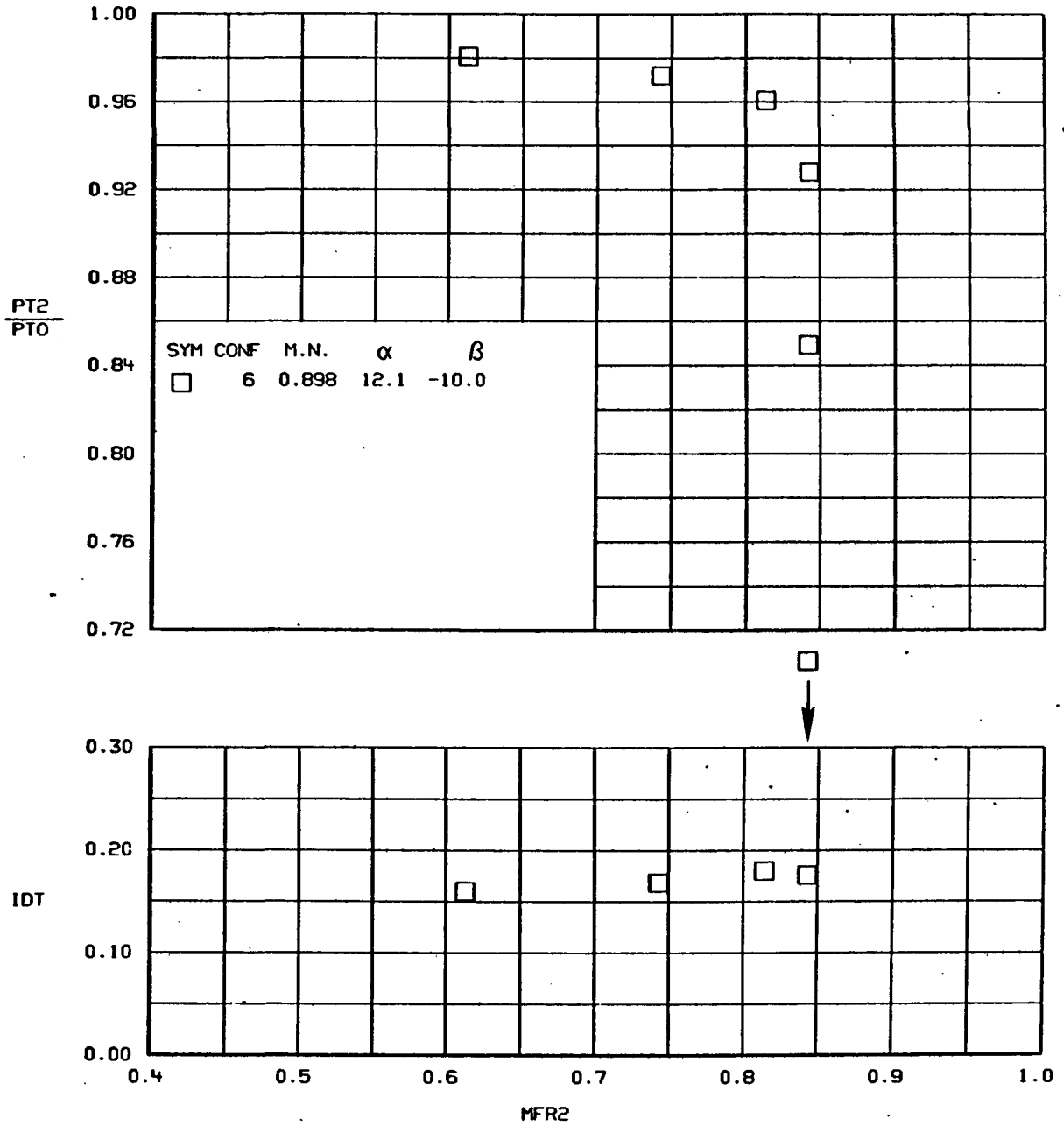

(i)

Figure 80.-Concluded.

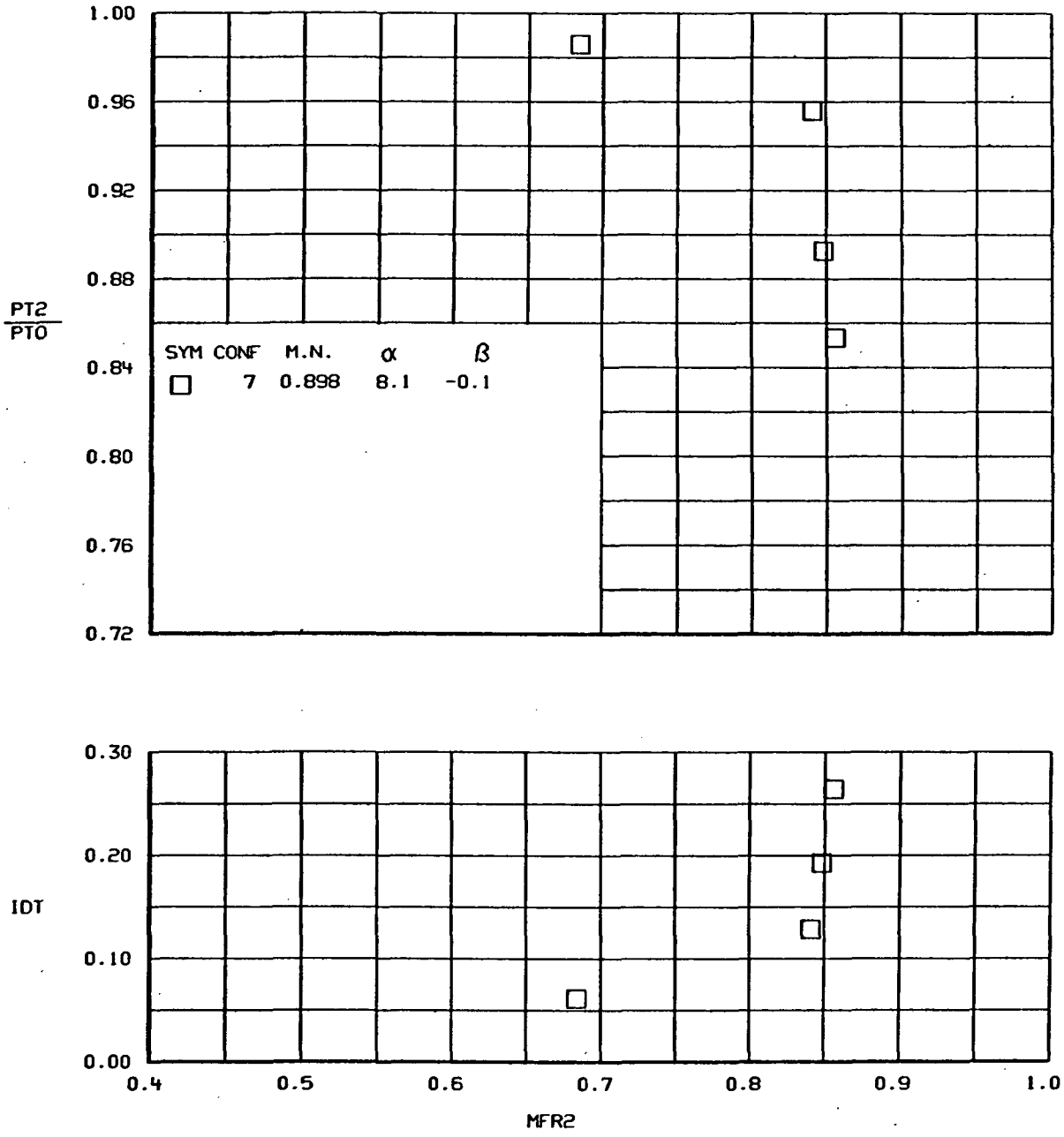

(a)

Figure 81.- TOTAL PRESSURE RECOVERY AND DISTORTION VERSUS MASS FLOW RATIO - Configuration 7.

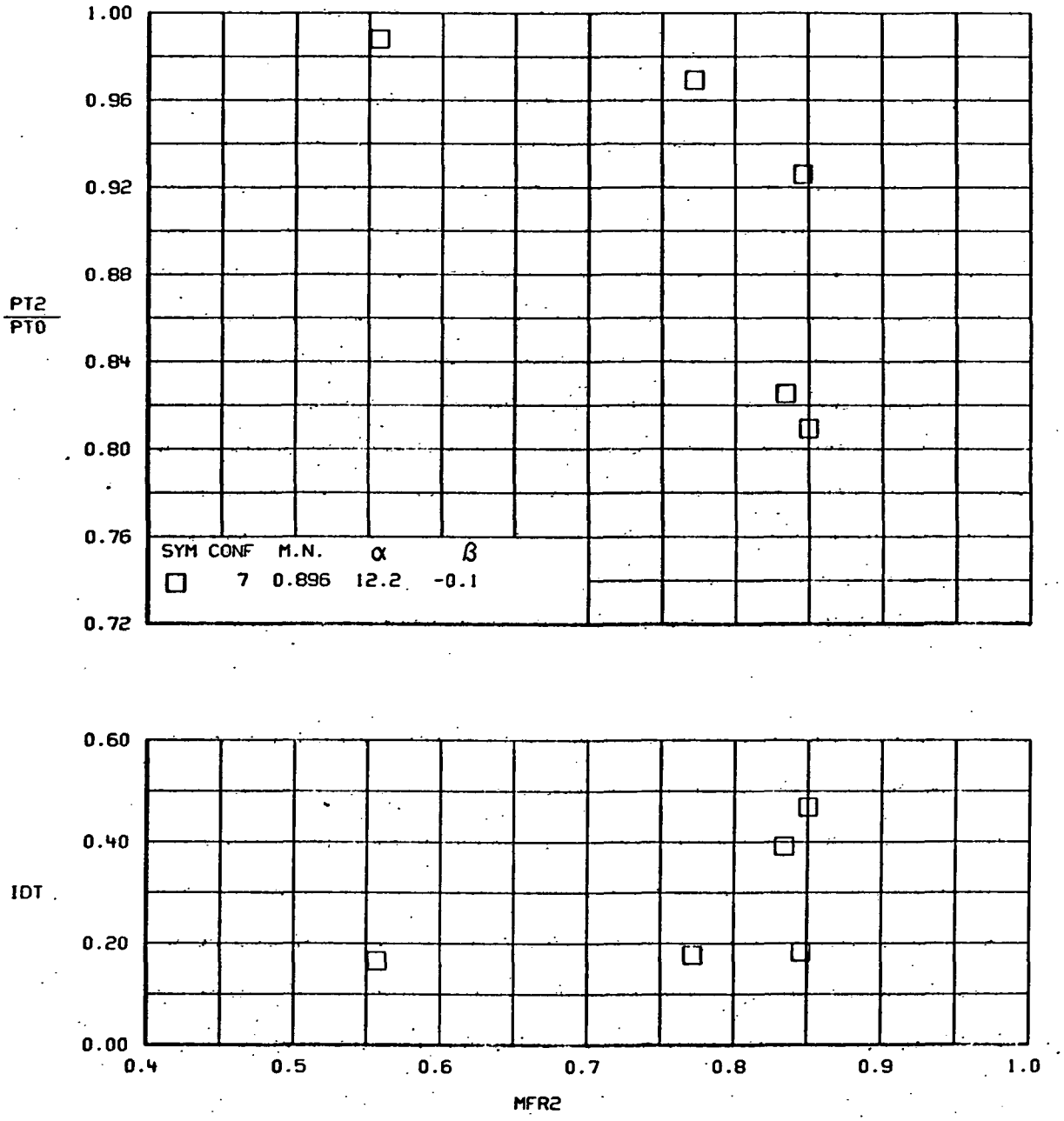

(B)
FIGURE 81.-CONTINUED.

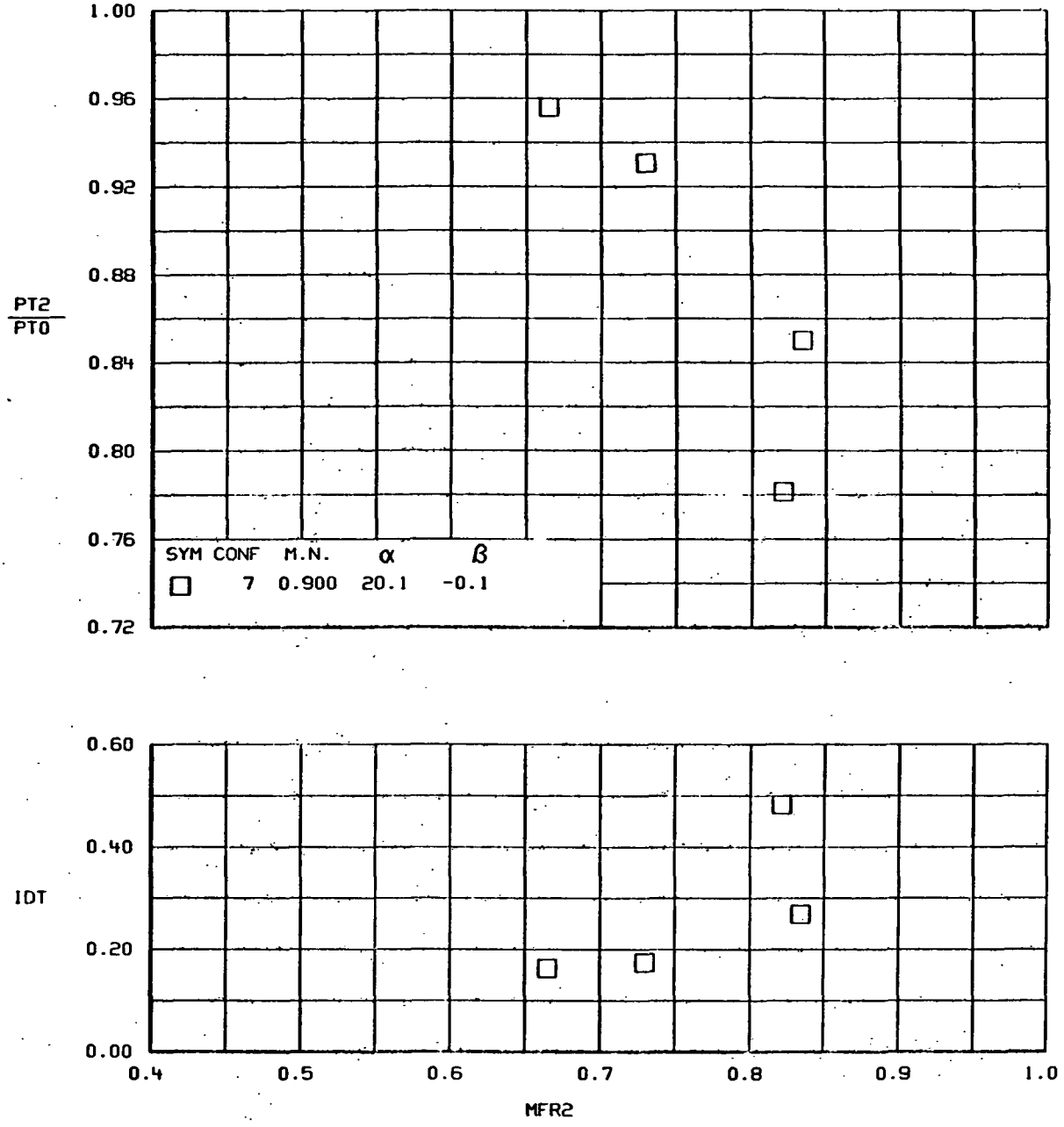

(C)
FIGURE 81.-CONTINUED.

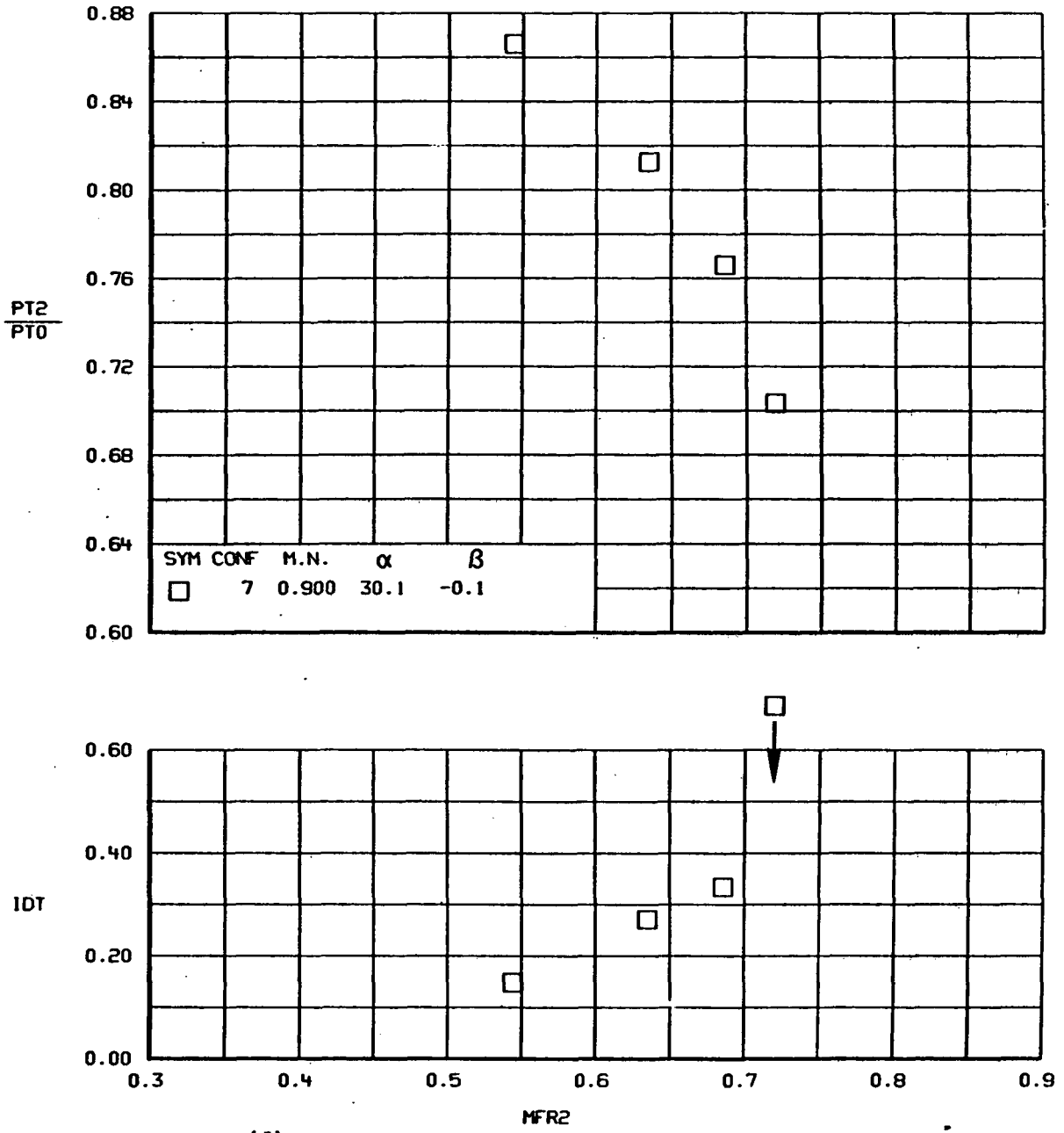

(d)

Figure 81.-Continued.

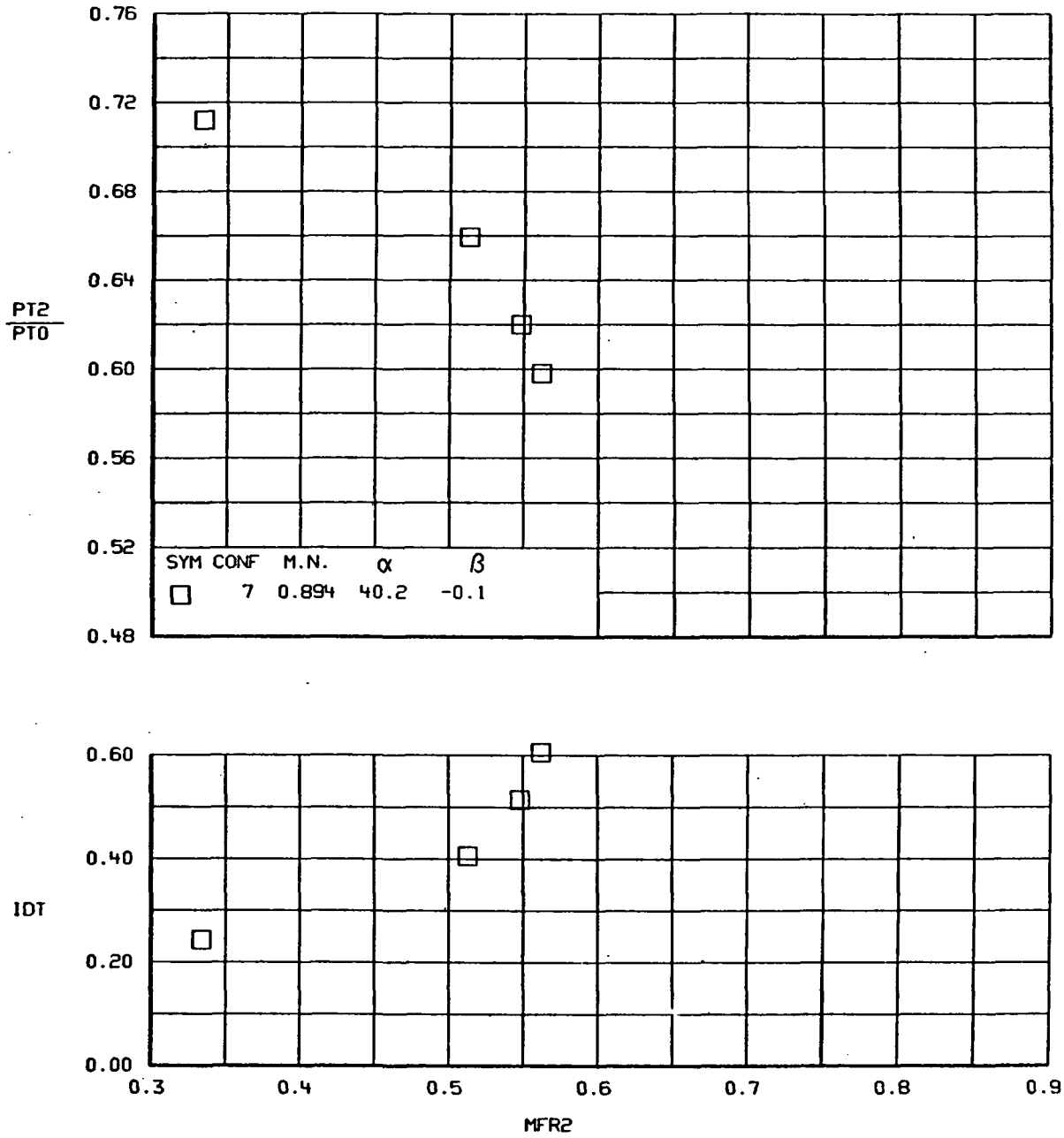

(e)

Figure 81.-Continued.

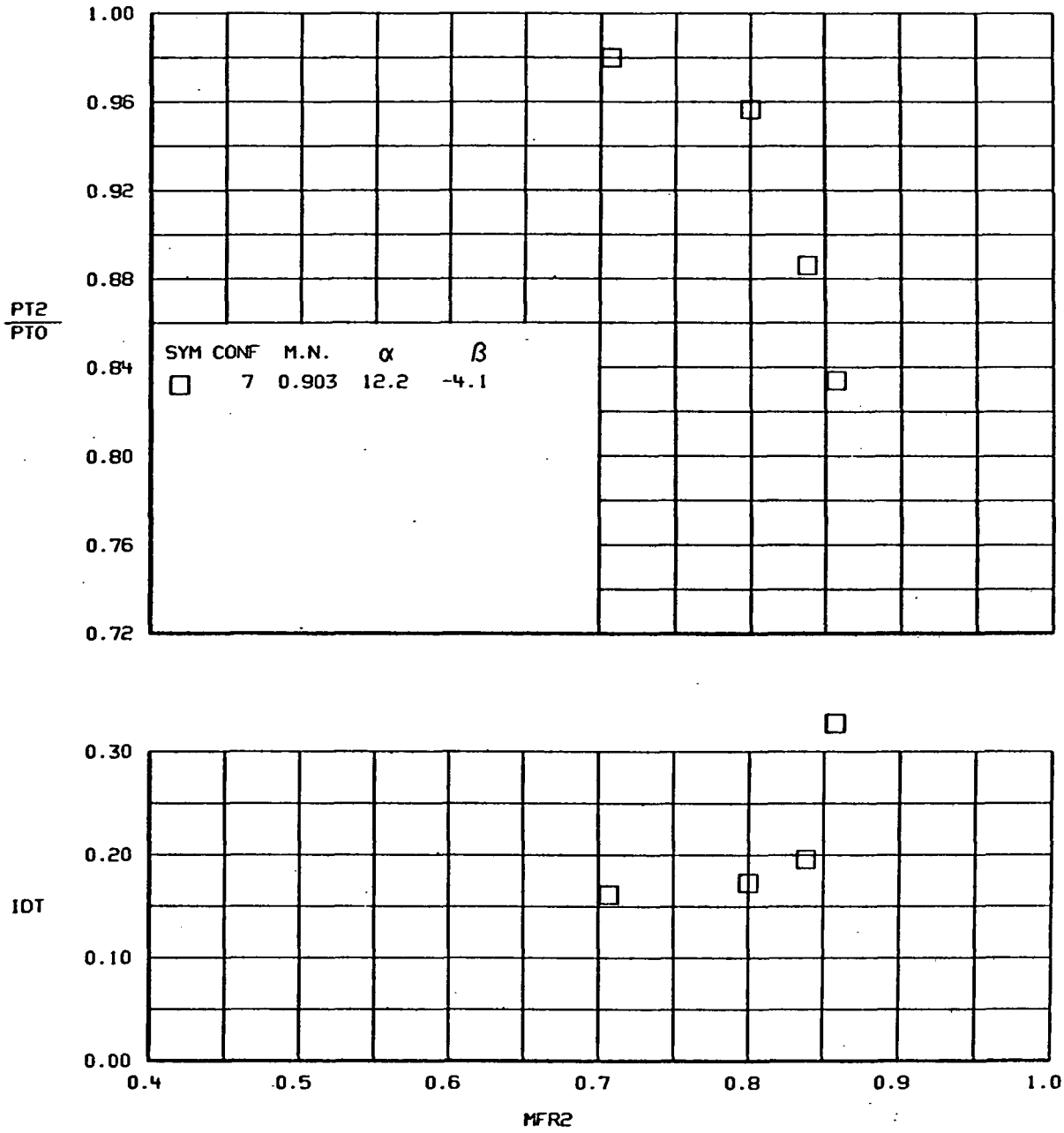

(f)

Figure 81.-Continued.

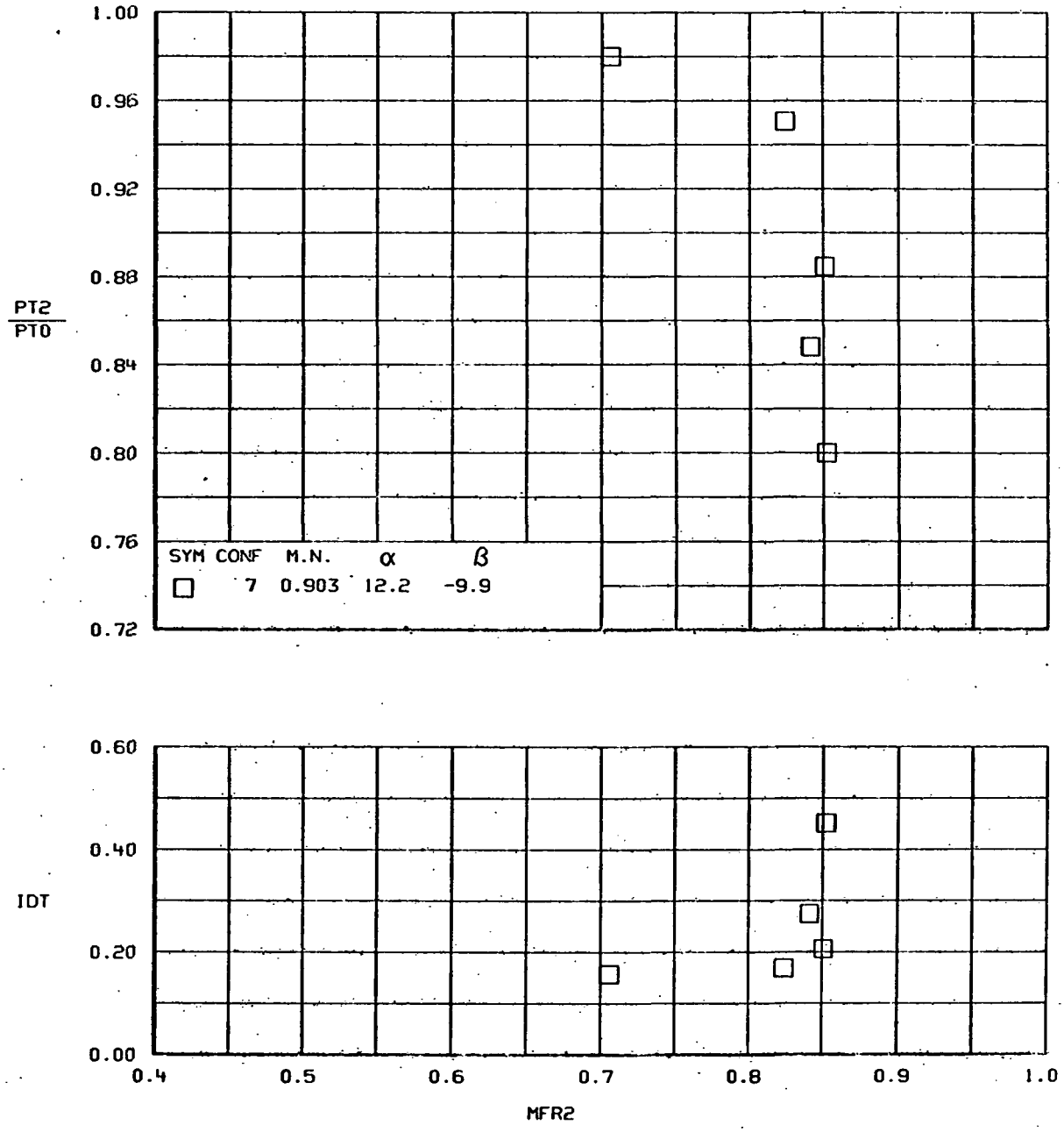

(G)
FIGURE 81.-CONCLUDED.

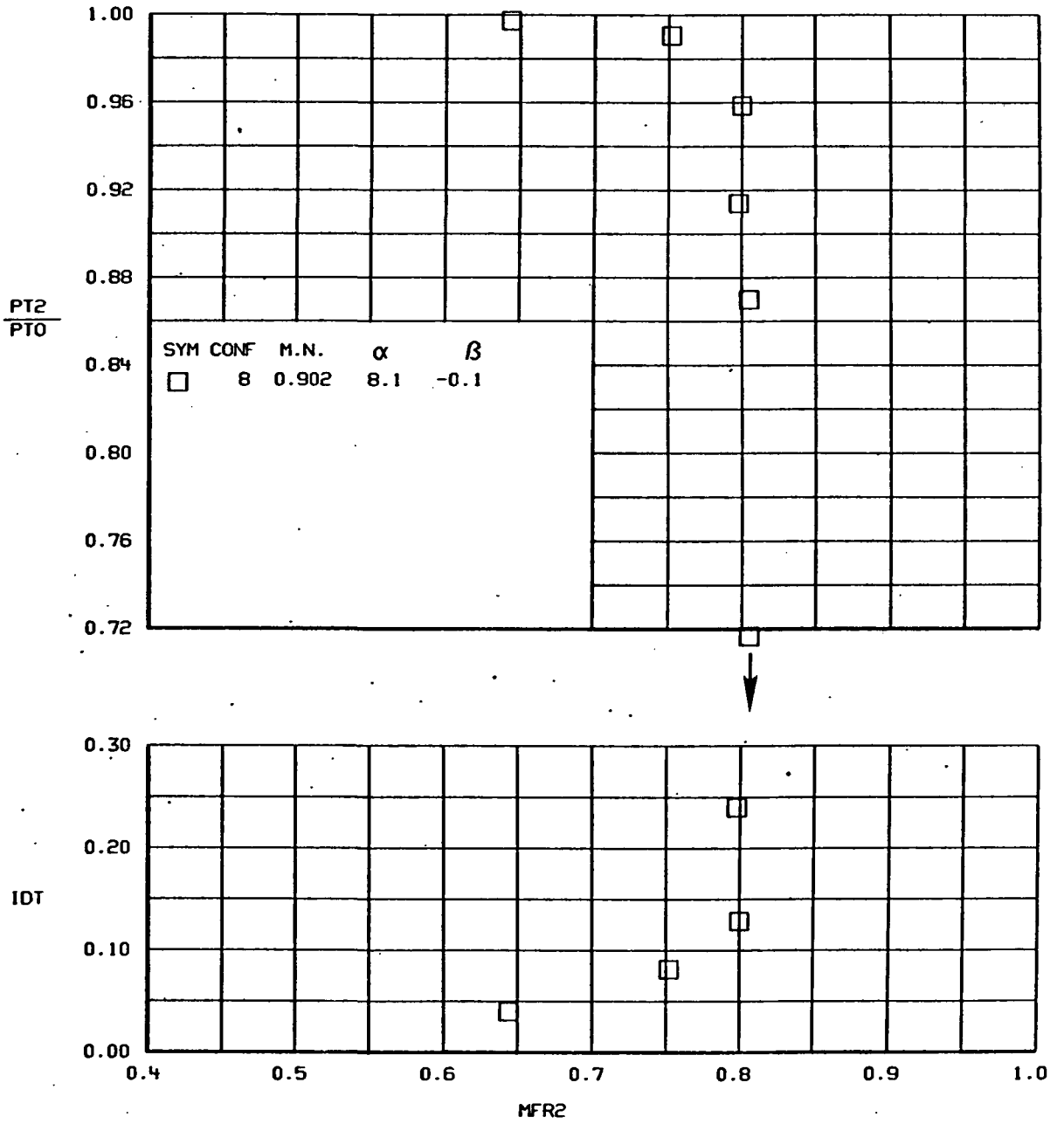

(a)

Figure 82.- TOTAL PRESSURE RECOVERY AND DISTORTION VERSUS MASS FLOW RATIO. Configuration 8.

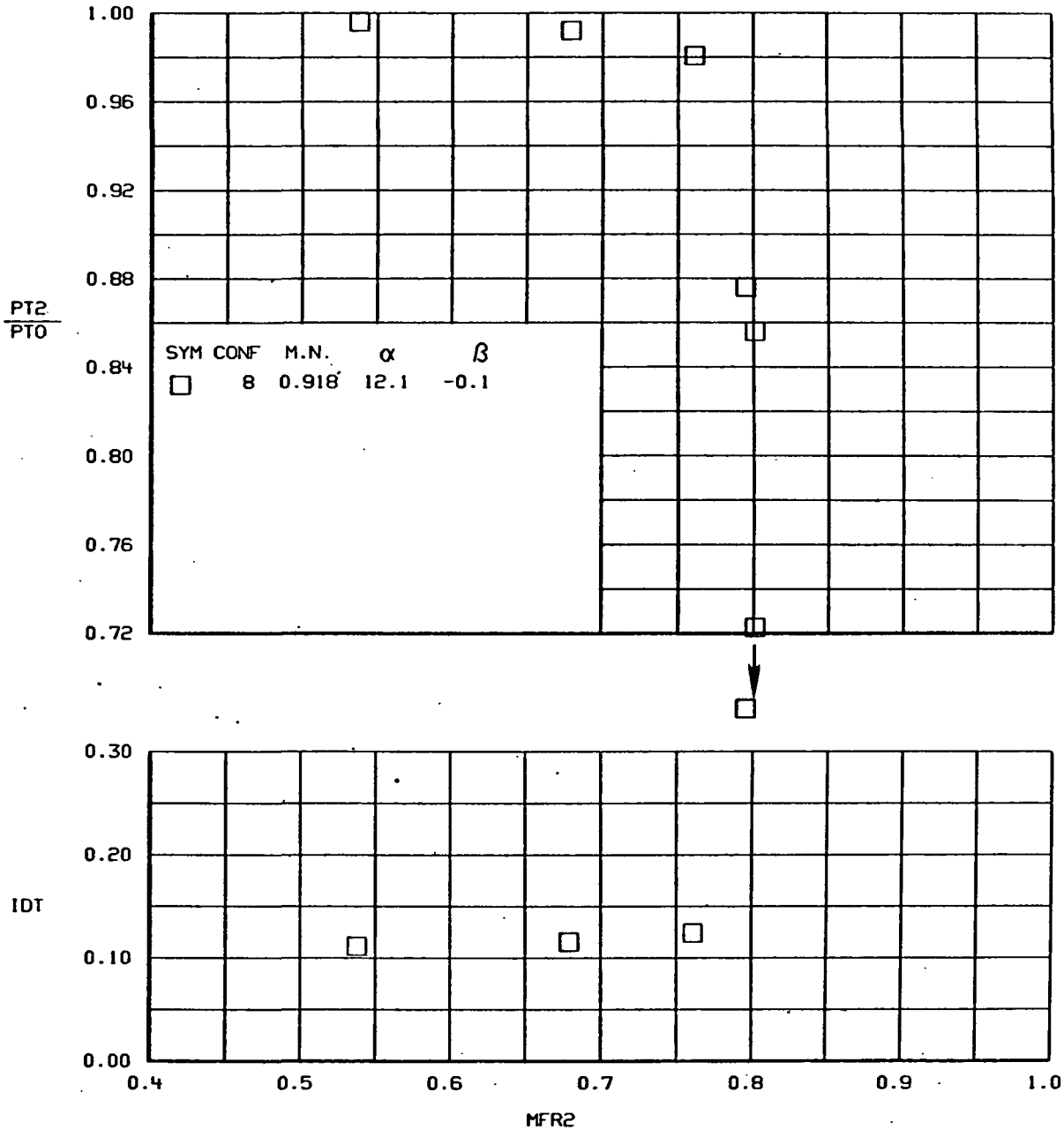

(b)

Figure 82.-Continued.

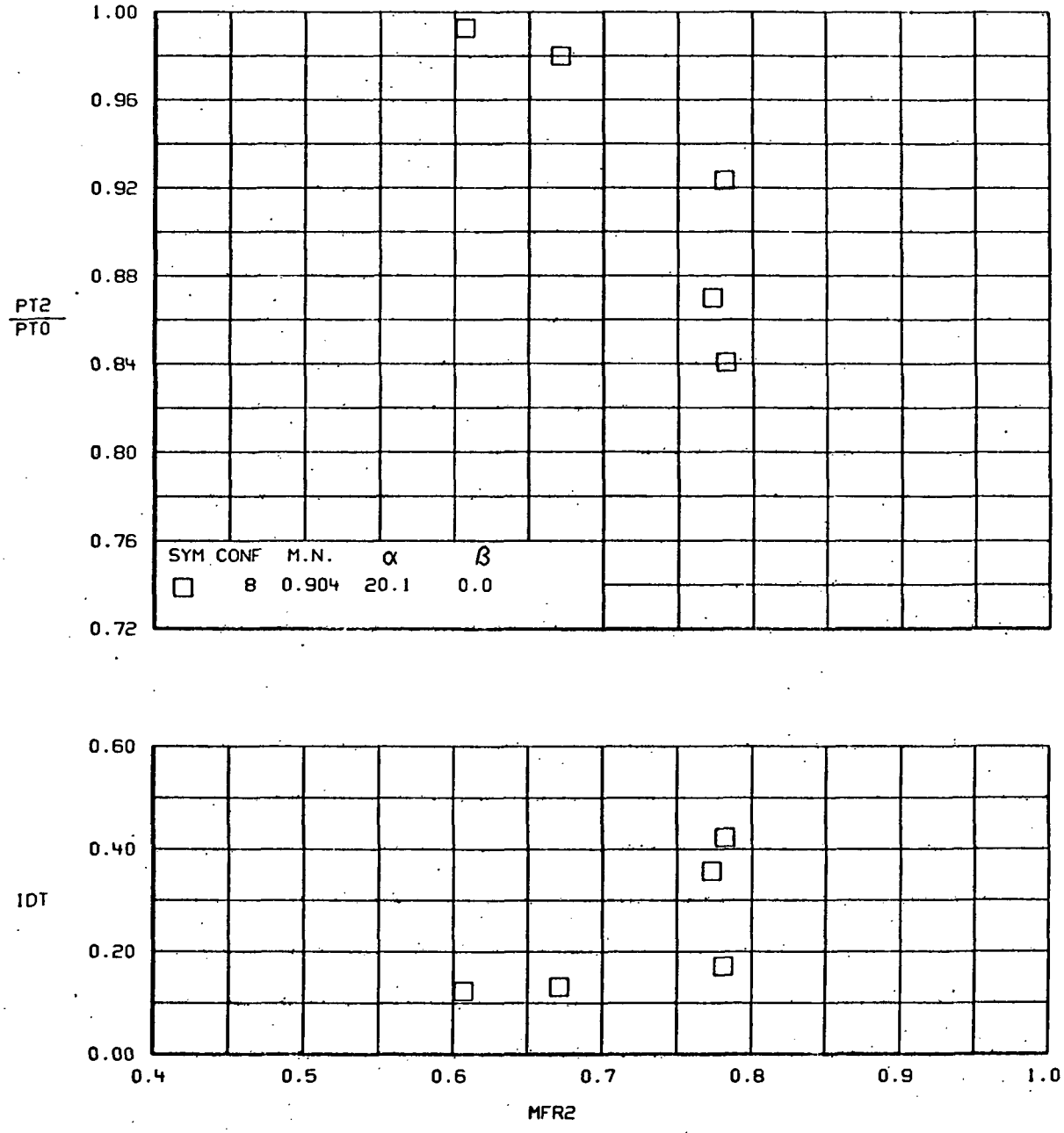

(c)
FIGURE 82.-CONTINUED.

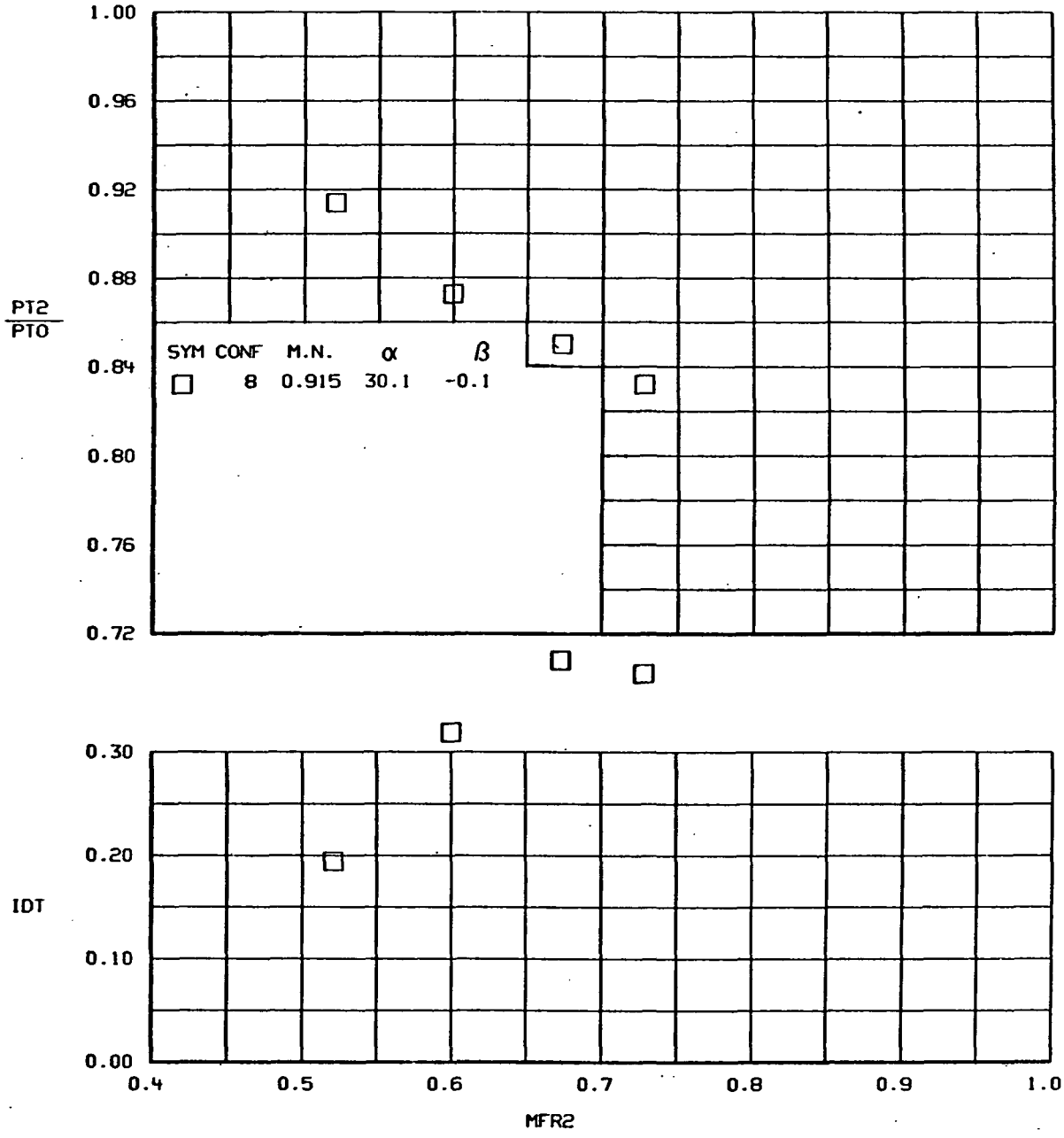

(d)

Figure 82.-Continued.

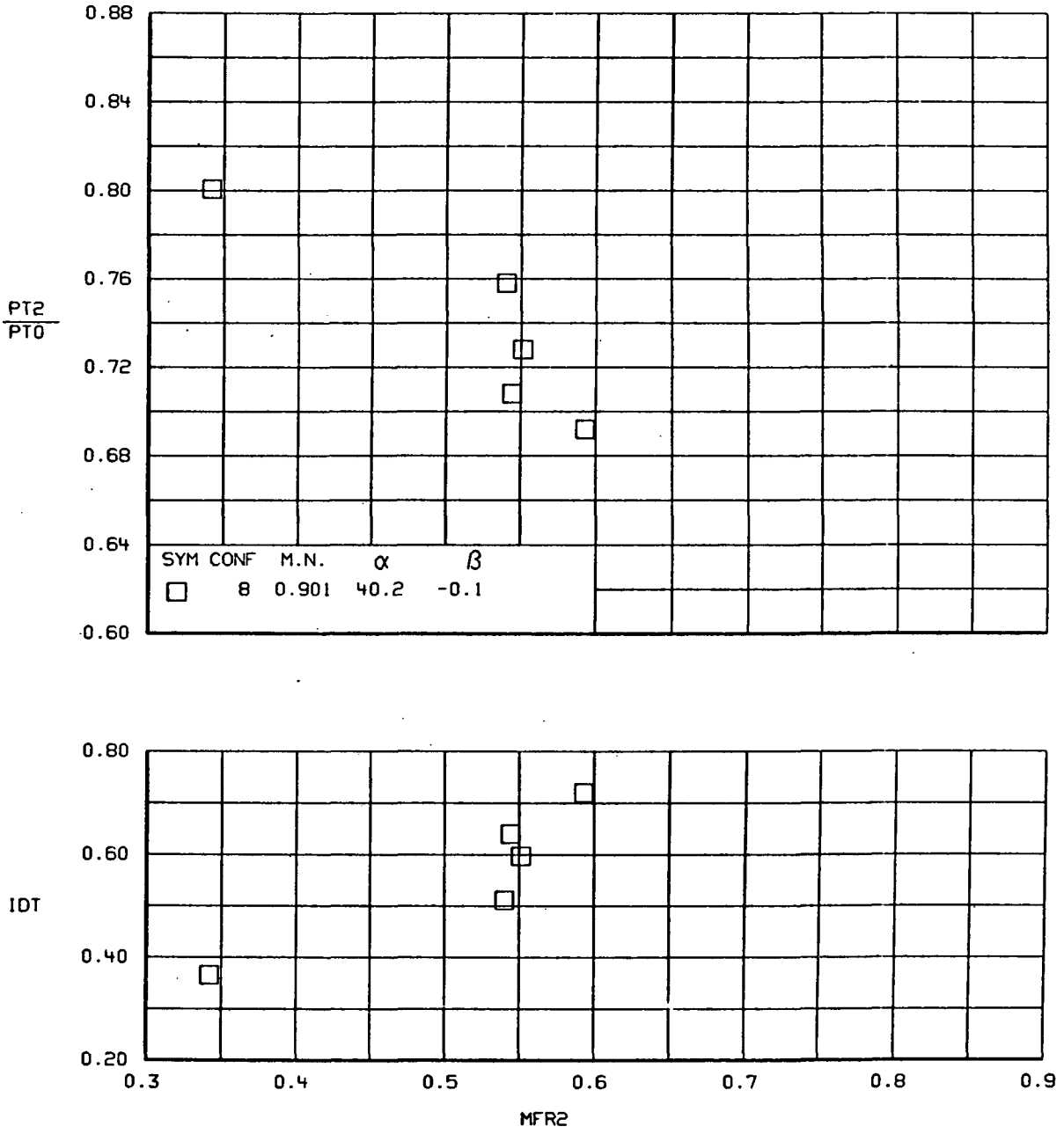

(e)

Figure 82-Continued.

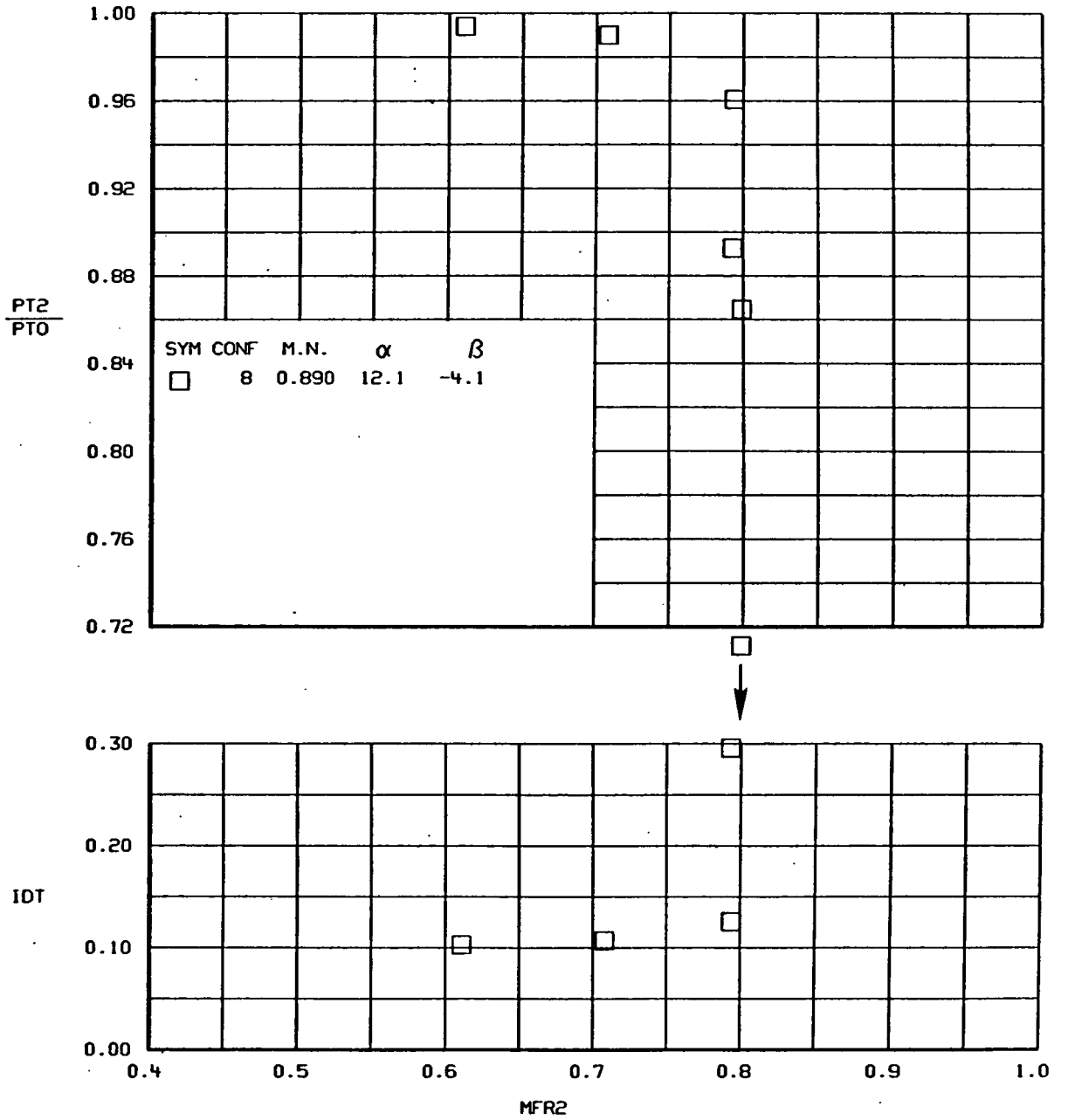

(f)

Figure 82-Continued.

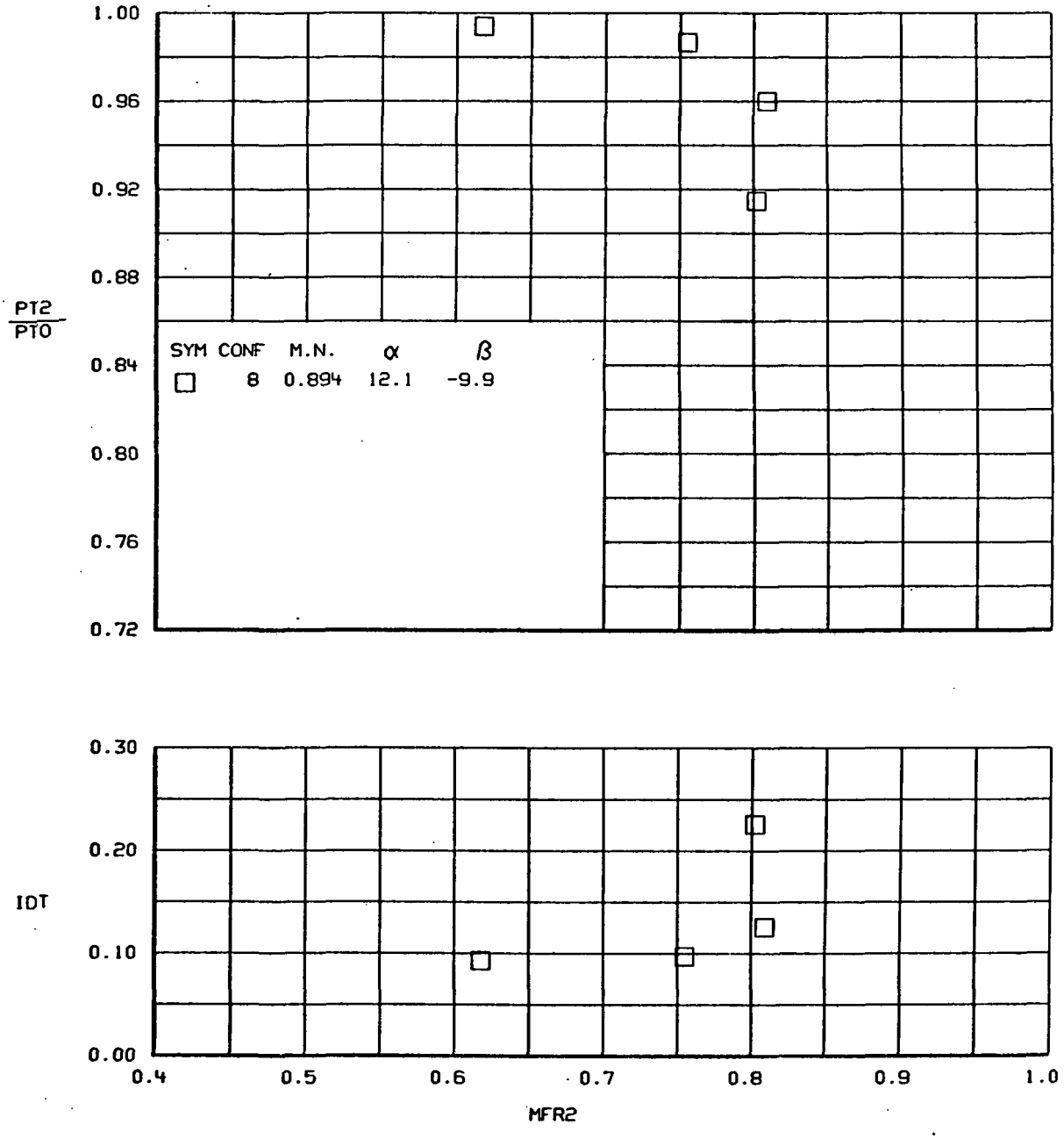

(g)

Figure 82-Concluded.

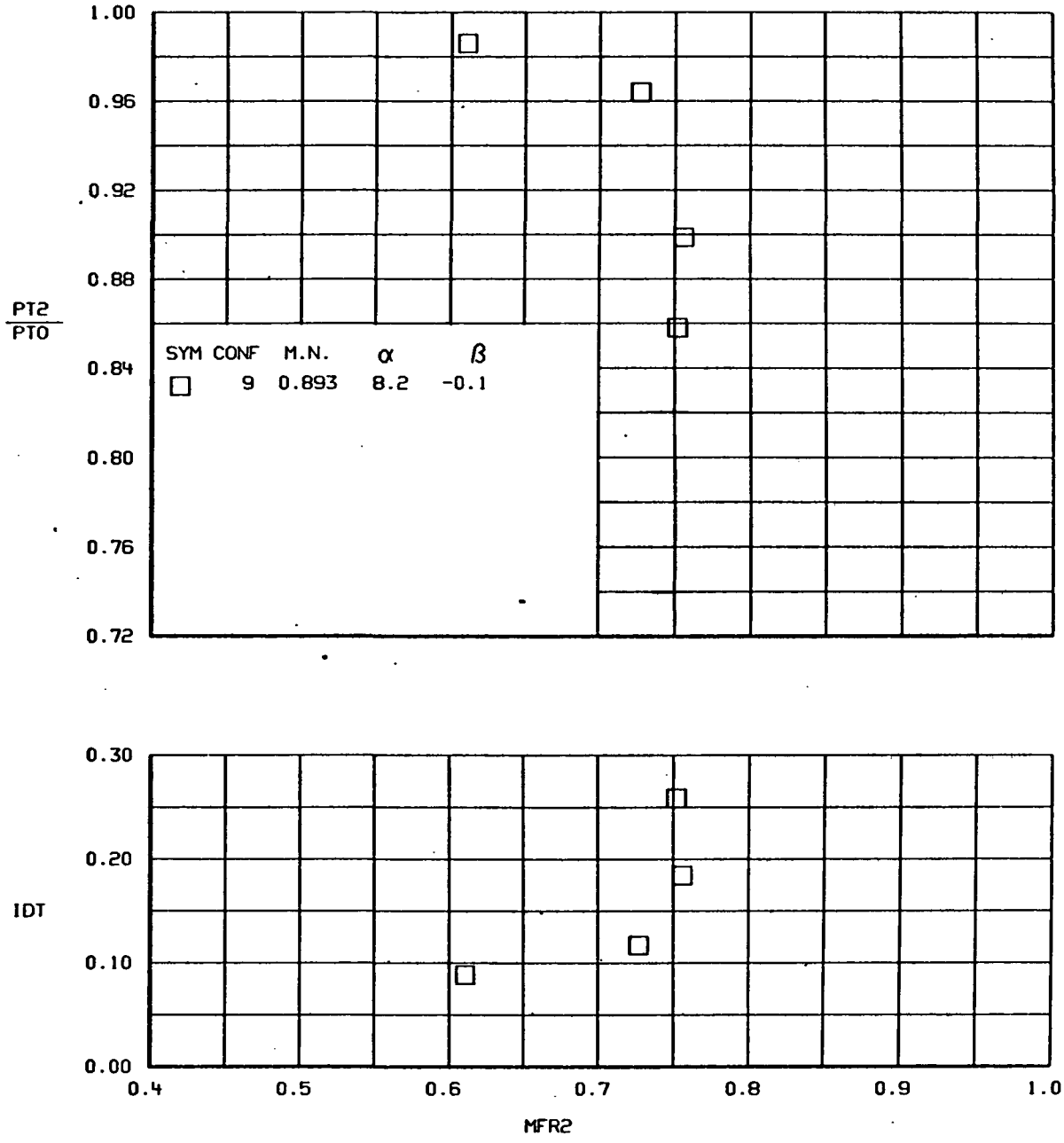

(a)

Figure 83- TOTAL PRESSURE RECOVERY AND DISTORTION VERSUS MASS FLOW RATIO Configuration 9.

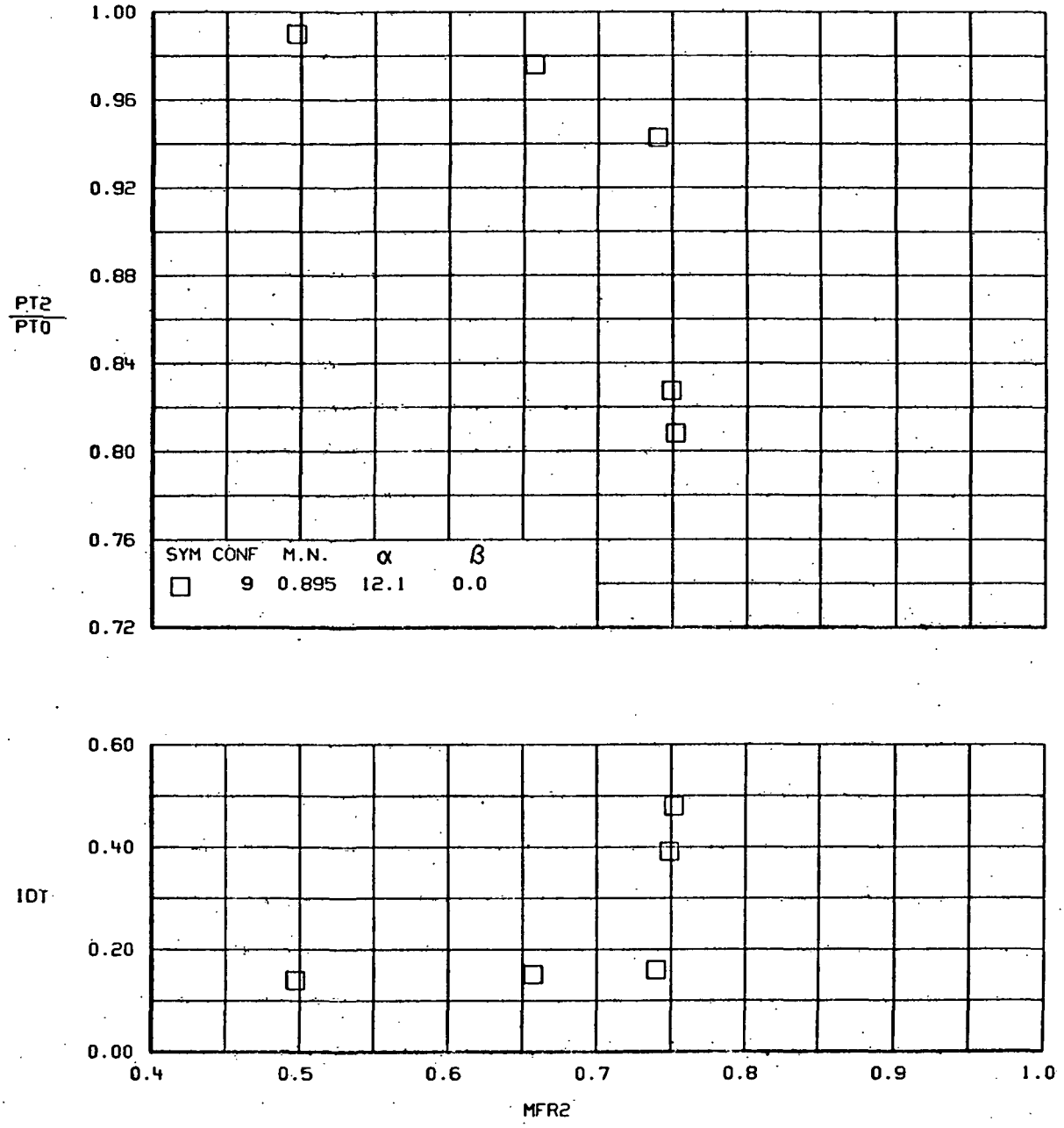

(B)

FIGURE 83.-CONTINUED.

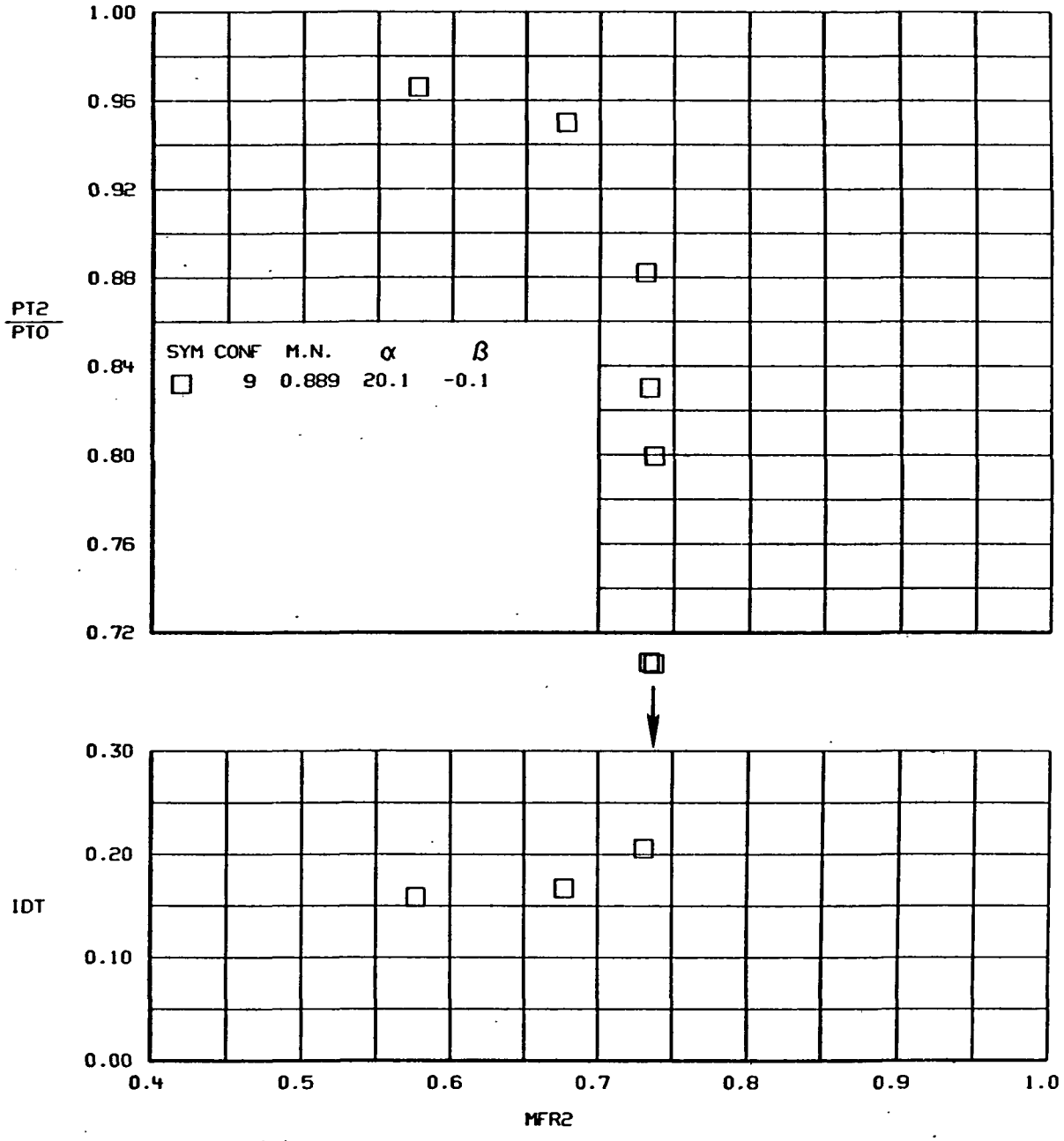

(c)

Figure 83-Continued.

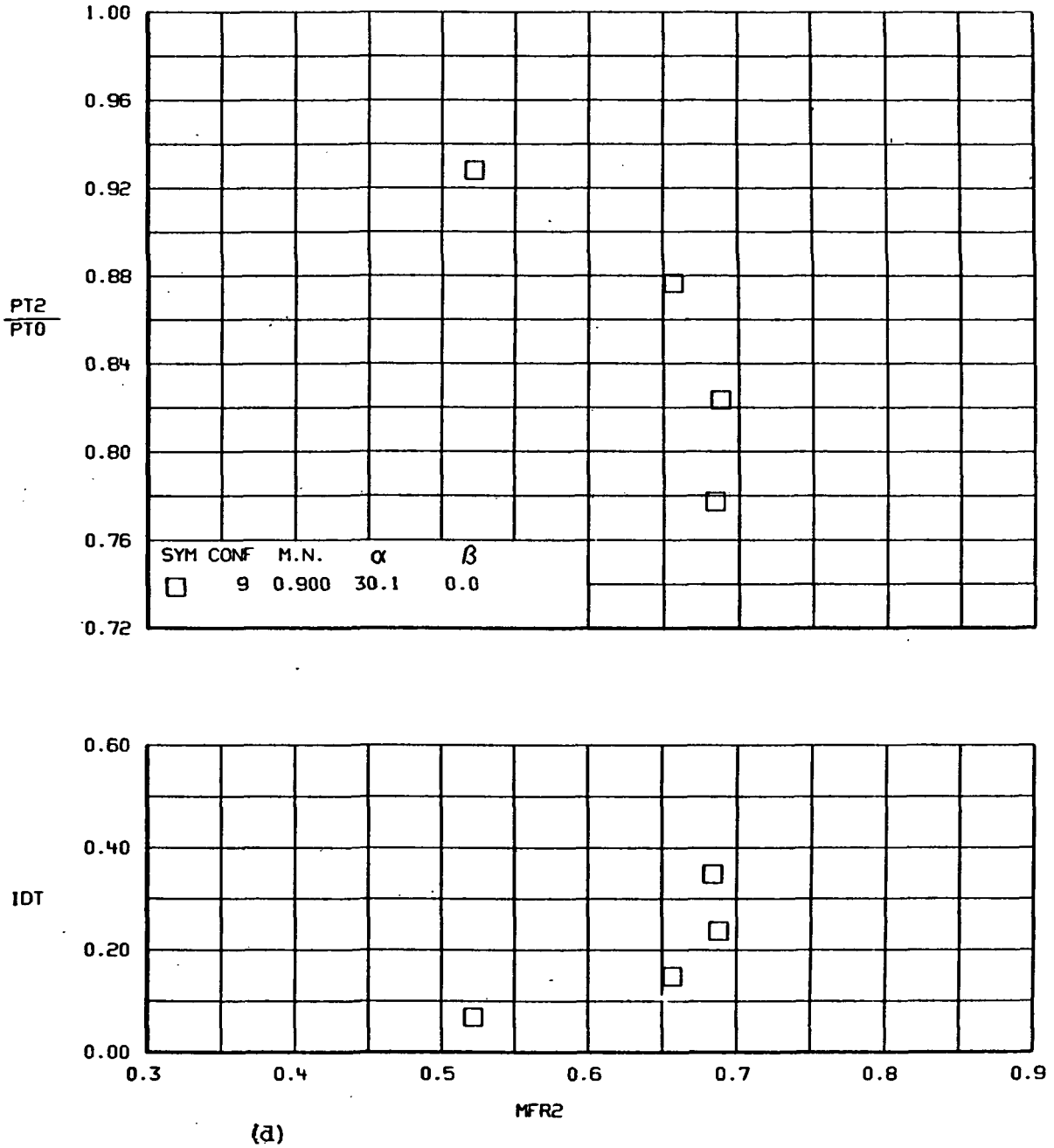

(d)

Figure 83-Continued.

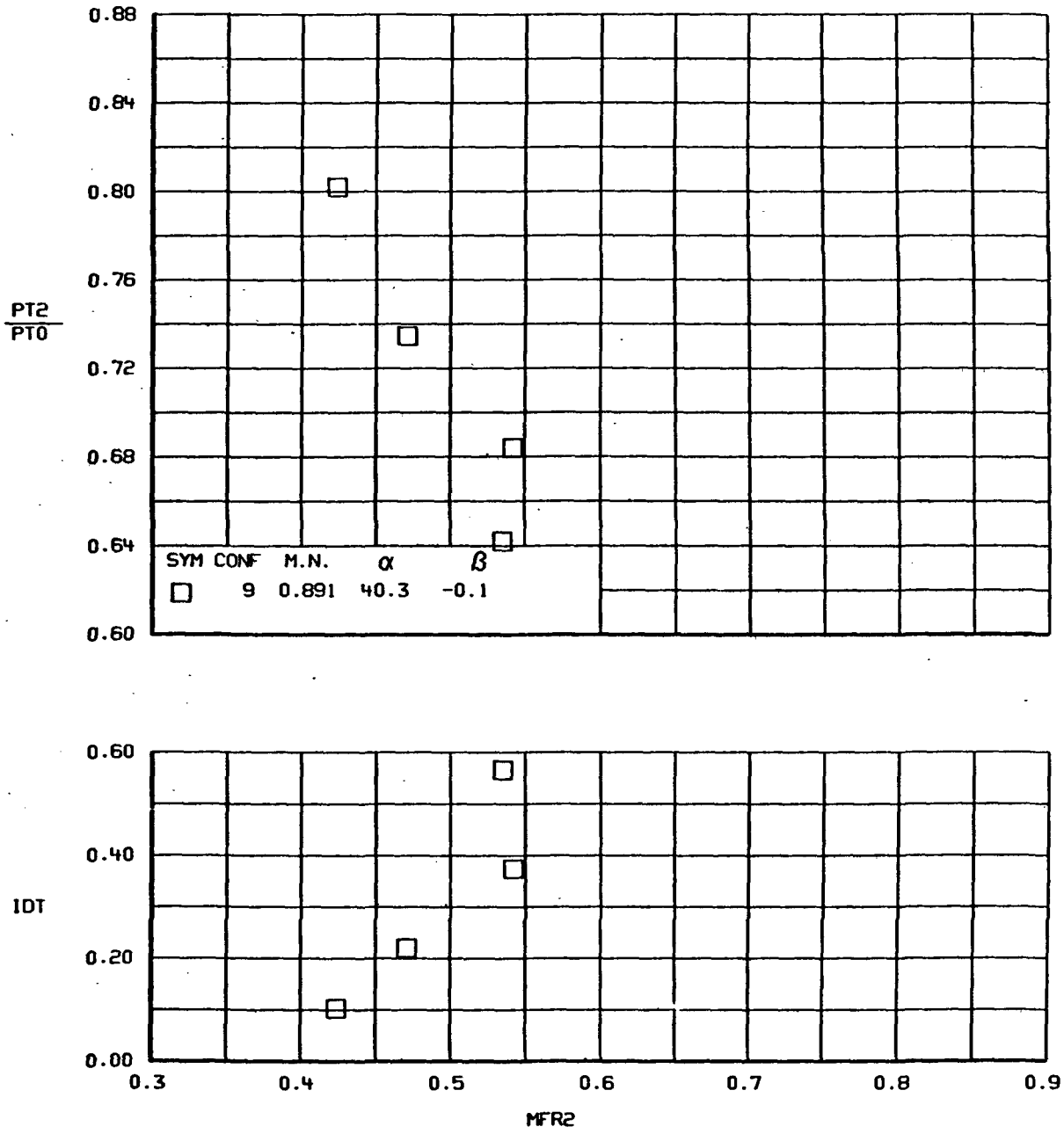

(e)

Figure 83-Continued.

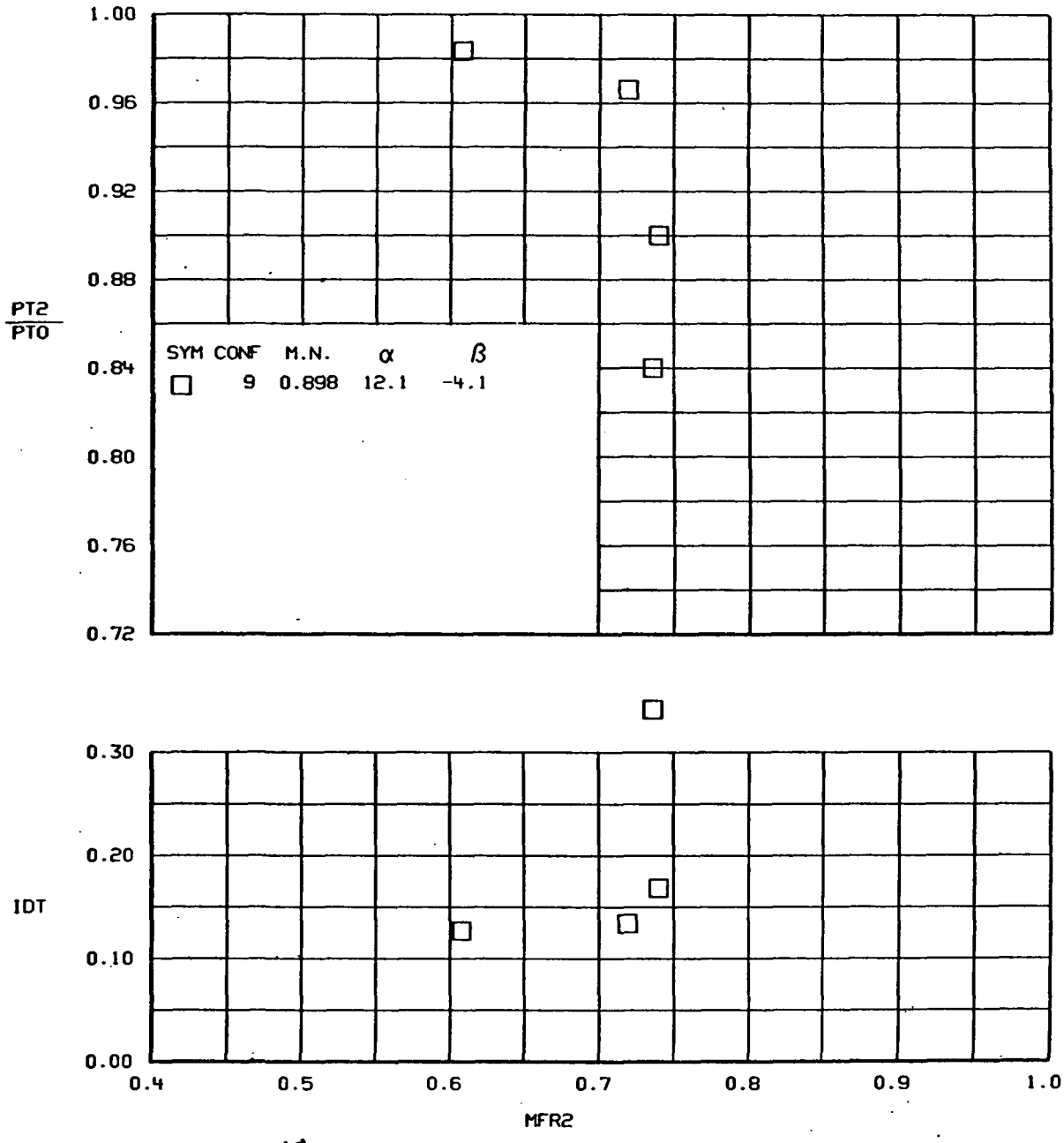

(f)

Figure 83-Continued.

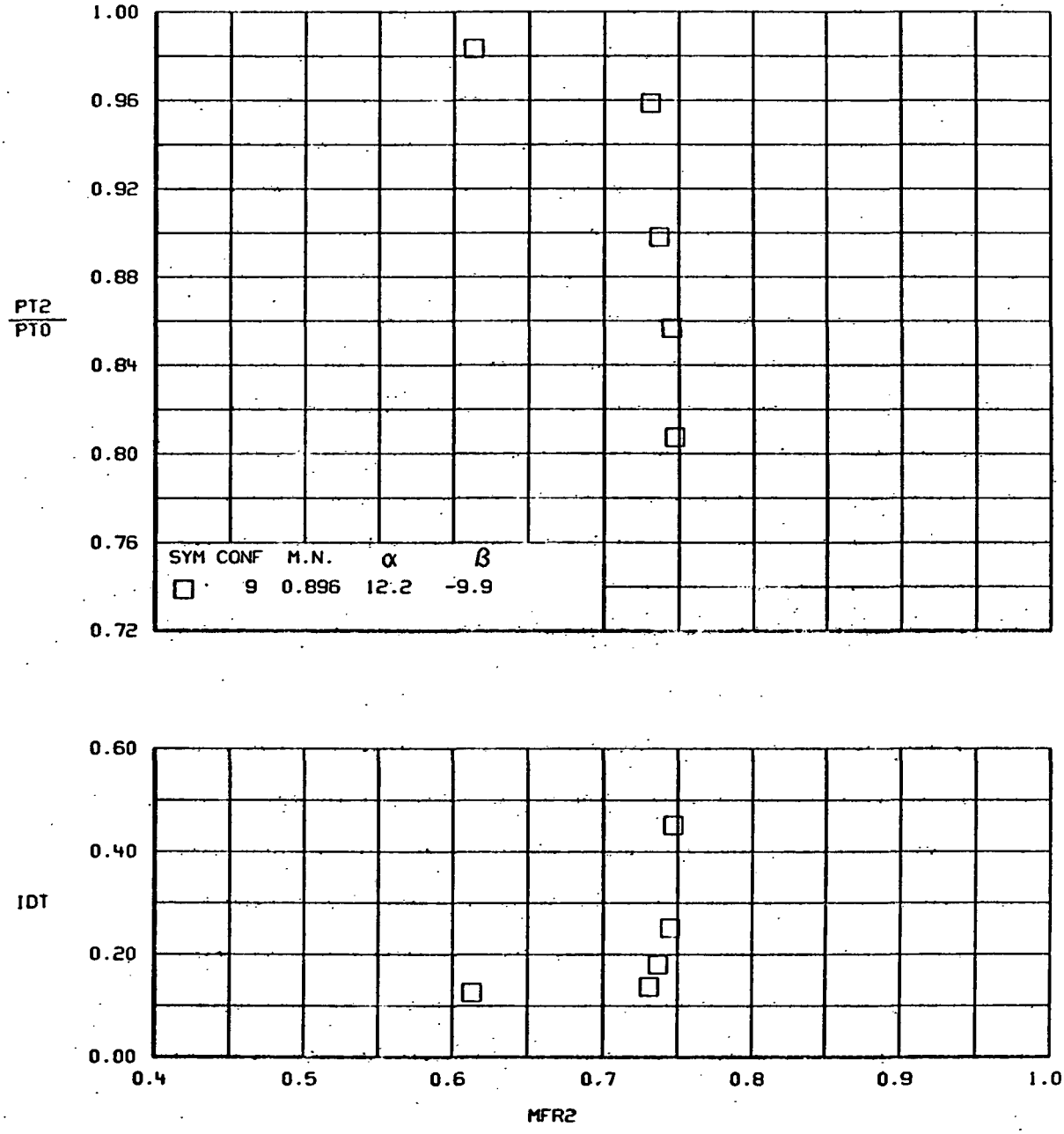

(G)
FIGURE 83.-CONCLUDED.

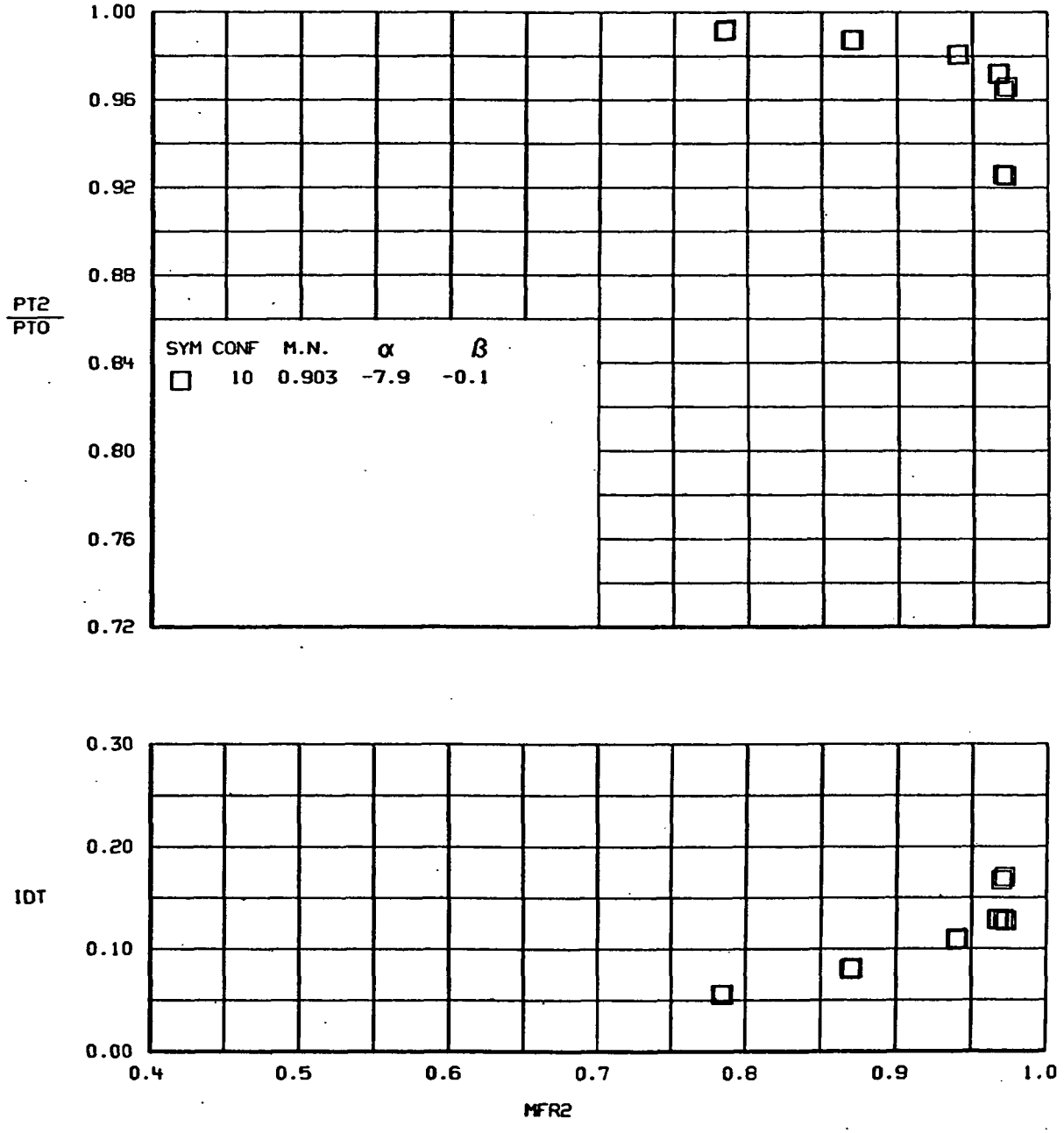

(a)

Figure 84.- TOTAL PRESSURE RECOVERY AND DISTORTION VERSUS MASS FLOW RATIO
Configuration 10, $\delta=0^{\circ}$

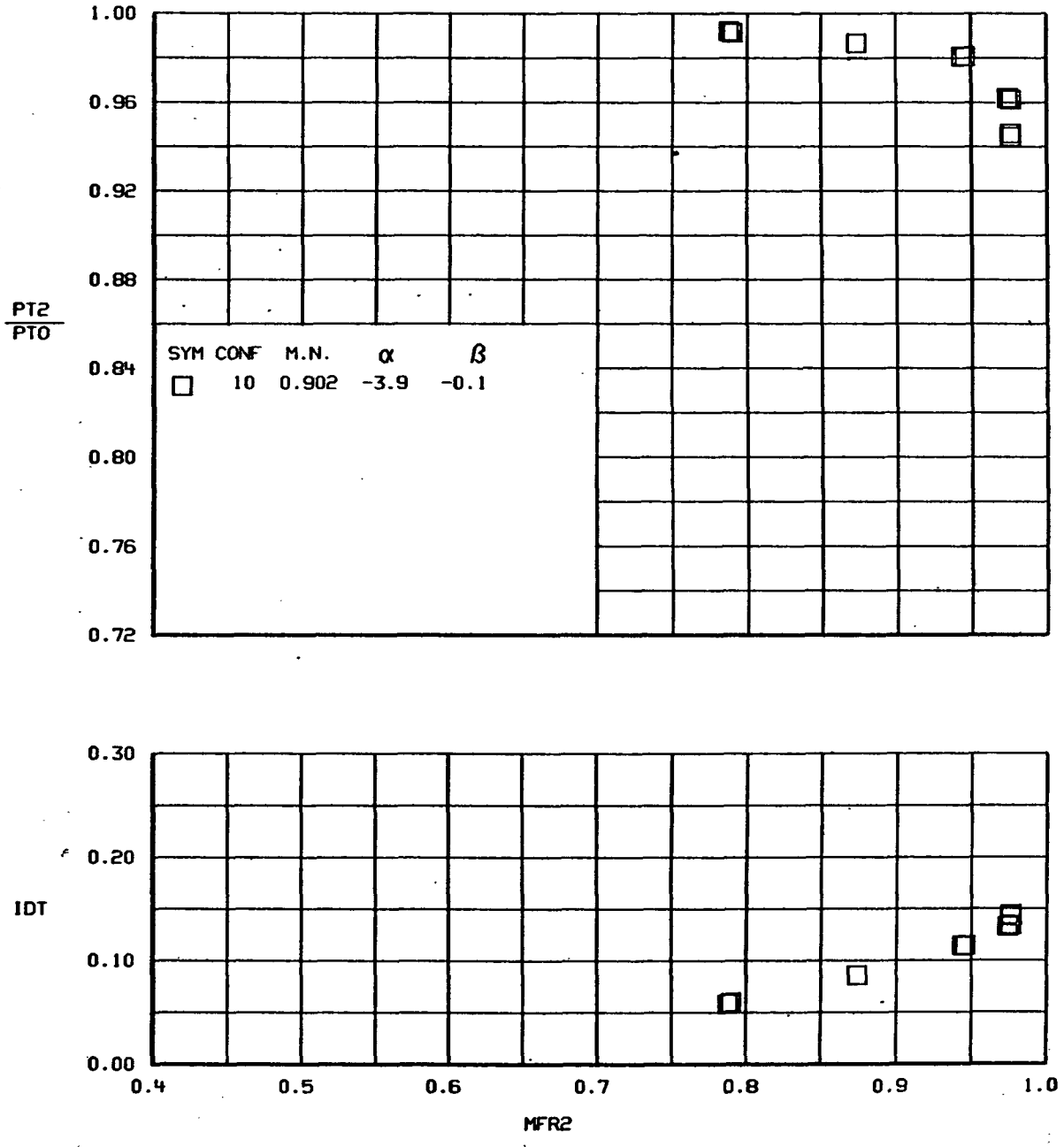

(b)

Figure 84.-Continued.

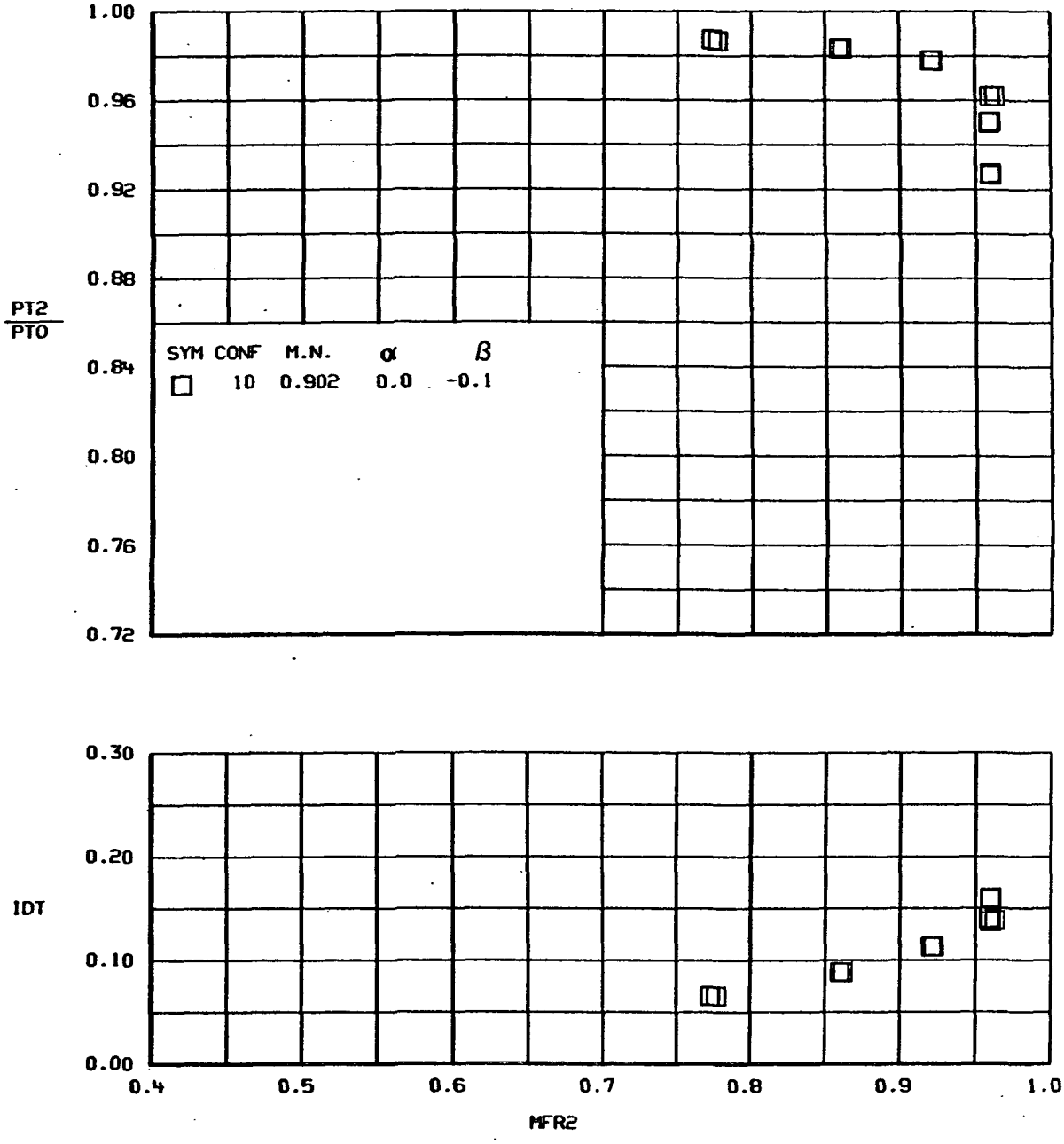

(c)

Figure 84.-Continued.

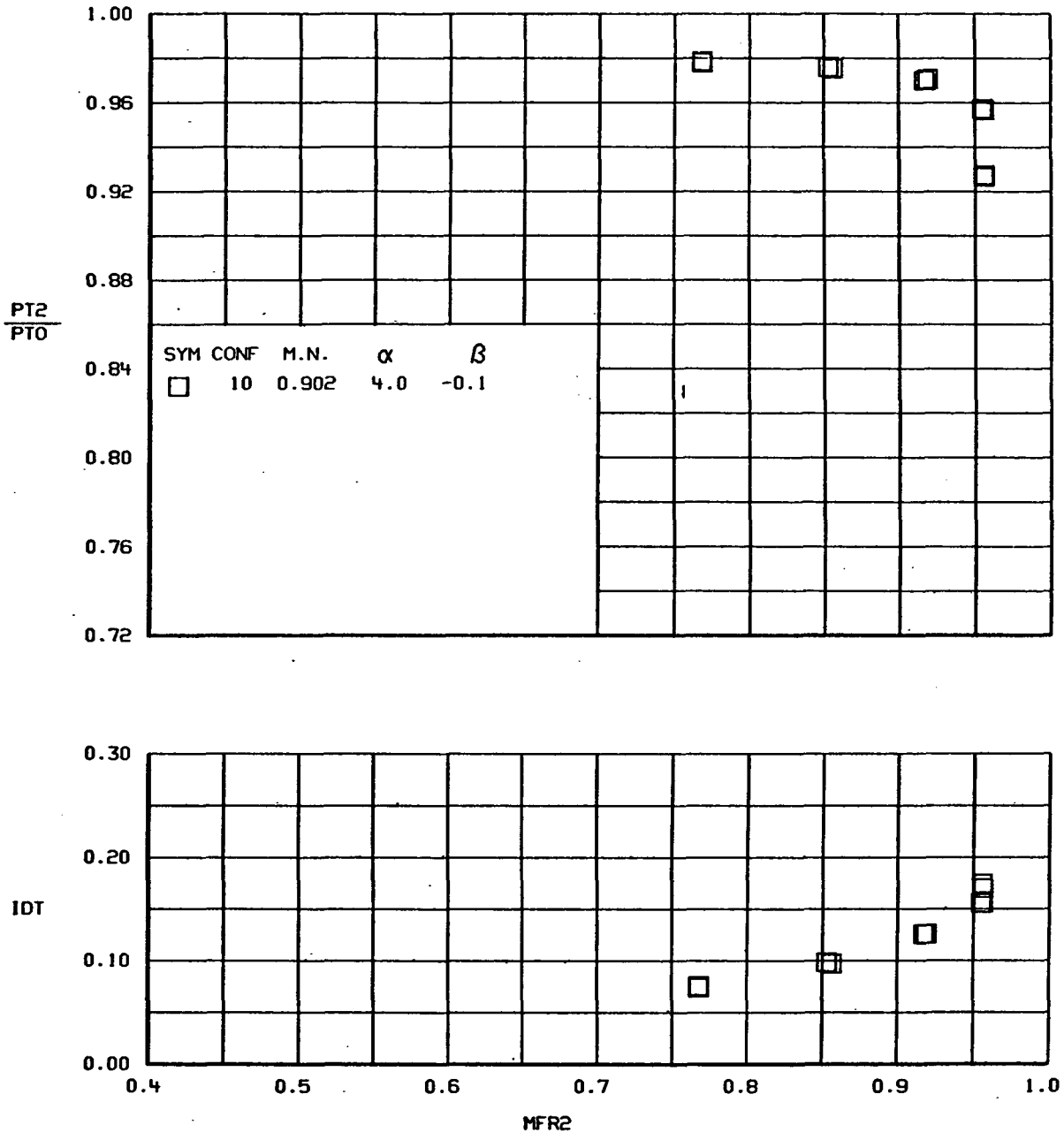

(d)

Figure 84.-Continued.

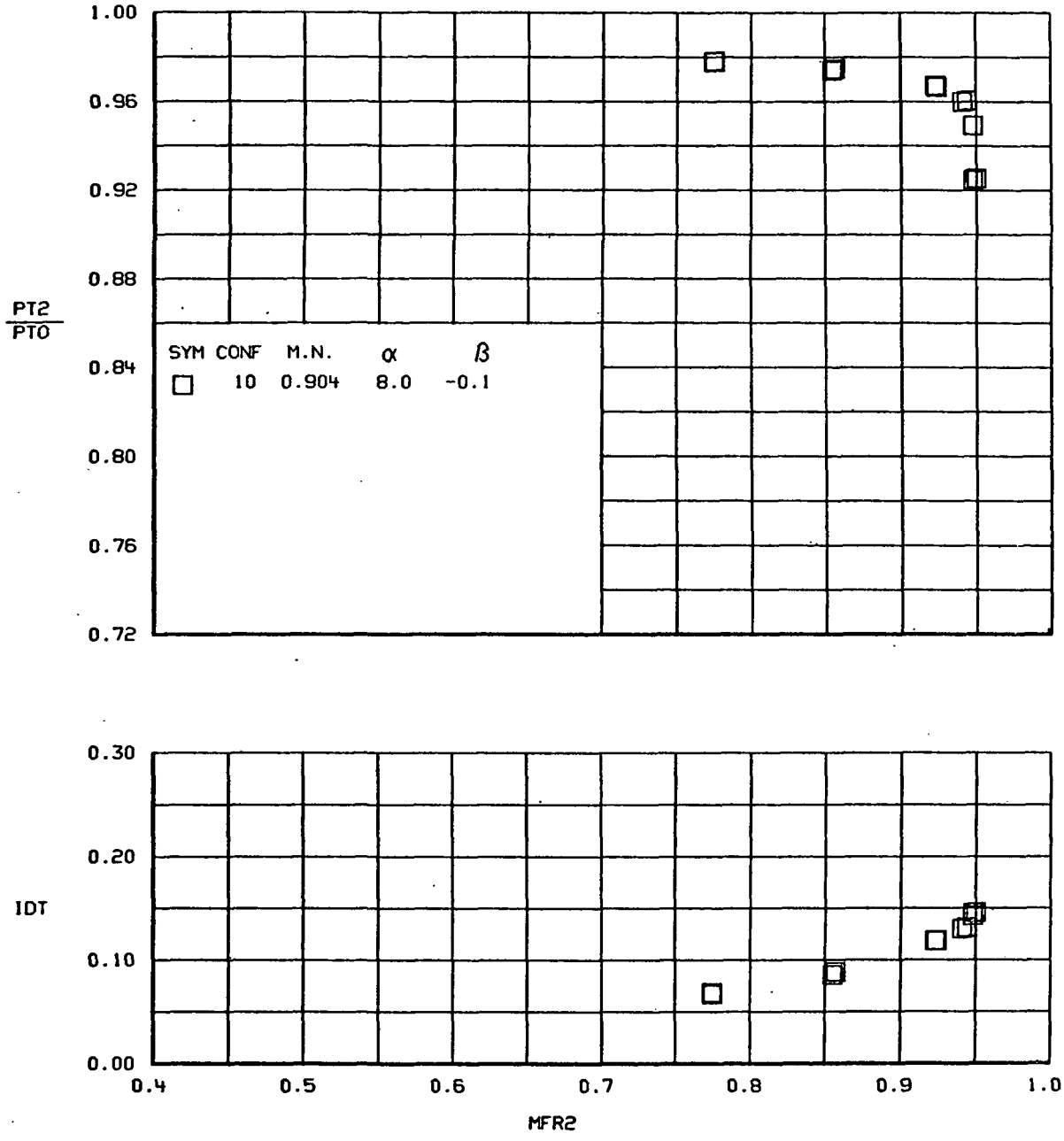

(e)

Figure 84.-Continued.

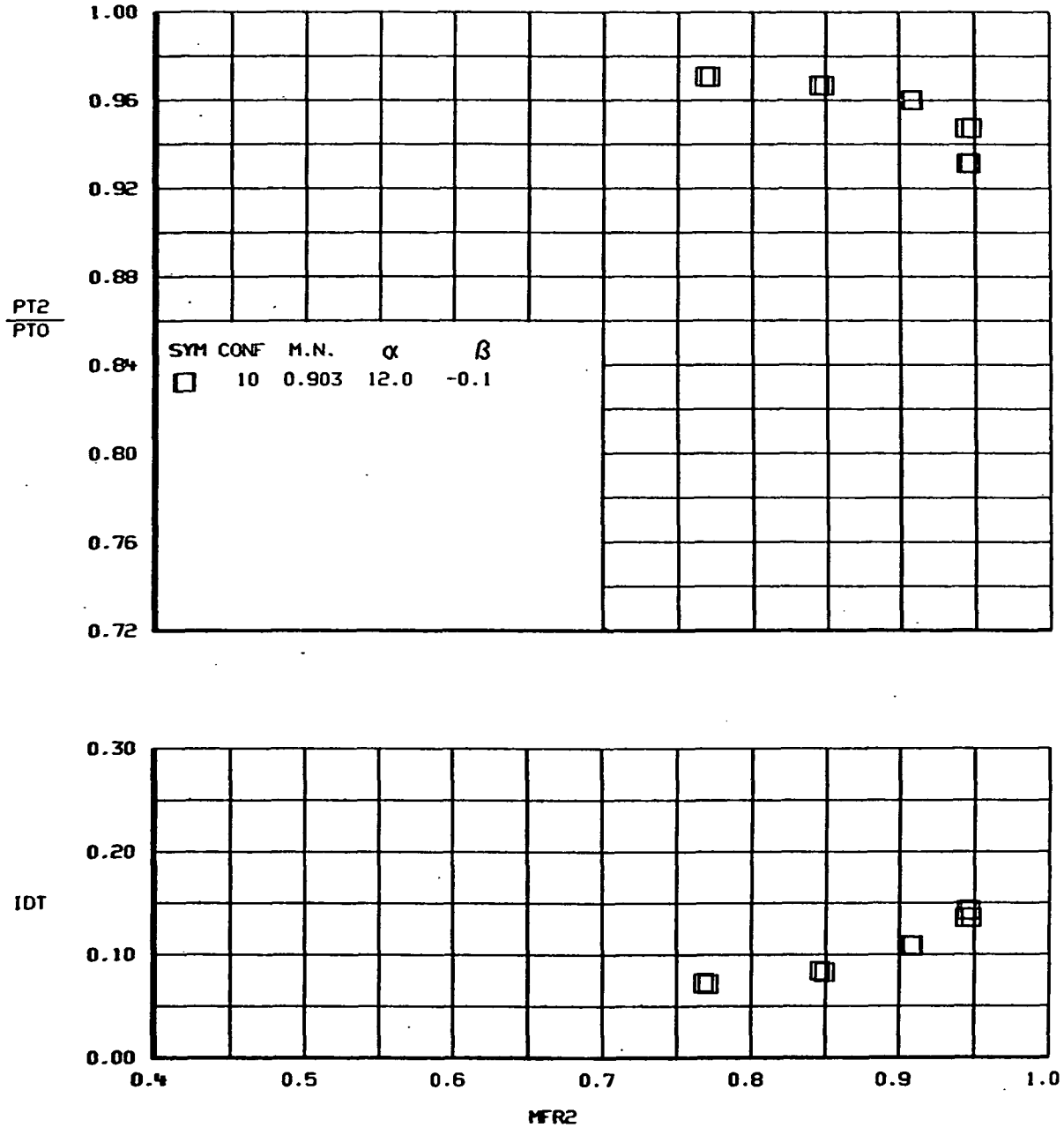

(f)

Figure 84.-Continued.

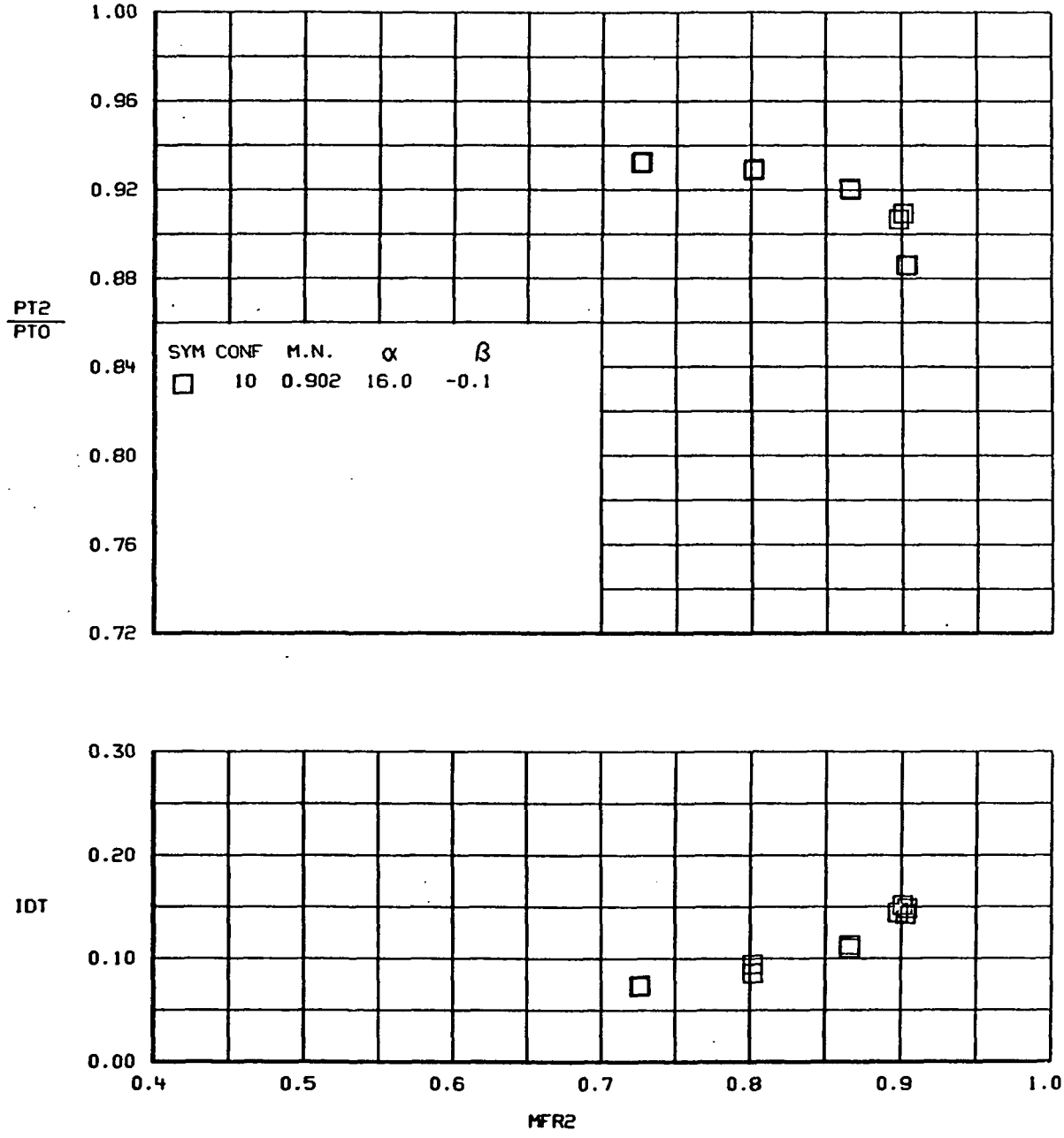

(g)

Figure 84.-Continued.

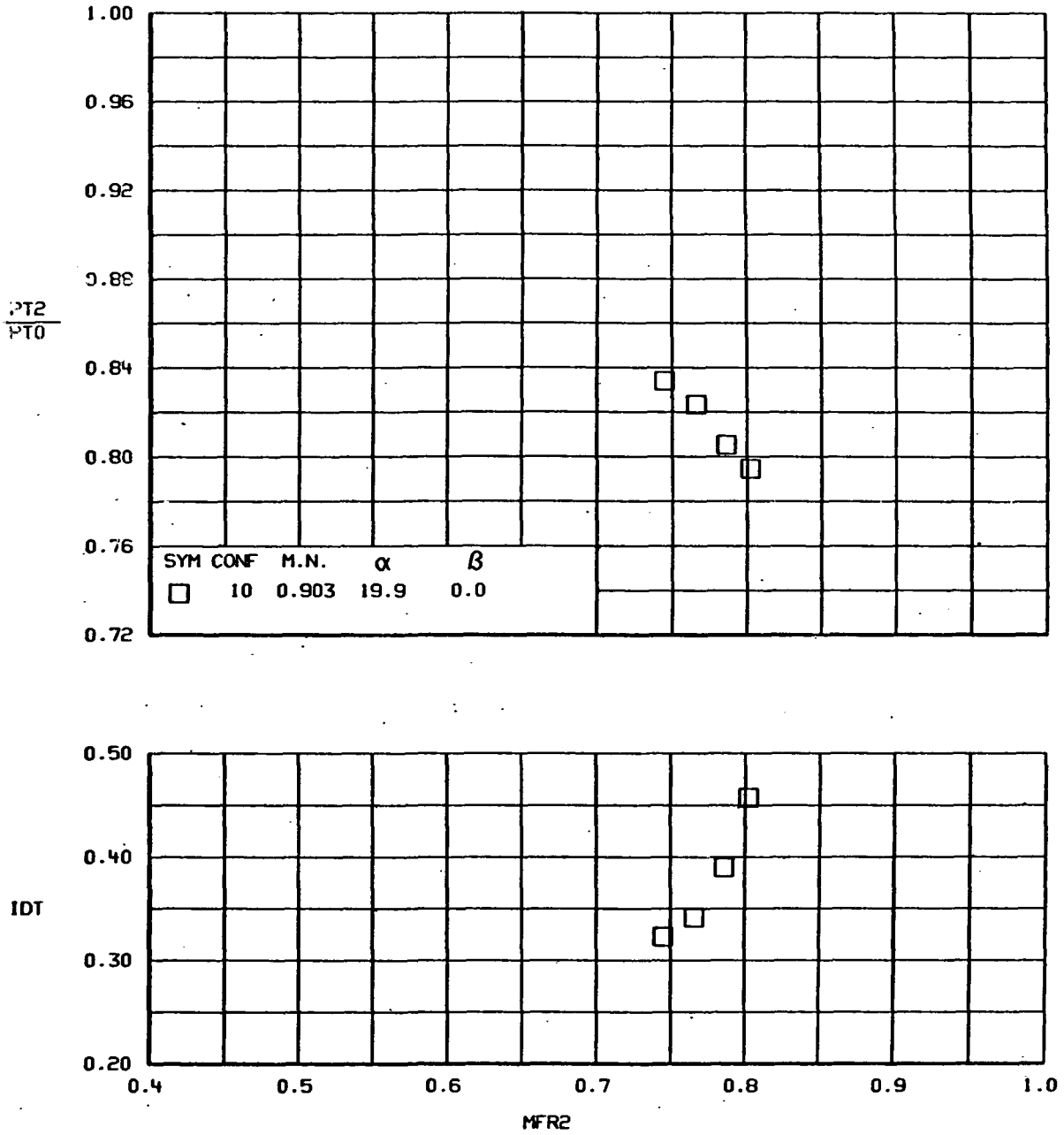

(h)

Figure 84.-Concluded.

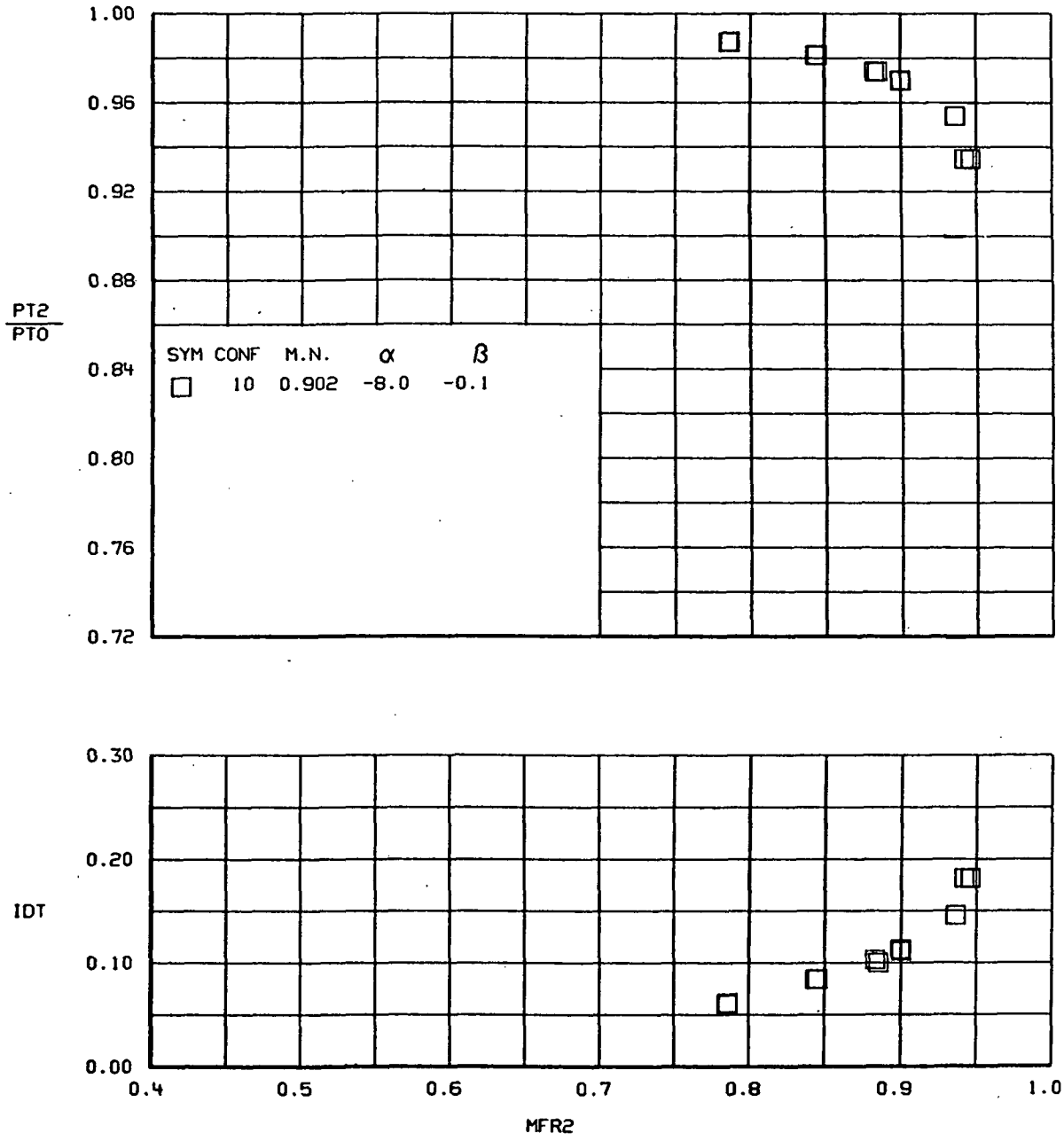

(a)

Figure 85.- TOTAL PRESSURE RECOVERY AND DISTORTION VERSUS MASS FLOW RATIO Configuration 10, $\delta=10^{\circ}$.

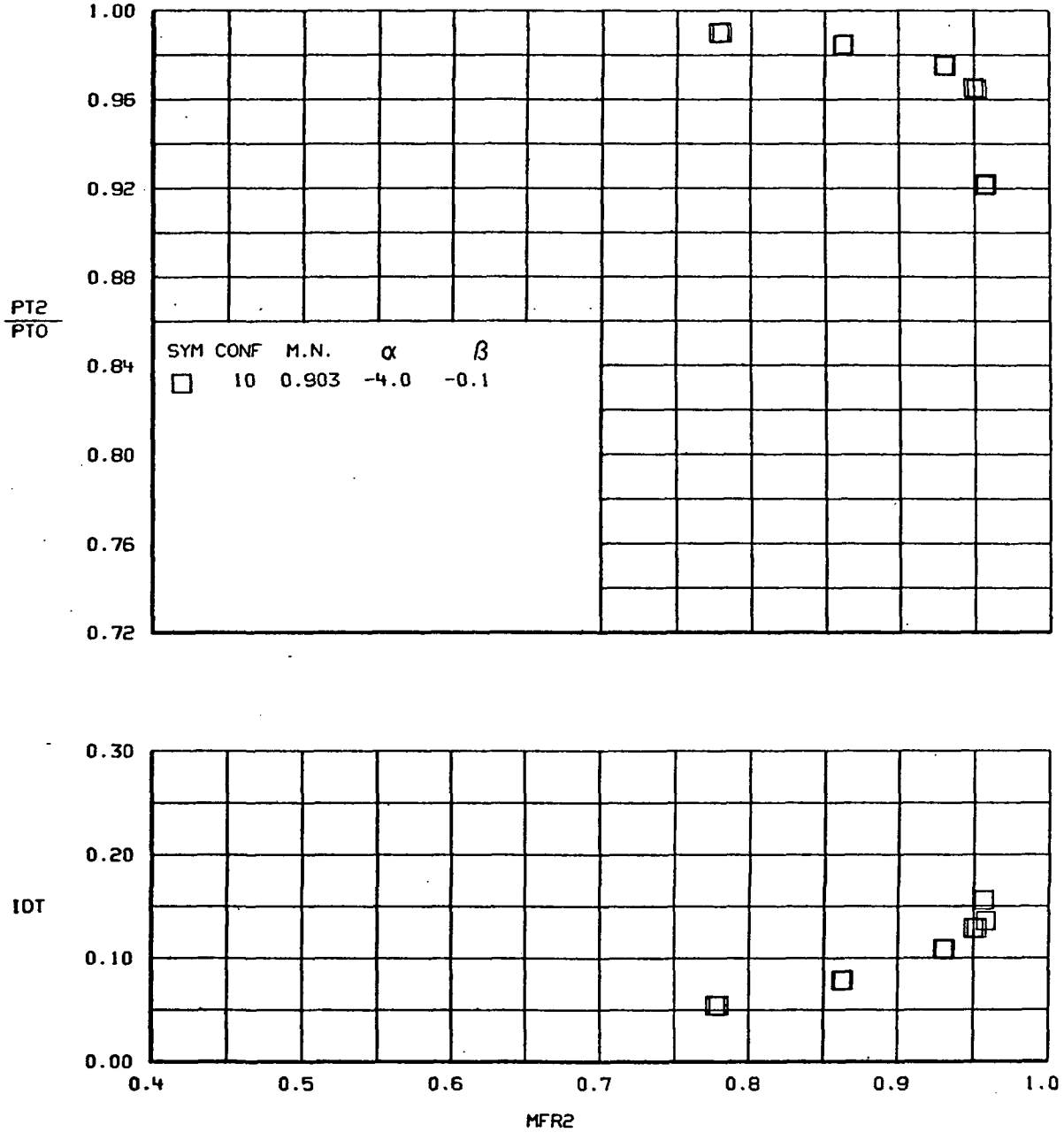

(b)

Figure 85.-Continued.

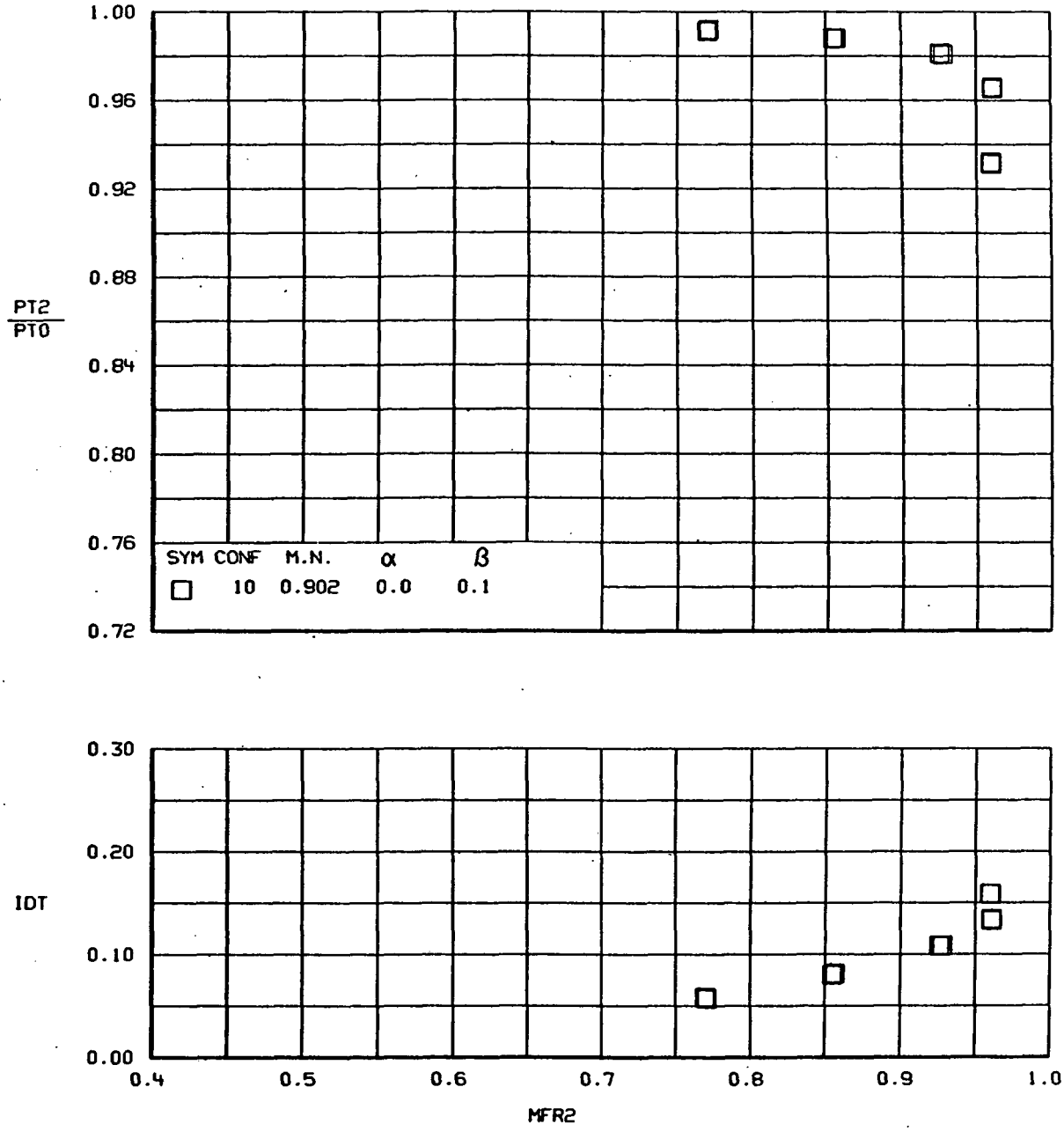

(c)

Figure 85.-Continued.

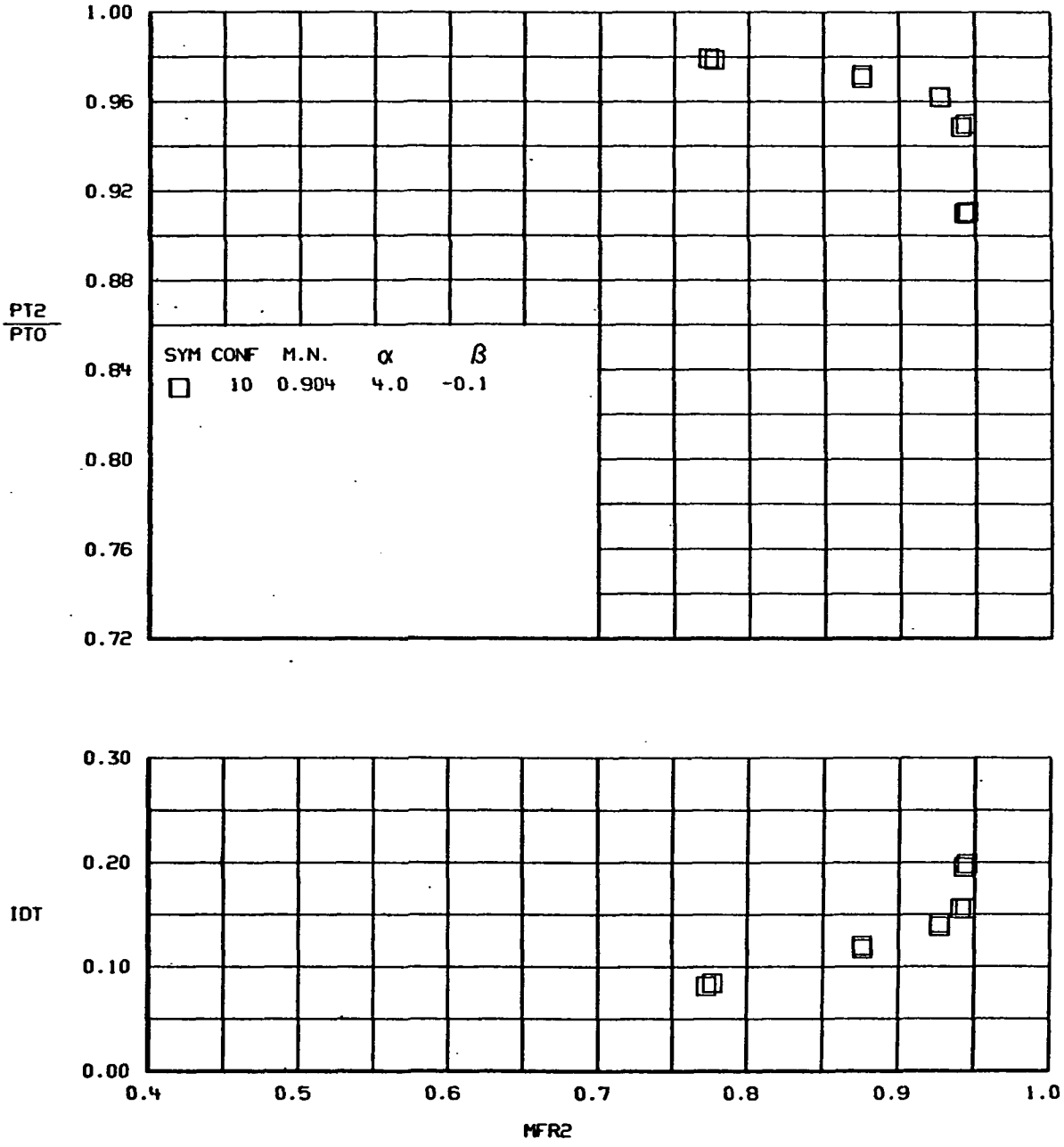

(d)

Figure 85.-Continued.

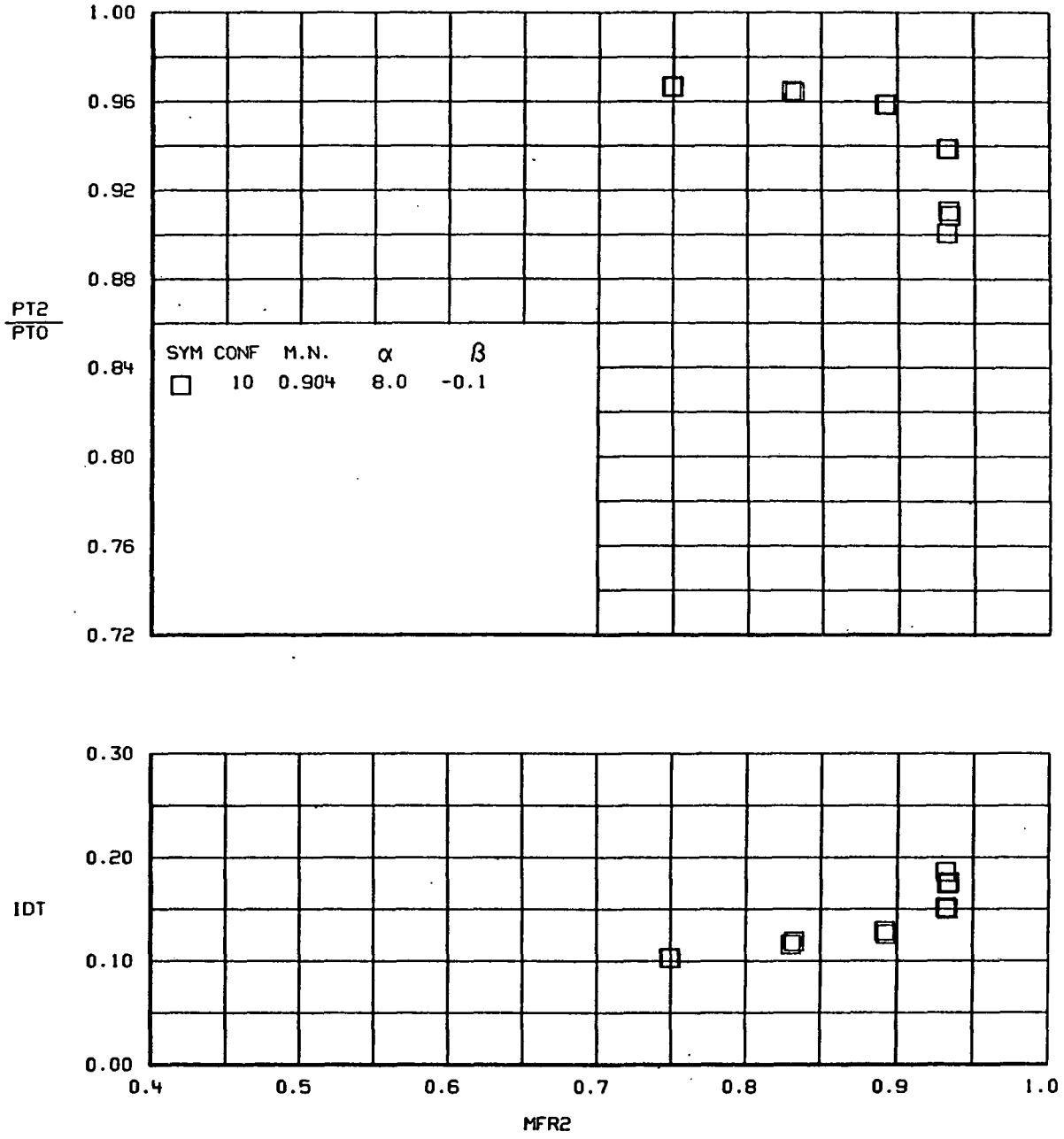

(e)

Figure 85.-Continued.

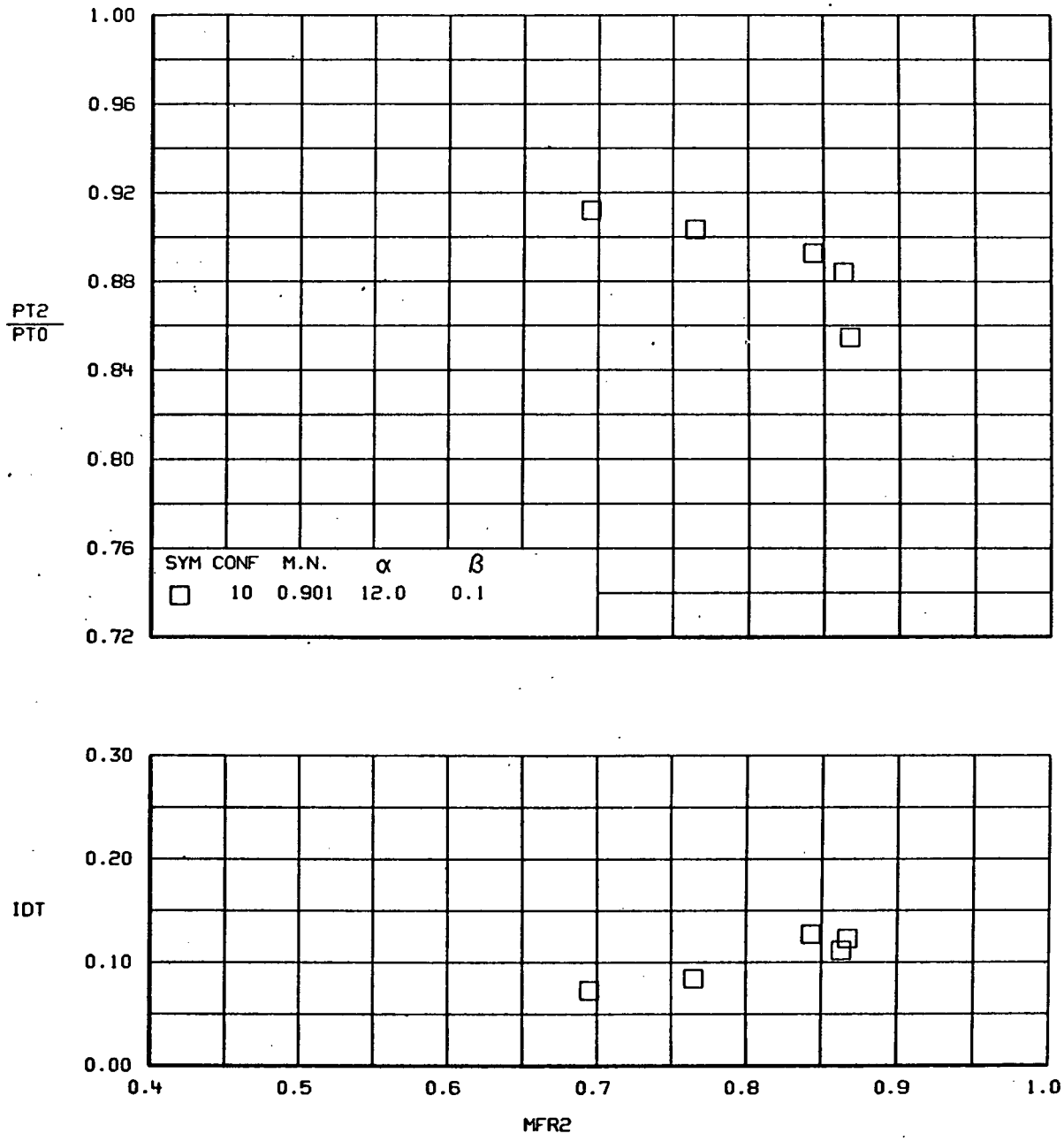

(f)

Figure 85.-Continued.

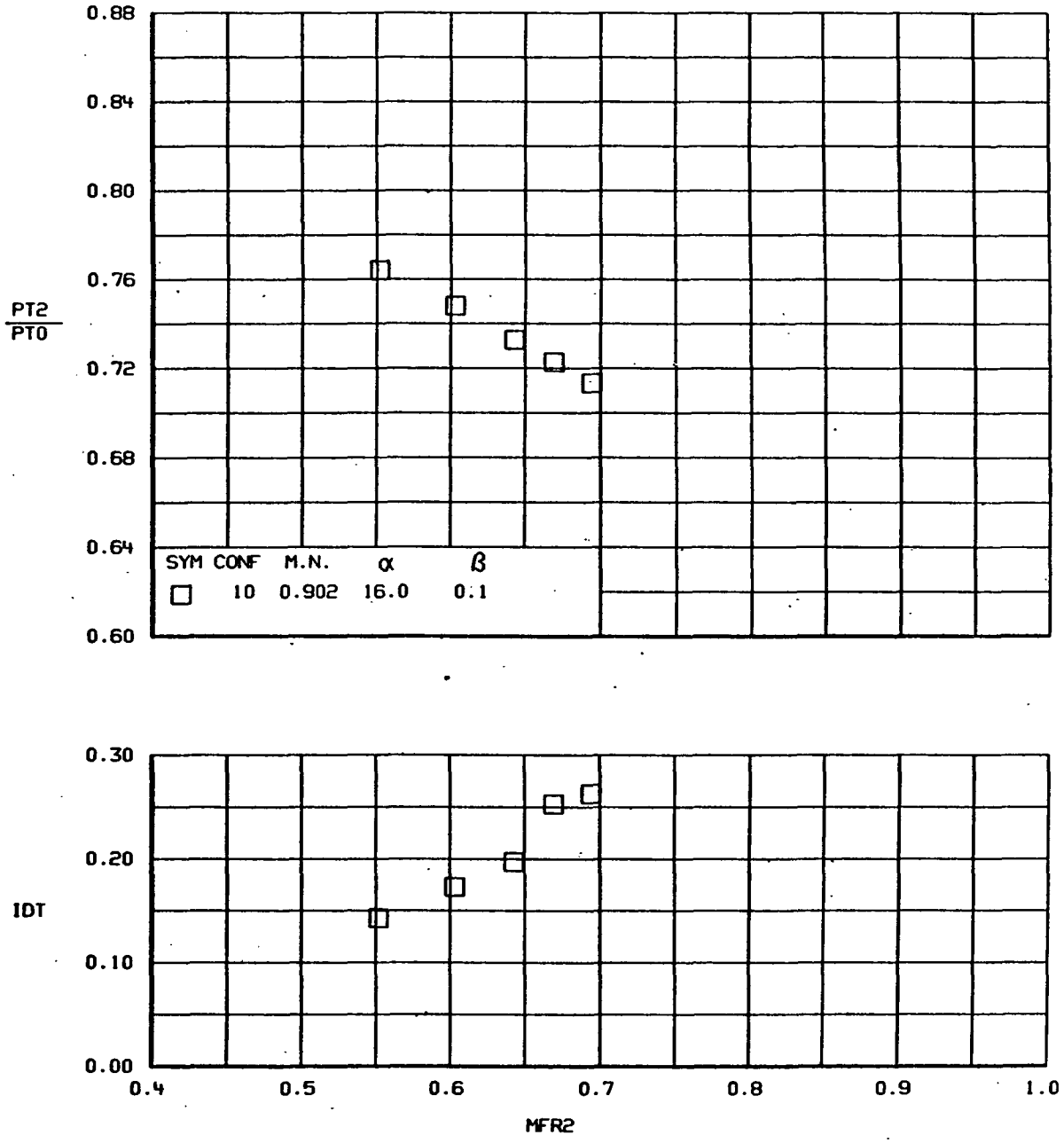

(g)

Figure 85.-Concluded.

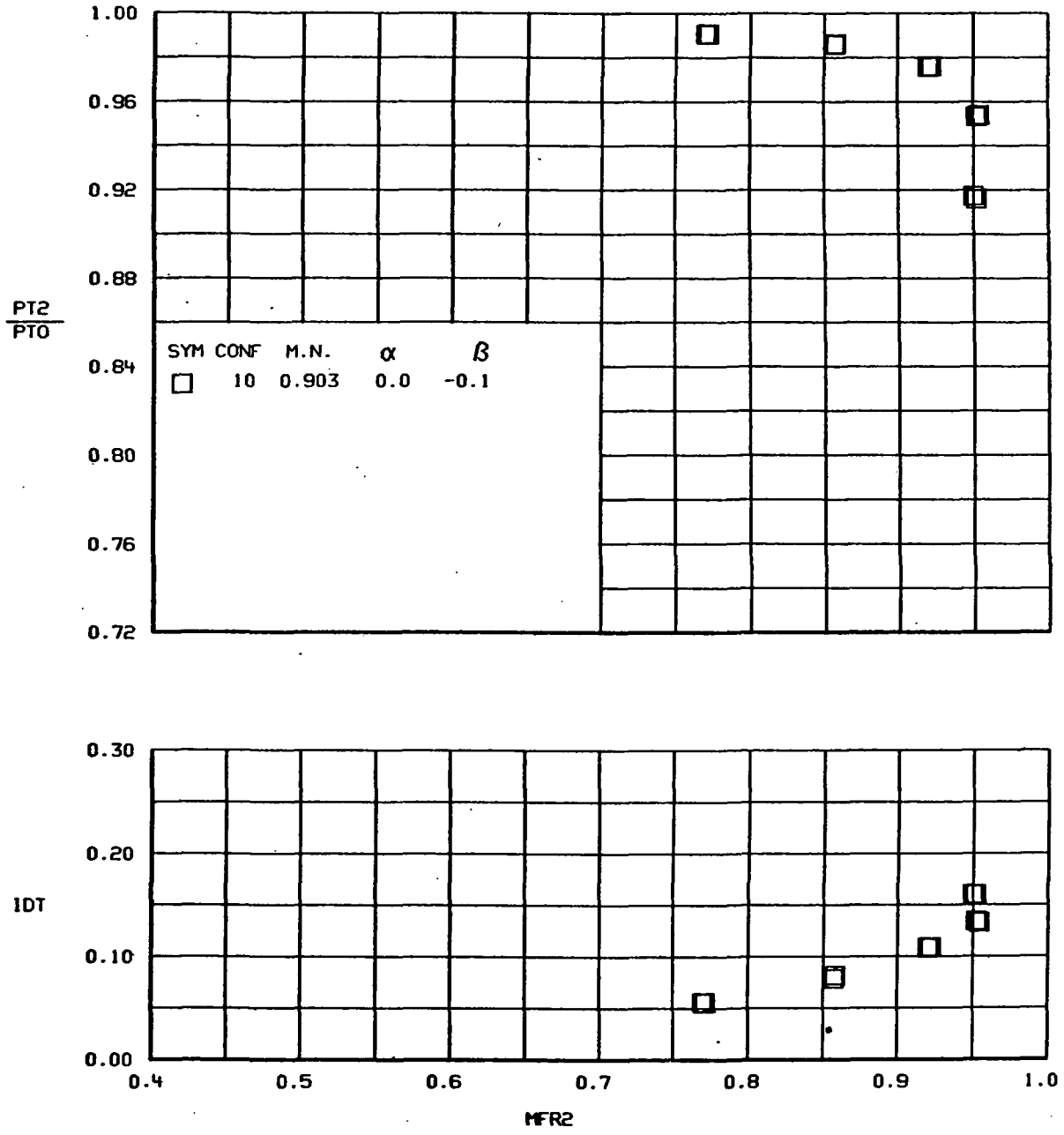

(a)

Figure 86.- TOTAL PRESSURE RECOVERY AND DISTORTION VERSUS MASS FLOW RATIO
Configuration 10, $\delta=15^{o}$

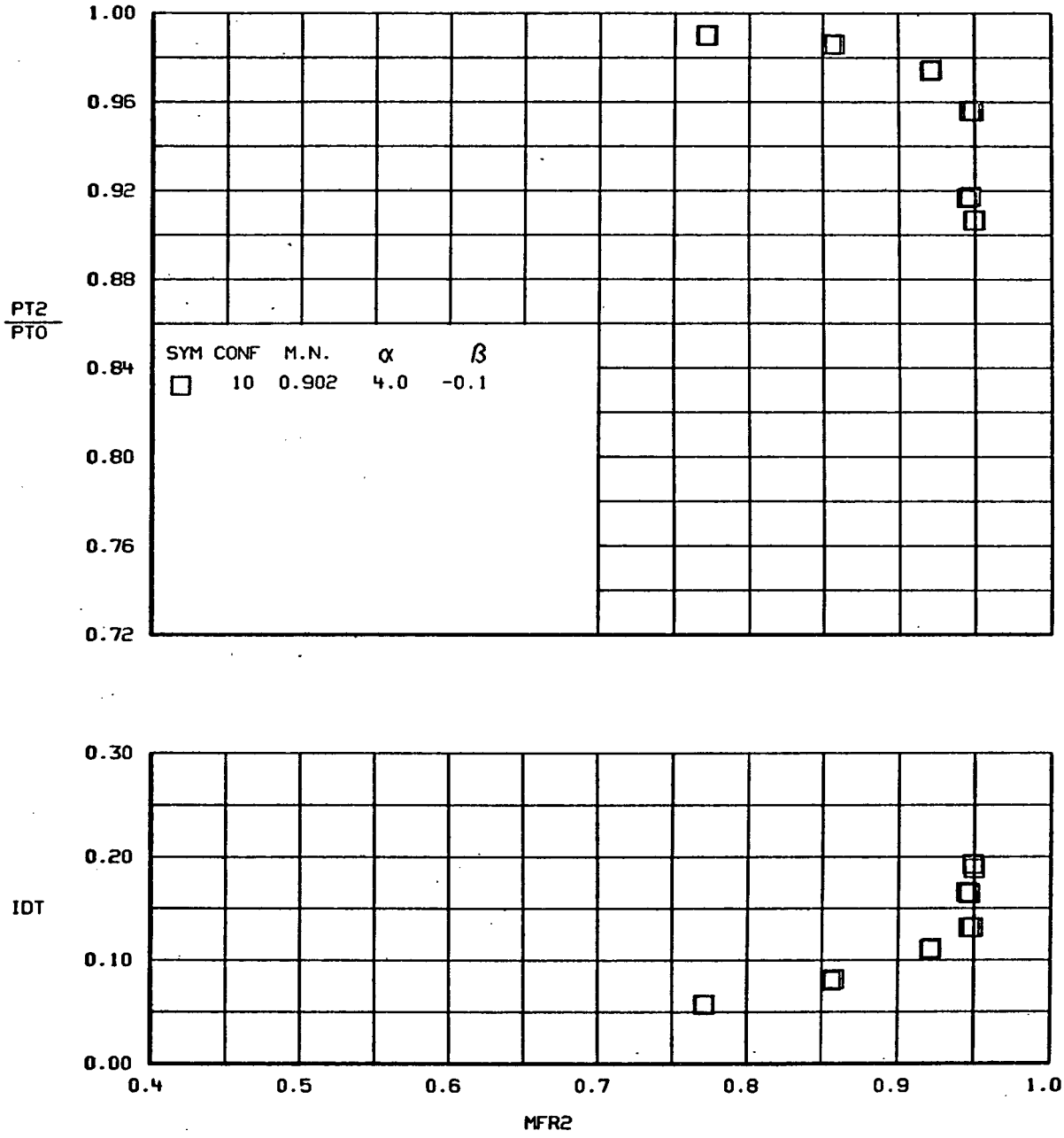

(b)

Figure 86-Continued.

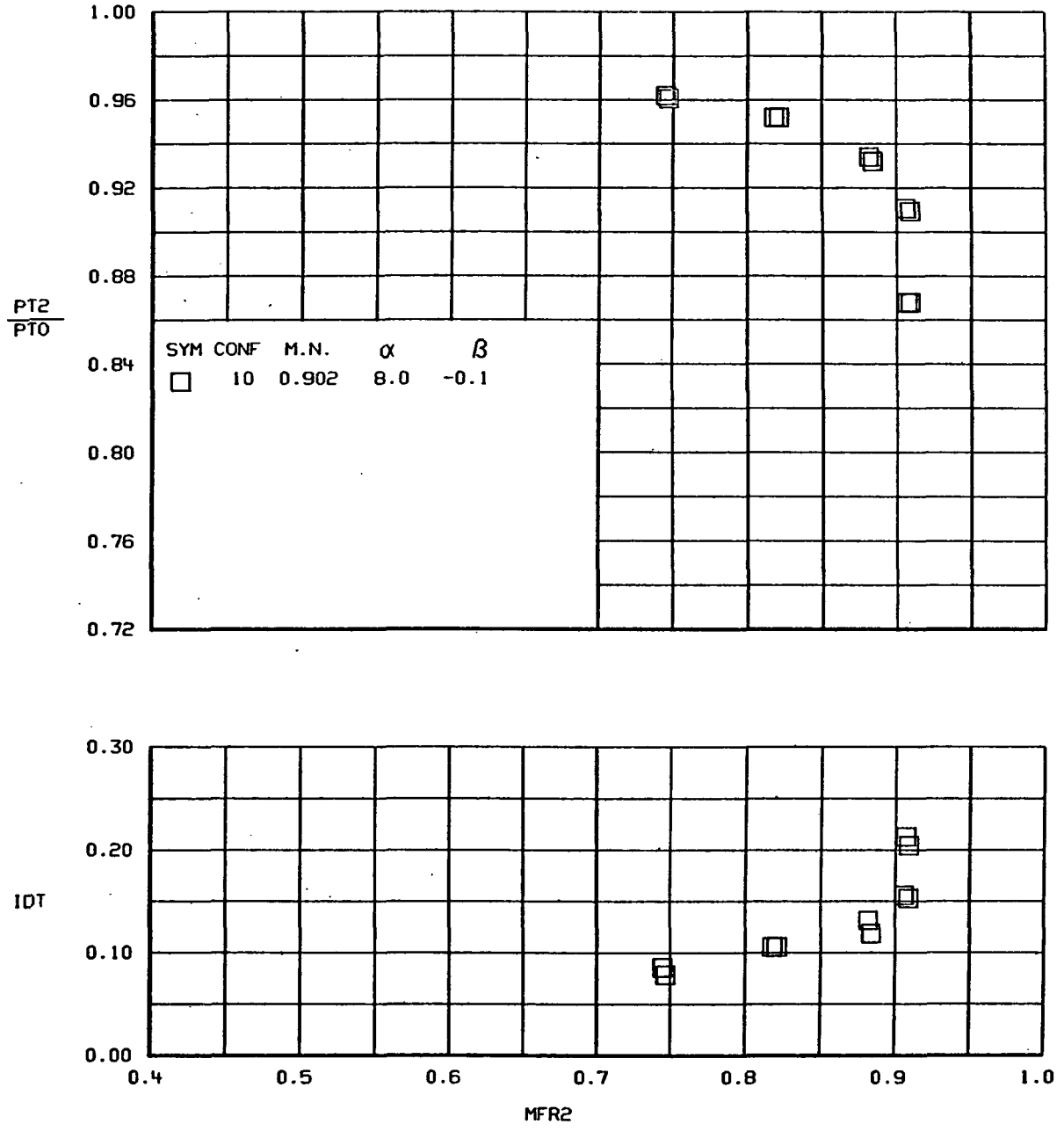

(c)

Figure 86-Continued.

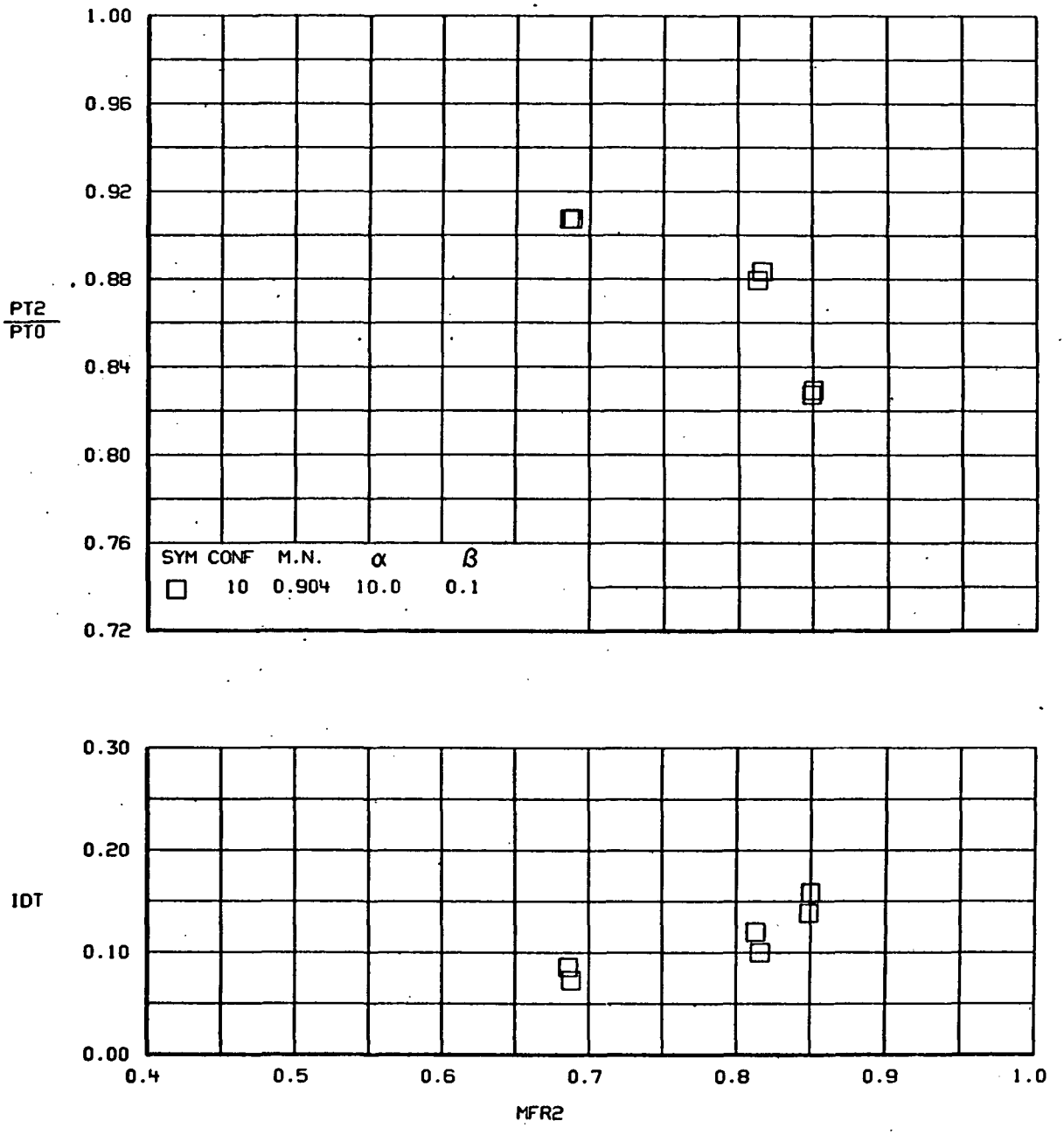

(d)

Figure 86-Continued.

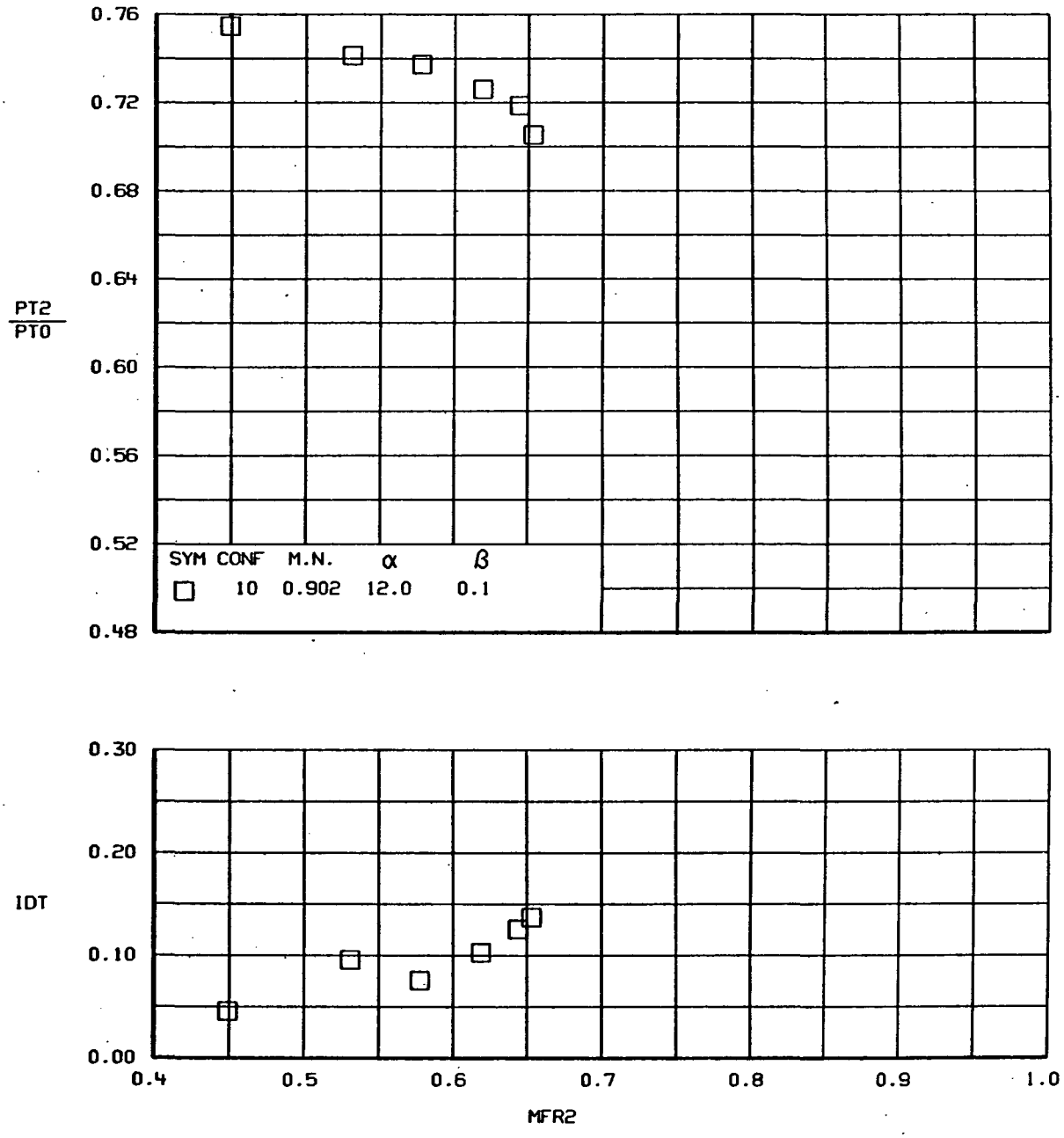

(e)

Figure 86.-Concluded.

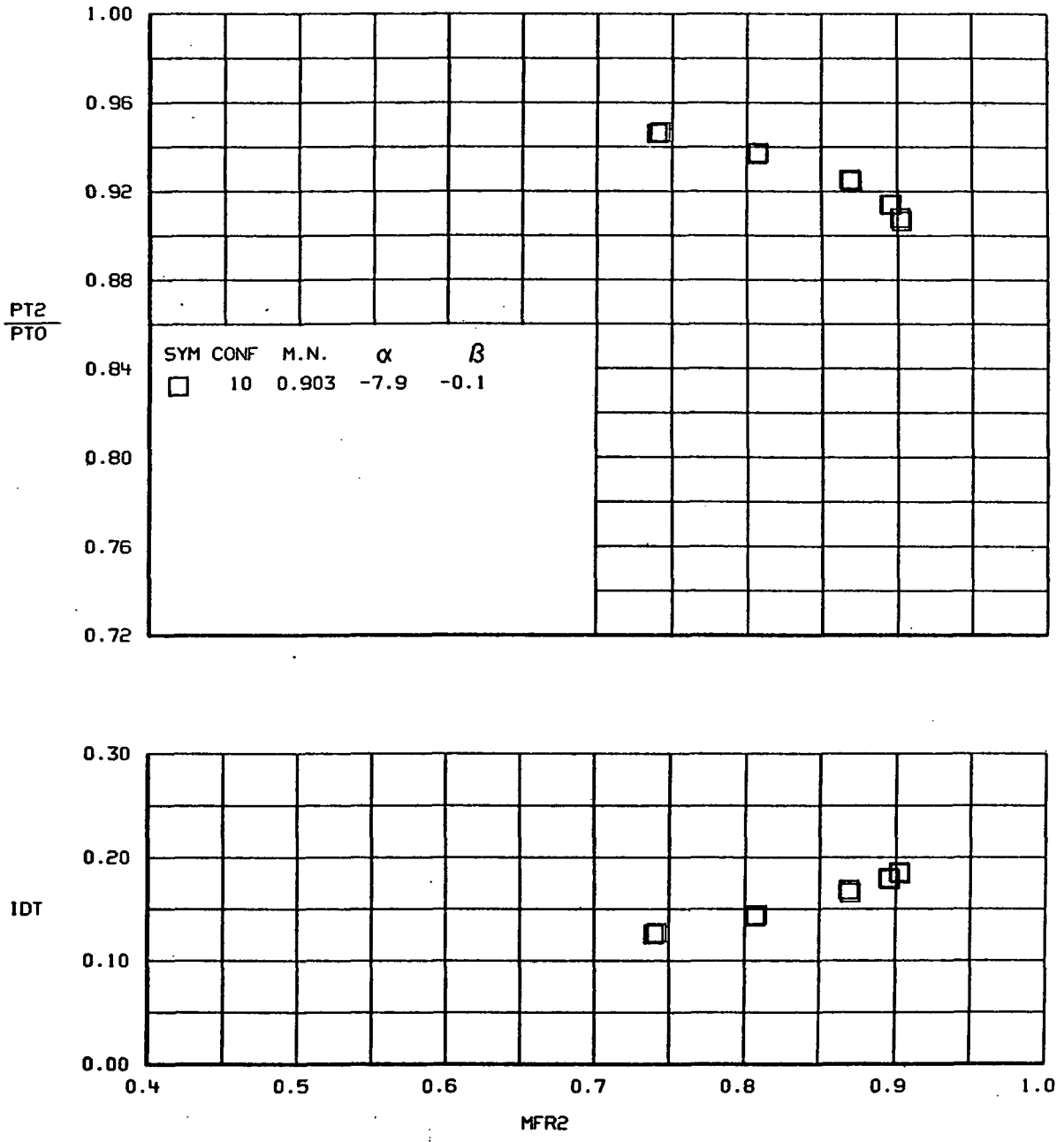

(a)

Figure 87.- TOTAL PRESSURE RECOVERY AND DISTORTION VERSUS MASS FLOW RATIO Configuration 10, $\delta=-10^{o}$.

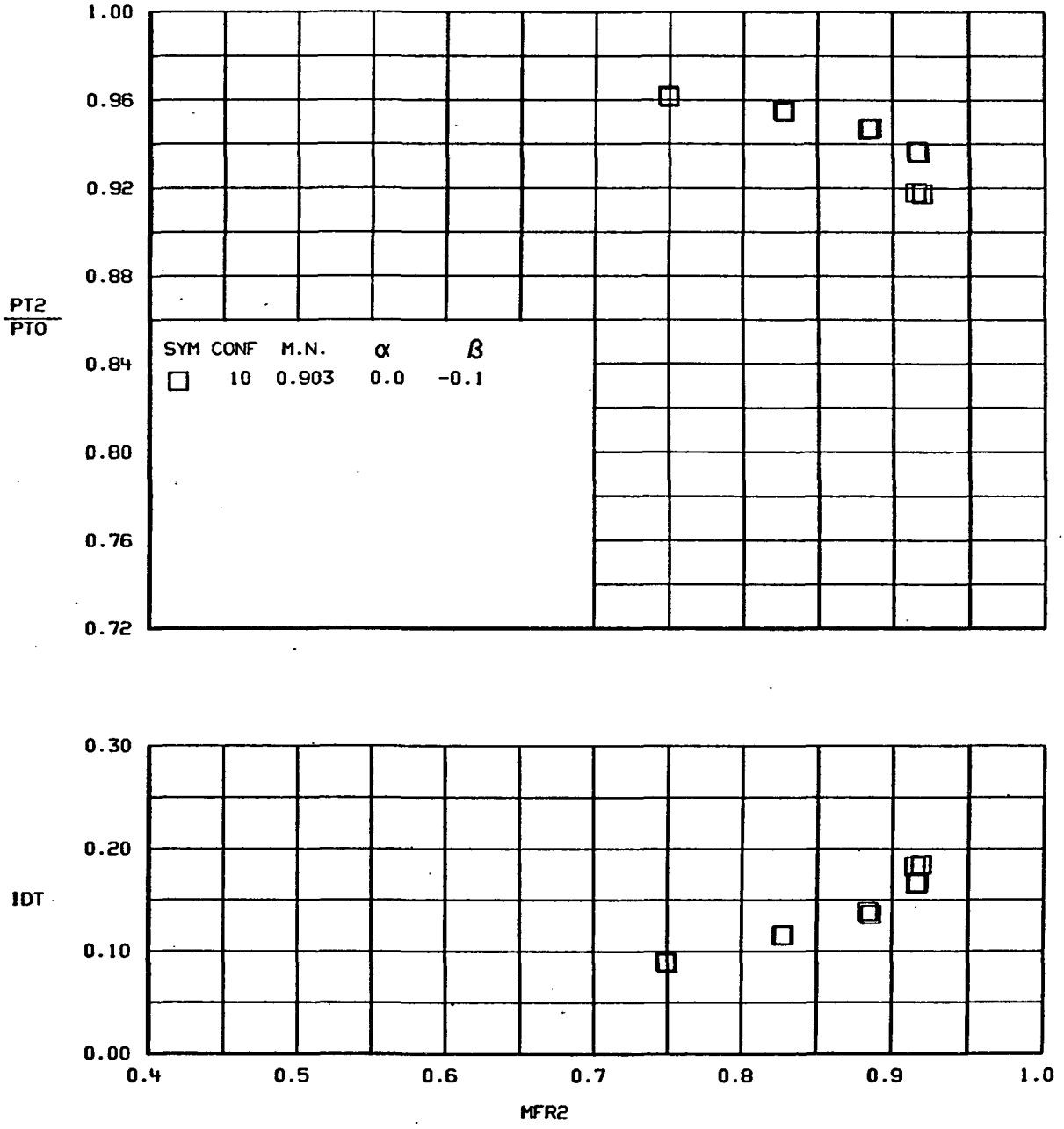

(b)

Figure 87.-Continued.

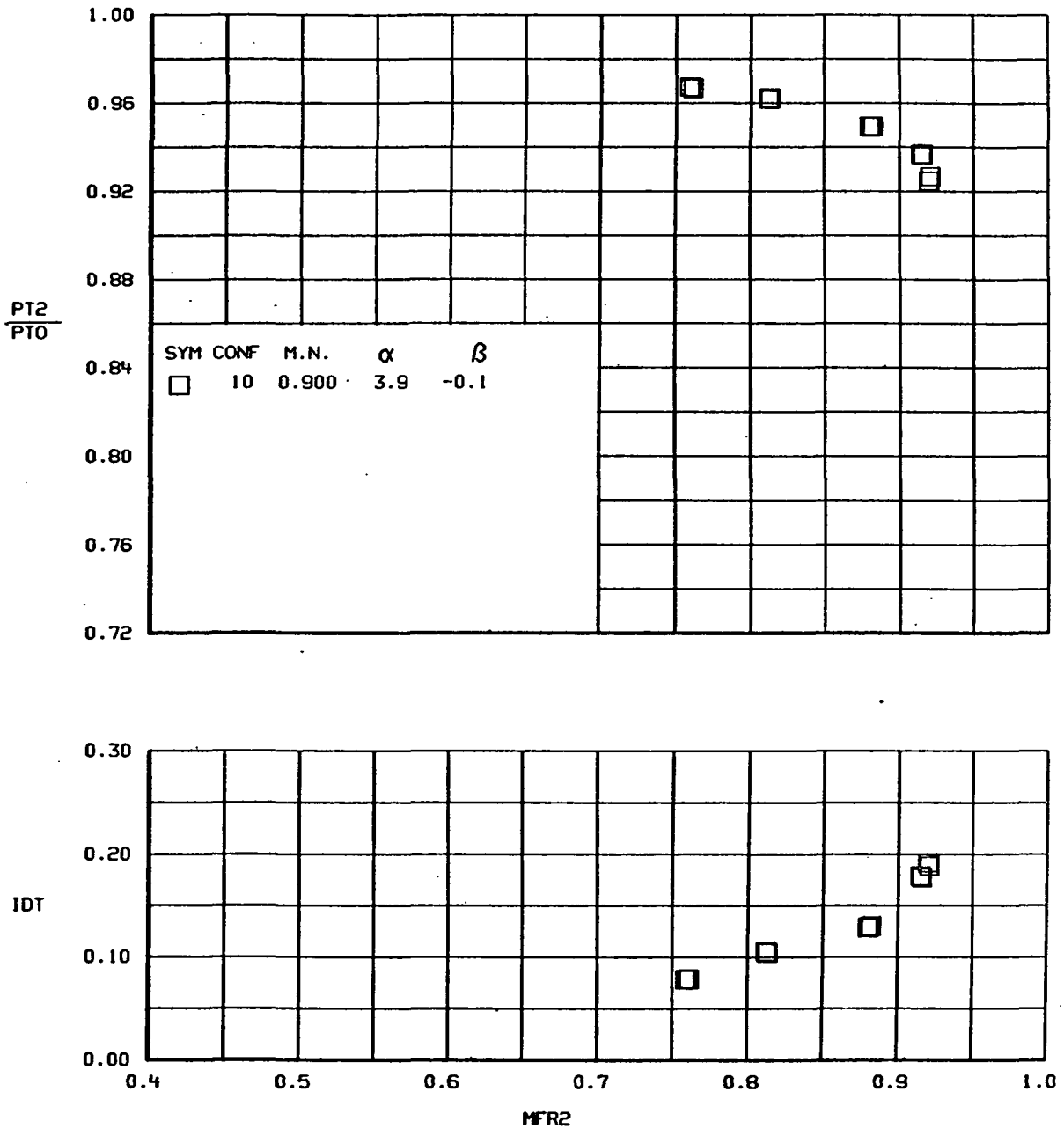

(c)

Figure 87.-Continued.

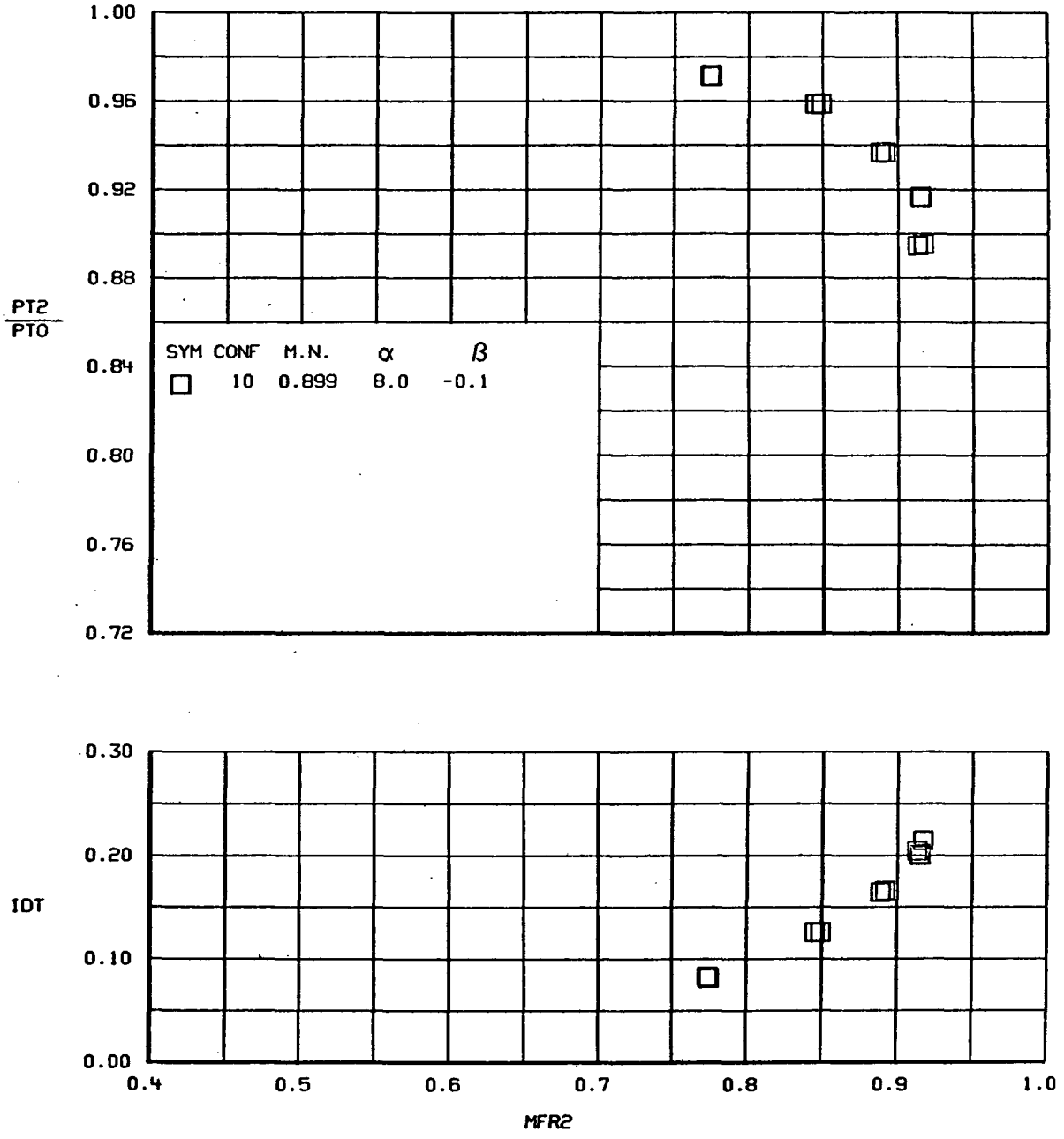

(d)

Figure 87.-Continued.

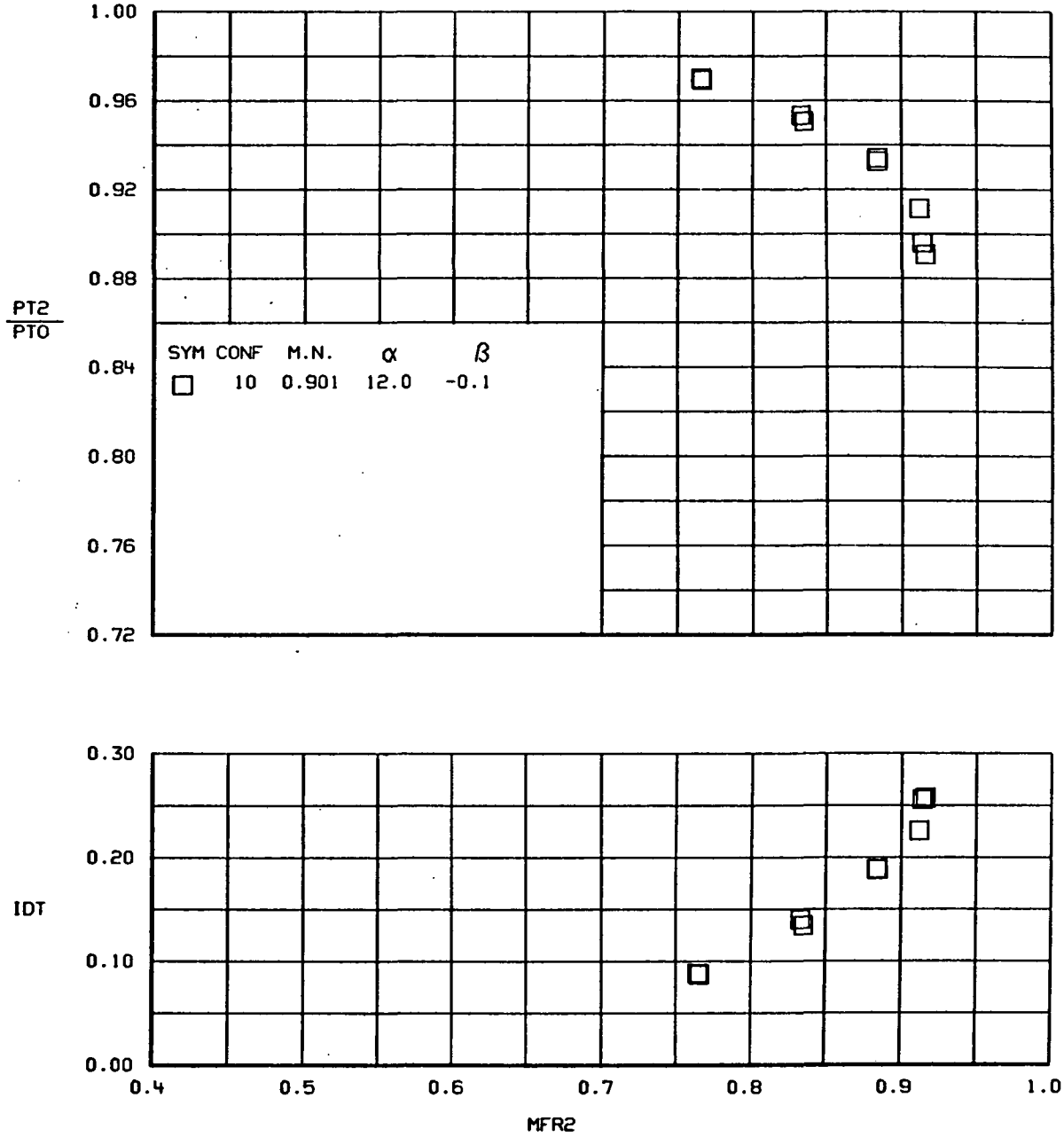

(e)

Figure 87.-Continued.

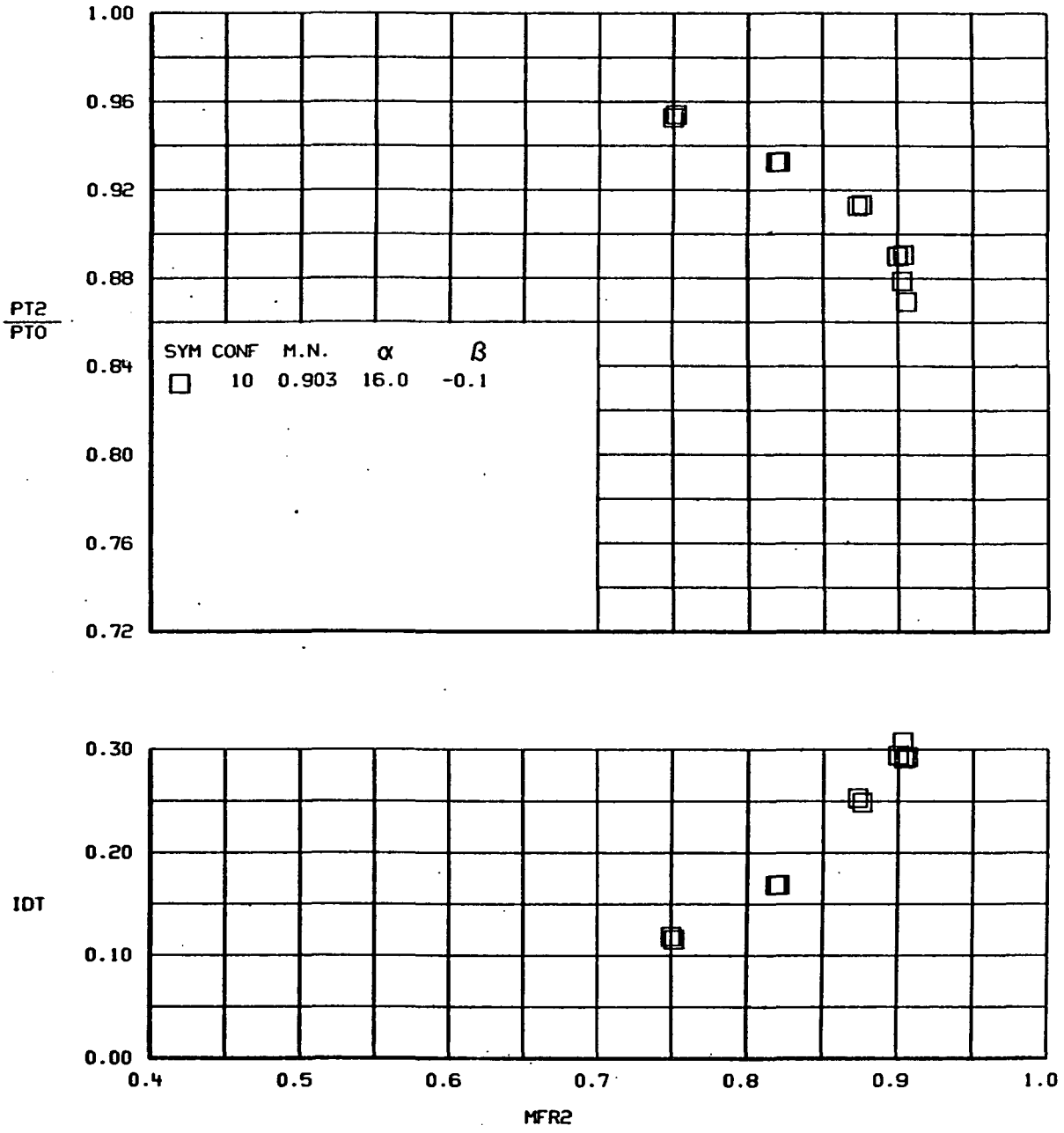

(f)

Figure 87.-Continued.

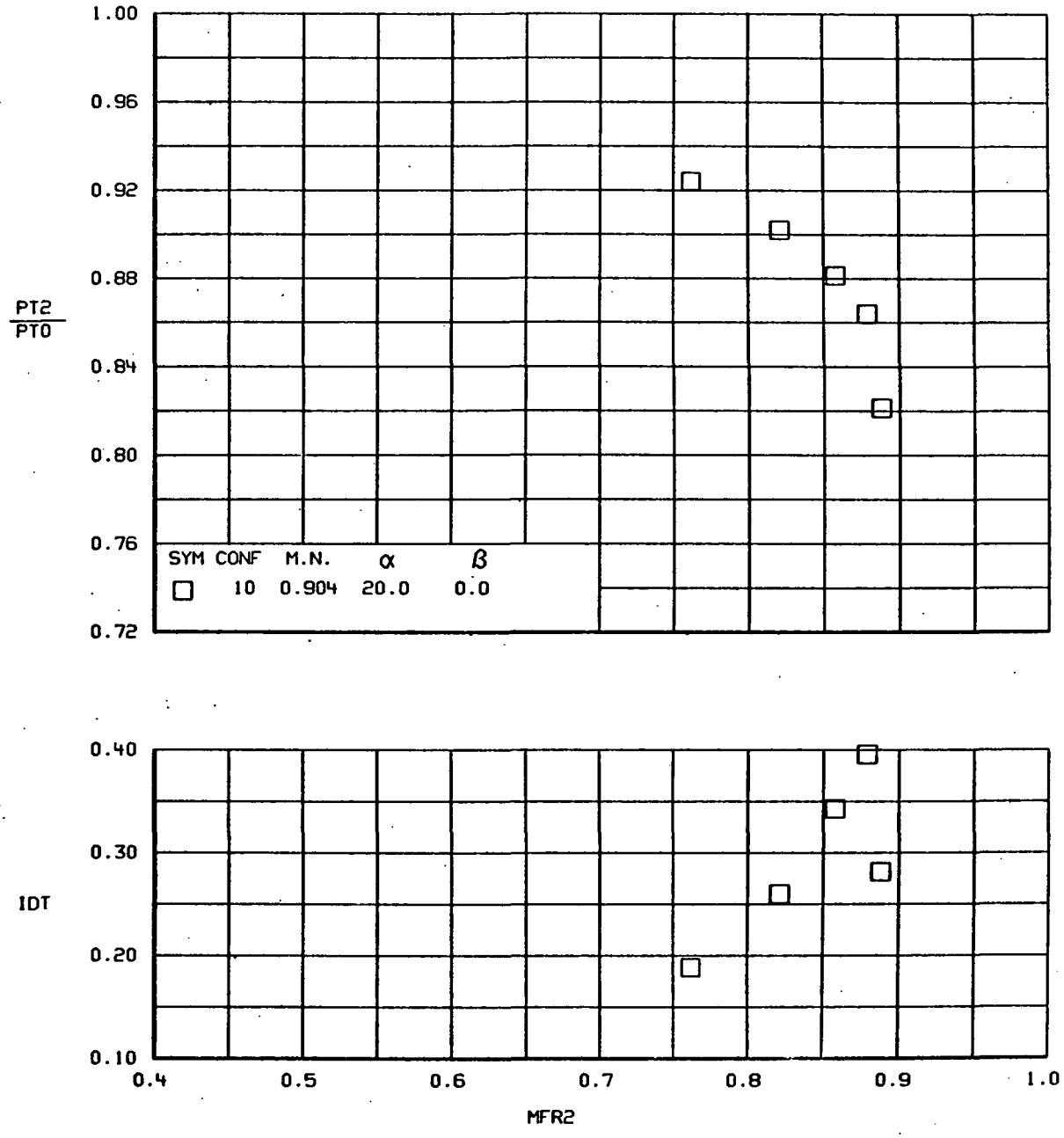

(g)

Figure 87.-Concluded.

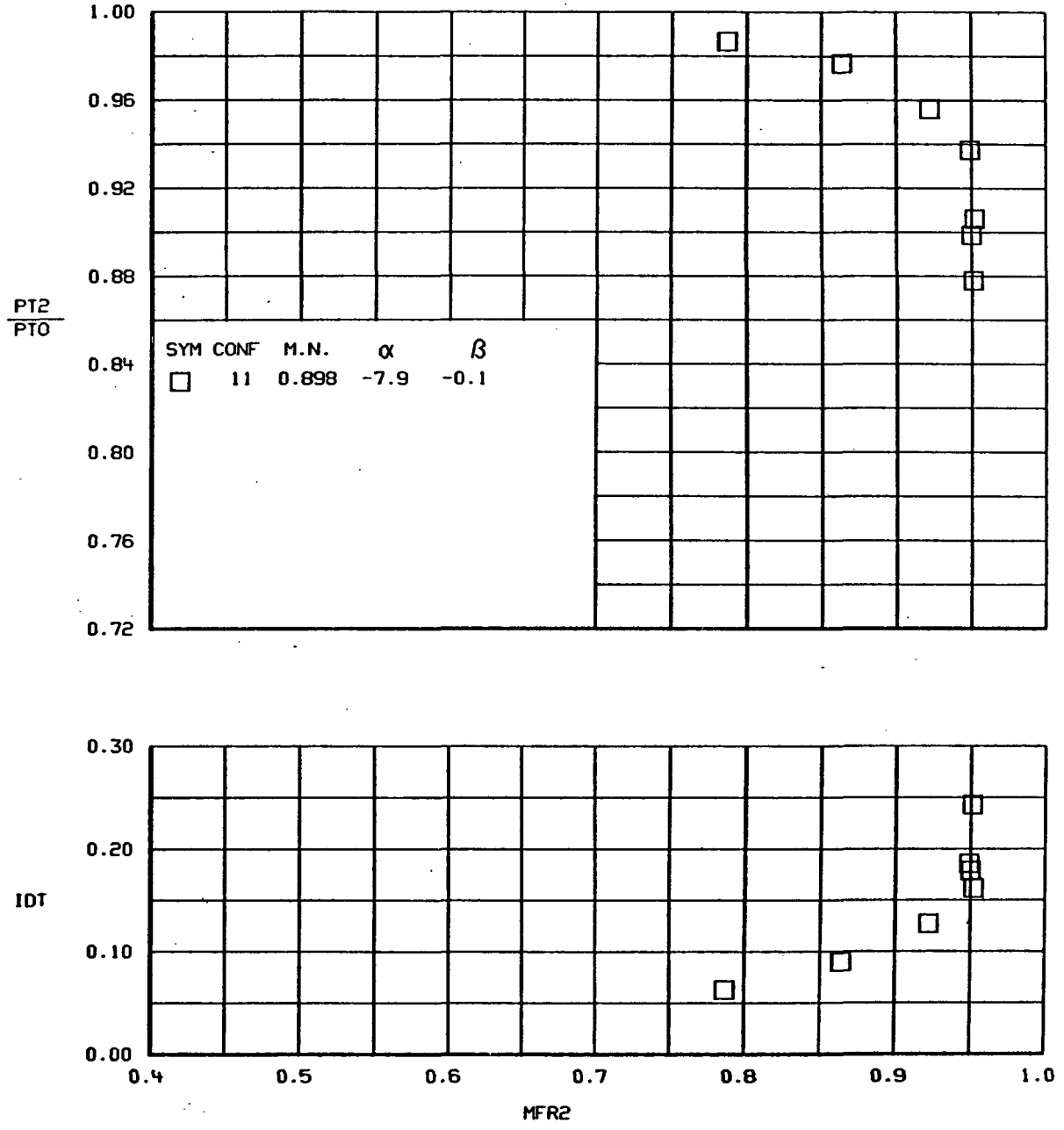

(a)

Figure 88.- TOTAL PRESSURE RECOVERY AND DISTORTION VERSUS MASS FLOW RATIO Configuration 11.

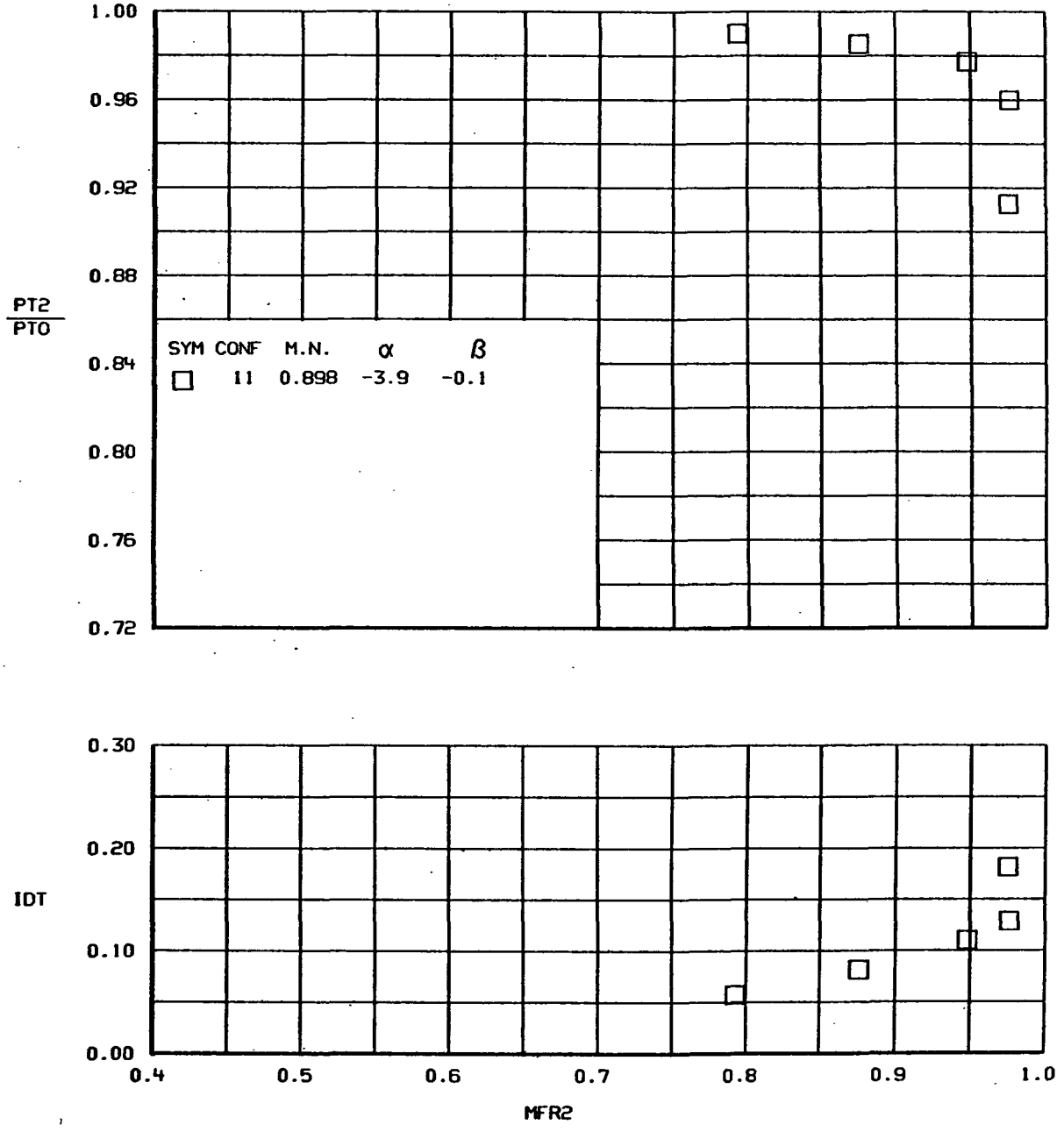

(b)

Figure 88.–Continued.

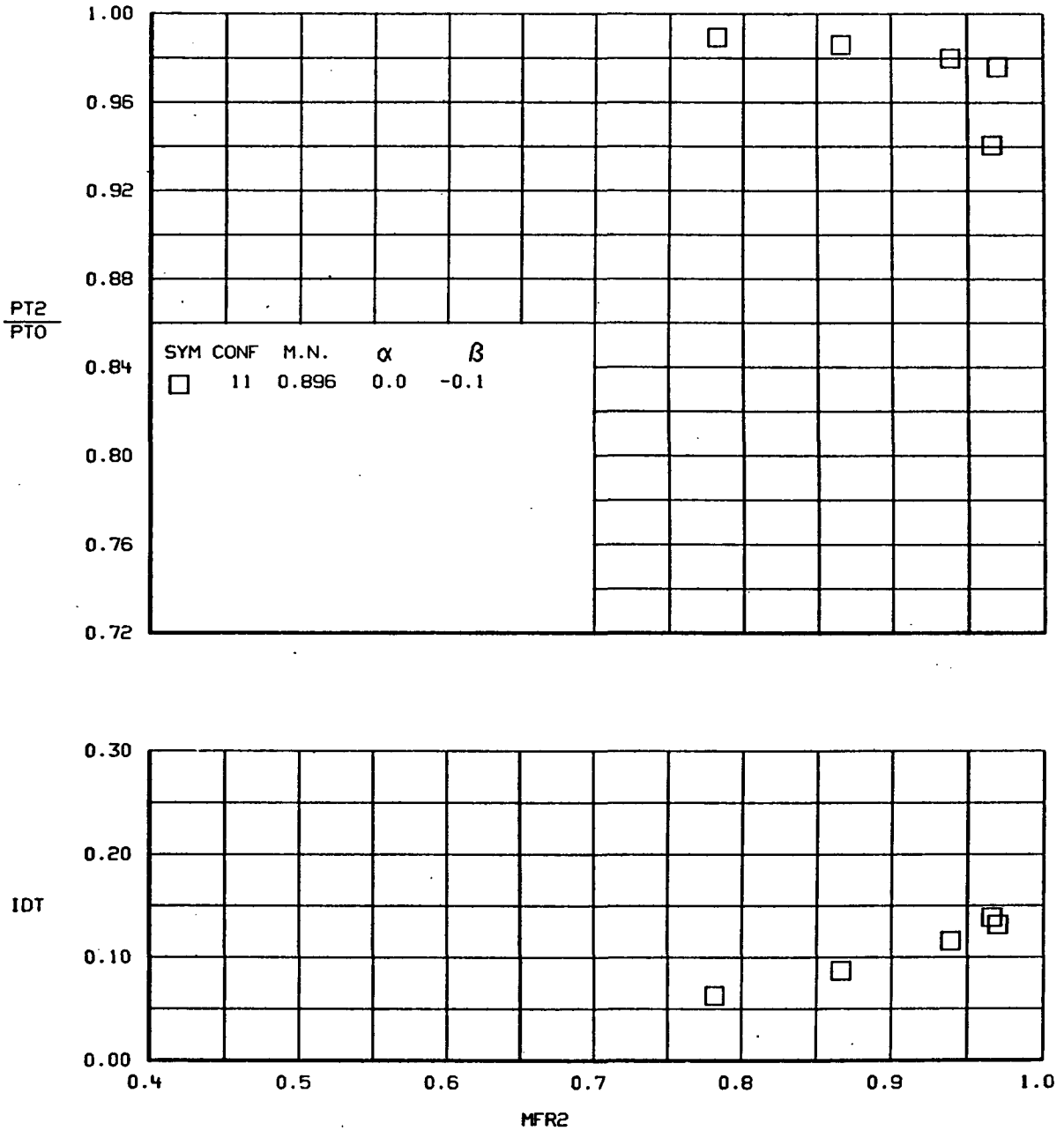

(c)

Figure 88.–Continued.

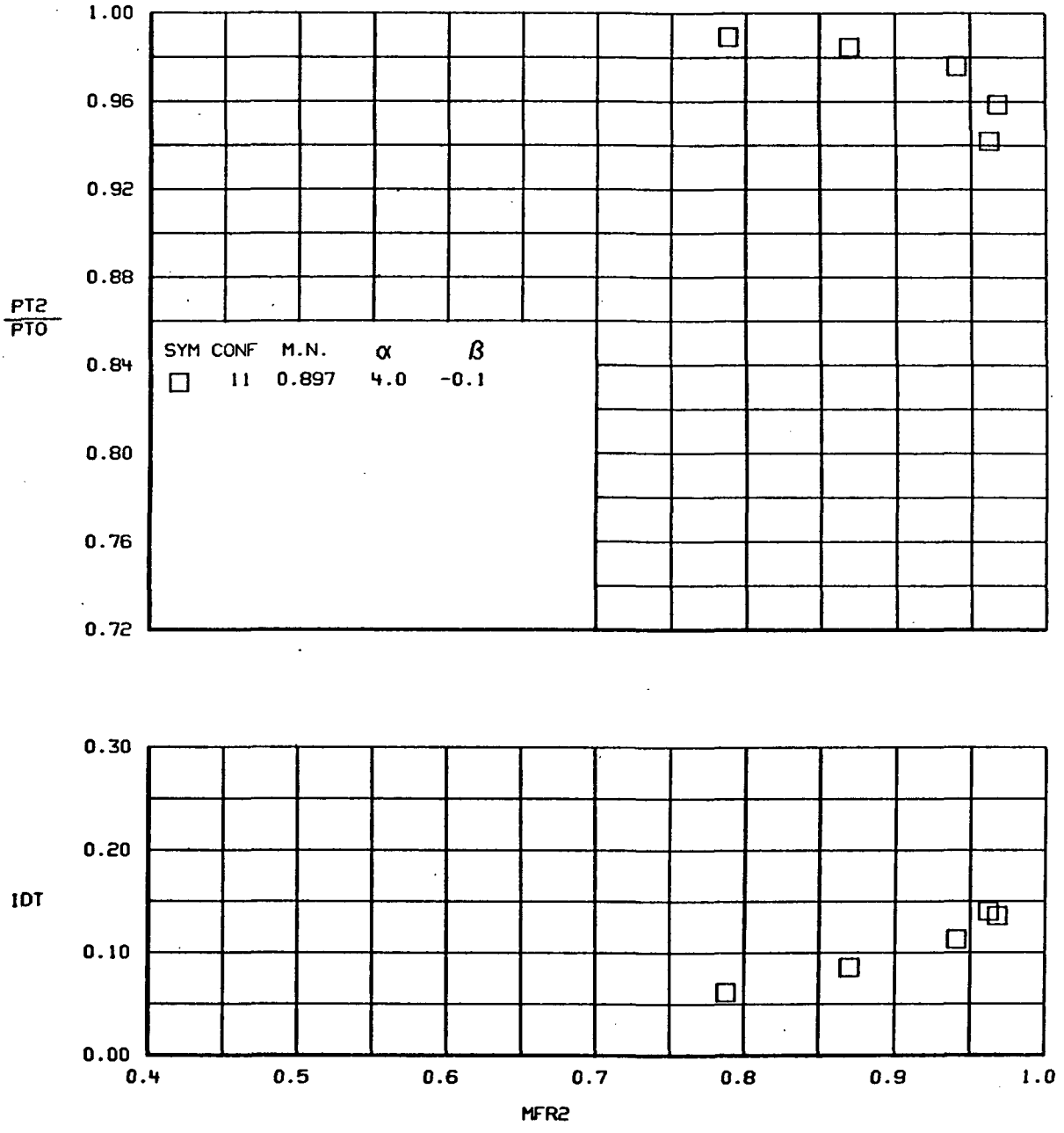

(d)

Figure 88.-Continued.

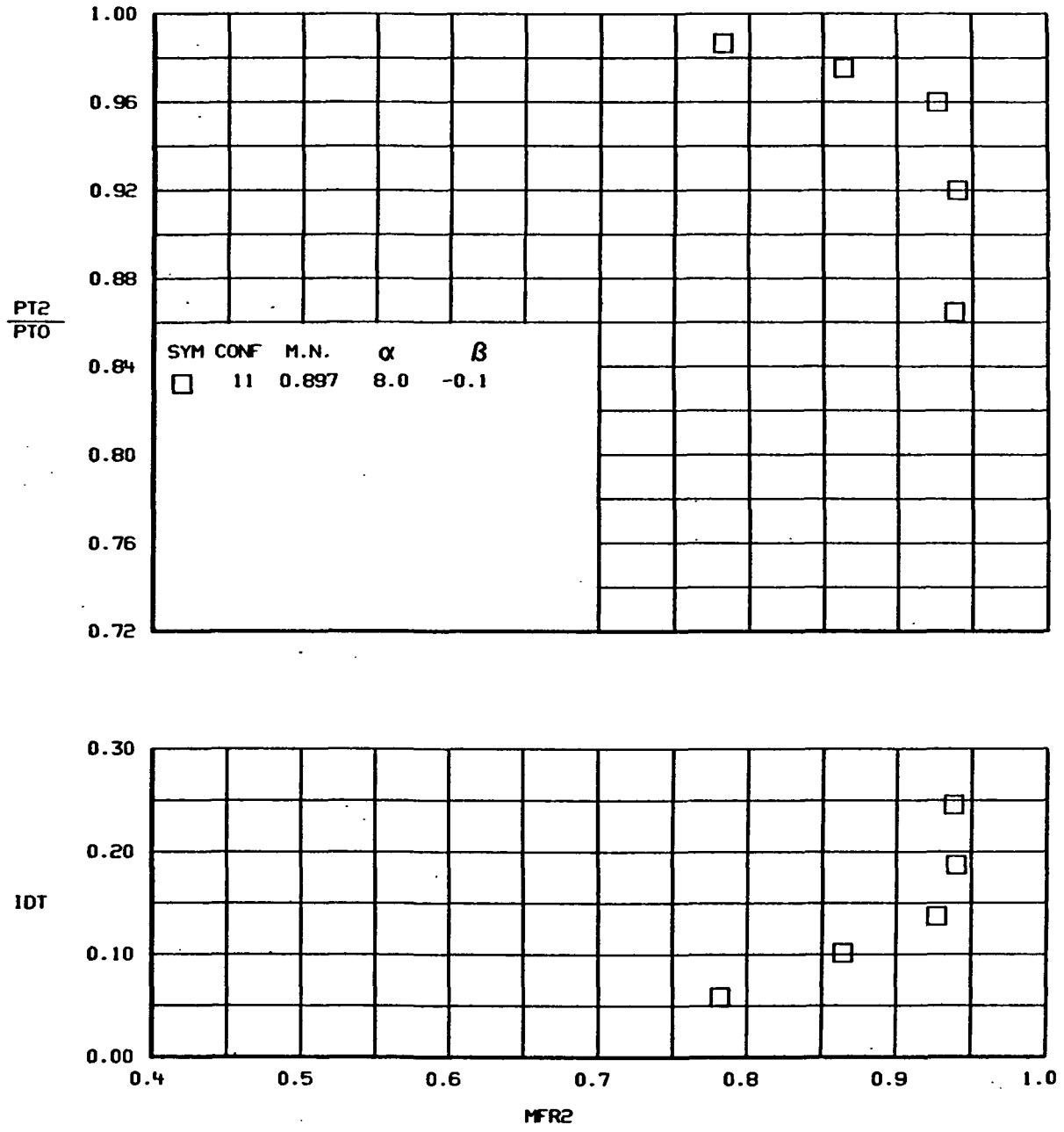

(e)

Figure 88.-Continued.

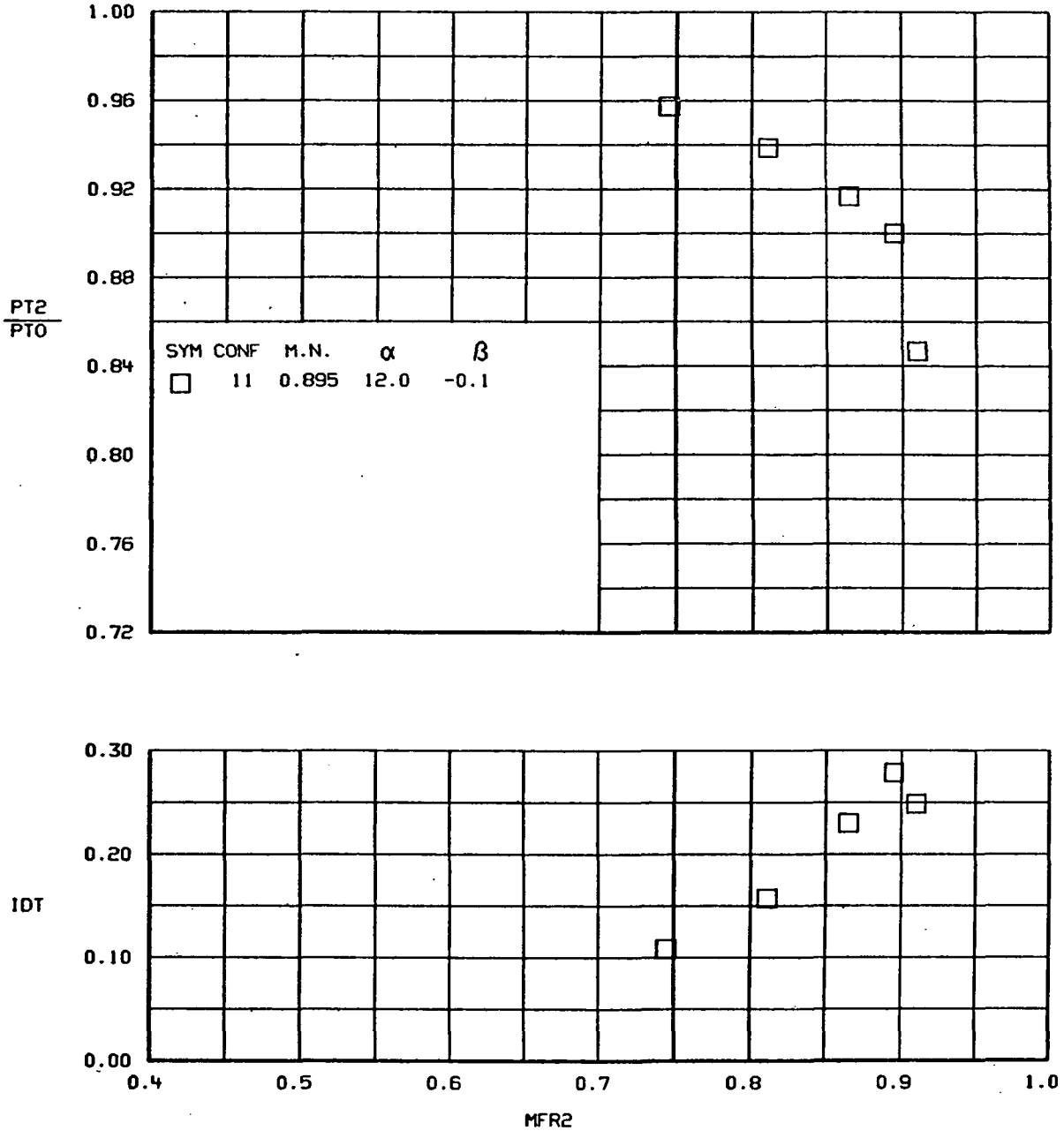

(f)

Figure 88.-Continued.

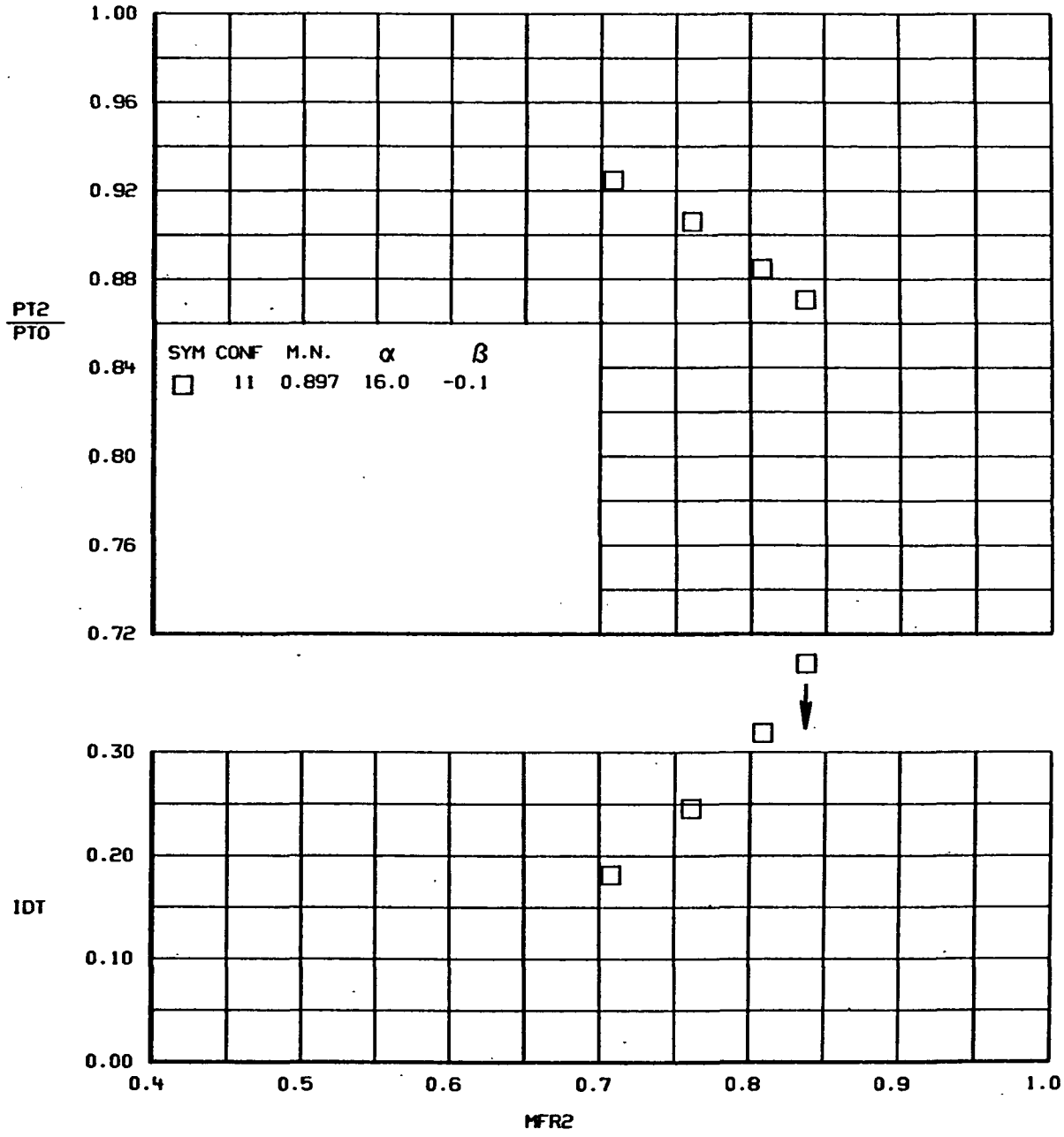

(g)

Figure 88.-Continued.

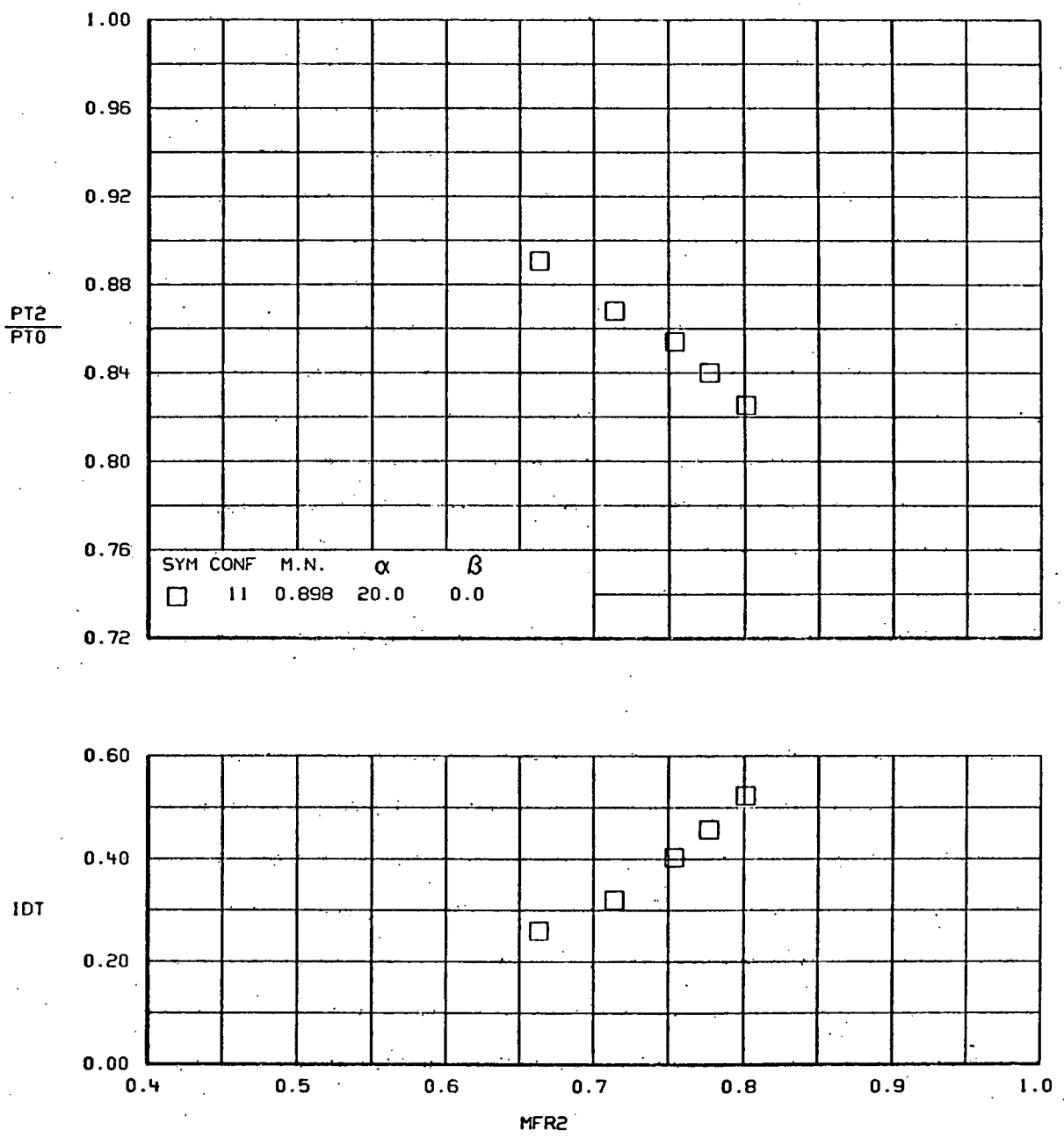

(H)
FIGURE 88.-CONCLUDED.